SPR-745 SEPTEMBER 2019

Developing Ultra High-Performance Concrete Mix Designs for Arizona Bridge Element Connections

Arizona Department of Transportation Research Center

ADOT

Developing Ultra High-Performance Concrete Mix Designs for Arizona Bridge Element Connections

SPR-745

September 2019

Published by:
Arizona Department of Transportation
206 South 17th Avenue
Phoenix, Arizona 85007
In cooperation with
U.S. Department of Transportation
Federal Highway Administration

This report was funded in part by the Federal Highway Administration, U.S. Department of Transportation. The contents of this report reflect the views of the authors, who are responsible for the facts and the accuracy of the data, and for the use or adaptation of previously published material, presented herein. The contents do not necessarily reflect the official views or policies of the Arizona Department of Transportation or the Federal Highway Administration, U.S. Department of Transportation. This report does not constitute a standard, specification, or regulation. Trade or manufacturers' names that may appear herein are cited only because they are considered essential to the objectives of the report. The U.S. government and the State of Arizona do not endorse products or manufacturers.

This report is subject to the provisions of 23 USC § 409. Any intentional or inadvertent release of this material, or any data derived from its use, does not constitute a waiver of privilege pursuant to 23 USC § 409, which reads as follows:

23 USC § 409 — Discovery and admission as evidence of certain reports and surveys

Notwithstanding any other provision of law, reports, surveys, schedules, lists, or data compiled or collected for the purpose of identifying, evaluating, or planning the safety enhancement of potential accident sites, hazardous roadway conditions, or railway-highway crossings, pursuant to sections 130, 144, and 148 of this title or for the purpose of developing any highway safety construction improvement project which may be implemented utilizing Federal-aid highway funds shall not be subject to discovery or admitted into evidence in a Federal or State court proceeding or considered for other purposes in any action for damages arising from any occurrence at a location mentioned or addressed in such reports, surveys, schedules, lists, or data.

Technical Report Documentation Page

1. Report No. FHWA-AZ-19-745	2. Government Accession No.	3. Recipient's Catalog No.
4. Title and Subtitle Developing Ultra-High–Performance Concrete Mix Designs for Arizona Bridge Element Connections		5. Report Date September 2019 6. Performing Organization Code
7. Author Barzin Mobasher, Aashay Arora, Matthew Aguayo, Farrokh Kianmofrad, Yiming Yao, and Narayanan Neithalath		8. Performing Organization Report No.
9. Performing Organization Name and Address Arizona State University School of Sustainable Engineering and the Built Environment Tempe, AZ 85281		10. Work Unit No. 11. Contract or Grant No. SPR-000 1(185) 745
12. Sponsoring Agency Name and Address Arizona Department of Transportation 206 S. 17th Ave. Phoenix, AZ 85007:		13.Type of Report & Period Covered FINAL 14. Sponsoring Agency Code
15. Supplementary Notes Prepared in cooperation with the U.S. Department of Transportation, Federal Highway Administration		

16. Abstract

This report addresses the development of non-proprietary mix designs for manufacturing ultra-high–performance concrete (UHPC) mixtures using materials commercially available in Arizona. The comprehensive work carried out addresses the development of paste, mortar, and concrete mixtures based on theoretical, analytical, and experimental optimization of particle packing at multiple scales, cement chemistry of the interacting phases, the rheology of mixture flow characteristics, and the mechanical properties of final mixture formulations. Several mix designs using all Arizona materials were developed and tested during the study. When tested, they exhibited characteristics that provided more than acceptable performance. Analysis showed these designs to be at a lower cost than UHPC incorporating proprietary materials.

17. Key Words Ultra-high performance concrete, ultra-high performance fiber reinforced concrete, non-proprietary UHPC, compressible packing model, microstructure modeling, rheology, durability, mechanical testing, multiple cracking,		18. Distribution Statement Document is available to the U.S. public through the National Technical Information Service, Springfield, Virginia 22161		23. Registrant's Seal
19. Security Classification	20. Security Classification	21. No. of Pages 347	22. Price	

SI (MODERN METRIC) CONVERSION FACTORS*

APPROXIMATE CONVERSIONS TO SI UNITS

Symbol	When You Know	Multiply By	To Find	Symbol
	LENGTH			
ft	inches	25.4	millimeters	m
yd	feet	0.305	meters	m
mi	yards	0.914	meters	km
	miles	1.61	kilometers	
	AREA			
in^2	square inches	645.2	square millimeters	mm^2
ft^2	square feet	0.093	square meters	m^2
yd^2	square yards	0.836	square meters	m^2
ac	acres	0.405	hectares	ha
mi^2	square miles	2.59	square kilometers	km^2
	VOLUME			
fl oz	fluid ounces	29.57	milliliters	mL
gal	gallons	3.785	liters	L
ft^3	cubic feet	0.028	cubic meters	m^3
yd^3	cubic yards	0.765	cubic meters	m^3
	NOTE: Volumes greater than 1000L shall be shown in m^3.			
	MASS			
oz	ounces	28.35	grams	g
lb	pounds	0.454	kilograms	kg
T	short tons (2000lb)	0.907	megagrams (or "metric ton")	mg (or "t")
	TEMPERATURE (exact)			
°F	Fahrenheit temperature	5(F-32)/9 or (F-32)/1.8	Celsius temperature	°C
	ILLUMINATION			
fc	foot-candles	10.76	lux	lx
fl	foot-Lamberts	3.426	candela/m^2	cd/m^2
	FORCE AND PRESSURE OR STRESS			
lbf				N
lbf/in^2				kPa

APPROXIMATE CONVERSIONS FROM SI UNITS

Symbol	When You Know	Multiply By	To Find	Symbol
	LENGTH			
mm	millimeters	0.039	inches	ft
m	meters	3.28	feet	yd
m	meters	1.09	yards	mi
km	kilometers	0.621	miles	
	AREA			
mm^2	square millimeters	0.0016	square inches	in^2
m^2	square meters	10.764	square feet	ft^2
m^2	square meters	1.195	square yards	yd^2
ha	hectares	2.47	acres	ac
km^2	square kilometers	0.386	square miles	mi^2
	VOLUME			
mL	milliliters	0.034	fluid ounces	fl oz
L	liters	0.264	gallons	gal
m^3	cubic meters	35.315	cubic feet	ft^3
m^3	cubic meters	1.308	cubic yards	yd^3
	MASS			
g	grams	0.035	ounces	oz
kg	kilograms	2.205	pounds	lb
mg (or "t")	megagrams (or "metric ton")	1.102	short tons (2000lb)	T
	TEMPERATURE (exact)			
°C	Celsius temperature	1.8C + 32	Fahrenheit temperature	°F
	ILLUMINATION			
lx	lux	0.0929	foot-candles	fc
cd/m^2	candela/m^2	0.2919	foot-Lamberts	fl
	FORCE AND PRESSURE OR STRESS			
N				lbf
kPa				lbf/in^2

CONTENTS

LIST OF FIGURES

LIST OF TABLES

List of Abbreviations and Acronyms

ADOT	Arizona Department of Transportation
ABC	Accelerated Bridge Construction
ACI	American Concrete Institute
APF	Atomic Packing Factor
ASR	Alkali Silica Reaction
ASTM	American Society for Testing and Materials
BCC	Body-Centered Cubic
CH	Calcium Hydroxide
CN	Coordination Number
C-S-H	Calcium Silicate Hydrate
CMOD	Crack Mouth Opening Displacement
$CTOD_C$	Critical Crack Tip Opening Displacement
F	Fly ash
FCC	Face-Centered Cubic
FRC	Fiber Reinforced Concrete
FHWA	Federal Highway Administration
HRWR	High-Range Water Reducer
HP	High-Performance
HPC	High-Performance Concrete
K	Metakaolin
M	Micro-silica
MCD	Mean Centroidal Distance
ND	Number Density
NS	Nano-silica
NSC	Normal Strength Concrete
OPC	Ordinary Portland Cement
PBES	Prefabricated Bridge Elements and Systems
REV	Representative Element Volume
RH	Relative humidity
S	Slag
SEM	Scanning Electron Microscopy
TPFM	Two-parameter fracture model
UHP	Ultra-high Performance
UHPC	Ultra-high Performance Concrete
UHPFRC	Ultra-high Performance Fiber Reinforced Concrete
w/b	Water-to-binder ratio
XRD	X-ray Diffraction

Nomenclature

Chapter 2

Symbol	Definition
γ_i	Virtual packing density of the mixture, achieved by placing each grain one by one in an appropriate position in a representative volume, when grains of size "i" are dominant
β_i	Virtual packing density of a mixture when only grains of class "i" are present
v_j	Volume fraction of grains of class "j"
n	Number of grain classes in packing density equation
τ	Shear stress
τ_y	Yield stress
η_p	Plastic viscosity
$\dot{\gamma}$	Shear rate
K	Consistency index - (a measure of the average viscosity of the fluid)
n	Flow behavior index in Herschel-Bulkley equation, ranges between 0 and 1 for shear thinning suspensions
n_∞	Viscosity at an infinite shear rate

Chapter 5

Symbol	Definition
MCD	Mean centroidal distance - average distance to the center of a given particle from the centroid of the microstructure
MCD_i	Mean centroidal distance of ith mixture
CN	Coordination Number - average number of nearest neighbor pairs in the microstructure
CN_i	Coordination number of ith mixture

N_d	Number density - number of particles in a unit volume
N_{d-i}	Number density of ith mixture
τ_y	Yield strength measured by rheometer
τ_{y-i}	Yield strength of ith mixture
μ_p	Plastic viscosity measured by rheometer
μ_{p-i}	Plastic viscosity of ith mixture
A_{ms}	Area of mini-slump measured as the spread from mini-slump test
A_{ms-i}	Area of mini-slump of ith mixture
γ	Packing Coefficient – measure of packing density of a microstructure
γ_i	Packing coefficient of the ith mixture
$\gamma_{UHP-Control}$	Packing coefficient of the control mixture containing ultra-high performance mixture composition (water-to-cement ratio is 0.2)
κ	Flow coefficient – measure of workability of a mixture
κ_i	Flow coefficient of the ith mixture
$\kappa_{UHP-Control}$	Flow coefficient of the control mixture containing ultra-high performance mixture composition (water-to-cement ratio is 0.2)

Chapter 6

Symbol	Definition
y_1	Volume fraction of aggregate size 1
y_2	Volume fraction of aggregate size 2
d_1	Diameter of aggregate size 1
d_2	Diameter of aggregate size 2
ϕ_1	Volume fractions of aggregate size 1
ϕ_2	Volume fractions of aggregate size 2

γ	Packing density of the mixture
β_1	Random packing density of mixture containing only aggregate size 1
β_2	Random packing density of mixture containing only aggregate size 2
a_{ij}	Loosening effect coefficient for aggregate size "i" due to the influence of aggregate size "j"
b_{ij}	Wall effect coefficient for aggregate size "i" due to the influence of aggregate size "j"
d_i	average diameter for aggregate size "i"
d_j	average diameter for aggregate size "j"
γ_i	Virtual packing density of the mixture, achieved by placing each grain one by one in an appropriate position in a representative volume, when grains of size "i" are dominant
β_i	Residual packing density of aggregate size "i," determined using dry-rodded unit weight testing
y_i	Individual volume fraction of the aggregate size "i" in the mixture
a_{ij}	Loosening effect coefficient for aggregate class "i" due to the influence of aggregate class "j"
b_{ij}	Wall effect coefficient for aggregate class "i" due to the influence of aggregate class "j"
ρ_{bulk}	Bulk density of aggregate
$M_{aggregate}$	Measured DRUW of aggregate
$V_{container}$	Volume of the cylindrical measure
$\phi_{aggregate}$	Packing density of the aggregate
K	Compaction index – measure of degree of compaction of aggregate mixture (typically ranges between 0 and 9, where 0 represents loose uncompacted aggregate, 9 represents packing of aggregates using vibration and compaction)
ϕ	Calculated packing density of the aggregate mixture
W_i	Weight fraction of aggregate size "i"

W_j	Weight fraction of aggregate size "j"
ρ_i	Specific gravity of aggregate size "i"
ρ_j	Specific gravity of aggregate size "j"
V_p	Perturbed volume by one single fiber present in an aggregate mixture
d_F	Diameter of fiber
l_F	Length of fiber
d	Mean size of the aggregates in a mixture containing fibers
k_F	Coefficient that depends on the size of the fibers (taken as 0.065 for all simulations)
$\acute{\Phi}$	Packing density of aggregate mixture containing fibers
α_F	Volume fraction of fibers in the mixture
N_F	Number of fibers present per unit volume of the mixture

Chapter 7

Symbol	Definition
σ_n	Nominal elastically equivalent flexural stress calculated for a specimen under flexural loading
P	Load acting on the specimen
L	Length of the specimen (span)
b	Width of specimen
d	Depth of specimen
k	Stiffness calculated from a cyclic load-deflection test
P_A	Load at point A for a cyclic load-deflection test
P_B	Load at point B for a cyclic load-deflection test
D_A	Displacement at point A for a cyclic load-deflection test

D_B	Displacement at point B for a cyclic load-deflection test

Chapter 8

Symbol	Definition
σ_{cr}	Tensile strength of concrete
ϵ_{cr}	Cracking tensile strain at first crack
E or E_c	Elastic modulus of concrete
σ_p	Post-peak tensile strength
μ	Residual strength parameter of concrete (ranges between 0 and 1), also called normalized post-peak tensile strength (ratio of the post-peak tensile strength to the cracking tensile strength)
ω	Ratio of compressive to tensile strength
γ	Ratio of compressive to tensile elastic modulus
ϵ_{cy}	Yield strain
ϵ_{cu}	Ultimate compressive strain
λ_{cu}	Non-dimensional constant factor to calculate ultimate compressive strain
α	Normalized tensile strain at peak strength
ϵ_{peak}	Peak tensile strain
η	Normalized post-crack modulus
β	Normalized tensile strain at bottom fiber
λ	Normalized compressive strain at top fiber
b	Width of beam cross-section
c	Depth of neutral axis
T_f	Tensile force carried by concrete
f'_c	Compressive strength of concrete

M_n	Ultimate moment capacity of a section
β_1	Factor that depends on the compressive strength of concrete used
β_2	Factor used in limit state design of concrete (=0.85)
M_{cr}	Cracking moment
κ	Normalized yield strain of steel
ϵ_{sy}	Strain in steel at yielding
E_s	Elastic modulus of steel
n	Normalized elastic modulus of steel
ρ_g	Reinforcement ratio
α	Normalized reinforcement depth
T_s	Tensile force carried by steel
ρ_b	Balanced reinforcement ratio
F_{c1}	Force in compression zone 1
F_{t1}	Force in tension zone 1
F_{t2}	Force in tension zone 2
y_{c1}	Centroid of section in compression zone 1
y_{t1}	Centroid in tension zone 1
y_{t2}	Centroid in tension zone 2
μ_{crit}	Critical value of residual tensile strength
ϕ_p	Reduction factor for post-crack tensile strength (typically between 0.75 and 0.90)
f_{150}^D	Residual strength of fiber reinforced concrete in flexure
ϕ_r	Reduction factor for moment capacity of member

Chapter 9

Symbol	Definition
D_{nssm}	Migration coefficient obtained from NSSM (non-steady state migration) test– measure of rate of chloride ion penetration in concrete
R	Molar gas constant (8.314 J/(K·mol))
z	Absolute value of ion valence, (1, for chloride ions)
F	Faraday's constant (9.648 ×10^4 J/(V·mol))
U	Absolute value of the applied voltage in NSSM test
T	Average value of the initial and final temperatures in the anolyte solution in NSSM test
L	Thickness of the specimen
t	Test duration for NSSM test
α	Coefficient that depends on C_d and C_0
C_d	Chloride concentration at which white silver chloride precipitates, (C_d ≈ 0.07 N for plain concrete and the UHPC concretes
C_0	Chloride concentration in the catholyte solution (C_0≈ 2N)
x_d	Average penetration depth of chloride ions in concrete during NSSM test
I	Absorption, calculated as the change in mass of the specimen divided by the product of its cross-sectional area and the density of water
m_t	Change in mass of the specimen during sorption test
a	Area of cross section of the test specimen during sorption test
d	Density of water
S_i	Initial sorptivity of the specimen
S_s	Final sorptivity of the specimen
b_1,b_2	Fitting constants for calculation of initial and secondary sorptivity

Chapter 10

Symbol	Definition
C_L	Life cycle cost of project
C_i	Initial cost of mobilization of the project
C_C	Construction cost of the project
C_M	Maintenance and repair cost of the project
C_R	Replacement cost of the project
C_S	Residual value of the project
$CU_{eq,j}$	Unit cost of equipment type "j" that needs to be purchased
n_{eq}	Amount of equipment of type "j" to be purchased
CU_{cr}	Unit cost per hour for training one worker
n_w	Number of workers to be trained
$CU_{rm,i}$	Unit cost of the i^{th} raw material
$m_{rm,i}$	Volume of the i^{th} raw material used in a unit volume of UHPC
v_{UHPC}	Total volume of UHPC used in the project
$C_{tn,i}$	Cost of transportation of i^{th} raw material to site
C_{rc}	Cost of steel reinforcement caging
C_{fw}	Cost of formwork to pour concrete
C_{asc}	Cost associated with aggregate sieving and crushing
C_{mc}	Cost of mixing and curing of UHPC
C_{qc}	Cost of quality control testing and verification of UHPC
C_{td}	Cost of traffic diversion for carrying out the construction activity
C_{rm}	Total raw material cost of UHPC for a project

EXECUTIVE SUMMARY

The ultra high-performance concrete (UHPC) project provides a detailed study on the development of UHPC from locally available materials and provides design guidelines to utilize UHPC for the construction of structural elements. The main objectives of the project were to design and characterize cost-effective UHPC mixes for Arizona bridge deck connections.

UHPC has been known to be an extremely high strength material with compressive strengths of the order of 150 MPa (22000 psi), high ductility, high impact resistance and a longer service life over traditional concrete. These properties of UHPC make it attractive for use in critical applications where strength and/or durability are of prime concern. However, the material formulation of UHPC has been proprietary to a large extent and because of its extraordinary properties as a construction material, the market costs for UHPC soar as high as $2000 per cubic yard, which is as much as 15-20 times the cost of ordinary concrete. Such high costs still do not outweigh the benefits of higher service life of UHPC but lead to low feasibility of implementation. This is where an understanding of the science of construction materials and mixture proportioning is used to come up with feasible and low-cost non-proprietary material solutions for UHPC applications.

In this report, UHPC has been addressed from a fundamental material science perspective. The report provides an understanding of the mechanisms that govern the ultra-high strength and performance aspect of UHPC materials, which is then utilized to develop UHPCs using a bottom-up approach. The entire project is divided into two major parts – (i) design of non-proprietary UHPC mixtures, and (ii) experimental characterization of non-proprietary UHPCs. In the first part, the microstructure of UHPC materials is designed by selecting the appropriate cement and cementitious materials which fall in the micron size range. In this process, several cementitious materials such as fly ash, slag, metakaolin, silica fume, and limestone are considered as potential UHPC components and trial mixtures are designed using combinations of these materials. The optimal mix proportion is determined as the combination of these materials which gives the maximum packing efficiency and at the same time also satisfies certain workability criteria. There are several variables that affect the packing and workability of the mixtures, the material composition, particle size distribution, reactivity between different components, amount of water and admixtures, mixing method, mixing temperature etc. Extensive analysis of these criteria was conducted, and a generic model based on microstructure packing efficiency and workability of the mixture was developed. The model consists of simple experiments and simulations to understand if a mixture composition is capable of performing as an ultra-high performance mixture. The model enables the identification of certain suitable mixture compositions using minimal number of tests and material.

The mixtures selected using the generic model as binder compositions were then coupled with an optimized aggregate gradation to create UHPCs. A compressible packing model was developed that calculates the packing density of any aggregate mixture. Several aggregate combinations were tested and then listed in decreasing order of their packing density. The aggregate combination with the maximum packing density was selected as the optimized aggregate gradation for the UHPC mixtures. It is sufficient to say that a high precision in aggregate gradation is required in order to achieve the highest packing density and using standard stockpiles available in the industry is not a feasible option for making

UHPC mixes. The packing density is critical to achieving high strengths and durability of the UHPC mixtures. Steel fibers were added at 1% to 3% dosage by volume to reinforce the matrix of these mixtures to create ultra-high performance fiber reinforced concretes (UHPFRCs).

In the second part of the study, the UHPC mixtures developed were subjected to mechanical testing to measure response under compression and flexure, and durability testing to determine service life. It was found that UHPC mixtures developed using this entire model demonstrated compressive strengths of 22000 psi (150 MPa) () or more, and flexural strengths of over 3000 psi (20 MPa) at 28 days. The effect of mixing environment, curing conditions, mixture design and fiber dosage has been addressed. The UHPFRC mixtures demonstrated high ductility maintaining more than 50% load carrying capacity beyond the peak load. Accelerated durability testing was conducted on the UHPC mixtures to measure the response to ion ingress and water absorption. The UHPC mixtures, by virtue of their high packing density, have extremely low porosity and therefore demonstrated very high resistance to chloride penetration and exhibited low surface absorption. The values were compared against the same values for ordinary concrete, and the UHPC mixtures fared about 10 times better than ordinary concrete, thus predicting a longer service life than that of ordinary concrete. It is sufficient to say that UHPC mixtures designed in this report meet the standard guidelines set in place by Federal Highway Administration and American Concrete Institute.

The design of UHPC structural elements was also addressed in this report. A detailed analysis method has been described to design UHPC beams and UHPC joint connections from a serviceability aspect. The key design parameters have been identified as (a) the ratio of compressive to tensile strength, (b) the post-crack tensile residual strength, and (c) the allowable compressive or tensile strain from a serviceability point of view. The design of UHPC elements takes into consideration the tensile capacity of UHPC since unlike ordinary concrete, UHPC has strength in both tension and compression. The design parameters are back-calculated using an inverse analysis procedure which utilizes the experimental load-deflection response and the design is formulated using limit state design procedures adopted from American Concrete Institute.

To present a holistic picture of the mixtures developed in this study, a detailed cost analysis model was formulated. The material cost of UHPC mixtures was found to be a fraction of the material costs for commercial UHPC. A material cost sensitivity analysis was also conducted, and it was discovered that the overall material cost has high variability with respect to the cost of steel fibers and admixtures.

Chapter 1 INTRODUCTION

Introduction

This chapter introduces the concept of ultra-high performance concrete (UHPC) and provides an outlook towards the benefits of UHPC over traditional and high performance concrete (HPC). Following key topics are addressed.

- Difference between UHPC, HPC and traditional concrete.
- Why should UHPC be preferred over HPC?
- Application of UHPC in accelerated bridge construction program
- Objectives on the ADOT-ASU project

Overview

Ultra-High-Performance Concrete (UHPC) is a special type of concrete designed to demonstrate exceptional strength, ductility, and durability properties. The high compressive strength of UHPC enables reduction in cross-section and self-weight of reinforced concrete structures. UHPC is constituted by employing a strictly controlled gradation of particles (including cement, cement replacement materials such as silica fume and fine and coarse aggregates), fibers, and a very low water-to-binder ratio (w/b) of 0.2 to 0.3. The very low w/b demands the use of higher than normal amounts of chemical admixtures, including high-range water reducers and viscosity modifiers. This complex mixture formulation, which is often proprietary, leads to a increase in the cost of production of UHPC. Development of economical, yet optimally performing UHPC mixtures is a major challenge for many users, including state departments of transportation. In the remainder of this section, answers to some of the commonly encountered questions about UHPC are provided to frame the discussions described later.

How is UHPC different from conventional concrete and high-performance concrete (HPC)?

While the 28-day compressive strength of conventional concrete ranges from 4,000 to 7,000 psi, and that of HPC lies between 7,000 and 14000 psi, the compressive strength of UHPC is on the order of 20,000 to 24000 psi. The higher tensile strength (1,000 to 1,500 psi) and bending strength also set UHPC apart from conventional concrete, and even traditional HPC. In addition, the use of a high dosage rate (of the order of one to three percent equivalent steel fibers) of fibers in UHPC increases the ductility of the member, in addition to allowing the UHPC to withstand tension and bending loads without any passive or active reinforcement. The use of a low w/b, coupled with optimal particle packing, increases the durability properties of UHPC by resisting the ingress of moisture and deleterious ions such as chlorides and sulfates. These special properties of UHPC have been utilized for the construction of several transportation structures as well as the connections for precast elements in the United States and Canada. Figure 1 shows the first UHPC bridge in the United States, which was built in Iowa, and the casting of longitudinal connections between precast bridge girders in the state of New York.

Figure 1. (a) The first UHPC bridge constructed in the U.S (in Wapello County, IA), (b) casting of longitudinal connections between deck-bulb-tee girders (Route 31 Bridge, Lyons, NY). Both figures courtesy of FHWA (https://www.fhwa.dot.gov/publications/research/infrastructure/structures/11038/)

Why should UHPC be preferred over HPC?

HPC presents several problems when used in bridge structures. These issues are listed below, along with the solutions to these issues which can be addressed by using UHPC.

1) High cracking potential and increased shrinkage cracking during service – Proper curing regimes and reduced use of portland cement in UHPC, through proper material selection and particle packing, increases the resistance to shrinkage cracking and enhances the service life. This results in a reduction in the amount of surface cracking as well as narrower crack widths. The reduction in the permeability of concrete, because of the narrower micro-cracks, contributes to longevity of concrete in transportation structures.

2) Interplay between water-to-cement ratio and air content – The w/b ratios used for HPC are in the 0.26 to 0.32 range, whereas they are in the 0.16 to 0.24 range for UHPC. The very low w/b ratios used in UHPC reduces the porosity and eliminates the need for air entrainment. Air entrainment is needed in concrete because the cement paste does not have enough tensile strength to resist stresses introduced by freezing and thawing. The high strength of UHPC paste overcomes this problem. The effective lower porosity will reduce permeability of concrete to water and corrosive ions and thus increase its durability.

3) Insufficient ductile behavior – Moderate- to high-volume fractions of fibers are used in UHPC to enhance post-cracking performance, control microcracking, obtain strain hardening, and prevent shrinkage cracking, as shown in Figure 2 (Park et al. 2012). The ductility of UHPC in tension and flexure are improved in comparison to HPC, which leads to superior energy absorption ability.

Obtaining a very high compressive strength is not the only criterion of importance, since increasing the compressive strength alone does not lead to other beneficial properties such as crack resistance, ductility, and durability. UHPC mixtures need to be designed for overall performance, including high

flexural, tensile, and shear capacity, as well as long service life, in addition to a higher compressive strength.

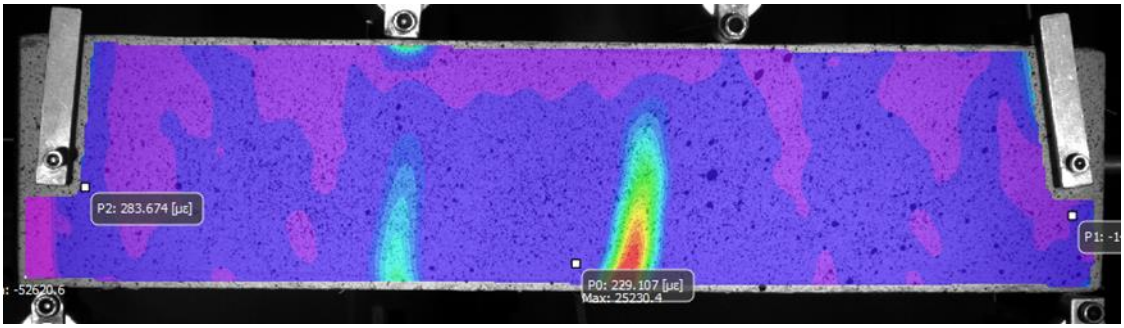

Figure 2. Multiple cracking of a UHPC specimen reinforced by steel fibers after flexure test

What are some other benefits of using UHPC?

- Adequate control of shear cracking in conventional concrete (also known as diagonal tension cracking) requires tightly formed rebar cages and stirrup arrangements that increases the cost of the finished structural member. The incorporation of fibers in UHPC provides enhanced tensile strength which leads to a subsequent increase in the shear strength and reduced tensile cracking.

- UHPC offers a high post-peak strength and high ductility due to the presence of discrete steel fibers and can sustain tensile loads for as much as 10,000 micro-strains beyond the tensile cracking strength.

- As seen in Figure 3, ordinary concrete requires the need for excessive and complex shear reinforcement. This problem can be avoided by utilizing the high ductility and increased crack resistance of UHPC.

- The mitigation of tensile cracks and reduction of crack opening in fiber-reinforced UHPC inhibit corrosion which improves the durability of the structures and helps to lower the long-term maintenance costs.

- The longevity of UHPC structures can be improved because of UHPC's exceptional durability. Ordinary concrete structures may experience deterioration from repeated freeze and thaw cycles, abrasion, fire, or rebar corrosion induced by chloride ingress, sulfate attack, and alkali-silica reaction (ASR). Because of UHPC's extremely low w/b ratio and dense packing of particles in the matrix, a very low permeability will be obtained, which is ideal to resist these detrimental effects.

Figure 3. Closely placed shear reinforcement for beam-column joint (courtesy of Gova steel & engineering http://www.govacarports.co.za/index.php?p=2_1_first-page)

Is cracked UHPC still durable?

UHPC elements exhibit very low deterioration even post cracking due to the extremely dense packing and presence of fibers. In the presence of environmental and mechanical loading conditions, discrete structural cracking can occur in UHPC members due to distributed steel fiber reinforcement, however the crack widths are likely to be much less than in lower-performing concrete, thereby resisting the harmful agents that may lead to corrosion. Steel fibers have also been found to demonstrate a different corrosion mechanism as compared to that of the traditional rebar in ordinary concrete structures due to the discrete nature of these fibers.

Application of UHPC in ABC Construction Program

Accelerated Bridge Construction (ABC) using Prefabricated Bridge Elements and Systems (PBES) is being widely implemented to ensure that construction and maintenance activities pose the least possible impediment to traffic. PBES is defined by FHWA in (FHWA 2016) as - "Structural components that are built offsite, or near the site of a bridge, and include features that reduce the onsite construction time as compared to conventional methods."

Such innovative and economic ways of planning, design, materials, and construction technologies are required for ABC either in the case of new bridge construction or in structural retrofitting projects to reduce the onsite construction time and the impacts to traffic. Prefabricated elements ensure reduced onsite construction time and minimal traffic interruption, which allows state departments of transportation (DOTs) to build and maintain durable bridges with increased safety. However, transverse connections between the precast elements using normal or high strength/performance concrete suffer from cracking and construction-related deficiencies, reducing their service lives. This makes UHPC a material of choice in ABC to ensure superior structural performance and long-term durability (Aaleti and Sritharan 2014; FHWA 2016).

Prefabricated elements can be manufactured as "deck" or "full-width" beam elements (e.g., adjacent deck bulb tee beams, double tee beams, post-tensioned box beams). Other types of components (FHWA

2013, 2016) include pier elements, abutment and wall elements, slabs, and joints, among others. Examples of full-width beam elements include truss spans, arch spans, and other types of beam elements without deck, as shown in Figure 4. Examples of pier elements are shown in Figure 5 and include precast spread footings and prefabricated columns among others. Examples of prefabricated abutment and wall elements include sheet piling made of steel or concrete, footings, backwalls, wing walls, concrete walls and abutments with or without precast elements, MSE walls, modular blocks, and geosynthetic reinforced soil. (FHWA 2013, 2016).

Figure 4. Prefabricated beam elements. Photo courtesy of Utah Department of Transportation (http://utcdb.fiu.edu/bridgeitem?id=257) and Manchester Evening News (http://www.manchestereveningnews.co.uk/news/greater-manchester-news/incredible-time-lapse-video-shows-new-8920375)

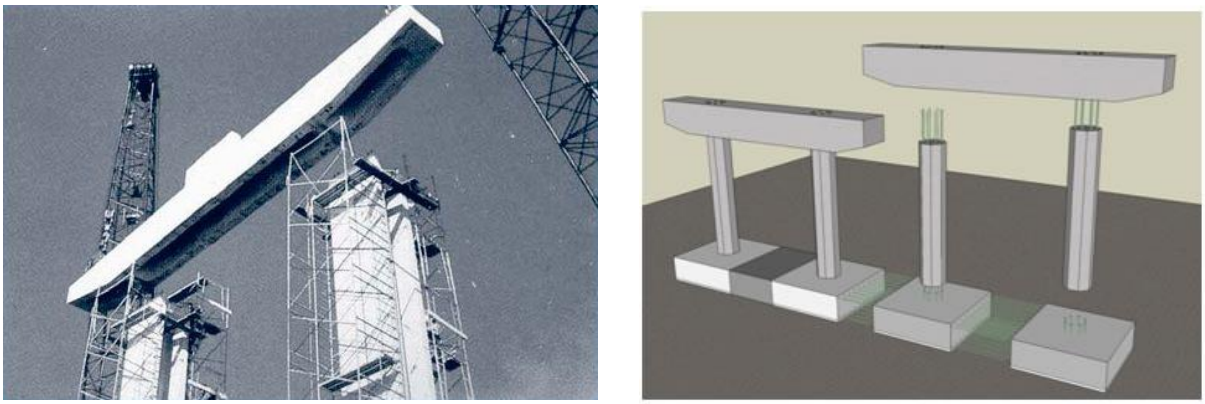

Figure 5. Examples of prefabricated bridge piers. Figure courtesy of FHWA (https://www.fhwa.dot.gov/bridge/prefab/facts.cfm)

The benefits of using UHPC connections in prefabricated bridge elements include simplified fabrication, faster construction, and the reduced requirement for overlays in deck-level connections. The constructed connections are usually stronger and more durable than the elements themselves (Benjamin A. Graybeal 2016). Due to the significantly higher bond strength between rebar and the UHPC matrix, the tension development length is a fraction of that in normal strength concrete, which facilitates connections between prefabricated elements by shorter and straight ends of rebars, greatly simplifying the configuration and expediting on-site construction. Figure 6 illustrates this simplicity with an example of lap-splice connection using UHPC. Due to the outstanding mechanical performance of

UHPC, such connections are able to transfer tensile and shear forces, as well as bending moments (FHWA 2014).

Figure 6. UHPC being used as connection joints between precast deck panels

Key Advantages of UHPC in Structural Applications

Use of innovative technologies such as UHPC enables construction of infrastructural components at lower life-cycle costs. UHPC can also be used in multitude of avenues such as high-performance decks, buried structures, box culverts (A. Meda, Plizzari, and Riva 2004). The use of UHPC can be extended to areas where excessive reinforcement is expected such as closure pours as well as areas with a requirement for high ductility, for instance, bridge decks.

Many of the advantages of using UHPC in structural applications, related to material and structural performance, were detailed earlier. Other major advantages are: (i) reduction in labor and construction time, (ii) reduction in the use of heavy equipment, facilitated by a reduction in the use of continuous reinforcement, (iii) significant ductility and reductions in structural weight provided by the employment of an elasto-plastic design approach, (iv) improved safety through the optimization of physical and labor-intensive tasks at the job site, and (v) improved mobility and safety of personnel because of the absence of layers of rebars.

Benefits to ADOT from Developing Economical UHPC Mixtures

This project addresses the development of economical, non-proprietary UHPC mixtures for bridge element connections in Arizona. The project is motivated by the need to develop UHPC mixtures to replace proprietary mixtures that are very expensive and sometimes require special treatment, such as heat curing, to attain desirable properties. The research wing of FHWA has published key findings with regards to the development of economical and non-proprietary mixtures for UHPC in the past few years. However, these mixtures have to be developed and calibrated locally in order to meet local performance specifications.

Project Objectives

The following objectives have been identified for this project:

- Review existing procedures for establishing appropriate costs for non-proprietary UHPC mixtures;
- Develop non-proprietary, sustainable UHPC mixtures incorporating locally available cement replacement and filler materials to: (a) achieve a significant cost reduction compared to the available proprietary UHPC systems, and b) meet early age and long-term performance requirements through a fundamental materials-engineering-based approach, rather than by trial and error;
- Optimize the material design to arrive at mixture proportions for UHPC based on performance criteria for bridge element connections, which will be arrived at in consultation with ADOT;
- Perform detailed testing on the mechanical (strength, ductility, volume changes, and crack resistance) and durability (resistance to chloride ion ingress and freezing and thawing) properties of the developed non-proprietary mixtures, in accordance with an ADOT-approved plan, and develop cost-and-performance matrices; and
- Provide recommendations to, and assist ADOT with, the development of specifications to use for UHPC mixtures.

Chapter 2 LITERATURE REVIEW

Introduction

This chapter summarizes the existing literature on UHPC, including its formulation and properties, along with a few case studies. Research conducted by various agencies, including FHWA, state DOTs, universities, and other research agencies, as described in journal and conference publications and reports, form the basis for this chapter. In the United States, FHWA has been at the forefront in researching UHPC for transportation elements (Ben Graybeal 2011, 2010a, 2014b, 2010b). As such, this chapter addresses the following key topics:

- Definitions of UHPC adopted by various agencies.
- Overview of the raw materials typically used for proportioning a UHPC mixture design.
- Existing scientific models available for proportioning materials to obtain the highest packing density for UHPC.
- Mixing and curing procedures implemented by researchers working on UHPC.
- Test methods used to quantify the behavior of UHPC, specifically pertaining to flowability, strength gain, and durability.

Overview

Structural applications requiring enhanced mechanical performance are candidates for UHPC (Attar et al. 2000; Schiessl et al. 2004; Porteneuve et al. 2001; Schrefler et al. 2002). The precursors of UHPC include HPC (T. Ahlborn et al. 2011), polymer modified concretes (Birchall et al. 1983), and reactive powder concrete (Cheyrezy, Maret, and Frouin 1995; Dugat, Roux, and Bernier 1996; Richard and Cheyrezy 1995; Zanni et al. 1996; Philippot et al. 1996; Feylessoufi et al. 1996), among others. ACI Committee 239 on UHPC defines it as ""Concrete that has a minimum specified compressive strength of 150 MPa (22,000 psi) with specified durability, tensile ductility and toughness requirements; fibers are generally included to achieve the specified requirement." FHWA has a rather generic and inclusive definition of UHPC - "A cementitious composite material composed of an optimized gradation of granular components, a water-to-cementitious materials ratio less than 0.25, and a high percentage of discontinuous internal fiber reinforcement."

The mechanical properties of UHPC include compressive strength greater than 22,000 psi (150 MPa), and sustained post-cracking tensile strength greater than 720 psi (5 MPa) (Ben Graybeal 2011; Russell and Graybeal 2013). The current research defines UHPC based on the conventional definitions as adopted by ACI Committee 239 and the FHWA.

Raw Materials in UHPC Proportioning

It has been understood that reduction of water-to-cement ratio, use of admixtures such as high-range water reducers and viscosity modifiers combined with an optimized gradation of aggregates as well as cementitious materials is important in the process of developing UHPCs (C. Wang et al. 2012). Short metallic fibers (usually steel) improve the strength, stiffness, and ductility of UHPC. Researchers at

Arizona State University (ASU) have gained expertise working with these materials in the past, in cooperation with ADOT. Relevant works (Bakhshi, Laungrungrong, Bonakdar, Mobasher, et al. 2013; Laungrungrong, Mobasher, and Montgomery 2008; Barzin Mobasher and Kaloush 2004) include the detailed study of materials, methodologies, and test methods to enhance the performance and durability of concrete. In addition, several new approaches to accomplish sustainable design of concrete have been showcased.

This section provides a brief overview of materials and their properties used in UHPC proportioning. Many of the materials (aggregates in particular), will be obtained from Arizona, while other raw materials, including ordinary portland cement (OPC) and admixtures, will be obtained from major national and international manufacturers, some of which may operate in Arizona.

Cementitious Materials

As in any conventional cementitious system, ordinary portland cement (OPC) constitutes the major binding material in UHPC systems. In addition to OPC, several waste/by-product materials containing reactive aluminosilicates (industrial by-products such as fly ash and slag, and natural pozzolans) are used in UHPC (Kosmatka, Kerkhoff, and Panarese 2002; Mitchell, Hinczak, and Day 1998) because of their potential to enhance the mechanical and durability properties of concretes (Figure 7). The mechanisms by which these materials improve the properties of cementitious systems are well known. These materials form secondary hydration products by reaction with the soluble calcium hydroxide (CH) produced as a result of OPC hydration. This increases the volume of solid products in the material structure and refines the pore structure, thereby enabling strength enhancement and increased resistance to the passage of deleterious agents such as chlorides and sulfates.

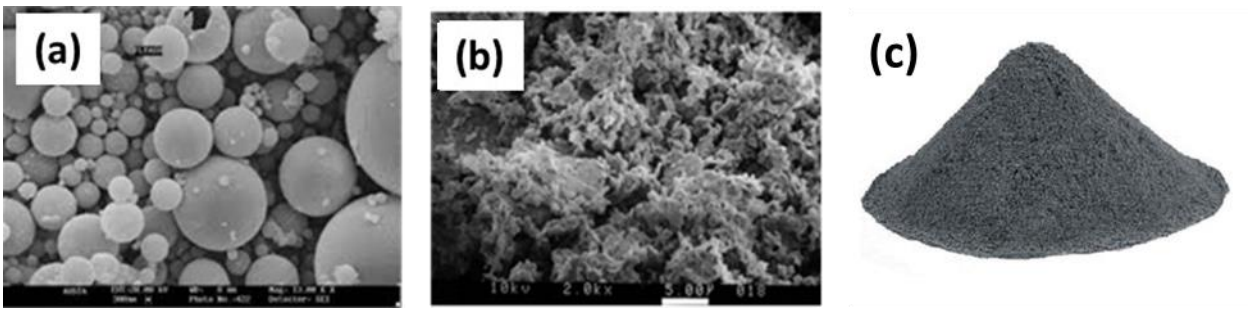

Figure 7. Micrographs of (a) fly ash and (b) metakaolin and (c) silica fume powder as supplementary cementitious materials (SCMs)

The common materials used to replace cement in UHPC are described below.

Fly Ash

Fly ash is a by-product of coal-fired electric power plants. Depending on the amount of calcium in the sly ash, it can be classified as high-calcium (Class C) or low-calcium (Class F). Class F fly ash is the more common in Arizona. Due to their spherical shape (Figure 7 (a)), fly ash particles have been shown to improve the workability of concrete. Fly ash is also a pozzolanic material, which means that it reacts with the by-product of cement hydration (calcium hydroxide) to form its own hydration product,

thereby improving concrete properties. However, the reaction of fly ash (in general, Class F) in cement-based systems is a slow process and therefore the use of fly ash in concrete leads to slower setting times, slower early age reaction kinetics as well as reduced early age strengths. At the same time, the combination of fly ash with certain cement replacement materials, such as silica fume and metakaolin, has been shown to accelerate property development at early ages (Vance, Aguayo, et al. 2013a). It is also well documented (Nochaiya, Wongkeo, and Chaipanich 2010; Richardson 1999) that fly ash lowers the heat of hydration, enhances the amount of hydration products (C-S-H gel), and thus improves the mechanical properties and durability of concrete, when used as a partial cement replacement. In general, the replacement levels of cement by Class F fly ash in concrete ranges from 10 to 30 percent by mass, while Class C fly ash can be used in higher proportions. The use of high volumes of fly ash in cementitious systems and the use of geopolymeric systems (where OPC is not used at all; fly ash is the sole cementing medium, aided by high concentration of alkali hydroxides and silicates) (Garcia-Lodeiro et al. 2011) are also becoming common.

Silica Fume

Silica fume is a by-product of the silicon manufacturing industry (Malhotra et al. 1987). Due to the nature of processing of silica, the particulate size of silica fume is an order of magnitude smaller than that of OPC which helps with the densification of the cement paste matrix. As a result of this, silica fume has an extremely high surface area by virtue of which it acts as a nucleation site for cement hydration, thereby enhancing the rates of reaction during the early stages of hydration (Cheng-yi and Feldman 1985). Silica fume is available in two forms - densified and undensified. The dry densified is the one more commonly used since it increases the bulk density of resulting concrete. There has been research to show that silica fume particles tend to agglomerate resulting in extremely low workability (Boddy, Hooton, and Thomas 2000; Nagataki, Otsuki, and Hisoda 1994; Mitchell, Hinczak, and Day 1998; Bonen and Diamond 1992) and therefore it is of important consideration to develop mixing methods and techniques to break and reduce the agglomerations to have a workable concrete mixture. Silica fume is also pozzolanic in nature and enhances the mechanical properties of the matrix due to pore size refinement as a result of formation of secondary hydration products (Yajun and Cahyadi 2003; Mazloom, Ramezanianpour, and Brooks 2004; Bayasi and Zhou 1993; C. S. Poon, Kou, and Lam 2006a; G. A. Rao 2003; Igarashi, Watanabe, and Kawamura 2005). The very high reactivity of silica fume, aided by its small particle size and large amounts of reactive silica, results in faster property development than occurs in other partial cement replacement materials. This is apparent from the strength activity indices of cementitious systems containing silicon fume or fly ash (Figure 8) (Neithalath, Persun, and Hossain 2009). An even finer version of silicon fume, termed nano-silica, is sometimes used for UHPC mixtures. While the very small particle sizes increase the reactivity in the system, the dispersion of mixtures containing such particles is a challenge, even when very large amounts of dispersion-helping chemical admixtures are used. The agglomeration of these particles sometimes causes reduction in mechanical properties.

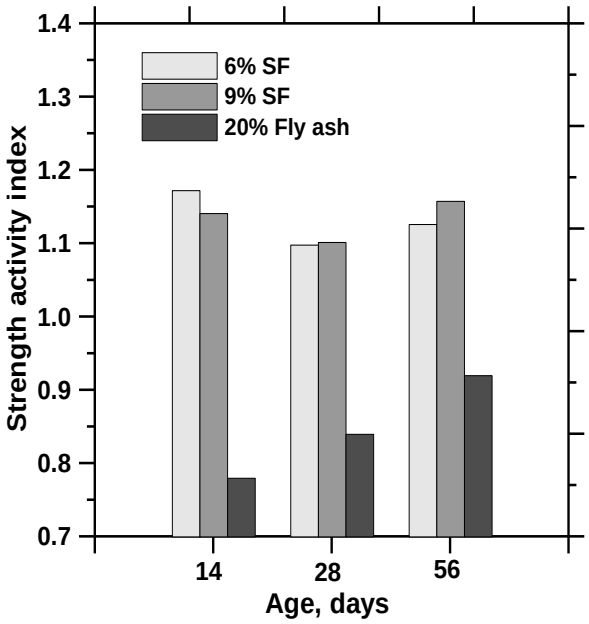

Figure 8. Strength activity indices of cementitious mortars containing silica fume or fly ash (Neithalath, Persun, and Hossain 2009)

Metakaolin

Metakaolin (MK) is produced by the thermal processing of kaolin clay (Gruber et al. 2001). Like fly ash and silica fume, metakaolin is also a pozzolanic material and has high reactivity towards calcium hydroxide formed during cement hydration due to its amorphous structure (see Figure 7). MK consists mostly of aluminosilicates and its high alumina content as well as high surface area are the reason for its high reactivity (C.-S. Poon et al. 2001). The higher reactivity, along with the reduction in cement content, leads to increase in heat of hydration per unit mass of cement (Figure 9 (a)) (Vance, Aguayo, et al. 2013a). The enhanced pozzolanic activity consumes more calcium hydroxide and forms more C-S-H than what is typical with other cement replacement materials such as fly ash. This is shown through thermal analysis results in Figure 9 (b) (Vance, Aguayo, et al. 2013a). The net result is an increase in the amount of hydration products, refinement of the pore structure, and consequent improvement in the mechanical properties and durability of concrete (C.-S. Poon et al. 2001; Vance, Aguayo, et al. 2013a; Shekarchi et al. 2010; Antoni et al. 2012; Kadri et al. 2011; Paiva et al. 2012).

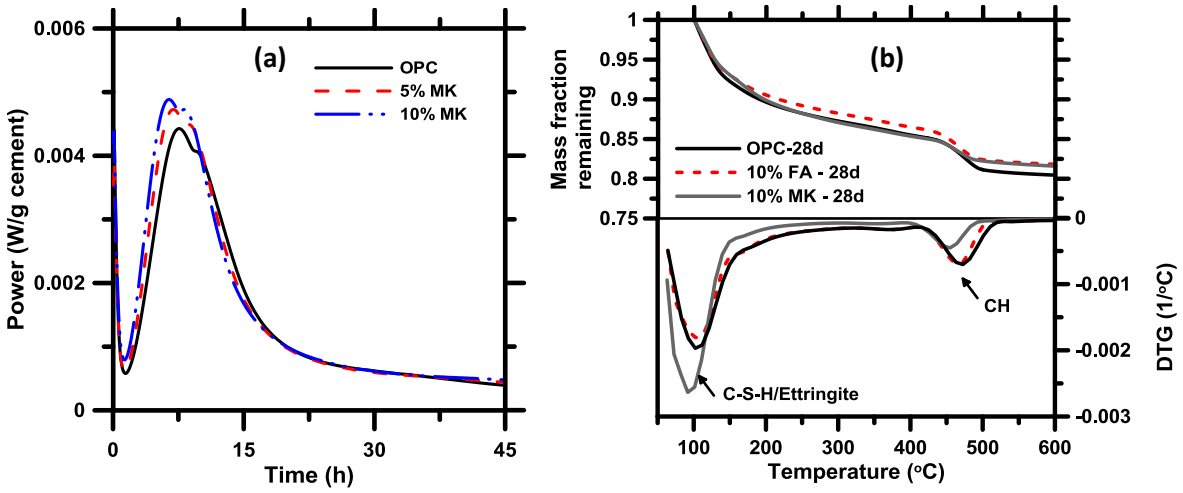

Figure 9. (a) Reduction in heat of hydration when cement is partially replaced by MK, (b) thermal analysis results showing reduction in CH and increase in C-S-H when MK replaces part of cement (Vance, Aguayo, et al. 2013a)

Limestone

The use of limestone as a partial cement replacement material has risen in recent years. Portland limestone cements are used in several countries, including the United States. ASTM C 595 has defined a Type IL cement that can include up to 15 percent limestone powder as a partial cement replacement material (Tennis, Thomas, and Weiss 2011). The use of appropriate sizes of limestone powder results in better particle packing and thus improves the properties. While reports on UHPC in the literature have not mentioned the use of limestone powder, it is an appropriate cement replacement material to be used in UHPC based on its capability to provide adequate particle packing, as well as to form space-filling reaction products in the presence of aluminate-rich materials. Limestone powder can chemically interact with the aluminate phases in cement to form a carboaluminate phase. Several studies address these topics (Arora et al. 2016; Puerta-Falla et al. 2016; Arora, Sant, and Neithalath 2016; Das et al. 2015b; Vance et al. 2015; Kumar et al. 2013; Vance, Aguayo, et al. 2013a). Previous work (Vance, Aguayo, et al. 2013a) has shown that fine limestone, in the presence of metakaolin or fly ash, enhances the amount of C-S-H gel formed as early as 28 days, and has a beneficial impact in strength development, as shown in Figure 10. This result provides the rationale for using fine limestone in UHPC mixtures in combination with other SCMs, which in turn may improve the sustainability of concrete.

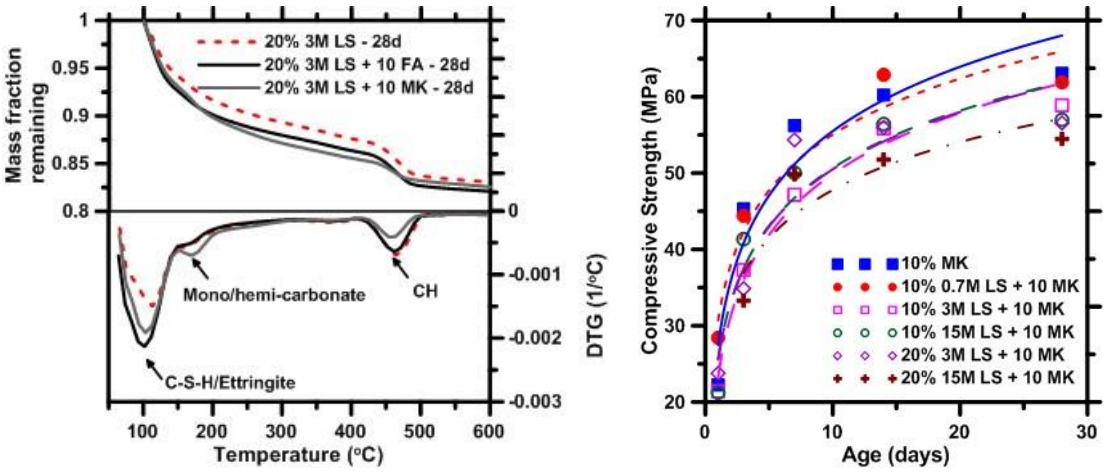

Figure 10. (a) Thermal analysis results showing reduction in CH and increase in C-S-H when MK or fly ash in combination with limestone replaces part of cement, and (b) strength development of limestone-metakaolin systems (Vance, Aguayo, et al. 2013a)

Particle-Packing-Based Mixture Proportioning of UHPC

Improved mechanical and durability properties of UHPC are a result of proper mixture proportioning that includes a low w/b ratio and the use of several materials that help refine the pore structure. Packing density of a cement paste is defined as the ratio of total volume of particles in the mixture to total volume of the overall paste. As explained earlier in this chapter, the incorporation of cementitious materials such as fly ash, silica fume, metakaolin helps refine the pore structure and reduce the overall porosity of the cement paste due to their pozzolanic action. This ultimately leads to a dense microstructure, increase in the packing density which is directly correlated with mechanical strength development and enhanced durability properties. This is schematically depicted in Figure 11 ("Fillers in Action: How to Achieve High Particle Loadings" 2015). Since packing in the matrix can be controlled by judicious selection of powders with appropriate particle sizes, it is a better means to design and produce economical UHPC mixtures than the use of expensive high-reactivity materials. A particle-packing-based mixture thereby ensures economy and sustainability.

(Stovall, de Larrard, and Buil 1986) described the linear packing density model to calculate the packing density of a system containing multi-sized aggregates as a function of the volume fraction of each aggregate size. In many packing models, it is assumed that there is at least one dominant particle size (defined as the particle size that has the highest packing density) among the grain sizes present. By sequentially considering each class of particles as dominant, a series of packing density functions can be obtained. The minimum packing density can then be conservatively taken to be the packing density of the mixture (De Larrard 1999; Lecomte 2006). The packing density functions can be represented as:

$$\gamma_i = \frac{\beta_i}{1 - (1 - \beta_i)\sum_{j=1}^{i=1} v_j - \sum_{j=i+1}^{n} v_j}$$ **Equation 1**

where γ_i is the virtual packing density of the mixture when class *i* is dominant, β_i is the virtual packing density of grains of class *i*, v_j is the volume fraction of grains of class *j*, and *n* is the total number of grain classes. Refer to (De Larrard 1999) for more details including the formulation and mathematical expressions that define packing-based mixture design.

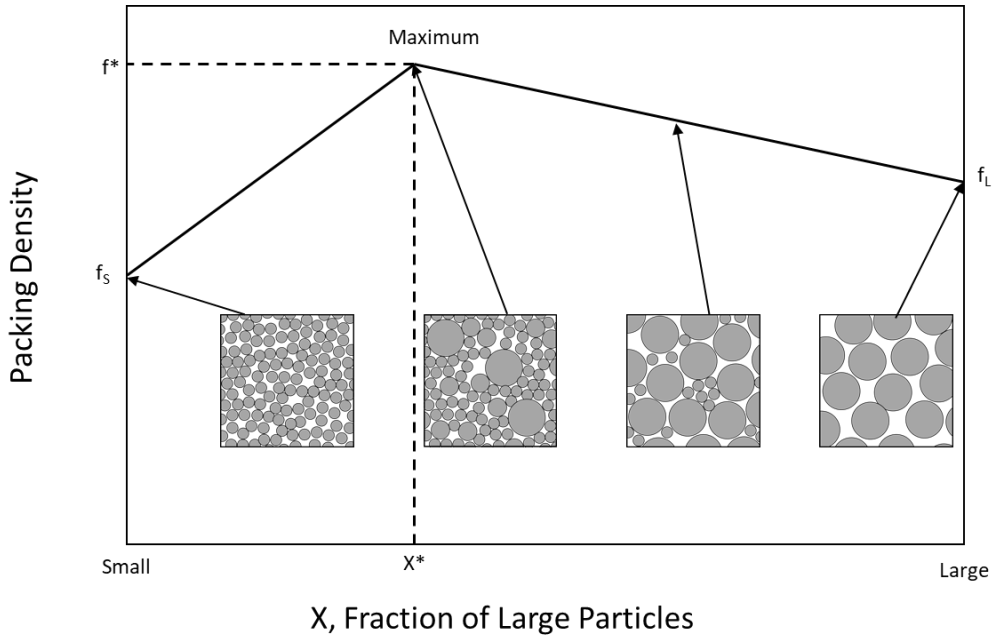

Figure 11. Schematic illustration of packing density as a fraction of larger particles in the mix ("Fillers in Action: How to Achieve High Particle Loadings" 2015)

The virtual packing density is defined as the theoretical value of maximum packing density where every particle is precisely positioned at a specific location within the representative volume. Such a precise arrangement cannot occur in the field and the distribution of particles in a system is always random. Hence, another parameter, the actual packing density is used and can be calculated using a compressible packing model (De Larrard 1999). Previous research (Vance, Kumar, et al. 2013) has indicated that packing densities can be calculated computationally by placing spheres that represent the actual particles in representative volume elements (RVEs) as shown in Figure 12. Though many of the cementitious materials, with the exception of fly ash, are not spherical, the spherical particle assumption is widely used in computational materials science. This is to ensure that the simulations run in a reasonable amount of time in a relatively high-powered computing environment. Assigning realistic particle shapes requires orders of magnitude larger computational time, and the refinement in the

results has not justified that choice in past studies. Virtual three-dimensional (3D) microstructures can be created using the particle size distributions of the powders present in the mixture. These microstructures can then be analyzed to calculate the packing density of the mixture. Such an approach will be used in the present study.

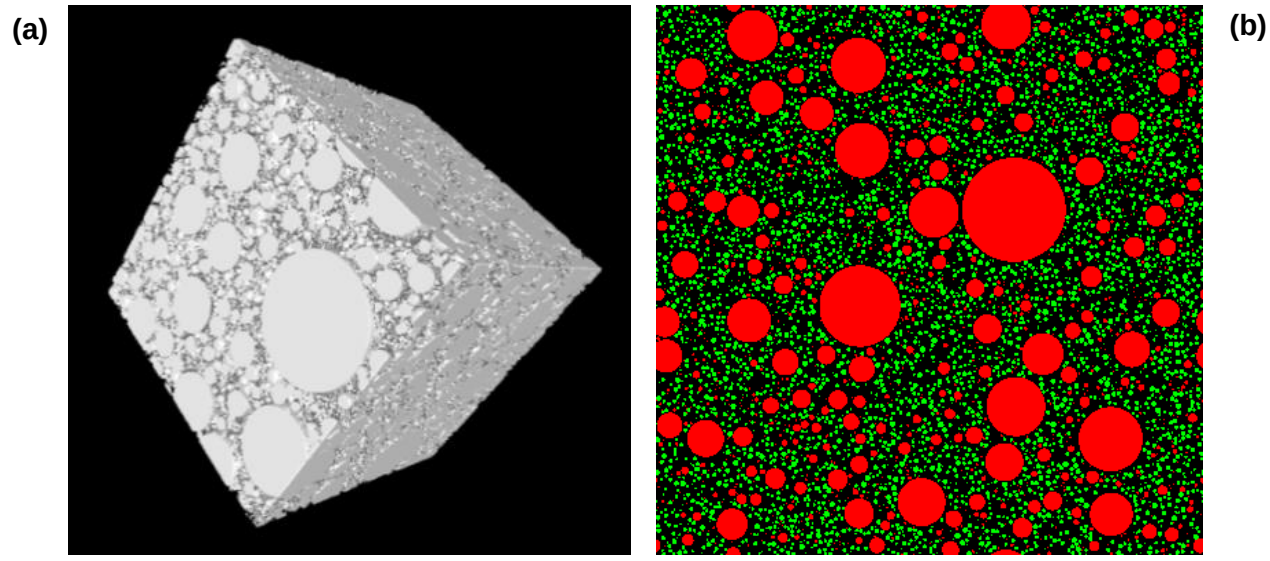

Figure 12. (a) A 3D system in which spheres of different sizes are packed, and (b) a 2D representation of the same, to calculate the particle contacts and proximities (Vance, Kumar, et al. 2013)

(Stroeven and Stroeven 1999a) showed that for dense mono-sized particles at two different grain fractions, the volumetric packing density exhibits an oscillatory phenomenon, as shown in Figure 13 (a). It is observed from Figure 13 (a) that the packing fraction (volume density) increases when using a combination of two particle sizes as opposed to having just mono-sized particles. Such an understanding is useful in selecting particle sizes of aggregates for mixtures such as UHPC where packing must be increased for optimal performance. Figure 13 (b-c) shows the particle arrangement of corresponding binary systems at 2 mm and 14 mm from the interface.

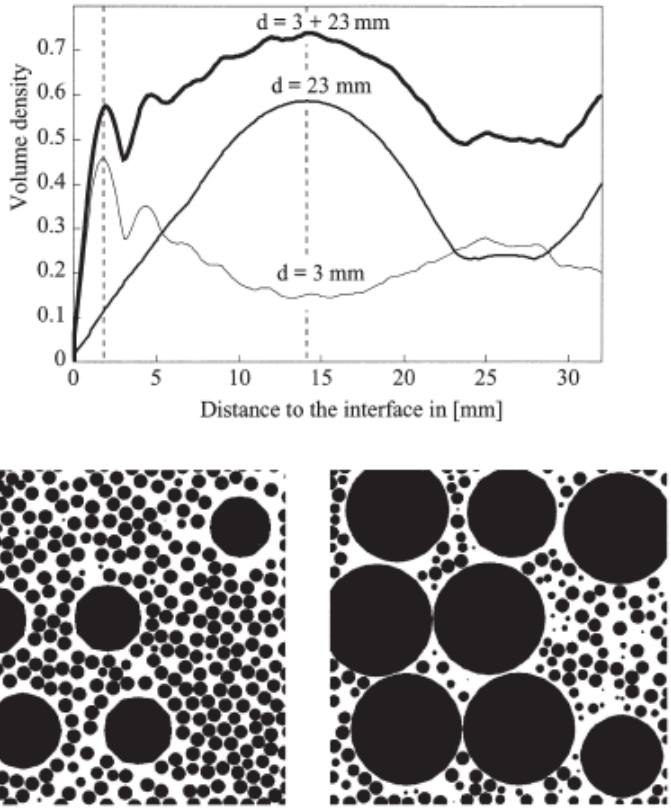

Figure 13. (a) Packing fraction (volume density) of a binary system expressed as a function of distance to the interface (Stroeven and Stroeven 1999b) (b-c) particle arrangement for two different volume proportions

Other models for particle packing exist. Yu et al. (2014) formulated a dense UHPC using the Andreasen model with a binder content of 650 kg/m^3. (Le et al. 2015) used the Funk and Dinger packing theory to proportion aggregates to obtain self-compacting high performance concrete. While these models provide adequate capabilities with respect to packing, they employ several questionable assumptions (e.g., size distribution of all grain classes are the same, the ratio of largest to smallest particle size is limited to a certain value). The virtual packing density-based model chosen for the present work eliminates many of these assumptions and provides a scientific methodology for mixture design which is repeatable and robust.

The degree of hydration is rather low in UHPC systems due to the low w/b ratios. Therefore, the workability as well as reactivity of UHPC can be improved upon by utilizing filler materials such as limestone and nanoparticles such as nano-silica (Camiletti, Soliman, and Nehdi 2012; W. Li et al. 2015). Table 1 gives an overview of the components in the binder phase of UHPC and their amounts in a typical UHPC mixture design, as reported in several studies (Yazıcı et al. 2008; Tafraoui et al. 2009; C. Wang et al. 2012; Elrahman and Hillemeier 2014; Yu, Spiesz, and Brouwers 2014, 2015; Yoo and Yoon 2015; Kay Wille and Boisvert-Cotulio 2015; Alkaysi et al. 2016). Paste or binder consists of the cementing materials, including SCMs, water, and chemical admixtures. Fibers are sometimes considered part of the matrix. The numbers given in this table are general guidelines based on the work of several researchers. These

values can be used as initial estimates of the contents of these materials, which will then be modified based on the particle-packing-based mixture design described earlier. Note that the use of limestone is not commonly reported, but this study will explore its use for the benefits noted earlier.

Table 1. Typical proportions of materials used for the paste (binder) phase of UHPC

	Materials in UHPC Binder phase	Percent by weight
Cement and Cement replacement materials	Cement	25-45
	Fly ash	5-25
	Silica fume	5-15
	Metakaolin	0-10
Fine aggregate	Sand	35-45
	Quartz	5-15
Water	Water	3-10
Fiber	Fiber	0-6

Mixing and Curing

The mixing procedure for UHPC has been described in several research publications. The generally accepted procedure is as follows. Initially, coarse and fine aggregates are mixed using a 1.25-gallon Hobart mixer with the dry powder containing cementitious materials at a low speed (60 rpm). The mixture of water and superplasticizer is then partially added to the mix with the mixer operating at low speed. The remaining superplasticizer and water is then added to the mixture at an intermediate speed (124 rpm). Finally, fibers are introduced and mixed at a higher speed (255 rpm). The entire mixing procedure takes about 15 to 20 minutes for the material to flow in a shear thinning manner (i.e., increase in workability with time). Specific mixing procedures reported in some publications are outlined here, so as to obtain an overall understanding of the process, and to help select the right mixing procedure for the UHPC systems. This study will review the available mixing procedures (Tafraoui, Escadeillas, and Vidal 2016; Kay Wille and Boisvert-Cotulio 2015; Yu, Spiesz, and Brouwers 2014) and develop a protocol based on the selected materials and desired workability. Figure 14 shows a step by step mixing procedure for UHPC as found from literature.

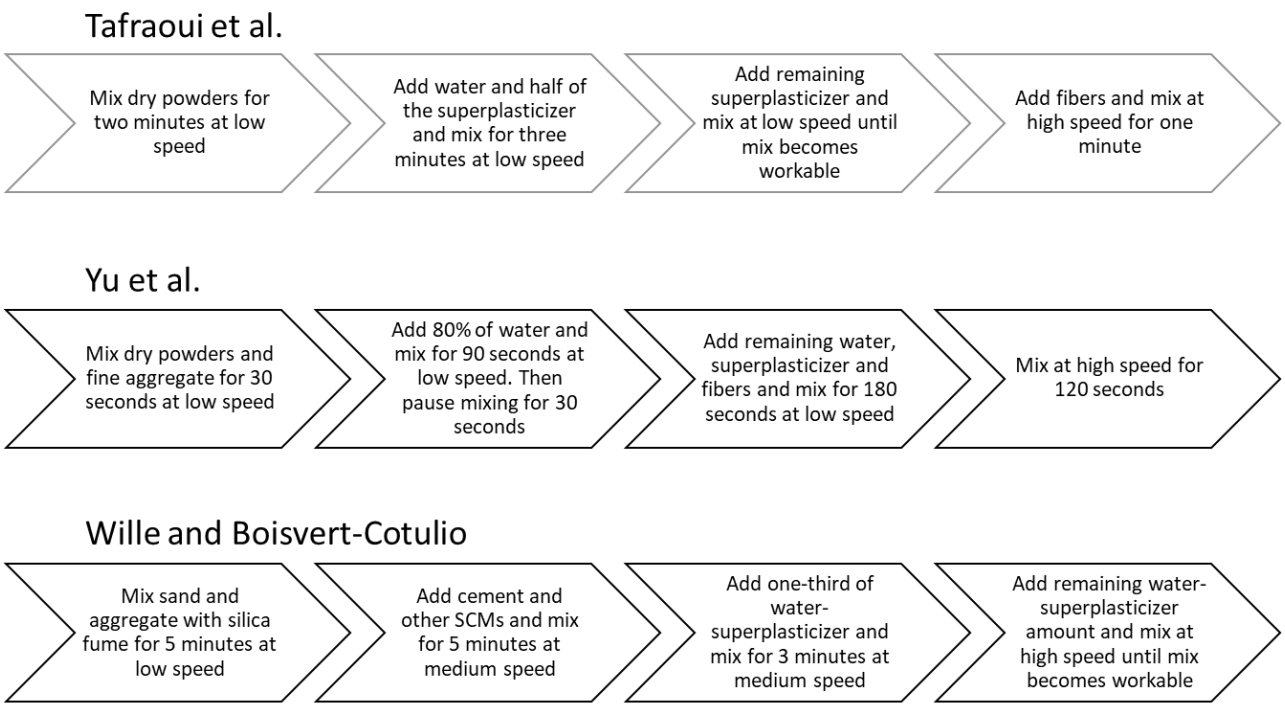

Figure 14. Step by step mixing procedures from three research studies to develop UHPC

The mixing procedure strongly depends on the material proportions in the mixture as well as the volume of the mixture to be cast. Longer mixing times are needed when materials like silica fume, which forms agglomerates, are used. Larger volumes of mixture may also need longer mixing times. The procedures listed above served as guidelines to arrive at a mixing procedure that can be adopted for the mixtures in this study.

Curing of UHPC is an important aspect for UHPC to develop compressive strengths in excess of 150 MPa (22 ksi). The easiest way is to cure the specimens under normal temperature and relative humidity. Special treatments such as pressure and extensive vibration are among the techniques that are sometimes used to accelerate curing and strength development (T. M. Ahlborn et al. 2008; Behloul, Bernier, and Cheyrezy 1996; Benjamin Graybeal and Davis 2008; Matsubara et al. 2008; Reda, Shrive, and Gillott 1999). Extremely high curing temperature (400°C) and pressure (50 MPa) have been used (Richard and Cheyrezy 1995) to attain a compressive strength of 800 MPa for reactive powder concretes. Needless to say, such temperatures and/or pressures would be cost-prohibitive in actual construction projects. Because of this reason, several studies have tried to formulate curing methods without the use of heat curing (Benson and Karihaloo 2005; Habel et al. 2006; Maeder et al. 2004; Ma et al. 2003). Thus, the emphasis ideally should be on adequate particle packing, a sufficient amount of reactive materials, a low water-to-binder ratio, and controlling the rheological properties of the UHPC mixtures. The present study considers such an approach.

Rheological properties of binders

Rheological testing is among the most important test methods to ascertain the fluidity and workability of cementitious materials. Rheology is defined as the study of the flow and deformation of matter. Rheology of fresh concrete is extremely important, especially for low water-to-binder ratio systems such as UHPC, because it determines the particle dispersion, and consequently the reactivity and the mechanical property development. Rheology is dependent on the particle characteristics and packing in the system, both of which are very important for UHPC. Rheological studies consider concrete as a fluid system with particles as the dispersed solids. Rheology of concrete changes with time and temperature. Rheological experiments are typically carried out on cement pastes using a rotational rheometer, which monitors the change in torque required to change the shear rate (constant strain), or the change in strain required to change the torque (constant stress) (Vance, Sant, and Neithalath 2015). Constant strain mode is usually preferred over constant stress mode due to the ease in measuring the yield stress and plastic viscosity of the cement pastes. Shear rate is the change in shear strain with time. A typical rotational rheometer is shown in Figure 15 (a). Several experimental parameters are important when carrying out rheological studies, including the testing geometry (parallel plate, coaxial cylinder, cup and vane), the gap between shearing surfaces, the roughness of the shearing surfaces, the testing temperature, the state of dispersion determined by the particle characteristics, and the mixing method. Common testing geometries, and when they can be used are depicted in Figure 15 (b).

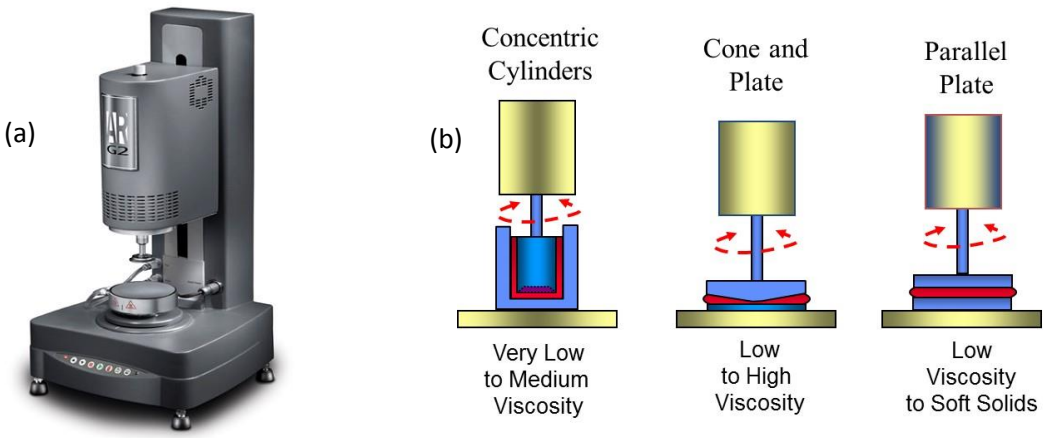

Figure 15. (a) A typical rotational rheometer and (b) common testing geometries for rheological tests on cement pastes

The shear stress versus strain rate is measured using the rheometer in a flow curve. Before the experiment is begun, the initial paste is sheared at a specific strain rate to reach an equilibrium state. This is called as the pre-shear phase. Beyond the pre-shear, the material response is captured by varying the shear strain rate along an up-ramp and a down-ramp curve. The shear strain rates used and their ranges are shown in Figure 16, based on previous work (Vance, Sant, and Neithalath 2015). Bingham, Herschel-Bulkley, and Casson models are commonly applied to the shear stress-shear rate response to extract the rheological parameters (mainly yield stress and plastic viscosity) that describe flow of cement

pastes (Nehdi and Rahman 2004; Schwartzentruber, Le Roy, and Cordin 2006). These three models are depicted below:

Bingham:

$$\tau = \tau_y + \eta_p \dot{\gamma}$$ **Equation 2**

Herschel-Bulkley:

$$\tau = \tau_y + K\dot{\gamma}^n$$ **Equation 3**

Casson:

$$\sqrt{\tau} = \sqrt{\tau_y} + \sqrt{\eta_\infty}\sqrt{\dot{\gamma}}$$ **Equation 4**

In these equations, τ is the shear stress (in Pa), τ_y is the yield stress (in Pa), η_p is the plastic viscosity (in Pa.s), $\dot{\gamma}$ is the shear rate (in s^{-1}), K is the consistency index (a measure of the average viscosity of the fluid), n is the flow behavior index, which ranges between 0 and 1 for shear thinning suspensions, and η_∞ (in Pa.s) is the viscosity at an infinite shear rate.

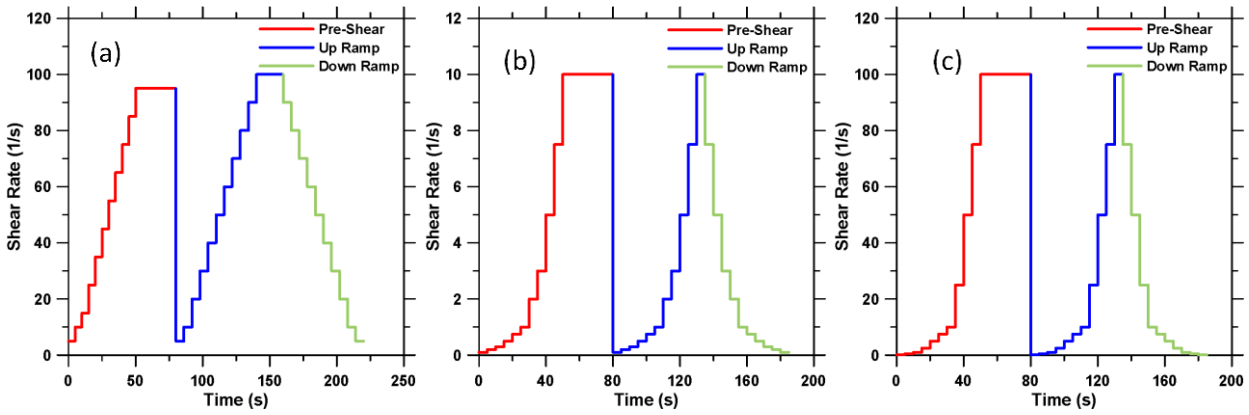

Figure 16. The rheological procedures applied over: (a) "normal" shear range, (b) "low" shear range, and (c) "wide" shear range (Vance, Sant, and Neithalath 2015). These experimental protocols will be tailored to this study based on the materials and proportions used

The mixing time and rheological properties of fresh UHPC are also influenced by the characteristics of the mixer (including its geometry, speed, and degrees of motion), the ambient environmental conditions in the mixer, and the elapsed time since blending of the premix (Benjamin A. Graybeal 2006). Dils et al. (2013) characterized the influence of the chemical composition of cement on the rheological response of UHPC binders. According to their study, a lower aluminate to sulfate ratio, and a lower alkali content

in cement is favorable to achieve low yield stress and plastic viscosity for UHPC binders. In general, low values of yield stress and plastic viscosity denote a fluid mixture. “Low” is a relative term here, since the use of chemical admixtures dramatically changes the rheological response of mixtures, and consistency requires comparisons between mixtures with similar admixture dosages. Schröfl et al. (2012) studied the effect of admixture on binary UHPC mixtures containing cement and silica fume. They found that the adsorption of admixture on the particle surfaces depended on the intrinsic composition and surface area of particles. They also found that a mixture of different polycarboxylate superplasticizers was more effective at adsorbing on particulate surfaces rather than an individual polymer, and thus provided better particle dispersion and better workability. Another way to determine the rheological properties of UHPC binder is the mini-slump test proposed by (Choi et al. 2016). This test measures the area of spread of the paste phase and correlates that with the fundamental rheological properties discussed earlier. In the present study, a similar attempt will be made to ensure that the binder selection process is made easy.

Hydration and Microstructure

It is important to evaluate the hydration of the binding materials in UHPC systems, since the property development is intimately related to the degree of hydration and the resultant microstructure. Understanding the hydration also provides indications of heat release and potential cracking probabilities, as well as degrees of reaction of the component materials. As an example, Figure 17 shows the cumulative heat released as a function of time for the first 72 hours of hydration when OPC is replaced partially with different amounts of slag (Arora, Sant, and Neithalath 2016).

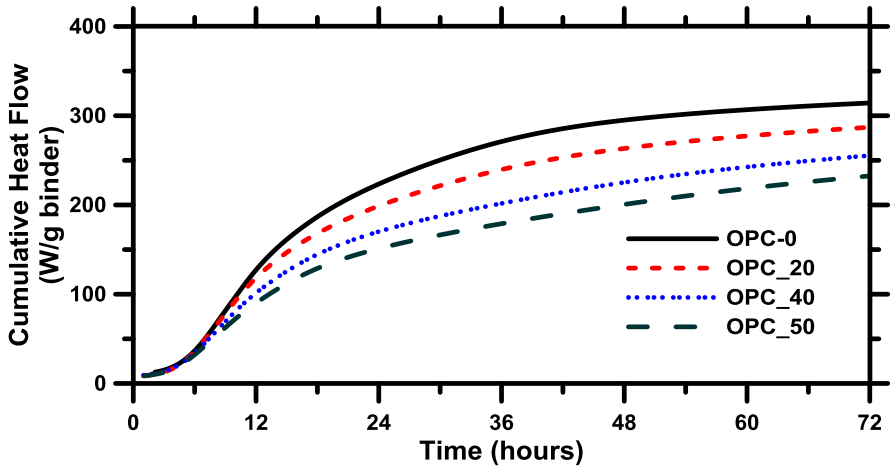

Figure 17. Cumulative heat released as a function of time for cement pastes where OPC is partially replaced with slag (Arora, Sant, and Neithalath 2016)

Several researchers have studied the microstructure of UHPC to quantify the reaction products being formed using advanced techniques such as scanning electron microscopy (SEM), X-ray diffraction (XRD) etc. (Reda et al. 1999) investigated carbon-fiber reinforced UHPC containing silica fume and silica flour. They discovered minimal traces of calcium hydroxide in the microstructure and attributed the consumption of calcium hydroxide to the pozzolanic activity of silica particles present in the binder.

(Ghafari et al. 2012) studied the effect on incorporation of nano-silica in UHPC. They found that the presence of nano-silica led to the refinement of pore-structure and significant reduction in sorptivity (sorptivity is the tendency of concrete to absorb water on its surface) as compared to a reference UHPC mixture without nano-silica. The influence of nano-silica on the reduction of capillary pores was quantified using mercury intrusion porosimetry and SEM analysis.

Mechanical Properties

The key mechanical property for UHPC is its compressive strength, although other important parameters were laid out in Chapter 1. A list of these parameters and corresponding test procedures to evaluate these parameters is shown below. Carrying out all these tests is beyond the scope of the research in this project, but the most important ones will be covered. This section provides a broad overview of past work in many of the topics listed below, in an attempt to guide the work in this study.

Compressive Behavior	Closed loop stress-strain tests, confinement, ductility, Poisson's ratio
Tensile Behavior	Closed-loop tension tests, tensile stress-crack width relationship
Shear Behavior	Structural and material tests in the presence and absence of rebars
Bond Behavior	Bond of UHPC with ordinary concrete, shear strength of the interface
Effect of Fibers	Fiber-matrix interaction, bond-slip, fiber pullout tests, interface effects of hooked or twisted fibers
Creep	Compression creep, tension creep, time dependent behavior
Shrinkage	Free and restrained shrinkage behavior, crack width in restrained shrinkage, effect of water-cement ratio and cement content on shrinkage
Thermal Properties	Thermal coefficient of expansion, curing
Cyclic Loading	Cyclic strength and stiffness degradation under fatigue loading, tension and compression
Impact Resistance	Drop weight test, strain rate effects
High Speed Testing	Strain rate effects

The standard test procedures available for evaluating the compression strength (ASTM C39/C39M or EN 12390-3) and elastic modulus (ASTM C469/C469M or EN 12390-13) of ordinary concrete are used for testing UHPC specimens as well. Size of the specimen has been found to significantly affect the mechanical properties of UHPC. (Magureanu et al. 2012) tested prismatic UHPC specimens under flexure loading and found that the flexural strength increased by about 50 percent when the size of the specimens reduced from 100 x 100 x 300 mm (3.94 x 3.94 x 11.81 in.) to 40 x 40 x 160 mm (1.57 x 1.57 x 6.29 in.). Skazlić et al. (2008) investigated the effect of test specimen geometry on the compression strength of UHPC. They detected that compressive strength of cylindrical specimens increased by 20 percent when the size reduced from 100 × 200 mm (3.94 × 7.87 in) to 70 × 140 mm (2.75 × 5.50 in).

(Bencardino et al. 2008) studied the effect of fiber factor on the failure behavior of UHPC specimens. Fiber factor is a function of the fiber volume fraction and geometry. Bencardino showed that the incorporation of steel fibers changes the UHPC failure mechanism from explosive brittle failure to a

ductile failure. They also related the direct influence of fiber factor on the mode of failure. Wille et al. (2011a) studied the direct tensile behavior of 10 fiber-reinforced UHPC (also referred to as UHPFRC) mixtures containing either smooth, deformed, or twisted fibers. The specimens containing deformed or twisted fibers demonstrated higher tensile strengths than those containing smooth fibers. They determined that the deformed fibers underwent higher deformation and dissipated more energy, which ultimately resulted in an increase in the fiber-matrix interaction and therefore tensile strengths.

The post-peak response of a specimen under compression can be determined using a closed-loop strain-controlled test. However, the use of axial strain control may lead to an unstable failure of the specimen because of sudden release of strain energy. A two-stage process has been implemented to solve this problem (Ariño and Mobasher 1999). During the first stage, the axial strain is used as the control parameter. The second stage is radial strain controlled and is initiated just prior to reaching the peak load.

The tensile strength of UHPC, both before and after tensile cracking, is significantly higher than that of normal concrete (Benjamin A. Graybeal 2006). This is of significance to designers working with UHPFRC elements where the non-negligible post-cracking tensile behavior may be used as a design parameter. Although several studies have conducted direct as well as indirect tensile tests on UHPC specimens, the availability of a standard procedure remains to be established.

The compressive strength of UHPC has been found to be a function of the curing methods (heat curing, steam curing etc.). An FHWA study (Benjamin A. Graybeal 2006) reported that steam-based treatment of UHPC significantly enhances the material properties as compared to curing in water. Three steam-based treatments − steam, delayed steam, and tempered steam − were compared with a curing treatment that did not involve steam after casting. Two other studies conducted on curing techniques for UHPC specimens (Magureanu et al. 2012; Prem, Murthy, and Bharatkumar 2015) also found that heat curing resulted in an increase in compressive strength between 30-50 percent as compared to water curing.

Flexure strength testing can be carried out to determine the flexural strength (ASTM C78/C78M for 4-point bending or C293/C293M for center-point loading) or the load-deflection behavior (ASTM C1609/C1609M) of UHPC specimens. A study by FHWA showed that the ASTM C1018 prism flexure test provided means of comparing the post-cracking tensile behavior of various UHPFRCs (Benjamin A. Graybeal 2006).

The two parameter fracture method (TPFM) can be used to characterize the fracture properties of UHPC. The fracture parameters such as the critical stress intensity factor (K_{IC}^{S}) and the critical crack tip opening displacement ($CTOD_C$), can be calculated from three-point bend tests on notched beams, as shown in Figure 18 (a). TPFM involves the use of loading and unloading compliances, peak load, specimen and notch geometry, and a geometry correction factor, to determine the values of K_{IC}^{S} and $CTOD_C$. A typical load-CMOD plot is shown in Figure 18 (b) with the loading and unloading compliances.

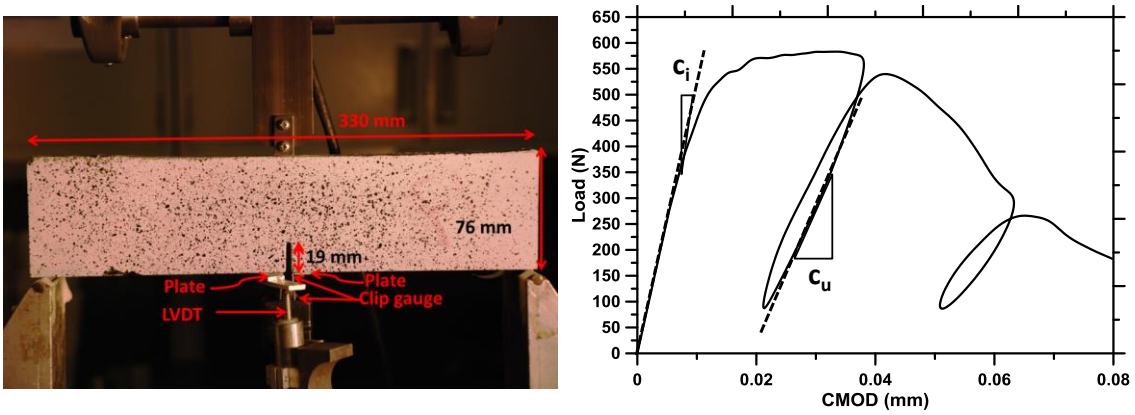

(a) (b)

Figure 18. (a) Experimental setup for the notched beam fracture test, and (b) a typical load-CMOD plot showing loading and unloading compliances (Das et al. 2015b)

In addition to the ASTM and EN standards discussed, many other standards are available to evaluate the flexural properties of fiber-reinforced cementitious systems such as UHPFRCs. One such method to evaluate flexural toughness of prismatic unnotched UHPFRC specimens is detailed in the Japan Concrete Institute standard, JCI-SF4.

Research (Benjamin A. Graybeal 2006) also suggests that UHPC shrinks more than conventional concretes, because of the higher binder content in UHPC mixtures, as well as the autogenous effects of very low water-to-binder ratios. It has been mentioned that the initiation of shrinkage in UHPC is affected by their delayed set times; the majority of the shrinkage occurs in a short time just after the concrete has set (Benjamin A. Graybeal 2006). Restrained shrinkage tests can provide indications of cracking susceptibility of UHPCs and potential means to mitigate them. The influence of fibers on improving the shrinkage behavior of UHPC also needs to be considered.

The fiber bond strength has been evaluated for fiber reinforced composites and studies have described the test setup as well as the influence of loading conditions on the test results (Grünewald 2004; Markovic 2006; Antoine E. Naaman et al. 1991; Banthia and Nandakumar 2003; Macedo, e Silva, and Martins 2010). No standard ASTM and EN procedures are available for fiber pullout testing.

Durability

Durability of concrete subjected to various aggressive environments (e.g. marine environments with high chloride concentration, acids and bases attack, sulfate attack) has been a subject of research for many years. Many commonly advocated methods for durability enhancement of concretes rely on a reduction in the water-to-cement ratio of the mixture and the use of partial cement replacement materials that positively impact hydration. Thus, UHPC mixtures should inherently be more durable than conventional concretes. However, several factors that are less understood play a significant role in concrete deterioration. The commonly evaluated durability criteria for concrete include resistance to abrasion, water permeation, freezing and thawing, alkali-silica reaction susceptibility, and ionic penetration.

Abrasion Resistance

Abrasion resistance is a standard method (ASTM C944 2012, 944) to measure the relative wear resistance of concrete when subjected to a rotating abrading cutter. Graybeal (Benjamin Graybeal and Tanesi 2007) studied the abrasion resistance of UHPC specimens aged with and without steam curing, and found that the steam cured specimens showed an order of magnitude higher abrasion resistance. (Peyvandi et al. 2013) tested three replicate UHPC cylindrical specimens and concluded that UHPC reinforced by steel fiber shows a greater abrasion resistance than UHPC reinforced by PVA fiber. (Le, Nguyen, and Ludwig 2014) determined the abrasion resistance of UHPC with and without silica fume after 28 days using the BÖhme test. They formulated an abrasive index as a measure of the abrasion resistance and their findings suggest that the silica fume mixture performed significantly better than the mixture without silica fume.

Water Absorption

Water absorption or water sorptivity is a standard method (ASTM C1585 2013) used to evaluate the susceptibility of a concrete surface to water ingress. The mass of the concrete surface exposed to water is recorded at regular intervals and the rate of water absorption is calculated to evaluate two sorptivity values – the initial sorptivity and the secondary sorptivity, both of which are characteristic of the internal microstructure of concrete. (Safeer Abbas, Soliman, and Nehdi 2015) investigated the water absorption in UHPFRC and found that the rate of sorption was independent of the fiber length and had an inverse relationship with the fiber dosage. This points to fewer connected pores and a denser microstructure when steel fibers are used. (Ghafari et al. 2014) showed that as the amount of nano-silica in the UHPC was increased up to four percent by mass of cement, there was a corresponding decrease in water absorption of up to 30 percent.

Freeze-Thaw Resistance

Freeze-thaw resistance is a standard method (ASTM C666-15) to quantify the resistance of concrete to freeze-thaw cycles. (Benjamin Graybeal and Tanesi 2007) conducted a long-term feeeze-thaw study in UHPC prism specimens placed in a water bath with the temperature cycling between -18 °C and 4.4 °C. The experiment was completed over a nine-month period and the results showed high resistance to freeze-thaw degradation in UHPC specimens. The results were independent of the curing method used prior to testing.

Alkali-Silica Reaction (ASR)

Alkali-silica reactivity of concrete is determined according to (ASTM C1260 2014). (Benjamin Graybeal and Tanesi 2007) conducted ASR study on UHPC mixtures containing no coarse aggregates. The UHPC bars were submerged in a 1 M sodium hydroxide solution maintained at 80°C for an extended duration of four weeks and their expansion was measured after 14 and 28 days of casting. They found that UHPC mixtures performed an order of magnitude better than the recommended expansion values prescribed by the standard. This study concluded that, due to the high reactive silica content that is utilized in the formation of a low Ca/Si ratio C-S-H gel and the low permeability of UHPC, ASR is not likely to occur. After 600 days, (Moser, Pfeifer, and Stark 2009) also studied ASR on UHPC and conducted the ASR

expansion test for 600 days. Their study determined the ASR expansion of UHPC to be at 0.02 percent which is 50% lower than the threshold value.

Chloride Permeability

Chloride permeability testing can be carried out using the rapid chloride permeability test (RCPT) ("ASTM C1202-12. Standard Test Method for Electrical Indication of Concrete's Ability to Resist Chloride Ion Penetration," 2012), which is a method to assess the chloride ion resistance of concrete. This test applies a 60-volt electrical potential difference across a concrete specimen 50 mm in thickness and 100 mm in diameter for six hours. (Benjamin Graybeal and Tanesi 2007) observed that the charge passed through the UHPC specimens cured for 28 or 56 days was negligible when measured according to this standard, thereby indicating very high resistance to chloride penetration. Another study conducted on chloride resistance of UHPC (Safeer Abbas, Soliman, and Nehdi 2015) showed negligible chloride permeation in UHPC specimens beyond 28 days.

History of UHPC Applications

Owing to its superior mechanical properties, UHPC has been used several structural applications, such as repair, rehabilitation, and retrofitting of existing structures, as well as in the construction of new infrastructure. The first ever large-scale construction project with UHPC was done in 1997 on a pedestrian bridge in Canada. This was soon followed by another UHPC bridge on the Bourg lès Valence bypass in Drôme, France in 2002 (Simon et al. 2002; Sorelli, Fanning, and Toutlemonde 2006), the first of its kind to carry vehicle traffic. Since then, several UHPC projects have been realized till date. Over 90 completed bridges using UHPC have been reported (S. Abbas, Nehdi, and Saleem 2016b; FHWA 2011). (Hadl et al. 2015) investigated the application of UHPC in the renovation of an existing motorway bridge in Austria and found that a thin layer of UHPC was sufficient to replace the waterproofing and the existing asphalt layer, due to its excellent durability and high load bearing capacity.

UHPC has recently been utilized in Ontario, Canada to connect precast segments for accelerated bridge deck construction (Perry, Krisciunas, and Stofko 2014; Young and Boparai 2013). This is estimated to have extended the life of the deck by more than 75 years, which is the typical design life of a traditional concrete bridge deck. The response of UHPC used as joint connections was studied by Graybeal (Benjamin A. Graybeal 2011) who found that the failure stress of UHPC under cyclic truck wheel loading was three times higher (197 MPa or 28600 psi) as compared to ordinary concrete (60 MPa or 8700 psi) for regular concrete.

Gunes et al. (Gunes et al. 2012) discussed the design of bridge structures using UHPC. Their study outlined the benefits of UHPC to design thin beam sections for the same span or alternatively design longer beam spans for the same cross-section as compared to ordinary concrete. Recent studies (Reichel, Sparowitz, and Freytag 2011; Freytag et al. 2009) have demonstrated the use of UHPC in creating complex arch sections. UHPC has also been shown to improve the service life of deep foundations (Suleiman, Vande Voort, and Sritharan 2010). Numerous other studies have explored the application of UHPC as waffle panels on bridge decks (Honarvar et al. 2016), for shear connections (Voo, Foster, and Voo 2015), in lightweight bridge deck systems (Ghasemi et al. 2016; S. Abbas, Nehdi, and

Saleem 2016b; Reichel 2009), and for accelerated construction (Royce 2014). (Zohrevand and Mirmiran 2013) investigated UHPC-filled tube columns with fiber reinforced polymer under seismic loading and found that the UHPC specimens outperformed the conventional concrete specimens subjected to the same loading conditions.

Summary

This chapter has presented a concise review of available literature on the raw materials used in UHPC, the mixing and curing procedure, and the different test procedures adopted to ascertain the fresh and hardened properties of UHPC. According to the literature review, the selection of raw materials (cementitious powders, such as cement, fly ash, silica fume, metakaolin, and limestone) on the basis of their chemical composition and mixture proportioning is the most important step to achieve maximum packing density of UHPC mixtures, which in turn is vital to formulate the most economical UHPCs.

In addition, the water-to-binder ratio and the amount of superplasticizer in the mixture are critical components that affect the mechanical strength development and the flowability of the mixture, respectively. Based on the literature reviewed, a water-to-binder ratio of 0.18 to 0.24 is ideal for UHPCs; therefore, this range will be used for the preliminary evaluation of trial mixtures in this study.

Based on past work, a superplasticizer content varying between two percent and five percent by weight of the binder can also be considered as the starting point. The exact superplasticizer dosage would be determined by the flowability of the UHPC mixture. The mixing and curing procedures mentioned in the literature will be used as the starting point and fine-tuned to arrive at standard procedures that are applicable for economical UHPCs designed as part of this work. The different test methods reported in the literature, with appropriate modifications, will ensure that mechanical and durability properties of the designed UHPCs are captured adequately in this study.

Chapter 3 OVERVIEW OF MATERIAL DESIGN METHOD FOR NON-PROPRIETARY UHPC

Introduction

This chapter provides an overview of material design to develop non-proprietary UHPC mixture formulations with performance capabilities similar to those of proprietary UHPCs. These formulations use a low water-to-binder ratio (w/b) of 0.24 or less as well as a high dosage of chemical admixtures; and incorporate supplementary cementitious materials such as slag, fly ash, and metakaolin to be able to achieve target strengths in excess of 22,000 psi (150 MPa) at 28 days. The following key topics are addressed.

- Fundamental steps involved in the design of UHPC.
- Strategy for UHP paste design.
- Process to select the appropriate aggregate proportions for UHPC
- Methods to evaluate the mechanical response and long-term durability of UHPC.

Figure 19, Figure 20, Figure 21 show the strategies implemented to obtain the optimized design of UHPC. The research approach is built around three fundamental steps: binder (paste) design, aggregate packing and optimization, and testing the final properties of the material. The first step is the binder design as Figure 19 shows. This step consists of selection of the source materials for the binder from a series of common cementing (or cement replacement) materials such as ordinary Portland cement (OPC), fly ash, silica fume, metakaolin, and slag. The selected components and their mass fractions are evaluated in an attempt to ensure maximum packing of the powder ingredients. The flowability of the selected binders at very low w/b, and in the presence of large amounts of chemical admixtures, is evaluated using fundamental rheological experiments. The goal is to use a blend of the cementitious materials that can be mixed with a very low w/b ratio and, with the aid of superplasticizers, can result in flowable and workable mixtures. In the second step, the packing of selected coarse and fine aggregates and fibers is optimized, and used along with the binders that demonstrated desirable performance. Selection of aggregates is based on a compressible packing model, which determines the maximum packing density using different sizes of coarse and fine aggregates. The packing efficiency reduces the capillary pores and therefore improves the strength and the impermeability significantly. This is shown in Figure 20. The finalized UHPC mixture(s) will be subjected to property-and-performance testing (see Figure 21) that includes mechanical testing (compression, tension, flexural, fracture) and durability evaluation (resistance to freezing and thawing, chloride penetration). Finally, a simple life-cycle cost analysis will be performed to inform the users of the overall cost and performance benefits from using the developed non-proprietary UHPC mixtures.

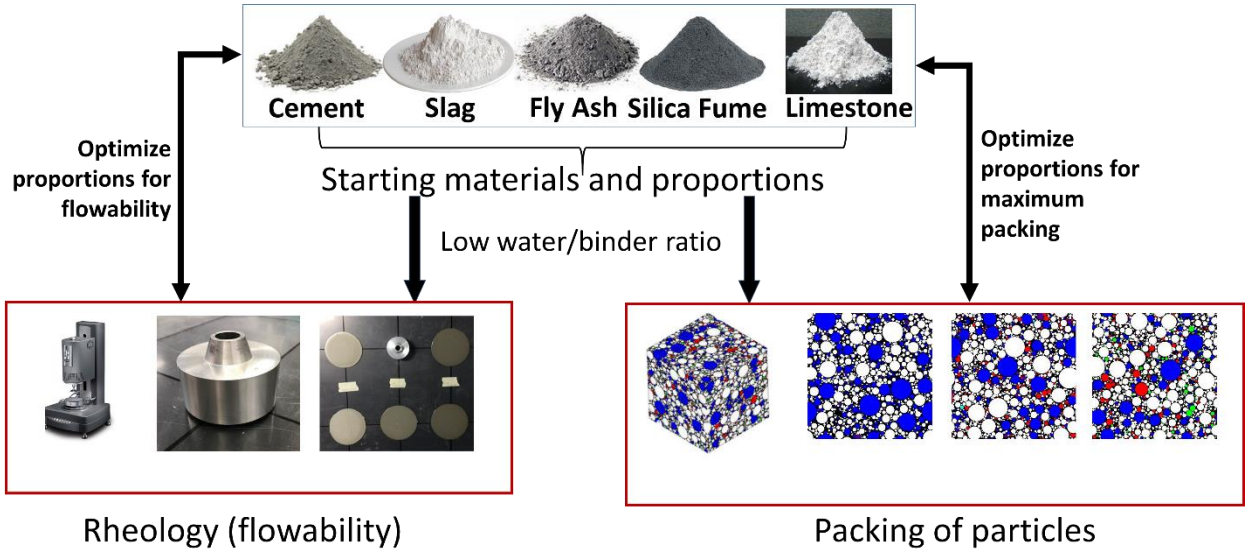

Figure 19. Schematic showing the binder (paste) design of UHPC

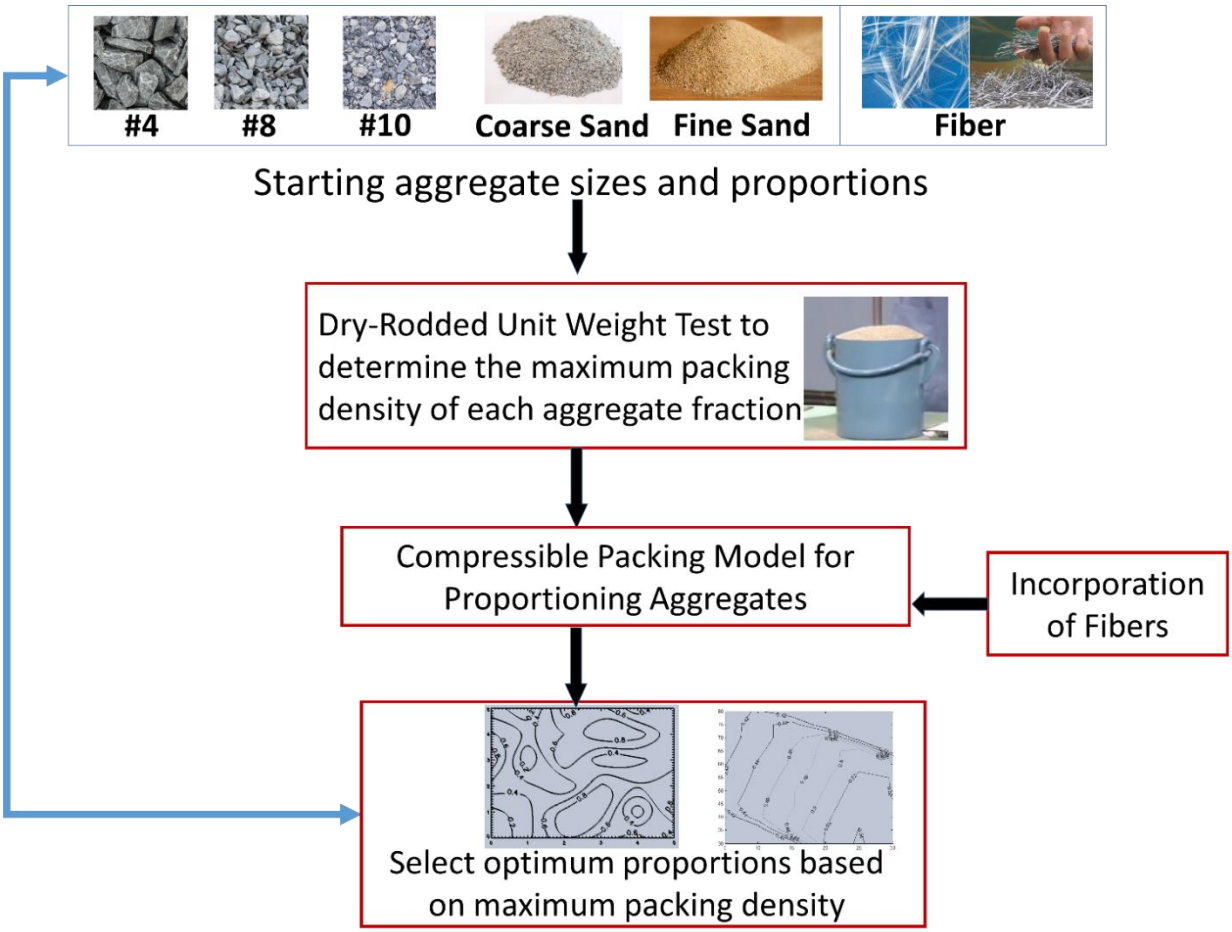

Figure 20. Schematic showing the aggregate packing of UHPC

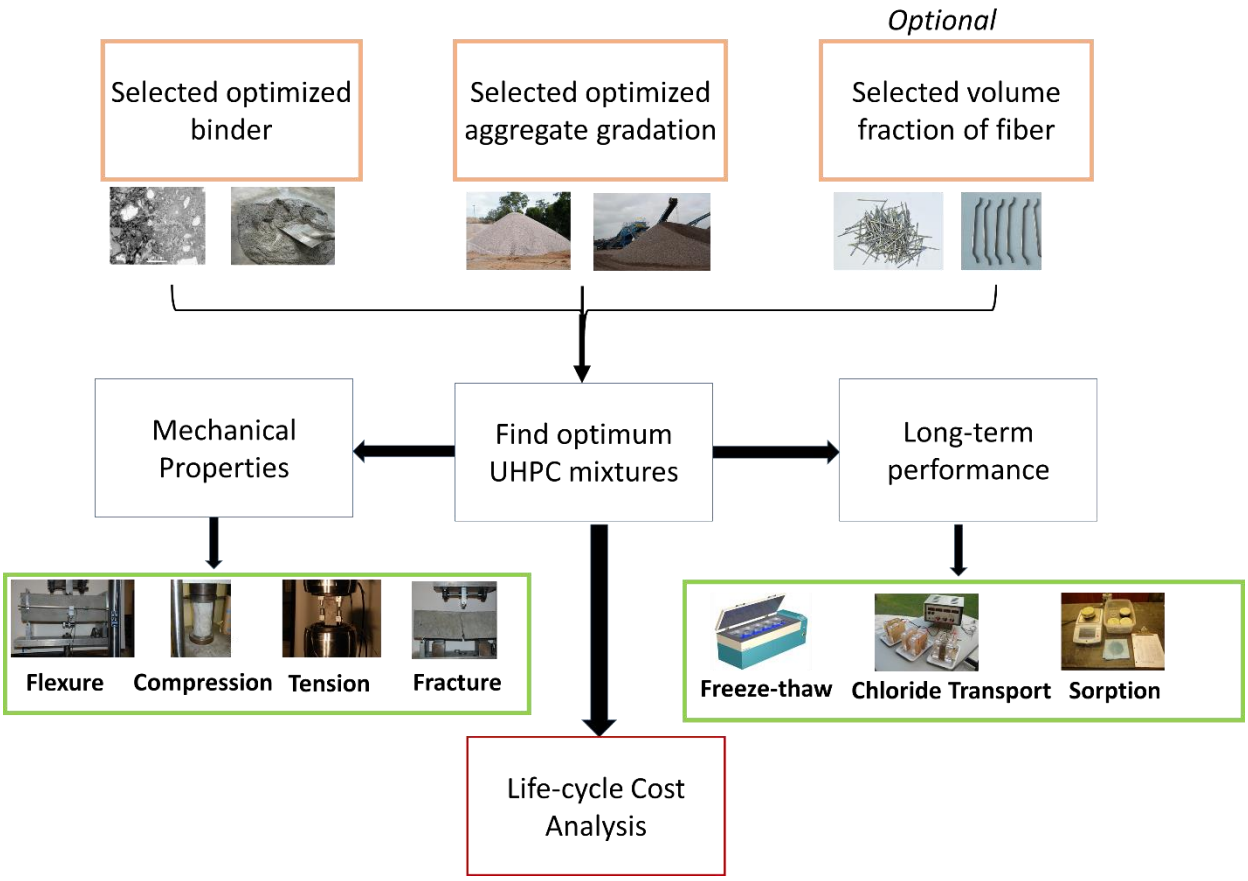

Figure 21. Schematic showing the overall design for UHP concretes and testing methods

Chapter 4 RAW MATERIALS, PRELIMINARY MIXTURES, AND STRENGTHS

Introduction

This chapter discusses the preliminary design of UHPC and examines the influence of various factors in the compressive strength of the preliminary mixtures. Following key topics are addressed.

- Basic raw materials used to design UHPC and their properties
- Influence of curing techniques and curing temperature on the compressive strength of UHPC
- Influence of the type of aggregate on the compressive strength of UHPC
- Determination of appropriate aggregate to paste proportion to obtain the highest compressive strength for a UHPC mixture.

Overview

The materials used for the preliminary mixture study include a Type I/II OPC conforming to ASTM C 150, Class F fly ash and metakaolin conforming to ASTM C 618, slag conforming to ASTM C 989, limestone powder conforming to ASTM C 568, and micro silica (silica fume) conforming to ASTM C 1240. All of these materials are commercially available in Arizona and none is proprietary. Limestone powders with two different median particle sizes (1.5 μm and 3.0 μm) were used to ensure improved particle packing. The idea of blending so many ingredients and components is to support the final packing density goal and ensure both physical space filling and chemical reactivity. Table 2 shows the chemical composition of the materials, while Figure 22 shows their particle size distribution (with the median size in microns in parentheses). The differences between the rates of reactivity, particle size, and chemical and surface affinity of the particles will ensure that the reactions occur quickly, are locally controlled within the microstructure, and progress in a time-released fashion.

Table 2. Chemical composition of starting materials used

Components of the binder	Chemical composition (percent by mass)						
	SiO_2	Al_2O_3	Fe_2O_3	CaO	MgO	SO_3	LOI
OPC	19.60	4.09	3.39	63.21	3.37	3.17	2.54
Slag (S)	39.41	8.49	0.37	35.53	12.05	2.83	1.31
Fly ash (F)	58.40	23.80	4.19	7.32	1.11	3.04	2.13
Metakaolin (K)	51.70	43.20	0.50	-	-	-	0.16
Micro silica (M)	> 90.0	-	-	< 1.0	-	-	-

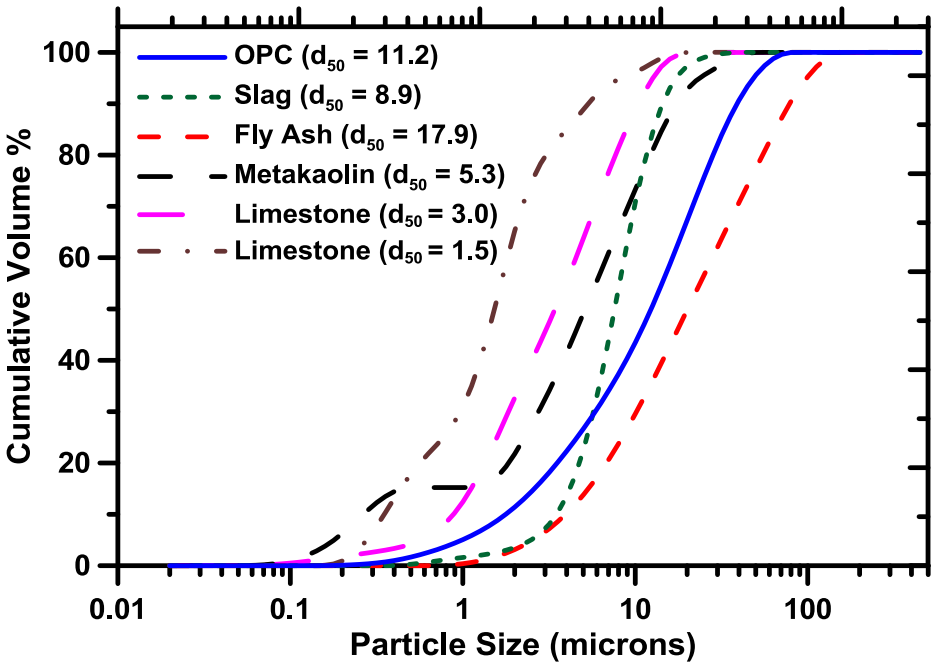

Figure 22. Particle size distribution plots for OPC, slag, fly ash, metakaolin, and limestone powders

Trial mixtures

Initial trial mixtures reported here are based on the literature review and prior experience. A sample set of five mixtures was designed to evaluate the effect of multiple cementing materials at early ages. Supplementary cementitious materials used included ground granulated blast furnace slag, Class F fly ash, dry densified silica fume (micro-silica), nano silica (NS) and metakaolin. Table 3 lists the mixtures considered for this part of the study. The overall cement replacement considered here was limited to 20 percent by weight of cement to make sure that these mixes were workable at the lower water content used. The main purpose of this portion of the study was to help formulate a mixing procedure for low w/b pastes or mortars.

Table 3. Mixture proportions for initial mixes evaluated in the study

Mixture Composition	Replacement material (percent by mass of cement)	
	Fly Ash (F)	Micro Silica (M)/Nano Silica (NS)/Metakaolin (K)
OPC	-	-
M15	-	15
M20	-	20
K10F10	10	10
F17NS0.5	17	0.5

Mixing and curing procedure

All mixtures were prepared using a mass-based w/b ratio of 0.22 to 0.24 and a superplasticizer content of 4 percent by mass of the cementitious materials. The powders were dry-mixed in a Hobart mixer [Figure 23(a)] for 5 to 10 minutes. The dry mixed powder was then added to an Omni high shear mixer [Figure 23(b)]. A third of the total amount of required water and superplasticizer was added to the dry powder and mixed for at least five minutes. The procedure was repeated until all of the water and superplasticizers were mixed in, each time at high speed. The mixing process continued until a cohesive final mixture was obtained. The silica fume mixtures took longer to mix than the mixtures containing fly ash, because the large diameter and spherical size of fly ash particles help make the mixture more workable and thereby reduce the mixing time. The blended mixes were poured in cubical molds [Figure 23(c)] and stored in an environmental chamber at greater than 98 percent RH for 24 hours before demolding. The demolded cubes were cured using two different curing regimes. One set of cubes was stored in the environmental chamber at a temperature of 23 ± 2 degrees Celsius (C) and greater than 98 percent RH. Another set was stored in a water bath [Figure 23(d)] set at 80 degrees C to estimate the impact of heat curing on the compressive strengths.

Figure 23. (a) Hobart mixer, (b) Omni high shear mixer, (c) cubical molds used for casting, and (d) water bath

Strength results

Figure 24 shows the compressive strengths of the trial mixtures at early ages. Strengths as high as 12,000 psi (80 MPa) were obtained at seven days for most of the mixtures. The strengths were comparable to that of plain OPC mortar, which also achieved 12,000 psi (80 MPa) strength at 7 days. The micro-silica mixture with 20 percent overall cement replacement was expected to attain a higher strength than the one with a cement replacement of 15 percent. However, the mixture with 20 percent cement replacement achieved a lower strength at seven days, which indicates that micro-silica particles present in the mixture with a higher micro-silica content did not disperse well in the cement paste.

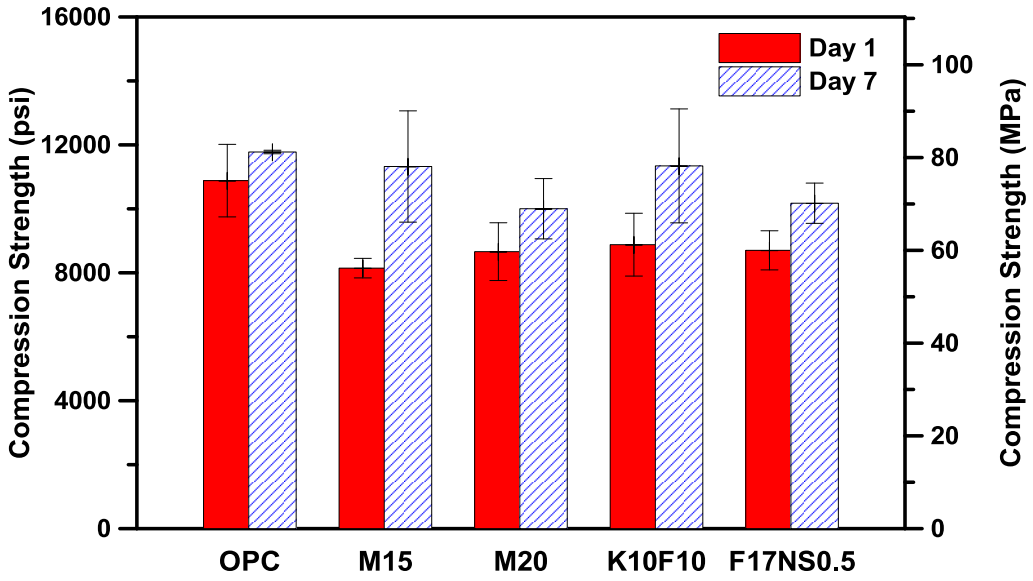

Figure 24. Compressive strengths of mortar mixtures studied on Day 1 and Day 7

Figure 25 shows the comparison of the strength results for the two curing techniques used. Curing at high temperature using a water bath leads to an increase of about 10 to 20 percent in the compressive strengths at seven days. However, although water bath curing would be an effective technique to produce high-strength concrete in a precast environment, it is not feasible for use in the field. In addition, water-bath curing is energy-intensive. To ensure that the UHPCs developed in this study can be replicated as cast in place under field conditions, heat curing is not adopted for any of the mixtures in the remainder of this study. Any of the mixtures developed, however, can also be evaluated for elevated temperature curing.

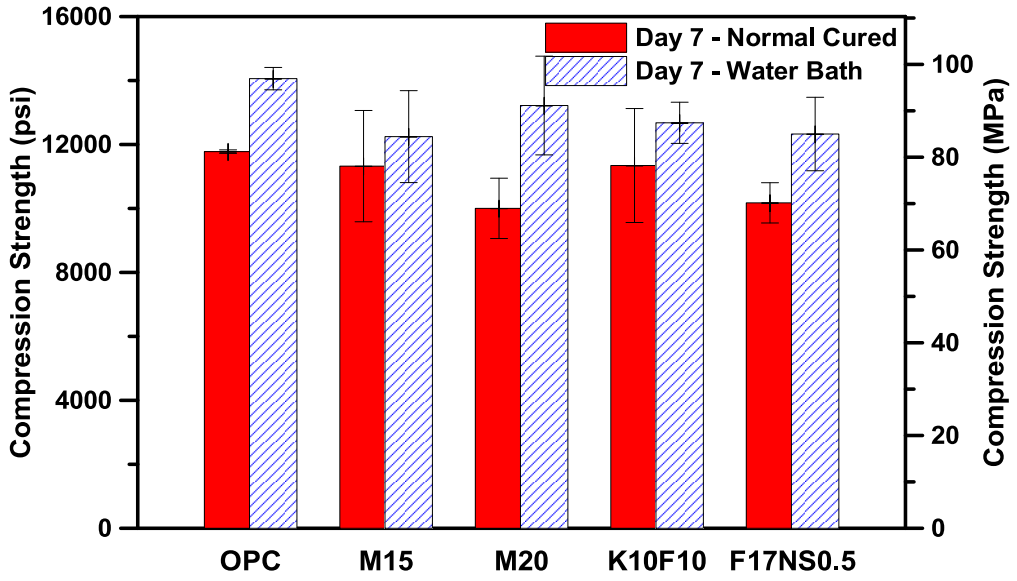

Figure 25. Comparison of high temperature curing using water bath versus normal curing at room temperature

Influence of different parameters on compressive strength

To determine the influence of several material and treatment options on the compressive strength of UHPC, six mortar mixtures were formulated, as shown in

Table 4. All of these mixture compositions were formulated using fly ash as the primary cement replacement material. This was done to ease the mixing process, since the spherical geometry of fly ash particles allows for better workability of the paste as compared to plain cement paste or the pastes containing micro-silica or metakaolin as the primary cement replacement material. Metakaolin, micro-silica and limestone (L) were used as secondary cement replacement materials. The limestone used here had a median diameter of three microns (Figure 22). A water-to-binder ratio of 0.24 and 4 percent by mass of superplasticizer was used for all the mixtures except HPC (high-performance concrete), which is a plain OPC mixture with a water-to-cement ratio of 0.32. The factors studied included the curing technique, the type of fine aggregate, the paste-to-sand ratio, and the compression testing technique. The mixing procedure was similar to the one used for the initial set of mixes, as described earlier.

Table 4. Mixture proportions for mixes evaluated in the second phase of the study

Mixture Composition	Replacement material (percent by mass of cement)			w/b
	Fly Ash	Micro Silica/Metakaolin	Limestone	
OPC	N/A	N/A	N/A	0.24
HPC	N/A	N/A	N/A	0.32
$F_{20}K_{10}$	20	10	N/A	0.24
$F_{20}M_{10}$	N/A	20	N/A	0.24
$F_{17.5}K_{7.5}L_5$	17.5	7.5	5	0.24
$F_{17.5}M_{7.5}L_5$	17.5	7.5	5	0.24

Figure 26, Figure 27, Figure 28show the compressive strengths of the mixtures under the different conditions studied. In Figure 26(a), wet curing refers to curing in the moist chamber at a relative humidity greater than 98 percent, and dry curing to curing at atmospheric RH and room temperature. Wet curing was observed to be slightly more effective than dry curing. Following this result, another set of samples was cured in the moist chamber, keeping half of them submerged in water and the other half covered under plastic sheets. The cubes were tested for compressive strengths at days 3 and 7 [Figure 26(b)]. Neither method had a significant advantage over the other in compressive strengths. From the results in Figure 26(a) and (b), it was decided to cure the rest of the samples in the environmental chamber at high relative humidity (more than 98 percent) and covered under plastic sheets.

Figure 27(a) shows the variation of compressive strength of OPC mortar with two types of fine aggregate. The interlocking of fine aggregates helps in load transfer; therefore, an optimum gradation of fine aggregate is important to be able to withstand higher loads. Concrete sand (river sand with median size of 0.024 inch) and mortar sand (commercially available medium grit sand with median size of 0.019 inch) were used to cast mortars. Use of mortar sand improved strength by about 10 percent over concrete sand. Further, a 50:50 mixture of concrete sand and mortar sand by volume led to increased strengths as compared to mortar sand only. Therefore, a 50:50 mixture was identified as the fine aggregate to be used for future mixtures. Figure 27 shows the change in compressive strengths for quaternary fly ash mixtures with change in the paste to fine aggregate ratio. The mixture labels in Figure 27 with (“A”) are the ones proportioned with 65:35 paste to fine aggregate content by volume, while the rest are proportioned with a 50:50 paste to fine aggregate content by volume. The mixtures with a paste to fine aggregate ratio of 65:35 have about 10 percent higher strengths than those with 50:50 ratios. Hence the paste to aggregate ratio was chosen to be 65:35 by volume. Figure 28 shows the comparison of compressive strengths when mortars were air dried for 24 hours prior to testing, as opposed to

testing immediately after removal from the curing chamber. A significant improvement of strength (approximately 5 to 10 percent) was observed in air dried samples.

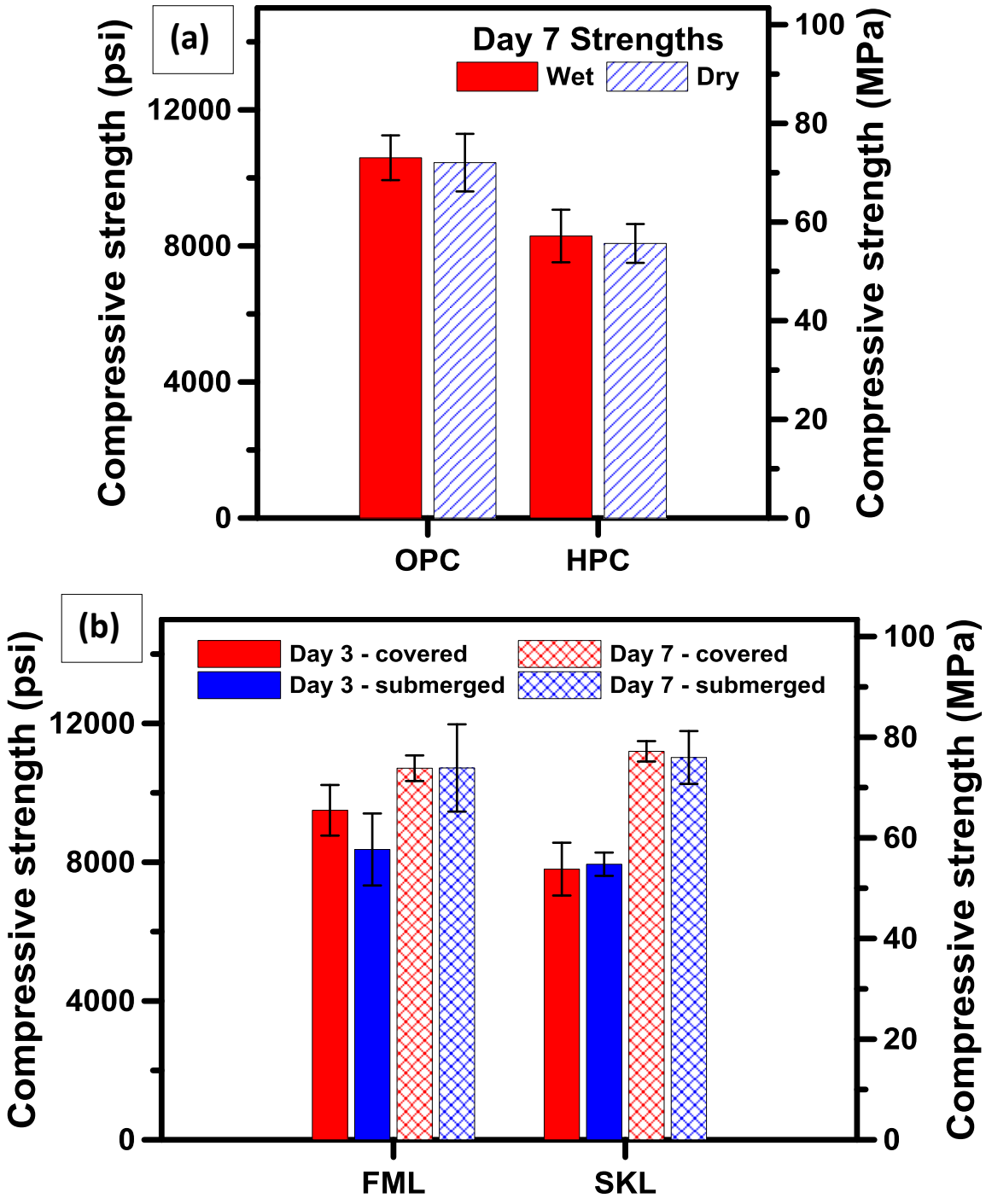

Figure 26. Plots showing the comparison in compressive strength values for (a) wet condition versus dry condition, (b) covered versus submerged curing regimes

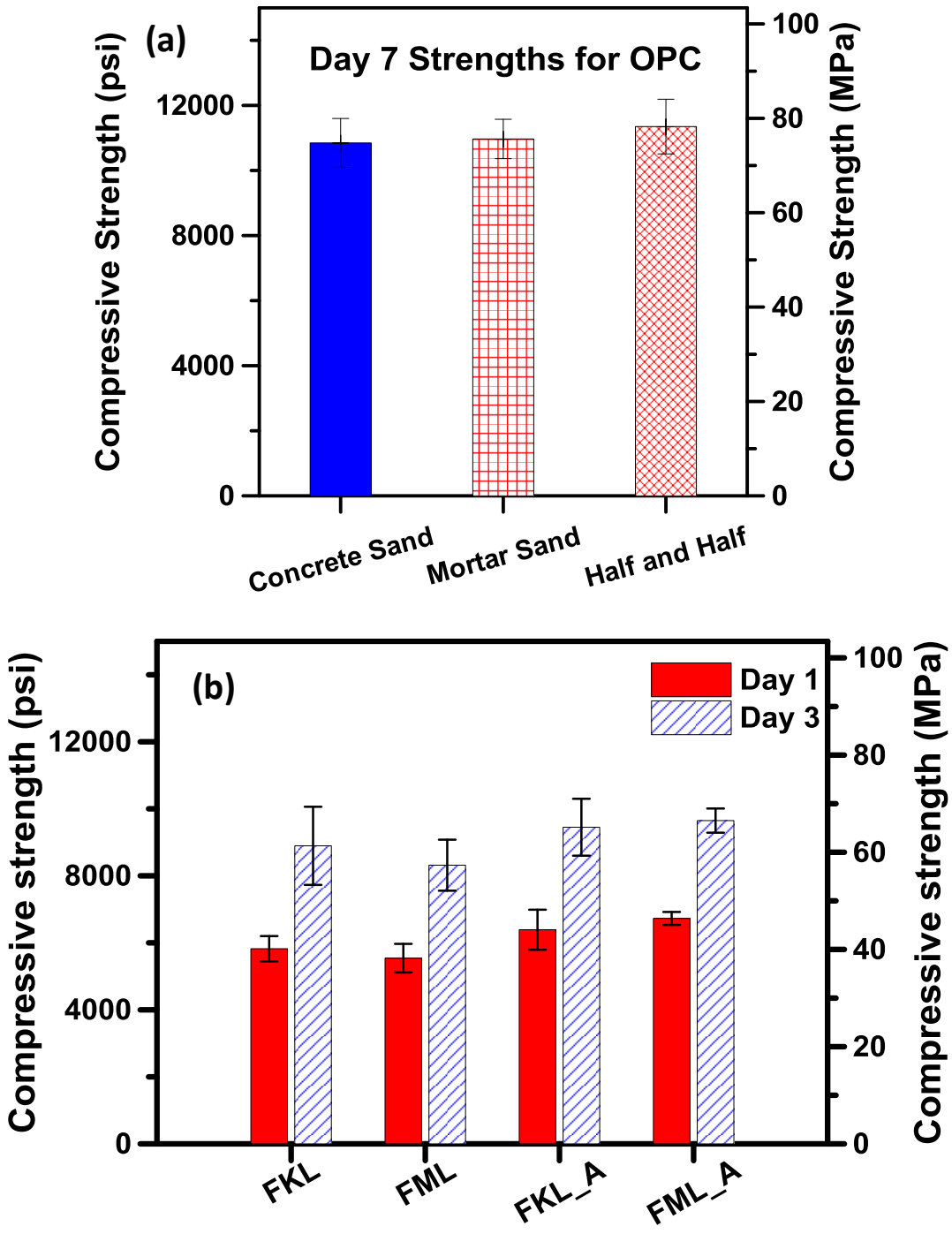

Figure 27. Plots comparing compressive strength values for (a) effect of type of fine aggregate concrete sand versus mortar sand on 7-day strengths of OPC, and (b) effect of relative volume of paste and fine aggregate in the mixture

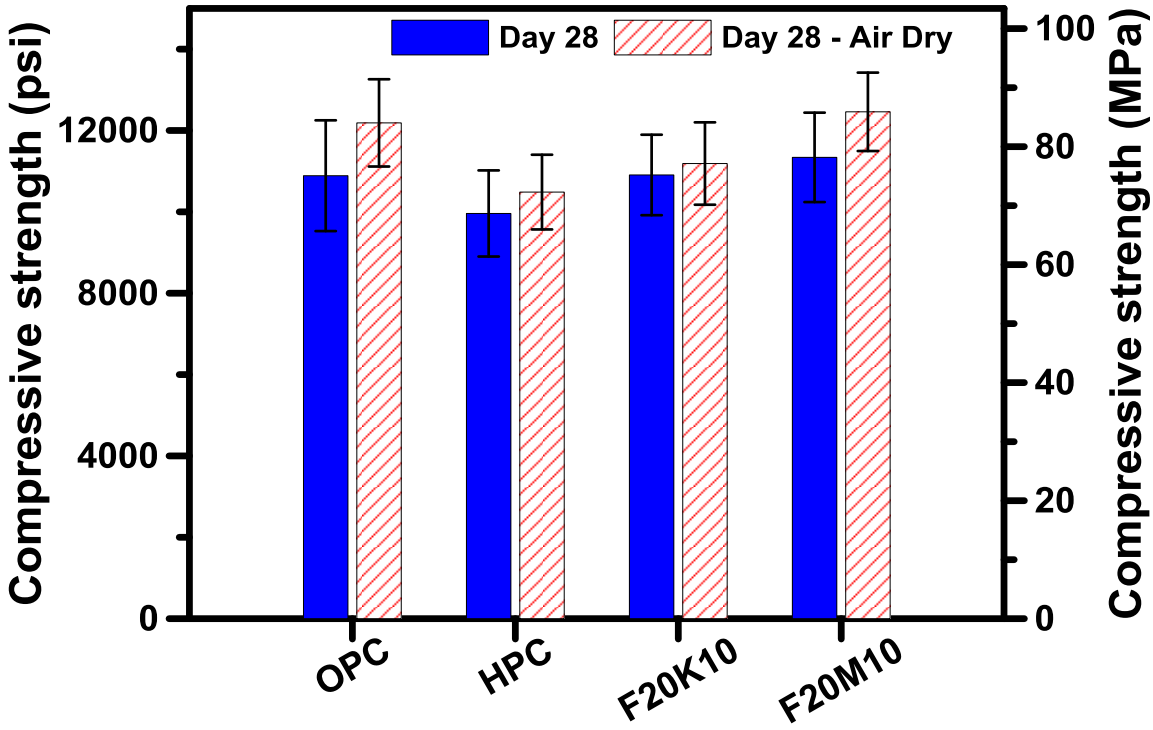

Figure 28. Comparison of normal testing versus air drying for compressive strength

Chapter 5 DETAILED STUDIES TO DESIGN UHP PASTES AND MORTARS: A SCIENTIFIC APPROACH BASED ON PARTICLE PACKING AND RHEOLOGY

Introduction

This chapter lays the foundation for a first principles-based approach to designing UHPC. It builds on the previous chapter which explored several factors that influence the strength of UHPC and utilizes the results to move forward towards a more fundamental method to understand and develop UHPC mix designs. Following key topics are addressed.

- Determination of criteria to design UHPC mixture from available materials.
- Assessment of any given mix design on the basis of particle packing and rheology and determination of its suitability for ultra-high performance.
- Mixing and curing procedure used to make UHPC mortars.
- Mechanical strength evaluation of selected UHPC mixtures.

Mix designs – evaluation for packing and rheology study

The preliminary investigations were intended to characterize the mixing efficiency as well as the procedures for blending mixtures with low w/b ratios. In order to document the process, certain key parameters affecting the compressive strengths of the mixtures were used as the primary indicators of efficiency. The objective of this chapter is to obtain ultra-high-performance pastes through a microstructure- and rheology-guided design, and then to cast these mixtures as mortars to obtain compressive strengths. For the pastes, the cement replacement level generally varied between 20 and 30 percent by mass of OPC.

In the ternary and quaternary blends, the replacement levels of fly ash or slag varied between 10 and 25 percent, while those of silica fume or metakaolin varied between 7.5 and 10 percent. Fly ash or slag were considered to be the primary cement replacement materials in ternary and quaternary blends because of their abundance and the larger OPC replacement levels that can be accomplished.

A total of 33 mixtures were evaluated in the initial phase of this work as identified by HP and UHP pastes and mortars referring to high-performance and ultra-high-performance samples. The breakdown of these mixtures was one UHP-control, one HP-control, and 31 UHP pastes. All the UHP pastes were proportioned using a volumetric water-to-powder ratio, $(w/p)_v$, of 0.63 (corresponding to a mass-based $(w/p)_m$ of 0.20). The ratio is adjusted to 0.22 when the water in the superplasticizer is also included in the calculations. In addition to the control UHP paste ($(w/p)_m$ of 0.20), a high-performance OPC paste (HP-control) with a $(w/p)_m$ of 0.32 was proportioned for comparative purposes. A commercially available superplasticizer (Master Glenium 7500, manufactured by BASF) was used at five percent by mass of the powder to improve the workability of the UHP pastes.

Table 5 shows the proportion of the mixtures used. UHP-control refers to the control mixture made using OPC alone and a $(w/c)_m$ of 0.20, and HP-control refers to the mixture made using a $(w/c)_m$ of 0.32. The HRWR dosage for the HP-control mixture was 2 percent by mass of the powder.

Table 5. Final mixture proportions for paste evaluated in this study*

Mixture composition	Replacement material (percent by mass of cement)			
	Fly Ash (F)/ Slag (S)	Metakaolin (K)	Microsilica (M)	Limestone (L); d_{50} of 1.5 or 3 µm[#]
UHP-control	0	0	0	0
HP-control	0	0	0	0
OPC + F/S	20, 30	0	0	0
OPC + M	0	0	10, 20	0
OPC + K	0	10	0	0
OPC + F/S + M	10, 20	0	10	0
OPC + F/S + K	10, 20	10	0	0
OPC + F/S + L	20	0	0	10_a, 10_b
OPC + F/S + L	25	0	0	5_a, 5_b
OPC + F/S + M + L	17.5	0	7.5	5_b,5_c
OPC + F/S + K + L	17.5	7.5	0	5_b,5_c

*All the pastes except HP-control were proportioned using a (w/p)m of 0.20.

[#]The subscripts ”a”, ”b” and ”c” along with the dosage of limestone powder indicate the type of limestone used in the mixture: ”a” = 1.5 µm limestone, ”b” = 3 µm limestone and ”c” = 50% 1.5 µm + 50% 3 µm limestone by mass.

Particle packing

In order to maximize the density of the mixture, the size distribution of the particles should be chosen such that the densest packing of particles varying in size is achieved. Sphere-packing theory is used to guide the design of mixes. The basis of sphere packing, also known as uniform packing, is shown in Figure 29. Figure 29(a) schematically illustrates the concept of a lattice consisting of a three-dimensional

array of particles with identical diameter. The problem gets more complicated when particles in the array have different diameters. The unit cell identified in the lattice represents the smallest repeating entities in a crystal structure. Figure 29(b) and (c) present two typical "theoretical" packing arrangements, referred to as body-centered cubic (BCC) and face-centered cubic (FCC). These arrangements are used to explain the idea of space filling using particles. In the former case (Figure 29[b]), if one considers a cube (illustrated by dark lines in Figure 29[a]), it consists of one-eighth of a particle at the vertices and one particle in the middle, thus providing the cube with two particles overall. In the latter case (Figure 29[c]), the vertices of the cube contain one-eighth of a particle, and each face contains half a particle, thus providing a total of four particles. The arrangements of the particles in such a manner changes the overall volume of the cube, but it is clear that more of the space in the cube is filled with particles in the latter case. The packing factor, also referred to as packing density or atomic packing factor (APF) when the arrangements of atoms in crystals are considered (which is broadly similar to filling particles in a unit volume to provide the densest configuration), defines the volume fraction of the solid particles in a unit cell and can be determined by computing the volume of spheres in the representative volume considered.

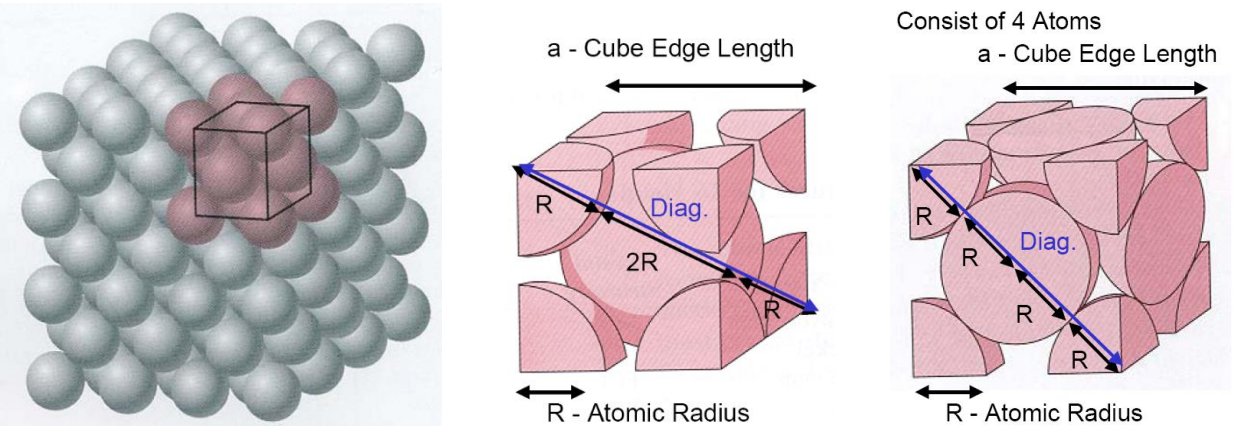

(a) (b) (c)

Figure 29. (a) Lattice and unit cell, (b) body-centered cubic (BCC), APF = 0.68, (c) face-centered cubic (FCC), APF=0.74

In the case of concrete mix design, however, the diameter of particles varies by a factor of 1,000, from 10^{-6} m to 10^{-3} m, where a uniform packing is not applicable. This difference of three orders of magnitude from the smallest to the largest particles complicates the calculation of packing densities. Therefore, random close packing (RCP) is used to achieve the maximum packing density of the mixture using all the given components. Instead of precise geometric definition, RCP is defined statistically, which requires a computer-aided computational model. The need is to define a specific volume (stipulated as a cube to make the computations easier) and pack the random particles in the cube so as to attain the maximum packing density. The cube is filled with particles one by one (iterative packing) until no more can be filled in.

Microstructure results

Microstructural models were created through iterative packing for all the paste mixtures, based on the particle size distribution of the component powders and their amounts. This information can be generated from sieve analysis or laser particle size analysis to measure the particle size distribution of individual phases. Figure 22 represents a starting point for the model where all the PSD for the ingredients of the paste phase are measured and reported from the manufacturers. The objective of this chapter is to analyze different aspects of particle packing that are important in influencing both the flow of the pastes and their mechanical properties. In order to accomplish this, a microstructural stochastic packing model with periodic boundary conditions was applied (D. P. Bentz 2005). The algorithm packs spherical particles in a three-dimensional representative element volume (REV), chosen here as 300 x 300 x 300 μm^3.

Figure 30(a) shows a representative virtual three-dimensional microstructure. Figure 30(b-d) show the two-dimensional slices corresponding to binary, ternary, and quaternary mixtures. Two-dimensional slices from the simulated three-dimensional microstructures are shown in (b) the binary OPC fly ash system, (c) the ternary OPC fly-ash-metakaolin system, and (d) the quaternary OPC fly-ash-metakaolin-limestone system. OPC is indicated in white, fly ash in blue, metakaolin in red, and limestone in green.

The binary mixture is formed using a combination of cement and fly ash particles, the ternary mixture using a combination of cement, fly ash, and metakaolin, and the quaternary mixture using a combination of cement, fly ash, metakaolin, and limestone. The mixture is designed based on the size distribution of the particles as well as the percentage of each component in the final mixture. The digital microstructures allow the extraction of several features that are influential in early and later age paste response. These parameters represent the characteristics of the blended powder mixture and include: the mean centroidal distance (MCD), coordination number (CN), and number density (N_d) as the key microstructural parameters that influence particle packing of the paste. These terms are explained as follows:

Mean Centroidal Distance (MCD) − the mean centroidal distance is a measure of the packing density of the microstructure. It is calculated as the average distance to the center of a given particle from the centroid of the microstructure.

Coordination Number (CN) − the coordination number is defined as the average number of nearest neighbor pairs in the microstructure. For any particle, the nearest neighbor is defined as a particle that lies either wholly or partially in the radial field of that particle, defined as a field with a radius of (r + i) µm, where "r" is the radius of the particle and "i" is the increment to the radius to define the field. When the CN determined using values of "i" and "i + 1" is relatively invariant, the corresponding CN value is used. By virtue of this, the coordination number represents the inter-particle contacts.

Number Density (N_d) − the number density is defined as the number of particles in a unit volume. The unit volume is measured in a three-dimensional microstructure in voxels, where a voxel is a three-dimensional representation of a pixel. It is directly related to the overall fineness of the powders in the paste.

More information on these microstructural parameters can be found in Arora et al. 2018.

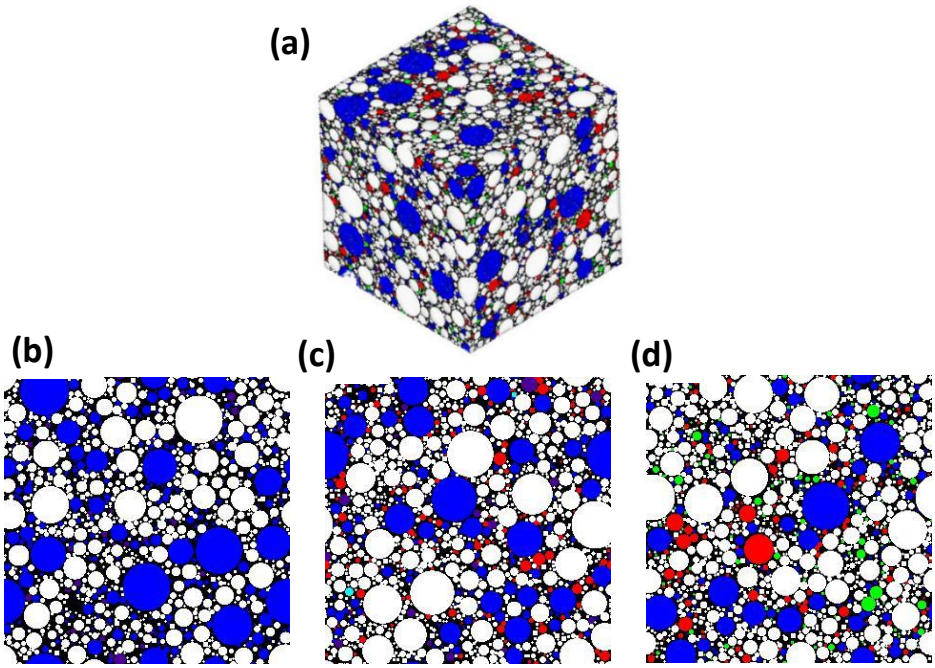

Figure 30. (a) RVE for a quaternary OPC-fly ash-metakaolin-limestone system. Two-dimensional slices from the simulated three-dimensional microstructures of: (b) binary OPC fly ash system, (c) ternary OPC fly-ash-metakaolin system, and (d) quaternary OPC fly-ash-metakaolin-limestone system. OPC is indicated in white, fly ash in blue, metakaolin in red, and limestone in green

Figure 31 shows the relationships between the microstructural parameters for the UHP pastes; filled symbols represent the values for the UHP-control pastes. As the number density increases, the mean centroidal spacing between the particles decreases and the coordination number increases. The coordination number and the number density indicate the inter-particle contacts in the microstructure, and thus can be related to the yield stress of the paste and its degree of hydration at early ages. Inter-particle contact density can be correlated with the degree of interlock that exists among particles. The greater the interlocking density, the higher the force required to activate and move the particles past one another. This correlates with the yield strength as measured in the rheology experiments. The slump of concrete is related to the yield stress between the particles, because flow requires overcoming the inter-particle stresses.

Plastic viscosity depends heavily on the solid volume fraction (and thus the surface contacts) in the paste, thereby relating to the above-mentioned parameters. These microstructural parameters can be considered to influence both the rheology and hydration in cementitious materials. The influence of improved particle packing of the paste on the mechanical and durability properties of cementitious mixtures, as well as their role in economizing concrete mixtures, is well documented (de Larrard and Sedran 1994; Lange, Mörtel, and Rudert 1997). For example, improved particle packing leads to a denser microstructure, and with cement hydration, the pore spaces can be filled more effectively. A denser microstructure also leads to disconnected pore space, thereby improving the durability of concrete, as will be shown in Chapter 9.

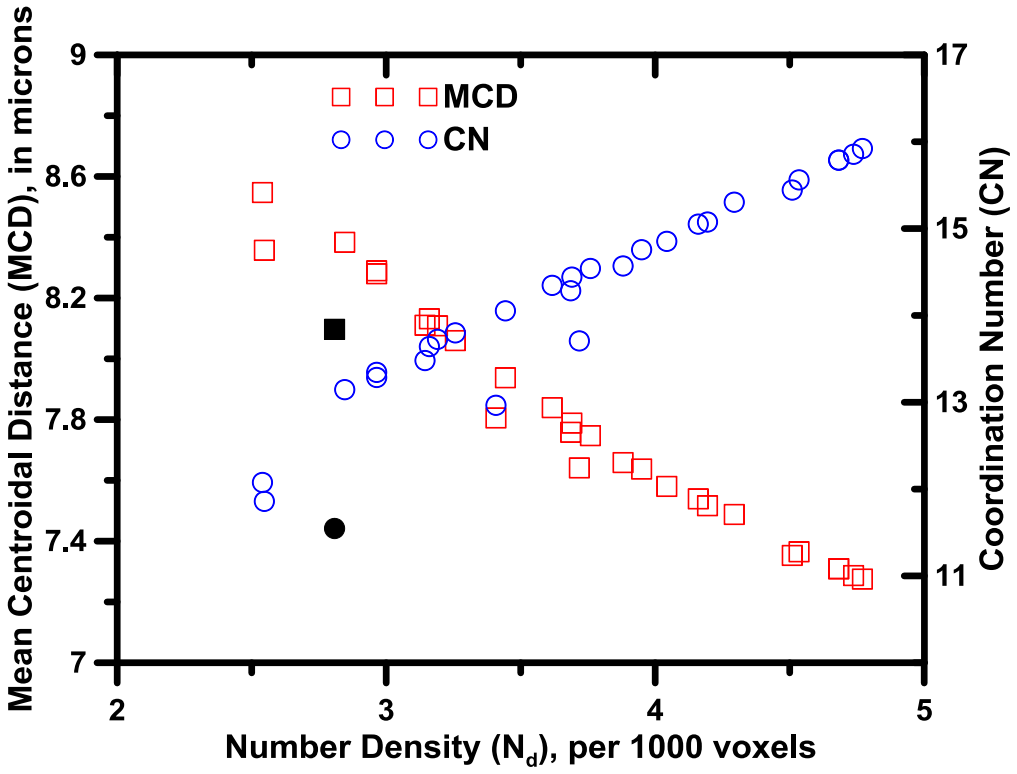

Figure 31. Relationships between the number density, mean centroidal distance, and coordination number for the UHP pastes

Rheology results (YS, PV, MS)

Chapter 2 provided a detailed review of the rheological experiments used in literature. The research team determined the rheological characteristics of all the pastes using a TA Instruments AR 2000EX rotational rheometer with a vane in cup geometry. This geometry eliminates issues with slip (the phenomenon by which the paste and the plates applying a torque in a rheology experiments become not in contact with each other) in rheological measurements.

All experiments were carried out with the set-up maintained at a temperature of 25 ± 0.1 degrees C. Approximately 40 mL of paste was placed in the rheometer using a disposable syringe. The amount of time between the addition of water and beginning the rheological experiment was approximately 5 minutes. A shear rate (rate of shear strain over time) ramp study (strain-controlled) was used to evaluate the yield stress and plastic viscosity of all the pastes.

The rheological procedure consisted of a pre-shear phase (ramp-up) increasing from 10 to 100 per second, lasting around 75 seconds to homogenize the paste, followed immediately by a reduction of shear rate (ramp-down) to 0.005 per second. This phase is followed by a ramp-up phase of shear strain from 0.005 to 100 in/in per second, and a ramp-down phase from 100 to 0.005 per second. Figure 32(a) represents this procedure. Note that shear rate is the time derivative of shear strain, or the slope of the shear strain-time plot. Excluding the pre-shear phase, data is acquired every second until three consecutive torque measurements are within eight percent of each other, at which time the experiment advances to the next shear rate.

The wide shear rate range (0.005 to 100 per second) is used to enable extraction of yield stress without the models. When a wide shear rate range is used, a stress plateau which corresponds to the yield stress is obtained, as shown in Figure 32(b). This method was shown to be more consistent than using any of the commonly used rheological models (such as Bingham or Herschel-Bulkley) for cementitious suspensions. The slope of the rising portion of the curve is the plastic viscosity of the paste, which is independent of the shear rate range (Vance, Sant, and Neithalath 2015). Replicate measurements on at least two separately mixed pastes were carried out for each mixture in this phase of the study.

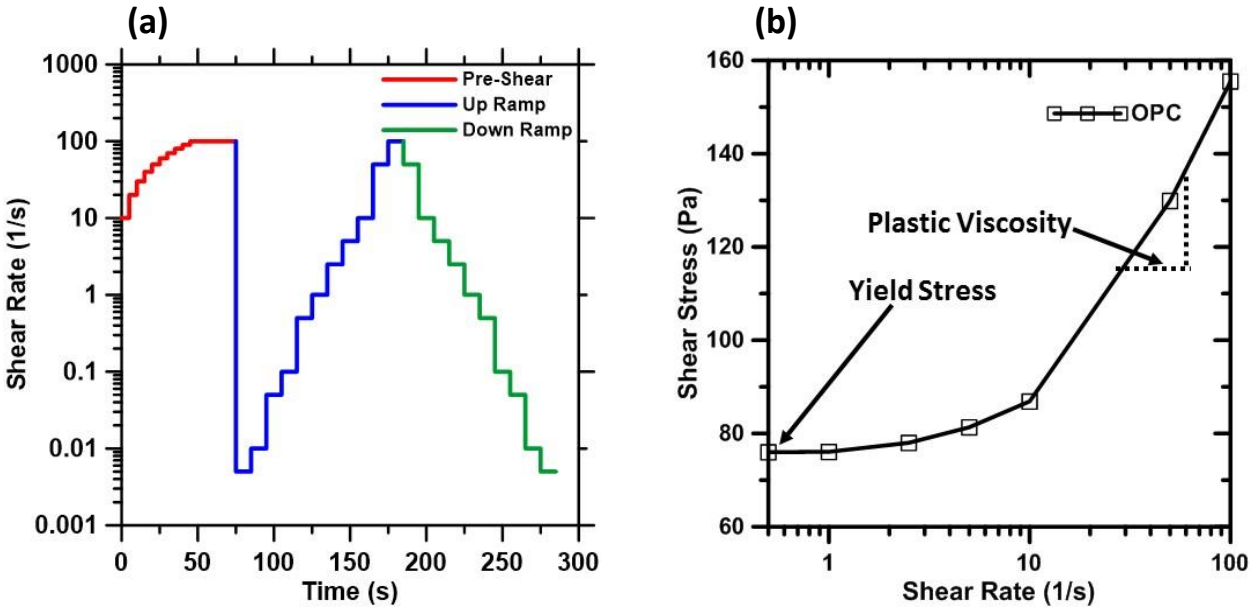

Figure 32. (a) Representation of the strain-controlled rheological procedure and (b) representative flow curves to illustrate estimation of yield stress without models

Testing methods

For all experimental mixing of the UHP pastes, the dry powders were first mixed by hand until the mixture became homogenous. Next, all the water and five percent superplasticizer for the specific mix were added to the mixer (Figure 33[a]). For 30 seconds the homogenized powder was slowly added to the mixer at a speed of approximately 4,000 rpm. Once this was completed, the mixing was continued at a higher speed (approximately 12,000 rpm) for 30 seconds. After 30 seconds, there was a two-minute waiting period during which the sides of the mixer were scraped. After the two minutes, the mix was again mixed at a high speed for 90 seconds. Immediately after mixing, the mix was poured directly into the rheometer (Figure 33[b]) and additional mix was poured into the mini-slump cone (Figure 34[a-b]).

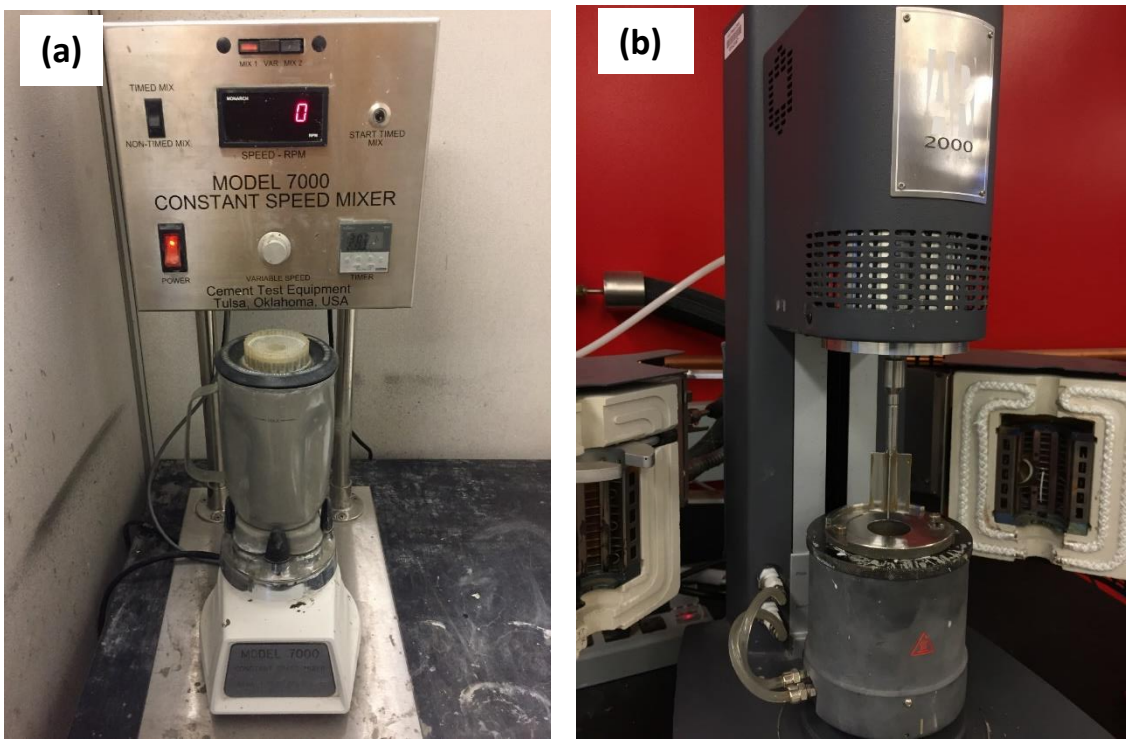

Figure 33. (a) M7000 constant speed mixer, (b) TA Instruments AR2000 EX rheometer

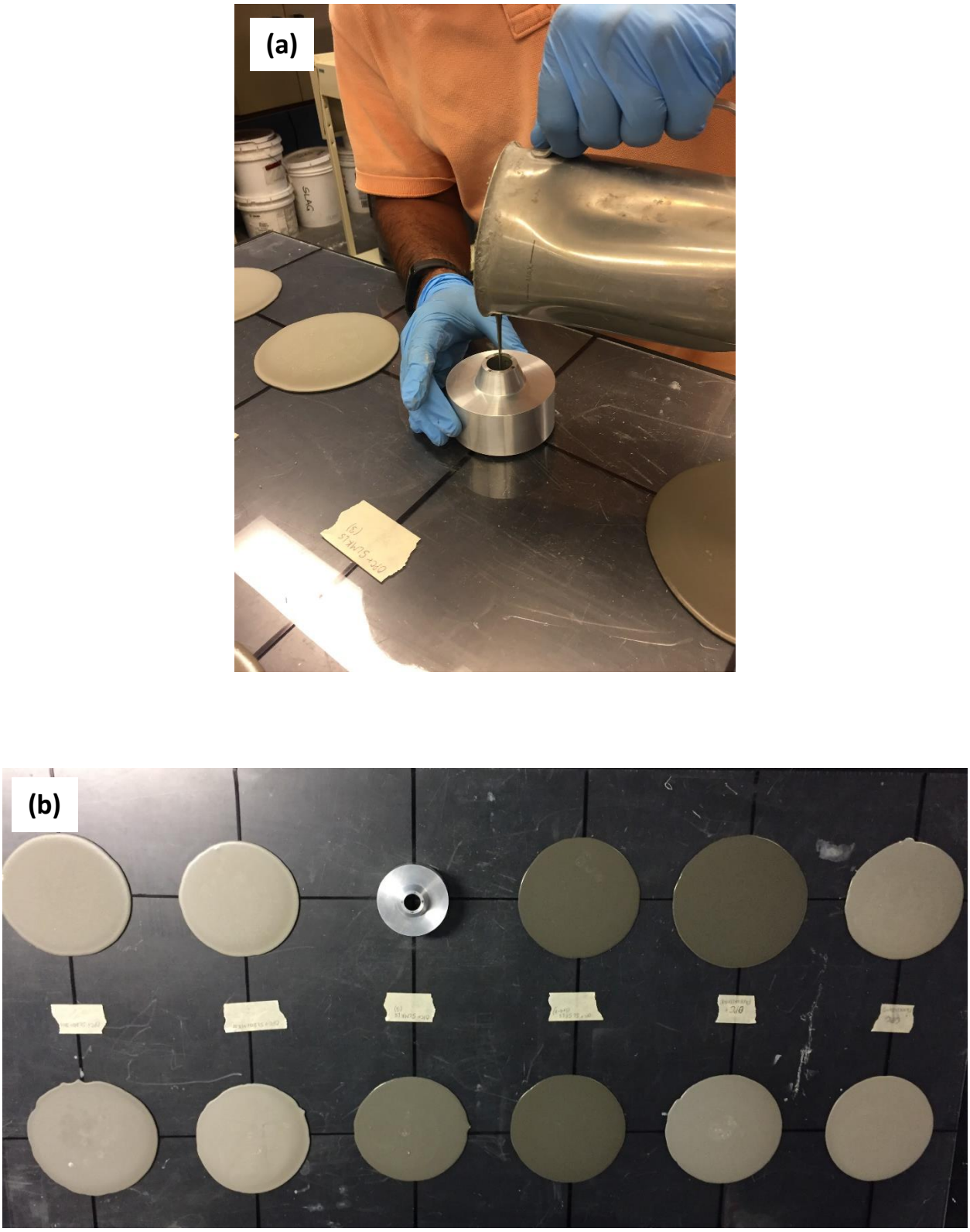

Figure 34. (a) Paste being poured in Mini-slump cone, and (b) mini-slump flow of different pastes

Figure 35(a) and (b) show the yield stress, plastic viscosity, and normalized mini-slump spread area (A_{ms}) for all the pastes in which fly ash and slag, respectively, are the dominant cement replacement materials. Subscript numbers here (and in Figure 37) represent the percentage by mass of the material replacing cement. The areas of the mini-slump spread are shown by normalizing them with respect to the spread area for the UHP-control paste. The numbers as subscripts in the mixture labels indicate the OPC replacement level with those materials. All the mixtures shown here contain five percent HRWR by mass of the powder.

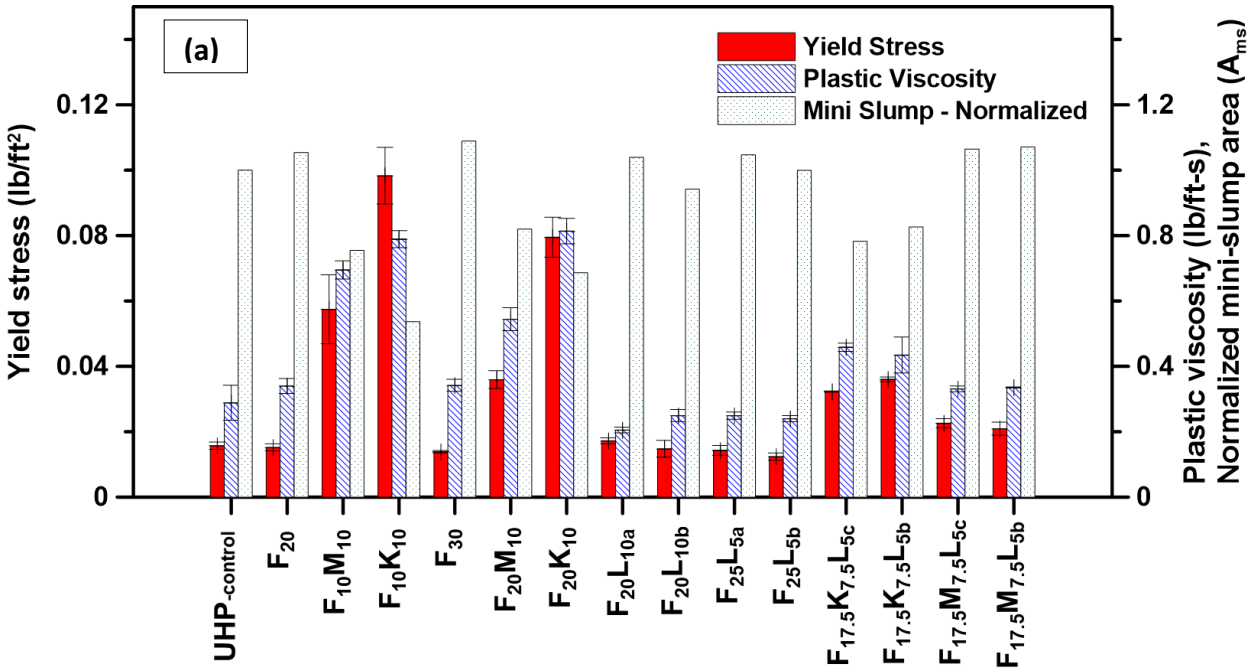

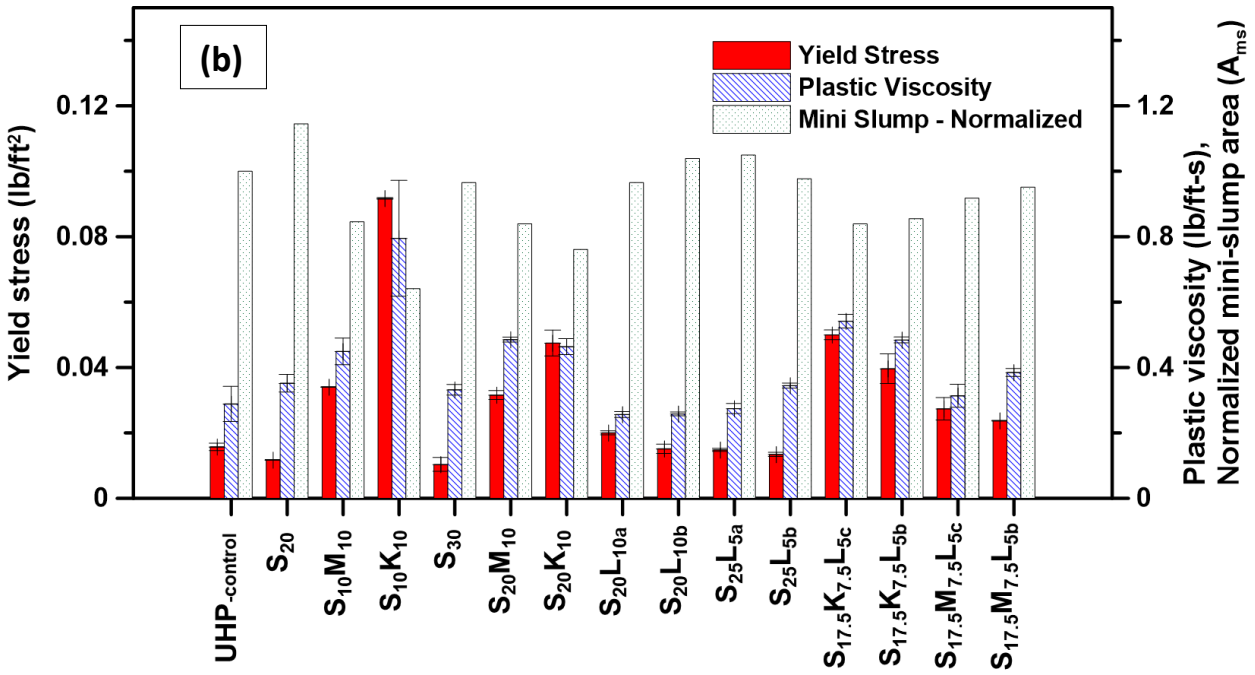

Figure 35. Yield stress, plastic viscosity and normalized mini-slump values for pastes containing: (a) fly ash as the primary cement replacement material, and (b) slag as the primary cement replacement material

Figure 35 shows that, in general, the yield stress and plastic viscosity values are directly related, with an increase in one causing the other also to increase, even if not proportionally. The mini-slump spread is inversely related to the yield stress and the plastic viscosity. The binary pastes containing fly ash or slag demonstrate relatively lower yield stress and plastic viscosity values than the UHP-control paste. This is due to the lower inter-particle frictional forces in these pastes, a result of particle sizes and surface characteristics. In addition, the ternary mixes containing metakaolin show high yield stress values, but incorporating fine limestone helps reduce the yield stress in quaternary mixtures. The presence of fine limestone improves the overall packing and reduces the inter-particle friction (Vikan and Justnes 2007; Vance, Aguayo, et al. 2013b) in the quaternary mixtures, thus lowering the yield stress and plastic viscosity and leading to increased flowability of these mixtures.

Selection of ultra-high-performance pastes based on microstructure and rheological parameters

The microstructural packing and rheological studies provide preliminary indicators of the applicability of these paste systems for UHPC. Packing influences rheology and mechanical/durability properties, while rheology influences placing and early-age structure development, which in turn influence the later age properties. In a composite binder that contains particles of different size distributions and surface characteristics, chemical admixtures are essential in controlling the rheological features. In order to select optimal and sustainable (e.g. low cement content) compositions for beneficial properties, well-defined strategies are needed. Based on the microstructure analysis (Figure 31) and the rheology results (Figure 35), two strategies or (approaches are proposed to select potential ultra-high-performing mixtures from the 31 initially considered for preliminary evaluation (see Table 5).

Strategy 1 – Selection based on independent consideration of microstructural and rheological parameters

The first strategy is a straightforward approach based on the independent consideration of microstructure packing and rheological parameters. Paste mixtures are selected from the list of mixtures in Table 5 that satisfy both packing and rheology criteria (Inequality 1, "Criteria based on packing," and Inequality 2, "Criteria based on rheology"). Figure 31 shows that a low mean centroidal distance, a high coordination number, and a high number density will lead to a densely packed microstructure. The control UHP paste is used as the baseline case. The choice of using several cement replacement materials is not just to reduce the cement content, but to obtain a paste that demonstrates improved properties compared to the control mixture. Hence, the potential UHPC binders should satisfy all three of the packing-based criteria listed below.

$$Criteria\ based\ on\ packing: \begin{cases} MCD_i \leq MCD_{UHP-control} \\ CN_i \geq CN_{UHP-control} \\ N_{d-i} \geq N_{d-UHP-control} \end{cases}$$ **Inequality 1**

Better workability is defined through a lower yield stress and plastic viscosity and a higher mini-slump spread. However, an examination of Figure 35 suggests that the yield strengths and plastic viscosities of the UHP control paste are already quite low, due to the use of high amounts of HRWR. Enforcing a criterion that requires τ_y and μ_p of the pastes to be lower than that of the UHP control paste would result in few or no pastes being selected. As a yield stress or plastic viscosity even two to three times higher than that of the UHP control would not detrimentally influence the workability, the research team imposed a subjective rheology-based selection criterion, as shown below in Inequality 2. This criterion can be modified based on the rheological parameters that the user is comfortable with, since the requirements of workability vary among applications. Here the potential mixture should satisfy all three rheology-based criteria. Absolute values of the rheological parameters, as opposed to those relative to UHP control paste, can also be used if the user decides so.

$$Criteria\ based\ on\ rheology: \begin{cases} \tau_{y-i} \leq 3 \times \tau_{y-UHP-control} \\ \mu_{p-i} \leq 3 \times \mu_{p-UHP-control} \\ A_{ms-i} \geq 0.75 * A_{ms-UHP-control} \end{cases}$$ **Inequality 2**

Figure 36(a) and (b) show Venn diagrams depicting the number of mixtures that satisfy (a) the microstructural packing and (b) the rheology criteria. From Figure 5-8(a), 30 mixtures (22 + 6 +2) satisfy the CN and N_d criteria, while 24 (22 + 2) satisfy the MCD criterion. From Figure 36(b), 23 mixtures satisfy the yield stress criteria, 27 (23+4) mixtures satisfy the mini-slump criteria and 31 (27+4+4) mixtures satisfy the plastic viscosity criteria. Of the 31 UHP mixtures evaluated here (from Table 5), 22 satisfy all three packing criteria, shown in Figure 36(a) and 23 meet all the rheology criteria, shown in Figure 36(b). Figure 36(c) shows the intersection of the 22 mixtures which satisfy the packing criteria and the 23 mixtures which satisfy the rheology criteria. It shows that 17 mixtures satisfy both the packing- and rheology-based criteria. (These criteria can be modified to further refine the mixture selection.) Figure 37 shows the matrix of 31 mixtures, among which the 17 selected ones are highlighted.

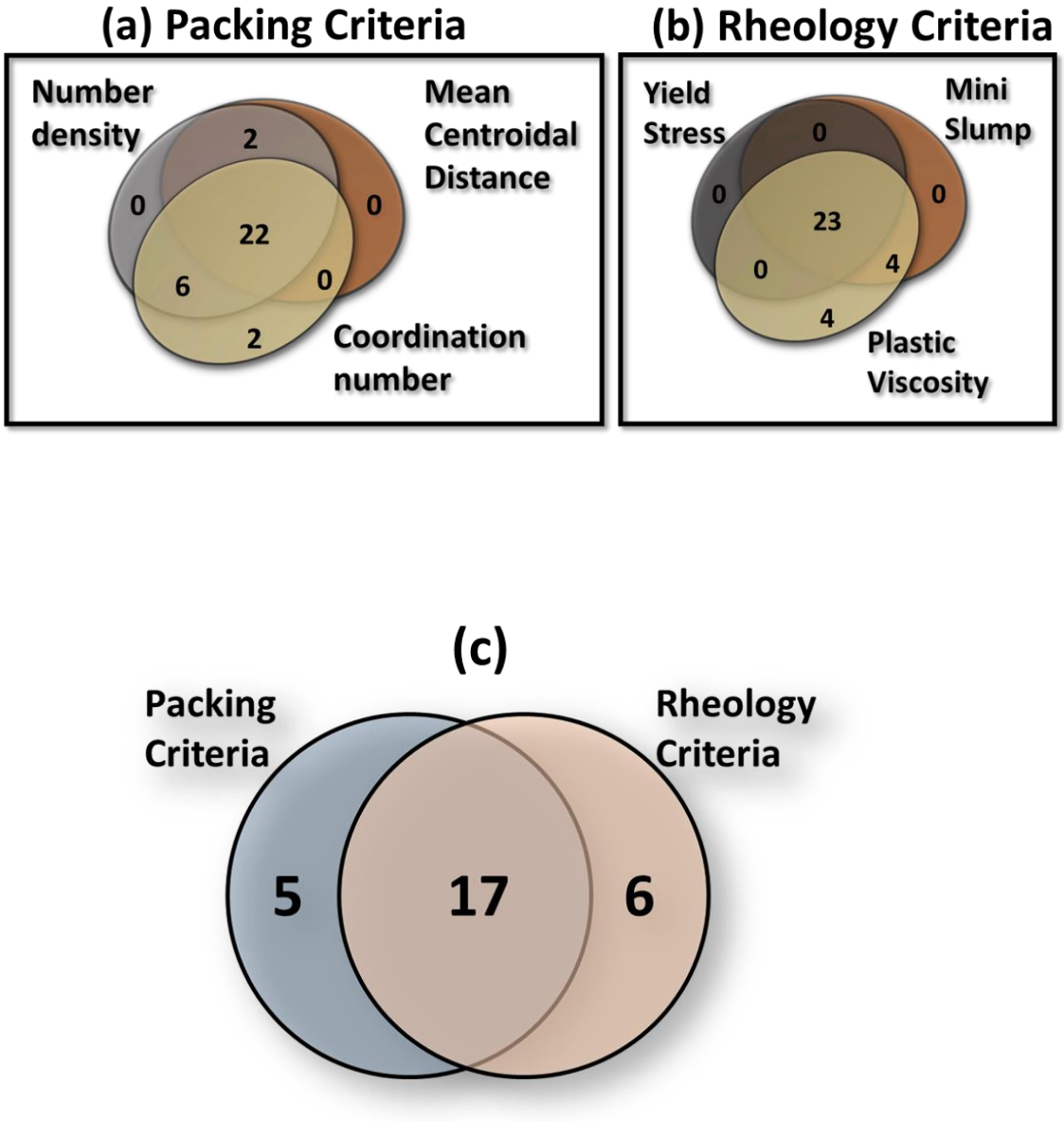

Figure 36. Venn diagrams showing the number of mixtures selected based on: (a) microstructural criteria, (b) rheology criteria, and (c) the intersection of both

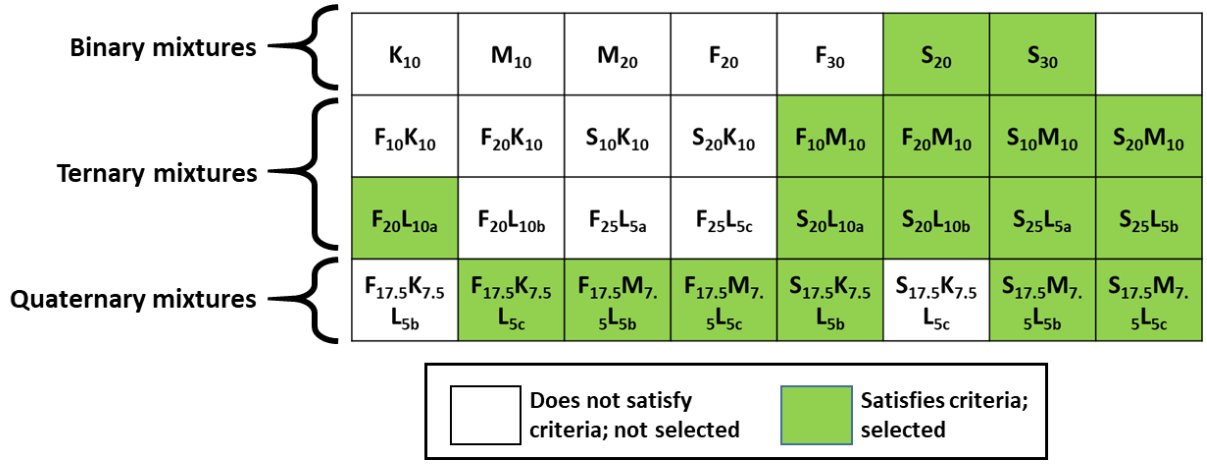

Figure 37. Matrix of mixtures with the highlighted cells showing the mixtures selected, based on independent consideration of microstructural and rheological parameters

Strategy 2 – Selection based on packing and flow coefficients

The second strategy involves the computation of the packing coefficient (γ) and flow coefficient (κ) for each mixture. These two parameters represent the microstructural packing and rheological properties respectively (Equation 5 and Equation 6).

$$Flow\ Coefficient\ (\kappa) = \sqrt{\frac{A_{ms}}{\tau_y\ X\ \mu_p}}$$

Equation 5

$$Packing\ Coefficient\ (\gamma) = \frac{CN\ X\ N_d}{MCD}$$

Equation 6

A higher value for γ indicates better packing, whereas a higher value for κ indicates better workability for the UHP paste. The subjective criteria adopted for mixture selection are given in Inequality 3 and 4.

$$\kappa_i \geq 0.25 * \kappa_{UHP-control}$$

Inequality 3

$$\gamma_i \geq 1.0 * \gamma_{UHP-control}$$

Inequality 4

As stated before, the constant multipliers used in these equations are subject to user requirements and can be changed depending on the type of application. This is why the criteria in Inequality 3 and 4 are subjective. Here, constants of 1.0 and 0.25 are adopted for packing and flow criteria, respectively. It is desirable to have packing better than that of the control UHP paste, which justifies the multiplier 1.0.

Higher values will be needed for more stringent requirements. A constant of 0.25 was chosen for the flow coefficient based on prior experience that even when the flow coefficient (defined in Equation 5) was four times lower than that of the control UHP paste, the evaluated paste demonstrated adequate workability. Out of the 31 UHP mixtures, 23 satisfy Inequality 1 and 28 satisfy Inequality 2.

The selected packing and flow coefficients yield 22 mixtures – a relatively large number − that satisfy the criteria. The criteria could be made more rigorous, however, to make the final selection more manageable and more selective. The research team devised rigorous criteria that impose additional constraints based on the following conditions:

(i) Consider only ternary and quaternary mixtures in view of their better packing, with limestone included only in the quaternary mixtures,

(ii) Use a total cement replacement level of 30 percent to ensure sustainable UHP binders,

(iii) Consider the use of limestone only in mixtures containing metakaolin or microsilica, because the size range of limestone is between those of fly ash/slag and microsilica/metakaolin, and because its low reactivity (Vance, Aguayo, et al. 2013b) limits the dosage to five percent, and,

(iv) When using limestone, apply equal proportions with d_{50} values of 1.5 µm and 3 µm to improve packing.

The combination of these criteria resulted in eight final mixtures, as shown in the dark shaded (red) cells in Figure 38. Either of the two methods presented here can be employed along with user-defined constraints to select optimal pastes for UHP mixtures. The methodologies are flexible enough to allow weighting of the packing or rheology criteria according to the users' demands.

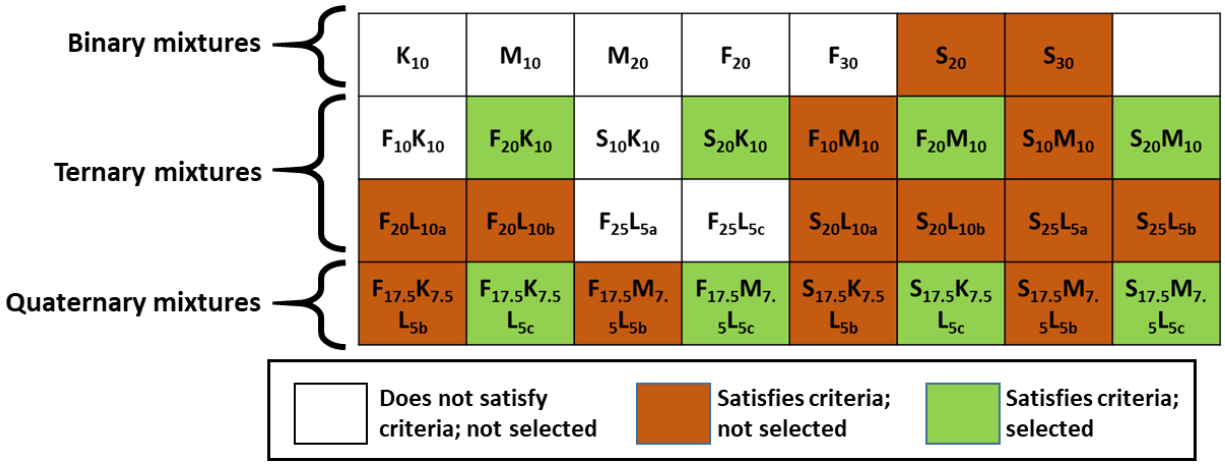

Figure 38. Matrix of mixtures with highlighted cells showing the ones selected based on packing and flow coefficients

Selected mix designs for paste composition

Table 6 lists the mixture proportions of the eight selected mixtures from Figure 38 along with a UHP control mixture and a HP control mixture selected after the evaluation.

Table 6. Final mixture proportions selected after preliminary evaluation

Mix type		Addition level (mass percent)				
	Mix ID	Fly Ash	Slag	Metakaolin	Silica Fume	Limestone (1.5 and 3 µm)
UHP − control	UHP	0	0	0	0	0
HP − control	HP	0	0	0	0	0
OPC + F + M	$F_{20}M_{10}$	20	0	0	10	0
OPC + F + K	$F_{20}K_{10}$	20	0	10	0	0
OPC + S + M	$S_{20}M_{10}$	0	20	0	10	0
OPC + S + K	$S_{20}K_{10}$	0	20	10	0	0
OPC + F + M + L	$F_{17.5}M_{7.5}L_5$	17.5	0	0	7.5	5_c
OPC + F + K + L	$F_{17.5}K_{7.5}L_5$	17.5	0	7.5	0	5_c
OPC + S + M + L	$S_{17.5}M_{7.5}L_5$	0	17.5	0	7.5	5_c
OPC + S + K + L	$S_{17.5}K_{7.5}L_5$	0	17.5	7.5	0	5_b

[#]The subscripts “b” and ”c” along with the dosage of limestone powder indicate the type of limestone used in the mixture: ”b” = 3 µm limestone and ”c” = 50% 1.5 µm + 50% 3 µm limestone.

Development of the mortar mixtures based on the optimized paste

An optimized paste formulation, as developed in the previous section, was used in the fabrication of mortar mixtures. There was an intermediate phase to use the paste with fine aggregate in order to obtain a proper mortar blend. The fine aggregate used here was a 50:50 mixture (by volume) of concrete sand and mortar sand as found in Figure 27(a). A constant sand to blended cement ratio of 1:1 by volume was used in the preparation of the mortars. Steel fibers were included as an integral component of the UHPC in this phase of the study. The idea is that the rheology of the paste formulation can accommodate both the sand and the steel fibers and still produce a flowable and workable mix.

Mixing and curing procedure for mortar

The objective of this section is to evaluate the compressive strength and find the effects of adding sand to the paste formulations. Since the size of the batch increased, the mixing protocol had to be changed. Therefore, mortars were mixed using a half-inch hand-drill attached to a spiral drill bit for better shearing of particles in the mixture (Figure 39[a]). First, the fine aggregate was dry blended with the metakaolin or silica fume for 5 to 10 minutes. This allowed shearing between the hard quartz particles and the fine metakaolin or micro-silica powder, which would cause any agglomerates to be broken up and properly dispersed. Next, the OPC and fly ash or slag was added to the mixture and mixed for an additional 10 minutes until the color of the mixture appeared uniform. If the mixture design required use of limestone, it was added after the OPC and fly ash or slag and mixed for another 10 minutes until the mix became homogenous.

The bottom and sides of the mixing bowl were scraped to remove any improperly mixed powder. After all the dry powders and fine aggregate were successfully mixed, about half of the mixing water and superplasticizer were added and mixed for another five minutes. Next, the bottom and sides of the mixing bucket were scraped and the mixture mixed for an additional five minutes. The remaining water and superplasticizer were added and mixing was continued for another 10 minutes. The bottom and sides of the mixing bucket were then scraped to eliminate any residue of dry powder. The final mixing lasted from 10 to 20 minutes, depending on the type of mix, until a homogeneous mixture was formed. If fibers were included, they were slowly added during the final mixing phase and mixed for 10 minutes more.

Immediately after mixing, the slurry was poured into the cube and/or cylindrical molds resting on a vibrating table. The molds were filled, rodded, and then vibrated for one to two minutes. During vibration, the workers ensured that any entrained air was removed and that no segregation occurred within the mix. Once molds were filled, they were covered first tightly with plastic cling wrap, and then loosely with a plastic sheet for 24 hours, after which they were demolded and labeled accordingly. Figure 39 (b-c) shows the fine sand and the steel fibers used for the formulation of mortar mixes.

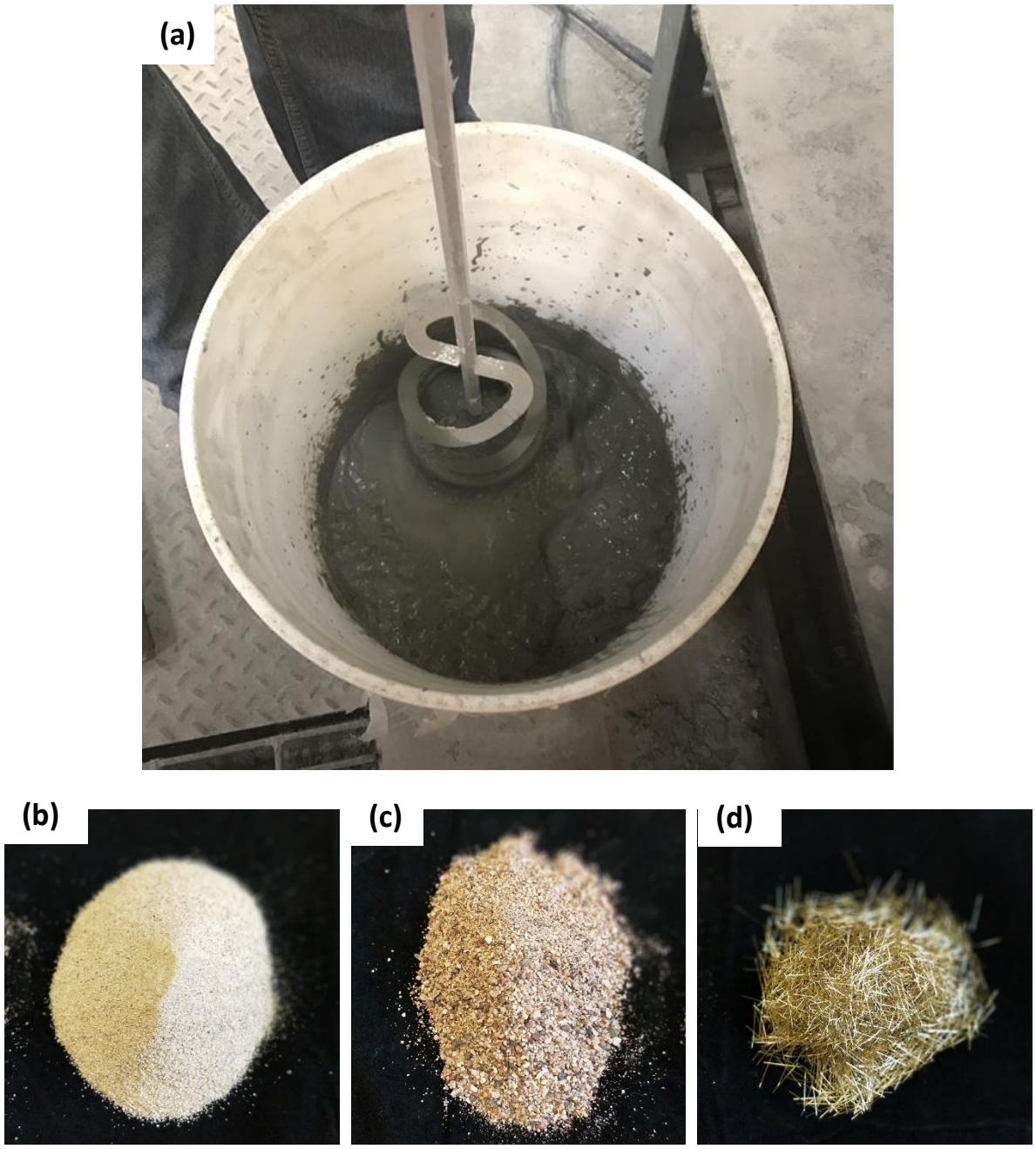

Figure 39. (a) Hand-drill with a spiral drill bit used to mix samples in a 5-gallon HDPE bucket, (b) Mortar sand, (c) Concrete Sand, (d) Steel fibers (1 inch length, 0.02 inch diameter)

Strength results

Figure 40 shows the compressive strengths of mortars made using the selected UHP pastes after 14 and 28 days of moist curing. Even with a cement replacement of 30 percent, most of the UHP mortars, especially the quaternary blends, demonstrated 28-day strengths comparable to, or higher than, those of the control UHP mortar. The mixtures containing slag demonstrated higher strengths than those containing fly ash at 28 days, but it is conceivable that the pozzolanic reaction of fly ash and its later

synergy with the other replacement materials could improve the strength with further curing. The addition of fibers, reduction of w/b ratio, and optimization of the aggregate size fractions could lead to a final mixture with 28-day compressive strengths in excess of 22,000 psi (150 MPa). This will be demonstrated in the following chapters.

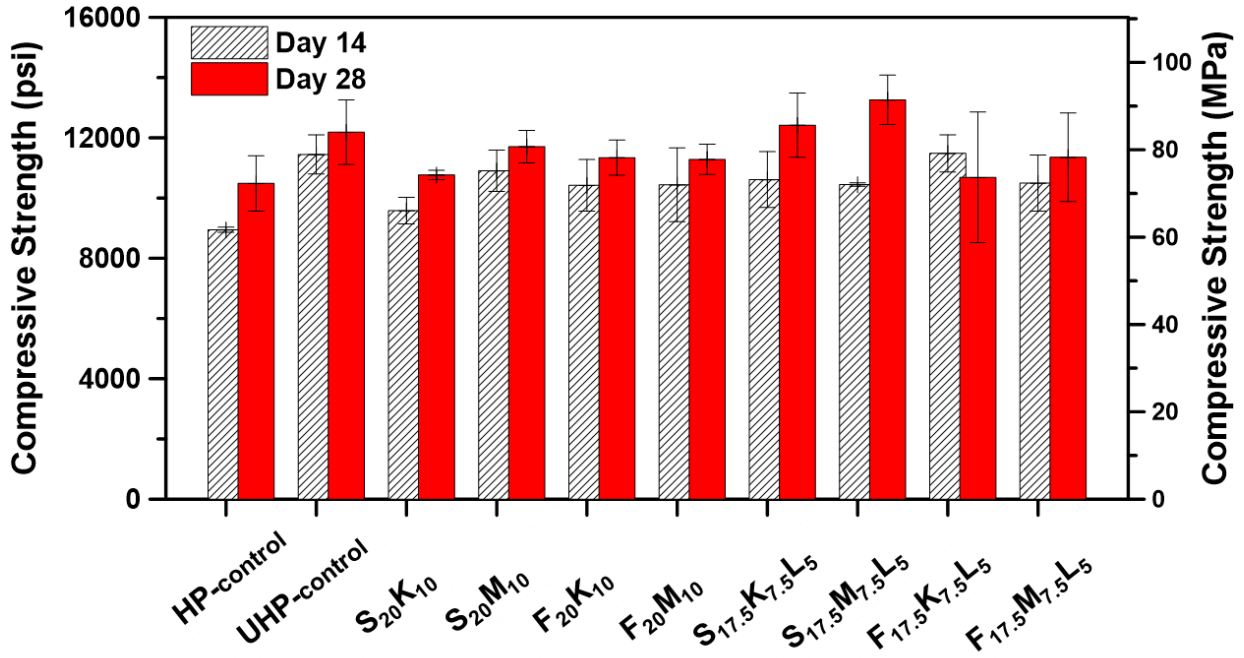

Figure 40. Day 14 and day 28 compressive strengths of eight UHP mixtures, plus controls (from Table 6)

The fifth mixture among those that demonstrated the highest strength in Figure 40 ($S_{17.5}K_{7.5}L_5$) and the UHP-control mixture were selected to study the influence of addition of steel fibers on the compressive strengths. While mixing, 2.5 percent steel fibers by volume (microfibers 1 inch long and 0.02 inch in diameter) were added to the UHP mortars; 3-inch by 6-inch cylindrical samples were cast for strength testing at 14 and 28 days. As compared to the mortars without fibers, inclusion of fibers increased the 28-day strengths by about 30 percent. Figure 41 shows the results obtained.

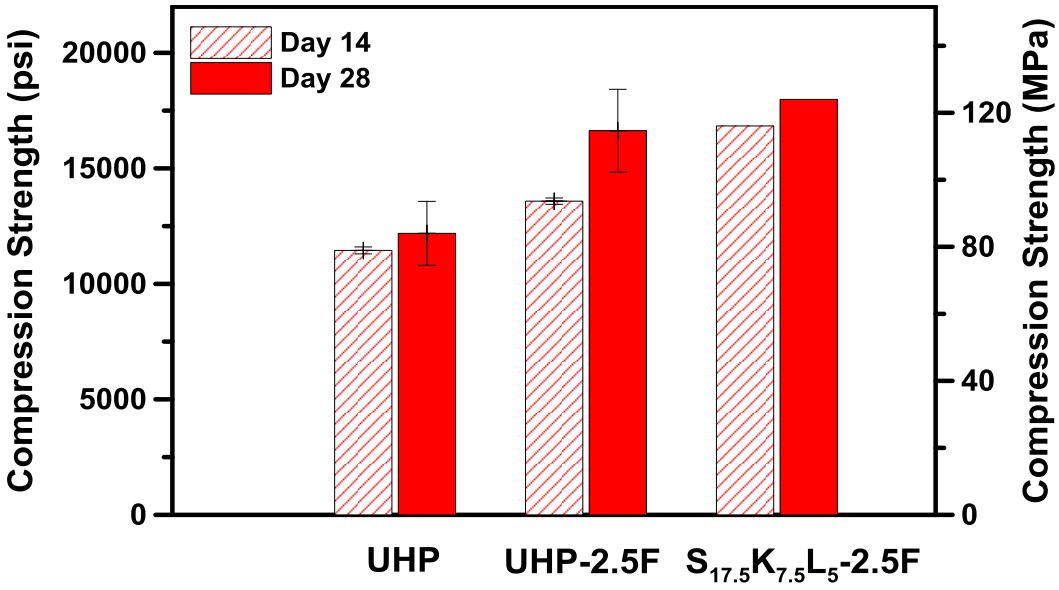

Figure 41. Day 14 and day 28 compressive strength results for UHP mortars with 2.5 percent steel fiber content

Chapter 6 PARTICLE-PACKING-BASED MIXTURE DESIGN FOR UHPC

Introduction

This chapter explores several aspects of design of UHPC mixtures in detail and addresses key components and steps in the design of mixtures using a science-based approach. The steps of the design are all integrated with the available information regarding the locally available ingredients, aggregate types and particle size distributions, admixture choices, and blended cement components. The key topics that this chapter addresses include the following:

- A description of particle-packing-based mix design, and its importance for the design of UHPC.
- An overview of the existing scientific models available for proportioning materials to obtain the highest packing density for UHPC.
- Development of a procedure to develop a straightforward and nonproprietary particle packing design that is based on computational tools and particle size distribution of various cementitious blends and aggregate combinations.
- Effects of aggregate size and fibers on the packing of UHPC.

Overview

The optimized composition for UHP pastes was determined according to the selection criteria based on the microstructure and rheology of the pastes, as explained in Chapter 5. In order to design UHPC, it becomes essential to incorporate an optimized aggregate gradation as well in the overall mixture composition to obtain ultra-high strength and provide effective load transfer. The volumetric ratio of paste to aggregate in UHPC is 65:35, as reported in several studies (Reda, Shrive, and Gillott 1999; Russell and Graybeal 2013; Yu, Spiesz, and Brouwers 2015). This is considerably different from conventional concrete, where the paste to aggregate ratio is 3:7 (See Figure 42).

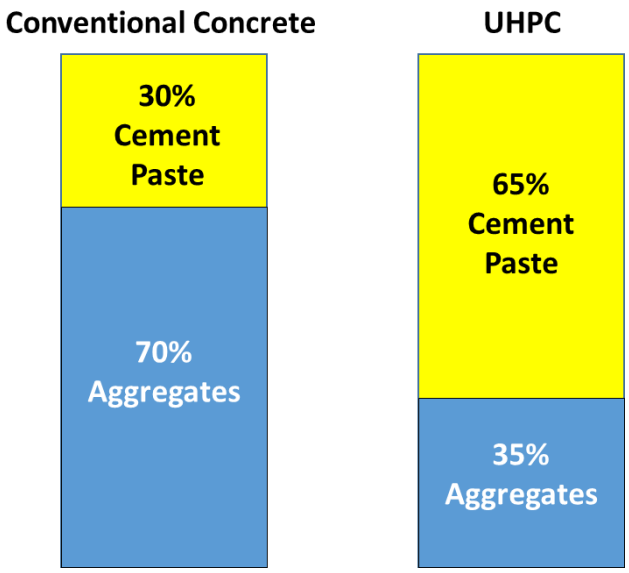

Figure 42. Volume proportions of cement paste and aggregate in conventional concrete versus UHPC

Several studies on UHPC consider the incorporation of fine aggregates which help to disperse the particles of cement, silica fume, and other materials sufficiently to prevent any agglomerations and thereby to ensure a uniform mixing environment. It is also worth noting that the coarse aggregate which forms a significant portion in regular PCC often gets replaced by fine quartz or silica flour in UHP concretes.

These predominantly fine aggregate-based mixture designs are suitable for small volumes of UHPCs (e.g. bridge connections) or for applications where larger aggregates are a hindrance (grouting and shotcreting). They are also suitable in applications where shrinkage is not a critical issue. However, for UHPC to be used in larger volumes such as in bridge decks and piers, the use of larger aggregates sizes (coarse aggregates) needs to be considered to minimize volume changes and to reduce cost. For this purpose, coarse aggregates (smaller than #4) are employed in addition to fine aggregates to provide stability to the paste phase. The aggregate network consists of size ranging from 0.008 inch (fine sand) to 0.25 inch (larger coarse aggregate).

Packing of Aggregates

The concept of packing was explained in detail in Chapter 5, where the focus was to have a low water to binder ratio to obtain a high packing density of the microstructure. As with the packing of powders at the microstructure level, the packing of aggregates at the meso-scale (intermediate size) level in concrete is equally essential to achieve an overall high packing density of concrete. However, as stated earlier, there is a huge size difference between the powders in the binder and the aggregates. Therefore, the packing of both the powder and aggregate phases needs to be considered individually. A high degree of aggregate packing ensures that the aggregates interlock well with each other to form a dense network for load transfer within concrete, whereas a high degree of powder packing ensures that the binder or the paste phase fills the voids between the aggregates with extremely low porosity.

There are a number of models available in literature to predict the packing density of aggregates. Yu et.al (Yu, Spiesz, and Brouwers 2014) employed the Andreasen and Andreasen particle-packing model to produce a dense UHPC with a binder content of about 650 kg/m^3. Stovall and de Larrard (Stovall, de Larrard, and Buil 1986) modified the suspension viscosity model by Mooney (Mooney 1951) to derive the linear packing density model, which considers the packing of solids as a suspension of infinite viscosity. The Funk and Dinger packing theory was used by Le (Le et al. 2015) in order to determine the grading of aggregates for self-compacting, high-performance concrete. Several other related particle packing models that can be used for concrete mixture proportioning are reported in (Toufar, Born, and Klose 1976; Dewar 2002; Goltermann, Johansen, and Palbøl 1997).

Random packing model, which calculates the virtual packing density of grains, is commonly employed to predict the packing efficiency of aggregates (Fu and Dekelbab 2003; Stroeven and Stroeven 1999b). Virtual packing density is defined as the maximum packing density, which can be achieved by placing each particle one by one in an appropriate position in a representative volume. On the other hand, the packing density obtained for a random arrangement of particles in a representative volume is known as the random packing density. For example, a mixture of single-sized spheres when placed one by one inside a box (not shown here) occupies a volume fraction of 74%. On the same side, when the same single-sized spheres are placed randomly, they occupy a volume fraction of about 60%. In this case, the random packing density for the single-sized spheres is 60% or 0.60. In two dimensions, circles packed one by one in an ordered packing arrangement occupy a volume fraction of 91%, whereas circles placed randomly only occupy a volume fraction of about 70% (see Figure 43). In case of random packing, it is possible to compact the particles to achieve a higher volume fraction, but the theoretical maximum volume fraction can only be achieved by placing the particles one by one.

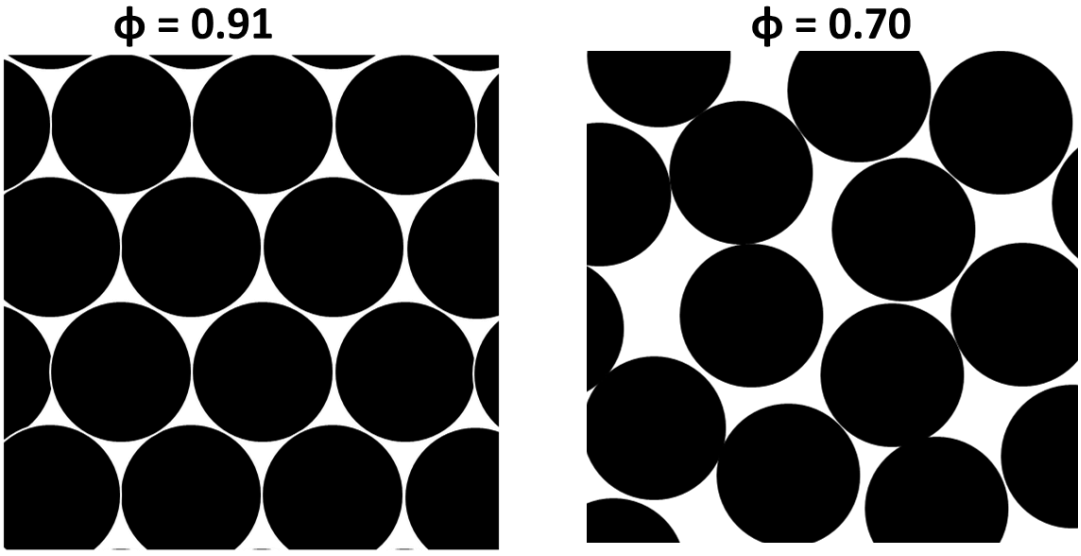

Figure 43. Two-dimensional packing showing ordered packing arrangement on the left versus random packing arrangement on the right

The challenges faced in the case of aggregate packing in concrete are twofold: (a) the shape of aggregates is irregular, and (b) there are different sizes of aggregates in the aggregate mixture. The compressible packing model (referred to as CPM hereafter) is a widely used model to predict the packing density of an aggregate mixture containing aggregates of different sizes (Stovall, de Larrard, and Buil 1986). CPM combines theoretical formulation with experimental results and can predict the packing density with higher accuracy than other packing models available in literature, as mentioned earlier in this section. For this reason, CPM is the preferred model used in this study to calculate the packing density of aggregate systems containing several aggregate sizes. CPM is discussed in detail in the next section.

Compressible Packing Model – Theory and Implementation

Theory of CPM

CPM is used to calculate the packing density of mixtures containing two or more aggregates sizes. The packing density of such a poly-disperse aggregate mixture can be expressed as a function of the individual packing densities of each aggregate size present in the mixture. We can understand the concept of CPM by using a simple example. Let us consider a mixture of only two aggregate sizes (d_1 and d_2) with the assumption that $d_1 >> d_2$, (d_1 is significantly greater than d_2, nearly 10 times or more) such that the packing of d_1 is not disturbed by the presence of d_2. Also, let us assume that the individual random packing densities of d_1 and d_2 are β_1 and β_2 respectively. We are interested in calculating the packing density of the mixture of these two aggregate sizes, when y_1% of d_1 is mixed with y_2% of d_2 (see Figure 44 (a)). Let "y_1" and "y_2" correspond to the relative volume fractions of "d_1" and "d_2." When the two aggregate sizes are packed inside a unit volume (Figure 44 (b), they occupy volume fractions ϕ_1 and ϕ_2 in the bulk volume. "ϕ_1" and "ϕ_2" are the volume fractions occupied by "d_1" and "d_2" in the bulk volume. Equation 7 and Equation 8 therefore describe the relationship between the volume fractions (y_1,y_2) and packing density (γ). It should be noted that the value of packing density lies between 0 and 1 as calculated in Equation 8. The porosity of the system can be obtained by subtracting the packing density (γ) from one ($Porosity = 1 - \gamma$).

$$y_1 = \frac{\phi_1}{\phi_1 + \phi_2} and\ y_2 = \frac{\phi_2}{\phi_1 + \phi_2}$$ **Equation 7**

$$\gamma = \phi_1 + \phi_2$$ **Equation 8**

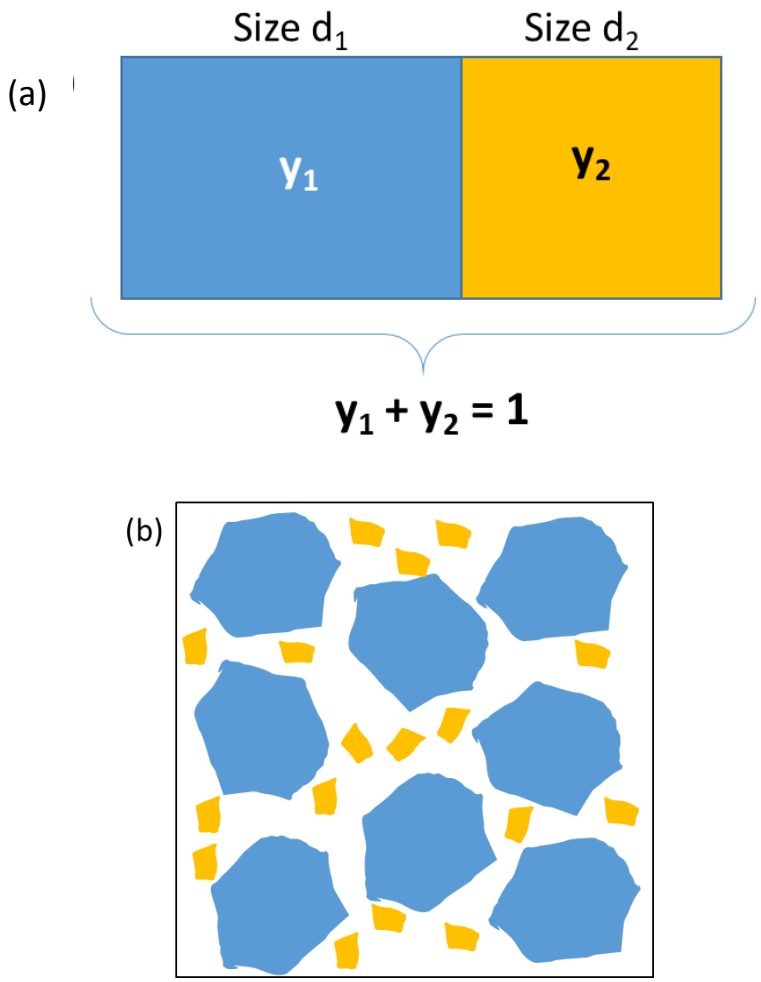

Figure 44. (a) Relative volume fraction of aggregates in granular mixture, (b) Binary aggregate mixture

Now, when d_1 has a higher volume fraction, the d_1 aggregates will occupy the available volume as if no other aggregate were present. In that case, $\phi_1 = \beta_1$, and the packing density (γ_1) can be calculated in Equation 9 using Equation 7 and Equation 8.

$$\gamma = \gamma_1 = \frac{\beta_1}{1 - y_2}$$ **Equation 9**

Similarly, when d_2 has a higher volume fraction, the d_2 aggregates will occupy all the available volume i.e. the porosity in between the d_1 aggregates. In this case, $\phi_2 = \beta_2(1 - \phi_1)$ and the packing density (γ_2) in this case can be calculated in Equation 10.

$$\gamma = \gamma_2 = \frac{\beta_2}{1 - (1 - \beta_2)y_1}$$ **Equation 10**

For any mixture of d_1 and d_2 aggregates, we can write the packing density of the mixture (γ) as:

$$\gamma \leq \min(\gamma_1, \gamma_2)$$ **Inequality 5**

Now, in this example, we considered that the packing of one aggregate size was not affected by the presence of another aggregate size. However, this may not be the case in an aggregate mixture containing several different sizes of aggregates. Therefore, we need to understand the concept of loosening effect and wall effect.

The loosening effect occurs when the packing density of a coarse grain mixture is decreased by the introduction of fine grains. Figure 45 (a) shows a schematic of an aggregate system containing single-sized coarse aggregates. When a few aggregates smaller than the coarse aggregates are added to this system, the original particle packing is disturbed and the system transforms to a new one, as shown in Figure 45 (b).

(a)

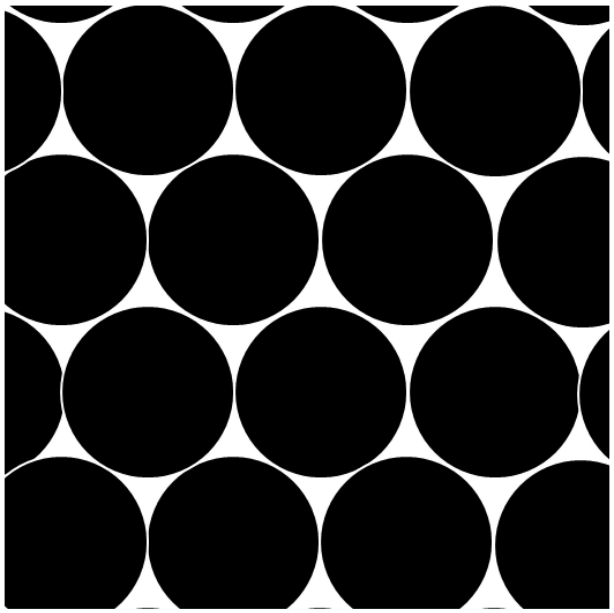

(b)

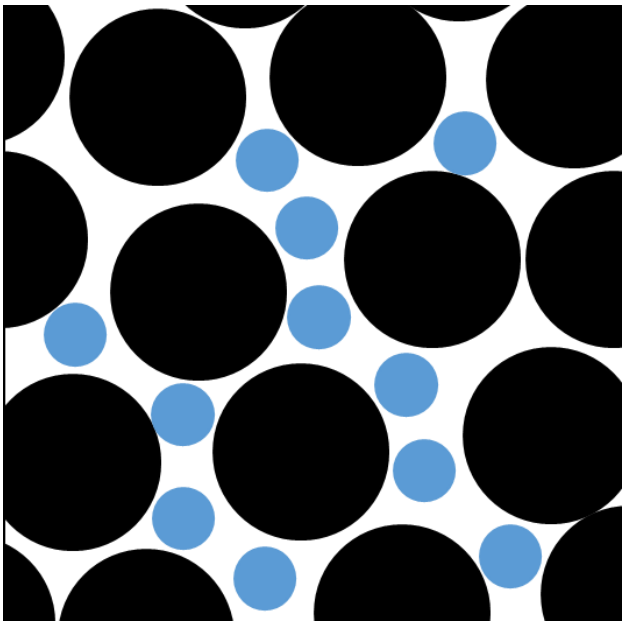

Figure 45. (a-b) Densely packed mixture of coarse grains disturbed in the presence of fine grains showing loosening effect

Wall effect is the opposite of loosening effect. It occurs when a coarse grain is introduced into a mixture consisting of fine grains, which decreases the packing density of the mixture (Figure 46 (a-b)).

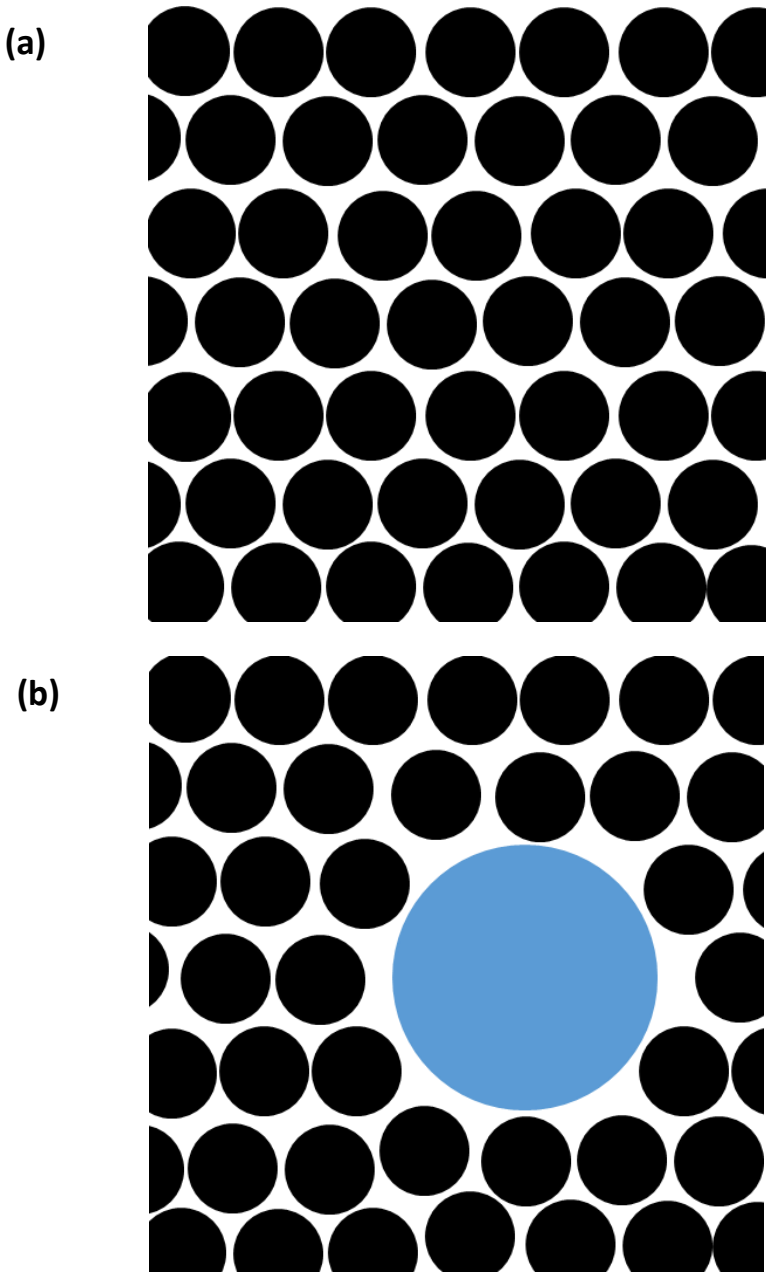

Figure 46. (a-b) Densely packed mixture of fine grains disturbed in the presence of a coarse grain illustrating wall effect

Since the aggregate introduced in Figure 46 (b) could not fit in the already existing voids present in the system in Figure 46 (a), the overall packing density of the new system is lower than that of the original system. This effect is termed as the ***wall effect***.

Equation 11 and Equation 12 are the empirical formulations to calculate the parameters that govern the loosening effect and the wall effect (De Larrard 1999). If we have two aggregate sizes "i" and "j," then a_{ij} and b_{ij} represent the loosening and wall effect coefficients for aggregate size "i" due to the influence of aggregate size "j." Both coefficients can be calculated as a function of the diameters d_i and

d_j of aggregate classes “i” and “j.” This procedure is done for each of the aggregate sizes present in the mixture.

Equation 11

$$a_{ij} = \sqrt{1 - \left(1 - d_j/d_i\right)^{1.02}}; d_j > d_i$$

Equation 12

$$b_{ij} = 1 - \left(1 - d_i/d_j\right)^{1.50};\ d_i > d_j$$

Here,

“i” and “j” refer to ith and jth aggregate sizes in the mixture,

a_{ij} is the loosening effect coefficient for aggregate size "i” due to the influence of aggregate size “j,”

b_{ij} is the wall effect coefficient for aggregate size “i” due to the influence of aggregate size “j,”

d_i is the average diameter for aggregate size “i,” and,

d_j is the average diameter for aggregate size “j.”

The same approach can be extended to an aggregate mixture containing “n” different sizes of aggregates. In an aggregate mixture, a **dominant aggregate size** is the one with the maximum volume fraction among all the aggregate sizes. This depends on the relative quantity of the aggregates in the system, the shape and size of the aggregates, and the individual packing densities of the aggregates.

The **virtual packing density** γ_i is defined as the theoretical value of packing density for the aggregate mixture when aggregate class “i” is dominant. Equation 13 is a linear formulation for the calculation of virtual packing density, which considers the interactions encountered by aggregate class “i” due to the presence of other aggregate classes in the mixture. These interactions generally manifest in the form of loosening effect and wall effect (De Larrard 1999).

Equation 13

$$\gamma_i = \frac{\beta_i}{1 - \sum_{j=1}^{i-1}\left[1 - \beta_i + b_{ij}\,\beta_i\left(1 - 1/\beta_j\right)\right]y_j - \sum_{j=i+1}^{n}\left[1 - a_{ij}\,\beta_i/\beta_j\right]y_j}$$

Here,

γ_i is the packing density of the aggregate mixture considering aggregate size “i” as the dominant aggregate size,

β_i is the residual packing density of aggregate size “i,” determined using dry-rodded unit weight testing,

y_i represents the individual volume fraction of the aggregate size “i” in the mixture,

a_{ij} is the loosening effect coefficient for aggregate class "i" due to the influence of aggregate class "j."

b_{ij} is the wall effect coefficient for aggregate class "i" due to the influence of aggregate class "j."

The individual random packing density of each aggregate size "i" is termed the **residual packing density** (β_i). The values for the residual packing density (β_i) are determined for each aggregate size "i," experimentally using the **dry rodded unit weight** (DRUW) testing. For this purpose, the aggregate stockpile must be sieved in order to obtain sufficient quantity of all the aggregate sizes to be used in the study. For the UHPC mixtures in this study, three size ranges of coarse aggregates were considered corresponding to nominal maximum sizes of #4, #8, and #10. Figure 47 shows the coarse aggregates used in this study. Two size ranges of fine aggregates – with d_{50} of 0.02 in coarse sand and 0.008 in fine sand – were chosen. The fine aggregates used are shown in Figure 48.

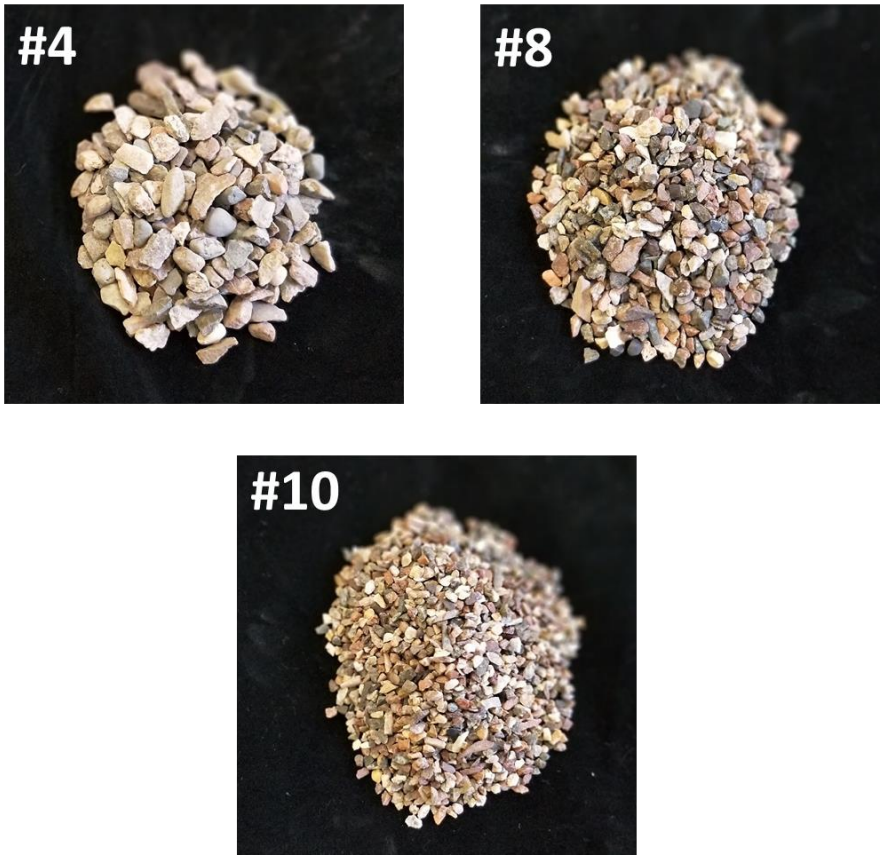

Figure 47. Coarse aggregate sizes used

Figure 48. Fine aggregates used

A large aggregate stockpile was sieved in order to obtain aggregate seizes corresponding to #4, #8, and #10. Due to the shortage of #10 sized aggregates in the stockpile, some #4 aggregates had to be crushed in a laboratory pulverizer and then sieved to obtain #10 aggregates. Fine and coarse sand were obtained directly from suppliers. Dry-rodded unit weight testing was conducted on each individual aggregate size in accordance with ASTM 1997. Figure 49 shows a schematic of DRUW testing in progress. Aggregates were oven dried at 110 ± 5° C for 24 hours prior to testing. The aggregates were then added to a cylindrical measure of fixed volume (0.25 ft^3) up to one-third full level. The aggregates were rodded evenly over the surface with 25 strokes of a tamping rod. Care was taken not to allow the rod to strike the bottom of the measure forcibly. The cylindrical measure was filled to two-thirds full and rodded again as above. Care was taken to apply only enough force to cause the rod to penetrate to the first layer. Finally, the measure was filled to the top and again rodded as above. It was ensured that only enough force was applied to cause the rod to penetrate to the second layer. The surface of the aggregate was levelled with a straightedge. After each successive turn the cylindrical measure was vibrated on a vibrating table to further consolidate the aggregates. Finally, the weight of the aggregate in the mixture was taken. The packing density was calculated as follows:

$$\rho_{bulk} = M_{aggregate} / V_{containe\ r} \quad \textbf{Equation 14}$$

$$\phi_{aggregate} = \rho_{bulk} / \rho_{aggregate} \quad \textbf{Equation 15}$$

Here,

ρ_{bulk} is the bulk density of aggregate,

$M_{aggregate}$ is the measured DRUW of aggregate,

$V_{container}$ is the volume of the cylindrical measure, and

$\phi_{aggregate}$ is the packing density of the aggregate.

Figure 49. DRUW test in progress

The packing densities obtained for these five aggregate sizes from the DRUW test are given in Table 7. These values are not unique for the particular aggregate size, because they depend on the shape and size of the aggregates. These values correspond to the aggregates used by the authors. For any new aggregate stockpile, these values need to be obtained by conducting the DRUW test.

Table 7. Packing density (unitless) values obtained from DRUW test for aggregate sizes used in this study

Aggregate Size	#4	#8	#10	Concrete Sand	Fine Sand
Packing Density ($\varphi_{aggregate}$)	0.572	0.544	0.520	0.620	0.527

Finally, the packing density of the aggregate mixture, Φ, is calculated using Equation 16. In this equation, "K" is a scalar index, also known as the compaction index, which depends on the physical effort involved in packing these particles in the mixture. A higher compaction index implies fewer voids and a higher packing density of aggregates. For instance, a "K" value of 9 is used when a combination of vibration and compression is used to pack the particles and a "K" value of 4.75 is used when only vibration is used. Equation 16 can be numerically solved (the Newton-Raphson method was used in this work) to obtain

the packing density Φ once all the other parameters are determined using Equation 11, Equation 12, and Equation 13.

$$K = \sum_{i=1}^{n} \frac{y_i/\beta_i}{1/\Phi - 1/\gamma_i}$$ **Equation 16**

Here,

K is the compaction index; K = 9 is used when aggregates are vibrated and compacted,

"n" is the number of different aggregate sizes in the aggregate mixture,

β_i is the residual packing density of aggregate size "i," determined using dry-rodded unit weight testing,

y_i is the individual volume fraction of the aggregate size "i" in the mixture,

ϕ is the packing density of the aggregate mixture, and

γ_i is the packing density of the aggregate mixture considering aggregate size "i" as the dominant aggregate size.

Implementation of CPM

The packing density for any given combination of aggregate sizes can be determined by solving Equation 16. For instance, let us consider an aggregate combination with the aggregate proportions listed in Table 8.

Table 8. Aggregate fractions for a random aggregate mixture

	Aggregate Mixture				
	#4	#8	#10	Concrete Sand	Fine Sand
Aggregate Weight Fractions	0.21	0.10	0.51	0.09	0.09
Specific Gravity	2.70	2.70	2.70	2.65	2.65
Average Diameter	0.22"	0.14"	0.08"	0.02"	0.009"
Aggregate Absolute Volume Fractions (y_i) (calculated)	0.2	0.1	0.5	0.1	0.1

In order to calculate the packing density of this aggregate mixture, we need to solve for packing density (ϕ) using Equation 16. There are five basic inputs required to obtain ϕ, which are listed as follows.

(a) number of aggregate sizes "n,"

(b) relative volume proportion of each aggregate size "y_i,"

(c) average diameter of each aggregate size "d,"

(d) packing density of each aggregate size "β_i," and

(e) compaction index "K."

The number of aggregate sizes (n) is five. The aggregate weight fractions are converted to aggregate volume fractions using a rule of mixtures approach (see Equation 17). The calculated values of volume fraction are listed in Table 8.

$$y_i = \frac{W_i/\rho_i}{\sum_{j=1}^{n} W_j/\rho_j}$$ **Equation 17**

In Equation 17,

y_i is the absolute volume fraction of aggregate size "i" (Note: since this is absolute volume fraction of aggregates, the volume of voids in the bulk aggregate stockpile is not considered here),

W_i , W_j are the weight fractions of aggregate sizes "i" and "j," and

ρ_i and ρ_j are the specific gravity values corresponding to aggregate sizes "i" and "j."

The y_i values are the volume fraction values obtained from Table 8 corresponding to each aggregate size. The average diameter of the coarse aggregate is taken as the size of the sieve on which the aggregates are retained: #4 aggregate corresponds to 0.22," #8 corresponds to 0.14," and #10 corresponds to 0.08." The average size of the fine aggregates was obtained from the size distribution of the sands. The average size of the concrete sand was calculated as 0.02" and average size of the fine sand as 0.008." The values for average size were input in Equation 11 and Equation 12 to calculate the loosening and wall effect coefficient matrices. Since there are five different sizes of aggregates, the size of the matrices containing the loosening and wall effect coefficients is 5 x 5.

The β_i values of each aggregate size are obtained from the DRUW test. These values are listed in Table 7. The values for β_i, y_i, and the wall and loosening effect coefficients are used to evaluate γ_i values using Equation 12.

Finally, the value of "K" is selected based on the kind of compaction to which aggregates are subjected. A "K" value of 9 was used for all the aggregate compositions, since both compaction and vibration were used to compact the aggregates. While mixing the concrete mixtures using these aggregates, compaction and vibration were employed as well. The values of "K," γ_i, $\beta_{i,}$ and y_i are used in Equation 16 to solve for the packing density ϕ. In this case, the packing density ϕ was solved to be 0.587. This value can be independently verified using the DRUW method, as specified earlier.

A detailed step by step approach to calculate packing density using CPM for an example problem is shown in Appendix A. Different aggregate combinations lead to different values of packing density. The combination of aggregates that gives the maximum packing density must be determined, since such an aggregate mixture will also lead to a higher strength of UHPC. The maximum packing density is calculated by solving Equation 16 for multiple aggregate combinations. There are infinite possible combinations for the five different aggregate sizes (#4, #8, #10, coarse sand, and fine sand) chosen in this study. The number of combinations is limited by varying the volume fraction of each size from 0.0 to 1.0 in increments of 0.1. The aggregate combinations were obtained such that the sum of volume fractions of individual aggregate sizes is always 1.0.

Implementation of the Model for Practical Applications

A total of 885 different aggregate combinations were formulated using the five different aggregate sizes. A computer program was developed in MATLAB to automatically choose the aggregate combinations and input them into the algorithm for packing density determination. The computer program computes the packing density for the 885 different aggregate combinations and then reports the maximum packing density obtained as well as the aggregate combination corresponding to the maximum packing density.

The distribution of packing density as a function of the volume fraction of coarse aggregates and fine aggregates in shown in Figure 51 (a-b). Coarse aggregate refers to the combinations of #4, #8, and #10 aggregates. Fine aggregate refers to the combinations of coarse and fine sand. In Figure 51 (a), for each value of volume fraction of coarse aggregate on the x-axis, there are multiple values of the calculated packing density. These values correspond to the packing densities obtained by using different combinations of the chosen aggregates that result in a net coarse aggregate volume fraction equal to that shown on the x-axis. For instance, a coarse aggregate volume fraction of 0.60 may be achieved using multiple aggregate combinations of coarse aggregates. Similarly, the fine aggregate volume fraction of 0.40 can be composed of different combinations of the two selected sizes of fine aggregates.

As examples, the volume fractions of aggregates in a combined mixture containing 60% coarse aggregates and 40% fine aggregates are shown in Figure 50. Each of these combinations would result in a unique aggregate packing and therefore present a unique value of packing density, which is plotted in Figure 51 and Figure 52. Note that concrete sand is the same as coarse sand here.

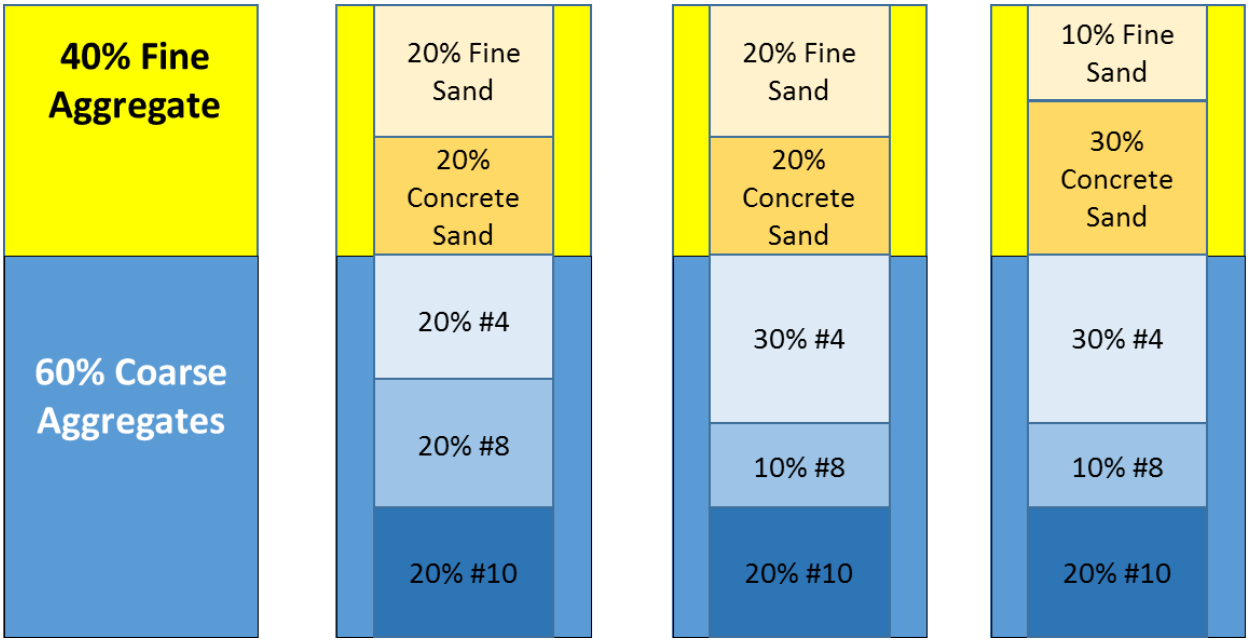

Figure 50. Example of a few aggregate combinations that have equivalent composition to 40% fine aggregate and 60% coarse aggregate

Figure 51 (a) shows that maximum packing density occurs when the volume fraction of *coarse* aggregates is 60%. On the other hand, Figure 51 (b) shows that maximum packing density occurs when

the volume fraction of *fine* aggregates is 40%. The plot of packing density as a function of aggregate size combinations illustrates the combined effect of coarse aggregate and fine aggregates on the packing density of the mixture.

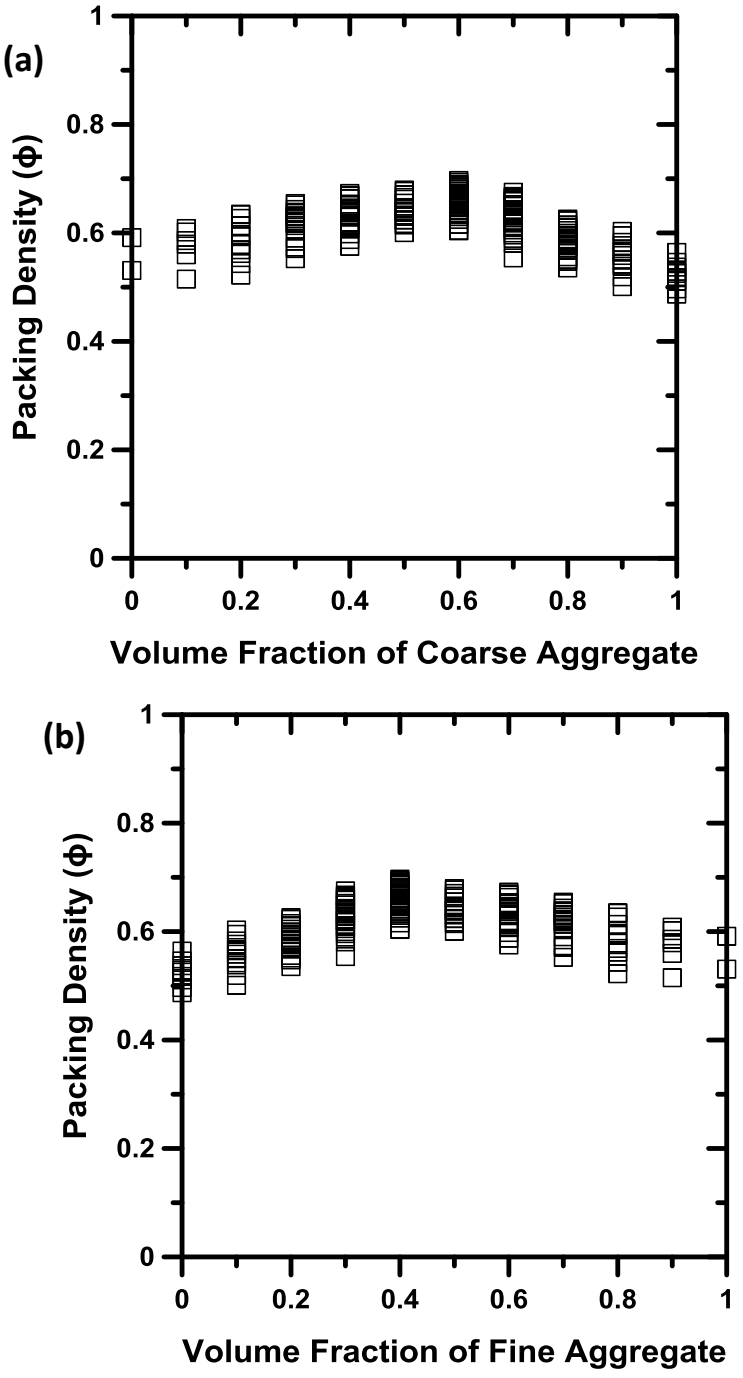

Figure 51. (a) Packing density as a function of the volume fraction of coarse aggregates, (b) Packing density as a function of the volume fraction of fine aggregates

Figure 52 (a-c) show the packing density as a function of the amount of individual coarse aggregate sizes. These plots help illustrate the effect of aggregate sizes on the total packing density. Figure 52 (a) shows that maximum packing density occurs when the volume fraction of #4 aggregate is 40% (equivalent to 0.4 in Figure 51 (a)) and the packing density gradually decreases when the volume fraction of #4 aggregate increases or decreases beyond that.

Similarly, Figure 52 (b) and Figure 52 (c) show that maximum packing density occurs when the volume fraction of #8 and #10 aggregate in the mixture is 10%. The net coarse aggregate content to obtain the maximum packing density corresponds to #4 – 40%, #8 – 10% and #10 – 10%, thereby providing an overall coarse aggregate content of 60%, which is the same as that obtained from Figure 51 (a).

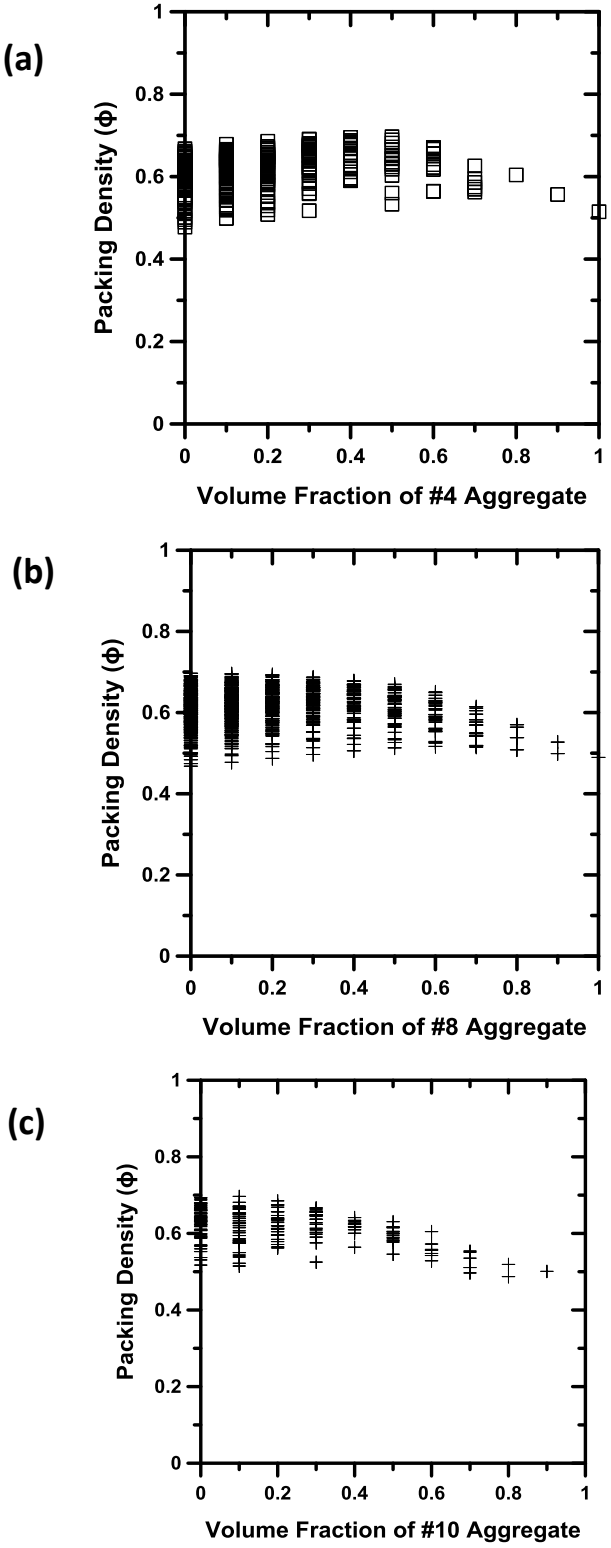

Figure 52. Packing density as a function of the volume fraction of (a) #4 aggregate, (b) #8 aggregate, and (c) #10 aggregate

Table 9 shows the packing density values obtained for a few aggregate combinations by solving Equation 17. As mentioned before, the individual values for the aggregates correspond to volume fractions. The first row in the table corresponds to the aggregate combination with the maximum packing density (Φ = 0.696).

Table 9. Packing density values for selected aggregate combinations

#4	#8	#10	Concrete Sand	Fine Sand	Packing density
0.4	*0.1*	*0.1*	*0.2*	*0.2*	*0.696*
0.3	0.1	0.2	0.2	0.2	0.685
0.1	0.3	0.1	0.3	0.2	0.675
0.5	0.1	0.1	0.2	0.1	0.671
0.1	0.3	0.2	0.3	0.1	0.657
0.2	0.1	0.4	0.1	0.2	0.634
0.1	0.1	0.1	0.2	0.5	0.599
0	0	0	0.6	0.4	0.591
0.2	0.1	0.5	0.1	0.1	0.587
0.4	0.1	0.5	0	0	0.546
0.1	0.1	0.8	0	0	0.494

Figure 53 shows the comparison of the particle size distribution of several aggregate stockpiles used in the construction industry, and compares them against the optimized aggregate mixture (marked by ϕ_{max}) obtained using CPM. The optimized aggregate proportion obtained is finer than any of the aggregate stockpiles. Therefore, in order to obtain the optimized aggregate proportion, existing stockpiles must be screened to obtain higher volume proportions of the finer aggregate sizes. An alternative to this is to blend different stockpiles of aggregates together in different proportions, and then screen the resultant aggregate distribution into individual sizes. Aggregate stockpiles #78 and #89 are the closest to the optimized packing gradation.

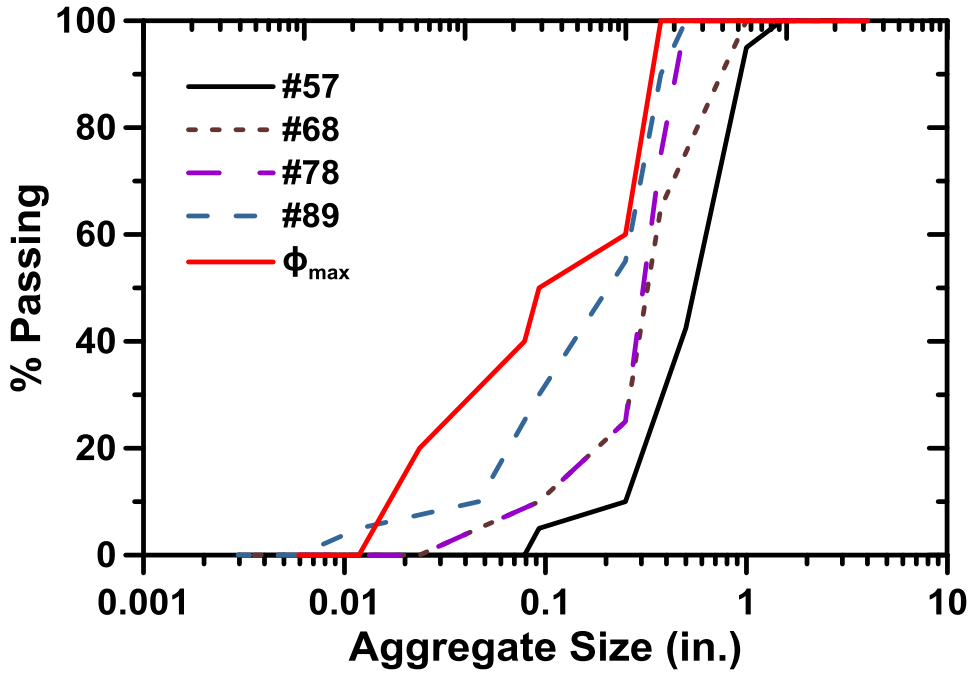

Figure 53. Comparison of particle size distribution of existing aggregate gradations and optimized gradation obtained in Table 9

The existing aggregate stockpile gradations were also prepared and their corresponding packing density values calculated using CPM. The results are presented in Table 10. Aggregate stockpile #89 gives the highest packing density (0.655) among all the stockpiles, whereas #57 gives the lowest density (0.600). The packing density of all the optimized aggregate gradations shown in Table 9 is the highest of all at 0.696. Since the packing of aggregates greatly affects the strength of UHPC, using the optimized gradation would result in a UHPC with high strength.

Table 10. Comparison of packing densities obtained

Aggregate Type	#57	#68	#78	#89	ϕ_{max}
Packing Density	0.600	0.612	0.613	0.655	0.696

Accommodating Fibers using Perturbation Model

Fibers provide enhanced ductility to a quasi-brittle material like concrete. Geometrically, fibers are considered as one-dimensional materials, that is volumes with a very high aspect ratio (>10) and where one side is significantly larger than the other two. However, fibers have a strong disruptive effect on the packing of aggregates, due to their oblong shape. The inclusion of fibers increases the fraction of voids in a poly-disperse mixture of aggregates.

The effect of fibers on the packing density can be accounted for by using a perturbed volume approach proposed by Ben-Aim (Aim and Le Goff 1969). The existence of fibers leads to the presence of a perturbed volume, which can be described as a disturbance in the overall packing of the mixture. The size of the perturbed zone is a function of the size of the fibers as well as the mean size of the

aggregates in the mixture. For a cylindrical fiber with diameter "d_F" and length "l_F", the perturbed volume (V_p) is given by Equation 18.

Equation 18

$$V_p = \pi(d_F + k_F d)^2 \left(l_F - \frac{d}{2}\right)$$

Where k_F is a coefficient that depends on the size of the fibers, it is taken as 0.065 for all the simulations, and "d" is the mean size of the aggregates in the mixture. Figure 54 shows a schematic of the size of the perturbed zone created due to the influence of a single fiber of length l_F and diameter d_F.

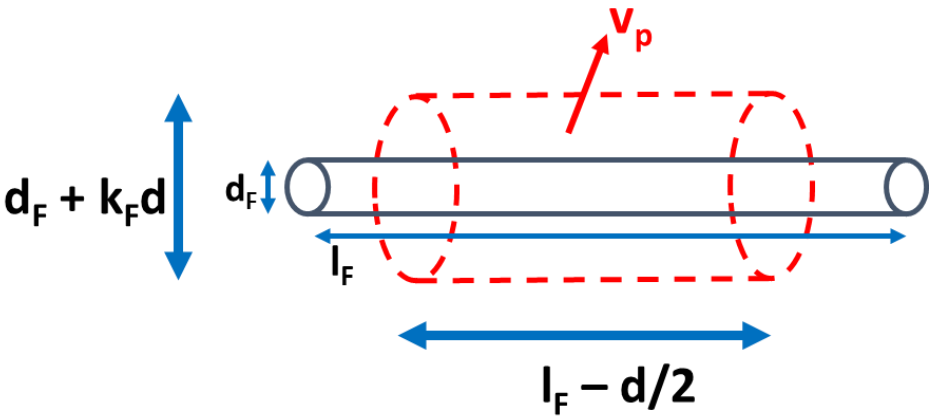

Figure 54. Perturbed volume for a cylindrical fiber

In the perturbed volume V_p, the mean packing density is reduced depending on the volume of a single fiber. Consequently, the overall packing in the mixture is reduced in proportion to the number of fibers in the mixture. The mean value of packing density for the whole system $\acute{\Phi}$ is then given by Equation 19.

$$\acute{\Phi} = \left[1 - \alpha_F - N_F V_p\right]\Phi$$

Equation 19

Where,

$\acute{\Phi}$ is the packing density of the aggregate mixture containing fibers,

Φ is the packing density of the aggregate mixture computed from Equation 17,

α_F is the volume fraction of fibers in the mixture,

N_F is the number of fibers present per unit volume of the mixture, and

V_p is the perturbed volume for one single fiber.

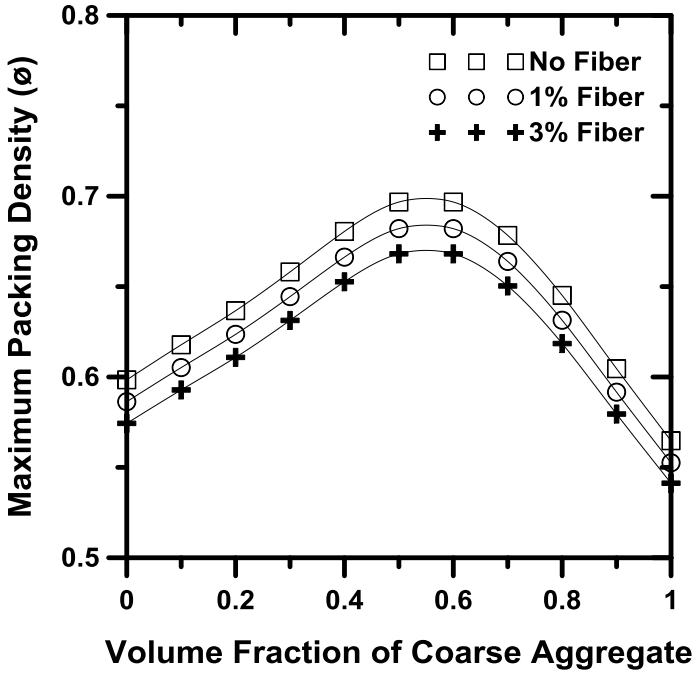

Figure 55. Maximum packing density as a function of volume fraction of coarse aggregates for different fiber volume fractions

Figure 55 shows the comparison of packing densities predicted by the model when two different volume fractions of fibers are introduced into the aggregate mixture. The perturbation model described earlier was used to determine the influence of fibers. To keep the figure concise, only the maximum packing density obtained for each volume fraction of coarse aggregate in the total aggregate mixture is plotted.

Since fibers disrupt the packing of the mixture due to their elongated shape, an increase in the fiber content reduces the maximum packing density. However, the locations of the packing density maxima are unchanged by the fiber content and the maximum packing density values occur for the same combination of aggregates. Thus, the combination of aggregates to achieve the maximum packing density can be considered independent of the fiber volume fractions commonly employed in UHPC mixtures.

Combining Particle Packing with Microstructure Packing and Rheology Results

The optimized aggregate gradation obtained in the previous section was coupled with the optimized paste compositions obtained in Chapter 5 to make concretes. Eight paste compositions were selected based on the analysis of microstructural packing and rheology of the pastes in Chapter 5. Mortars were cast for all the eight selected mixtures and all the mixtures attained compression strengths of more than 10,000 psi at 28 days. Based on these results, a smaller subset of binders was selected for casting concretes and further evaluation of mechanical and durability properties. The selection process made sure that UHPC mixtures with a high amount of cement replacement were selected such that sustainable UHPC mixtures could be formulated.

Two binder compositions were selected. One was a quaternary blend of cement, silica fume, limestone, and fly ash with an overall cement replacement of 30% by mass, and the second was a ternary blend of

cement, silica fume, and limestone with an overall cement replacement of 50% by mass. Concrete batches were prepared for each binder mixture, one without any steel fiber reinforcement and the other incorporating 1% of steel fiber by volume. Furthermore, the UHPC made using quaternary blend binder was proportioned using 3% of steel fibers by volume to compare with commercially available UHPCs, which use such high fiber content to obtain higher levels of ductility. These mixtures are shown in Figure 56. Table 11 provides the details of the mixture proportioning for all these mixtures. Table 12 lists a simplified mixture proportions data by grouping data from Table 11 into fewer categories.

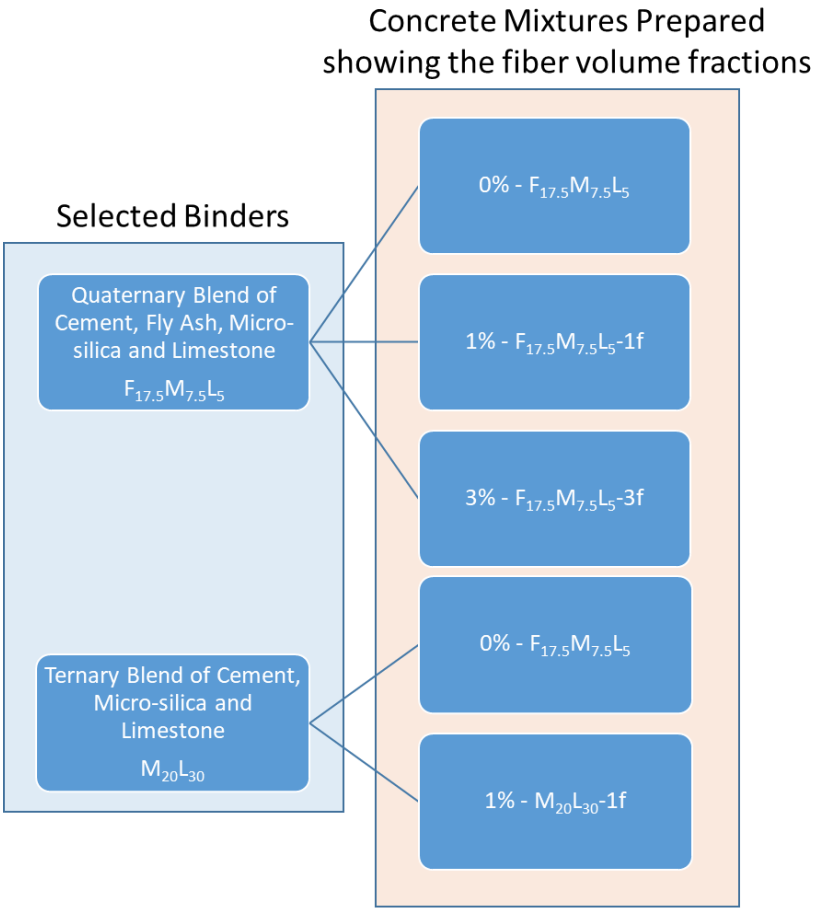

Figure 56. Schematic showing the concrete mixtures prepared with fiber volume fractions varying from 0% to 3%

Table 11. Mixture proportions of UHPCs obtained using optimized aggregate and paste compositions

Content of materials (lb/yd^3)	$F_{17.5}M_{7.5}L_5$	$M_{20}L_{30}$	$F_{17.5}M_{7.5}L_5$ – 1f	$M_{20}L_{30}$ – 1f	$F_{17.5}M_{7.5}L_5$ – 3f
OPC	1595	1321	1579	1310	1539
Fly ash (F)	280	0	276	0	270
Micro silica (M)	120	265	118	261	115
Lime stone (L)	79	396	79	393	78
Coarse aggregate (#4)	580	555	575	549	560
Coarse aggregate (#8)	145	138	143	138	140
Coarse aggregate (#10)	145	138	143	138	140
Fine aggregate (Concrete Sand)	290	278	287	275	280
Fine aggregate (Fine Sand)	290	278	287	275	280
Water	280	288	276	285	265
Fibers	0	0	126	126	379
Superplasticizer (% solids content by mass of binder)	1.25	1.45	1.3	1.5	1.37

Table 12. Simplified mixture proportions of UHPCs obtained using optimized aggregate and paste compositions

Content of materials (lb/yd^3)	$F_{17.5}M_{7.5}L_5$	$M_{20}L_{30}$	$F_{17.5}M_{7.5}L_5$ – 1f*	$M_{20}L_{30}$ – 1f*	$F_{17.5}M_{7.5}L_5$ – 3f*
Cementitious Materials	2073	1982	2053	1964	2001
Coarse Aggregate	870	831	861	826	839
Fine Aggregate	580	556	573	549	560
Water	280	288	276	285	265
Superplasticizer	104	115	107	118	110
Water to Binder Ratio	0.17	0.19	0.17	0.19	0.17

The water to binder ratio was adjusted to be lower than 0.20 for the concrete mixtures by adding a higher superplasticizer content. The water-to-powder ratio for all the concrete mixtures varied from 0.17 to 0.19. A higher water-to-powder ratio was required for the mixtures with a higher amount of silica fume because of its higher water demand owing to large surface area. Since fibers disrupt the packing of the microstructure, mixtures containing a high fiber content required a higher superplasticizer dosage than the ones without fibers.

Mixing and Curing of Concretes

The selected UHPC mixtures in Table 11 were mixed in a Croker RP150XD rotating pan mixer with a capacity of 10 cubic feet (see Figure 57). The mixer consists of two shearing paddles which are held in place, while the pan containing the concrete rotates at a pre-defined rate of 74 rpm. This mixing arrangement simulates the mixing of concrete in a truck mixer. A fixed scraper blade attached to the assembly removes the paste adhering to the sides of the wall and provides a uniform mixing environment.

Figure 57. Croker RP150XD rotating pan mixer

Prior to mixing, all aggregates were washed and dried to eliminate surface impurities that enhance the water demand and compromise the mechanical properties (see Figure 58).

Figure 58. Washed and dried coarse aggregates - #10, #8, and #4 from left to right

The washed and dried aggregates were mixed first along with the predetermined amount of mixing water that was required to bring them to a saturated surface-dry (SSD) condition (Figure 59 through Figure 62). The amount of water required for the aggregates to reach SSD condition was determined during the laboratory testing of aggregates.

Figure 59. Coarse aggregates (#4, #8 and #10) added to the mixer

Figure 60. Fine aggregates (concrete sand and fine sand) added along with the coarse aggregates

Figure 61. Mixing water added to the aggregate to attain SSD condition

Figure 62. Aggregate mixture in SSD condition after addition of mixing water

Powders were incrementally introduced in the aggregate mixture in decreasing order of fineness (micro silica, limestone, cement, and fly ash, in that order). This helps ensure adequate shearing of powders and restricts any agglomerations that might occur otherwise. Every successive powder addition was followed by a mixing time of approximately 3 to 4 minutes. Figure 63 (a-f) shows the addition of powders to the aggregate mixture and the state of the mixture after each mixing cycle. Finally, a mixture of water and superplasticizer was introduced in one-third increments and mixed for 5 minutes after every addition. Figure 64 (a-e) shows the visuals of each step.

Fibers were added after the other components were uniformly mixed. A further mixing for 3 to 4 minutes was carried out after the addition of fibers to ensure that they were uniformly dispersed. Figure 64 (e) and Figure 65 (a-c) show the addition of fibers to the concrete mixture and the final mixture ready to be poured into the beam and cylinder molds.

a) Addition of micro-silica to aggregate mixture

b) Blending the micro-silica and aggregates

c) Addition of limestone to the aggregate blend

d) blending of limestone and aggregate blend

e) Addition of fly ash to the blend

f) Addition of cement to the final blend

Figure 63. (a-f) Addition of powders to the aggregate mixture

a) Addition of first 1/3 of water & superplasticizer

b) Post-addition of the 1/3 water and SP

c) Addition of 2/3 of water & superplasticizer

d) Post-addition of 2/3 water and SP

e) Addition of all of the water and SP

f) Addition of steel fibers to concrete mixture

Figure 64. (a-f) Addition of water, superplasticizer (SP) and fibers to the mixture

a) Final state of mixture after mixing with steel fibers

b) Final state of mixture showing its workability

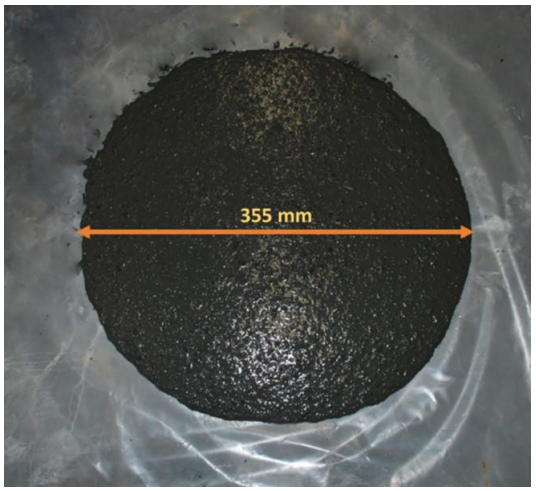

c) Slump flow test conducted on fresh UHPC, showing no segregation

Figure 65. (a-c) Final state of the mixture

As can be noticed from the description of the mixing procedure, it is quite intense and requires continuous shearing of the aggregates and the powder components. Proper mixing procedure is essential to obtain a flowable and consistent mixture at the low water to binder ratio employed. UHPC cylinders (50 mm diameter and 100 mm long for compressive strength, 100 mm diameter and 200 mm long for moisture and ionic transport tests), and beams (50 mm x 65 mm x 380 mm and 100 mm x 100 mm x 400 mm) were prepared for mechanical property testing and stored in a moist chamber at >98% RH and 23 $\pm$ 2^{o}C until the age of testing, after removal from the molds after 24 hours. The molds prepared for casting the specimens are shown in Figure 66 (a-c).

a) Two wooden beam molds of size 4” x 4”x 18” for casting large UHPC beam specimens

b) Six wooden beam molds of size 2” x 2.5”x 15” for casting small UHPC beam specimens

c) Two plastic cylindrical molds of diameter 3” and height 6” prepared for casting UHPC cylinder specimens

Figure 66. (a-c) Molds prepared to cast the UHPC concrete mixture

Chapter 7 MECHANICAL TESTING AND EFFECT OF FIBER REINFORCEMENT IN UHPC BEAMS

Introduction

This chapter describes the flexural tests performed on the UHPC beams. Effect of fibers on the suppression of cracking and toughening mechanisms are addressed in detail. Some of the variables in the experiments include the effect of specimen size, mix designs, mixing methods, curing periods, and fiber volume percent. The key components of this chapter include:

- The effect of fibers on toughening and mechanisms of crack growth in UHPC is characterized.
- The effect of mix design is compared for two mix designs discussed in detail in Chapters 5 and 6. These include quaternary and tertiary mixes F17.5M7.5L5 and M20L30.
- The effect of the mixing method is investigated by comparing the results for the materials mixed with Croker mixer and Hand-Drill mixing.
- The size effect on the strength parameters is addressed for several sets of small and large beams.
- The effect of duration of curing period was studied using 14 days and 28 days of curing.
- The effect of fiber content was examined for several sets of beams with 1% and 3% steel fiber content.

Overview

One of the most important mechanical properties of UHPC is its resistance to cracking due to enhanced tensile strength and ductility. This enhanced response is attributed to the strength of the matrix phase as well as the toughening mechanism due to fiber reinforcement. Flexural testing is commonly used as an indirect method in lieu of tensile testing because the complexities of specimen preparation and gripping make it difficult to conduct a tensile test. Tension tests are also associated with various challenges such as localization of failure after the first crack, the effect of fixed versus rotating free supports (which may lead to sample rotation or asymmetric crack growth), and potential for growth of multiple cracks (Van Mier 2017). Unlike a compression test or tensile test, a flexure test does not measure fundamental material properties. When a specimen is placed under flexural loading all three fundamental stresses − tension, compression, and shear stresses − are present. Therefore, the flexural properties are due to the combined effect of all three stresses.

A comprehensive discussion of the effect of fibers on the toughening in concrete materials was presented in an earlier report AZ633 (Bakhshi, Laungrungrong, Bonakdar, and Mobasher 2013). Concrete materials produced with short, randomly distributed fibers may be superior to forms of reinforcing concrete using welded wire mesh or rebars. Both the tensile strength and the toughness, especially the post-crack strength, are improved (Bentur and Mindess 1990). It has been shown that due

to the reduced specific spacing, fibers strengthen the composite at the micro level by bridging the microcracks before they reach the critical flaw size (Barzin Mobasher and Li 1996). The small diameter of the individual fibers ensures a better and more uniform distribution of reinforcement. In addition, the high surface area offers significant bond capability. Since the bond strength of glass, steel, or even polymeric fibers is far superior to reinforcing bars, this increases the efficiency of reinforcement so that there is limited crack opening due to the debonding and pullout of reinforcement. The fibers are distributed randomly, offering efficiency in load transfer by the fiber phase. Finally, because the fibers that bridge the matrix cracks are resilient and highly compliant, they can orient to carry the load across the crack faces. This factor is expected to increase the durability of concrete substantially, since the crack width control affects long-term durability.

The sample in a flexural test is a prismatic beam that is simply supported at its ends, and loaded at one or two contact points. These testing configurations are referred to as three-point and four-point bending tests, respectively. These geometrical differences in the test configurations result in variations in the stress distribution in the specimen and the overall flexural response. Beam specimens in these tests may be notched or un-notched to determine several parameters pertaining to the mechanical strength of the specimen. Hence it is important to identify the specimen geometry and characterize the type of loading in a flexural test.

Fundamentals of Toughening Cement Composites by Controlling the Crack Growth Mechanisms

One of the main problems observed with HPC and UHPC is that the high strength and stiffness result in a brittle behavior of the material. The cracks, which initiate due to the concentration of stresses, may extend with a minimal amount of energy and lead to fracture. This low strength post-cracking response is concerning and limits many potential applications. The addition of sufficient fibers would help bridge the potential microcracks and lead to the toughening of fiber-matrix composite, due to processes such as fiber bridging and crack deflection; it would also carry the load post-peak after the matrix failure. The high cost of fibers is always a deterrent that inhibits the use of extremely high percentage of fibers. Therefore, the fiber volume percent in UHPC needs to be optimized to utilize their strength, stiffness, and bond capacity in reinforcing the brittle matrix. The efficiency of fibers also depends on their volume percent, stiffness, type, and aspect ratio.

Toughening is affected by the interaction of the fiber, the matrix, and the interface. In the presence of fibers, the propagation of a matrix crack results in fiber debonding, and as the pullout force on the fiber increases, cracks are closed and fail to propagate easily as a decrease in the stress intensity at the crack tip is observed. Further growth of the matrix crack depends on the extent of fiber debonding, which itself dissipates energy. Two mechanisms play a key role in toughening in the case of UHPC. First, the particle packing results in a densified mixture using particles with different size distribution achieving a maximum packing efficiency, as shown in Figure 67 (a). Second, the use of fibers aids in bridging the cracks, and therefore significantly increases the potential for toughening (see Figure 67(b)).

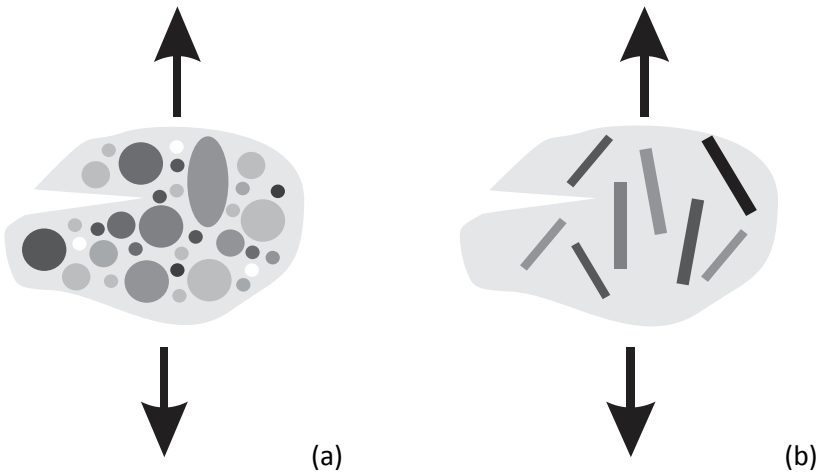

Figure 67. Potential toughening due to a) particle packing and porosity reduction, and b) fiber toughening

Several complementary techniques such as those based on fracture mechanics, non-linear finite element, and closing pressure formulations have been used to relate the fiber, interface, and matrix properties to the strength, toughness, and fracture response of HPC materials as they affect the toughness. In fiber-reinforced concretes, the critical volume percent of fibers for the transition from strain softening to hardening, or distributed cracking, is available from (Chote Soranakom and Mobasher 2009, 2007), (A. E. Naaman and Reinhardt 2006), and (Tjiptobroto and Hansen 1993).

Figure 68 (a) and (b) show the contribution of fibers to the resistance to crack propagation. Whether they are continuous fibers or short uniformly-distributed fibers, in unnotched or notched specimens, the results in terms of toughening are similar in nature. As a single crack grows in the concrete, it crosses one, or several fibers which remain intact and result in bridge across the two crack faces. Additional force applied to the specimen, would attempt to open the crack, which is resisted by the bridged fibers, therefore, the fiber, may start to debond, while still transferring the load. The fibers therefore create the bridging mechanism by forming a closing pressure, that resists crack opening and increase the material's fracture toughness. Propagation of a matrix crack, resisted by the debonding of fibers in an unnotched specimen with continuous fibers, is shown in Figure 68 (a). Note that the bridging zone may contain the entire sample width. Propagation of a crack in a notched specimen with short fibers would also result in crack closure due to stress-crack width relationship, however in this case the bridging zone is rather limited and dimensionally related to the number of fibers that are able to transfer load. Several studies have shown that if the bridging zone is sufficiently large, it would actually increase the strength of the material significantly. The strengthening of the matrix phase by means of a critical volume percent of fibers was also studied using micromechanics (I. H. Yang, Joh, and Kim 2010; J. Yang and Ye 2002). Another approach includes a model to

describe the stages of fiber pullout and crack growth toughening. Using closed-loop pullout experiments, the interfacial region can be characterized as the non-linear response of the ascending part of the pullout curve which affects the stiffness of the pullout force versus slip response. To consider incremental crack growth, an algorithm allowing for gradual fiber debonding is used to allow for the crack opening to take place. To simulate the changes in compliance and of the pullout-slip response, nonlinear fracture models based on R-Curves have recently been used (B. Mobasher and Li 1995; Ouyang, Pacios, and Shah 1994).

Figure 69 shows the bridging effect of fibers in the samples with 1% and 3% fiber content. It demonstrates that the crack bridging is due to the presence of fibers.

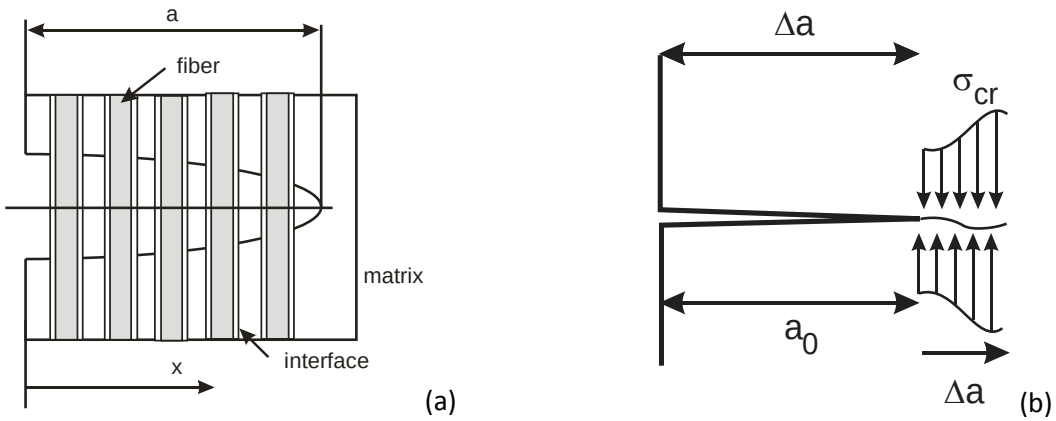

Figure 68. Propagation of a matrix crack, resisted by the debonding of fibers in (a) an unnotched specimen with continuous fibers, and/or b) a notched specimen which results in crack closure due to stress-crack width relationship

(a) (b)

Figure 69. Bridging effect of fibers on samples with: (a) 1% fiber content; (b) 3% fiber content

Flexural testing as a Crack Growth Characterization process

A closed loop flexural testing procedure was applied to the UHPC beams. Closed loop systems are far superior to open-loop systems, which apply a constant load rate or displacement rate until the sample fails. The equipment used in a closed-loop, strain-controlled test has the ability to detect initiation of failure and small changes in the stiffness of the sample as the point of maximum strength is reached. In a closed loop system, the rate of loading can be tied to sensitive parameters such as rate of opening of a crack or a critical deflection measure. These parameters are continuously measured at rates as high as 5000 Hz. As the specimen approaches the point of failure, the equipment is capable to detect the change in stiffness and gradually reduce the load on the specimen in a controlled manner so that the failure is not catastrophic and may proceed using the input requirement of the test. Closed-loop systems are often called feedback control test devices, which use the sample feedback to maintain the loading. For more detailed discussion about the difference between closed- and open-loop testing refer to (Barzin Mobasher 2011).

Experimental Program

As discussed in Chapter 6, two sets of mixtures were evaluated and selected as ideal candidate samples to be evaluated using flexural tests. These mixtures are the quaternary OPC-fly ash-micro silica-limestone binder mixture ($F_{17.5}M_{7.5}L_5$) designated as FML and the ternary OPC-micro silica-limestone binder mixture ($M_{20}L_{30}$) designated as ML. A series of ten sets of concrete beams from different mixture formulations was used in the flexural tests. The variables in these experiments included: two specimen sizes, the effect of notched versus unnotched samples, two different mixing methods, two fiber volume percents, and monotonic and cyclic tests. Each of these topics is addressed in the pertinent section.

Table 13 shows the scope of the study conducted. The presented items address the mixtures, specimen sizes, curing time, and fiber content of the flexural tests. Due to the number of possible combinations, only selected variables were used to address all the various effects. The variables chosen include:

1) Effect of size of beams − small beams of dimensions 2”x 2.5” x 15” (51 mm x 64 mm x 381 mm) and large beams of dimensions 4” x 4” x 18” (102 mm x 102 mm x 457 mm).
2) Effect of curing duration was measured at 14 and 28 days of moist curing for selected samples. All the specimens were cured under identical conditions in a curing room maintained at a temperature of 72 ($\pm$ 3)°F and >95 % relative humidity until the day of testing.
3) Effect of mix formulation − ML and FML.

4) Effect of fiber content – control mixture with no fibers and mixtures with 1% and 3% steel fibers.
5) Effect of cyclic loading – the FML mixture with the larger fiber volume (3%) was subjected to three-point notched beam cyclic tests.
6) Each set consists of three to six replicate beams. A four-point bending (4PB) test in accordance with a modified version ASTM C 1609 was performed on these beams.

The $M_{20}L_{30}$ mixture (referred to as ML mixture) was used only in small beams, 2"x 2.5" x 14" (51 mm x 64 mm x 356 mm), cured for 28 days at 0% and 1% fiber volume. The $F_{17.5}M_{7.5}L_5$ mixture (referred to as FML mixture) was used to evaluate the influence of specimen size, fiber volume percent, and curing age. The FML mixture was selected based on its higher 28-day compressive strength (see Chapter 6). This mixture had a more economical set of ingredients based on material costs (see Chapter 10) than the $M_{20}L_{30}$ mixture.

Table 13. Mixtures and test details for the flexural response of UHPC beams

Set ID	Mix Design	Beam Series	No. of Replicates	Beam Size*	Fiber Content (% by volume)	Curing Period (days)	Testing Method	Mixing Method
1	$M_{20}L_{30}$ (ML)	ML_S_0_28_4PB_D	3	Small 2"×2.5"×14"	0%	28	4PB	Drill Mixer
2		ML_S_1_28_4PB_D	6		1%	28		
3	$F_{17.5}M_{7.5}L_5$ (FML)	FML_S_0_28_4PB_D	6		0%	28		
4		FML_S_1_28_4PB_D	6		1%	28		
5		FML_S_1_14_4PB_C	3		1%	14		Croker Mixer
6		FML_S_1_28_4PB_C	3		1%	28		
7		FML_L_3_28_4PB_C	3	Large **(4"×4"×16")**	3%	28		
8		FML_L_1_14_4PB_C	3		1%	14		
9		FML_L_1_28_4PB_C	3		1%	28		
10		FML_L_3_28_3PB_C	3		3%	28	3PB-Fracture (Cyclic)	

***The nominal dimension of the small beams is 2"×2.5"×14" and of the large beams 4"×4"×16".**

Test Setup

A servo-hydraulic MTS 810 mechanical testing machine equipped with the flexural fixture, two displacement transducers, and software capable of controlling the test and recording/analyzing the data were used. The test setup is shown in Figure 70. The two-transducer arrangement uses a setup attached to the concrete specimen directly above the support members and at the specimen so the spurious deformations are excluded from the measured response. Four-point bending tests were performed on replicate UHPC beams corresponding to the mixture designs shown in Table 13. A spring-loaded Linear Variable Differential Transformer (LVDT) was mounted at the center of the beam to measure the mid-span deflection with a range of 3.8 mm. Results were used for parameter estimation such as the initial stiffness, post-peak residual strength and toughness.

The Modified ASTM C 1609 testing process consists of load and stroke-controlled phases. The test procedure is conducted in three steps based on the mode of control during the test as summarized in Table 14. The first phase is force-controlled and is based on a constant rate of increase of the load applied to the specimen. A loading rate of 2.2 N/sec was used and the deflection measured. This initial loading range covers about 30% of the initial linear load-deflection response and is followed by the subsequent steps that are both displacement controlled at rates of 8.5 µm/sec and 1.7 µm/sec, as specified in Table 14.

Table 14. Testing procedure used in the MTS station manager to control the test

Phase	Control Mode	Loading Rate	Phase Limit
1	**Load**	**2.2 N/sec**	**134 N**
2	**Actuator (Deflection)**	**8.5 µm/sec**	**3.8 mm**
3	**Actuator (Deflection)**	**1.7 µm/sec**	**19 mm**

The raw experimental data collected from the test was analyzed using a MATLAB code developed by the authors. The original data file contains several data points and the code allows for data reduction using interpolation and smoothing algorithms for better data handling. The code also calculates post-cracking parameters that represent the role of the fiber efficiency in carrying the load in the crack propagation phase of testing. Parameters such as load capacity, residual strength, and toughness were computed at two deflection limits of L/600 and L/150, where L is the span of the beam. These parameters are summarized in Table 15.

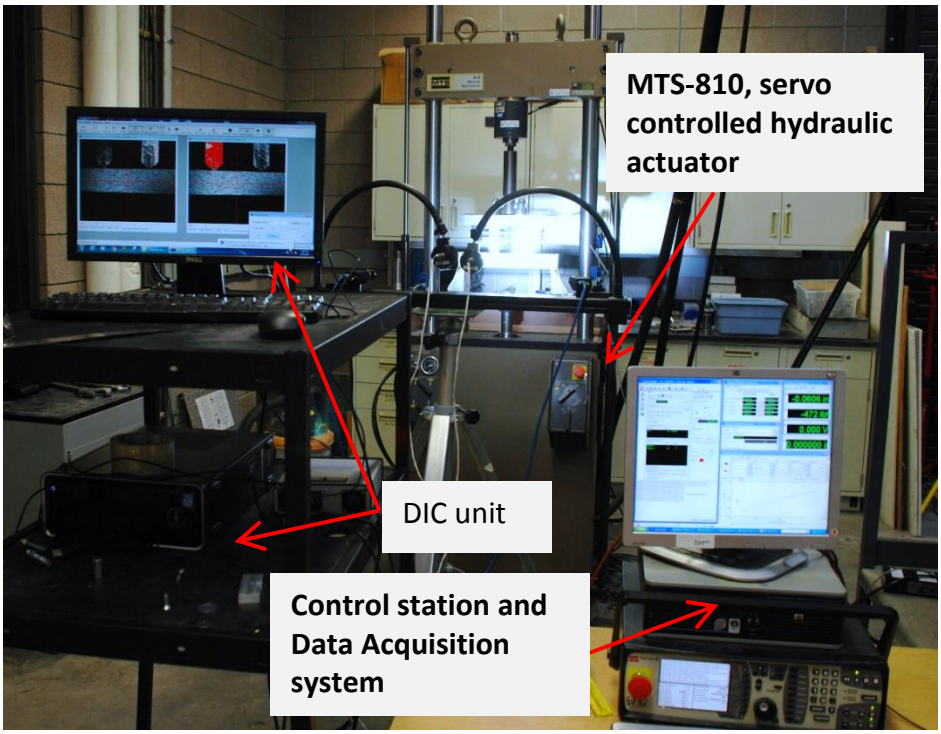

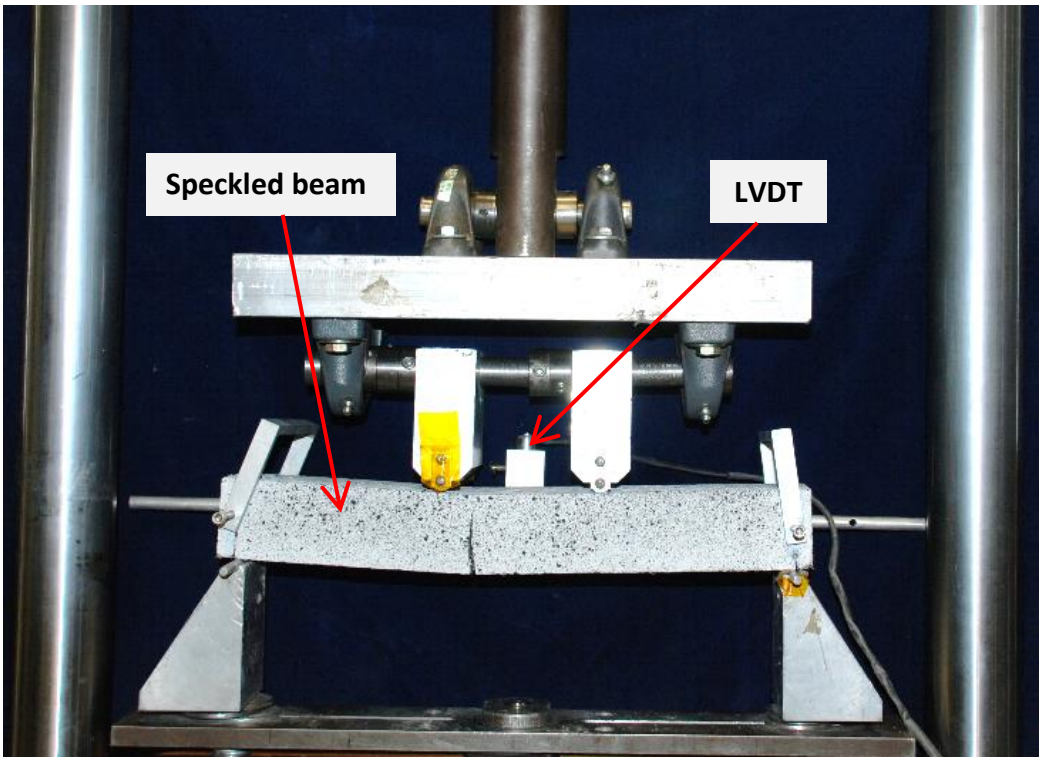

Figure 70. Experimental setup used for standard four-point bending tests on UHPC beams

Introduction to Digital Image Correlation (DIC)

Traditional displacement measuring techniques such as Linear Variable Differential Transformer (LVDT) measure the deformation of a single point on the specimen. Digital Image Correlation (DIC) is a more advanced technique that can capture the entire displacement field at every point on the surface of the specimen. As a non-contact optical speckle-tracking measurement method, DIC obtains full-field surface deformations through consecutive post-processing of digital images taken at specific time intervals. This method has been widely applied for composites, fabrics, structural materials, etc. (Gao et al. 2015; Rajan et al. 2010; Zhu, Mobasher, and Rajan 2010). The principle and applications of DIC are well documented (Gao et al. 2015; X. Wang et al. 2017; Xing et al. 2017). This method is superior to alternative strain measurement systems at an isolated spot or within a gage length by conventional devices such as LVDT, extensometer, clip gage, or strain gages, since the latter result in single values and are insufficient to study the spatial variations or changes due to non-homogeneous deformations.

Application of DIC to specimens that undergo cracking provides a unique opportunity to keep track of the beam's deformations and crack growth during the test by measuring full field deformations and crack opening. In order to perform DIC, a speckle pattern is prepared on the specimen surface using flat paint to create a random texture that is non-periodic and with a clear contrast of gray levels as shown in Figure 71**.** A single camera can be used to obtain two-dimensional deformation pattern in the sample. For three-dimensional displacement measurements, multiple images are needed; hence two cameras from different angles are pointed toward the beam to capture the deformation. Post-processing of the data provides the three-dimensional (u, v, and w) displacements (Das et al. 2015a, 2014).

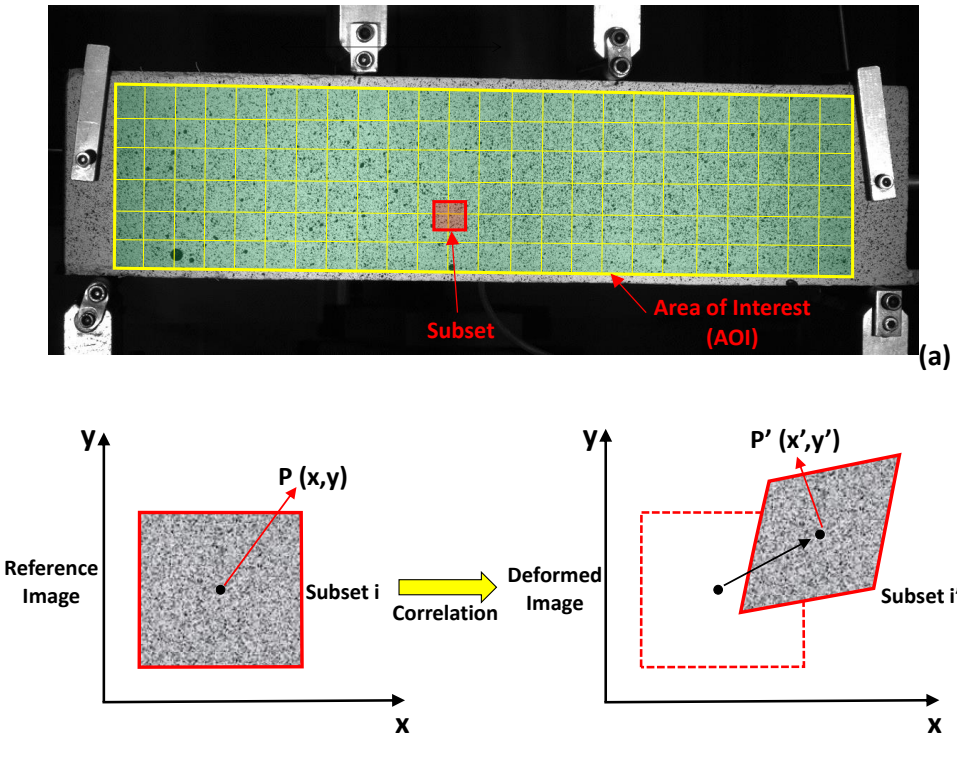

Figure 71. Basic principle for DIC method: (a) Illustration of the area of interest (AOI) and subset, (b) schematic presentation of a reference and deformed subset

A CCD (Charged-Coupled Device) camera was used to record images every second. A commercial software, Vic-2D 2009, developed by Correlated Solutions Inc., was used to conduct image analysis ("Correlated Solutions – VIC-2D™" n.d.). As shown in Figure 71, post-processing of the data starts by manually specifying an area of interest (AOI) in the software. This area is divided by the software into an evenly spaced virtual grid. The displacements are computed at each point of the virtual grids *P(x, y)* by tracking the movement of each point from the reference image (before deformation) to the images in the deformed state of the specimen *P'(x', y')*. The computation is based on the assumption of a certain window of deformation and the maximum likelihood of matching the intensity of the grid 6.9 the undeformed and deformed images. The cross-correlation function is a mathematical computation of the likelihood of displacement within the grid and is conducted by pattern matching of the grid speckles.

The red square in Figure 71(a) is defined as a subset (a set of pixels) and its gray scale distribution is used in the identification of a certain subset of deformed images. The tracking of the subset is conducted using selected correlation functions such as cross-correlation (CC) or normalized cross-correlation (NCC). Subsequently, the strain fields can be derived by smoothing and differentiating the displacement fields. Figure 72 shows the speckled beam after cracking, at different loading stages. Figure 72 (a) shows the initial stage of the deformation in the beam. Figure 71 (b-e) represent the crack propagation as a result of the increasing load on the specimen.

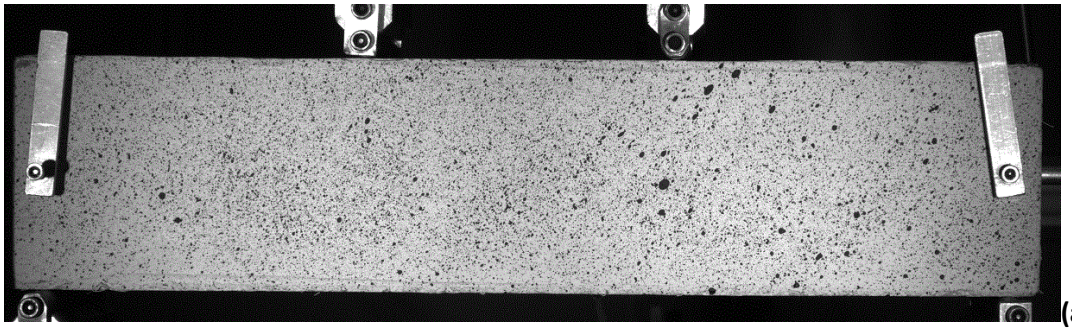
(a)

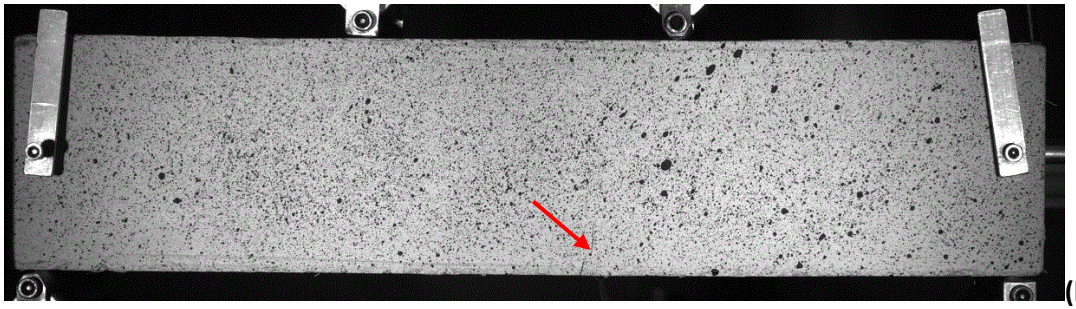
(b)

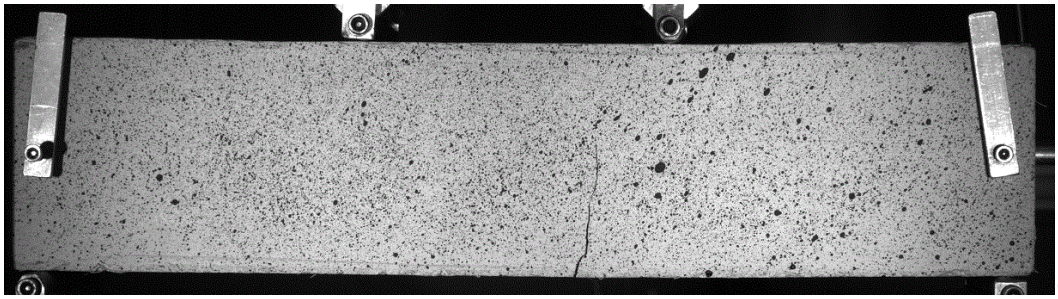
(c)

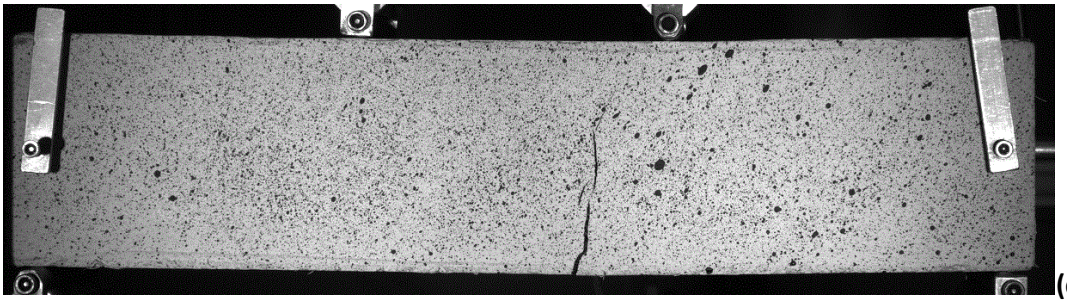
(d)

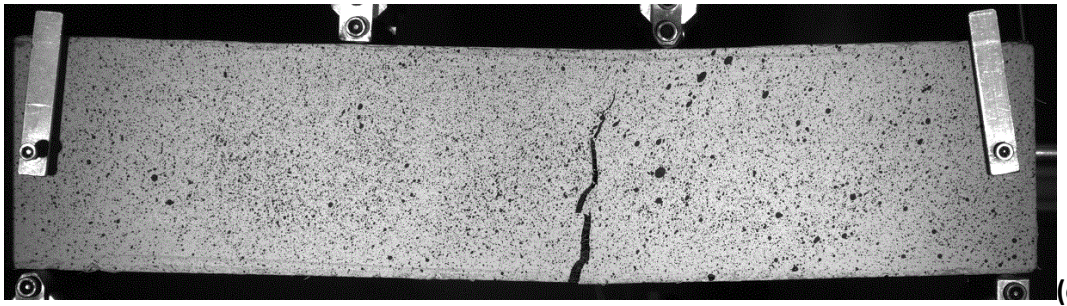
(e)

Figure 72. Speckled beam at different stages of testing

Analysis of Test Results

Analysis of Plain UHPC and Effect of Fiber Reinforcement on the Flexural Response

Figure 72 compares the flexural response of a UHPC control specimen with a UHPC sample containing 1% steel fibers by volume (V_f = 1%). As shown in the figure, the unreinforced UHPC beam (V_f = 0%) behaves as a brittle material and the load-deflection response increases linearly up to a load of 799 lbs, which is equivalent to a mid-span deflection of 0.004 in. At this point, the failure is imminent as a crack forms in a sample which propagates to the full depth of the specimen. The brittle response is clearly shown in the figure and the entire load-carrying capacity is exhausted as a single crack propagates without any resistance from the matrix. This figure also shows the flexural response of the beam containing 1% fiber volume. Note that significant ductility is obtained with the addition of the fibers. This ductility enhancement can be studied at various stages of load-deformation response as discussed below:

1) The first cracking point in the fiber-reinforced specimen is identified by the initiation of nonlinearity in the ascending response and shown to be at higher loads as compared to the plain unreinforced UHPC. This nonlinearity is related to the crack initiation and takes place prior to reaching the maximum load, with a distinct separation from the first cracking point. The nonlinear pre-peak zone corresponds to the stable growth of microcracks, which leads to the accumulation of damage at the peak load.
2) The peak load for the fiber-reinforced specimen (with 1% fiber volume) is 22% higher, compared to the unreinforced control specimen.
3) The post-peak response, however, is significantly dominant in the fiber reinforced specimen and the sample is able to carry a significant portion of the maximum load even beyond the peak.

Figure 73 shows that the incorporation of 1% steel fibers has a beneficial effect on the flexural behavior and the post-peak response of the sample. While there is no post-peak response for the unreinforced specimen due to its brittle behavior, the fiber-reinforced specimens demonstrate a considerable non-linear response after the occurrence of the first crack.

The flexure testing was terminated at an ultimate mid-span deflection of 4 mm for the fiber-reinforced specimens. This value is nearly 40 times greater than the mid-span deflection at the first cracking point in the unreinforced UHPC beams. Additionally, the load carrying capacity at this level is as high as 60% of the peak load. This indicates that after reaching the peak load, the sample is capable of maintaining a large percent of load carrying capacity for a significant range of deformation. The peak load sustained by the UHPC beams containing 1% fiber volume is about 976 pounds, 22% higher than the peak load of 799 pounds in the unreinforced UHPC beams.

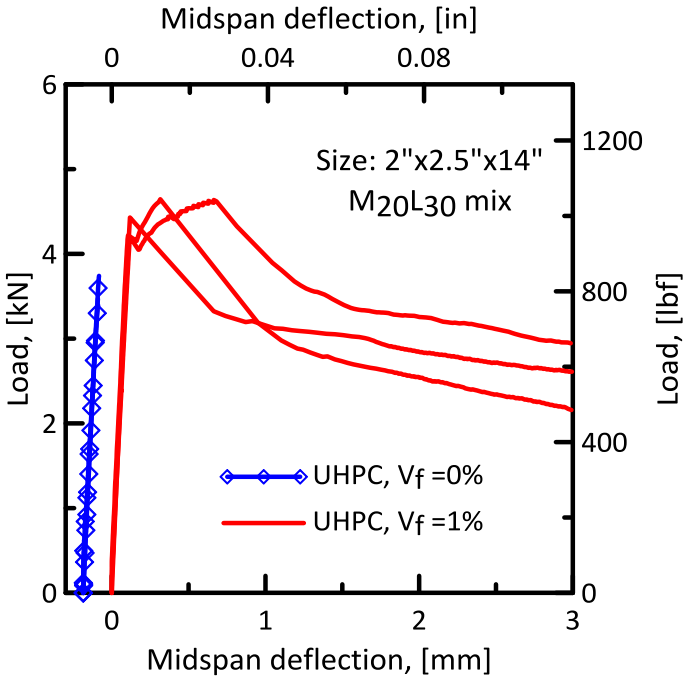

Figure 73. Fiber effect, with and without 1% fiber on $M_{20}L_{30}$ samples

Figure 74 shows similar results for the effect of fibers on the mix FML. Post-cracking results due to the role of fibers are shown for samples with 1% fiber volume of FML samples, and compared to the control samples containing no fiber. Similar results are obtained for specimens which show an improvement in load-carrying capacity beyond the first cracking point as well as a strain softening region beyond the peak load.

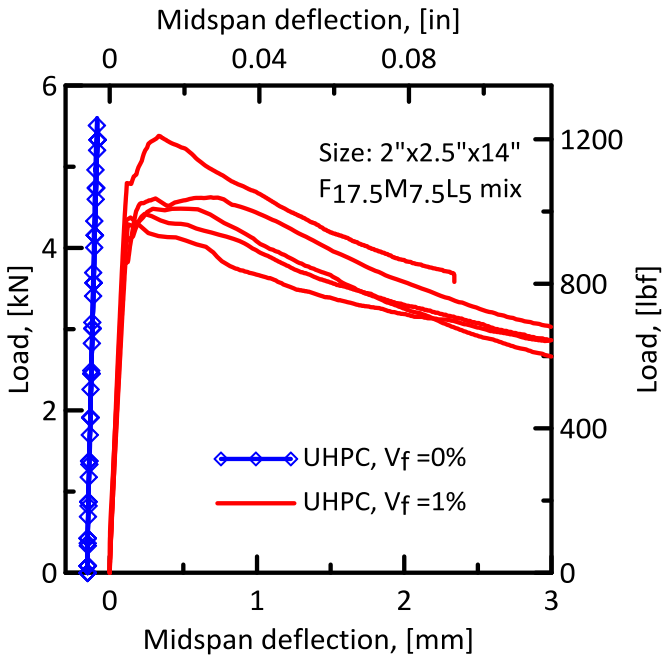

Figure 74. Comparison of the load-deflection response of control sample with a composite containing 1% fiber volume mix series $F_{17.5}M_{7.5}L_5$

Effect of Fiber Volume Percent on the Flexural Response of the UHPC Beams

The area under the load-deflection curve is used as a measure of energy absorption in terms of flexural toughness or the ductility of the material. The rapid loss of load-bearing capacity beyond the peak load in the unreinforced UHPC mixtures indicates a brittle failure and minimal flexural toughness. In the case of the fiber-reinforced specimens, the energy absorption is significantly enhanced. The flexural toughness values are calculated in accordance with ASTM C 1609 at the mid-span deflections of L/600 (area under load-deflection curves from 0 to L/600) and L/150 (area under load-deflection curves from 0 to L/150), where L is the nominal span of the beam (in this case, for small beams, L=14 in).

Figure 75 shows the effect of the inclusion of 1% fiber volume on the toughness of the UHPC beams. The absorbed energy in the fiber-reinforced UHPCs is two to three orders of magnitude higher than that obtained for the unreinforced UHPCs at the peak load. Furthermore, there is no significant post-peak response for the unreinforced UHPC samples as shown in Figure 73 and Figure 74; while the fiber-reinforced specimens show forty times higher toughness values at a mid-span deflection of L/150 than those of samples without fiber, in which the toughness was measured at the deflection corresponding to the cracking. Figure 75 also shows that the FML samples have better post-cracking toughness than that of the ML samples. This is attributed to better particle packing and hydration in this mixture, as shown in Chapters 5 and 6.

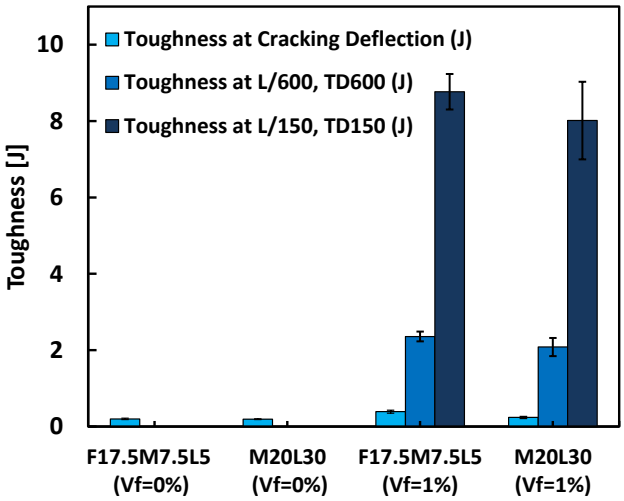

Figure 75. Comparison of toughness between FML and ML mixtures with and without fiber reinforcement (1% fiber volume)

Figure 76 shows the effect of fiber content on the flexural load-deflection response, comparing two samples with fiber volumes of 1% and 3%. The addition of fibers significantly improves the pre-peak response and doubles the flexural load-bearing capacity of the specimen. Post-peak response is also improved significantly by the increase in the volume percent of fibers.

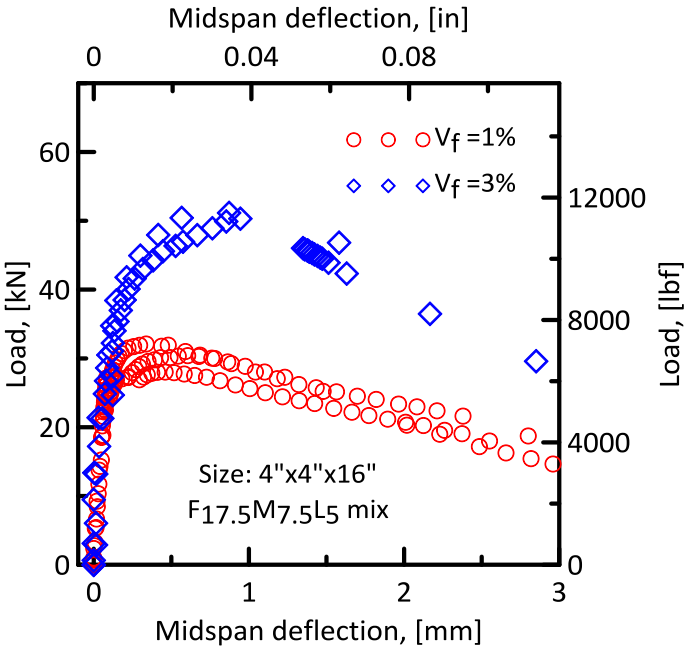

Figure 76. Effect of fiber volume percent on the load-deflection response of large beams after 28 days of curing

Figure 77 shows the plot of equivalent flexural stress versus mid-span deflection for the fiber-reinforced FML specimens. The elastic equivalent flexural stress can be defined as the nominal stress, calculated based on the assumptions of linear elasticity by dividing the load by the section modulus of the uncracked specimen, as shown in Equation 20. Nominal flexural stresses as high as 3000 psi (20 MPa) are calculated for the specimen with 3% steel fibers.

$$\sigma_n = \frac{PL}{bd^2}$$ **Equation 20**

Here σ_n is the nominal elastically equivalent flexural stress, *P* is the load, *L* is the length of the beam, and *b* and *d* are the width and depth of the section.

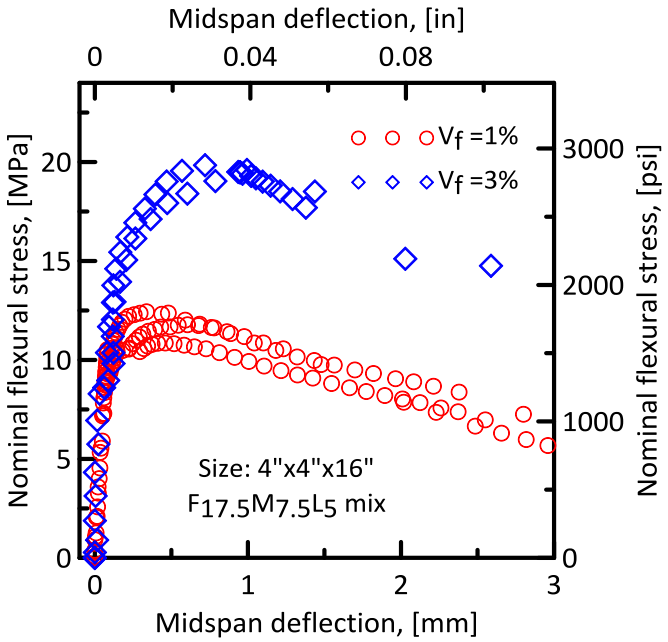

Figure 77. Effect of fiber volume percent on the nominal flexural response of the large beams after 28 days of curing

Figure 76 demonstrates that the initial stiffness (the slope of the nominal flexural stress versus mid-span deflection in the linear region prior to peak load) for the specimens containing 3% fibers is similar to that of the specimens containing 1% fibers. The specimens with 3% fibers also show a much larger region of pre-peak nonlinearity which extends from 13 MPa to 19 MPa in flexural capacity. This is attributed to the effect of additional fibers that bridge the matrix cracks and make it possible for the transfer of the load across crack surfaces. The average maximum load-bearing capacity of the beams with 3% fiber

volume (11,417 lb.) is found to be 68% higher than that of the beams with 1% fiber (6,793 lb). This is a significant contribution of the fibers to enhancing the load carrying capacity.

Figure 78 compares the flexural strengths of the beams containing 1% and 3% fiber volume. Samples containing 3% fibers show significantly higher flexural strengths as well as higher residual strength in the post-peak region. The post-crack response greatly improves the toughness, and is primarily a function of the fiber content in the mixture.

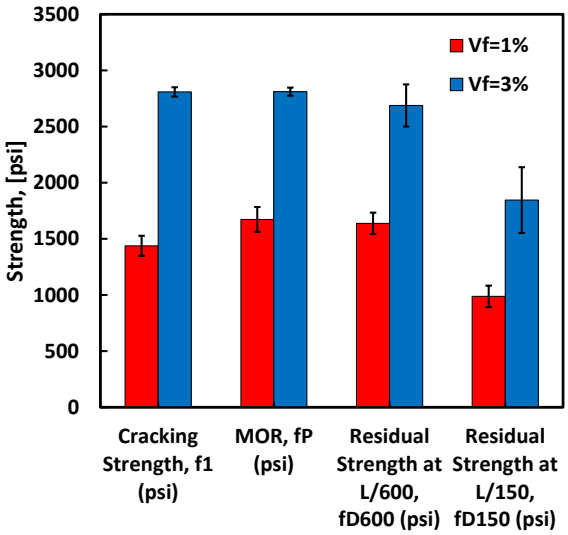

Figure 78. Effect of fiber volume percent on the flexural parameters of large beams, 4" x 4" x 16" (102 mm x 102 mm x 406 mm), after 28 days of moist curing (FML mixture)

Effect of Binder Composition

The influence of binder composition on the flexural response is shown in Figure 79. Figure 80 shows a comparison of the strength values for the FML and ML mixtures. The FML mixture shows better flexural behavior (Figure 78) and higher flexural strength (Figure 79) than the ML mixtures. The post-peak response of this mixture also shows a higher residual strength than the ML mixture. This improvement is attributed to the improved interaction between the matrix and fibers in the FML mixture. Because of this, the FML mixture was chosen for the remaining tests, as shown in Table 13. The remaining experiments were conducted using the FML mixture, to address the effect of different sizes and curing periods (14 and 28 days). The following sections present the key conclusions only. Detailed tables and plots appear in the appendix.

Post-cracking parameters were also calculated. Parameters such as load capacity, residual strength, and toughness were computed at two deflection limits of L/600 and L/150, where L is the span of the beam. These parameters are summarized in Table 15.

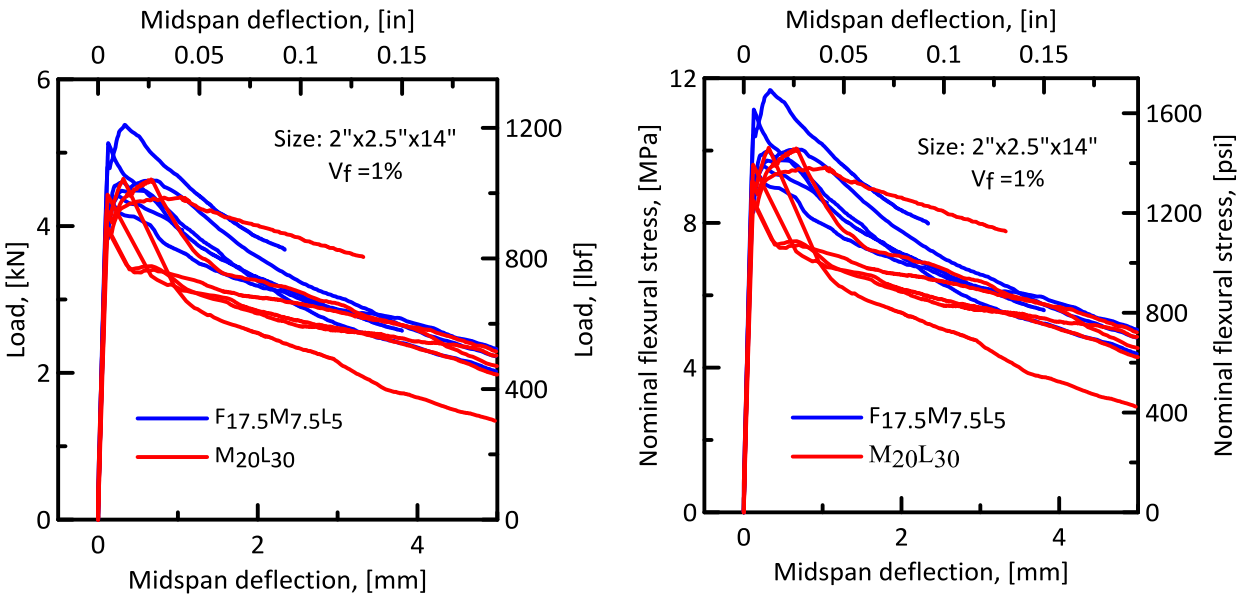

Figure 79. Effect of mixture design on the flexure response for the small beams (2" x 2.5" x 14") with 1% fiber volume

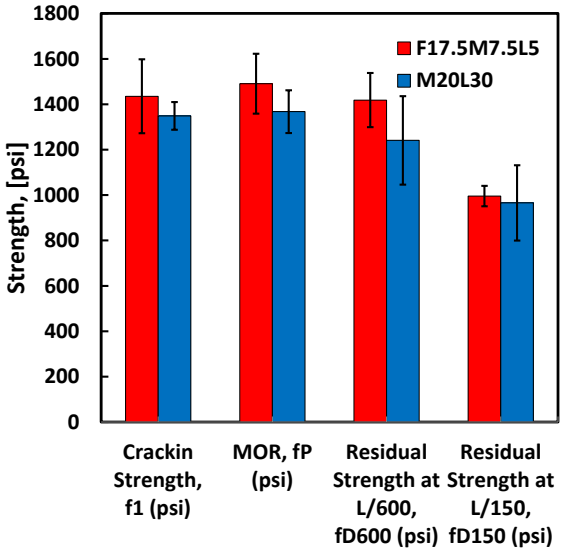

Figure 80. Strength parameters for the tested beams for FML and ML mixtures (the error bars correspond to one standard deviation from the mean, calculated for a total of six replicate samples)

Table 15. Summary of the calculated parameters, based on ASTM C1609

($F_{17.5}M_{7.5}L_5$ Replicates)

Group	Specimen ID	First Peak Deflection, δ1 (in)	First Peak Load, P1 (lb)	First Peak Strength, f1 (psi)	Deflection at Maximum Load, δp (in)	Peak Load, Pp (lb)	MOR, fP (psi)	Load at L/600, PD600 (lb)	Residual Stress at L/600, fD600 (psi)	Toughness at L/600, TD600 (in-lb)	Load at L/150, PD150 (lb)	Residual Stress at L/150, fD150 (psi)	Toughness at L/150, TD150 (in-lb)	Equivalent Flexural Strength at L/150, Re_3 (%)
$F_{17.5}M_{7.5}L_5$	FML1	0.005	1155.5	1680.3	0.005	1153.5	1614.9	1015.3	1421.5	20.7	--	--	--	--
	FML2	0.004	852.5	1239.6	0.027	1039.5	1455.4	1035.8	1450.1	19.8	756.3	1058.8	83.0	85.6
	FML3	0.004	901.5	1310.9	0.019	1008.0	1411.2	1006.1	1408.6	21.3	681.5	954.1	77.8	82.6
	FML4	0.005	1077.3	1566.6	0.013	1209.5	1693.2	1159.8	1623.8	22.9	--	--	--	--
	FML5	0.004	974.8	1417.5	0.006	983.5	1377.0	909.2	1272.8	20.1	697.8	976.9	73.0	79.6
	FML6	0.005	960.2	1396.2	0.009	993.5	1390.8	953.1	1334.3	20.4	709.2	992.9	76.6	82.6
Average		**0.005**	**986.9**	**1435.2**	**0.013**	**1064.6**	**1490.4**	**1013.2**	**1418.5**	**20.9**	**711.2**	**995.7**	**77.6**	**82.6**
Std. Dev		**0.000**	**112.1**	**163.0**	**0.009**	**94.2**	**131.9**	**85.5**	**119.6**	**1.1**	**32.2**	**45.0**	**4.1**	**2.4**
Coef. of Var.		**7.8%**	**11.4%**	**11.4%**	**64.9%**	**8.8%**	**8.8%**	**8.4%**	**8.4%**	**5.4%**	**4.5%**	**4.5%**	**5.3%**	**3.0%**

($M_{20}L_{30}$ Replicates)

Group	Specimen ID	First Peak Deflection, δ1 (in)	First Peak Load, P1 (lb)	First Peak Strength, f1 (psi)	Deflection at Maximum Load, δp (in)	Peak Load, Pp (lb)	MOR, fP (psi)	Load at L/600, PD600 (lb)	Residual Stress at L/600, fD600 (psi)	Toughness at L/600, TD600 (in-lb)	Load at L/150, PD150 (lb)	Residual Stress at L/150, fD150 (psi)	Toughness at L/150, TD150 (in-lb)	Equivalent Flexural Strength at L/150, Re3 (%)
$M_{20}L_{30}$	ML1	0.005	995.5	1447.7	0.005	995.7	1394.0	747.1	1045.9	21.1	623.9	873.4	64.3	69.2
	ML2	0.005	942.5	1370.6	0.026	1042.2	1459.0	1024.6	1434.5	19.0	713.3	998.6	76.4	78.6
	ML3	0.004	946.6	1376.6	0.012	1044.2	1461.8	1037.0	1451.8	10.0	563.9	789.4	59.8	61.3
	ML4	0.005	885.6	1287.8	0.005	892.4	1249.3	774.2	1083.9	15.9	--	--	--	76.5
	ML5	0.004	893.8	1299.7	0.041	989.0	1384.6	974.1	1363.7	19.3	877.4	1228.3	84.1	91.1
	ML6	0.004	901.9	1311.5	0.004	898.2	1257.4	762.3	1067.2	16.7	669.9	937.9	66.0	78.8
Average		**0.004**	**927.6**	**1349.0**	**0.015**	**976.9**	**1367.7**	**886.5**	**1241.2**	**17.0**	**689.7**	**965.5**	**70.1**	**75.9**
Std. Dev		**0.000**	**41.9**	**60.9**	**0.015**	**67.3**	**94.2**	**139.2**	**194.9**	**3.9**	**118.7**	**166.1**	**9.9**	**10.0**
Coef. of Var.		**7.9%**	**4.5%**	**4.5%**	**97.0%**	**6.9%**	**6.9%**	**15.7%**	**15.7%**	**23.1%**	**17.2%**	**17.2%**	**14.1%**	**13.2%**

Effect of Mixing Method

Figure 81 shows the effect of mixing method on the flexural response of the FML mixtures incorporating 1% fibers. The two mixing methods are i) a drill mixer, and ii) a high-volume, high-shear Croker mixer. The details of mixing methods were discussed in Chapters 5 and 6. The load-deflection results show that the mixtures cast using the high-volume, high-shear mixer are stronger in flexure and have a higher residual flexural strength than those cast using the hand-drill mixer. This can be attributed to the better mixing, dispersion, and uniform fiber distribution obtained using the high-shear mixer (also see Figure 82).

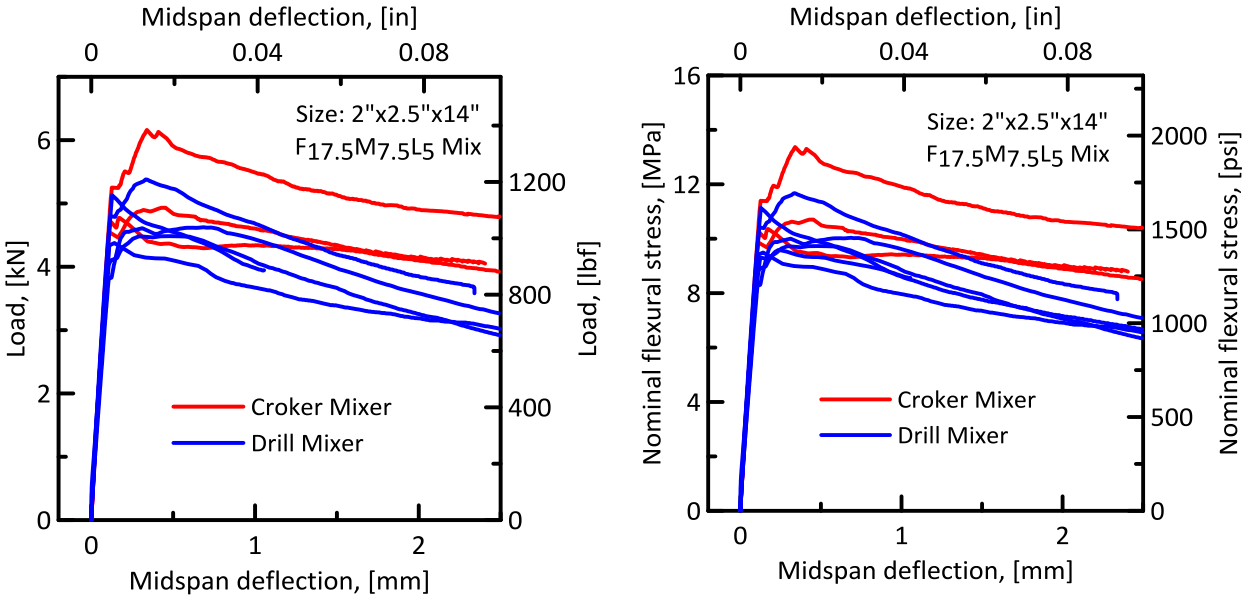

Figure 81. Effect of mixing method

The comparative analysis of the flexural results for hand-drill and high-shear mixers is shown in Figure 82. Beams made using the high-shear mixer have about 12% higher flexural strength, at different stages of loading, than those made with the hand-drill mixer. The improved performance using the high-shear mixer is due to the uniform dispersion of powders and fibers in the mixture.

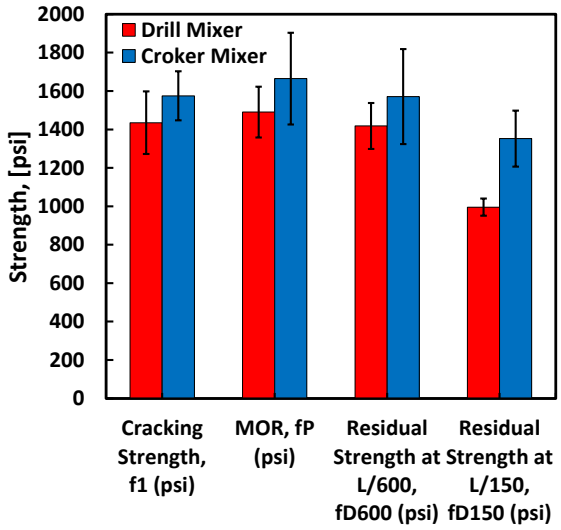

Figure 82. Comparison of flexural strengths obtained via drill mixer and high-shear (Crocker) mixer for small beams with 1% fiber content after 28-day curing period

Effect of Specimen Size

Figure 83 compares the effect of specimen size, measured by the load-deflection curves and flexural stress-deflection curves for the small, 2”x 2.5” x 14” and large, 4” x 4” x 16” beams. The figure shows that there is no significant difference in first-cracking stress, maximum stress, and residual strength between small and large specimens. However, these results will be discussed in Detail in Chapter 8 where the strain, as observed from the predicted stress-strain curves, is higher for the large beams and shows more smooth post-peak response than for the small beams. This may be due to the greater depth of the large specimens, which promote better crack growth, than of the smaller beams that are only 2” deep. This results in a higher bending and deformation capacity for the larger beams. It is also observed that the small beams show a higher maximum stress, about 5%, than do the large beams.

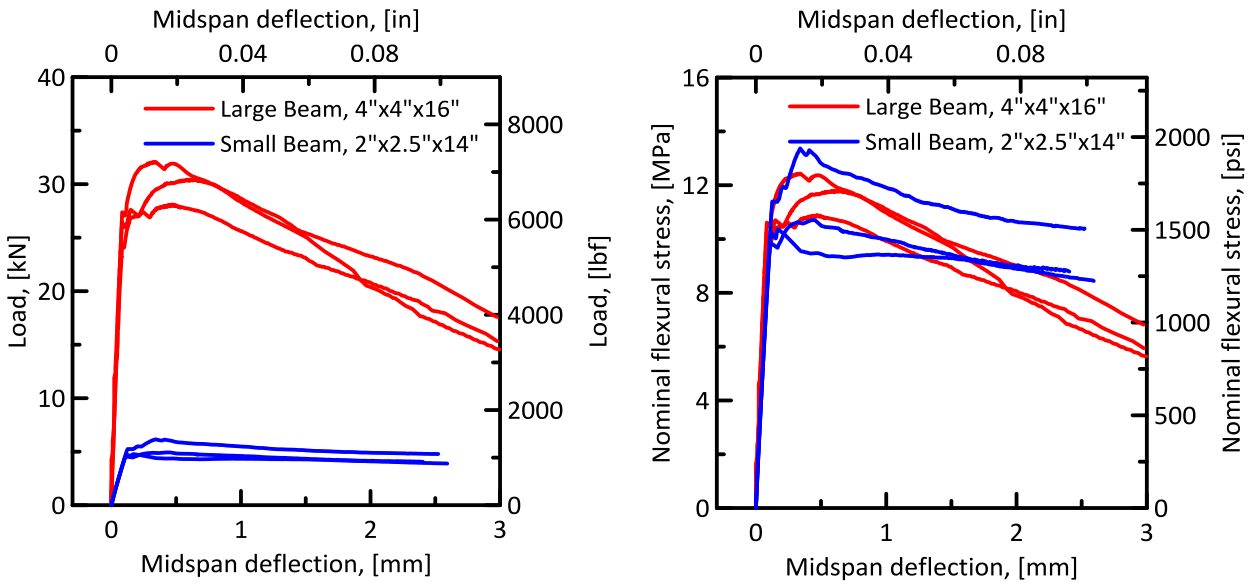

Figure 83. Size effect (2x2.5x14 in beams vs. 4x4x16 in beams)

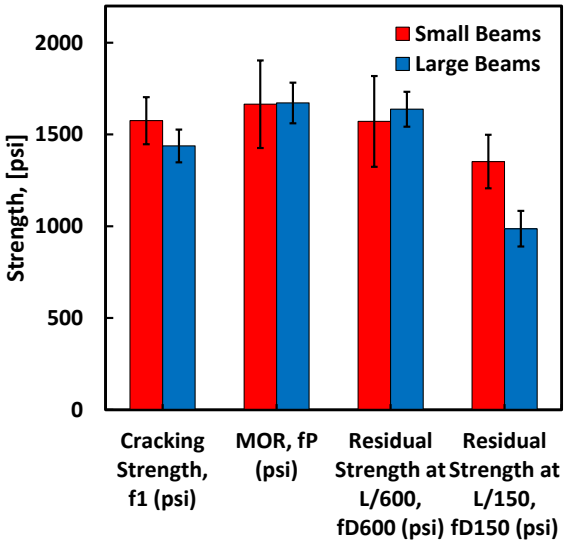

Figure 84. Size effect: (a) small beams, 2"x 2.5" x 14" (51 mm x 64 mm x 356 mm); (b) large beams, 4" x 4" x 16" (152 mm x 152 mm x 406 mm); $F_{17.5}M_{7.5}L_5$ mixes after 28 days

Effect of Curing Duration

Figure 85 compares the effect of curing period on the load-deflection response of the small beams after 14 and 28 days of curing. The strength of the small beams was almost 43% higher after 28 days than after 14 days of curing (see

Table 16). Similar ratio is maintained for the residual strength of small beams, which is 47% higher after 28 days than after 14 days of curing.

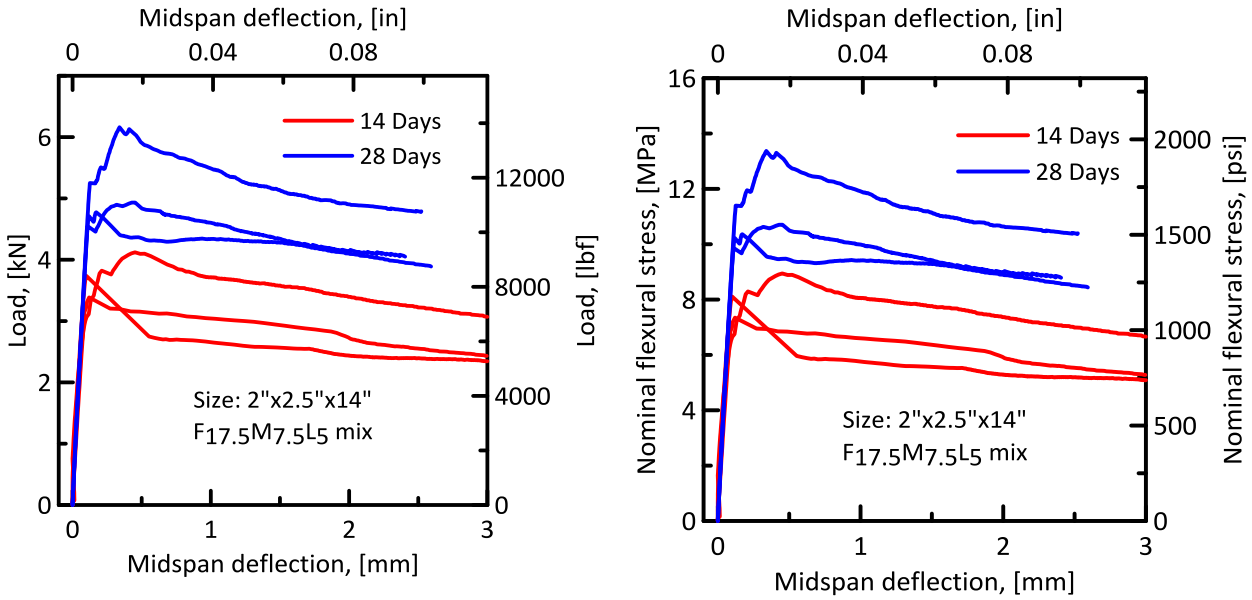

Figure 85. Effect of moist curing on the load-deflection response of the small beams, 2”x 2.5” x 14” (51 mm x 64 mm x 356 mm)

Figure 86 shows the same trend of strength increase due to curing of the large beams. However, the increase in strength is lower than for the small beams.

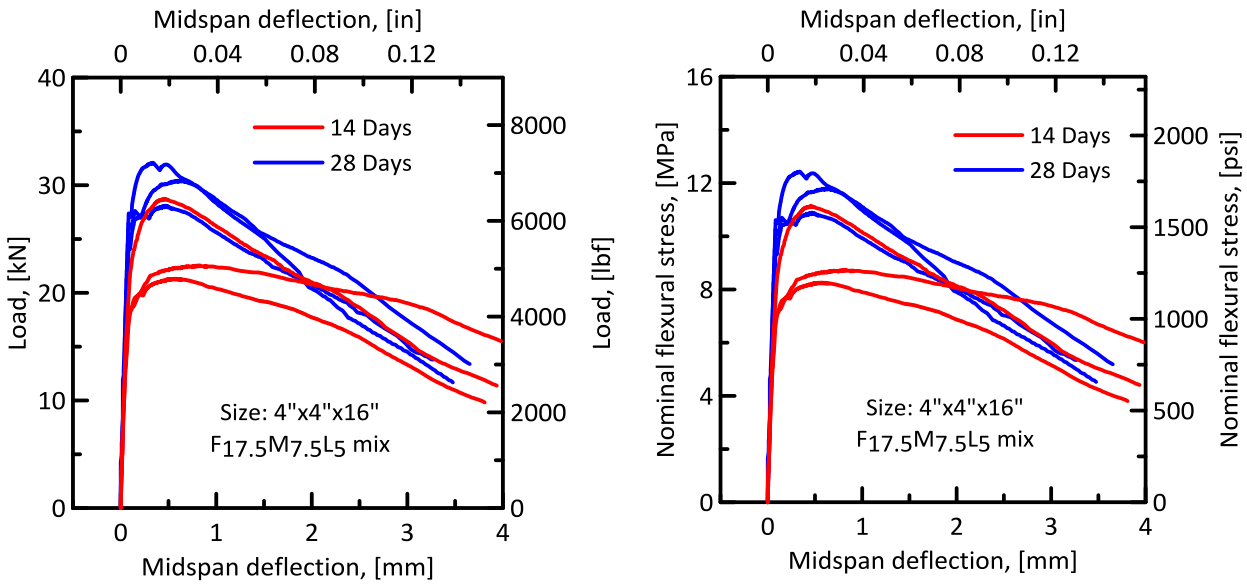

Figure 86. Effect of moist curing on the load-deflection response of the large beams, 4” x 4” x 16” (152 mm x 152 mm x 406 mm)

Figure 87 shows a comparative graph of the effect of the curing duration on the small beams with 1% fibers. Beams cured for 28 days have a 50% higher flexural strength than those cured for only 14 days. This increase is observed at all stages of the loading process.

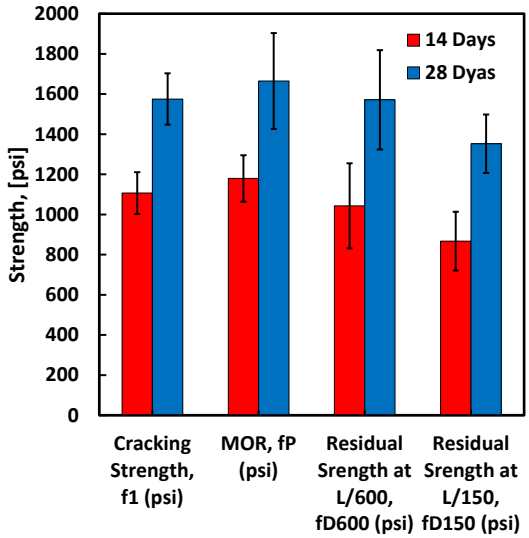

Figure 87. Effect of curing duration on the strength parameters of small beams, 2”x 2.5” x 14” with 1% fiber content

Figure 88 shows a bar chart of the effect of curing duration on the large beams with 1% fiber content. After 28 days of curing, the beams show as much as 30% higher strength than after 14 days.

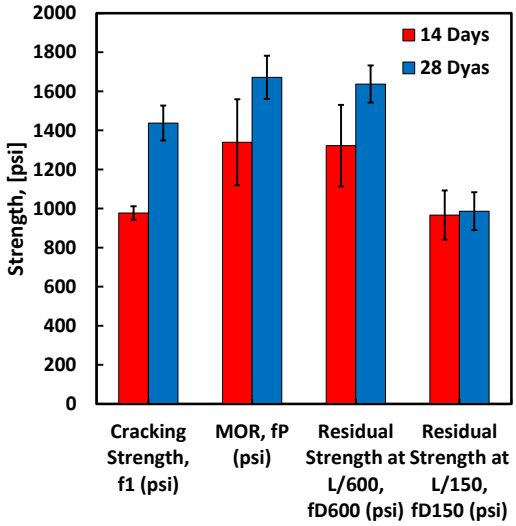

Figure 88. Effect of curing period on large beams, 4" x 4" x 16" (152 mm x 152 mm x 406 mm) with 1% fiber content

As a summary, a list of average values for each set of experimental tests is presented in Table 16. The last column of Table 16 shows that, in almost all of the fiber-reinforced beams, at least 80% of the maximum bending strength is maintained until the equivalent deflection of L/150.

Table 16. Average of experimental parameters for each set of tests according to ASTM C1609

Test Set	Beam Series	No. of Replicates	First Peak Deflection, δ1 (in)	First Peak Load, P1 (lb)	First Peak Strength, f1 (psi)	Deflection at Maximum Load, δp (in)	Peak Load, Pp (lb)	MOR, fP (psi)	Load at L/600, PD600 (lb)	Residual Strength at L/600, fD600 (psi)	Toughness at L/600, TD600 (in-lb)	Load at L/150, PD150 (lb)	Residual Strength at L/150, fD150 (psi)	Toughness at L/150, TD150 (in-lb)	Equivalent Flexural Strength at L/150, Re_3 (%)
1	ML_S_0_28_4PB_D	3	0.004 (±0.0001)	799.7 (±39.4)	1163.0 (±57.3)	0.004 (±0.0001)	799.7 (±39.4)	1119.6 (±55.2)	0.0	0.0	0.0	0.0	0.0	0.0	0.0
2	ML_S_1_28_4PB_D	6	0.004 (±0.0003)	927.6 (±41.9)	1349.0 (±60.9)	0.015 (±0.02)	976.9 (±67.3)	1367.7 (±94.2)	886.5 (±139.2)	1241.2 (±194.9)	17.0 (±3.9)	689.7 (±118.7)	965.5 (±166.1)	70.1 (±9.9)	75.9 (±10.0)
3	FML_S_0_28_4PB_D	6	0.003 (±0.0001)	1138.9 (±104.6)	1656.2 (±152.1)	0.003 (±0.0001)	1138.9 (±104.6)	1594.5 (±146.4)	0.0	0.0	0.0	0.0	0.0	0.0	0.0
4	FML_S_1_28_4PB_D	6	0.005 (±0.0001)	986.9 (±112.1)	1435.2 (±163.0)	0.013 (±0.0001)	1064.6 (±94.2)	1490.4 (±131.9)	1013.2 (±85.5)	1418.5 (±119.6)	20.9 (±1.1)	711.2 (±32.2)	995.7 (±45.0)	77.6 (±4.1)	82.6 (±2.4)
5	FML_S_1_14_4PB_C	3	0.004 (±0.0001)	761.1 (±71.9)	1106.8 (±104.5)	0.009 (±0.0001)	842.6 (±82.7)	1179.6 (±115.8)	745.2 (±151.3)	1043.2 (±211.9)	15.8 (±1.7)	619.3 (±104.5)	867.0 (±146.3)	63.1 (±9.6)	80.2 (±8.4)
6	FML_S_1_28_4PB_C	3	0.005 (±0.0001)	1083.2 (±88.1)	1575.1 (±128.0)	0.013 (±0.006)	1189.1 (±170.7)	1664.8 (±238.9)	1122.4 (±176.6)	1571.4 (±247.3)	22.0 (±2.4)	966.0 (±104.2)	1352.4 (±145.8)	94.4 (±11.1)	85.3 (±2.2)
7	FML_L_3_28_4PB_C	3	0.032 (±0.006)	11410.2 (±166.9)	2807.6 (±41.1)	0.034 (±0.003)	11417.2 (±145.5)	2809.7 (±35.8)	10920.1 (±764.1)	2687.4 (±188.0)	187.7 (±52.8)	7493.3 (±1191.3)	1844.1 (±293.2)	1032.7 (±11.3)	86.1 (±1.2)
8	FML_L_1_14_4PB_C	3	0.003 (±0.0001)	3971.6 (±141.7)	977.3 (±34.9)	0.024 (±0.007)	5441.1 (±894.9)	1339.0 (±220.2)	5371.3 (±847.9)	1321.8 (±208.7)	117.3 (±17.2)	3926.6 (±511.8)	966.3 (±126.0)	492.2 (±57.5)	86.6 (±4.9)
9	FML_L_1_28_4PB_C	3	0.003 (±0.0001)	5842.5 (±363.2)	1437.6 (±89.4)	0.019 (±0.006)	6793.2 (±450.1)	1671.8 (±110.8)	6653.5 (±386.0)	1637.4 (±95.0)	149.3 (±9.2)	4008.9 (±392.9)	986.6 (±96.7)	575.1 (±28.2)	80.7 (±3.9)

Characterization of Crack Growth Mechanisms Using Digital Image Correlation (DIC)

The objectives of this section are to address the mechanisms of crack formation and propagation as well as of multiple crack formation and crack opening. These observations will be compared with the analytical models in Chapter 8. This section presents experimental results for one small beam with 1% fiber and two large beams with 1% and 3% fiber. All samples were tested after 28 days of curing.

One of the first benchmarks of these experiments was to validate the two measurements of sample deflection at the loading point. By comparing the measurements using DIC and LVDT-based instrumentation, the accuracy of the two methods were checked against one another. In addition, the researchers chose up to four stages of deformation (designated A through D) that correspond to critical stages of loading. Each stage is listed in Table 17. The results for additional samples are provided in the appendix.

Table 17. Different stages of data analysis using DIC method

Stage	Characteristic
A	Initiation of the deformation
B	Initiation of the non-linear response
C	Response to the peak load
D	End of the DIC data analysis (beam failure)

Figure 89 to Figure 91 show good agreement between the results from the LVDT and the DIC. However, obtaining correct results from the DIC is very sensitive to the data analysis procedure used. A detailed description of the DIC data analysis is given in the appendix.

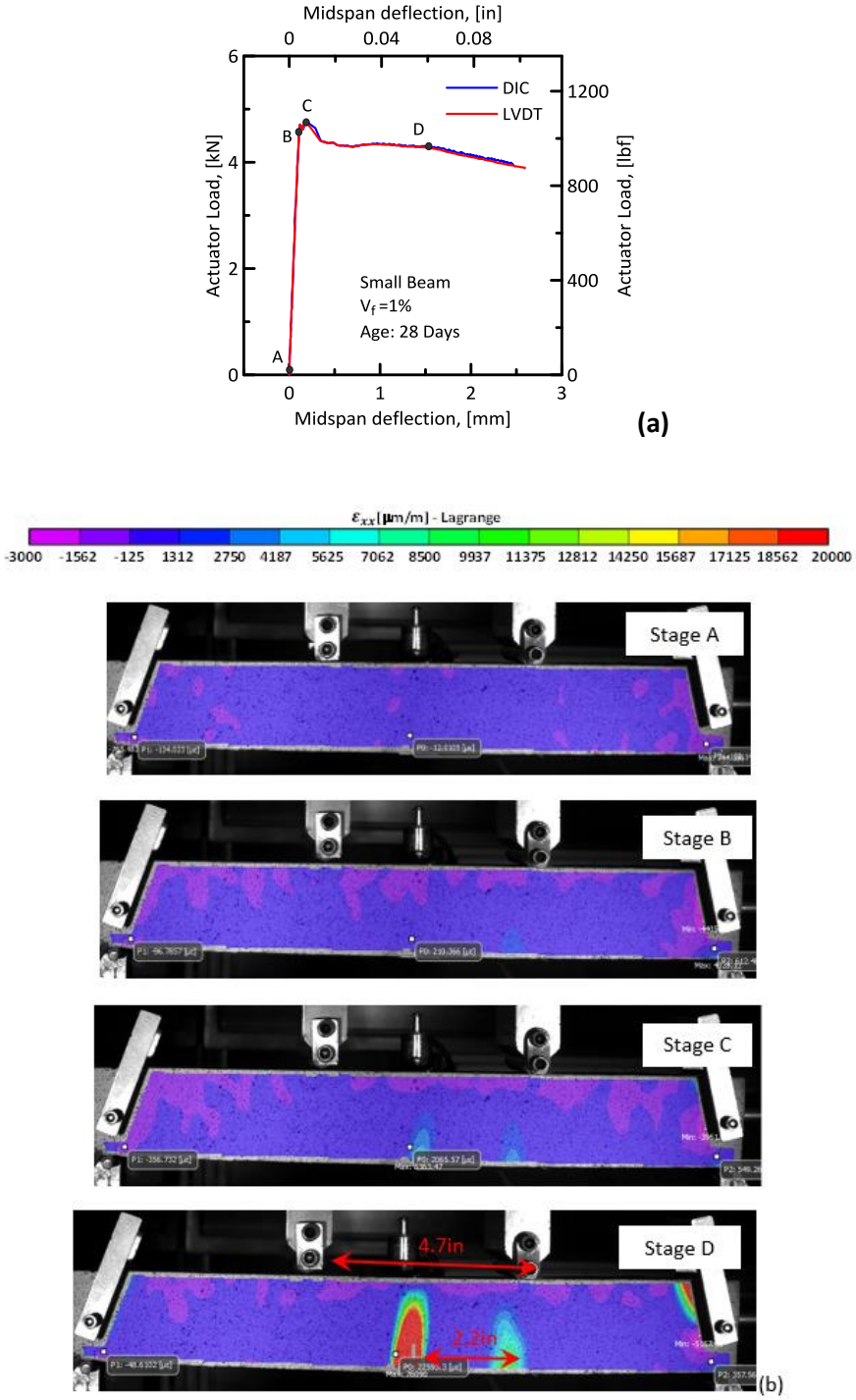

Figure 89. Small beam with 1% fiber, after 28 days of curing: (a) Load-deflection curves, the comparison between DIC results and LVDT results; (b) DIC results at different stages of the test

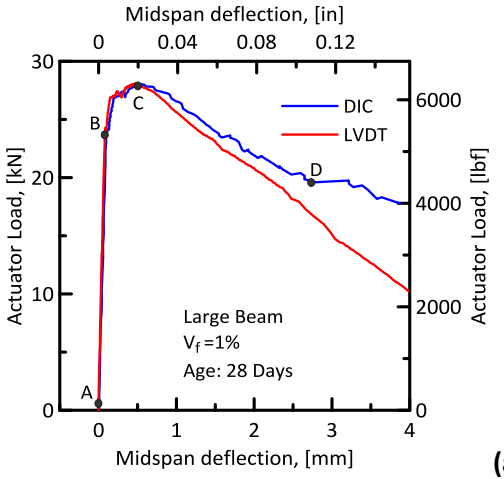

(a)

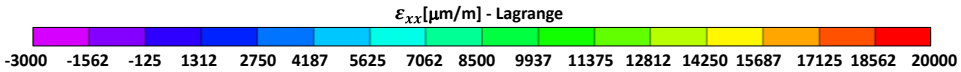

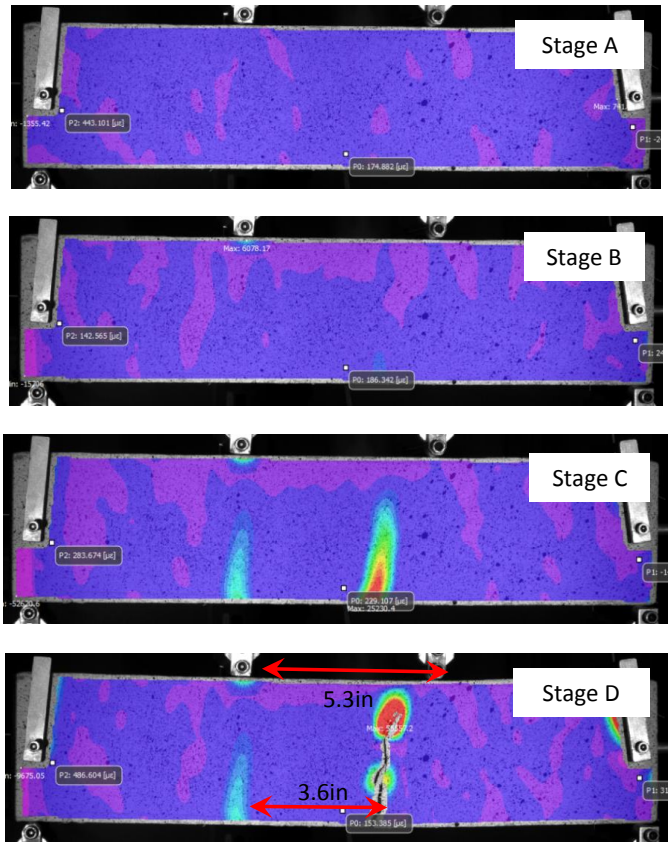

(b)

Figure 90. Large beam with 1% fiber, after 28 days of curing: (a) Load-deflection curves, the comparison between DIC results and LVDT results; (b) DIC results at different stages of the test

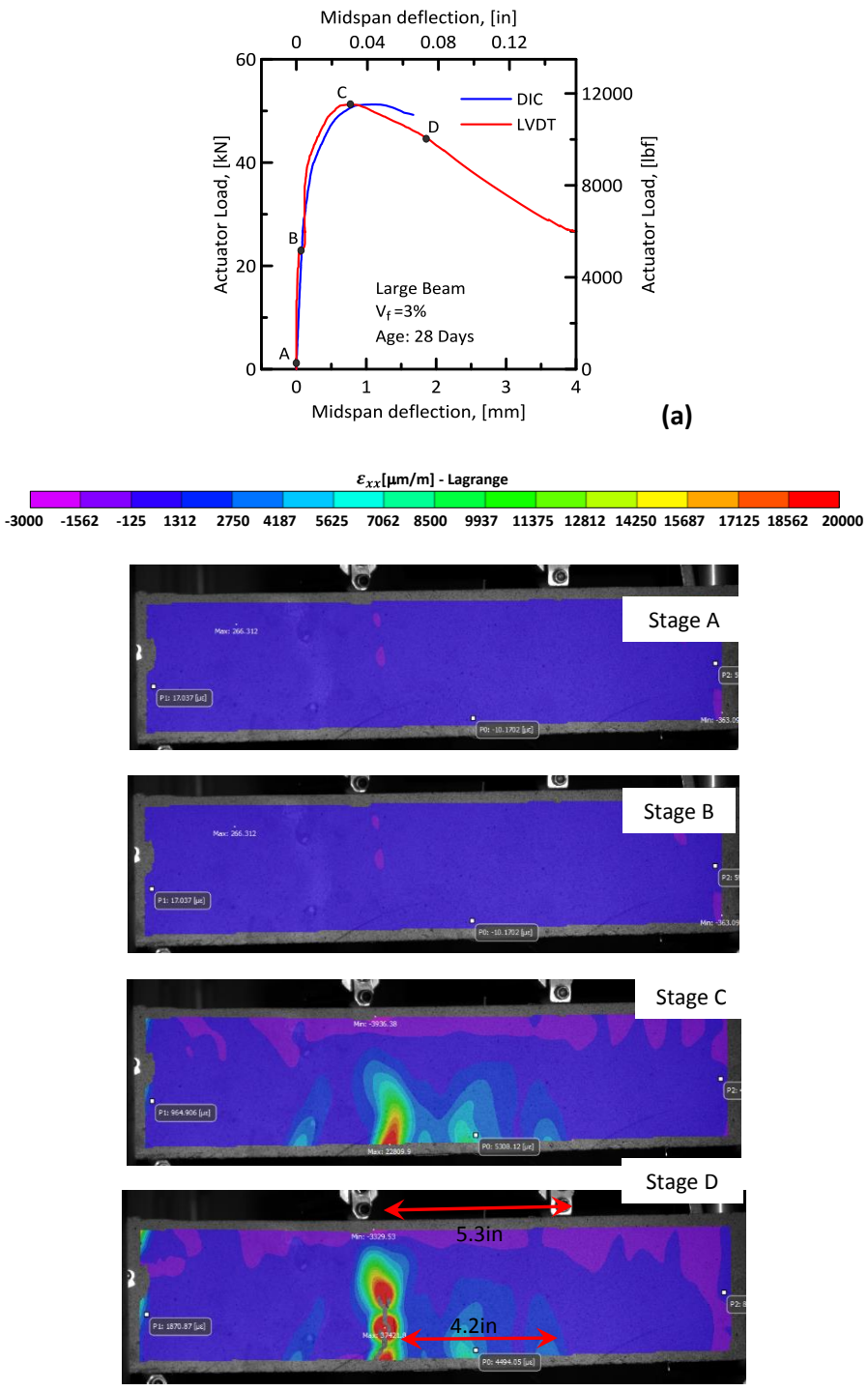

Figure 91. Large beam with 3% fiber, after 28 days of curing: (a) Load-deflection curves, the comparison between DIC results and LVDT results; (b) DIC results at different stages of the test

Fracture Tests (Cyclic)

One of the areas of improvement in UHPC as compared to plain concrete is its exceptional response to repeated cyclic loading such as earthquake loads as well as fatigue loading. This is especially in the reverse cyclic and tension loading-unloading cycles. A detailed literature search of the fatigue studies conducted on UHPC has been presented by Abbas et al. (Abbas et al., 2016). A fatigue test helps determine a material's ability to withstand cyclic loading conditions. By design, a material is selected to meet or exceed service loads that are anticipated in fatigue testing applications. Cyclic fatigue tests produce repeated loading and unloading in tension, compression, bending, torsion, or combinations of these stresses. Additional papers for discussion in the fatigue test results can be found in the literature (S. Abbas, Nehdi, and Saleem 2016a; Ríos et al. 2017).

Graybeal and Hartmann (Benjamin A. Graybeal and Hartmann 2003) conducted flexural fatigue tests on 2-inch (51-mm)-square beams. In one set of tests, uncracked specimens were loaded to produce different stress ranges. Most specimens survived more than 6 million cycles of loading. In the second series of tests, the specimens were pre-cracked and then tested for fatigue with loads cycling from 10 to 60 percent of the cracking load. One specimen failed after 9,950 cycles, while the other failed after 129,700 cycles. In these tests, some of the steel fiber reinforcement was observed to have fractured rather than pulling out of the UHPC matrix.

Behloul et al., (2005) conducted flexural fatigue tests on 4- by 4- by 16-inch (100- by 100- by 400-mm) prisms made of two different UHPC formulations. Prior to fatigue loading, the specimens were loaded to produce a crack opening of 0.012 inches (0.3 mm). The specimens were then cycled at 5 Hz between 10 and 90 percent of the first cracking strength. After 1 million cycles, the specimens were loaded statically, and the results were compared with specimens not subjected to fatigue loading. The fatigue loading appeared to have no effect on the overall mechanical behavior.

Herein the results of the cyclic tests on the large notched beams, 4" x 4" x 16" (152 mm x 152 mm x 406 mm), are presented. Fracture cyclic tests were conducted using a closed loop, servo-hydraulic MTS test frame and cyclic three-point bending (3PB) procedure. The beams were loaded along the notch to monitor crack growth, as shown in Figure 92. An Instron clip-on gage type extensometer was used to measure the crack mouth opening displacement (CMOD). A Linear Variable Differential Transformer (LVDT) with a range of ±4 mm was used to measure the deflection of the mid-span. Initially, the testing procedure was controlled monotonically under load control to apply load on the specimen equivalent to about 10% of the peak load. The feedback control was then switched to CMOD control at a constant rate of 0.004 in/min up to the peak load. The first unloading cycle started at the peak load and the specimen was unloaded to about 1% of the peak load, under load control. Cycles of loading-unloading were then applied under CMOD and load control until 10 such loading-unloading cycles were completed at 1.2 mm of crack opening. A schematic side view of the test setup is presented in Figure 93. Three beams were tested and the results are shown in Figure 94 to Figure 96.

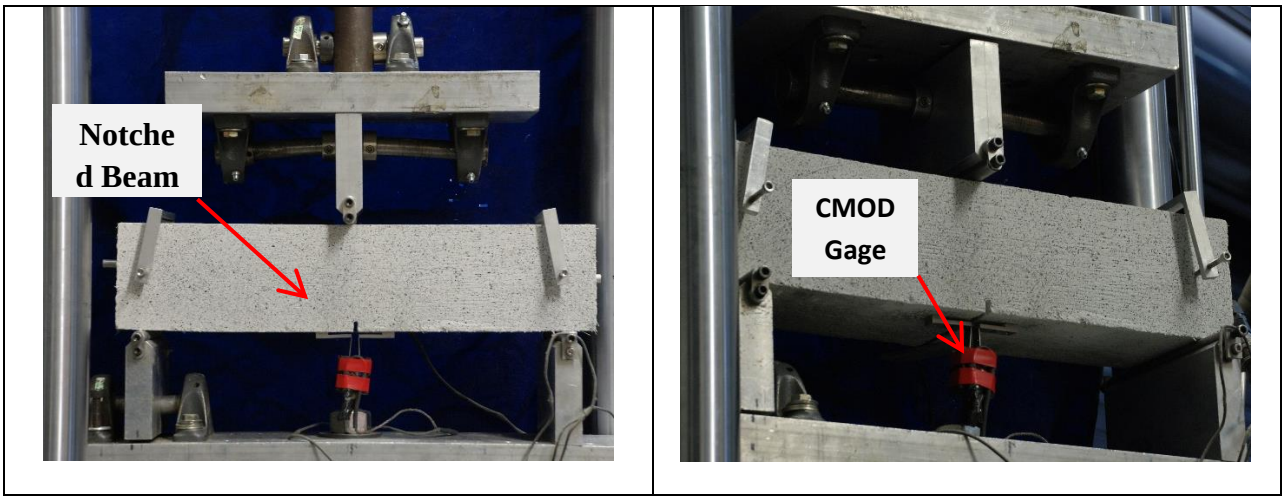

Figure 92. Fracture test setup

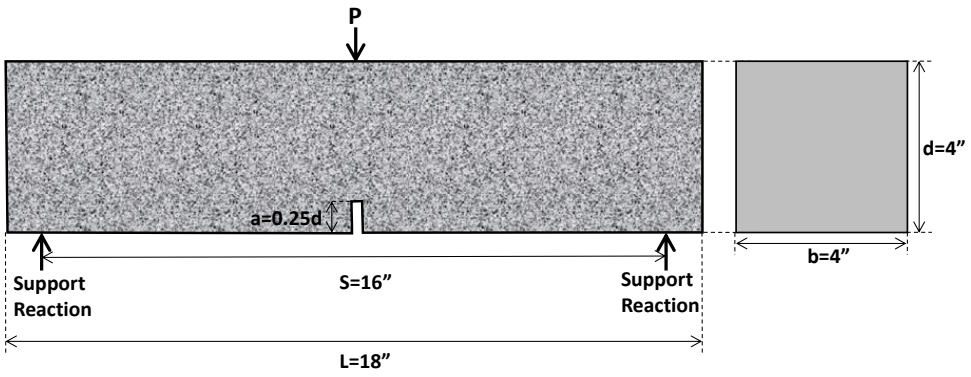

Figure 93. Schematic side view of the 3PB test setup and the beam dimension

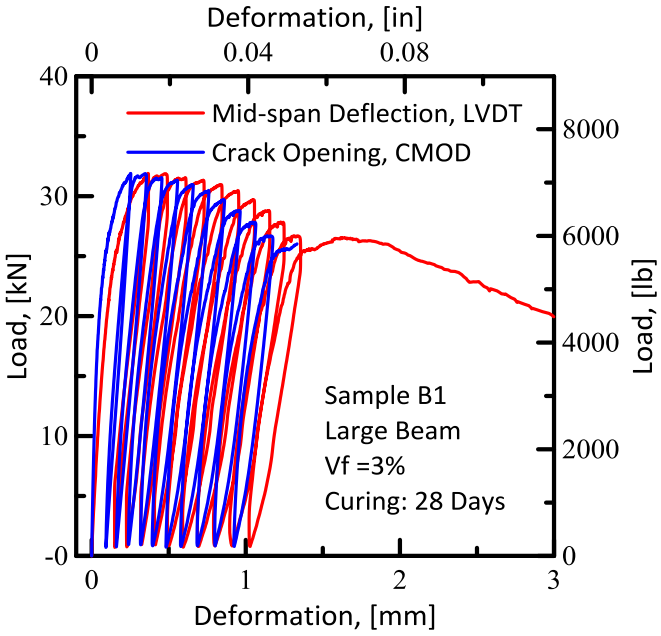

Figure 94. Cyclic test results: (a) Mid-span deflection against load; (b) CMOD against the load, for the large beams with 3% fiber content after 28 days of curing

Figure 95 represents load against mid-span deflection and crack opening. These plots were obtained after ten cycles of loading and unloading of another beam under 3PB-fracture tests.

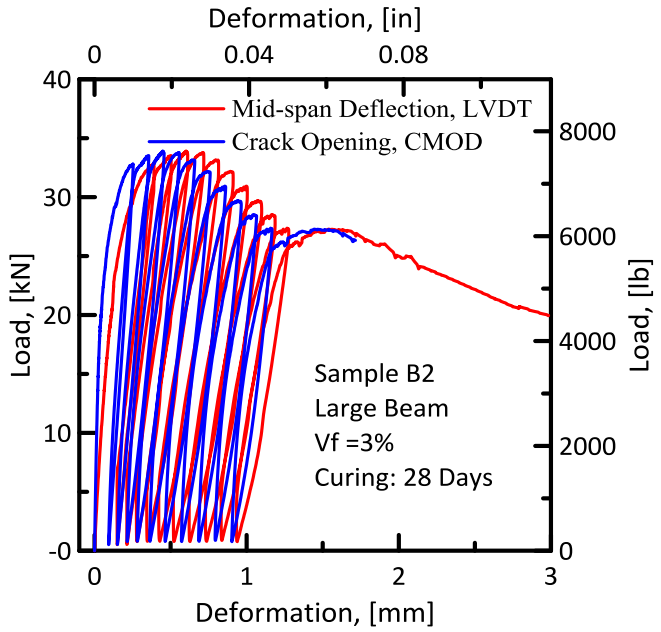

Figure 95. Cyclic test results: Mid-span deflection (LVDT) and Crack Mouth Opening (CMOD) against the load, for the large beams with 3% fiber content after 28 days of curing

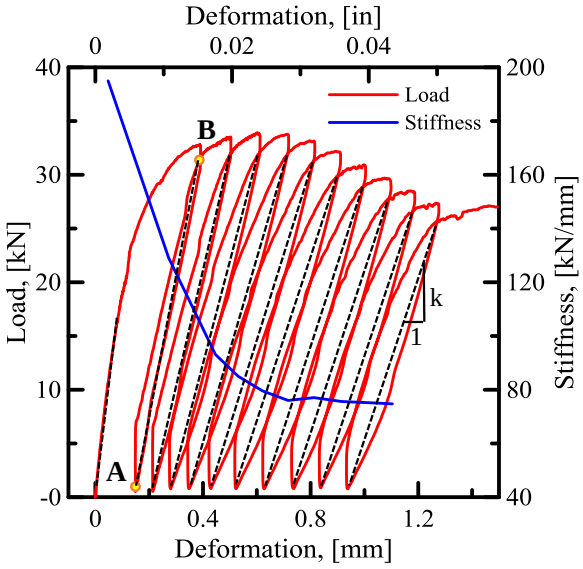

Figure 96. Chosen the part of the cyclic load-deflection response that is used for the stiffness degradation calculation (Sample B2)

Figure 96 shows a part of the load-deflection loops, which were used for the stiffness degradation curves. For doing the calculations, nodes at the minimum point of unloading, points A, and the points located at the joints of loading and unloading curves, points B, were chosen to calculate the stiffness for each loop, black dashed lines in the figure.

$$k = \frac{P_B - P_A}{D_B - D_A}$$ **Equation 21**

In this equation, 'P' is the loading, 'D' is the displacement and the subscripts represent the equivalent point in which the parameter is extracted.

Displacement at the midpoint of line AB was chosen as the equivalent deflection of each loop to plot the stiffness versus deformation.

As it is shown in the figure, at the start of the cyclic loading there is a sudden drop in the stiffness, but, as the number of cycles increases, it converges to a stable stiffness value, i.e., 78 kN/mm in this specific test. The remaining stiffness of the UHPC section is about 40% of its initial value; i.e., 195 kN/mm. This shows that the section is still able to keep its stiffness after numerous cycles of loading and unloading.

Compression Stress-Strain Tests

Compression tests were conducted using a 220 Kip (55 ton) testing machine operated under closed-loop control. The controller used for these experiments was developed by CGTS Corp, Tempe, AZ. The 2"x 4" cylinders tested were ground to a flatness level of 1/1000" by using grinding equipment. This is an

important factor in uniformly distributing the load over the whole specimen. Although the top platen swivels to enable a uniaxial load application, it is preferable to have parallel ends for each specimen in order to minimize the eccentricity of the applied load.

A special fixture was developed to attach the two LVDTs to measure the axial strain in the specimen. A constant gage length of 2.5 inches was used for all specimens. This apparatus is shown in Figure 97. The instrumentation includes LVDT to measure change in length of the specimen, radial strain gage to measure radial deformation, and ultrasonic pulse velocity transducers.

The displacement measuring fixture was attached to the specimen using spring plungers which allow the transducers to move freely as the specimen deforms. The fixture permits the axial and circumferential deformations to be measured as the specimen undergoes the post-peak response and cracking results in significant dilatation of the sample. A chain type fixture is used to measure the circumferential strain in the specimen. The test was controlled by LVDTs which measure the axial strain and an extensometer which measure the circumferential strain. Using a combination of these two control parameters in sequence, it was possible to capture the post-peak response. By achieving well-controlled post-peak behavior, the specimens do not experience an explosive failure mechanism and the true stress-strain response is measured.

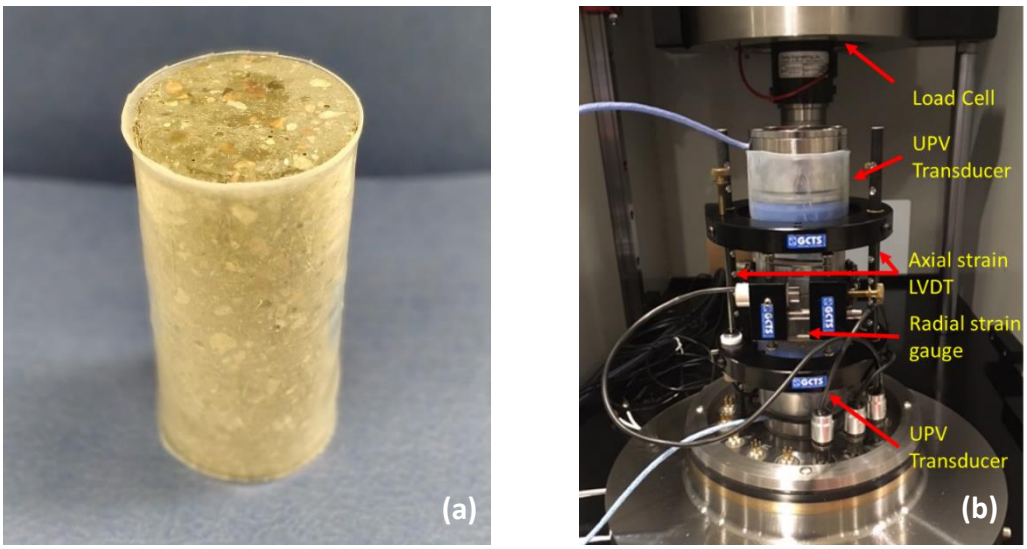

Figure 97. (a) 50 mm diameter cylinders cored from 75 mm diameter specimens, and prepared for compression testing, and (b) test setup to determine compressive stress-strain response of UHPC cylinders

Figure 98 compares the axial and circumferential stress-strain results from the control specimen. These samples show the extreme brittleness of the control UHPC specimens. As the peak load is reached, the brittleness of UHPC indicates that sufficient energy is stored in the specimen to be self-driving the failure. The instrument can't remove the load fast enough, so the energy is dissipated in the specimen

leading to a dynamic fracture mode. Data collected from both the LVDTs for the axial response and the extensometer are shown in the figure.

As shown in the figure, the control UHPC reached an axial strain of 0.0032 at an ultimate load of 22.2 ksi, while with the addition of 1% steel fibers, the strain at peak load increased to 0.0041. Fiber addition is best demonstrated in the response under the transverse direction, which shows significantly higher dilatation and higher strength and ductility than the control samples.

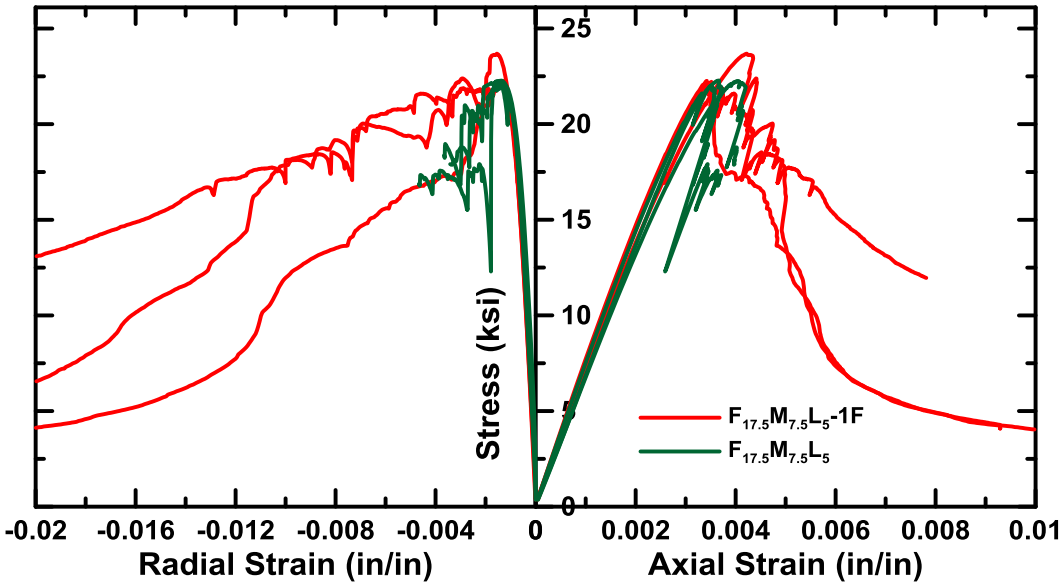

Figure 98. Compressive Stress-Strain Curves of UHPC comparing control specimens of FML (green) and 1% fiber (red)

Examination of the strain-softening region indicates that the plain UHPC specimens behave in a brittle manner while much ductility is observed in the fiber-reinforced samples. This is typical of high-strength materials when the strength of the interface increases to the level of aggregates and mortar, so that the cracks have a lower likelihood of following along the mortar–aggregate interface and goes straight through the aggregate particles. This behavior is negated in the presence of fibers, which provide the toughening mechanism due to fiber pullout along the path of crack growth and increase toughness by the bridging. A larger area under the stress-strain diagram indicates a more ductile failure mode. It has also been observed that stiffness as measured by the slope of the stress-strain response in the initial linear range is higher for the fiber-reinforced samples. The stiffness as calculated from the stress-strain plots in Figure 98 for the unreinforced FML specimen is 6.89 x 10^6 psi, whereas the stiffness for the 1% fiber-reinforced FML specimen is 7.23 x 10^6 psi. This increase in stiffness with fiber reinforcement is due to the presence of fibers that bridge the microcracks in the matrix and help toughen the fiber-matrix composite, as described in section 7.2.

Figure 99 compares the axial and radial strain for UHPC with different fiber contents. These samples were part of both mixes (ML and FML) and were tested at an age of 28 days. As expected, the samples with 3% fiber content resulted in similar strength while the softening response was more stable than the control, or 1% fiber systems. The ductility of all mixtures was similar among the 1% and 3% fiber. Only limited data are available from this study. Differences in strength response may be attributed to the fiber's contribution in the pre-peak region of the response when micro-cracking under compression in forming at stress levels corresponding to 18,000 to 20,000 psi and approximate strain levels of 0.003-0.004. The micro-cracking in this range is expected to be affected by the presence of fibers which would provide bridging and crack growth suppression. Additionally, confinement of the concrete under compression is also expected to increase the compressive strength and ductility. These experiments indicate that all fiber reinforced samples behaved in a similar manner and exhibited a less brittle response than the control samples.

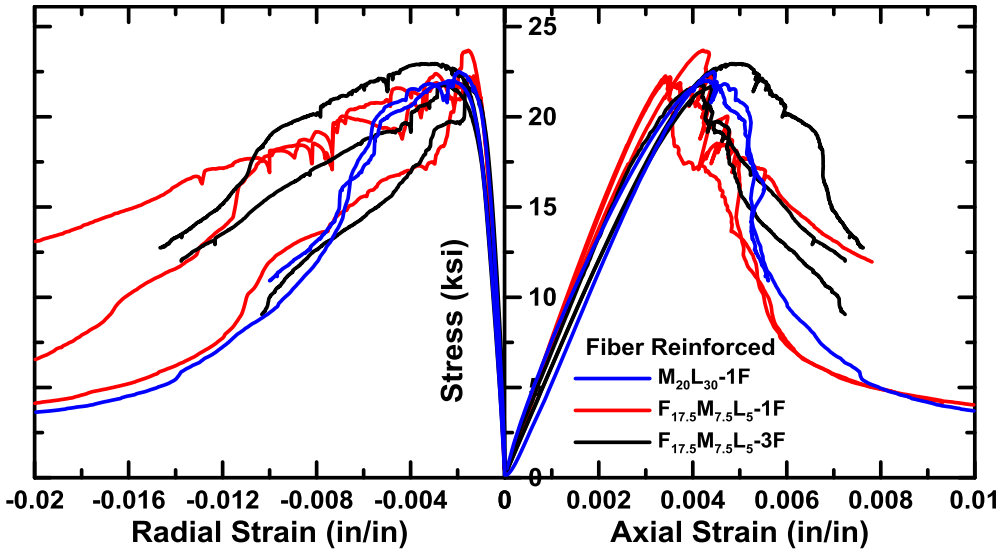

Figure 99. Compressive Stress-Strain Curves of UHPC comparing effect of fiber content on specimens of ML (blue) and FML (red, 1% fiber; black, 3% fiber)

Summary

- One of the most useful mechanical properties of UHPC is its resistance to cracking and its enhanced tensile strength and ductility. Generally speaking, in all FRC materials, including HPC and UHPC, the resistance to cracking and its propagation in brittle matrix is significantly affected by steel fibers. This resistance to crack growth is therefore more due to the higher percent of fibers used in UHPC. As the amount of fibers increases, more ductile behavior is expected and observed.
- Flexure tests are generally used to determine the flexural modulus or flexural strength of a material. Unlike a compression test or tensile test, a flexure test does not measure fundamental

material properties. When a specimen is placed under flexural loading, all three fundamental stresses are present: tensile, compressive, and shear. The flexural properties of a specimen are the result of the combined effect of all three stresses as well as − to a lesser extent − the geometry of the specimen and the rate at which the load is applied. Results of the flexural tests can be correlated to the fundamental tension, compression and shear response.

- Steel fibers are added to concrete to improve the structural properties, particularly tensile and flexural strength. The level of improvement in the mechanical properties depends on several factors, such as shape, size, volume, percent, and distribution of fibers.
- The results of the flexural response for the beams are very sensitive to the fiber volume percent. As the micro-cracks develop, the stress in fiber increases gradually with the increase of crack opening.
- Addition of 1% of straight steel fibers to the UHPC mixture affects the post-peak flexural behavior by increasing the toughness values up to 40 times. The absorbed energy (toughness) in the fiber-reinforced beams is two to three times higher than the toughness of the unreinforced beams at peak load.
- Unreinforced beams don't show a considerable post-peak behavior, while the fiber-reinforced beams show a high level of energy absorption after the post-peak. The total absorbed energy (toughness) at L/150 is 40 times higher than the energy measured at the peak load for unreinforced beams.
- A comparison between two different fiber volume percents, while holding other parameters constant, reveals that the E-modulus of the beams with a 3% fiber volume is 20% higher than this value for a beam with a 1% fiber volume. Furthermore, the ultimate strength of the beams with 3% fiber volume is 70% higher than that in the beams with 1% fiber content.
- $F_{17.5}M_{7.5}L_5$ beams have a superior flexural behavior compared to the $M_{20}L_{30}$ beams. This means that the partial replacement of micro-silica and limestone with fly ash is a good approach to make stronger members and joints. However, the portions and values are very important in the mix design of the UHPC material and a small change in the portions can cause a dramatic change in the results.
- Mixing procedure and methods have a considerable effect on the results. Beams mixed with the high-shear mixer have a residual strength 12% greater than that of beams made using the hand-drill. This can be attributed to a more uniform fiber distribution during the mixing procedure. The more uniform distribution of the admixtures and fibers may be a reason for this better performance.
- Although there is no meaningful difference between the maximum stresses in the beams with different sizes, there is a significant increase in the strain for the large beams. This may be due to the greater depth of the large beams, which can provide more space for crack growth than the small beams.

- As the curing period increases, the strength and post-peak response of the beams increase as well.
- This increase in strength due to extended curing period is larger in the small beams than in the large beams.
- The loading capacity of small beams after 28 days is almost 43% higher than that of the beams tested after 14 days of curing. The same holds true of the residual strength: the average residual stress for 28-day beams is 47% higher than that of 14-day beams.
- The UHPC section with 3% fiber volume of steel fibers can maintain 40% of its initial stiffness even after numerous cycles of loading and unloading.

Chapter 8 DEVELOPMENT OF STRUCTURAL DESIGN PROCEDURES FOR UHPC BEAMS AND JOINTS

Introduction

UHPC materials are designed to exhibit noticeable ductility, energy absorption capacity, and post-cracking strength under tension by employing a relatively high dosage of fiber reinforcement (Yao et al. 2017). The use of fibers improves the mechanical response behavior by increasing the stiffness and residual strength in the serviceability range of loading, which is the dominant mode of loading during the life of a structure. The improvement in mechanical response is accomplished by preventing the cracks from opening and therefore restraining excessive deformations (Alberto Meda, Minelli, and Plizzari 2012). Unreinforced UHPC materials are extremely strong in compression, and brittle in tension and flexure. In order to increase UHPC's ductility even when used with conventional reinforcement, a proportion of reinforcement must be replaced by steel fibers to provide both flexural capacity and ductility. The improvement in the load-bearing capacity and ductility depend on the fiber parameters such as type, shape, aspect ratio, bond strength, and volume fraction (Singh and Jain 2014). Furthermore, fiber reinforcement improves shear resistance by transferring tensile stresses across flexural cracks and enhances aggregate interlock by reducing the spacing and width of diagonal cracks. The enhanced post-cracking tensile strength and improved crack control due to the distributed fiber reinforcement can improve shear behavior and may potentially substitute or reduce conventional transverse reinforcement (Dinh, Parra-Montesinos, and Wight 2010). Results have shown that even a limited amount of diffused steel fiber reinforcement increases the post-cracking toughness and ductility of concrete considerably (Batson 1976; Vandewalle 1999; Balaguru, Narahari, and Patel 1992; Lee, Cho, and Vecchio 2011).

Computational models provide opportunities for robust analysis and design with Hybrid UHPC. Various research groups have accomplished extensive work in the development, design, analysis, and fieldwork with FRC in order to develop design guides (di Prisco, Plizzari, and Vandewalle 2009; Vandewalle 2002; Soranakom and Mobasher 2009). Several procedures for design of UHPC use formulations based on a strain compatibility analysis, which can be extended to a serviceability-based design by incorporation of full material stress-strain relationship. The material models can be implemented in finite element and elastic-plastic solution methodologies in order to close the gap among properties, analysis, modeling, and design. The tensile characteristics of UHPC can be defined in the context of fiber content and response after the matrix has fully cracked. The general terms of strain softening and/or strain hardening are defined, and additional sub-classes of deflection-softening and -hardening may be outlined based on the behavior in bending (A. E. Naaman and Reinhardt 2006).

UHPC mixtures exhibit tensile strain softening or strain hardening depending on the amount and effectiveness of fiber contribution to the overall composite. The bridging force is expressed in terms of an average smeared tensile residual strength parameter which applies over a large strain range. By

representing the bridging force as an average effective tensile stress-crack width relationship (or stress-strain relationship for a specimen of finite width referred to as a localized plastic hinge), one can model the material property as nonlinear spring elements to simulate the residual capacity of a cracked section (A. E. Naaman and Reinhardt 2006; Barros et al. 2005).

Use of UHPC concrete in the structural design of beams, columns, thin sections, link slabs, and panels is an important area of opportunity. With the use of a high-volume fraction of fibers, UHPC design components can be also applied to hybrid flexural and shear reinforcement as well as the connection of precast components in the field. ACI guidelines have recently been developed for general flexural design, elevated slabs, tunnel lining, etc. [ACI-544-8R, ACI-544-7R, ACI 544-6R]. The methodology for analysis and design is based on minimum and ultimate strength as well as sustainability and serviceability requirements. Serviceability can be designed based on user-defined and specified strain, crack width, deflection, or curvature ductility. Design for serviceability requires a better understanding of the load path and state of nonlinear behavior vis-à-vis cracking. Determination of design parameters such as load capacity at a certain level in the load-deformation history is, therefore, an important aspect of the modeling.

Simplified equations to account for the contribution of fibers to the tensile and shear response, cracking strength, and post-crack softening response are widely used to evaluate the mechanical performance. In many situations, direct interpretation of results primarily based on the strength can be misleading, since the interactions due to variables are not considered. For example, the interaction of factors such as longitudinal reinforcement, compression block, tension residual strength field, and fiber reinforcement make the interpretation of the results quite challenging. Different cracking mechanism often yields to conservative interpretations which underestimate the effect of real parameters (Minelli, Plizzari, and Vecchio 2007; Bernard 2004). Structural or quasi-full-scale tests, however, represent the concrete volume, modes of failure, and competing mechanisms more realistically and the overall toughness or ductility is a function of such interacting mechanisms. Many of these interacting parameters can be integrated into a representative plastic hinge element and its mechanical properties. Such models integrate cross-sectional dimensions with the tensile and compressive stress strain, as well as the reinforcement's contribution. The nonlinear hinge can then be used in a non-linear structural model.

A schematic drawing of the idealized plastic hinge which relates the axial and bending moment with the stress distribution and average curvature across the section is shown in Figure 100. The entire length of the element, L_p, is taken as a non-linear hinge which, due to cracking, exhibits large-scale rotation. This rotation engages the reinforcement and fibers which cross the crack; therefore the tensile and compressive stresses across the section can be related to the rotational and axial deformation using the moment-curvature (M-ϕ) that is obtained for a single cross-section (Yao et al. 2018). Derivation and use of a non-linear moment curvature relationship is an essential component of interaction between the geometrical parameters, material properties, and the choices for types of reinforcement.

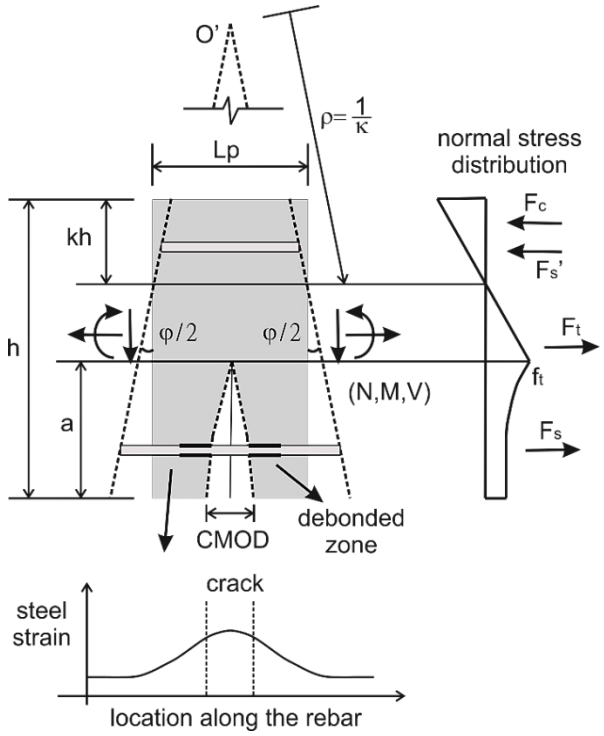

Figure 100. Schematic presentation of the localized zone for a beam section as a non-linear hinge, normal stress distribution, and strain distribution in steel rebar (Yao et al. 2018)

Generalized Yield Hinge Modeling Plan

This section addresses the methods employed in the analysis of flexural UHPC members. Closed-form relationships based on the non-linear design of reinforced concrete are used in the calculation of the load-deflection response of UHPC (Chote Soranakom and Mobasher 2009, 2007, 2008). The procedures followed from the recent code-based guidelines are briefly addressed here (ACI 544-8R 2016; ACI 544-7R 2016, ACI544-4R-2018), as are procedures to calibrate test methods to obtain material properties from experiments. Equations that relate the material properties to the structural design and analysis procedures of UHPC are also discussed. In order to develop serviceability-based design procedures, one has to formulate the problem using a strain compatibility approach that tracks the path of loading. Computations are extended to hybrid reinforcement systems with flexural rebars in conjunction with UHPC in beams and joints.

The developed procedures are used in obtaining material properties from the flexural data using procedures that are based on back calculation of material properties from the experimental results. Model simulations are compared with other results available in the literature. Performance of flexural reinforced UHPC concrete beam sections tested under different types of loading is addressed using a combination of fibers and rebars. The objective is to validate the proper design procedures for UHPC flexural members and UHPC connection elements. The proposed solutions can be used to increase the

ductility of the UHPC mixtures by increasing the amount of fibers in the mixture. Added fiber can also be used to develop alternatives to reduce the cost factors such as labor, and to reduce the total amount of continuous reinforcement used. The cracking, serviceability deflection, and ductility response can be analyzed using the moment-curvature expressions for homogenized UHPC concrete.

Simplified Approach for Incorporation of Fibers in Flexural Model

This section presents the classic ACI approach, based on the Whitney rectangle concept, for computing the bending capacity of a plain UHPC beam. This is an ultimate limit state approach based on strength analysis. In ordinary reinforced concrete design the contribution of tensile concrete is ignored due to its low magnitude. The present method employs linear strain distribution, but it ignores the stress-strain constitutive relationship by assuming a constant compressive stress block and a constant residual stress distribution in the tensile region. Due to this simplification, the approach is unable to simulate all stages of the flexural process, although it can be used as a simplified approach for designing the FRC and HRC sections. The basic assumptions of plane sections remaining plane are used. It is assumed that the tensile strength of concrete is $\sigma_{cr} = E\varepsilon_{cr}$ and the residual strength is represented by parameter μ (0< μ <1), representing a fraction of the tensile strength that is transmitted after cracking. This indicates that the stress crack width relationship is a constant function and equal to $\mu\sigma_{cr}$ in tension.

Figure 101 presents a constitutive model for homogenized strain softening and hardening of FRC with two fundamental material parameters: Elastic modulus, E, (equal in tension and compression) and first cracking tensile strain, ε_{cr} . Two non-dimensional parameters, normalized post-peak tensile strength μ and compressive to tensile strength ratio ω , were also defined. The compressive response in Figure 101(a) is represented as an elastic-plastic response with an initial modulus defined as γE up to the compressive strength of $\omega\gamma\sigma_{cr}$. Parameter ω represents the ratio of compressive to tensile strain. In most of the cases, elastic modulus for tension and compression are equal and therefore $\gamma = 1$. Thus, parameter ω can be considered as the ratio of compressive to tensile strength, $\sigma_{cy} = \omega\sigma_{cr}$.

The tension model in Figure 101(b) is described by a trilinear response with an elastic range defined by E, and then post-cracking modulus E_{cr} . By setting E_{cr} to either a negative or a positive value, the same model can be used to simulate strain-softening or strain-hardening materials. The third region in the tensile response is a constant stress defined with stress σ_{cst} in the post-crack region. The constant stress level μ can be set to any value at the transition strain, resulting in a continuous or discontinuous stress response. Two strain measures are used to define the first cracking and transition strains (ε_{cr} , ε_{trn}). The tensile response terminates at the ultimate tensile strain level of ε_{tu} .

The parameter μ represents the ratio of the post-peak tensile strength to the cracking tensile strength $\mu = \sigma_p / \sigma_{cr}$ and may be a function of the fiber volume fraction, geometry, stiffness, and bond. Figure 101(b) describes the compression model with stress increasing linearly up to the yield strain $\varepsilon_{cy} = \omega\varepsilon_{cr}$, and remaining perfectly plastic until the termination point at the ultimate compressive strain $\varepsilon_{cu} = \lambda_{cu}\varepsilon_{cr}$

. The non-dimensional strain measures β_{tu} and λ_{cu} are defined as limits for terminating the algorithm. They also facilitate a simplified parametric model based on serviceability limit state (SLS) and ultimate limit state (ULS) criteria for the design of FRC flexural members (Chote Soranakom and Mobasher 2009). The model can be implemented both for strain-softening and strain-hardening FRC. As an extension to the model, one can also consider a combination of fibers and plain reinforcement in the context of HRC, which addresses structural members that combine continuous reinforcement with randomly distributed chopped fibers in the matrix. An analytical model for predicting the flexural behavior of HRC, which is applicable to conventional reinforced concrete and FRC, presented by Mobasher et al. (2015) (Barzin Mobasher, Yao, and Soranakom 2015), will be discussed in the next section as well.

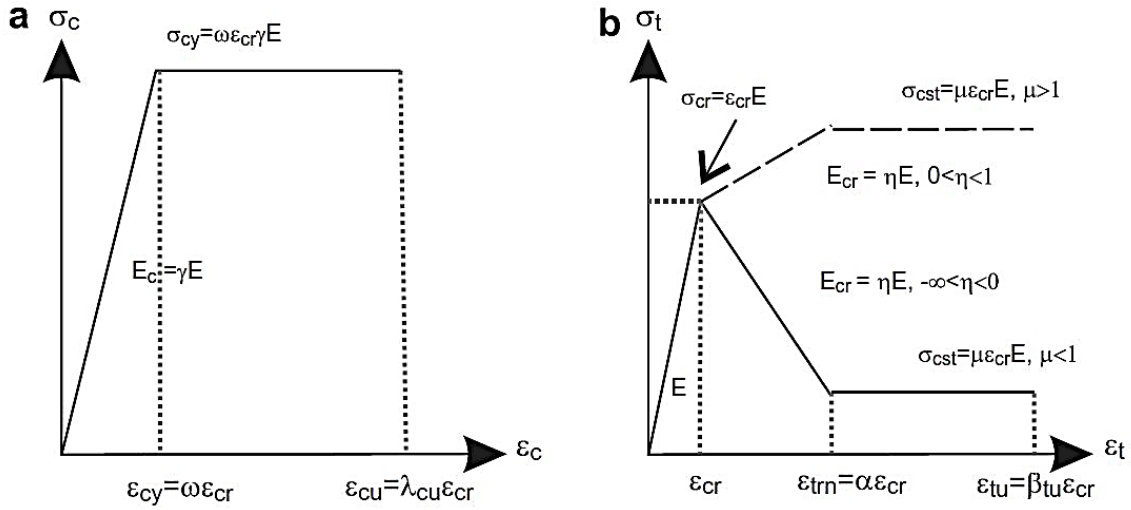

Figure 101. Material models for homogenized fiber reinforced concrete: (a) compression model and (b) tension model (Chote Soranakom and Mobasher 2007)

Material parameters required for the simplified models are summarized as follows:

Cracking tensile strain,

$$\varepsilon_{cr} = \frac{\sigma_{cr}}{E}$$ **Equation 22**

Normalized tensile strain at peak strength,

$$\alpha = \frac{\varepsilon_{peak}}{\varepsilon_{cr}}$$ **Equation 23**

Normalized post-crack modulus,

$$\eta = \frac{E_{cr}}{E}$$ **Equation 24**

Normalized yield compressive strain,

$$\omega = \frac{\sigma_{cy}}{E\varepsilon_{cr}} = \frac{\sigma_{cy}}{\sigma_{cr}}$$ **Equation 25**

Normalized tensile strain at bottom fiber,

$$\beta = \frac{\varepsilon_t}{\varepsilon_{cr}}$$ **Equation 26**

Normalized compressive strain at top fiber,

$$\lambda = \frac{\varepsilon_c}{\varepsilon_{cr}}$$ **Equation 27**

Designing with UHPC differs from designing with normal concrete, due to differences in stress-strain diagrams. The stress-strain relationship in compression has a similar shape for UHPC and normal concrete, but the fibers cause a different stress-strain relation in tension. Normal concrete has a small tensile capacity that will be neglected whenever the concrete has cracked and the reinforcement is activated. However, the fibers in UHPC provide a tensile capacity that cooperates with reinforcement as well. For design purposes, VSL Australia (Gowripalan and Gilbert 2000) has developed an idealized stress-strain relationship as shown in Figure 102. In this study, for design purposes, the VSL approach has been chosen. The French Standards for UHPC have the same approach (ACI Committee 239, 2018).This approach is compared with the typical stress-strain compressive relationship and the method proposed by (Almansour and Lounis 2010). The proposed models are shifted to the right for better clarity.

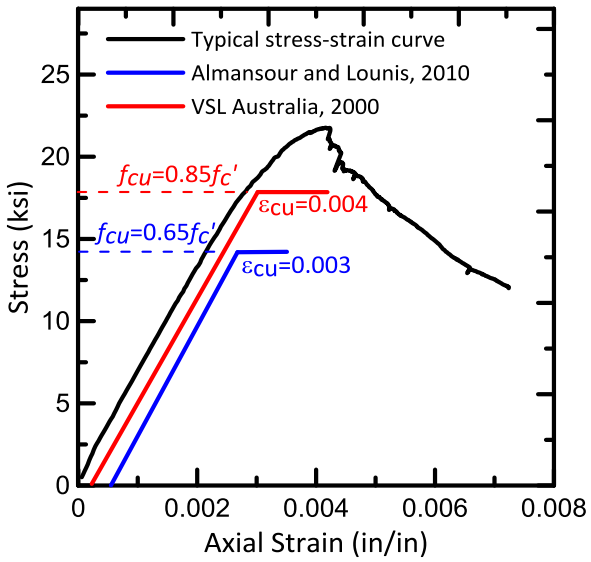

Figure 102. Comparison between design stress-strain relationships in compression

Fiber Reinforced Concrete (FRC)

Figure 103 shows the stress-strain block diagrams for an FRC section. In this case, due to the low tensile strength, it is very unlikely that we have a compressive failure in the section. Accordingly, a linear elastic response, with a maximum compressive stress value of $\sigma_{cy} = E_c \varepsilon_{cy}$, is chosen. As shown, the tensile response of the section is replaced with a uniform distributed loading equal to $\mu\sigma_{cr}$ representing the tensile post crack capacity.

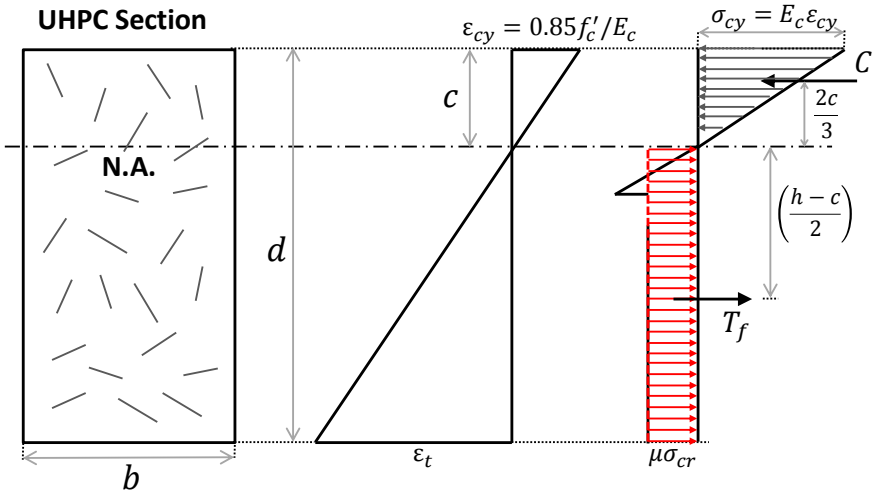

Figure 103. FRC cross-section stress-strain diagrams

The first step to achieve the moment capacity of the section is to calculate the depth of the neutral axis, c. The section is in a stable status and the tensile and compressive forces are equal. This can be used to calculate c.

$$C = \frac{b}{2} c \times \sigma_{cy} = \frac{bc}{2} \times E_c \varepsilon_{cy} \qquad \textbf{Equation 28}$$

$$T_f = b(h-c) \times \mu\sigma_{cr} = \mu b(h-c) \times E_c \varepsilon_{cr} \qquad \textbf{Equation 29}$$

By requiring $T_f = C$, we have,

$$c = \frac{2h\mu\varepsilon_{cr}}{\varepsilon_{cy} + 2\mu\varepsilon_{cr}} = \frac{2\mu}{\omega + 2\mu} \times h \qquad \textbf{Equation 30}$$

Based on the current research, the range for cracking strain, ε_{cr}, is between 0.00010 to 0.00017, but a more accurate value can be obtained using $\varepsilon_{cr} = E_c / \sigma_{cr}$, tensile tests, back-calculation approach (which will be discussed in the next section), or the empirical relationship between tensile and compressive strength; i.e. $\sigma_{cr} = 6.7\sqrt{f_c'}$ in U.S. customary units, pounds per square inch (psi) (and $\sigma_{cr} = 0.56\sqrt{f_c'}$ in SI customary units, MPa), for ordinary concrete; or $\sigma_{cr} = 0.04 f_c'$, for UHPC (Ben Graybeal 2014a). A similar approach can be used for E_c with the empirical relationship between elastic modulus and compressive strength; i.e., $E_c = 57000\sqrt{f_c'}$ in U.S. customary units, psi (and $E_c = 4700\sqrt{f_c'}$ in SI customary units, MPa) for ordinary concrete; or $E_c = 49000\sqrt{f_c'}$, for UHPC (Ben Graybeal 2014a). Since these equations are empirical relationships based on the tests on FRC beams, for UHPC sections, the more accurate approach is to test the samples, based on the applicable standard, and then conduct a back-calculation procedure in accordance with ACI-544-8R, in order to get the accurate value of residual strength, $\mu\sigma_{cr}$. By using the data reported under flexural tests in Chapter 7, we obtain σ_{cr} values in the range of $700\ (\pm 70)$ psi and $1050\ (\pm 50)$ psi for beams with 1 percent and 3 percent fiber content, respectively. The μ values lie between $0.55\ (\pm 0.07)$ and $0.85\ (\pm 0.07)$ for beams with 1 percent and 3 percent fiber content. The inverse analysis procedure will be discussed later.

The moment capacity of the section can be calculated as:

$$M_n = T_f(\frac{h-c}{2}+\frac{2}{3}\text{c})$$ **Equation 31**

By substituting c, from $c=\frac{2h\mu\varepsilon_{cr}}{\varepsilon_{cy}+2\mu\varepsilon_{cr}}=\frac{2\mu}{\omega+2\mu}\times h$

Equation 30 into $M_n = T_f(\frac{h-c}{2}+\frac{2}{3}\text{c})$

Equation 31,

$$M_n=\frac{\omega\mu(3\omega+8\mu)}{(\omega+2\mu)^2}\times M_{cr}$$ **Equation 32**

Where,

$$M_{cr}=\frac{\sigma_{cr}bh^2}{6}$$ **Equation 33**

Assuming the compressive strength is limited to $0.85f_c'$ (i.e., $\beta_2=0.85$), the normalized compressive strength ω is shown as:

Equation 34

$$\omega=\frac{\varepsilon_{cy}}{\varepsilon_{cr}}\approx\begin{cases}\frac{\beta_2 f_c'}{\sigma_{cr}}=\frac{0.85f_c'}{6.7\sqrt{f_c'}}=0.127\sqrt{f_c'} & (f_c' \text{ in psi})\\ \frac{\beta_2 f_c'}{\sigma_{cr}}=\frac{0.85f_c'}{0.56\sqrt{f_c'}}=1.518\sqrt{f_c'} & (f_c' \text{ in MPa})\end{cases}, \text{for FRC}$$

$$\omega=\frac{\varepsilon_{cy}}{\varepsilon_{cr}}\approx\frac{\beta_2 f_c'}{\sigma_{cr}}=\frac{0.85f_c'}{0.04f_c'}=21.25 \quad \text{, for UHPC}$$

Therefore, if one uses a value up to 21 in $c=\frac{2h\mu\varepsilon_{cr}}{\varepsilon_{cy}+2\mu\varepsilon_{cr}}=\frac{2\mu}{\omega+2\mu}\times h$

Equation 30, the nominal moment capacity as a function of cracking moment can be expressed within 0.5% degree of accuracy as $M_n=2.85\mu M_{cr}$, based on the suggested values by (Ben Graybeal 2014a).

Later in this chapter it is shown that the analytical solution for the ultimate design capacity is $M_n = 3\mu M_{cr}$ which is very much in line with the experimental predictions of $M_n = 2.85\mu M_{cr}$.

Hybrid Reinforced Concrete (HRC)

HRC is referred to as a structural member that combines continuous reinforcement with FRC matrix (Barzin Mobasher, Yao, and Soranakom 2015). Combinations of FRC and rebars, or welded wire mesh, may be used to meet the strength criteria (Taheri, Barros, and Salehian 2011; T. Y. Lim, Paramisivam, and Lee 1987; Lok and Pei 1998; Vandewalle 2002). An approach similar to that for FRC can be implemented to derive the moment capacity for reinforced UHPC sections by taking into account the contribution of steel rebars.

Figure 104 shows the material behavior (Mobasher et al. Barzin Mobasher, Yao, and Soranakom 2015), used to derive an analytical model for predicting the flexural behavior of HRC which is applicable to conventional and fiber-reinforced concrete (FRC). Figure 104a represent the material (a) tensile and (b) compressive, constitutive stress-strain responses for FRC. Figure 104c represents the elastic, perfectly plastic model for steel reinforcement.

As Figure 104(a) shows, the tensile response of the section is replaced with a uniform distributed loading over the tensile part of the section. Figure 104(b) shows the stress-strain block diagrams for an HRC section. In spite of the FRC section, the plastic compressive failure is likely in this case, so a uniform compressive tension is assumed for the compressive part of the section, $\beta_2 f_c'$. β_2 can be chosen as 0.85 for UHPC (see Figure 102)(ACI Committee 239).

By mixing the properties of FRCs with those of other type of composites, high strength and an excellent ductility are achievable for a broad range of composites such as textile-reinforced concrete (TRC), high-performance FRC, ultra-high-performance FRC, and ultra-high-performance hybrid reinforced concrete (UHPHRC). This strain-hardening behavior enhances the durability of concrete structures, because of the ability to (a) arrest the width of cracks and (b) carry tensile stresses (due to the bridging effect of fibers) (Destrée, Yao, and Mobasher 2015; Barzin Mobasher 2011). The arrangement of the rebars within a cross-section of width *b* and depth *h* (Figure 104d) shows that the depth of the center of gravity of the reinforcement is at a distance $d = \alpha h$.

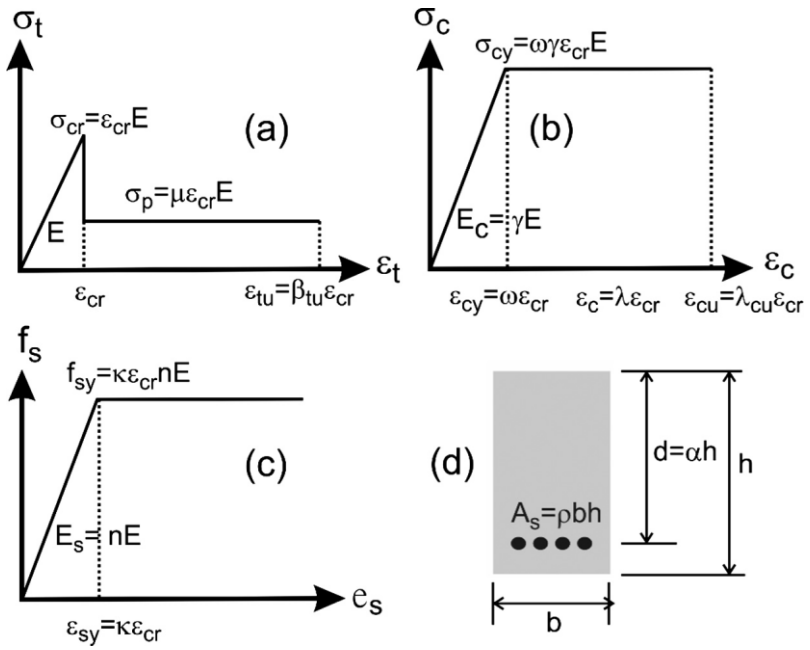

Figure 104. Material model for single reinforced concrete design (a) tension model; (b) compression model; (c) steel model; (d) beam cross-section (Barzin Mobasher, Yao, and Soranakom 2015)

In this report, the HRC analytical model presented by (Mobasher et al. Barzin Mobasher, Yao, and Soranakom 2015) is used in a design approach applied to the UHPFRC members. Equations to determine the moment-curvature relationship, ultimate moment capacity, and minimum flexural reinforcement ratio were explicitly derived (Mobasher et al. 2015, (Barzin Mobasher, Yao, and Soranakom 2015)). Figure 104 (a) and (b) represent all the combination tensile and compressive response of steel and UHPC models used in the analytical expressions of moment-curvature and load–deflection of HRC beams. The derivation includes the interaction of compression and tension failure of FRC, as well as a failure by tension yielding of steel.

Parameter-based tensile and compressive strain-stress diagrams of composite and steel sections are shown in Figure 104(c) for a typical hybrid-FRC cross-section. Reinforcement material parameters required for the simplified models are shown in Figure 104 and summarized as follows (see Figure 104):

Normalized yield strain of steel,

$$\kappa = \frac{\varepsilon_{sy}}{\varepsilon_{cr}}$$ **Equation 35**

Normalized elastic modulus of steel,

$$n = \frac{E_s}{E_c}$$ **Equation 36**

Reinforcement ratio,

$$\rho_g = \frac{A_s}{bh}$$ **Equation 37**

Normalized reinforcement depth,

$$\alpha = \frac{d}{h}$$ **Equation 38**

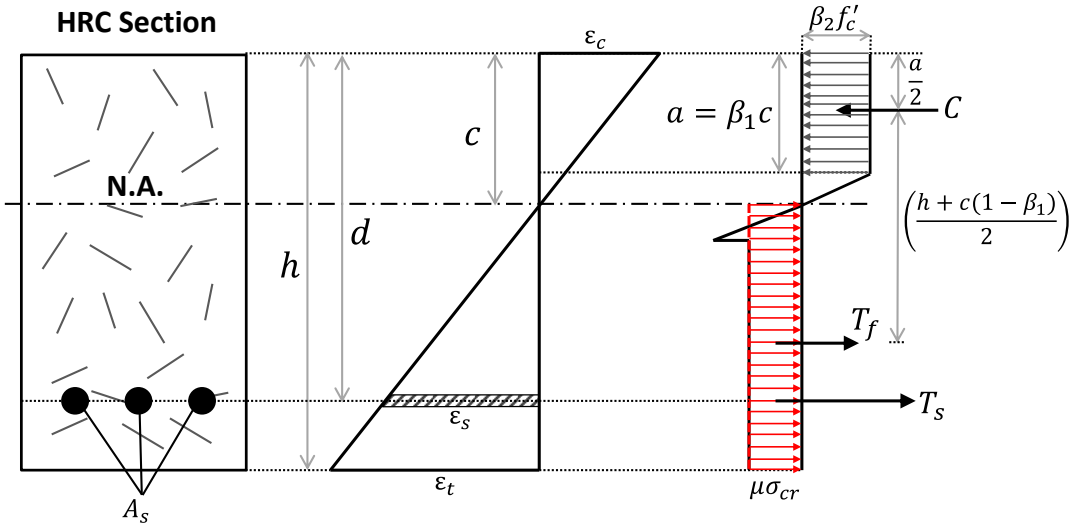

Figure 105. FRC cross-section stress-strain diagrams

As in the process used for FRC section, the first step is to calculate the depth of the neutral axis by setting tensile and compressive forces equal to each other. The tensile force due to the cover concrete is ignored.

$$C = ab \times \beta_2 f_c' \quad \textbf{Equation 39}$$

$$T_f = b(h-c) \times \mu\sigma_{cr} \quad \textbf{Equation 40}$$

$$T_s = A_s f_y = \rho_g bhf_y \quad \textbf{Equation 41}$$

Requiring the equilibrium of internal forces, i.e. $C = T_f + T_s$, depth of the neutral axis can be calculated as

$$c = \frac{hb\mu\sigma_{cr} + A_s f_y}{b(\beta_1\beta_2 f_c' + \mu\sigma_{cr})} = \frac{\mu + \rho\kappa n}{\beta_1\omega + \mu} \times h \quad \textbf{Equation 42}$$

Where,

$$\beta_1 = \begin{cases} 0.85 & \text{for } f_c' \le 4000 \text{ psi} \\ 0.85 - 0.05\left(\dfrac{f_c' - 4000}{1000}\right) & \text{for } 4000 < f_c' \le 8000 \text{ psi} \\ 0.65 & \text{for } f_c' > 8000 \text{ psi} \end{cases} \quad \textbf{Equation 43}$$

And $\beta_2 = 0.85$ (see Figure 102). The moment capacity of the section can be calculated as,

$$M_n = T_f\left(\frac{h + c(1-\beta_1)}{2}\right) + \mathrm{T}_s\left(\alpha h - \frac{\beta_1 c}{2}\right) \quad \textbf{Equation 44}$$

Substituting $C = ab \times \beta_2 f_c'$

Equation 39, $T_f = b(h-c) \times \mu\sigma_{cr}$

Equation 40, and $T_s = A_s f_y = \rho_g bhf_y$

Equation 41 into the above equation, the capacity of the section can be obtained.

$$M_n = 3\left[\mu(1-A)\left(1+A(1-\beta_1)\right)+2\rho\kappa n\left(\alpha-\frac{A\beta_1}{2}\right)\right]\times M_{cr}$$ **Equation 45**

Where,

$$A=\frac{\mu+\rho\kappa n}{\beta_1\omega+\mu}$$ **Equation 46**

M_{cr} can be obtained using $M_{cr}=\frac{\sigma_{cr}bh^2}{6}$

Equation 33. Balanced reinforcement can be calculated assuming that the steel reinforcement and compressive concrete yield at the same time. Based on this assumption, the depth of the neutral axis, in a section with balanced reinforcement, can be calculated as follows:

$$c_b=\frac{\varepsilon_{cy}}{\varepsilon_{sy}+\varepsilon_{cy}}d$$ **Equation 47**

Using the equilibrium of internal forces, i.e. $C=T_f+T_s$, the amount of the balanced reinforcement, ρ_b, can be calculated. Substituting C_b from $c_b=\frac{\varepsilon_{cy}}{\varepsilon_{sy}+\varepsilon_{cy}}d$ Equation 47 into $T_s=A_sf_y=\rho_gbhf_y$

Equation 41, $c=\frac{hb\mu\sigma_{cr}+A_sf_y}{b(\beta_1\beta_2f_c'+\mu\sigma_{cr})}=\frac{\mu+\rho\kappa n}{\beta_1\omega+\mu}\times h$

Equation 42, $\beta_1=\begin{cases}0.85 & \text{for } f_c'\le 4000 \text{ psi}\\ 0.85-0.05\left(\frac{f_c'-4000}{1000}\right) & \text{for } 4000<f_c'\le 8000 \text{ psi}\\ 0.65 & \text{for } f_c'>8000 \text{ psi}\end{cases}$

Equation 43, and $C=T_f+T_s$ we have,

$$\rho_b = \frac{\beta_1\beta_2\varepsilon_{cy}f_c' - \varepsilon_{sy}\mu\sigma_{cr}}{(\varepsilon_{sy}+\varepsilon_{cy})f_y} = \frac{\beta_1\omega^2 - \kappa\mu}{(\kappa+\omega)n\kappa}$$ **Equation 48**

If the reduction factors are assumed equal to 1 ($\beta_1 = \beta_2 = 1$), then $\omega = 25$ and

$$\rho_b = \frac{625 - \kappa\mu}{(\kappa+25)n\kappa}$$ **Equation 49**

To have a ductile failure it is necessary that the reinforcement ratio be less than the balanced ratio, $\rho_g < \rho_b$. A solved example, using this method, is presented in the appendix.

For steel rebar Grade 60 and UHPC with $f_c' = 20$ ksi, if $\kappa = 15$ and $n = 5$ then

$$\rho_b = 0.21 - \frac{\mu}{200}$$ **Equation 50**

Given that μ is usually less than 1, it can be concluded that ρ_b is independent of μ.

Closed-Form Solutions for Flexural Response of FRC Beams (Model for UHPC)

The simplified approach was based on the ultimate limit state (ULS) design. This section presents another approach, which can be used for serviceability limit state (SLS) design. The generalized fiber-reinforced concrete model used in this section is based on the idealized model suggested by Lim et al, 1987 (T.-Y. Lim, Paramasivam, and Lee 1987) and presented in the form of closed form solutions by Soranakom and Mobasher, 2007 (Chote Soranakom and Mobasher 2007). The proposed constitutive model for general fiber-reinforced concrete materials consists of a bilinear elastic-perfectly plastic model for compression and an elastic-constant post-peak response for tension.

Figure 106 shows the interactions of the parameters of elastic and inelastic zones of tension and compression response based on a linear strain distribution. The constitutive response relates the strains to stresses, forces, and the bending moment. Note that the interaction of any two zones in the tension and compression behavior results in a specific stress distribution which must be solved in closed form to get the location of neutral axis for that specific set of values. After solving for the depth of neutral axis, the value of moment and curvature are calculated at each range of applied strain and used to construct the moment-curvature response for that case.

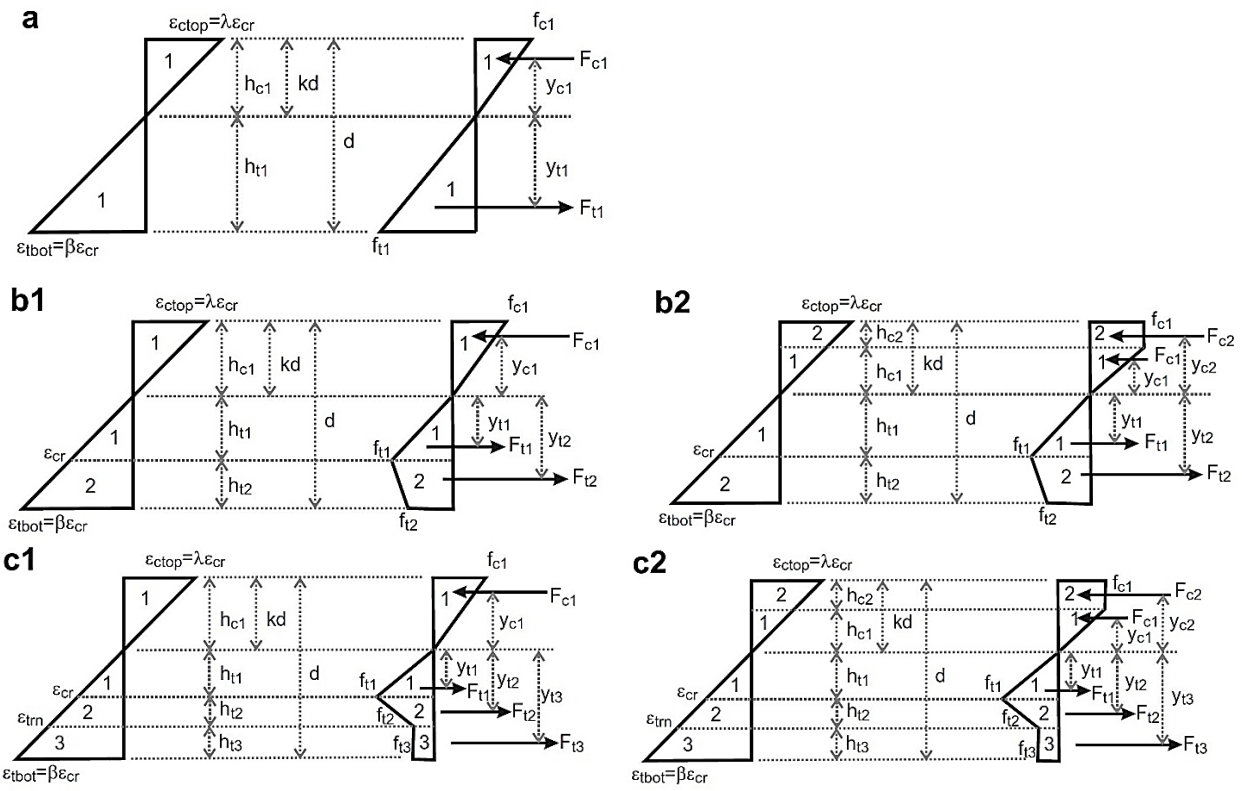

Figure 106. Stress-strain diagram at different stages of normalized tensile strain at the bottom fiber (β): (a) Elastic for compression and tension, $0 \le \beta \le 1$ and $0 < \lambda \le \omega$); (b.1) Elastic for compression but non-linear for tension, $1 < \beta \le \alpha$ and $0 < \lambda \le \omega$); (b.2) Plastic for compression and non-linear for tension, $1 < \beta \le \alpha$ and $\omega < \lambda \le \lambda_{cu}$); (c.1) Elastic for compression but non-linear for tension, $\alpha < \beta \le \beta_{tu}$ and $0 < \lambda \le \omega$; (c.2) Plastic for compression and non-linear for tension, $\alpha < \beta \le \beta_{tu}$ and $\omega < \lambda \le \lambda_{cu}$ (Chote Soranakom and Mobasher 2007)

The moment capacity of a beam section according to the imposed tensile strain at the bottom fiber ($\varepsilon_t = \beta\varepsilon_{cr}$) can be derived by the following steps: (1) determine linear strain and stress distributions, (2) force components by integration of stresses, (3) solve for the depth of neutral axis location, *k*, by force equilibrium, and obtain the strain-curvature relationship. The internal moment is obtained from the force and strain distribution. Based on the tensile response of the concrete, three major ranges were defined. In the first range, both compression and tension parts of the section behave in an elastic manner. In the second range, the component of the cross section that is under the tensile stress exceeds the tension cracking stress, therefore the section is in the post-peak transition range. The compressive part may be linear or non-linear. Therefore this tension cracking criterion introduced two ranges identified as 2-1 or 2-2, depending on the compression zone's being linear or non-linear. In the third range, the segment above the neutral axis that is under compressive stress may follow the linear or non-linear portion of the stress strain response, while the tensile part of the section has already reached the

residual tensile response. For this section, only Range 2-1 is described, and the bases for the other ranges will be the same. At this range, the tensile part of the section is cracked but the compressive part is still in the linear part of its response. Force component and its centroid to the neutral axis in each zone can be expressed as:

$$\frac{F_{c1}}{bh\sigma_{cr}} = \frac{\beta\gamma k^2}{2(1-k)}; \qquad \frac{y_{c1}}{h} = \frac{2}{3}k$$ **Equation 51**

$$\frac{F_{t1}}{bh\sigma_{cr}} = \frac{(1-k)}{2\beta}; \qquad \frac{y_{t1}}{h} = \frac{2}{3}\frac{(1-k)}{\beta}$$ **Equation 52**

$$\frac{F_{t2}}{bh\sigma_{cr}} = \frac{(1-k)(\beta-1)(\eta\beta-\eta+2)}{2\beta}; \quad \frac{y_{t2}}{h} = \frac{2\eta\beta^2-\eta\beta-\eta+3\beta+3}{3\beta(\eta\beta-\eta+2)}(1-k)$$ **Equation 53**

where *F* and *y* are the force and its centroid, respectively; subscripts *c1,t1,t2* designate compression zone 1 and tension zones 1 and 2; *b* and *h* are the width and the height of the beam. The neutral axis parameter *k* is found by solving the equilibrium of net internal forces equal to zero, $F_{c1} + F_{t1} + F_{t2} = 0$.

$$k = \frac{C_1 - \sqrt{\beta^2 C_1}}{C_1 - \beta^2}$$ **; where** $C_1 = \eta(\beta^2 - 2\beta + 1) + 2\beta - 1$ **Equation 54**

The nominal moment capacity M_n is obtained by taking the first moment of force about the neutral axis, $M_n = F_{c1}y_{c1} + F_{t1}y_{t1} + F_{t2}y_{t2}$, and expressed as a product of the normalized nominal moment m_n and the cracking moment M_{cr} as follows:

$$M_n = m_n M_{cr}$$ **Equation 55**

$$m_n = C_2\frac{k^2-2k+1}{\beta^2} + \frac{2\beta k^3}{1-k}$$ **;** where $C_2 = C_1 + 2C_1\beta - \beta^2$ **Equation 56**

Additional discussions of these methodologies and equations are presented in the original Soranakom and Mobasher publication, which has been incorporated in ACI 544-8R, ACI544-6R, and ACI544-7R (ACI 544 2016; Committee 544 2016).

Table 18 presents the general derivation of all potential combinations for the interaction of tensile and compressive response. The methodology used in the design of conventional reinforced concrete according to ACI-318 (ACI Committee 318 and American Concrete Institute 2014) is adopted next. The nominal moment capacity of a flexural member M_n must be decreased by a reduction factor to account for variability in materials and workmanship. The reduced capacity must be greater than the ultimate moment M_u due to factored loading by ACI Sec. 9.2, i.e., $\phi_r M_n \geq M_u$, where ϕ_r is the reduction factor for strain-hardening FRC and taken as 0.65, equal to the reduction factor for compressive failure of plain concrete stipulated by ACI Sec. C.3.5. Although the post-crack flexural response of HPFRC is ductile, so that it can sustain large deflections after cracking, it fails abruptly with little warning after passing the ultimate moment. For this reason, a conservative reduction factor for compressive failure of plain concrete is adopted.

According to bilinear tension and elastic compression models, shown in Figure 104, the maximum moment capacity is obtained when the normalized tensile strain at the bottom fiber ($\beta = \varepsilon_t/\varepsilon_{cr}$) reaches the tensile strain at peak strength ($\alpha = \varepsilon_{peak}/\varepsilon_{cr}$). However, the simplified $\frac{F_{c1}}{bh\sigma_{cr}} = \frac{\beta\gamma k^2}{2(1-k)}$;

$\frac{y_{c1}}{h} = \frac{2}{3}k$ Equation 51, $\frac{F_{t1}}{bh\sigma_{cr}} = \frac{(1-k)}{2\beta}$;

$\frac{y_{t1}}{h} = \frac{2}{3}\frac{(1-k)}{\beta}$ Equation 52, $\frac{F_{t2}}{bh\sigma_{cr}} = \frac{(1-k)(\beta-1)(\eta\beta-\eta+2)}{2\beta}$

; $\frac{y_{t2}}{h} = \frac{2\eta\beta^2-\eta\beta-\eta+3\beta+3}{3\beta(\eta\beta-\eta+2)}(1-k)$ Equation 53 for moment capacity are applicable to the compressive stress in the elastic region only. The elastic condition must be checked by computing the normalized compressive strain developed at the top fiber λ and comparing it to the normalized yield compressive strain ω. The general solutions for all the cases are presented in Table 18. Using the strain diagram in Figure 106, one can obtain the relationship between the top compressive strain and bottom tensile strain as follows:

$$\frac{\varepsilon_c}{kh} = \frac{\varepsilon_t}{(1-k)h}$$ **Equation 57**

Substituting $\varepsilon_c = \lambda\varepsilon_{cr}$ and $\varepsilon_t = \beta\varepsilon_{cr}$ in $\frac{\varepsilon_c}{kh} = \frac{\varepsilon_t}{(1-k)h}$

Equation 57 relates the maximum compressive strain to the tensile strain. Finally, the condition can be expressed in a normalized form as:

Table 18. Neutral axis parameter *k*, normalized moment *m*, and normalized curvature ϕ for each stage of normalized tensile strain at bottom fiber (β) (Barzin Mobasher, Yao, and Soranakom 2015)

Stage	K	m = M/M_{cr}	$\phi=\Phi/\Phi_{cr}$
1 **0 < β≤ 1**	$k_1=\begin{cases}\frac{1}{2} & \text{for } \gamma=1\\ \frac{-1+\sqrt{\gamma}}{-1+\gamma} & \text{for } \gamma\neq 1\end{cases}$	$m_1=\frac{2\beta\left[(\gamma-1)k_1^{\,3}+3k_1^{\,2}-3k_1+1\right]}{1-k_1}$	$\phi'_1=\frac{\beta}{2(1-k_1)}$
2.1 **1 < β≤ α** **0 < λ ≤ ω**	$k_{21}=\frac{D_{21}-\sqrt{D_{21}\gamma\beta^2}}{D_{21}-\gamma\beta^2}$ $D_{21}=\eta(\beta^2-2\beta+1)+2\beta-1$	$M'_{21}=\frac{(2\gamma\beta-C_{21})k_{21}^{\,3}+3C_{21}k_{21}^{\,2}-3C_{21}k_{21}+C_{21}}{1-k_{21}}$ $C_{21}=\frac{(2\beta^3-3\beta^2+1)\eta+3\beta^2-1}{\beta^2}$	$\phi'_{21}=\frac{\beta}{2(1-k_{21})}$
2.2 **1 < β≤ α** **ω< λ≤ λ_{cu}**	$k_{22}=\frac{D_{22}}{D_{22}+2\omega\gamma\beta}$ $D_{22}=D_{21}+\gamma\omega^2$	$M'_{22}=(3\gamma\omega+C_{22})k_{22}^{\,2}-2C_{22}k_{22}+C_{22}$ $C_{22}=C_{21}-\frac{\gamma\omega^3}{\beta^2}$	$\phi'_{22}=\frac{\beta}{2(1-k_{22})}$
3.1 **α < β≤ β_{tu}** **0 < λ ≤ ω**	$k_{31}=\frac{D_{31}-\sqrt{D_{31}\gamma\beta^2}}{D_{31}-\gamma\beta^2}$ $D_{31}=\eta(\alpha^2-2\alpha+1)$ $+2\mu(\beta-\alpha)+2\alpha-1$	$M'_{31}=\frac{(2\gamma\beta-C_{31})k_{31}^{\,3}+3C_{31}k_{31}^{\,2}-3C_{31}k_{31}+C_{31}}{1-k_{31}}$ $C_{31}=\frac{(2\alpha^3-3\alpha^2+1)\eta-3\mu(\alpha^2-\beta^2)+3\alpha^2-1}{\beta^2}$	$\phi'_{31}=\frac{\beta}{2(1-k_{31})}$

3.2 $\alpha < \beta \leq \beta_{tu}$ $\omega < \lambda \leq \lambda_{cu}$	$k_{32} = \frac{D_{32}}{D_{32} + 2\omega\gamma\beta}$ $D_{32} = D_{31} + \gamma\omega^2$	$M'_{32} = (3\gamma\omega + C_{32})k_{32}^{\ 2} - 2C_{32}k_{32} + C_{32}$ $C_{32} = C_{31} - \frac{\gamma\omega^3}{\beta^2}$	$\phi'_{32} = \frac{\beta}{2(1-k_{32})}$

Table 18 shows that the moment and curvature can be obtained as a function of the strain in the tensile fiber of the section, β . Figure 107 represents the typical moment-curvature diagrams with different fiber contents. Fiber-reinforced sections exhibit post-peak residual strength depending on their fiber content. As the amount of the fiber increases, the maximum bending capacity of the section and the residual (post-peak) strength increase as well.

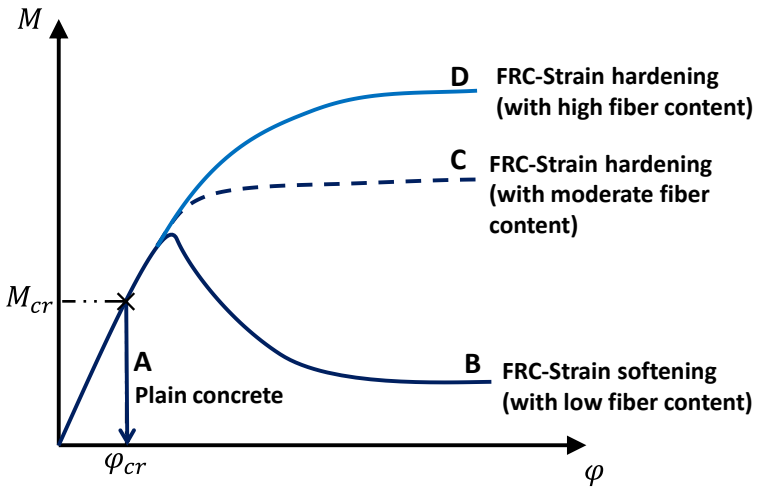

Figure 107. Typical moment-curvature diagrams for FRC sections with various fiber content

Load Deflection Computation

Moment-curvature diagrams are calculated for the sections depending on the number and interaction of flexural stages (see Figure 108). For any given curvature, the lowest magnitude of the moment from the stages was selected as the governing load, which would allow the transition from one loading stage to the other. The final moment-curvature diagram is a composite of the several interacting flexural stages. To have a load-deflection response for a beam element, it is necessary to have the moment-curvature response for various sections (elements) along the beam length and then calculate the deflection using moment-area method or direct integration. For a statically determinate simply supported beam, equilibrium is used to obtain support reactions and moment distribution along the length of beam directly from the applied forces. Using the moment-curvature distribution, this response is converted to the curvature distribution along the length using a look-up table.

The slope and deflection distributions along the length of the beam are obtained by applying the slope-deflection method to the curvature distribution. The strain at the tensile fiber is increased incrementally at a control point such as the midpoint, and used to establish the curvature distribution, which is in turn used to calculate both moment distributions used in the deflection computation (Chote Soranakom and Mobasher 2007).

Figure 108 and Figure 109 show the typical moment-curvature diagram for the four-point bending test and the moment distribution along the beam length. The three depicted patterns of curvature distribution are needed in the derivations for the mid-span deflection. Figure 109(a) shows the curvature distribution before cracking (Stage A). After cracking (stages B and C), as the post-crack curvature increases, the moment continues to increase as shown by the red line in Figure 109(b). At stage B, after reaching the maximum loading, the moment cannot go higher than the maximum bending capacity; thus it decreases at the levels below the maximum moment. At this point, two types of response are possible, depend on the location of the section along the axis. If the section is located in the non-localized length, (L_n) crack will be closed during the unloading (Stage C1), but if the section is located on the localized length (L_l) the crack opening will continue (Stage C2). The same approach can be taken for 3PB tests and another type of RC sections as well (Chote Soranakom and Mobasher 2007; Iyengar, Raviraj, and Jayaram 2002).

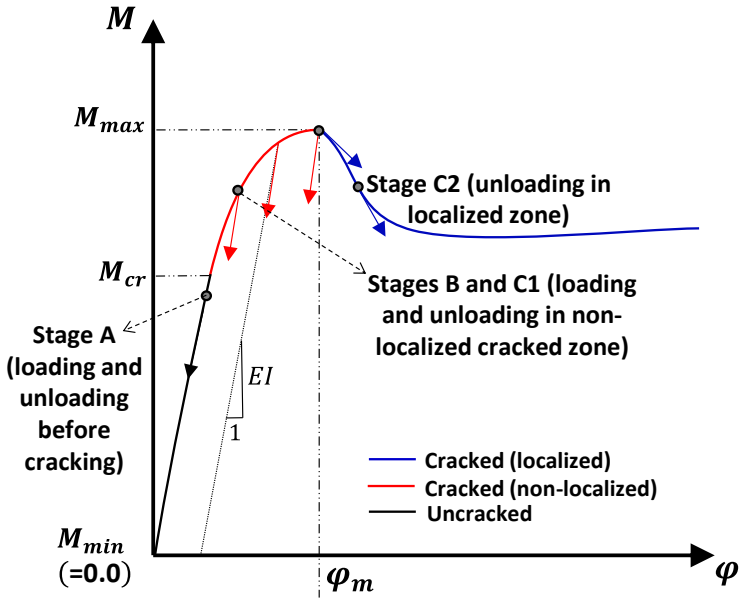

Figure 108. Generalized M-C diagram; during different stages of loading and unloading

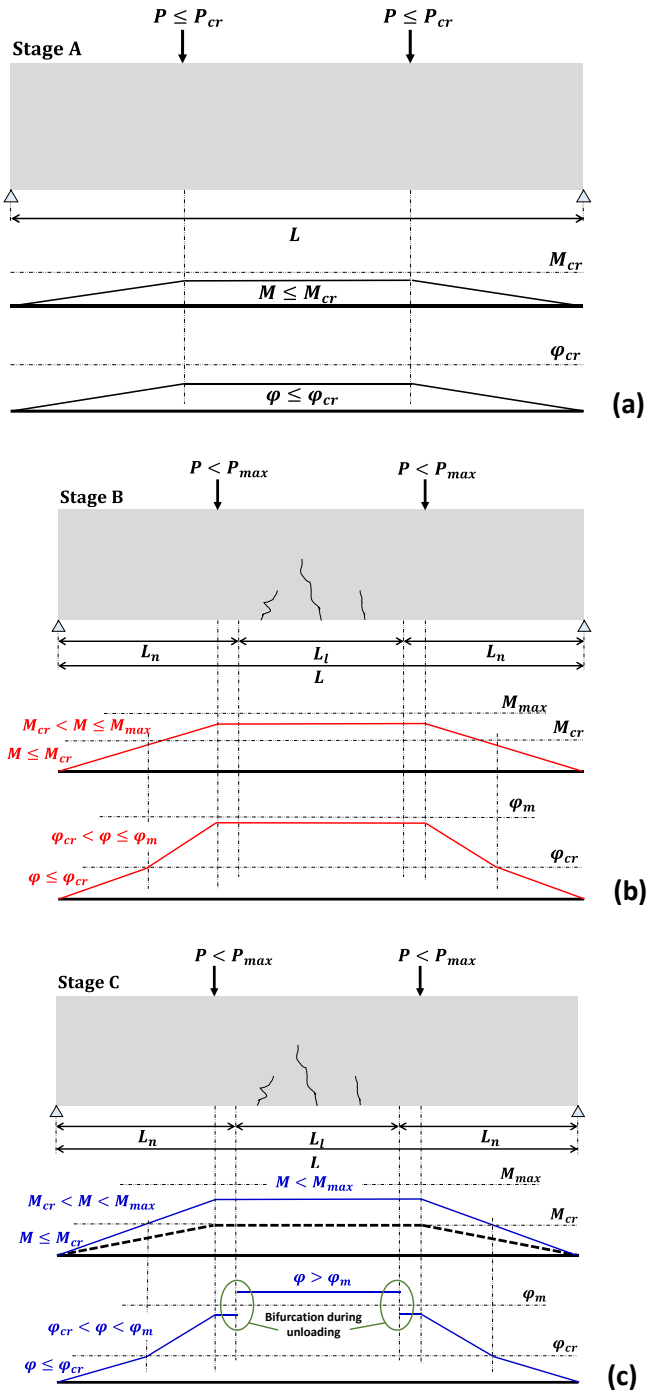

Figure 109. Moment and curvature distribution in FRC beams at different stages: (a) Stage A: un-cracked section; (b) Stage B: cracked beam, loading at localized and non-localized zones; (c) Stage C: cracked beam, unloading at localized and non-localized zones

The procedures for the calculation of the load-deflection are described in detail in earlier publications (Soranakom and Mobasher 2007; Mobasher, Yao, and Soranakom 2015; Committee 544 2016).

Applications of the UHPC Model

Computation of Material Tensile Property Using Inverse Analysis

In this section, an inverse analysis procedure is used in order to obtain the basic tensile material properties from the experimental tests reported in Chapter 7. Using this approach, one can obtain design parameters from experiments and simulate the flexural response of any member by starting from a known or back-calculated tensile and compressive constitutive model. This approach enables us to simulate the responses of various specimens in the context of load-deflection. Using the procedures that have been developed in ACI4544-8R (ACI 544 2016, 544) (Committee 544 2016) it is will be possible to obtain a model fit to the experimental data. The output of the model is the material property values. Material properties obtained from this model can be used in finite element analysis (FEA), structural design, or any other type of numerical analysis method.

The experimental results of the current research were exhibited in Chapter 7. In this section, only the comparative simulation results and the back-calculated parameters are given in the following figures. Furthermore, the average of the back-calculated parameters for each set of tests is listed in Table 19.

The first step for the inverse analysis is to import the experimental data as two columns representing the load and deflection experimental results. This is followed by the values for the beam dimensions and the test method (3PB or 4PB). There is also an Excel spreadsheet developed for this purpose which can be found on the ACI web site (Committee 544 2016).

We start the simulation by fitting the initial linear response with the linear part of the experimental results. This involves only changing the Young's modulus parameter to obtain the best fit for the Young's modulus of the linear elastic phase. This is done by increasing or decreasing the value of the elastic modulus (Young's modulus) *E*. Normal FRC has a Young's modulus in the range of 3000-5000 ksi (20-35 GPa), but for UHPC this value can be as high as 9400 ksi (65 GPa).

Next, the value of first crack strain ε_{cr} is chosen to fit the approximate point where the linear elastic behavior ceases and non-linear behavior begins. The type of FRC being tested, the first crack flexural strength of the sample, the fiber type, and the fiber dosage all contribute to the point where cracking is observed. In this research, a range between 100 and 170 microstrains was used. The next step is to address the post-peak response of the section. The post-cracking slope for strain hardening is represented by E_{cr} which is normalized by the parameter η. This parameter is dependent on the values of α and μ through the following equation, after some manipulations on $\alpha = \frac{\varepsilon_{peak}}{\varepsilon_{cr}}$

Equation 23, $\eta = \frac{E_{cr}}{E}$

Equation 24, $\omega = \frac{\sigma_{cy}}{E\varepsilon_{cr}} = \frac{\sigma_{cy}}{\sigma_{cr}}$

Equation 25, $\beta = \frac{\varepsilon_t}{\varepsilon_{cr}}$

Equation 26, $\lambda = \frac{\varepsilon_c}{\varepsilon_{cr}}$

Equation 27 (also see Figure 101).

$$\eta = \frac{E_{cr}}{E} = -\frac{(1-\mu)}{(\alpha-1)} \qquad \textbf{Equation 58}$$

By manipulating α and μ, the post-cracking slope can be fitted to the load-deflection curve. The parameter α adjusts the horizontal location of the transition point, while μ adjusts the vertical position of the transition point and of the tail of the curve. Increasing μ will raise the post-crack residual portion of the simulated curve. The parameter η is automatically calculated per $\eta = \frac{E_{cr}}{E} = -\frac{(1-\mu)}{(\alpha-1)}$ Equation 58 and should reflect the post-crack slope as negative in the softening case and positive in the hardening case. Both of these responses have been observed for UHPC samples with 1 percent (strain-softening) and 3 percent (strain-hardening) fiber content. The relationship between the parameters α and μ have other effects on the shape of the simulated curve. Changes made in ε_{cr} will also require changes to the parameters α and μ to realign the simulation curve. Parameter θ_{tu} depends on the user's preference on the termination point of the simulation curve. In some cases the entire deflection curve is not necessary, so appropriate adjustments can be made.

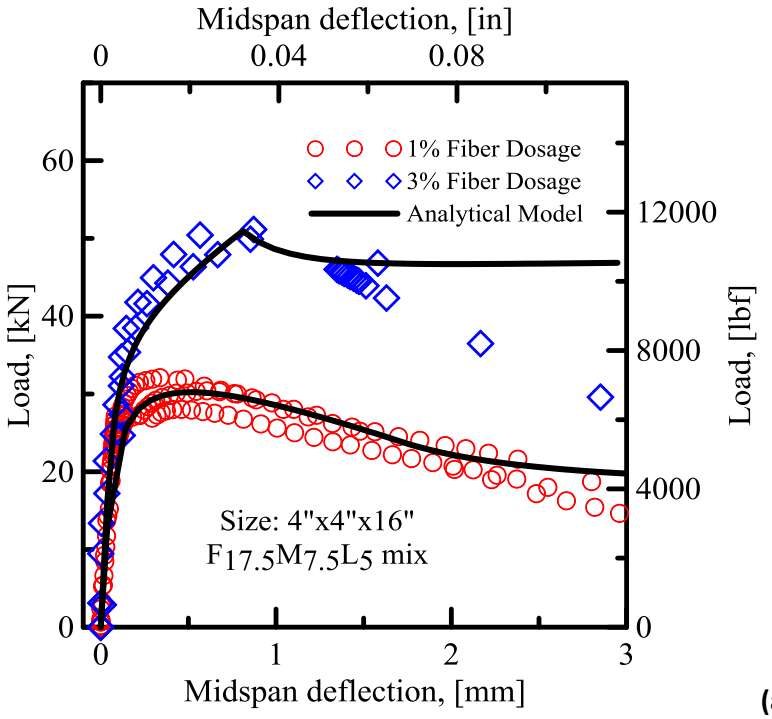

(a)

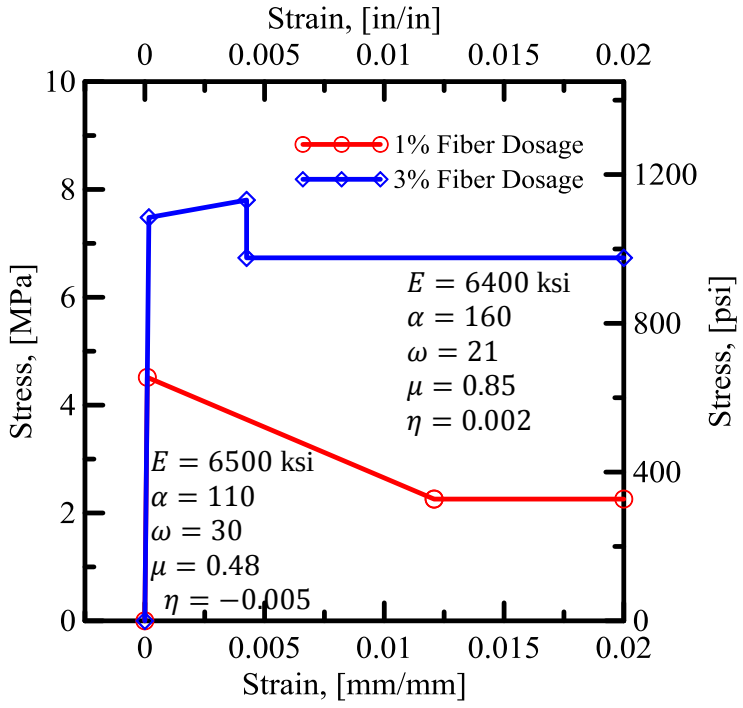

(b)

Figure 110. Effect of fiber volume fraction, large beam after 28 days curing: (a) load-deflection curves; (b) stress-strain diagrams

Figure 110 represents the effect of fiber content on large UHPC specimens (4" × 4" × 16") tested after 28 days of curing. The capacity of the section increases significantly from 1 percent to 3 percent of fibers. The post-peak response also remains at the same elevated level for a large range of displacements. With a residual strength of at around 970 psi after 3 millimeters of deflection, samples with 3 percent fibers have as much as twice the residual strength of the 1 percent fiber samples. The simulated tensile curve for these specimens shows that the strain softening response at the Vf = 1 percent content is now replaced with strain hardening. The first crack strength of beams with 3 percent fiber content is about 1100 psi (7.5 MPa), which is significantly higher than the first crack strength of 650 psi (4.5 MPa) for the beams with 1 percent fiber content. On the other hand, the residual strength of the section in samples with 3 percent fiber content is three times higher than that in the samples with 1 percent fiber content, with an increase from 320 to 987 psi. The slope of the post-crack transition zone, after crack and before stable residual strength, is negative for strain softening and positive for strain hardening. The back-calculated parameters are also presented in Figure 110. The same approach has been chosen for other sets of data in the experimental program. The average of all back-calculated parameters for each set of analysis is listed in Table 19.

Figure 111 represents the effect of mix design for the two mixtures of ML and FML on large size specimens (4" × 4" × 16") tested after 28 days of curing. The flexural capacity of the material FML is higher than that of the ML mixtures. This is due to the better interaction between the matrix and fibers, as addressed in Chapter 7. These two systems, however, are close to one another in general response. The tension back-calculation responses are similar to a strain softening response simulating both samples. A tensile strength of 625 psi and 790 psi and a nominal residual strength of approximately 380 to 400 psi are obtained for FML and ML mixtures, respectively.

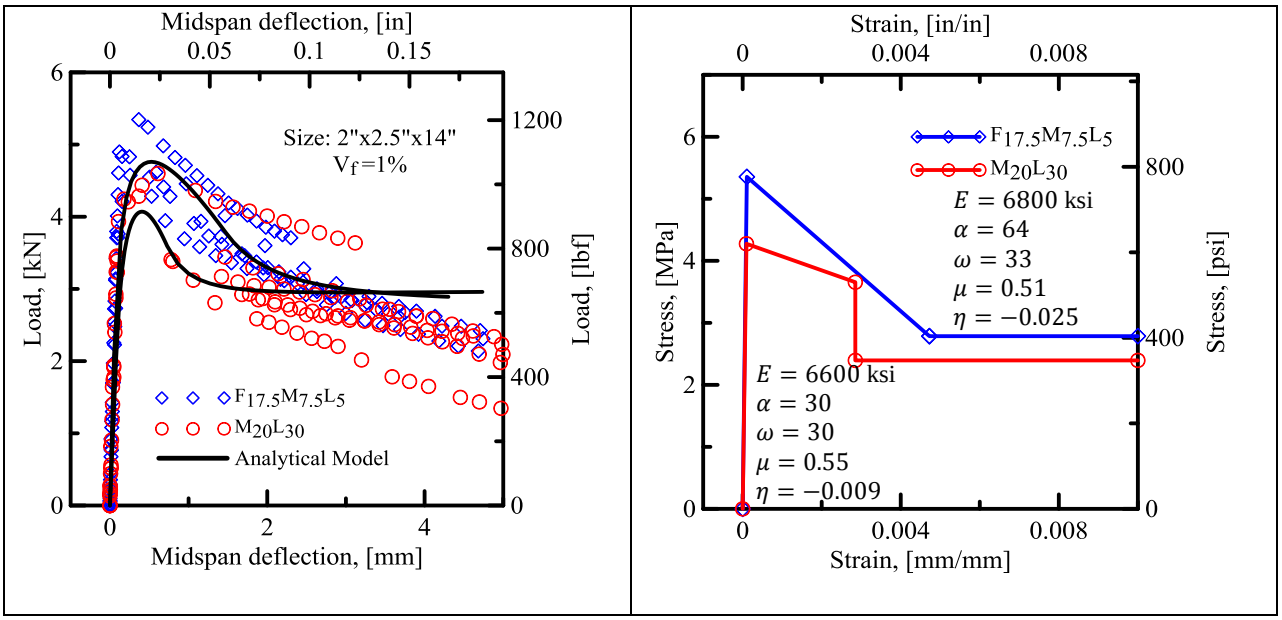

Figure 111. Effect of mix design on the flexure response and tensile stress-strain

The effect of mixing method is shown in Figure 112. The two samples selected as representatives are quite close to the overall samples. If we choose these two similar samples, the tensile responses also fall into the similar category, i.e., strain-softening, with a similar tensile response. In practice, one can fit the curves independently and report all of the data, or attempt to fit a representative simulation to the collection of all experimental data.

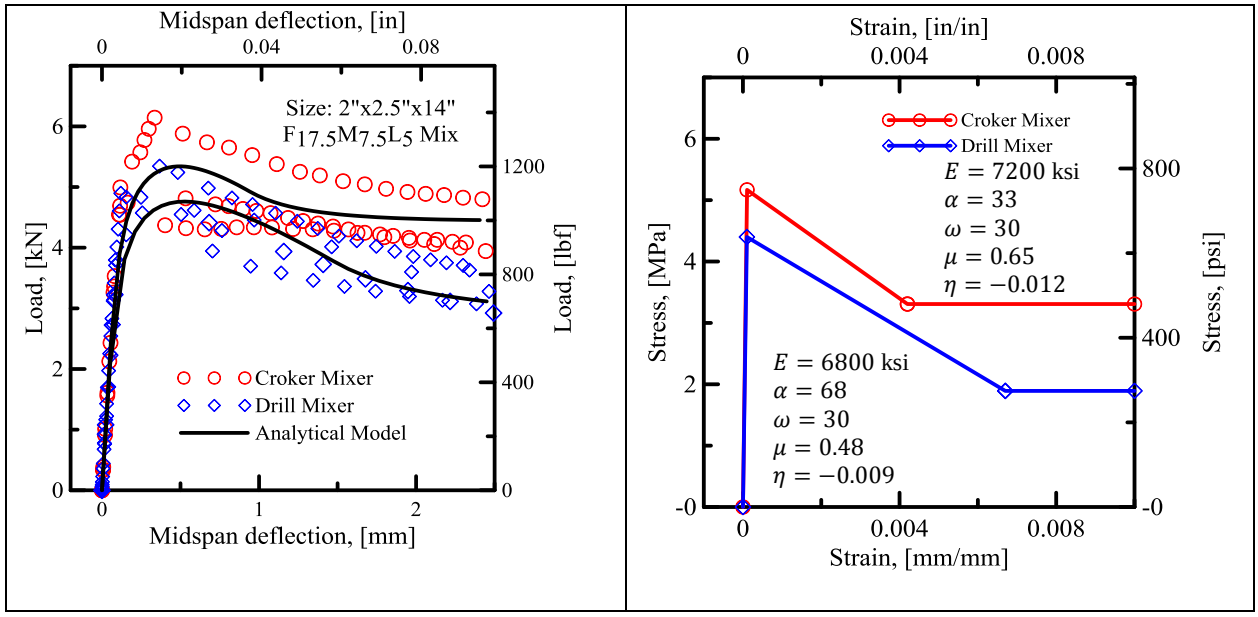

Figure 112. Effect of mixing method

The effect of specimen size is shown in Figure 113. While the geometry of the two samples is different, the proposed procedure uses a nearly constant stress-strain response in the post-cracking stage in order to simulate the load deflection results. The post-cracking residual stress of the large beam samples is higher than that of the smaller beams. This may be attributed to the small beams' lack of sufficient depth for the growth of the crack and activation of all the fibers in its path before the crack reaches the full depth of the beam. The size effect is therefore shown in this figure as a dominant response. Larger specimens, therefore, yield more accurate results than smaller ones.

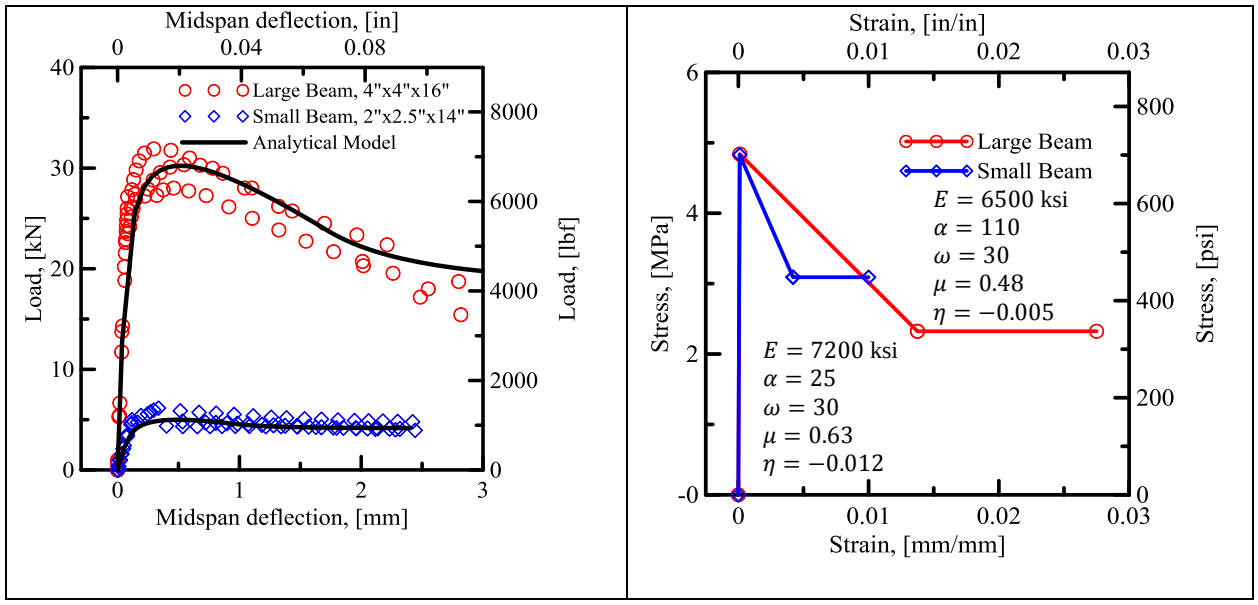

Figure 113. Size effect (2x2.5x14in beams vs. 4x4x16in beams)

The effects of curing on both large and small beams are shown in Figure 114 and Figure 115. In both cases, increasing the curing period increases the strength and ductility significantly. The larger beams show a strength measure of the same order of magnitude obtained from the smaller beams. While in the small beams, prolonging the curing period increases the tensile strength by 60 percent and residual strength by 50 percent, in the large beams the increase is around 10 percent for both tensile and residual strengths.

Table 19 summarizes all the back-calculated parameters.

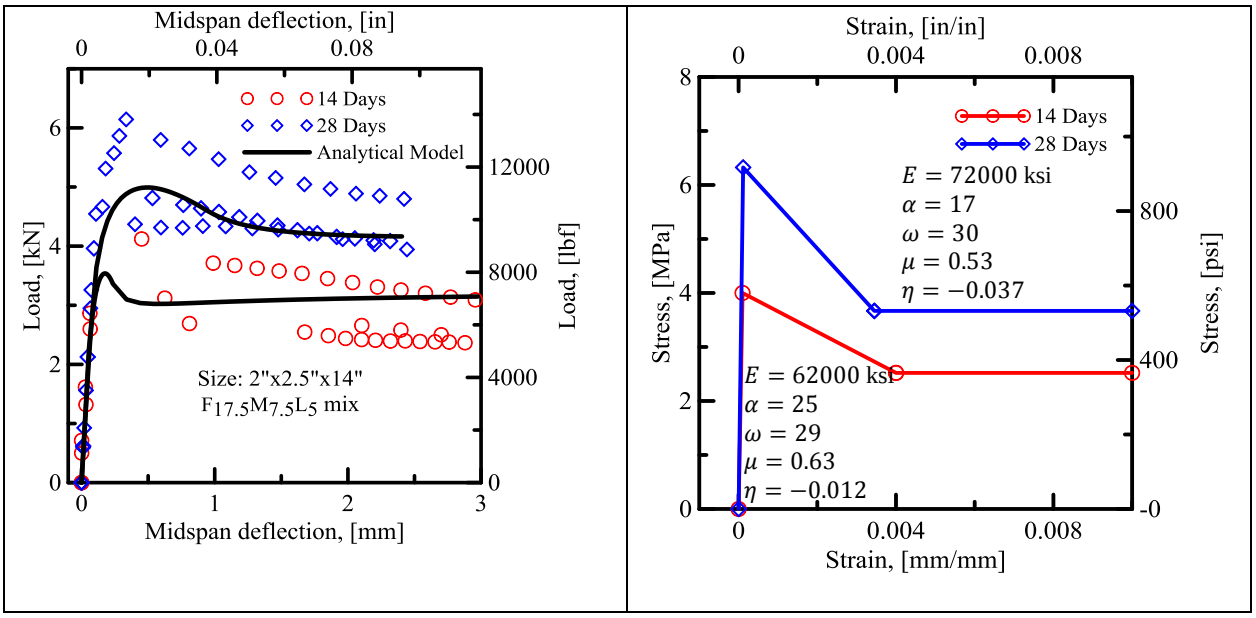

Figure 114. Effect of curing period on small beams (2x2.5x14in)

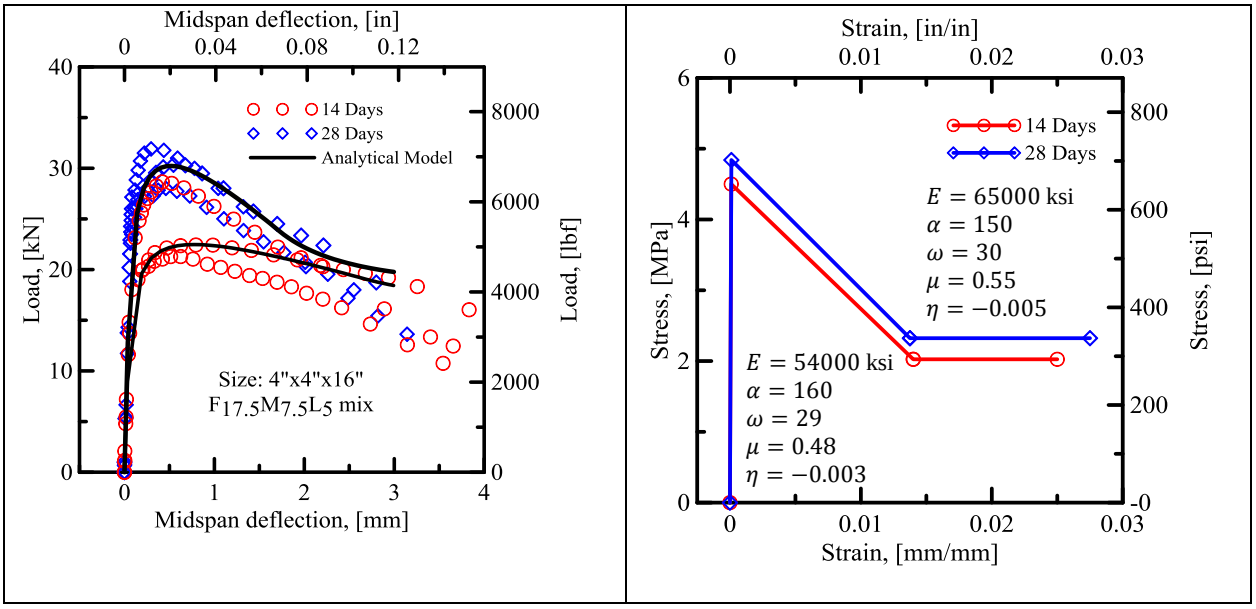

Figure 115. Effect of curing period on large beams (4x4x16in)

Table 19. Average of inverse analysis parameters for each set of tests

Set	Beam Series	No. of Replicates	Elastic Modulus, E (ksi)	Cracking Tensile Strain ε_{cr} (micro-strain)	Cracking Strength (psi)	α, Transition Strain/ Cracking Strain	γ, Normalized compressive modulus	ω, Normalized Compressive Yield Strain	η, Modulus Ratio	μ, Normalized Residual Tensile Strength	β_{tu}, Normalized Tensile Strain	Compressive Strength (ksi)
1	**ML_S_0_28_4PB_D**	**3**	**6346.9 (±229.4)**	**99 (±6.7)**	**628 (±65)**	**--**	**--**	**--**	**--**	**--**	**--**	**17.4 (±0.7)**
2	**ML_S_1_28_4PB_D**	**6**	**6599.2 (±177.6)**	**100 (±8.4)**	**660 (±68)**	**17 (±8)**	**0.98 (±0.04)**	**30.3 (±1.4)**	**-0.025 (±0.025)**	**0.51 (±0.07)**	**197 (±45)**	**19.6 (±0.7)**
3	**FML_S_0_28_4PB_D**	**6**	**6425.5 (±391.0)**	**91 (±3.7)**	**585 (±61)**	**--**	**--**	**--**	**--**	**--**	**--**	**20.2 (±0.8)**
4	**FML_S_1_28_4PB_D**	**6**	**6787.8 (±402.5)**	**98 (±4.4)**	**665 (±64)**	**64 (±11)**	**0.96 (±0.05)**	**32.6 (±1.1)**	**-0.009 (±0.0013)**	**0.46 (±0.04)**	**218 (±61)**	**20.8 (±1.0)**
5	**FML_S_1_14_4PB_C**	**3**	**6284.9 (±509.4)**	**100 (±0.1)**	**628 (±51)**	**17 (±11)**	**1.00 (±0.01)**	**28.4 (±0.1)**	**-0.037 (±0.039)**	**0.53 (±0.12)**	**163 (±12)**	**17.6 (±1.4)**
6	**FML_S_1_28_4PB_C**	**3**	**7203.6 (±685.4)**	**110 (±9.0)**	**792 (±121)**	**25 (±18)**	**1.0 (±0.01)**	**30.0 (±0.1)**	**-0.012 (±0.004)**	**0.63 (±0.05)**	**127 (±12)**	**22.0 (±3.6)**
7	**FML_L_3_28_4PB_C**	**3**	**6381.7 (±98.9)**	**170 (±0.1)**	**1084 (±11)**	**33 (±11)**	**1.0 (±0.01)**	**20.6 (±0.8)**	**0.002 (±0.0002)**	**0.85 (±0.07)**	**250 (±1)**	**21.8 (±0.1)**
8	**FML_L_1_14_4PB_C**	**3**	**5463.1 (±921.1)**	**100 (±0.1)**	**546 (±92)**	**160 (±53)**	**1.0 (±0.01)**	**29.3 (±1.2)**	**-0.003 (±0.001)**	**0.55 (±0.09)**	**263 (±23)**	**16.0 (±3.1)**
9	**FML_L_1_28_4PB_C**	**3**	**6526.7 (±383.7)**	**110 (±0.9)**	**707 (±55)**	**110 (±18)**	**1.0 (±0.01)**	**30.0 (±0.1)**	**-0.005 (±0.001)**	**0.48 (±0.03)**	**250 (±1)**	**21.2 (±1.7)**

Validation of the DIC Measurements in Flexural Crack Growth

The objective of this section is to address the mechanisms of crack formation and propagation using a quantitative analysis of the DIC displacement measuring technique. (An introduction to the DIC method is in the first section of Chapter 7.) The accuracy of the test methods allows for the determination of displacements of the order of few microns within a range of full specimen size (of the order of 500 millimeters). This resolution allows clear measurement and detection of formation of cracks under the entire domain of failure. Additional features that can be detected include multiple crack formation, crack opening profile, crack spacing, and stress concentration. The results can be used as a means to compare the experimental results with the analytical models. This section presents detailed experimental results for one small beam with 1 percent fiber and two large beams with 1 percent and 3 percent fiber tested after 28 days of curing.

The deflection of the specimen at the mid-span was measured using the DIC approach and results were compared with the LVDT-based instrumentation. At least four stages of deformation during the loading process were chosen to correspond to critical stages of loading and identified as Stages A through D. A description of each stage as listed in Table 20 and also shown in Figure 7-18a. Results for all additional samples are provided in the appendix.

Table 20. Different stages of data analysis using DIC method

Stage	Characteristic
A	Initiation of the deformation
B	Initiation of the non-linear response
C	Response to the peak load
D	End of the DIC data analysis (beam failure)

Figure 116 shows that during the loading process stable crack forms and propagates throughout the depth of a small beam with 1 percent fiber content after 28 days of curing period. These results are only possible in the case of fiber reinforced UHPC, since it is not possible to control the rate of crack growth in plain UHPC. Addition of fibers stabilizes the crack growth and allows for incremental measurement of crack extension. Stages A and B show a uniform loading in the sample. Cracks are not observable at stages A and B (representing nominal tensile stress level of 290 and 900 psi) when the load reaches stage C (tensile stress of 970 psi) we observe two cracks forming which the crack on the left dominates the response and additional load causes it to grow significantly. At level D only a main crack is active and a second crack is in the process of forming.

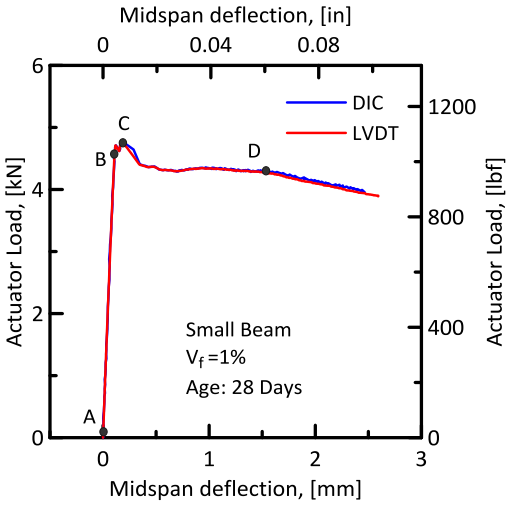
Midspan deflection, [in]
0
0.04
0.08
6
4
2
0
1200
800
400
0
DIC
LVDT
C
B
D
A
Small Beam
V_f =1%
Age: 28 Days
Actuator Load, [kN]
Actuator Load, [lbf]
0
1
2
3
Midspan deflection, [mm]

(a)

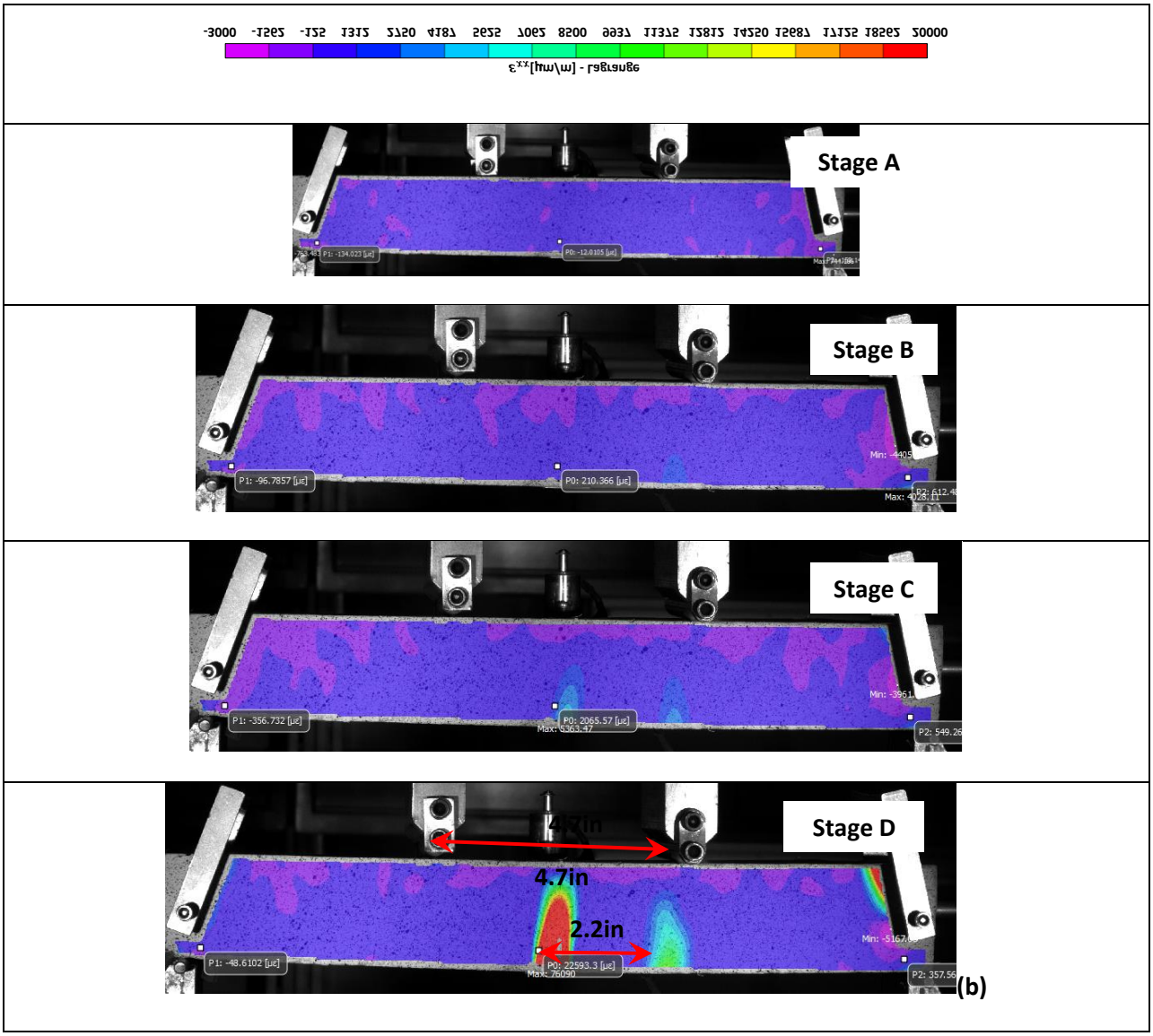

Figure 116. Small beam with 1% fiber, after 28 days of curing: (a, previous page) Load-Deflection curves, the comparison between DIC results and LVDT results; (b) DIC results at different test stages

For the large and small beams with 1 percent fiber content, at least two cracks occurred in the tension fiber. As the load increases, one of the cracks becomes dominant and the other one will be closed, due to the stress redistribution after crack growth. As the figure demonstrates, the cracking length is about 50 percent of the loading distance. The same trend was observed in the other small beams with 1 percent fiber content. For the large beams, this value is about 70 percent of the loading distance.

Stresses and strains along the section depth for each one of the four stages have been calculated (with the back-calculation process) and are shown in Figure 117. This figure shows that, as the moment

increases, the neutral axis moves toward the compressive part of the section. Furthermore, the stress diagram shows that the compressive part remains in the linear response region. This was also observed in other beams and shows that our assumption, in the simplified solution, that the compressive part of the FRC-UHPC section does not fail is acceptable. On the other hand, a stress softening behavior, due to the low (1 percent) fiber content, is detected. At the same time, a comparison with the model shows that the crack has extended as much as 1.7 inches (44 millimeters), or about 84 percent of the beam depth, and the nature of stress distribution over the cracked zone is dominated by the flexural cracking. Comparison of the stresses and the applied moments match, since for the applied bending moment at point D this is equivalent to 2,255pound-inches. We thus obtain a moment equal to 2,341 pound-inches in accordance with the stress distribution.

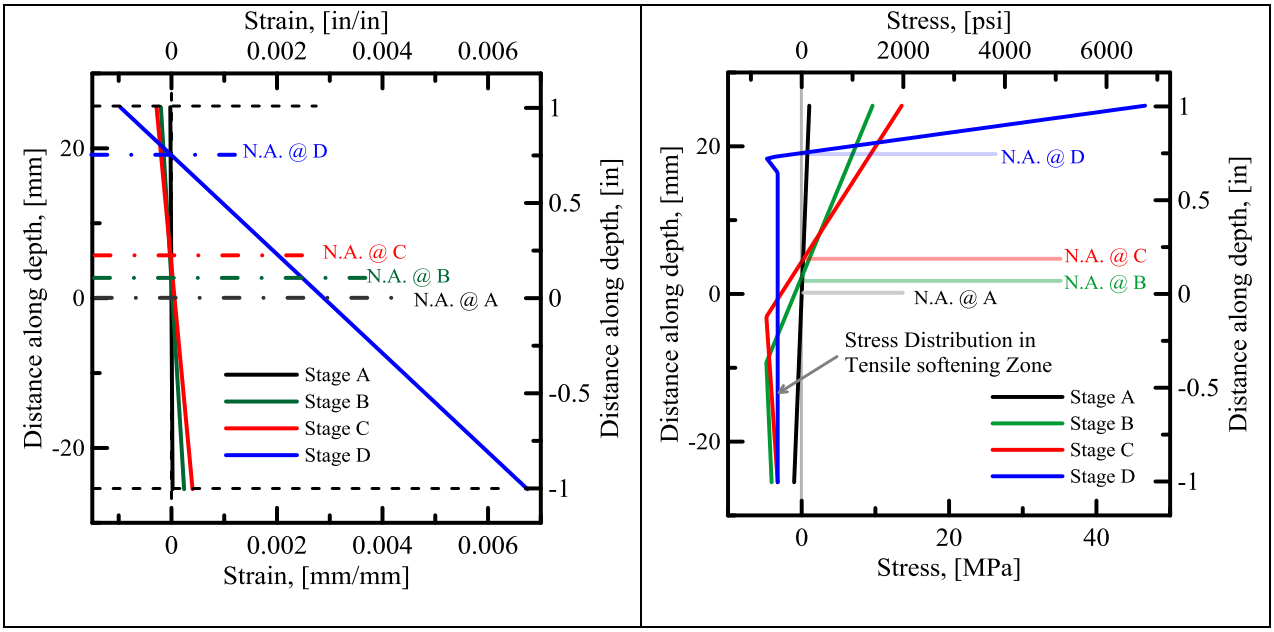

Figure 117. (a) Strain and (b) stress along the section depth, for a small beam with 1% fiber, after 28 days of curing (FML_S_1_28_4PB_C_B3)

A comparison between the results from LVDT and DIC for the large beams with 1 percent fiber (Figure 118) shows good agreement between the results from both methods. As in small beams, two cracks form in the large beams with 1 percent fiber. At stage C, which corresponds to the maximum load, the crack has grown as much as 3.35 inches (85 millimeters), or 84 percent of the height of the beam. While the load increases, one of the cracks becomes dominant and the other will be closed. The cracking length is about 70 percent of the loading distance. At stage D, the main crack is still visible and is opening significantly. There is a significant degree of unloading, as evidenced by the smaller secondary crack.

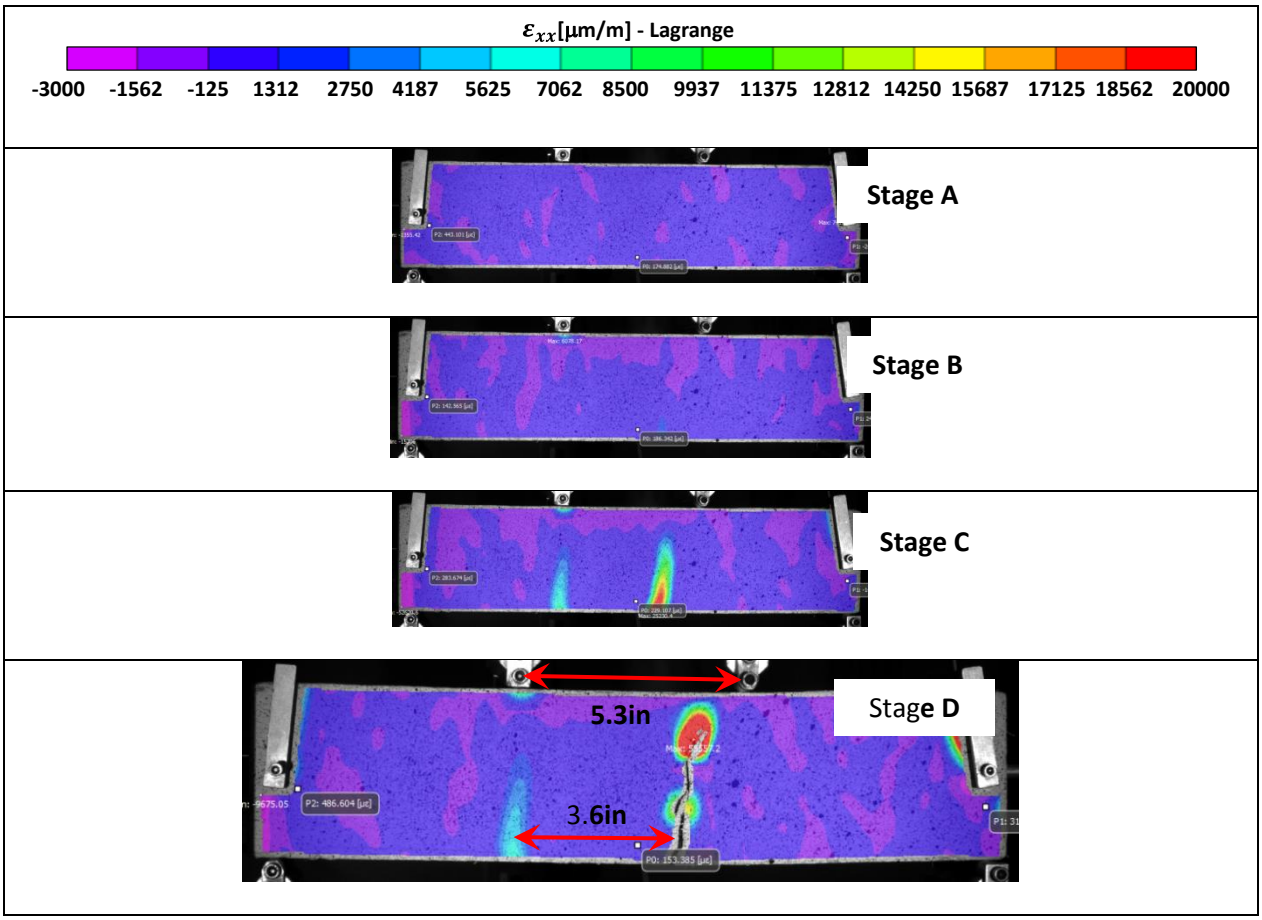

(a)

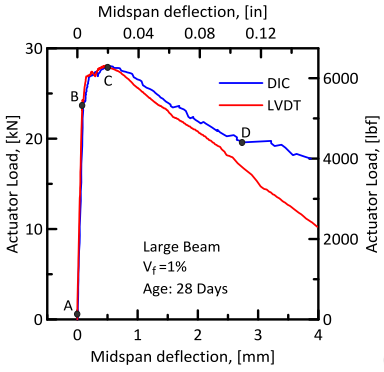

(b)

Figure 118. Large beam, 1% fiber, after 28 days of curing: (a) DIC results at different stages of the test; (b) load-deflection curves, the comparison between DIC results and LVDT results

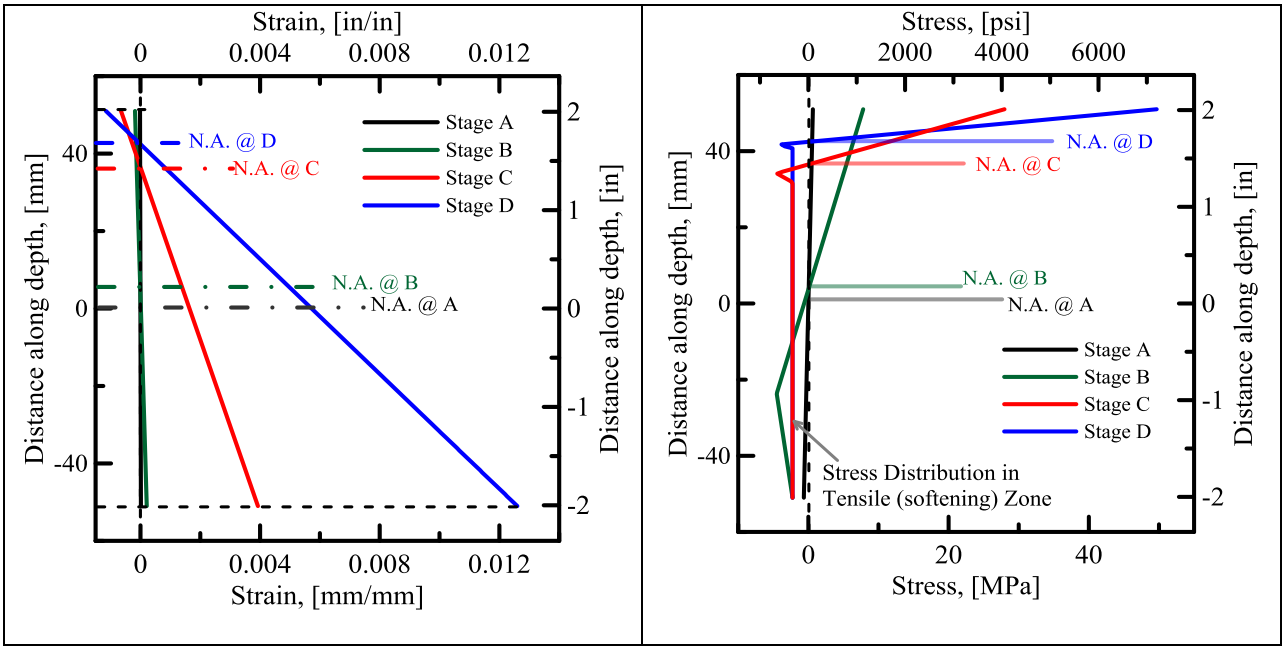

Figure 119. (a) Strain and (b) stress along the section depth, for a large beam with 1% fiber, after 28 days of curing (FML_L_1_28_4PB_C_B2)

Figure 119 shows the stresses and strains along the section depth for each one of the four stages obtained from the back-calculation process. As the moment increases, the neutral axis moves toward the compressive part of the section. At stage D, before failure, only 8 percent of the section is under compression and the rest is under tension. It can be seen from the stress diagram that the compressive part remains in the linear response region. This was also observed in other beams. Due to the low fiber content, a stress softening behavior is detected in the tensile zone. A comparison between Figure 117 and Figure 119 shows that as the beam size increases, the deformation capacity increases considerably. Strain levels for the large beam, at different stages, are much higher than for the small beam.

The results for one of the large beams with 3 percent fiber content, after 28 days of the curing period, are presented in Figure 91. DIC contours show a distributed cracked rejoin which is about 90 percent of the loading distance. The same cracking trend, a distributed cracked rejoin with at least three major cracks, was monitored for all of the beams with 3 percent fiber content. Like the beams with 1 percent fiber, one of the cracks becomes the major crack and the rest are closed as the load increases. On the other hand, as the fiber content increases, the distance between the major cracks decreases. The major crack's distance in the large beams with 1 percent fiber content is about 4 inches, while this parameter in the beams with 3 percent fiber content is about 2 inches, which represents a 50 percent decrease. This shows that there is a more distributed cracking pattern in the samples with higher fiber content and higher energy dissipation.

(a)

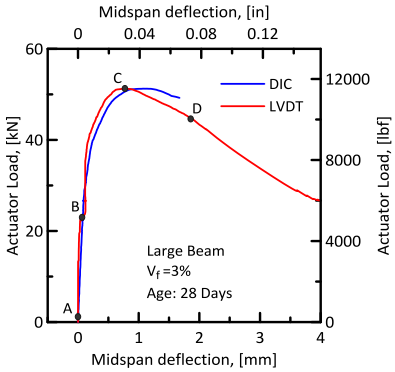
Midspan deflection, [in]
0
0.04
0.08
0.12
60
40
20
0
12000
8000
4000
0
DIC
LVDT
A
B
C
D
Large Beam
V_f =3%
Age: 28 Days
Actuator Load, [kN]
Actuator Load, [lbf]
0
1
2
3
4
Midspan deflection, [mm]

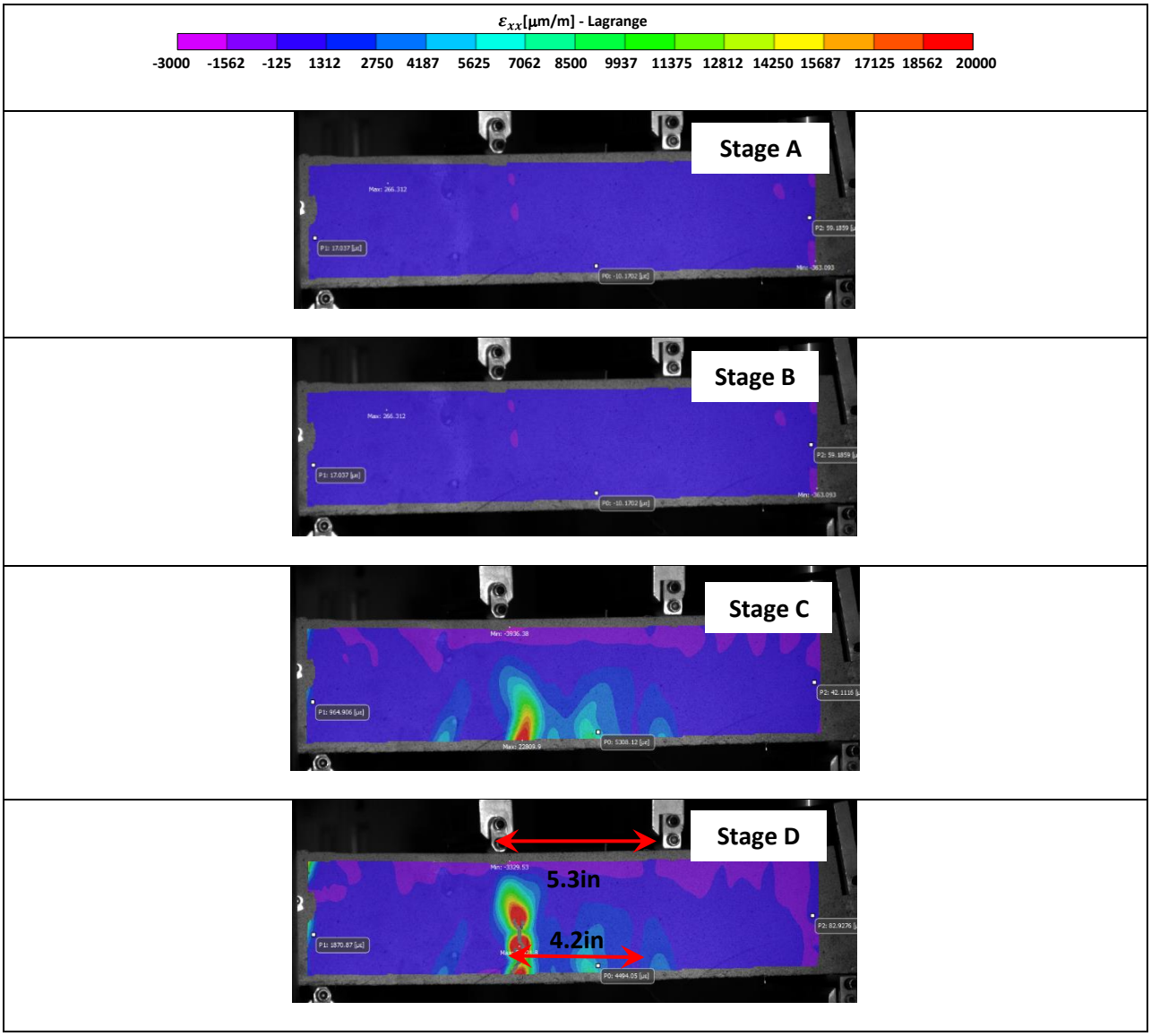

(b)

Figure 120. Large beam with 3% fiber, after 28 days of curing: (a, previous page) load-deflection curves, the comparison between DIC and LVDT results; (b) DIC results at different stages of the test

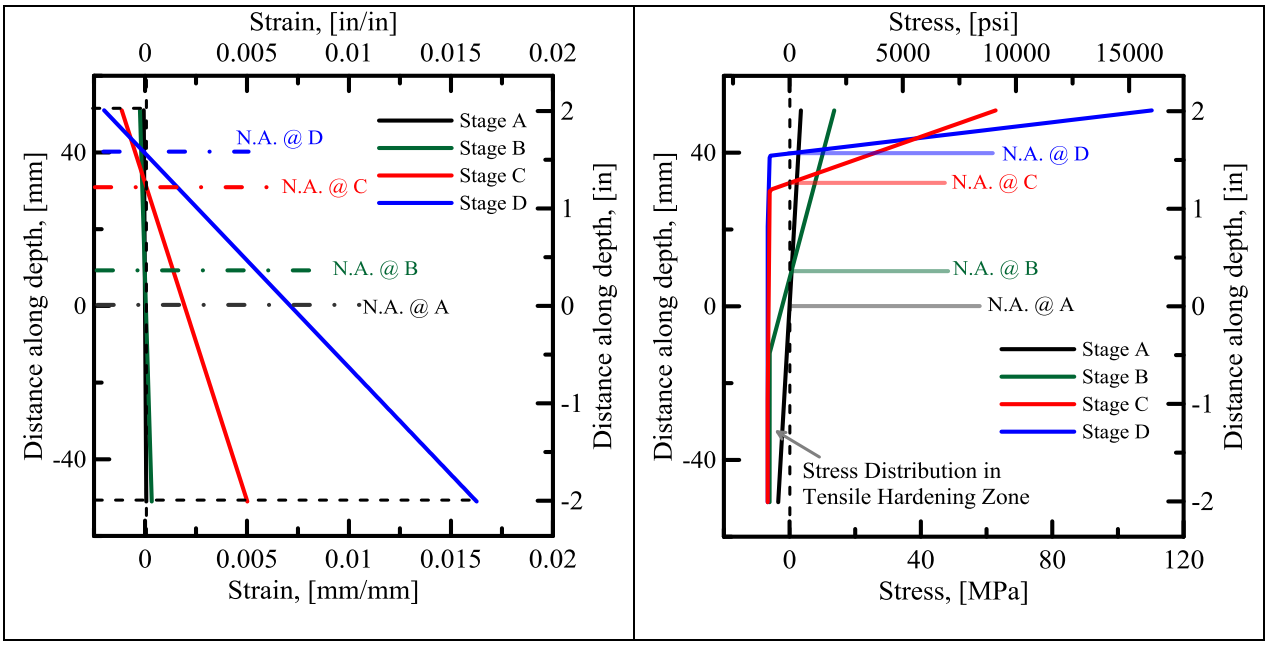

Figure 121. (a) Strain and (b) stress along the section depth, for a large beam with 3% fiber, after 28 days of curing (FML_L_3_28_4PB_C_B2)

Figure 121 shows the stresses and strains along the section depth for each one of the four stages obtained from the back-calculation process for the large beams containing 3 percent fiber content. As the applied moment on the beam increases, the flexural crack extends upwards and the neutral axis moves toward the compressive part of the section. The portion of the area carrying compression force is about 14 percent of the gross section area, which is 6 percent greater than that in the same section with lower fiber content. This is because as the fiber volume fraction increases, the crack growth is arrested by the fibers and less of the section enters the tensile phase of the response. In spite of the beam with 1 percent fiber content, for this set of beams a strain-hardening type of response is observed. For this type of the response, a perfectly plastic stress-strain diagram can be assigned to the material. Compressive failure was observed in none of the beams and the material remained in the linear-elastic region during the loading process.

Comparison with other experimental results

The back-calcuation procedure was applied to experimental flexural results of UHPC mixtures conducted by research colleagues and partners, using mixtures developed at Missouri Science and Technology University. Meng et al. (Meng et al. 2017), tested UHPC beams with a dimension of 400 x 75 x 75 millimeters (16 x 3 x 3 inches). These were notched specimens and the test results were in accordance with JCI method (Standard 2003). The effect of notch-to-depth ratio was evaluated at a level of N/D= 1/6, corresponding to notch depth of 12.5 millimeters (1/2 inch) (Zhang et al. 2014). Using a constant rate of the mid-span deflection as the control parameter, loading rates ranging from 0.05 millimeters/minute (0.002 inch/minute) to 5.00 millimeter/minute (0.2 inch/minute) were used in

accordance with available test methods (Pyo et al. 2015). Figure 122 shows the schematics of the testing system.

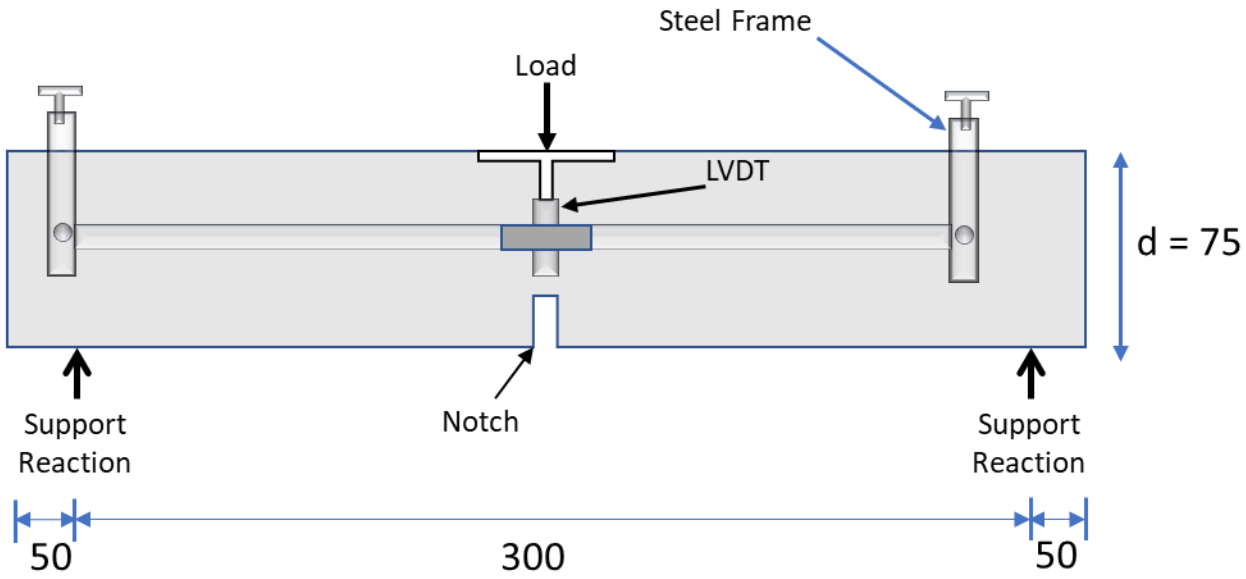

Figure 122. Flexural test setup and notched beam specimen. Unit: millimeter, (Meng et al. 2017)

Figure 123 compares the simulated and experimental flexural stress-deflection responses of the UHPC beams with different notch depths and loading rates. In this figure, the black dashed line shows the tensile response of the samples measured using a direct tensile test. Both tension and bending tests apply tensile stresses to the sample, which result in initiation and propagation of cracks. Both types of tests are routinely used to evaluate the strength and fracture response of materials.

The two tests are different because the stress and strain states in tension and bending are not the same. With a tensile test, the maximum tensile stresses occur throughout the entire volume (and surface area) of the test piece; in bending (where the sample sees tensile stress above the neutral axis and compressive stresses below), the maximum tensile stresses are conversely concentrated in a small region on the top surface above the neutral axis. Accordingly, for similarly sized test pieces, the tensile sample sees the maximum stresses throughout its entire gauge length, i.e., over a much larger volume than the corresponding bend sample. In brittle materials which are highly sensitive to the defect population, this change in statistical sampling volume means that strength and fracture properties measured in tensile tests are likely to be somewhat lower than the corresponding properties measured in bending, because there is a higher statistical probability of finding a larger defect.

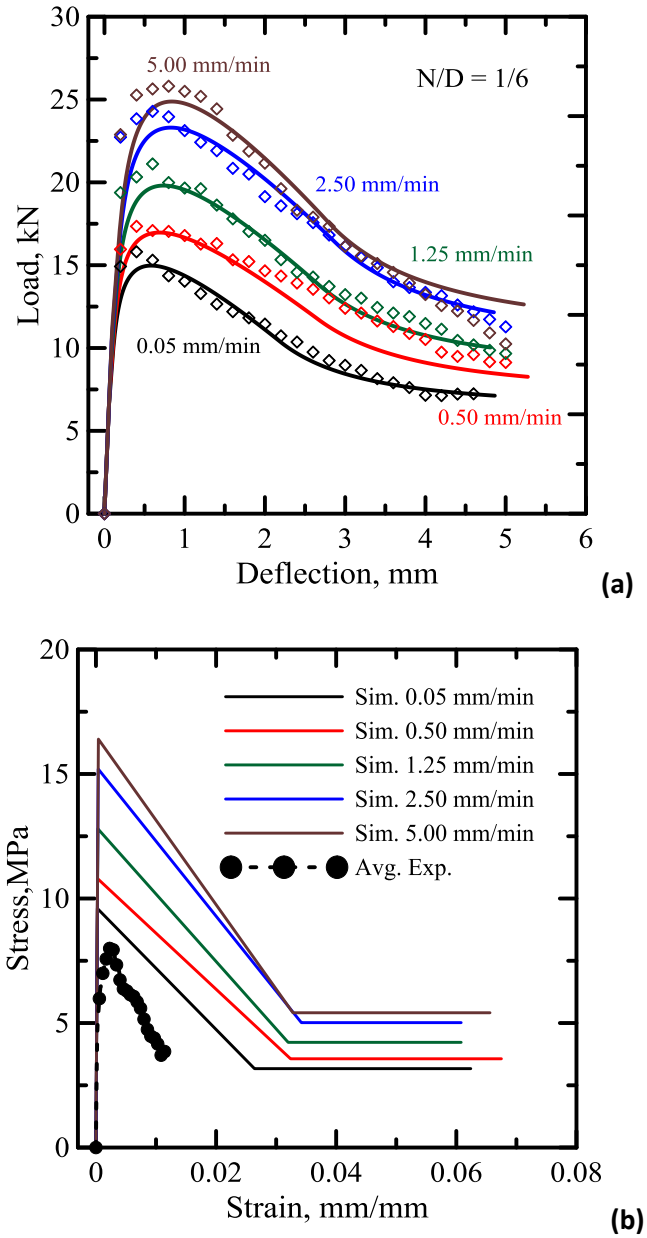

Figure 123. Comparisons between experimental and simulated flexural stress-deflection responses for the HRC samples with different loading rates: (a) load-deflection; (b) back-calculated tension models

The flexural strength would be the same as the tensile strength if the material were homogeneous. In fact, most materials have small or large defects in them which act to concentrate the stresses locally, effectively causing a localized weakness. When a material is bent, only the extreme fibers are at the largest stress, so if those fibers are free from defects, the flexural strength will be controlled by the strength of these intact fibers. However, if the same material was subjected to only tensile forces, then all the fibers in the material experience the same stress, and failure will initiate when the weakest fiber

reaches its limiting tensile stress. Therefore, it is common for flexural strengths to be higher than tensile strengths for the same material. Conversely, a homogeneous material with defects only on its surfaces (e.g., due to scratches) might have a higher tensile strength than flexural strength.

In Figure 123 the tensile material properties illustrated as multi-linear, stress-strain diagrams were back-calculated by fitting the experimental flexural responses for N/D of one-sixth, as shown in Figure 123(a). Results show that in order to fit the experimental loading rate effect, the tensile and residual strength have to increase from 9.5 to 15.9 MPa and 3.1 to 5.2 MPa (67 and 68 percent, respectively). The loading rate effects as measured by the increasing strength of the tested samples agree with the experimental investigations of tensile properties of UHPC under varying strain rates (Meng et al. 2017; Zhang et al. 2014; Pyo et al. 2015). The percentages of improvement are consistent with those of flexural strength measured in the experiment. General procedures for analysis of beams, panels and two-dimensional slabs have been developed based on this approach in recent publications and calibrated against a wide range of published work (Yao et al. 2017).

Development of Ultimate Limit State Design Procedures for UHPC

In this section, we use the original closed-form derivations discussed at the beginning of the chapter, and use them as a basis for the design of the UHPC beam sections.

The ultimate bending capacity of the section can be used in a design approach based on the ultimate limit state ($\beta = \beta_{tu}$). A minimum number of parameters for use in this model are three: (a) the ratio of compressive to tensile strength, ω (b) the post-crack tensile residual strength, $\mu\sigma_{cr}$ and (c) the allowable compressive or tensile strain from a serviceability point of view ($\beta_{tu}\varepsilon_{cr}$). The parameters for the constitutive models are obtained from either ASTM C1609/C1609M or BS EN 14651:2005 based on the recommendations of a parametric design method, as discussed in (ACI 544.8R-16, 2016).

The solution for the plain fiber reinforced concrete section is presented first for the case in Figure 106 specified by a cracked section under tension and the maximum compressive strain at the elastic-plastic compression zone. For the given applied strain distribution, the location of neutral axis is assumed as *kd*, and using the strain and stress profile across the section, the force equilibrium equation is obtained. The neutral axis depth *k* is found by solving the equilibrium of net internal forces, or $F_s + F_{c1} + F_{c2} + F_{t1} + F_{t2} = 0$ representing the forces due to internal stresses. As defined for a specified serviceability limit for maximum allowable compressive strain, compressive strain cannot be more than compression yield strain, $0 < \lambda \le \omega$ and $\beta = \beta_{tu}$; therefore the neutral axis depth is obtained as (stage 3.1):

$$k = \frac{\mu + \beta_{tu}\left(-2\mu + \sqrt{\mu(2\beta_{tu} - 1)}\right)}{\beta_{tu}^{\,2} - 2\mu\beta_{tu} + \mu}$$ **Equation 59**

$$k = \frac{\mu + \beta_{tu}\left(-2\mu + \sqrt{\mu(2\beta_{tu} - 1)}\right)}{\beta_{tu}^{\,2} - 2\mu\beta_{tu} + \mu}$$ Equation 59 is for the plain FRC section. The full derivation for a hybrid reinforced case is presented by Mobasher et al. (2015); a brief summary of their procedure will be presented in the next section. The magnitude of the moment M_n is obtained by taking the first moment of internal forces about the neutral axis, $M_n = F_{c1}y_{c1} + F_{c2}y_{c2} + F_{t1}y_{t1} + F_{t2}y_{t2}$, calculated as shown in

$$M_n = \left(\frac{\left(3\mu\beta_{tu}^{\,2} - \mu - 2\beta_{tu}^{\,3}\right)k^3 + \left(3\mu - 9\mu\beta_{tu}^{\,2}\right)k^2 + \left(9\mu\beta_{tu}^{\,2} - 3\mu\right)k - 3\mu\beta_{tu}^{\,2} + \mu}{\left(k-1\right)\beta_{tu}^{\,2}} \right) M_{cr}$$ Equation 60

and $M_{cr} = \frac{\sigma_{cr} bh^2}{6}$ Equation 61 as:

$$M_n = \left(\frac{\left(3\mu\beta_{tu}^{\,2} - \mu - 2\beta_{tu}^{\,3}\right)k^3 + \left(3\mu - 9\mu\beta_{tu}^{\,2}\right)k^2 + \left(9\mu\beta_{tu}^{\,2} - 3\mu\right)k - 3\mu\beta_{tu}^{\,2} + \mu}{\left(k-1\right)\beta_{tu}^{\,2}} \right) M_{cr}$$ **Equation 60**

$$M_{cr} = \frac{\sigma_{cr} bh^2}{6}$$ **Equation 61**

If one conducts an asymptotic analysis to compute the moment capacity in the limit case, a simplified design equation for normalized moment capacity is obtained. This resembles a case when the cracked section in flexure opens significantly to go beyond serviceability limit, but due to the presence of fibers, the section can still transmit the flexural load applied. The moment capacity, in this case, is defined by the limit case of compressive cracking strain λ_{cu} reaching a relatively large number (Soranakom and Mobasher 2009). In order to simplify the calculation of several specified moments, one can compute the neutral axis parameter k_{∞}, by substituting $\lambda_{cu} = \infty$, to obtain the normalized moment at very large strains, m_{∞} as shown in Equation 62. The equation for ultimate moment capacity is derived by substituting m_{∞} for m_{cu}. Thus, the design equation for nominal moment capacity M_n is expressed in Equation 62.

$$k_\infty = \lim_{\lambda \to \infty} k = 0,\ m_\infty = 3\mu,\ M_n = m_\infty M_{cr} = 3\mu M_{cr}$$ **Equation 62**

The limit between the strain-hardening and strain-softening response of the section can be achieved by setting m_∞ equal to the normalized cracking moment ($m_\infty = 1$). Rewriting Equation 62 will give the critical value for the residual tensile strength, μ_{crit}.

$$\mu_{crit} = \frac{1}{3}$$ **Equation 63**

The LRFD basis for the ultimate strength design is based on the reduced nominal moment capacity $\phi_p M_n$ exceeding the ultimate demand moment M_u ($\phi_p M_n \geq M_u$), which is determined by linear elastic analysis using factored load coefficients according to ACI318 section 9.2 (ACI 318-14). A reduction factor ϕ_p is applied to the post-crack tensile strength, and the value ϕ_p = 0.75-0.9 has been tentatively used based on statistical analysis of limited test data in the earlier work. In order to further simplify Equation 62, from the previous equations, an empirical relationship between tensile and compressive strength is used, i.e. $\sigma_{cr} = 6.7\sqrt{f_c'}$ in U.S. customary units (and $\sigma_{cr} = 0.56\sqrt{f_c'}$ in SI customary units). However, this relationship can be used only for normal concrete. FHWA (Ben Graybeal 2014a) has suggested that the tensile strength of the UHPC is equivalent to 4 percent of its compressive strength, i.e., $\sigma_{cr} = 0.04 f_c'$. For a typical fiber-based system, the residual strength of FRC in flexure is approximately three times its residual strength in tension (Bakhshi et al. 2014, (Bakhshi, Barsby, and Mobasher 2014)). Based on the experiments in this research, this value for the UHPC material is 2.42 (see Figure 124).

$$f^{D}_{150} = 2.42\mu\sigma_{cr}$$ **Equation 64**

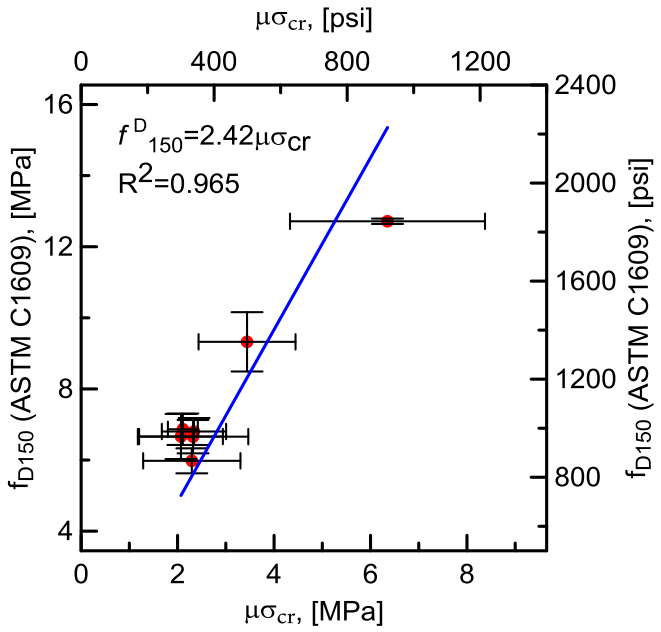

Figure 124. Comparison of residual strength ($\mu\sigma_{cr}$) with ASTM C1609 residual parameter (f^{D}_{150})

Substituting $f^{D}_{150} = 2.42\mu\sigma_{cr}$

Equation 64 into $M_{cr} = \frac{\sigma_{cr} bh^2}{6}$

Equation 61, we have

$$M_n = \frac{3f^{D}_{150}}{2.42\sigma_{cr}} M_{cr} = \frac{31f^{D}_{150}}{f_c'} M_{cr}$$ **Equation 65**

However, these equations are estimations of the relationship between the experimentally obtained standard's parameters, such as $f_{eq,3}$ or f^{D}_{150}, and the normalized residual strength, μ. These equations are empirical relationships. A more accurate approach is to test the samples, based on the relevant standard, and then to do back-calculations, according to ACI-544-8R, to get the accurate value of residual strength. A detailed approach for the back calculation can be found in the appendix, as well as in (Chote Soranakom and Mobasher 2007, 2009; Barzin Mobasher, Yao, and Soranakom 2015).

Using an LRFD approach, the nominal moment capacity of a flexural member M_n must be adjusted by a reduction factor to account for variability in materials and workmanship according to ACI-318 Sec. 9.2, (ACI Committee 318 and American Concrete Institute 2014), where ϕ_r is the reduction factor:

$$\phi_r M_n \geq M_u$$ **Equation 66**

Hybrid Reinforced Concrete (HRC) Beams

In a similar manner to the FRC section, closed form solutions are achievable at different stages of loading and deformation. All detailed derivations can be found in (Barzin Mobasher, Yao, and Soranakom 2015). However, as an ultimate limit approach, the ultimate moment capacity as a function of residual tensile strength and reinforcement (at $\beta = \beta_{tu}$) can be used as a convenient design tool for combinations of reinforcements, calculated as shown in

$$M_n \approx m_\infty M_{cr} = \frac{6\rho_g n\kappa\left(\mu\alpha - \mu + \alpha\omega\right) + 3\omega\mu - 3\left(\rho_g n\kappa\right)^2}{\omega + \mu} M_{cr}$$ Equation 67.

$$M_n \approx m_\infty M_{cr} = \frac{6\rho_g n\kappa\left(\mu\alpha - \mu + \alpha\omega\right) + 3\omega\mu - 3\left(\rho_g n\kappa\right)^2}{\omega + \mu} M_{cr}$$ **Equation 67**

Figure 125 shows a design chart for the parametric design model with various grades of steel at ultimate moment capacity. Flexural design using this chart requires ultimate moment M_u due to factored loads normalized with respect to cross-sectional geometry. The demand ultimate moment capacity M_u' is obtained from this chart used to select any combination of normalized residual tensile strength μ, grade of steel, and reinforcement ratio ρ_g that meets the demand for M_u'. The moment capacity is strongly dependent on the reinforcement ratio. Results are scaled to numerical values using the section cracking moment M_{cr}. An Excel spreadsheet has been developed as a design guide for both the FRC and HRC and is available for use as well (Barzin Mobasher, Yao, and Soranakom 2015). This graph is characterized based on the parameters obtained for the UHPC (with a compressive strength more than 20 ksi). The graphs for the ordinary concrete have been presented in previous researches (Barzin Mobasher, Yao, and Soranakom 2015).

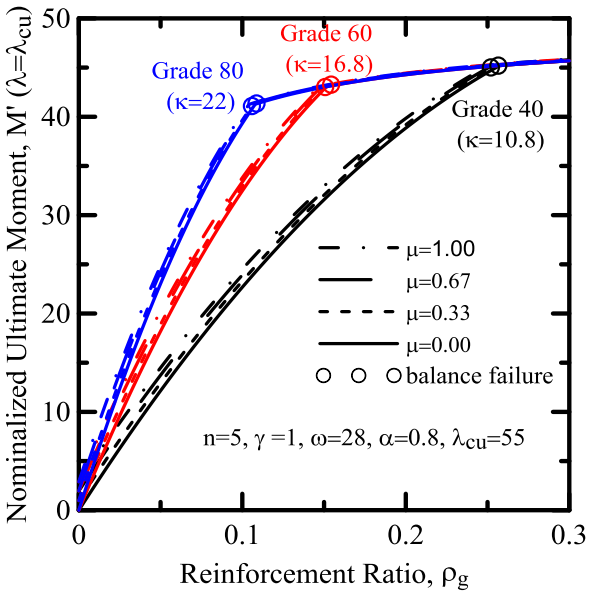

Figure 125. Design chart for normalized ultimate moment capacity (determined at $\lambda = \lambda_{cu}$) for different levels of post-crack tensile strength μ and reinforcement ratio ρ_g (1 MPa=145 Psi)

A parametric study was carried out on the effect of parameters μ and β on the normalized moment and curvature diagrams with two different values of reinforcement ratio, ρ_g =A_s/A_c. Figure 126 illustrates the results of the first set of simulations. In this set of simulation, a ductile failure ($\rho_g \leq \rho_{bal}$) mode was assumed. For this purpose, a longitudinal set of steel rebars, Grade 60, with a reinforcement ratio of ρ_g =7% was chosen. Other parameters are same as those used in Figure 125.

Figure 126 shows both the moment and curvature as a function of the tensile strain in the flexural concrete beam section. This figure demonstrates that residual tensile strength provides extra moment capacity for the section, but also increases the stiffness of the section. In fact, the fibers in FRC sections play the same role as the longitudinal reinforcements in ordinary RC sections.

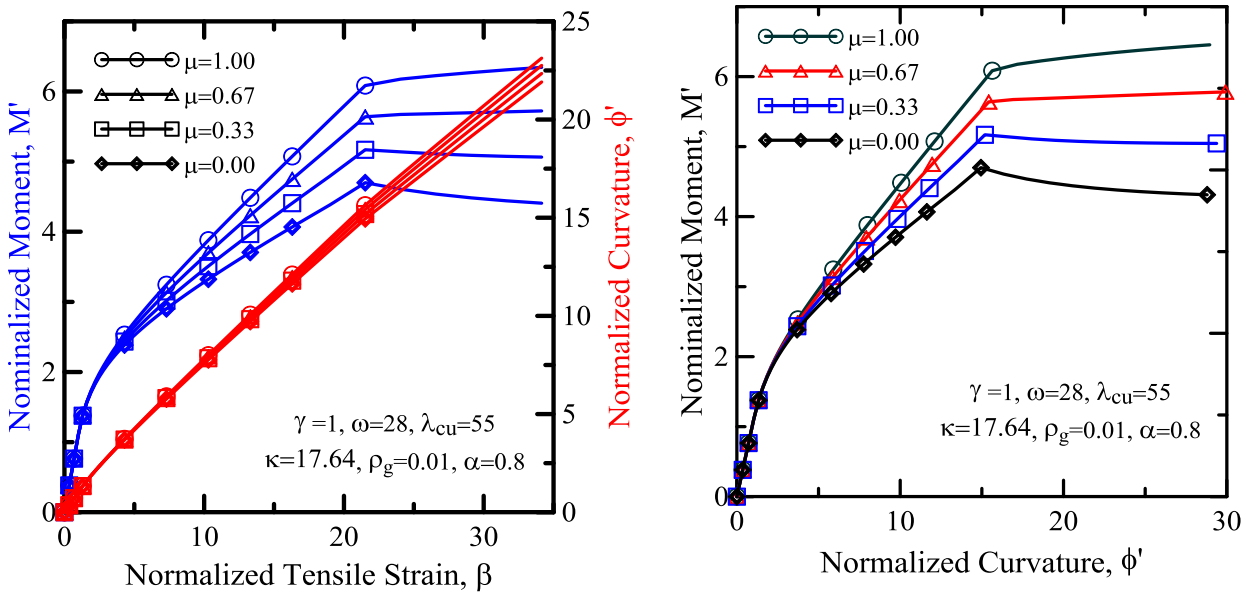

Figure 126. Parametric studies of the normalized moment and curvature diagrams as a function of normalized tensile strain, β , for different levels of post-crack tensile strength (residual strength) parameter, μ (with 1% longitudinal reinforcement, steel rebar grade 60)

Figure 127 shows both the moment, the blue line, and the curvature, the red line, as a function of the tensile strain in the lower fiber of the concrete section. This figure illustrates that residual tensile strength provides extra moment capacity for the section and increases the stiffness of the section as well. On the other hand, compared to a section with a decreased amount of longitudinal reinforcement (such as 1 percent or less), the effect of fibers in HRC sections with a higher amount of reinforcement is smaller.

Figure 128 shows the results of the other set of simulations. In this set, it was assumed that the section has a brittle failure ($\rho_g > \rho_{bal}$). For this purpose, a longitudinal set of steel rebars, grade 60 with a reinforcement ratio of 16 percent, was chosen. Other parameters are same as those used in Figure 125. A comparison between this figure and Figure 127 shows that, although the moment capacity of the section increases, the ductility decreases considerably, in such a way that the ultimate normalized curvature decreases from 31 to 22 (a 30 percent decrease) and the failure mode changes from ductile to brittle.

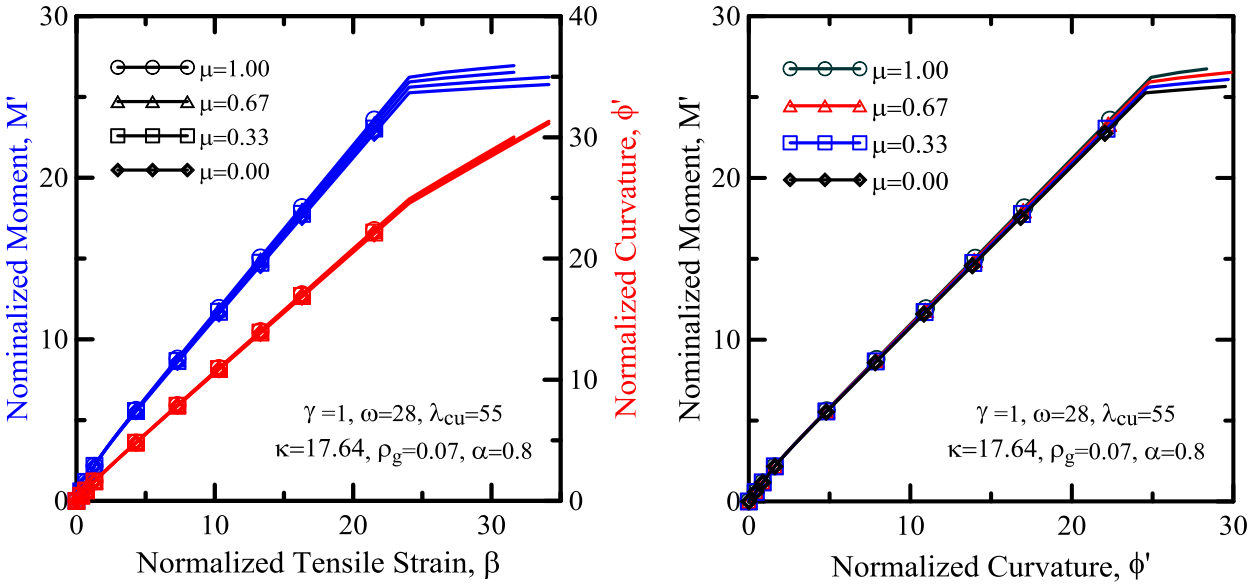

Figure 127. Parametric studies of the normalized moment, the blue line, and curvature, the red line, diagrams as a function of normalized tensile strain, β , for different levels of post-crack tensile strength (residual strength) parameter, μ (with 7% longitudinal reinforcement, steel rebar grade 60)

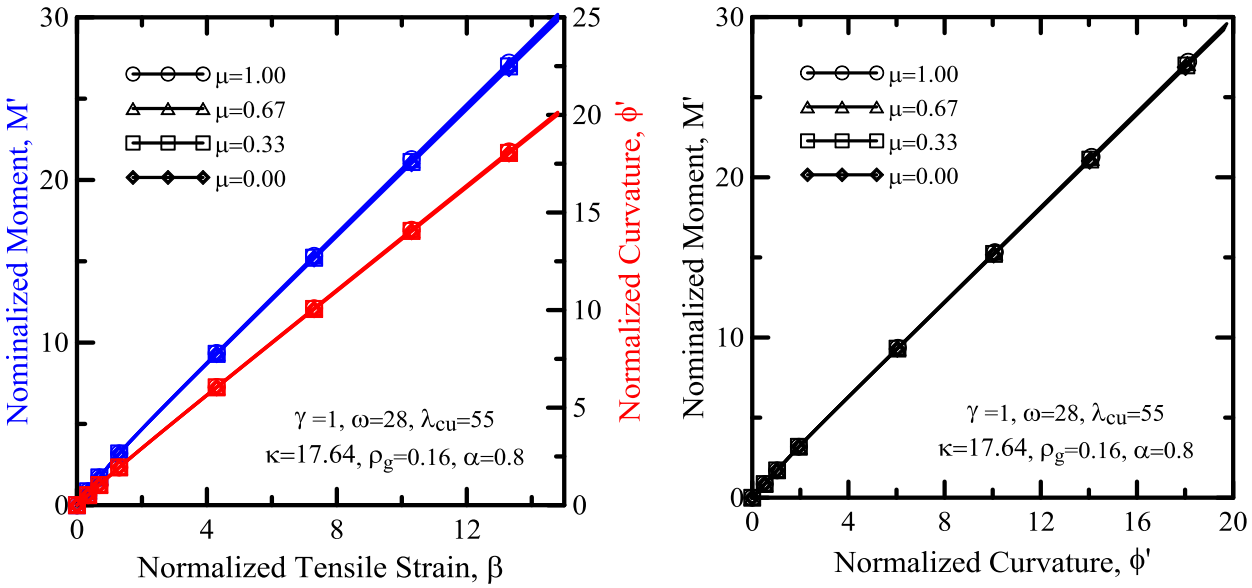

Figure 128. Parametric studies of the normalized moment, the blue line, and curvature, the red line, diagrams as a function of normalized tensile strain, β , for different levels of post-crack tensile strength (residual strength) parameter, μ (with 16% longitudinal reinforcement, steel rebar grade 60)

Figure 129 illustrates the effect of the reinforcement ratio on the normalized moment and curvature diagrams with no fiber reinforcement, $\mu = 0.0$. Again, as the amount of the reinforcement increases, the ductility of the section decreases, and the failure mode changes from ductile to brittle, so that for 10 percent reinforcement the response of the section is completely brittle, causing a compressive failure. However, for the reinforcements less than 8 percent there is a ductile failure, followed by a compressive failure as deformation continues. Crosses represent the brittle compressive failure before the reinforcement yields.

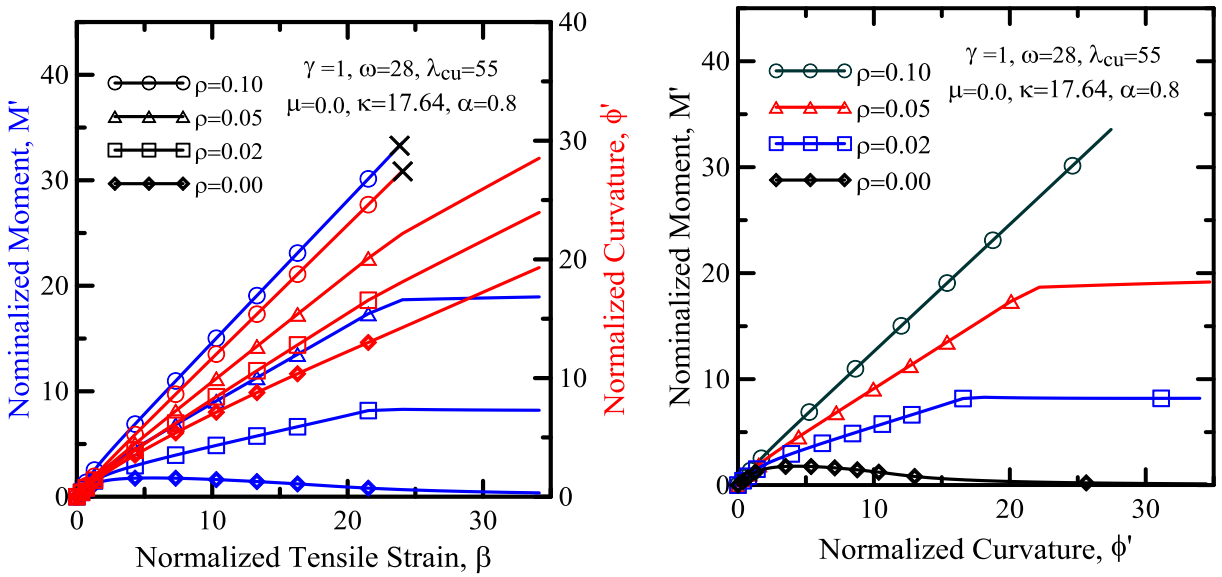

Figure 129. Parametric studies of the normalized moment, the blue line, and curvature, the red line, diagrams as a function of normalized tensile strain, β, for different levels of longitudinal reinforcement, with no fiber reinforcement (residual tensile strength equal to zero)

Figure 130 illustrates the effect of the reinforcement ratio on the normalized moment and curvature diagrams with the perfectly-plastic tensile response, $\mu = 1.0$. In this case, the section has a good moment capacity and ductility with 5 percent of reinforcement, and as the amount of the reinforcement increases, so does the stiffness of the section, while the failure mode changes from ductile to brittle. Using these figures it is possible to evaluate a specific moment and curvature for a specific value of tensile strain in the lower fiber of the beam, by drawing a vertical line from the interested tensile strain value; then the intersection with the curvature (red) curves and the moment (blue) curves will be the equivalent curvature and moment for that tensile strain value. This method can be used in serviceability limit state.

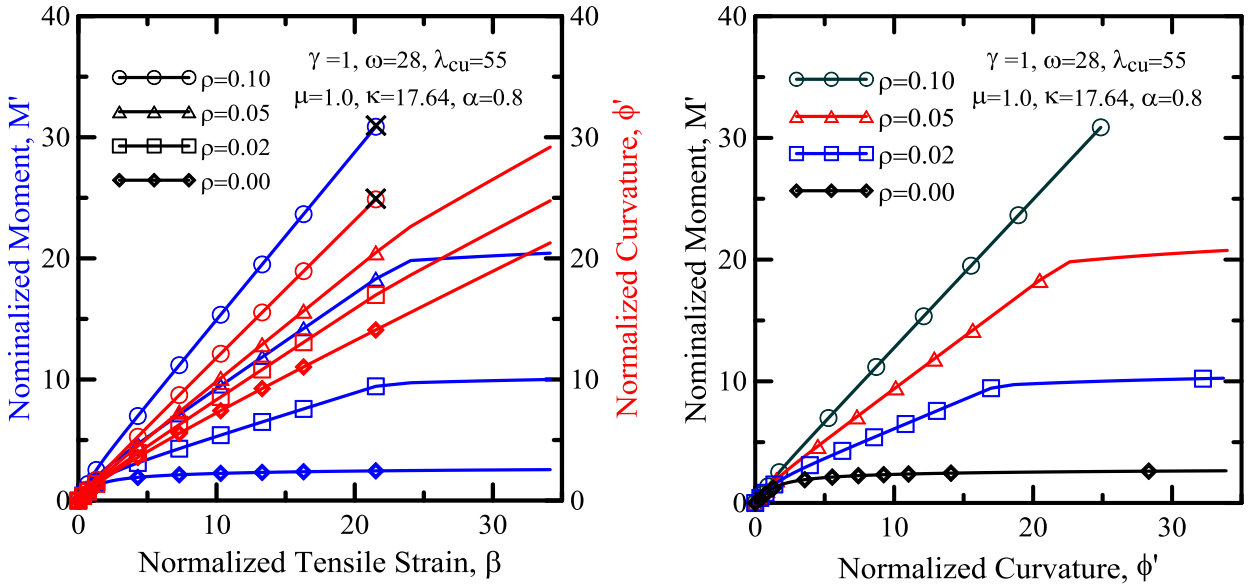

Figure 130. Parametric studies of the normalized moment, the blue line, and curvature, the red line, diagrams as a function of normalized tensile strain, β , for different levels of longitudinal reinforcement, with perfectly plastic tensile response ($\mu = 1.0$)

Comparison with other experimental results on HRC

Yang et al. (2010) provided some experimental test results for the flexural behavior of UHPC beams. The experimental parameters comprised the amount of rebar and the placing method for the UHPC. The flexural behavioral features were inspected with respect to test results on UHPC beams with rebar ratios less than 0.02 and steel fibers with a volumetric ratio of 0.02. Before doing the bending tests on the beam samples, Yang performed some basic compressive tests, on cylindrical specimens with a diameter of 100 millimeters and a height of 200 millimeters, to obtain the material properties of the UHPC, such as compressive strength and Young's modulus. For the flexural tests, the experimental program included tests on 14 beam specimens with rectangular cross-sections. The beam specimens included a basic specimen without rebar, which was designated as specimen NR in Figure 131. The other specimens had varying rebar ratios that were gained by changing the amount of rebar and the number of layers. For this study, two different set of samples with two sets of rebars (sections R-13 and R-14) were simulated using a HRC-TL model (two samples from R13 and one sample from R14). Nominal diameters were 13 millimeters for R13 rebars and 14 millimeters for R14 rebars.

Specimen	R13	R14
Cross-section	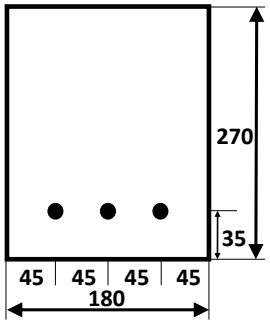	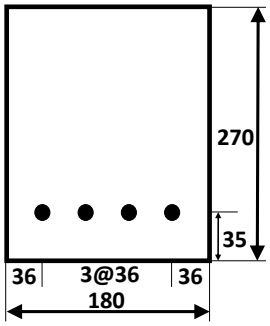
Rebar	**3-13mm ϕ, 1 layer**	**4-13 mm ϕ, 1 layer**
Rebar area (mm^2)	**380.1**	**506.8**
Rebar ratio	**0.009**	**0.012**
Batch number	**2**	**3**

Figure 131 Parameters used in experiments by Yang et al. , [33] (all dimensions in millimeters)

Figure 132 shows the arrangement of the beam and test setup. Electrical resistance strain gauges were used to measure the strain of the concrete and steel rebar. Five strain gauges were placed on the side surface of the beam at mid-span to measure strain at different heights. The loads were applied to the beams at the top face using hydraulic actuator in the form of four-point loading, as shown in Figure 132. A loading steel frame was installed between the beam and the actuator to transfer the load from the latter to the former at the specified points.

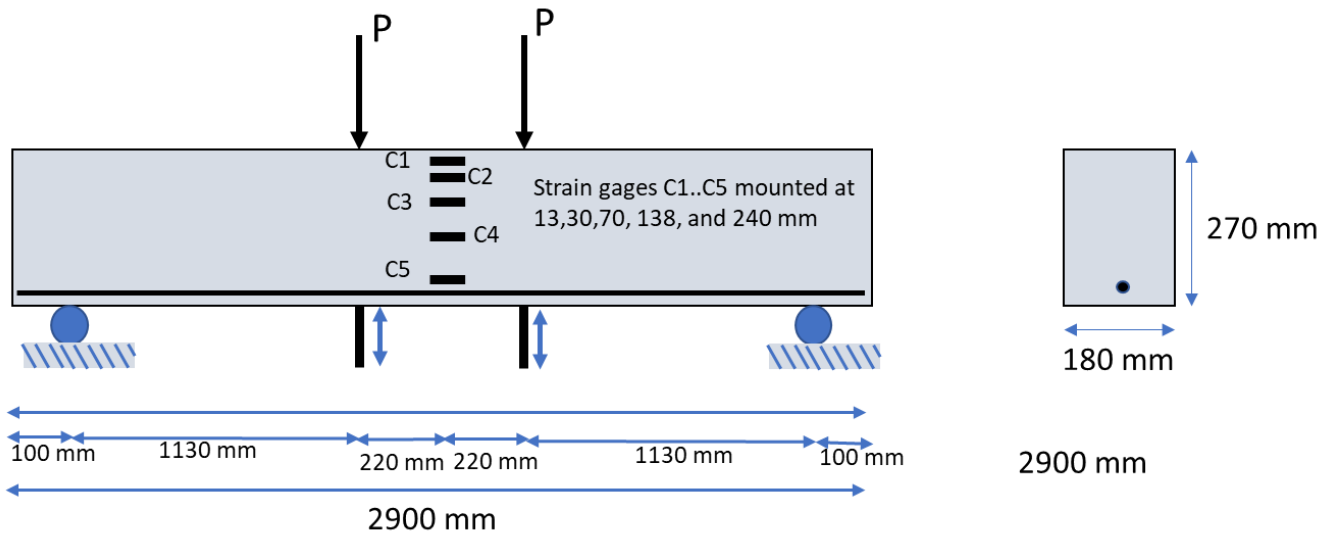

Figure 132. Instrumentation used for the beam flexural test

For the simulation part, the research team used a MATLAB code which was developed based on the parameters and stress-strain diagrams introduced above. More detailed description of the mathematical approach and the closed form solutions can be found in (Yao et al., 2017 Yao et al. 2017). The comparison graphs for these sets of simulations are represented here. All simulated samples achieved their maximum tensile capacity before reaching a strain of 0.5 percent. Their tensile capacity then decreased to zero (which is comparable to the ultimate tensile capacity of the steel rebars) with tensile strain of 2 percent.

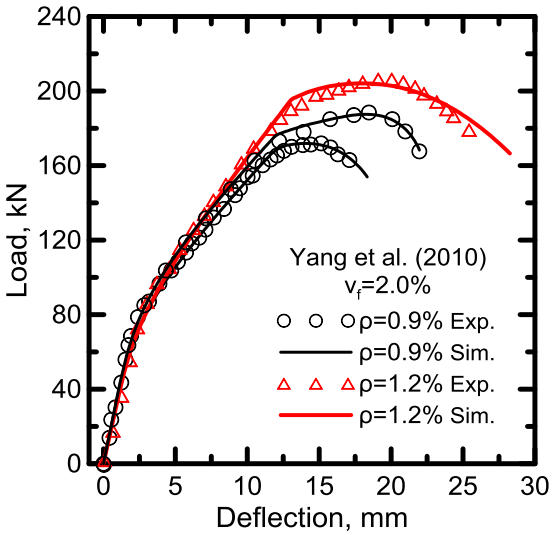

(a)

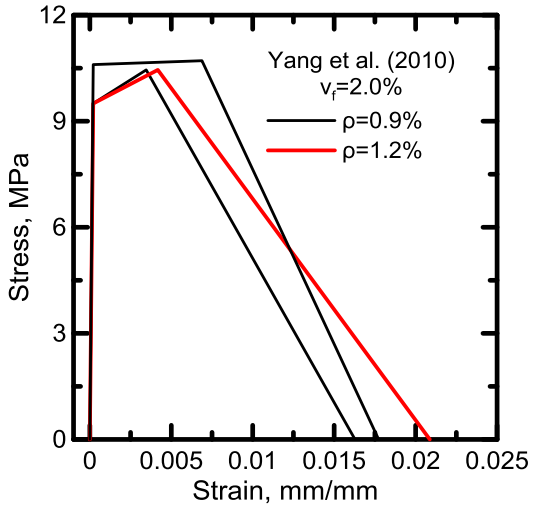

(b)

Figure 133. a) Simulated load-deflection curves; b) Stress-strain graphs for tensile behavior

Figure 134 demonstrates the comparison between the experimental strain distributions at different elevations along the beam depth (C1 to C5; also see Figure 132) (I. H. Yang, Joh, and Kim 2010), and the simulated results obtained from the constitutive model. These simulated results were calculated based on the linear strain distribution along the beam section (see Figure 105). The required values (i.e., the depth of the neutral axis, strains at lower and upper fibers of the section) were attained from the back-calculation process; then the strains at different elevations can be determined based on the linear strain distribution along the beam depth. This figure (Figure 134) shows that the experimental and simulated results agree very well, which proves that linear strain distribution along the beam depth is an acceptable assumption for both pre-peak and post-peak regions.

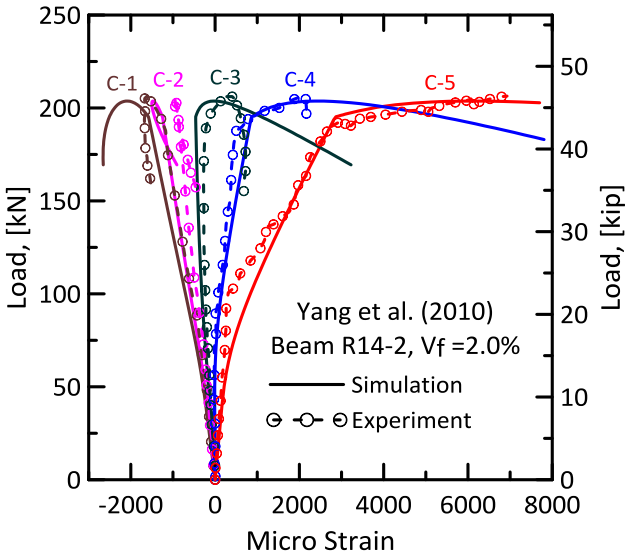

Figure 134. Comparison between simulated and experimental strain distribution along the beam depth, C-1 to C-6 strain gages (Yang et al., 2010) (I. H. Yang, Joh, and Kim 2010)

Another test data set which is used as a basis for simulations is the research done by Kamal et al., [34]. In their research, they evaluated the behavior of ultra-high strength concrete beams and the effect of adding fibers, and explored the effect of the fibers on the performance and strength of the reinforced concrete beams. Twelve simple concrete beams with and without shear reinforcements were tested. The main variables taken into consideration were the type of fibers and the percentage of longitudinal reinforcement as well as the presence or absence of the web reinforcement. Two types of fibers were used: steel and polypropylene. Plain steel fibers 0.2 millimeters wide and 13 millimeter long with an aspect ratio (L/D) of 65 were used. The polypropylene fibers, produced by SI Concrete systems, USA, had a length of 20 millimeters and an aspect ratio (L/D) of 12.5.

The beams were designed to have acceptable resistance against flexure failure. Simply supported beams (100 x 150 x 1,000 millimeters) were cast and tested until failure. The beams under investigation were reinforced with two bottom rebars either 10 millimeters wide (reinforcement ratio $\rho = 1.2\%$) or 12 millimeters wide ($\rho = 1.7\%$). The geometrical and reinforcement details of the tested beams are shown in Figure 135.

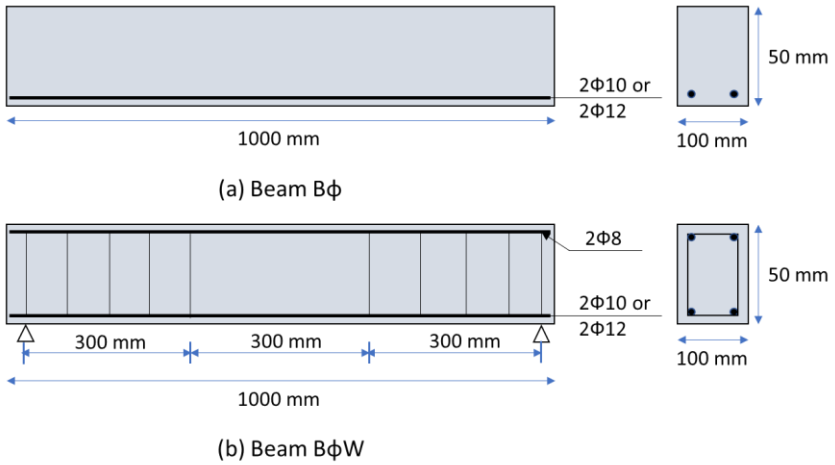

Figure 135. Geometrical and reinforcement details of the tested beams (Kamal et al. 2014)

A test beam was defined by the letter B followed by the diameter of the two reinforcing main bars (10 or 12 millimeters), followed by W in case of beams having web reinforcement and P or S denoting polypropylene or steel fibers. B10 (P or S) and B12 (P or S) were chosen as the reference for analytical simulation using the HRC-TL model. The simulated load-deflection curves and stress-strain diagrams for B10 and B12 beams are shown in Figure 136.In these samples, the number after B refers to the rebar number and S and P stand for steel and polymeric fibers.

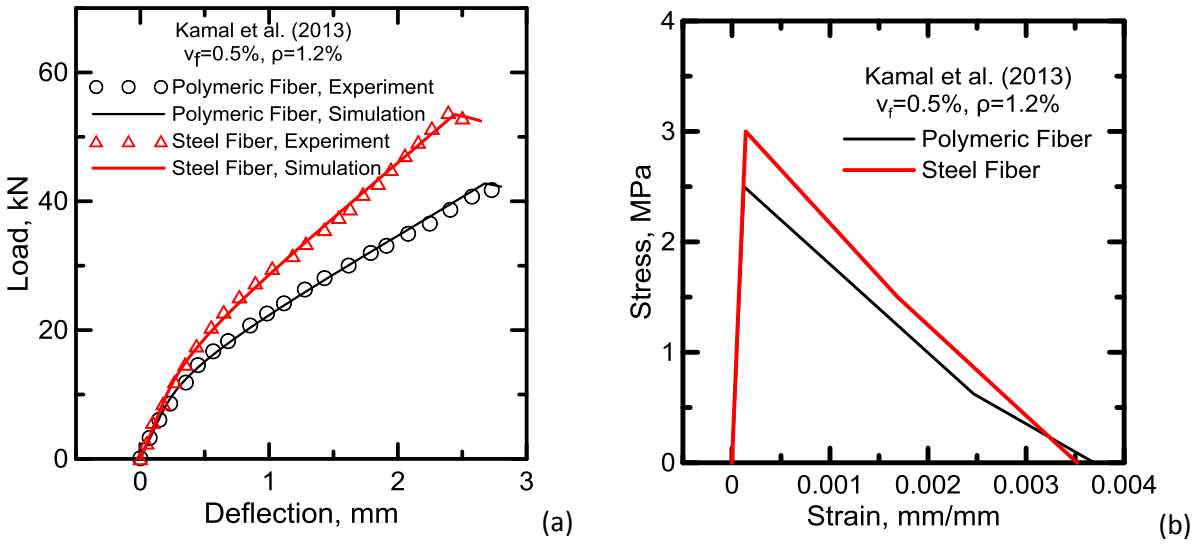

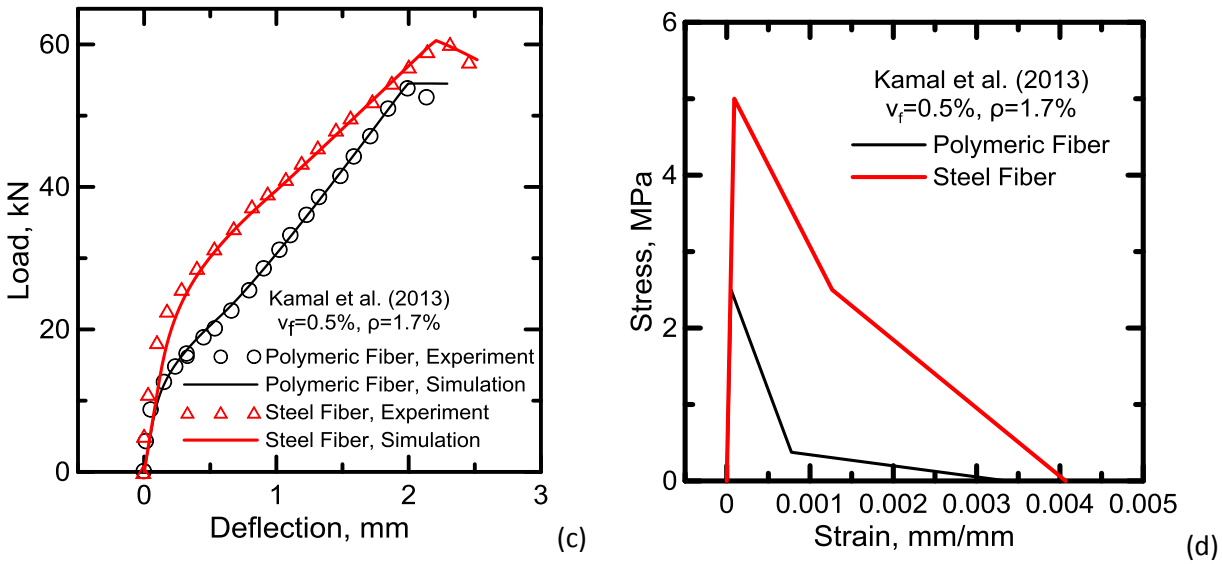

Figure 136. (a) simulated load-deflection curves, and (b) stress-strain graphs for tensile behavior for B10 samples; (c) simulated load-deflection curves, and (d) tress-strain graphs for tensile behavior for B12 samples

Back-calculated stress-strain graphs show that the steel fibers have better performance than the polymeric fibers with the same fiber content. On the other hand, a comparison between the results of this research and those of the previous study (Yang et al., 2010) demonstrates that the fiber content has a considerable effect on the tensile response of the FRC section. While in the current research (with 0.5 percent fiber content) the ultimate tensile strain of the section is about 0.4 percent, in the previous study (with 2 percent fiber content) the tensile strain was five times higher at about 2 percent. Similar results occur for the tensile strength. While the tensile strength in the samples with 2 percent fiber content is around 10 MPa, this value for the samples with 0.5 percent fiber content is about 3 MPa.

Another important issue is that in most of the experimental research performed so far, a reinforcement ratio of less than 2 percent was chosen. However, as the parametric studies demonstrated, due to the high compressive strength of UHPC it is possible to employ more reinforcement (up to 15 percent for UHPC section with a compressive strength more than 20 ksi and grade 60 rebars). This enables proper exploitation of the advantages of UHPC's high compressive strength.

Design and Analysis of UHPC Joints

One of the large and specific challenges facing bridge authorities is the long-term durability of bridge decks which receive continuous impact loading from trucks and changing environmental conditions. The

years of continuous flexural and thermal stresses and exposure to corrosive elements create long-term deterioration and maintenance issues for bridge decks. The use of HPC precast deck panels is a common method to speed construction and reduce the user inconvenience, but the joining of the precast system requires greater maintenance and can even cause failure (Vic Perry et al. 2010).

Joints are considered the vulnerable link in a structure; this is where structural deterioration often originates. Joints convey the stresses from superstructure to substructure and are subjected to large stresses during the process. However, the introduction of new methodologies and innovative material technologies facilitates the implementation of new solutions. One of these solutions is composite UHPC material, which offers superior technical characteristics, including ductility, strength, and durability, while providing highly moldable products with a high-quality surface aspect and a short bond development length (B. A. Graybeal 2004; Bierwagen, Moore, and Perry 2006). UHPC, when used as a jointing material with reinforced HPC panels, provides a new approach for reconstruction of bridge superstructures.

Opportunities to modify and improve prefabricated element connection details exist by taking advantage of the material and durability properties that UHPC has to offer. In addition to the high compressive and post-cracking tensile strengths, the dense, discontinuous pore structure and steel fiber reinforcement of UHPC provide further material property benefits. Resulting improvements include better internal distribution of stresses, better confinement of embedded rebar, and reduced rebar development and splice lengths. Currently, the most popular application of UHPC in US bridge construction is for connections between prefabricated bridge deck elements (Zachary B. Haber et al. 2018). UHPC was successfully used by the state of New York (NYSDOT; see Figure 137) and the Iowa DOT in many bridges as various components, and proved to help with Accelerated Bridge Construction (ABC) which made its use economical and time-saving (Rallabhandhi 2016). The performance of prefabricated bridge systems is highly contingent on the design of connections and joints, however.

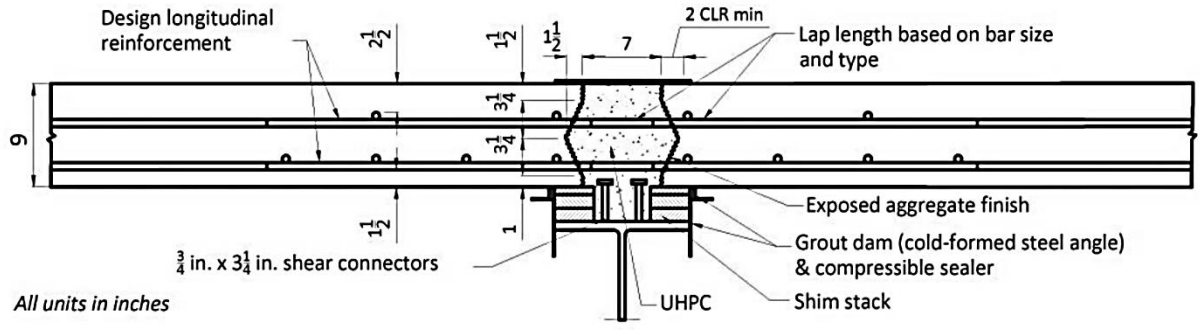

Figure 137. Combined UHPC deck-level and composite connections as deployed by NYSDOT on I-81 near Syracuse, NY (Ben Graybeal 2014a)

Figure 138. Transverse (LLC) joints filled with UHPC

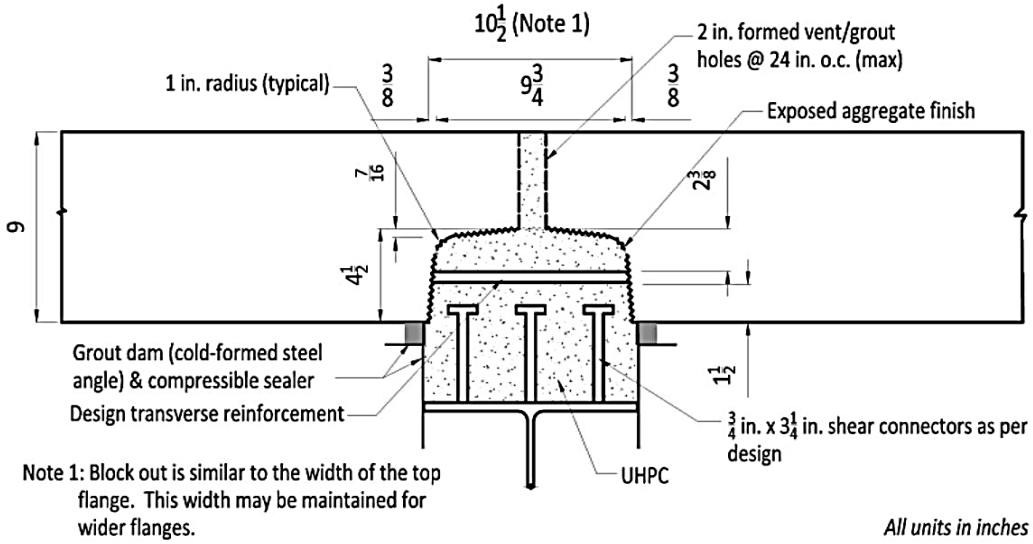

Figure 139. UHPC composite connection between deck panel and steel girder (Ben Graybeal 2014a)

Figure 140. Longitudinal connection detail above first interior girder line with shear studs stopping below the bottom mat of rebar (Ben Graybeal 2014a)

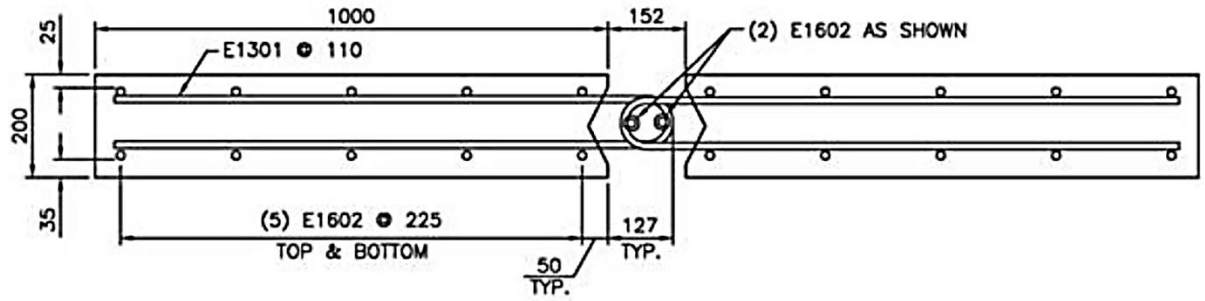

Figure 141. Prototype panel (pairs) for testing joint fill performance (Vic Perry et al. 2010)

The flexural reinforcement in the connection region typically requires hooked or U-shaped bars to meet the length requirements (L. Li et al. 2009). Additional bars are usually required to withstand secondary loads such as temperature and shrinkage. Using UHPC, however, there is no need for hooked flexural reinforcement or lacer bars, thus greatly simplifying the detailing and increasing the constructability

(Zachary B. Haber et al. 2018). The advanced properties of UHPC allow simple reinforcement details inside the connection region while using conventional non-shrink grouts.

To design the UHPC joint, a similar approach can be used for FRC and HRC sections. First, it is necessary to have the moment-curvature response to the section and then use that response to simulate the load-deflection response of the element. For this purpose, consider the most general case which covers all the possible situations with a different type of materials (i.e., curve C in Figure 107). It is possible to simplify the model as a beam with two different sections: section 1 for the beam body parts and section 2 for the joint. This is depicted in Figure 142.

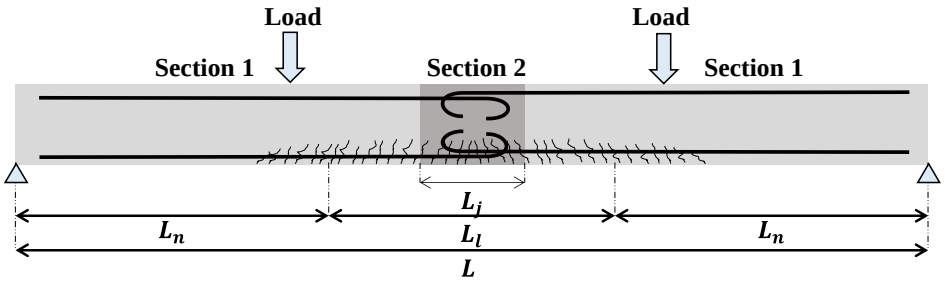

Figure 142. Typical RC beam with a joint at the middle part under four-point loading

In this figure, L_j represents the joint length and L_n and L_l represent non-localized and localized zones, respectively. As shown, the joint (Section 2) is totally located in the localized zone. Part of Section 1 is also located in the localized zone. It is assumed that the cracks in this zone continue to grow even after unloading, but the cracks in the non-localized zone will be closed after unloading. This kind of response in different segments of the beam affects the load-deflection response of the beam as well.

Each section has its own M-C diagram and is divided into several subsections or elements along with the beam axis. The moment due to external loading will be calculated for each element and the corresponding curvature extracted from the related M-C diagram. The mid-span deflection can be calculated using the moment-area method and direct integration of the element curvatures along the beam axis (C. Soranakom and Mobasher 2007). This process is performed using a MATLAB code for a generalized beam with two sections and two types of external loading (four-point and three-point bending tests; see Figure 143).

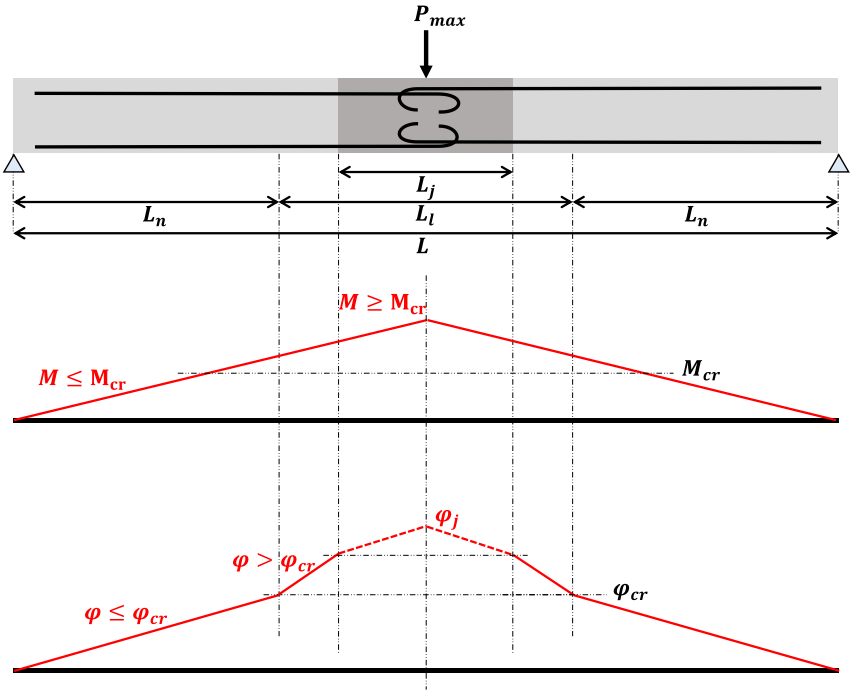

(a)

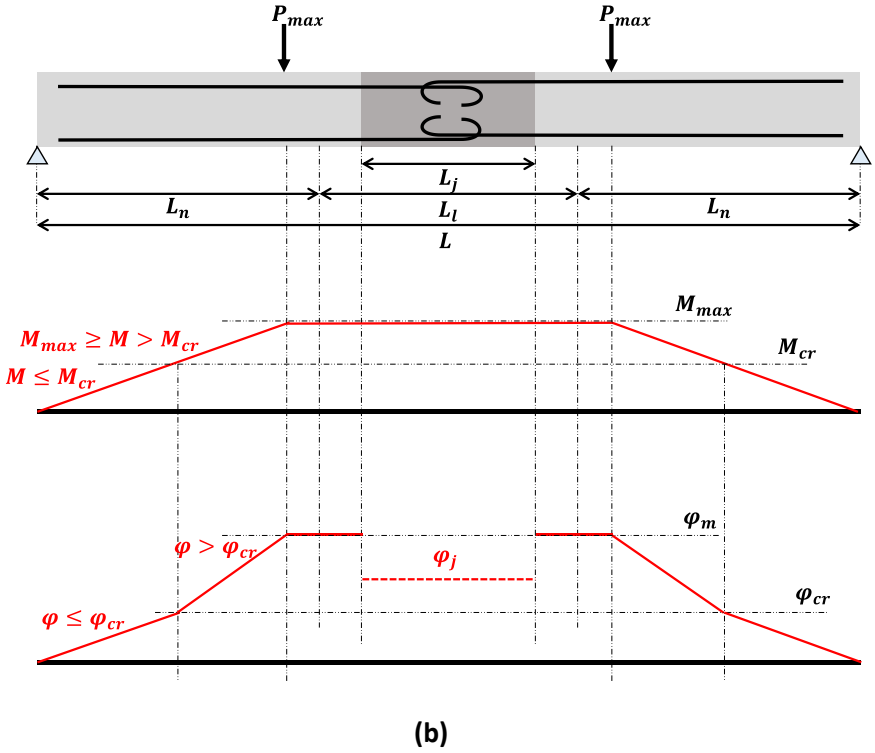

(b)

Figure 143. Schematic drawing of moment and curvature distributions: (a) 3PB; (b) 4PB

In these diagrams, it is assumed that the stiffness of the joint (section 2) is higher than the stiffness of the element (section 1). These figures demonstrate the schematic views of the moment and curvature diagrams at the maximum loading and bending moment. As it was mentioned before, each section has its own M-C diagram and this relationship is linear only for the initial part of the response.

The same approach applies to a beam with a UHPC joint at the middle. The difference in this case is that there are two different sections along the beam axis. The M-C diagrams for HRC sections, single- or double-reinforced, can be obtained using the models that were presented previously. To obtain a general solution to calculate the load-deflection response of a beam with a joint at the middle, a general form of the M-C diagrams should be utilized for each section. Different forms of a typical M-C diagram for FRC sections were shown in Figure 107.

Parametric Study and Comparison with Experimental Data

An experimental study on six commercially-available UHPC materials was conducted by FHWA (Haber et al. Zachary B. Haber et al. 2018; Haber and Graybeal, n.d.). The objective of the study was to obtain a comprehensive set of mechanical and physical properties for the field cast UHPC materials that are used in the closure pours. The objective of the closure pours is to connect adjacent prefabricated bridge elements; these are employed in many ABC projects in North America. The mix designs for components for each of the UHPC types are listed in

Table 21. The UHPC-class materials were assessed using 14 different ASTM, AASHTO, or FHWA-TFHRC-developed test methods. Their 4PB test setup is shown in Figure 144.

Table 21. Components of each type of proprietary UHPC material (Haber and Graybeal, n.d.)

ID		U-A	U-B	U-C	U-D	U-E	U-F
Mix Design		lb/yd^3	lb/yd^3	lb/yd^3	lb/yd^3	lb/yd^3	lb/yd^3
Pre-blended dry powders		3503	3516	3600	3700	3236	3725
Water		278	354	268	219	379	241
Chem admix	Liquid	23	48	N/A	89	73	65.7
	Solid	N/A	N/A	Pre-blended	N/A	N/A	1.5
Steel fiber content (2%) Short / Long Fibers		277	88/ 179	272	263	263	284
Tensile strength, ksi		160	≥305	348	399	399	399
Length, in		1.18	0.5 / 0.79	0.5	0.5	0.5	0.5
Diameter, in		0.022	0.012	0.012	0.008	0.008	0.008
E_c, ksi		7500	6300	6300	7200	5300	--
f_c', ksi		21	22	19	18	17	--
σ_{cr}, ksi		1.06	1.10	0.76	1.23	1.01	--

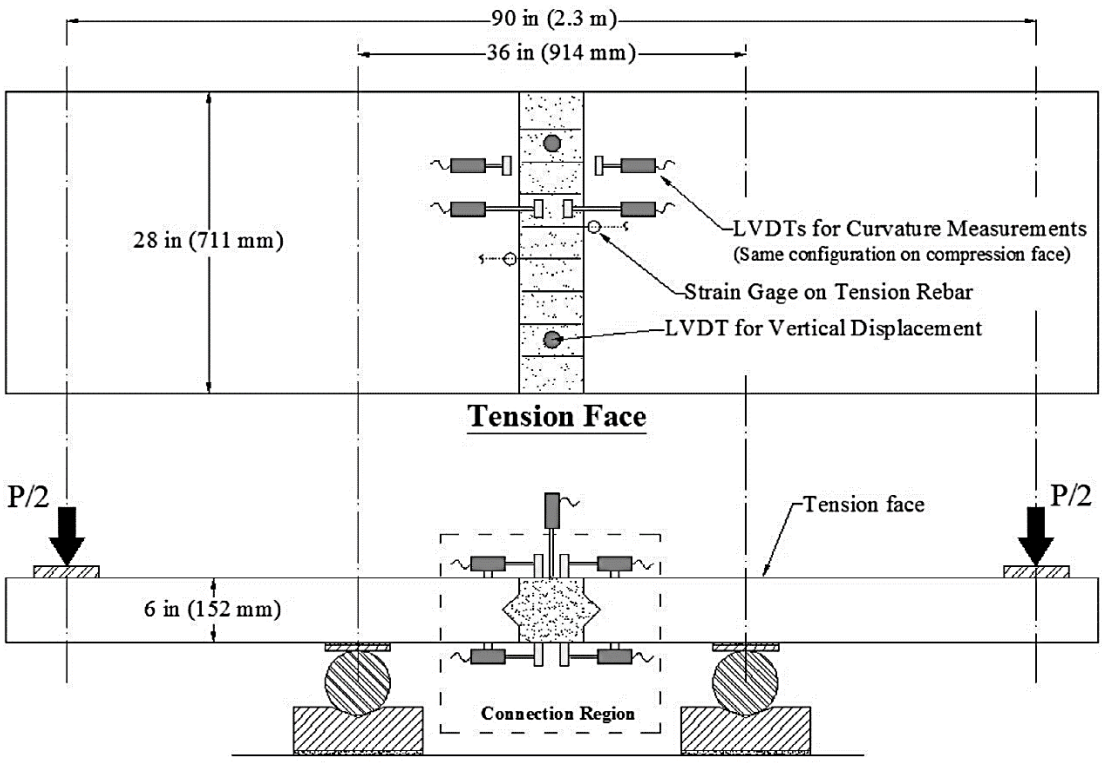
90 in (2.3 m)
36 in (914 mm)
28 in (711 mm)
LVDTs for Curvature Measurements
(Same configuration on compression face)
Strain Gage on Tension Rebar
LVDT for Vertical Displacement
Tension Face
P/2
Tension face
P/2
6 in (152 mm)
Connection Region

(a)

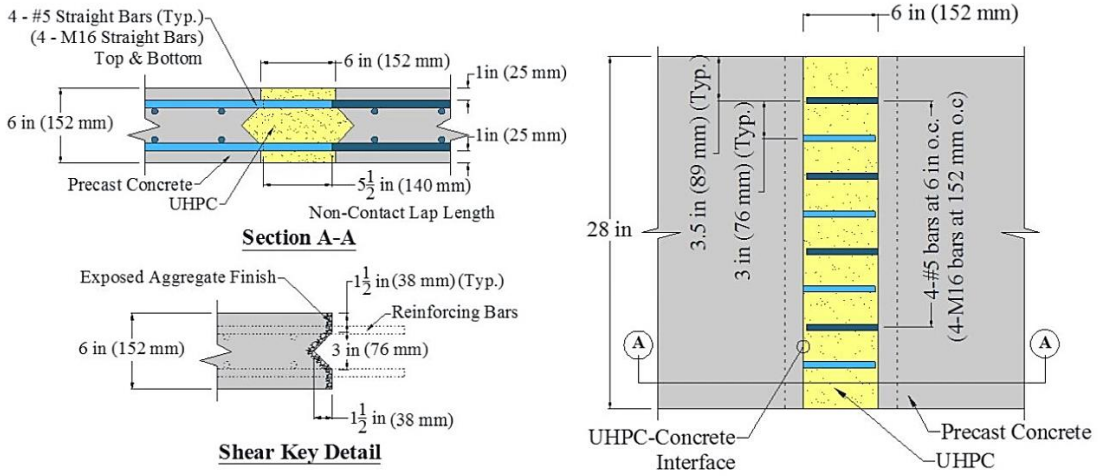
4 - #5 Straight Bars (Typ.)
(4 - M16 Straight Bars)
Top & Bottom
6 in (152 mm)
1in (25 mm)
1in (25 mm)
6 in (152 mm)
Precast Concrete
UHPC
5½ in (140 mm)
Non-Contact Lap Length
Section A-A
Exposed Aggregate Finish
1½ in (38 mm) (Typ.)
Reinforcing Bars
6 in (152 mm)
3 in (76 mm)
1½ in (38 mm)
Shear Key Detail
6 in (152 mm)
28 in
3.5 in (89 mm) (Typ.)
3 in (76 mm) (Typ.)
4-#5 bars at 6 in o.c.
(4-M16 bars at 152 mm o.c)
A
A
UHPC-Concrete
Interface
Precast Concrete
UHPC

(b)

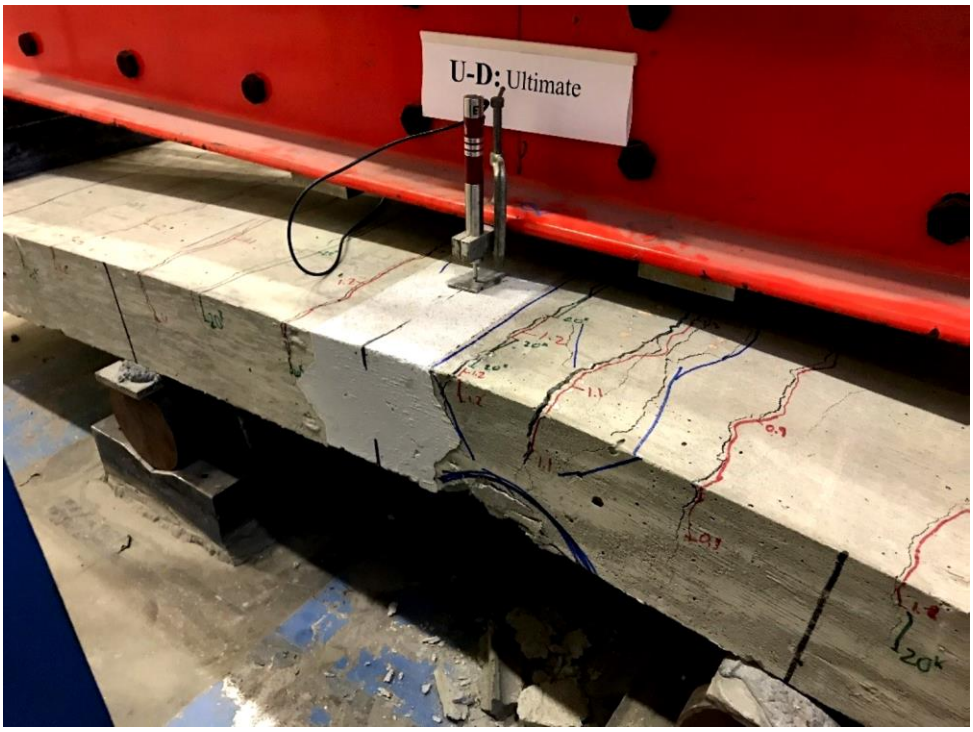

(c)

Figure 144. Instrumentation and loading configuration of 4PB test setup (Zachary B. Haber et al. 2018)

The Haber team performed 4PB tests on five sets of beams, each made of a different commercially available UHPC material. Four sets of tests were used in the back-calculations and load-deflection simulations. The details of each mix design and the comprehensive tests (including compression, tension, and bending) can be found in the original research (Zachary B. Haber et al. 2018). The current study is designed to simulate the full-scale tests conducted using these materials in order to develop a design guideline and procedure.

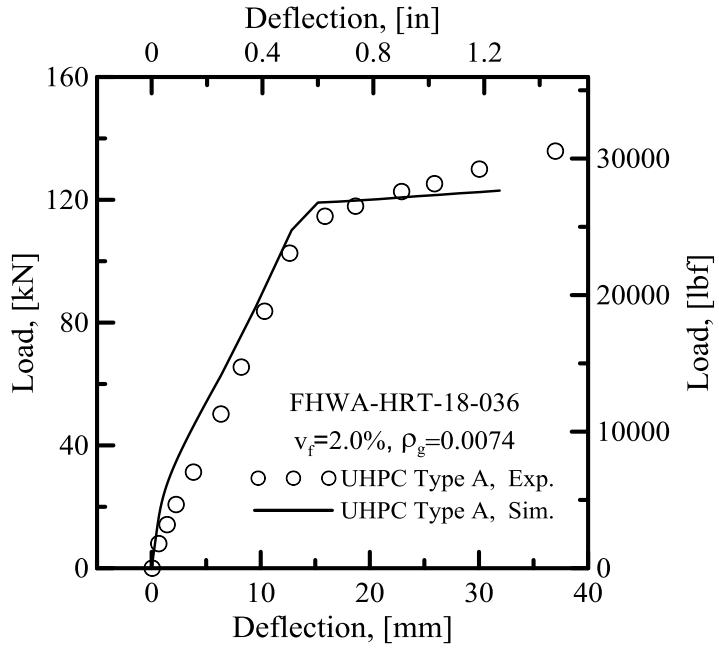
Deflection, [in]
0
0.4
0.8
1.2
160
120
80
40
0
Load, [kN]
30000
20000
10000
0
Load, [lbf]
FHWA-HRT-18-036
v_f=2.0%, ρ_g=0.0074
UHPC Type A, Exp.
UHPC Type A, Sim.
0
10
20
30
40
Deflection, [mm]

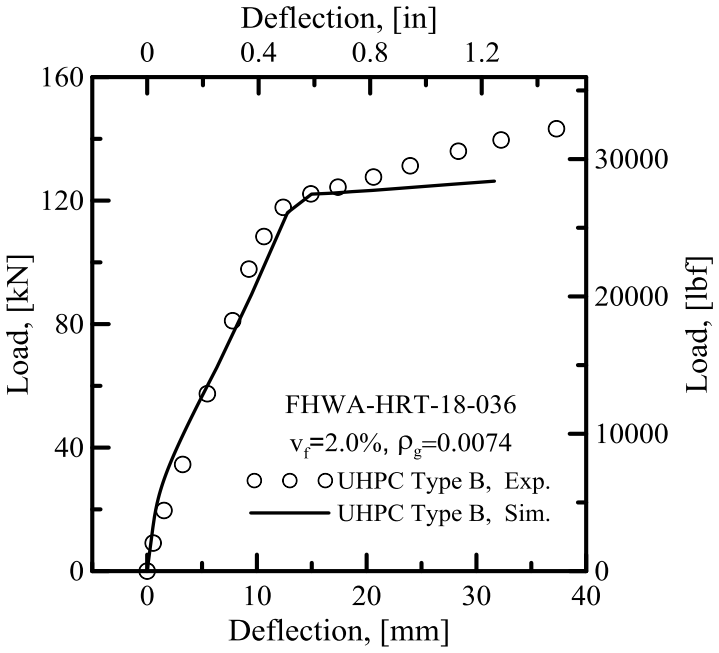
Deflection, [in]
0
0.4
0.8
1.2
160
120
80
40
0
Load, [kN]
30000
20000
10000
0
Load, [lbf]
FHWA-HRT-18-036
v_f=2.0%, ρ_g=0.0074
UHPC Type B, Exp.
UHPC Type B, Sim.
0
10
20
30
40
Deflection, [mm]

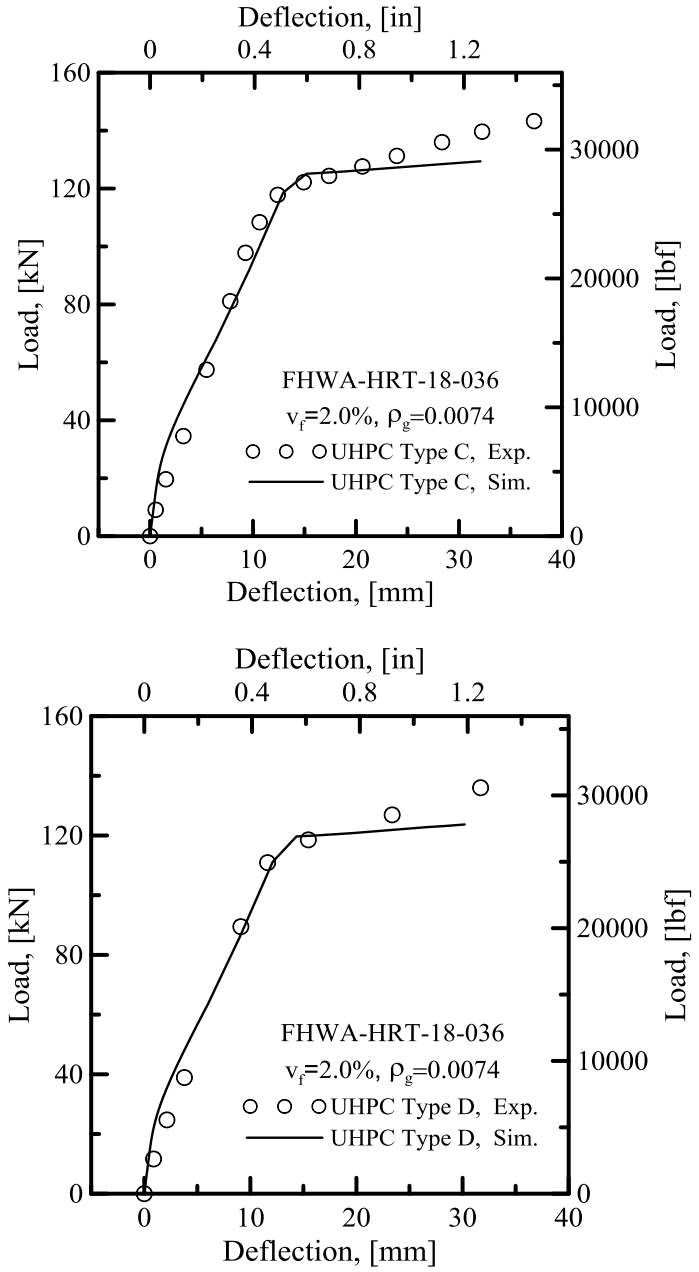

Figure 145. Results from inverse analysis and comparison with the experimental data (Zachary B. Haber et al. 2018)

Haber employed 0.74 percent reinforcement, which is acceptable for normal RC members with UHPC joints. For members fully made of UHPC, however, it is possible to use up to 15 percent reinforcement, grade 60. A parametric study on this beam-joint system is presented next. The dimensions and material properties are as follows (Figure 144):

Table 22. Material properties of the joint and the slab concrete

Properties	RC	UHPC joint
L	**90 inches**	
L_j (joint length)	**--**	**0.5, 1.0, and 1.5 ft**
b (section width in inches)	**28**	**28**
d (section depth in inches)	**6**	**6**
E (ksi)	**4600**	**6700**
$f_{c1}^{'}$ (ksi)	**4.3**	**19**
σ_{cr} (psi)	**500**	**1200**
ω	**9**	**17**
γ	**1**	**1**
μ	**0**	**1**
E_s (ksi)	**29000**	**29000**
$\rho_s (= \rho_s')$	**0.0074**	**0.0074**
f_{sy} (ksi)	**61**	**61**

Figure 146 shows the moment-curvature responses for both sections, i.e., RC used as the standard section and the UHPC joint. The moment capacity of the section is dominated by the capacity of the weaker section (RC section); therefore the moment capacity cannot exceed this value (42 kN-m) and, although the UHPC is cracked, it does not reach its maximum moment capacity and never enters its localized region (after maximum moment). However, these curves show that making stronger joints will not help to improve the capacity of the member and that the member itself, not the joint, dominates the capacity of the entire structural configuration.

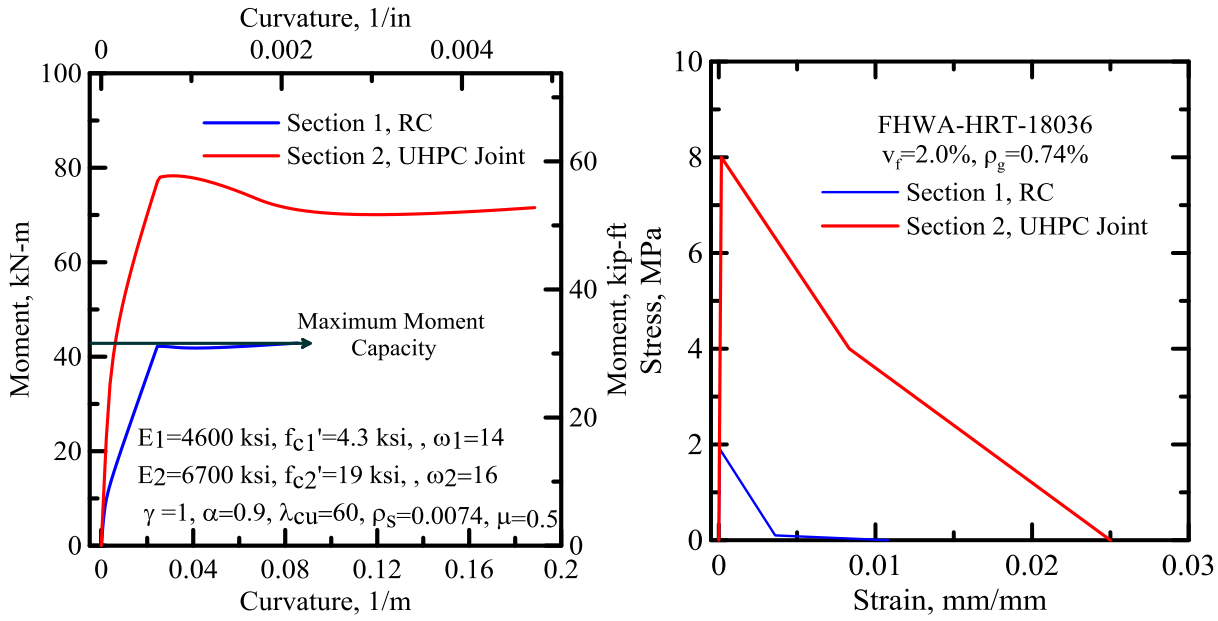

Figure 146. Moment-curvature response for two different sections (RC and UHPC joint)

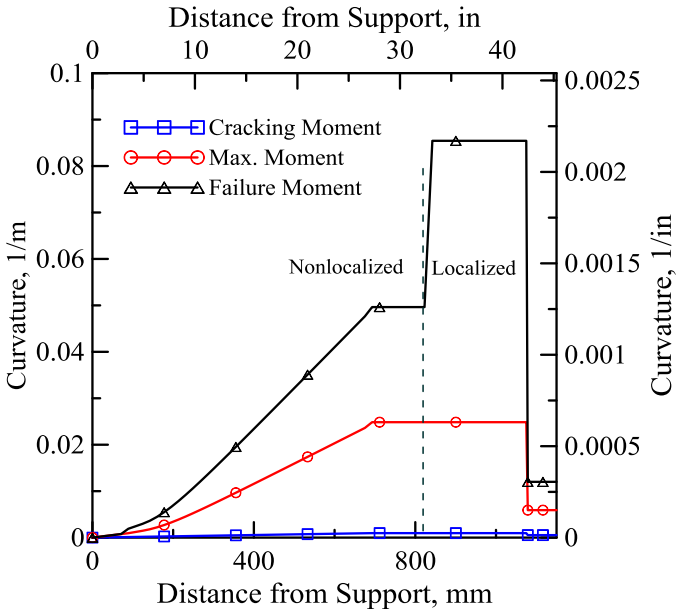

Figure 147. Curvature distribution along the beam axis (for half of the simulated beam)

Figure 147 demonstrates the curvature distribution along the beam axis obtained from the MATLAB simulation. Before reaching the maximum moment (the red curve in the figure), there is no difference between the curvature in the localized and non-localized zones. During the unloading, however, there is

a significant difference between the curvature in the two due to the localization. The curvature in the joint never reaches its maximum capacity and the localization never happens at this part. As the joint length increases, the stiffness of the member increases as well. Figure 148 shows the effect of the joint length on the load-deflection response of the beam-joint element under 4PB simulation.

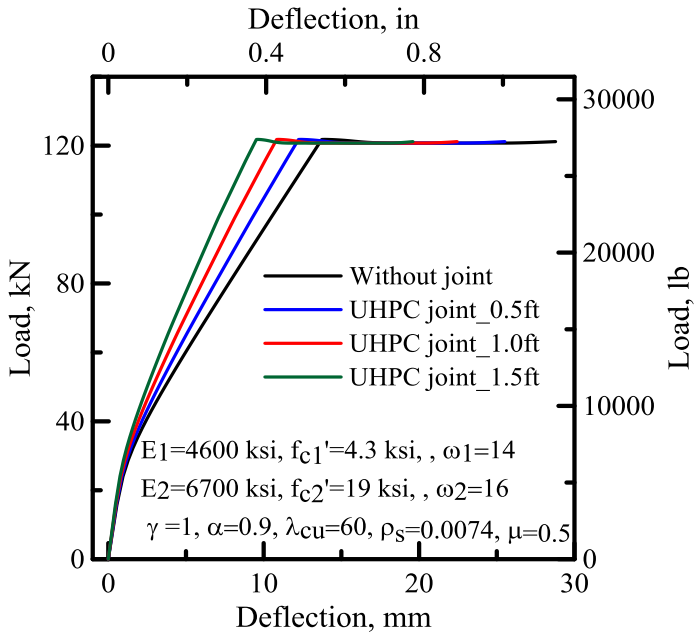

Figure 148. The effect of the joint length on the load-deflection response of the example beam-joint element

In this simulation, it is assumed that the joint is made of UHPC and the beam element of normal concrete. As the length of the UHPC joint increases, the stiffness of the system increases so the mid-span deflection decreases. On the other hand, the extra strength in the UHPC joint cannot be used as long as the RC section itself is not able to carry that extra strength; therefore, a UHPC joint which is about 20% stronger than the RC section is a rational design.

Chapter 9 DURABILITY PROPERTIES OF UHPC

Introduction

The serviceability and life expectancy of civil structures depend to a great extent on the environmental and service conditions they are subjected to. As such, durability of concrete mixtures used in infrastructure is one of the key aspects of every construction project. This chapter explores in detail several durability aspects regarding UHPC mixtures designed in this study. The key topics addressed include the following:

- An overview of the effect of transport processes such as chloride diffusion on UHPC type concrete
- A description of test methods to quantify the durability of UHPC mixtures
- Interpretation of the results of durability tests for UHPC mixtures and their comparison with ordinary portland cement concrete.

Overview of Moisture and Ionic Transport in Concretes

Concrete structures may be subjected to ingress by several aggressive ions present in the environment. These ions may react with aggregates in concrete (alkali-silica reaction) or with the reaction products formed in concrete due to hydration of cement/cementitious materials. As a result, the strength of the structure could be severely compromised and service life drastically reduced. Understanding these mechanisms that could adversely affect the strength of UHPCs over time is crucial to the determination of the service life of structures constructed using UHPCs. Chloride ions affect the durability of structures exposed to sea water, marine environments containing chloride-bearing air, and de-icing salts. Beyond a threshold level, the presence of chloride ions leads to the corrosion of concrete as well as the steel present in the concrete.

Chloride ions react with calcium hydroxide present in concrete to form calcium oxychloride, which is expansive and causes destruction of concrete (Suraneni et al. 2016). Chloride ions destroy the protective ferric oxide layer on steel rebar which protects the steel from corrosion. Water acts as the carrier of these harmful ions in concrete and therefore the rate of their movement through concrete depends strongly on the transport of water/moisture through concrete.

The corrosion process depends on the chemical composition and physical microstructure of concrete. The primary mechanisms that govern the movement of ions and moisture in concrete are sorption and diffusion. Sorption is defined as the absorption of water on the surface by capillary pores and transport by capillary action. Diffusion is defined as the long-term movement of moisture through gel pores driven by a gradient. The gradient can be a pressure gradient, electrical potential, or a concentration gradient. Under normal conditions, diffusion takes places due to a concentration gradient. However, the penetration of chloride ions or moisture in concrete is a slow process; therefore, accelerated testing methods have been developed in order to measure the impact of chloride ions or moisture on concretes

in a reasonable amount of time (testing time of seven days or less). These accelerated tests measure diffusion and sorption of chloride ions or water in concrete subjected to a chemical potential or concentration gradient. The most common form of measuring diffusion is through an electric potential.

Accelerated chloride migration tests such as the rapid chloride permeability test (ASTM C 1202, 2017) and the non-steady-state migration test (NT Build 492, 1999) are used in this study to determine the effectiveness of UHPCs against the transport of chloride ions. Both of these tests cause the chloride ions to penetrate under an externally applied electrical field and a concentration gradient (Neithalath and Jain 2010). Moisture transport in UHPCs has been evaluated using the sorption test (ASTM C 1585, 2013).

Description of Test Procedures

Chloride Transport – Sample Preparation

Two cylindrical concrete samples (4” x 8”) were prepared for NSSM and RCP tests. Specimens were cured for 28 days in an environmental chamber maintained at a temperature of 73.5 ± 3.5°F at a relative humidity of 95 percent or higher. Two-inch-thick slices were cut from the 28-day cured samples using a laboratory grade water-cooled diamond saw (Figure 149). The cut sample is shown in Figure 150. Two samples corresponding to the same mixture obtained from different cylinders were used for the transport tests.

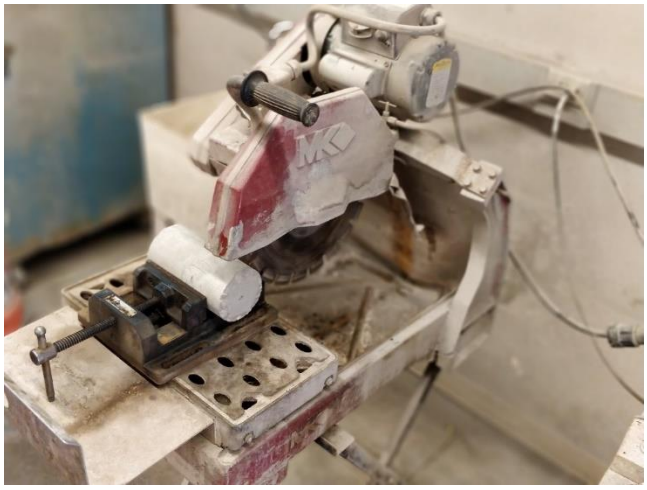

Figure 149. Water saw used for sample preparation

Figure 150. 50-mm thick disk sample cut from 200-mm long cylinder

Chloride Transport – Pre-conditioning

The prepared samples (2" thick) were air dried for one hour after cutting. Both samples were then immediately placed in a vacuum desiccator for three hours, maintaining a pressure at 0.15-0.7 psi. The vacuum desiccator setup is shown in Figure 151. After three hours, the funnel was filled with de-aerated water while the vacuum was still running. Sufficient water was allowed to drain into the vacuum desiccator by opening the stopcock such that the samples were completely submerged. The stopcock was then closed, and the vacuum allowed to run for one additional hour to make sure that all the voids in the specimen were saturated with water. After this step, the vacuum pump was turned off and the air allowed to enter the desiccator. The specimen was left to soak underwater for 18 ± 2 hours. This procedure is valid for the pre-conditioning of samples for the RCP test. The sample pre-conditioning procedure for NSSM testing deviates slightly from this procedure. Instead of adding water to submerge the specimens, a saturated solution of calcium hydroxide (obtained by dissolving 2 g of calcium hydroxide in 1 liter of water) was used.

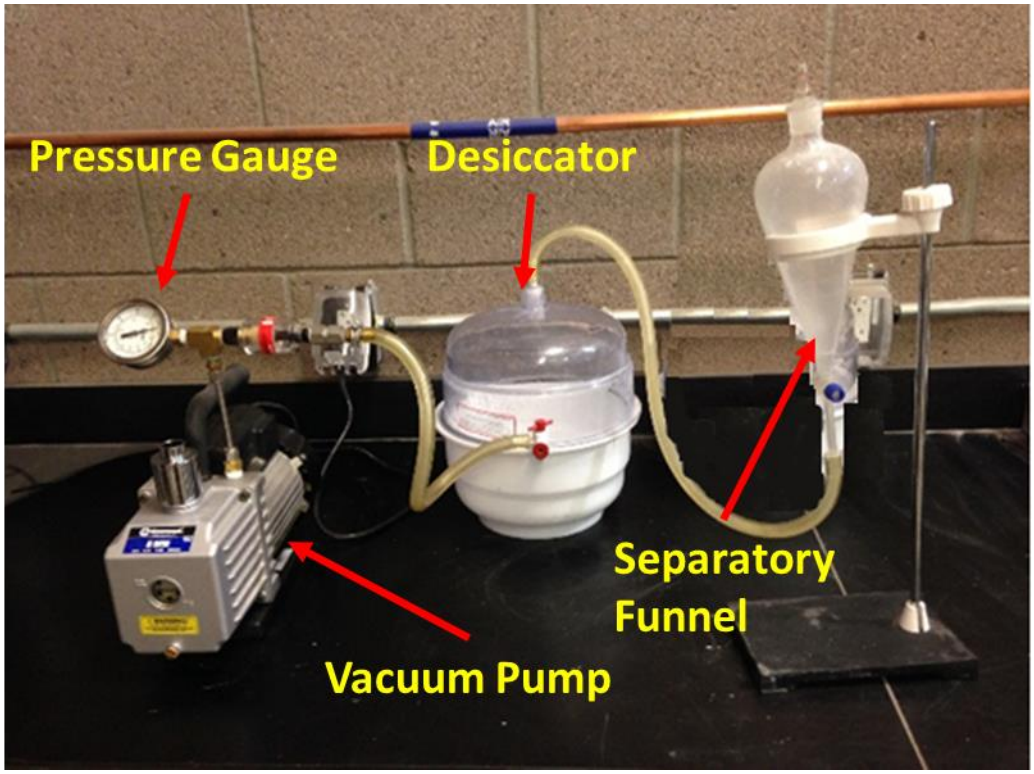

Figure 151. Experimental set-up for pre-conditioning samples using vacuum saturation apparatus

Chloride Transport – Test Setup

The experimental set-up for the RCP and NSSM test is a Germann Instruments PROOVE'it Rapid Chloride Permeability Test System shown in Figure 152. The RCP test was performed in accordance with ASTM C 1202. This test determines the resistance to chloride penetration through the electrical conductance of the concrete when subjected to an externally applied potential of 60V. The electric current is monitored for six hours and the total charge (in coulombs) passed is expressed as the result.

The setup shown in Figure 152 uses a three percent sodium chloride solution (3g sodium chloride in 100 g water) in the catholyte compartment and a 0.3 N sodium hydroxide solution (1.2 g sodium hydroxide in 100 g water) in the anolyte compartment during the RCP test. During the RCP test, the temperature and current were monitored and recorded by the system every five minutes and at the end of the test the total charge passed was displayed.

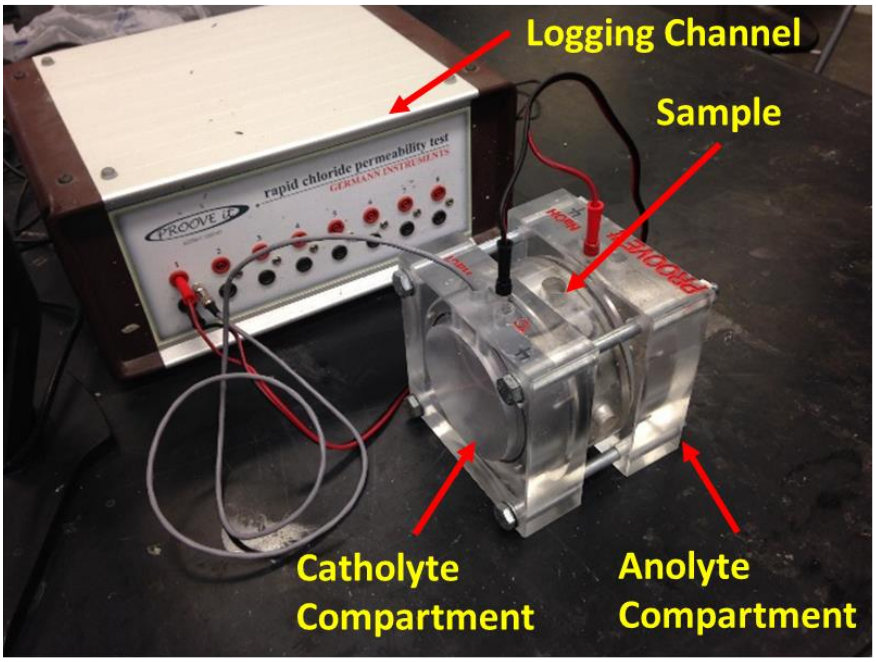

Figure 152. Experimental set-up for NSSM and RCP test

The NSSM test was performed in accordance with the Nordtest method (NT BUILD 492). This test also determines the resistance of chloride penetration through the measurement of the penetration depth and calculation of the migration coefficient. The NSSM test differs from the RCP test in several aspects: (i) the test lasts appreciably longer (24 hours or more) and (ii) due to this longer duration, the externally applied voltage used is determined from the initial current in the specimen when a 30V electric potential is applied.

For the NSSM test, the migration cell shown in Figure 152 uses a 2 N (10 percent) sodium chloride solution in the catholyte compartment and a 0.3 N sodium hydroxide solution in the anolyte compartment. After completion of the test, the specimens were split axially (along the z-axis of the sample) and a 0.1 N silver nitrate solution was sprayed on the split surfaces. After a few minutes, a visible white silver chloride precipitated on the surface and five to seven measurements were taken representing the chloride penetration depth. Figure 153 shows an example of the white silver chloride penetration profile.

Figure 153. Axially split specimen tested under NSSM showing chloride penetration

The average value of the penetration depth (x_d) per sample was used to calculate the NSSM migration coefficient, D_{nssm} (m^2/s), described in Equation 68, Equation 69, and Equation 70.

$$D_{nssm} = \frac{RT}{zFE}.\frac{x_d - \alpha\sqrt{x_d}}{t} \quad \textbf{Equation 68}$$

where

$$E = \frac{U-2}{L} \quad \textbf{Equation 69}$$

$$\alpha = 2\sqrt{\frac{RT}{zFE}}.\mathrm{erf}^{-1}\left(1 - \frac{2c_d}{c_0}\right) \quad \textbf{Equation 70}$$

Here, R is the molar gas constant (8.314 J/(K·mol)),
z is the absolute value of ion valence, (1, for chloride ions),
F is the Faraday's constant (9.648×10^4 J/(V·mol)),
U is the absolute value of the applied voltage,
T is the average value of the initial and final temperatures in the anolyte solution (K),
L is the thickness of the specimen (m),
t is the test duration (s),
α is a coefficient that depends on C_d and C_0,
C_d is the chloride concentration at which white silver chloride precipitates, ($C_d \approx 0.07$ N for plain concrete and the UHPC concretes in this study, because the changes in C_d do not influence the NSSM migration coefficient to a noticeable degree),
C_0 is the chloride concentration in the catholyte solution ($C_0 \approx$ 2N), and

x_d is the average penetration depth (mm).

Sorption Test – Sample Preparation

The sample preparation for the sorption test is similar to that of the chloride transport tests mentioned above in the subsection "Chloride Transport – Sample Preparation."

Sorption Test – Pre-conditioning

The two-inch-thick specimens are vacuum-saturated with water using the same procedure as mentioned earlier. The mass of each specimen after vacuum saturation is recorded to the nearest 0.01 g. The specimens are then conditioned for three days in a controlled environment at a temperature of 122 ± 3.5° F and a relative humidity of 80 ± 3 percent. For this purpose, the specimens are kept in a desiccator placed inside an oven maintained at a temperature of 74° F. The relative humidity is maintained using a saturated solution of potassium bromide (KBr) prepared by adding 161 g of KBr to 200 g of water. Care is taken so that the specimens are not in contact with the KBr solution. A picture of the desiccator with the sample is shown in Figure 154 and Figure 155. Here, the KBr solution is placed in the bottom of the desiccator below the perforated plate. The specimens are then stored individually in a sealed container at 73.5 ± 3.5° F for 15 days, after which the test procedure is started. This ensures that the internal humidity of the samples reaches 50 to 70 percent, similar to that found in field structures near the surface.

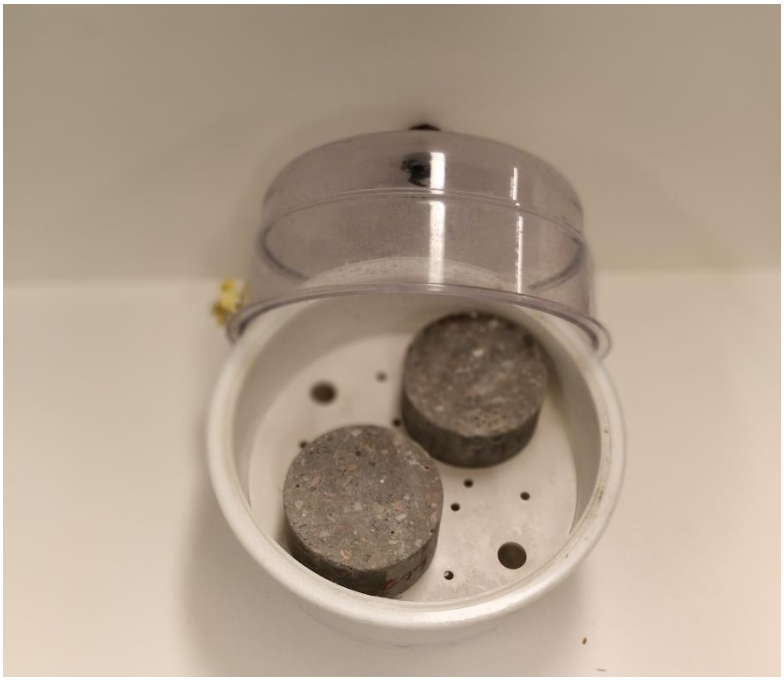

Figure 154. Samples placed inside the desiccator containing Potassium Bromide (KBr) solution at the bottom

Figure 155. Sample placed inside desiccator placed in an oven

Sorption Test – Test Setup

The specimens are removed from the storage containers and their mass is recorded to the nearest 0.01 g. The average diameter of each specimen is also recorded to the nearest 0.1 mm. The specimen is then sealed on the sides using duct tape. The end of the specimen that will not be exposed to water is sealed using a plastic wrap. The prepared sample is sealed from three sides, leaving only one side exposed for the water absorption to take place. Figure 156 shows the sealed specimen.

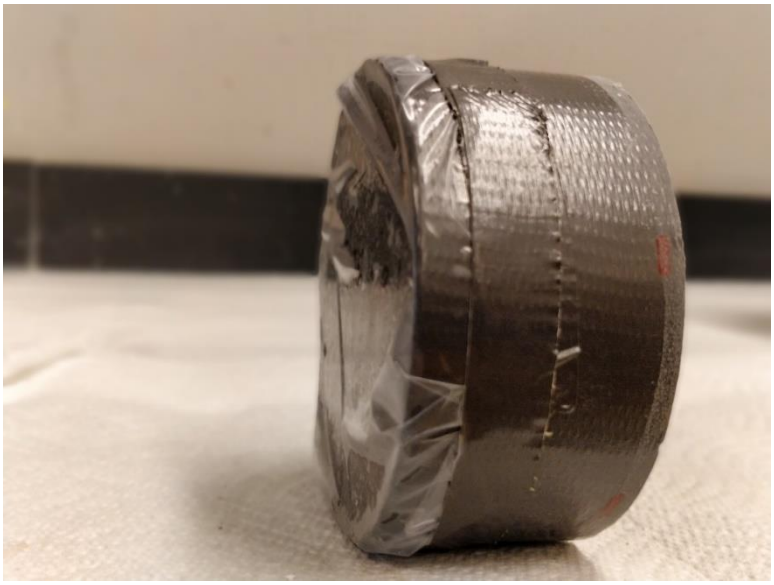

Figure 156. Sample prepared for sorption testing

The mass of the sealed specimen is recorded to the nearest 0.01 g as the initial mass for the water absorption procedure. Each specimen is placed in an individual polyethylene storage container fitted with a support device at the bottom. Water is then added to the container so that the water level is between 1 mm and 3 mm above the top of the supporting device. Figure 157 shows the container with the support device and Figure 158 shows the container with the sample placed inside the container.

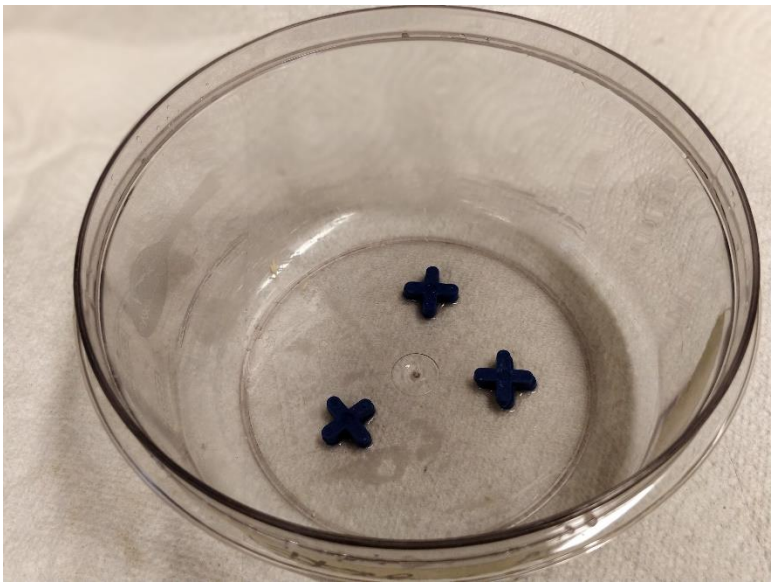

Figure 157. Polyethylene container with support devices installed

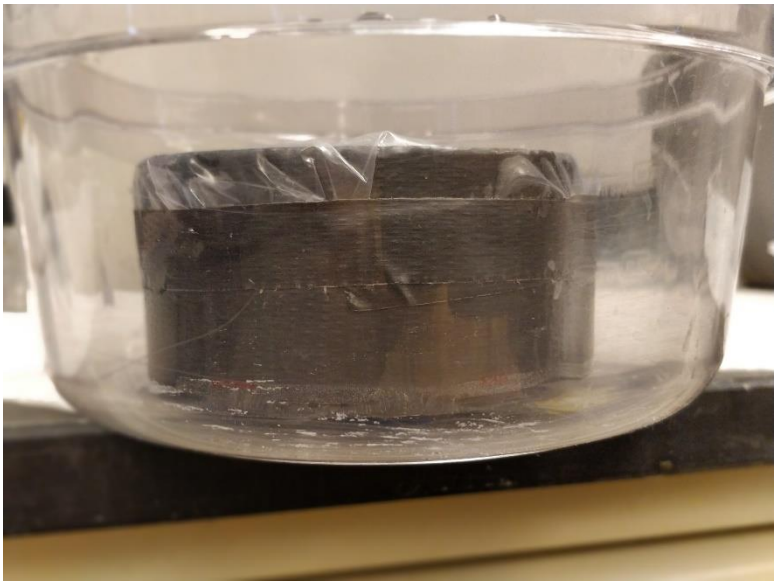

Figure 158. Specimen placed inside the container for absorption measurements

The mass of the specimens was measured at regular intervals of 1, 5, 10, 20, 30, 60 minutes, every hour up to 6 hours, and once every day up to 10 days. The absorption, I (in units of length) is calculated as the change in mass of the specimen divided by the product of its cross-sectional area and the density of water (Equation 71)

$$I = \frac{m_t}{a * d}$$ **Equation 71**

Here, I is the absorption (mm),
m_t is the change in mass of the specimen,
a is the area of cross section of the test specimen, and
d is the density of water.

The absorption, I when measured against the square root of time is a bilinear plot indicating initial and secondary absorption. Initial absorption (Equation 72) occurs in the first few hours of the test when the sample comes in contact with water and is related to the surface adsorption of the specimen. Secondary absorption (Equation 73) occurs over a longer period from 24 hours to 10 days, and is related more to the internal pore structure and pore sizes of the specimen. The slopes of the initial and final absorption curves are referred to as the initial and final sorptivity of the specimen.

$$Initial\ absorption, \quad I = S_i\sqrt{t} + b_1$$ **Equation 72**

$$Secondary\ absorption, \quad I = S_s\sqrt{t} + b_2$$ **Equation 73**

Here, I is the absorption (mm),
t is the time (s),
b_1, b_2 are constants,
S_i and S_s are initial and final sorptivities of the specimen.

Results

Chloride Transport Test

RCP and NSSM tests were used to determine the resistance of the UHP mixtures to chloride ion transport as mentioned above. Since both are electrically accelerated tests, the steel fiber reinforced mixtures were not considered. Figure 159 compares the results for total charge passed for the UHPC mixtures during the RCP test with known values for regular OPC concrete (w/c = 0.40) and high-

performance concrete (HPC; w/c = 0.32) obtained from previous studies (Cam and Neithalath 2010; C. S. Poon, Kou, and Lam 2006b; Neithalath and Jain 2010). The total charge passed during the RCP test is extremely low for the UHPC mixtures selected. This is attributed to the following reasons: (a) refinement of pore structure through the use of a very low w/p and cement replacement materials, and (b) the changes in pore solution conductivity brought about primarily by the use of silica fume. This is more evident in the case of the mixture with 20 percent of silica fume (by mass) replacing OPC, the reasons for which have been extensively detailed (Neithalath and Jain 2010).

Figure 159 also shows the range for charge passed as per ASTM C 1202 classification using dashed horizontal lines. The charge passed for a regular OPC concrete specimen (in Coulombs or Ampere.second, and abbreviated as C) lies in the range of 2000 C to 4000 C, which is considered in the "moderate" rapid chloride permeability category. Similarly, the charge passed for an HPC specimen lies in the range of 1000 C to 2000 C, which is classified as "low" rapid chloride permeability. On the other hand, both of the UHPC mixtures designed in this study fall under the "very low" rapid chloride permeability category. Figure 159 also shows that the charge passed for the UHPC specimens is at least ten times lower than that of the regular OPC concrete specimen.

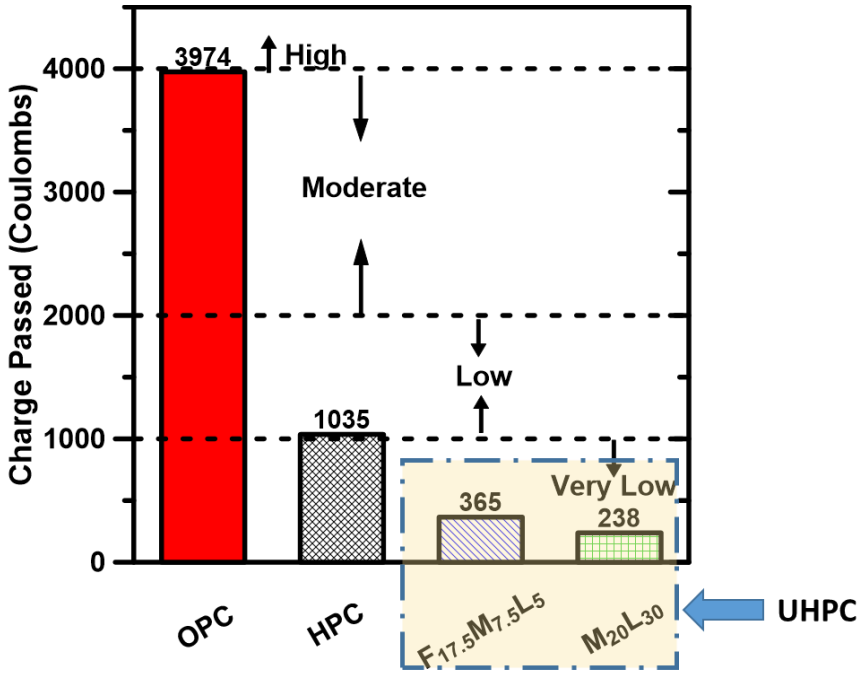

Figure 159. Charge passed during the RCP test applied to OPC and HPC compared with FML and ML series of UHPC mixtures

The NSSM test overcomes some of the drawbacks of the RCP test and provides a migration coefficient (D_{NSSM}) that is more realistically related to chloride ion transport through concrete. A lower D_{NSSM} value

indicates better chloride ion penetration resistance under electrically accelerated conditions. The non-steady state migration coefficient (D_{NSSM}) was calculated based on Equation 68, Equation 69, Equation 70, described earlier. The NSSM test carried out in accordance with NT Build 492 specifies different voltage values to be applied to the specimens, based on the initial value of current under an applied voltage of 30 V (potential of 600 V/m). For UHPCs, because of the very dense microstructure, the initial current was very low, and thus a higher applied voltage of 60 V (1200 V/m potential) was needed.

The NSSM coefficients for both UHPC mixtures are shown in Figure 160 along with the corresponding values for OPC concrete and HPC. The UHPCs demonstrate much lower migration coefficients than OPC or HPC, even under a higher applied voltage that accelerates ionic transport. The selected UHPCs have migration coefficients that are an order of magnitude lower than those of conventional OPC concrete. This level of impermeability offers a promise of significantly extending the service life of concrete structures designed using UHPCs, thus leading to lower life-cycle costs.

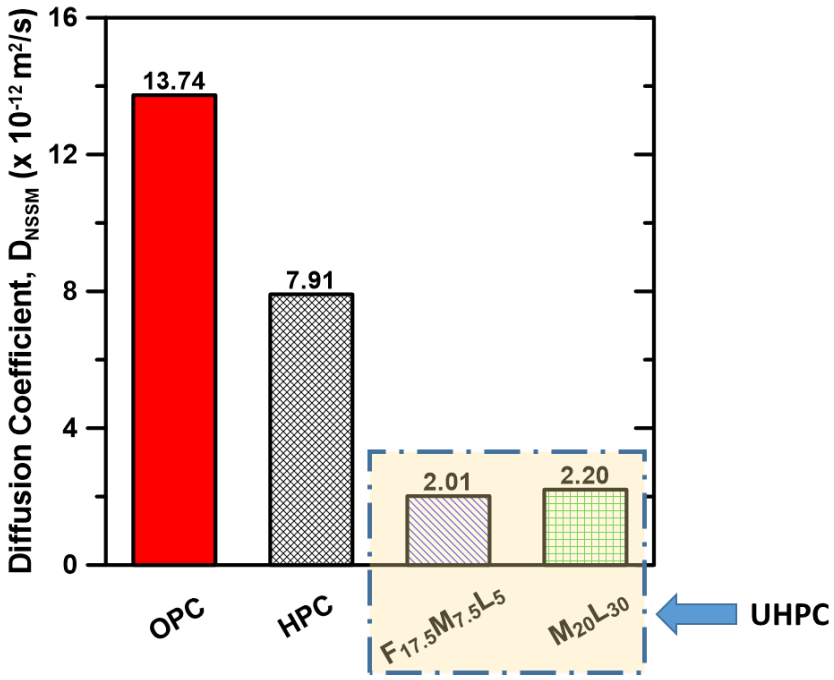

Figure 160. Non-steady-state migration coefficients (m^2/s) of OPC and HPC compared with FML and ML series of UHPC mixtures

Sorption Test

Figure 161 shows the absorption, I, as a function of the square root of time. Figure 161 shows that both UHPC mixtures show a very low value of absorption compared with the plain OPC concrete. Among the two UHPC mixtures, the ternary silica fume-limestone mixture (with an overall cement replacement level of 50 percent) shows a lower value of absorption than the quaternary fly-ash mixture. The high volume of extremely fine silica fume and limestone particles present in the ternary mixture helps in pore refinement and reduction of overall porosity. The initial sorptivity is calculated as the slope of the linear fit of the data in Figure 161 for the first six hours; the secondary sorptivity is the slope of the linear fit of the absorption data from the first seven days.

Figure 162 shows the initial and secondary sorptivities of the selected UHPCs and compares them to the values obtained for conventional OPC concrete proportioned with a w/c of 0.40. The initial sorptivity has been found to be related to the porosity of the paste phase and the threshold diameter of the pores; the secondary sorptivity is related to the critical pore diameter in the paste (Cam and Neithalath 2010). Figure 162 shows that the initial and final sorptivities for the UHPCs are much lower than those of conventional OPC concrete. The secondary sorptivities of UHPCs show a much more dramatic reduction (by a factor of five), since the critical pore diameter of UHP pastes show much larger reductions than the porosities when compared to a conventional OPC paste (Arora et al. 2018).

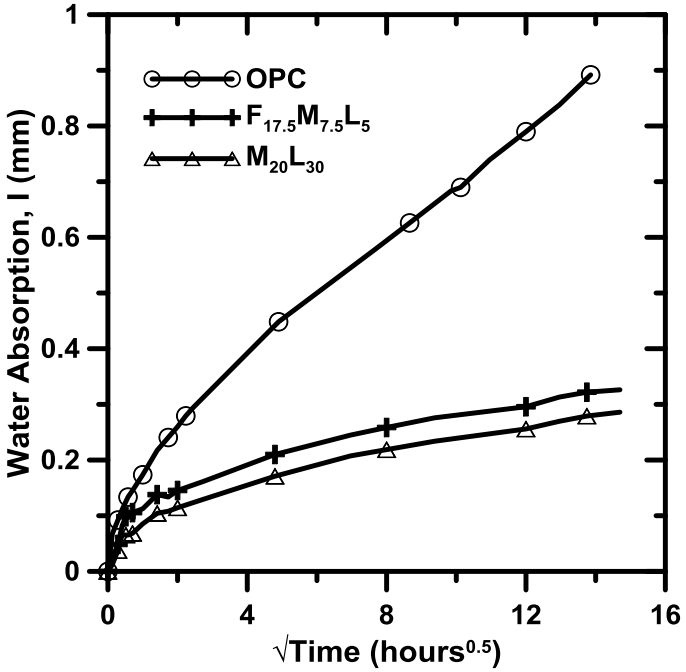

Figure 161. Water absorption as a function of time for UHPCs

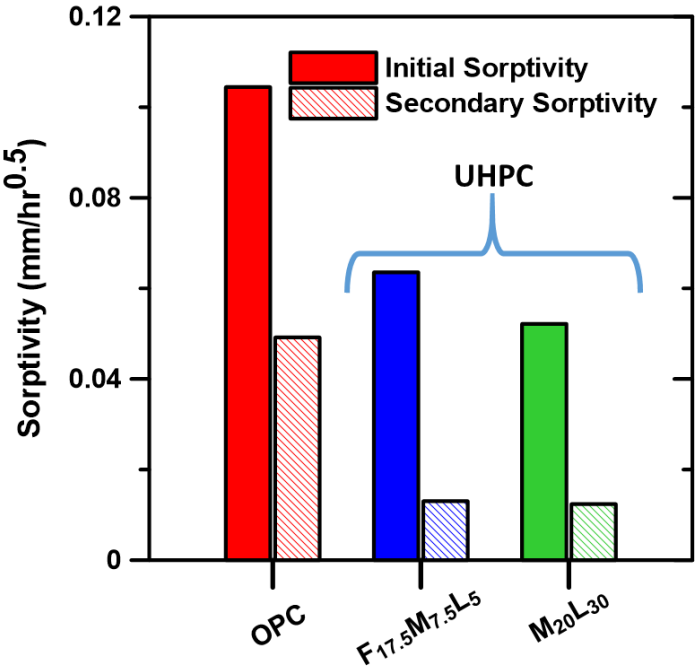

Figure 162. Initial and secondary sorptivity values of UHPCs and their comparison to a conventional OPC concrete with w/c of 0.40

Chapter 10 COST ANALYSIS

Introduction

This chapter explores in detail the cost aspects of carrying out a commercial project using the non-proprietary UHPC mixtures designed in this study. The chapter gives an overview of the cost analysis model to understand the cost implications of incorporating UHPC in an infrastructure project. The primary focus of the chapter is the analysis of the cost of raw materials required to make UHPC and how it compares with that of proprietary UHPC. The chapter explores the following topics in detail -

- The different aspects that would govern the cost of a UHPC project
- Cost benefits for infrastructure construction with UHPC versus regular concrete
- Cost of raw materials of the UHPCs designed in this study, and what materials govern the cost of the UHPC mixtures
- Possible strategies to reduce the material costs of the UHPC mixtures, and how the raw material costs of UHPC mixtures designed in this study compare with proprietary UHPC

Overview of Cost Model

Because of its high strength and durability properties, UHPC is proving to be a very useful material in infrastructural applications. However, the extremely high cost of UHPC has limited its use to a minimal number of specialized projects. Market material costs for commercial UHPC products start upwards of $\$2500/yd^3$ as compared to nearly $\$150/yd^3$ for regular concrete. In a project where UHPC will be utilized, however, several other factors besides the costs of materials, such as equipment and labor, might drive the overall cost of the project. Therefore, a thorough cost estimate and analysis is necessary to identify the significant cost components for a project.

Accurate cost estimation and forecasting techniques require a complete knowledge of the scope of the project, its scale, and the uncertainties involved in money and time. Several cost analysis models have been developed in the industry to arrive at cost estimates at different stages of a project. The accuracy of the cost models and the level of confidence depend on the level of detail carried out. Four methods primarily used for estimation of costs are (a) parametric cost estimating, (b) area and volume estimating, (c) assembly and system estimating, and (d) unit price and schedule estimating. More explanation of these cost models can be found at (Daschbach and Apgar 1988; Phaobunjong 2002). Data for cost estimates can be obtained from historical sources and existing databases (Means 2012). However, accurate cost values dependent on the project location will need to be provided by ADOT and contractors working with ADOT to obtain a precise cost estimate.

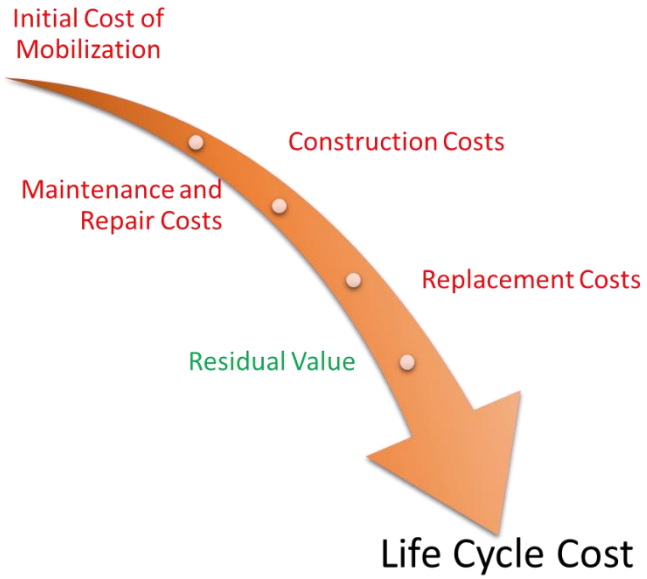

Figure 163. Life-Cycle Cost Analysis Model for UHPC

The construction costs, along with several other costs estimated over a period, such as maintenance and repair costs, determine the life-cycle costs of the project. Figure 163 shows a simple schematic of the cost model. The overall life-cycle cost of the concrete structure (C_L) is given by:

$$C_L = C_I + C_C + C_M + C_R - C_S$$ **Equation 74**

Here,

C_I is the initial cost of mobilization of the project,
C_C is the construction cost of the project,
C_M is the maintenance and repair cost of the project,
C_R is the replacement cost of the project, and
C_S is the residual value of the project.

A brief description of these costs is given below:

i. Initial cost of mobilization (C_I) – This type of cost may also be termed the initial cost or startup cost of the project. Being an unconventional material, the use of UHPC on a project would require specialized training for the workers responsible for proportioning, mixing and laying it. Specific equipment for storing the raw materials for UHPC as well as a high shear mixer for mixing UHPC would also be required. The initial cost (C_i) can be represented by Equation 75.

Equation

$$C_I = \sum_{j=1}^{j=z} (CU_{eq,j} \times n_{eq,j}) + CU_{tr} \times n_w \times hours \quad \textbf{75}$$

Here, Cu_{eq} represents the unit cost of equipment type "j" that needs to be purchased,
n_{eq} represents the amount of equipment of type "j" to be purchased,
Cu_{tr} represents the unit cost per hour for training one worker, and
n_w represents the number of workers to be trained.

ii. Construction costs (C_C) – The cost of construction includes the raw material costs (the cost of transportation to the site, the cost of aggregate sieving and crushing, the cost of preparing the formwork for pouring concrete, the cost of steel reinforcement caging, the cost of mixing and curing, the cost of quality control, the cost of traffic diversion, and the cost of energy for carrying out these activities). The cost of raw materials can be calculated using the unit price approach when the mix design is known. Other costs need to be determined from previous experience. UHPC offers a reduction in the overall volume of material used for a specific application because of its ultra-high strength, which is five to six times greater than that of regular concrete. The cost of preparing the steel reinforcement will be reduced as well, since UHPC contains embedded steel fibers between one and three percent by volume. UHPC requires an extremely high packing of aggregates, which requires aggregates conforming to a specific particle size distribution. To achieve such a gradation, aggregate crushing and sieving will lead to an increase in the overall construction cost. UHPC mixtures contain a very low water-to-binder ratio and therefore need longer mixing time to homogenize the mixture, which will drive up the energy costs for mixing. Curing for UHPC follows the same protocol and would use the same resources as that of regular concrete, so there is no incremental cost expected. In summary, the construction cost (C_c) is given by Equation 76.

Equation

$$C_C = \sum_{i=1}^{i=n} \left(C_{tn,i} + CU_{rm,i} \times m_{rm,i}\right) v_{uhpc} + C_{rc} + C_{fw} + C_{acs} + C_{mc} + C_{qc} + C_{td} \quad \textbf{76}$$

Here,

$CU_{rm,i}$ is the unit cost of the i^{th} raw material ($/lb),

$m_{rm,i}$ is the volume of the i^{th} raw material used in a unit volume of UHPC (lb/yd^3),

v_{uhpc} is the total volume of UHPC used (yd^3),

$C_{tn,i}$ is the cost of transportation of i^{th} raw material to site,

C_{rc} is the cost of steel reinforcement caging,

C_{fw} is the cost of formwork to pour concrete,

C_{asc} is the cost associated with aggregate sieving and crushing,

C_{mc} is the cost of mixing and curing of UHPC,

C_{qc} is the cost of quality control testing and verification of UHPC, and

C_{td} is the cost of traffic diversion for carrying out the construction activity.

iii. Maintenance and repair costs (C_M) – These costs include the cost of material and labor used to maintain an acceptable condition of the structure depending on a serviceability criterion. These may include filling up cracks in existing concrete structure or using carbon fiber wraps to rehabilitate the strength of the structure. The durability of UHPC is extremely high, and lab testing has shown that UHPC is nearly ten times more resilient than regular concrete against the ingress of harmful ions that cause corrosion. Therefore, it is expected that UHPC structures will last longer and require less maintenance costs than regular concrete structures when subjected to the same environmental conditions.

iv. Replacement Costs (C_R) – The replacement costs include the capital costs of removal or demolition of the existing structure and replacing it at the end of its service life. The typical service life of a regular concrete structure may range from 25 to 75 years depending on the application and type of concrete used. Since UHPC is highly resistant to moisture and corrosion, the service life of UHPC structures is expected to be much longer than that of regular concrete structures, so that the frequency of UHPC structure replacement is expected as much as five times lower than that of regular concrete.

v. Residual Value (C_S) – The residual value refers to salvage value of the materials after the service life of the structure. There has been an increase in the use of recycled concrete (Hansen and Narud 1983; Sagoe-Crentsil, Brown, and Taylor 2001; A. Rao, Jha, and Misra 2007; Tabsh and Abdelfatah 2009) in infrastructure as an aggregate over the past few years. Beyond its service life, UHPC may be used for the same purpose.

Cost Comparison – UHPC versus Regular Concrete Project

A UHPC project intended to replace a regular concrete project in the field has several sources of additional cost and several opportunities for savings. Figure 164 summarizes these factors.

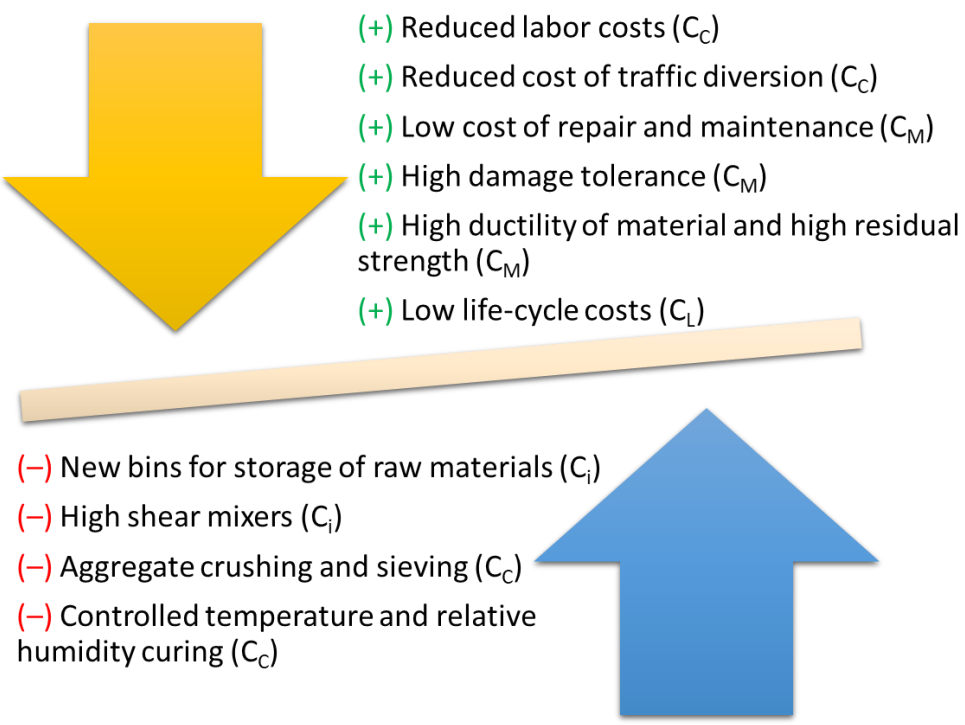

Figure 164. Additional costs and benefits of UHPC project relative to a regular concrete project

Use of UHPC would lead to lower labor costs, since it reduces the amount of material and saves time in compacting and leveling (due to its high flowability). Labor costs are also reduced in preparation of steel cage reinforcement, as the material already contains dispersed steel fibers. The cost of traffic diversion may be significant with regular concrete, which takes a long time to gain strength. Regular concrete may also entail additional cost if addition of accelerators is required to speed up the hydration process. UHPC, in contrast, gains strength in less than 72 hours, so the structure may be opened to traffic sooner. UHPC is much more durable than regular concrete and nearly five times as strong, with high damage tolerance and ductility. Therefore, UHPC has a low probability of cracking and corrosion, and hence a low expected cost of repair and maintenance.

A 2007 Michigan DOT report compared the life-cycle cost of a bridge structure (bridge girders and deck panels), constructed with normal strength concrete (NSC), to the cost of a structure built with proprietary UHPC (Ductal @ $2000/yd^3). The overall cost estimate of construction and maintenance was analyzed for a design life of 180 years. A cost sensitivity analysis was carried out with the unit material cost of UHPC as the variable, and the assessment showed that over the life cycle, a target material cost of UHPC at $1750 per cubic yard would lead the overall cost of the UHPC structure to be lower than that of the NSC structure.

Material Costs of UHPC Designed in this Study

Although several considerations affect the cost of a UHPC project, the current cost analysis is limited to analysis of the cost of raw materials and how it compares with that of proprietary UHPC. Any change in the cost of raw materials can significantly impact the overall project cost.

The material designs of proprietary UHPCs include a large amount of materials with high manufacturing and processing costs, such as nano-silica, nano-metakaolin, silica fume, silica flour, and fine ground quartz. Another material that adds to the high cost of UHPC is superplasticizer. Since UHPCs use a very low water to binder ratio (less than 0.20), a superplasticizer is necessary to compensate for the low amount of water and to attain good workability of the mixture. The UHPC mixtures in the current study have been designed using locally available materials such as fly ash, blast furnace slag, and limestone, which help reduce the costs of materials. Typical material costs obtained from local suppliers and literature (Wille and Boisvert-Cotulio 2013, Berry 2015) are shown in Table 23.

Table 23. Unit cost of raw materials

Material	$/US Ton
Coarse Aggregate	$8.25
Fine Aggregate	14
Fly Ash	50
GGBFS	17
Limestone	180
Metakaolin	400
Micro Silica	550
Nano Silica	2500
OPC	250
Silica Flour	200
Steel Fibers	3000
Superplasticizer	$15/gallon

The mixture compositions of the UHPCs selected in this study are given in Table 24.

Table 24. UHPC mixture proportions (lb/yd^3) in the study

	$F_{17.5}M_{7.5}L_5$	$M_{20}L_{30}$	$F_{17.5}M_{7.5}L_5$ – 1f	$M_{20}L_{30}$ – 1f	$F_{17.5}M_{7.5}L_5$ – 3f
OPC	1595	1321	1579	1310	1539
Fly ash (F)	280	0	276	0	270
Micro silica (M)	120	265	118	261	115

Limestone (L)	79	396	79	393	78
Coarse Aggregate	870	831	861	826	839
Fine Aggregate	580	556	573	549	560
Water	280	288	276	285	265
Fibers	0	0	126	126	379
Superplasticizer (gal/yd^3)	11.8	13.1	12.2	13.4	12.5

The total raw material cost for a UHPC mixture can be calculated using the unit price approach as shown in Equation 77.

Equation 77

$$C_{rm} = \sum_{i=1}^{i=n} (CU_{rm,i} \times m_{rm,i}) v_{uhpc}$$

Here,

C_{rm} is the total raw material cost of UHPC

$CU_{rm,i}$ is the unit cost of the ith raw material ($/lb),

$m_{rm,i}$ is the volume of the ith raw material used in a unit volume of UHPC (lb/yd^3),

v_{uhpc} is the total volume of UHPC used (yd^3),

Using Equation 77 and data from Table 23 and Table 24, we can calculate the total cost of UHPC mixtures designed in this study. The cost calculations for one cubic yard of UHPC ($F_{17.5}M_{7.5}L_5$) are shown below, resulting in a total of $417 per cubic yard. Cost calculations can be carried out for the remaining four UHPC mixtures as well.

Equation 78

$$C_{rm} = \left(1595\ \frac{lb}{yd^3} \times 0.125 \frac{\$}{lb} + 280 \frac{lb}{yd^3} \times 0.025 \frac{\$}{lb} + 120 \frac{lb}{yd^3} \times 0.275 \frac{\$}{lb} + 79 \frac{lb}{yd^3} \times 0.090 \frac{\$}{lb} + 870 \frac{lb}{yd^3} \times 0.004 \frac{\$}{lb} + 580 \frac{lb}{yd^3} \times 0.007 \frac{\$}{lb} + 280 \frac{lb}{yd^3} \times 0 \frac{\$}{lb} + 0 \frac{lb}{yd^3} \times 1.5 \frac{\$}{lb} + 11.8 \frac{lb}{yd^3} \times 1.710 \frac{\$}{lb}\right) \times 1.0\ yd^3$$

$$C_{rm} = \$417$$

Figure 165 shows the cost of raw materials required to proportion the selected UHPC mixtures, with and without fibers, while Figure 166 provides the relative cost of each of the mixture components as a fraction of the total cost of the mixture. It should be noted here that the cost of water is not accounted for in these calculations. These figures clearly demonstrate that, from a cost perspective, superplasticizer and fibers comprise the major portion of the cost of UHPC, followed by OPC. In mixtures where the paste fraction is not optimized, the OPC cost can be still higher. A higher OPC content leads to

other environmental impacts associated with such mixtures, reinforcing the importance of a mixture selection strategy as explained in Chapters 5 and 6. Please note that the costs shown here are in 2018 constant dollars.

In conjunction with the material design strategy described in Chapters 5 and 6, an understanding of the materials' costs, local availability, and energy/environmental implications can be used to conduct life-cycle cost and impact analyses which help decision-makers choose the appropriate material combinations for UHPC applications. This analysis does not address the capital investment necessary for equipment required to crush, sieve, and proportion large volumes of aggregates. The analysis also does not address the cost of energy and environmental impacts.

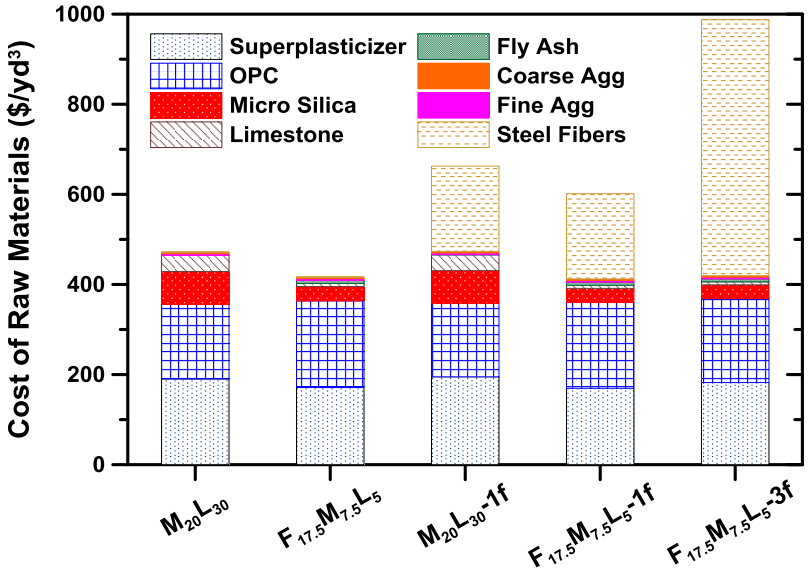

Figure 165. Cost of raw materials per yd^3 of selected UHPC mixtures

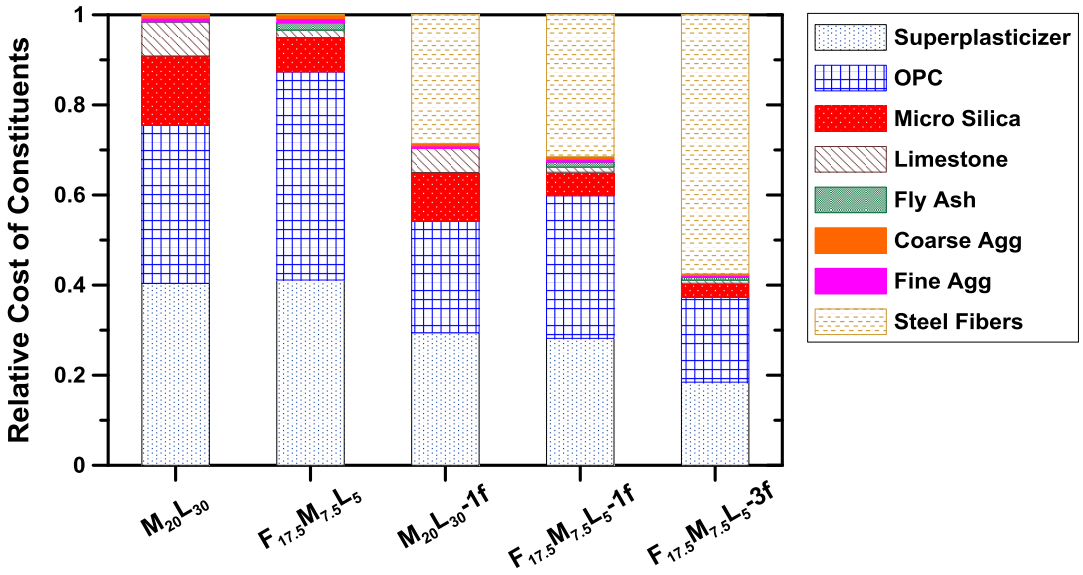

Figure 166. Relative cost of the individual components in the UHPC mixtures

Alternative scenarios to reduce material costs

Figure 166 shows that the four major components of cost in the UHPC mixtures are steel fibers, superplasticizer, OPC, and silica fume. Therefore, to reduce the overall cost of UHPC mixtures, these component materials need to be replaced, wholly or partially, with a less expensive material. Of course, all materials are in the mix to serve a specific purpose, and substitutions may sacrifice quality, thereby raising cost in the long run. A change in the mix design will compromise one or more properties of UHPC, such as workability, mechanical strength, or durability. For instance, OPC is the most massive ingredient in the mixtures and reacts with water to form hydration products that gain strength over time. Similarly, steel fibers improve the ductility of the mixture, silica fume reduces porosity to improve durability, and superplasticizer improves the workability.

One scenario to reduce costs would be to reduce superplasticizer and add more water instead, such that the water to binder ratio remains the same. This would lead to a reduction in the workability and longer mixing times. However, it would not compromise the strength or durability. Figure 10-5 shows a cost comparison of the five mixtures with a 20 percent reduction in the superplasticizer content. The mixtures with the superplasticizer reduction are shown on the right next to their original costs.

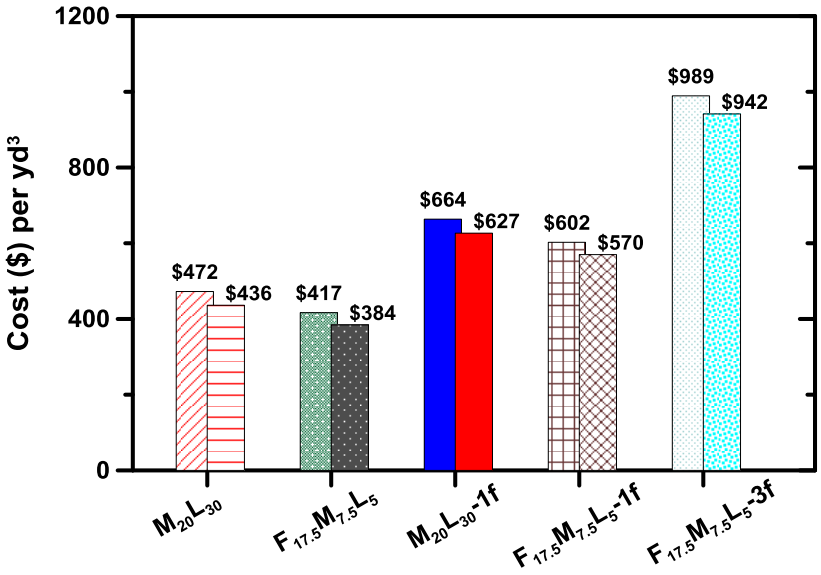

Figure 167. Cost comparison of concrete mixtures – original versus new with a 20% reduction in superplasticizer

The cost of materials and the relative cost of the components for this scenario are shown in Figures 10-6 and 10-7 respectively.

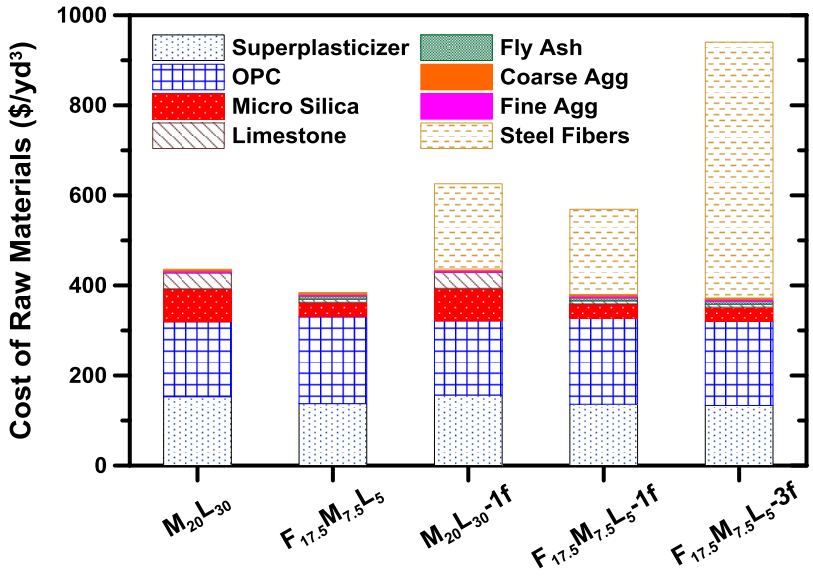

Figure 168. Cost of raw materials per yd^3 of selected UHPC mixtures accounting for 20% reduction in superplasticizer content

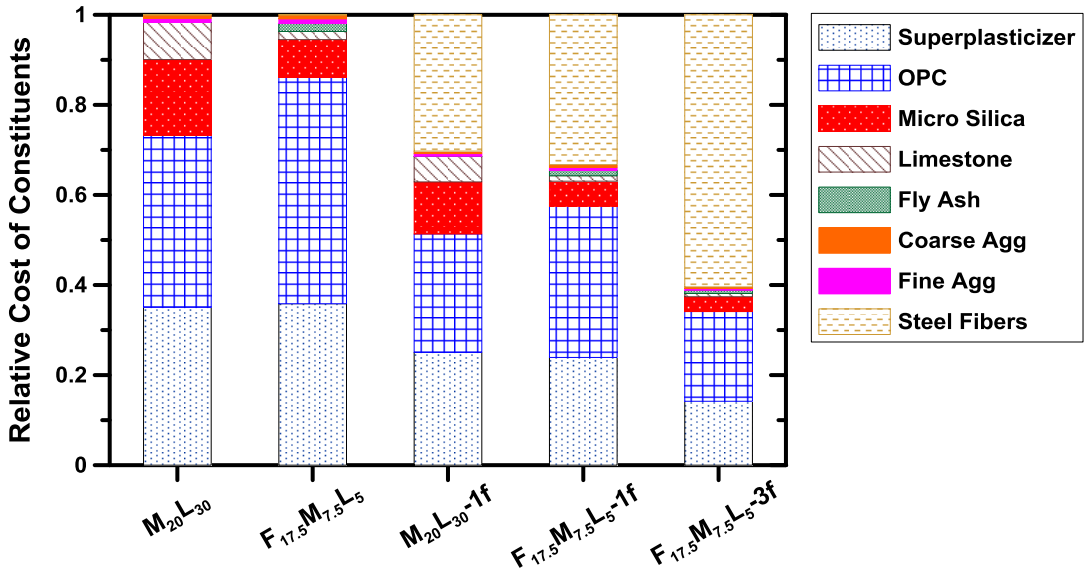

Figure 169. Relative cost of the individual components in the UHPC mixtures accounting for 20% reduction in superplasticizer content

Another scenario is increasing the water to binder ratio from 0.20 to 0.24, which would reduce the overall amount of cement and other cement replacement materials and therefore reduce costs significantly. However, this would cause a significant reduction in strength, as more water would lead to more pores in the microstructure as well as a reduction in the packing. The increased porosity would also detrimentally affect the durability of the concrete formed. However, if having an extremely high strength is not the prime concern, a higher water to binder ratio may be preferred. The workability in this scenario will depend on the superplasticizer content. The costs associated with this scenario are presented in Figure 170. All the results in Figure 170, Figure 171, Figure 172 are presented for a water to binder ratio of 0.24 and a superplasticizer content of 4 percent.

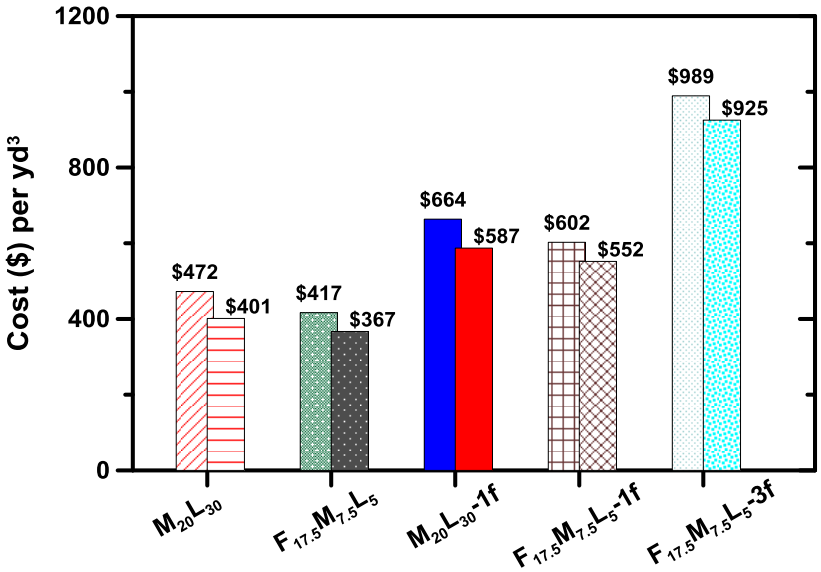

Figure 170. Cost comparison of concrete mixtures – original versus new with a water to binder ratio of 0.24 and superplasticizer content of 4%

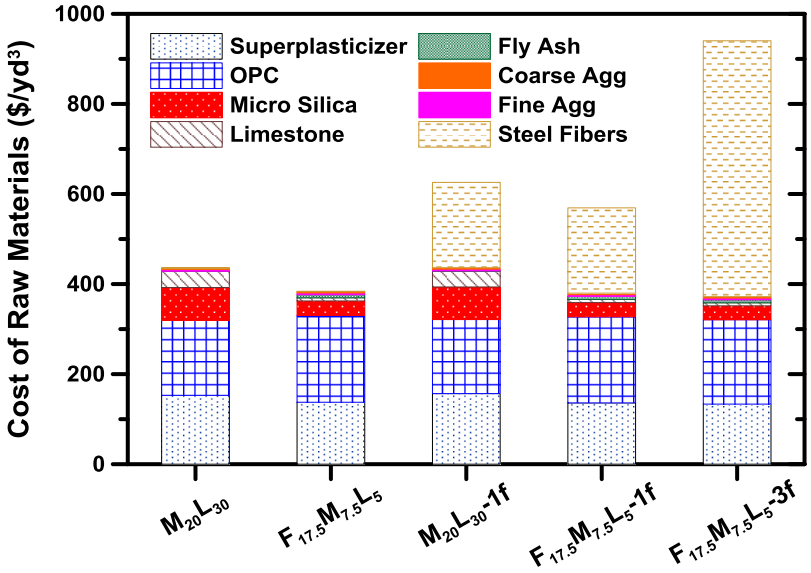

Figure 171. Cost of raw materials per yd^3 of selected UHPC mixtures accounting for a water to binder ratio of 0.24

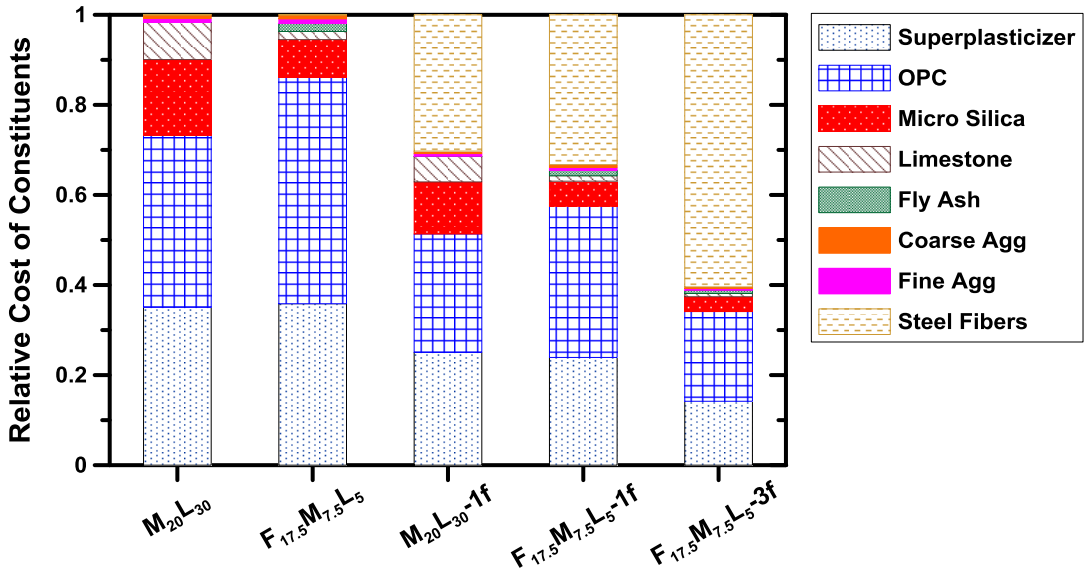

Figure 172. Relative cost of the individual components in the UHPC mixtures accounting for a water to binder ratio of 0.24

These scenarios provide a cost comparison of two ways to alter the mixture design to reduce the overall cost of the concrete. A cost analysis tool is provided to aid the user with the cost analysis of UHPC mix designs different from the ones already analyzed in this chapter. However, any change in the mix design must be accompanied with the results for strength and durability to make sure that the required values are attained for a particular infrastructural application.

Comparison of Costs Obtained and Overall Cost Estimation

Figure 173 shows a comparison between the material costs of the UHPC mixtures designed in this study and the UHPC mixtures designed by Wille et. al. in an earlier study in 2013. While all of the mixtures here meet the minimum strength requirement for being classified as UHPC mixtures (20 ksi), the costs for the mixtures designed in this study are slightly lower than the costs calculated by Wille et. al. The mix designs in Wille's 2013 study contain a large amount of silica fume, which is the main reason for the higher costs.

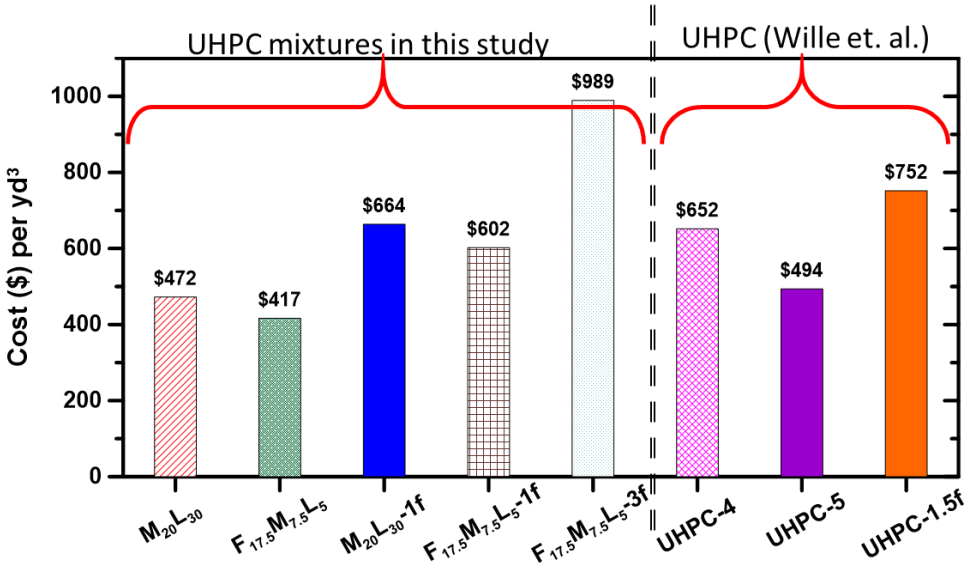

Figure 173. Comparison of material cost of UHPC mixtures designed in this study versus UHPC mixtures designed by Wille and Boisvert-Cotulio 2013

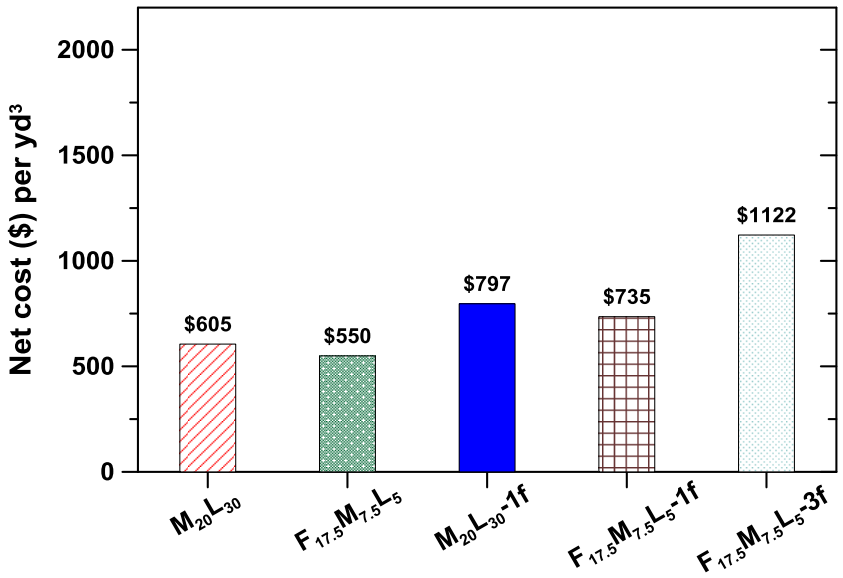

Figure 174. Net cost per yd^3 of UHPC mixtures designed in this study

To use UHPC in real-life applications and infrastructure projects, material costs need to be supplemented with operational costs for mixing, handling, and delivery, as elaborated in the previous sections. Quality control will add to the cost of the mixture as well. While these costs may vary between projects, a simplified cost calculation is presented in Figure 174. The operational costs are based on the cost of ordinary concrete and are estimated as a 30 percent surcharge on the cost of ordinary concrete. The cost of quality control testing and verification is estimated at $100/yd^3.

Cost Sensitivity

The cost of raw materials may vary over the course of a single project for several reasons. Therefore, it is important to understand the changes in the cost of the UHPC mixtures when the material costs are affected by fluctuations in the market. The overall material cost variations for the UHPC mixture is calculated due to fluctuations in the cost of a single ingredient within the range of -80% to +200% percent of its current cost as obtained from Table 23. The cost sensitivity as a function of spikes in the price of a single ingredient were conducted for coarse aggregates, superplasticizer, micro-silica, and steel fibers.

The results of the cost sensitivity analysis are presented in Figure 175 and Figure 176 for one non-fiber-reinforced mixture and one fiber-reinforced mixture. The zero mark on the x-axis corresponds to the current cost of the materials in the mix design. Any value on the right side of the current cost signifies a percentage increment in the material cost, whereas any value on the left side of the current cost signifies a percentage decrease in the material cost. The slope of each line on the cost sensitivity analysis plot indicates the degree of fluctuation of the overall cost with respect to a change in the cost of that material. While a change in the cost of coarse aggregates to even twice the current cost structure does not significantly affect the overall cost of the mixture, a slight change in the cost of superplasticizer or steel fibers leads to a substantial changes in the cost model. This is because the unit cost of coarse aggregates by weight/volume is relatively low compared to that of superplasticizer. Similar trends are identified in both figures.

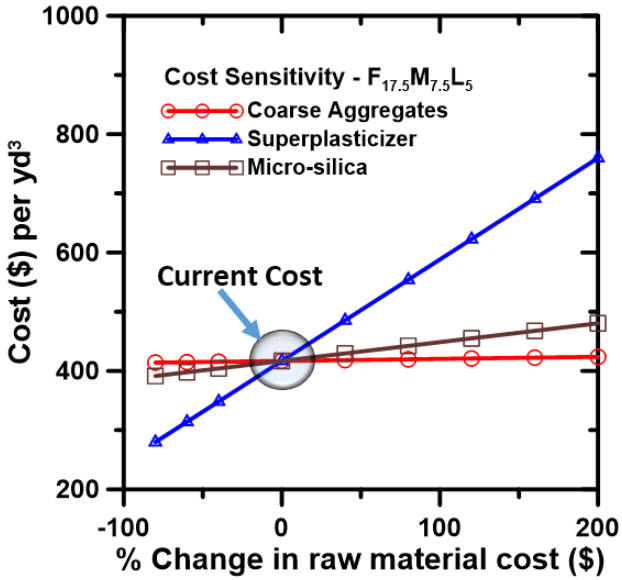

Figure 175. Cost sensitivity analysis for the non-fiber-reinforced mixture ($F_{17.5}M_{7.5}L_5$)

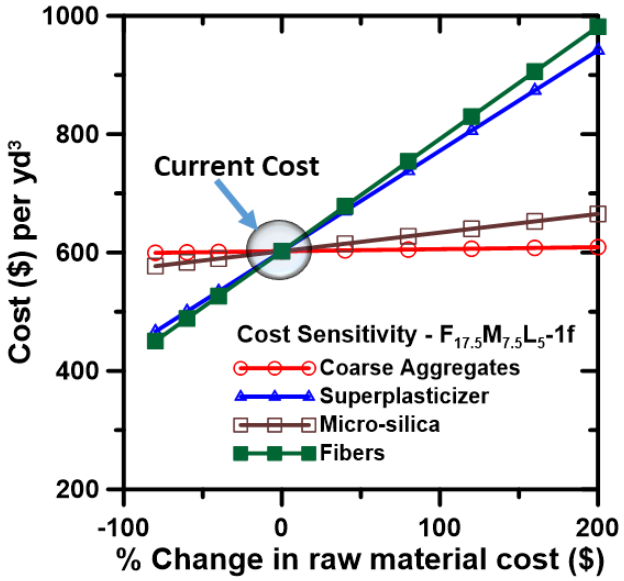

Figure 176. Cost sensitivity analysis for the fiber-reinforced mixture ($F_{17.5}M_{7.5}L_5$-1f)

Summary of Material Cost Analysis

The cost per cubic yard and the strength-normalized cost (cost normalized by the 28-day compressive strength) of the selected UHPC mixtures are shown in Figure 177 and Figure 178. The material costs are calculated using the unit price approach (Equation 78). The cost for ordinary concrete (w/c = 0.40) has also been calculated in Figure 177. The cost of proprietary UHPC has been obtained from FHWA reports (B. Graybeal 2011).

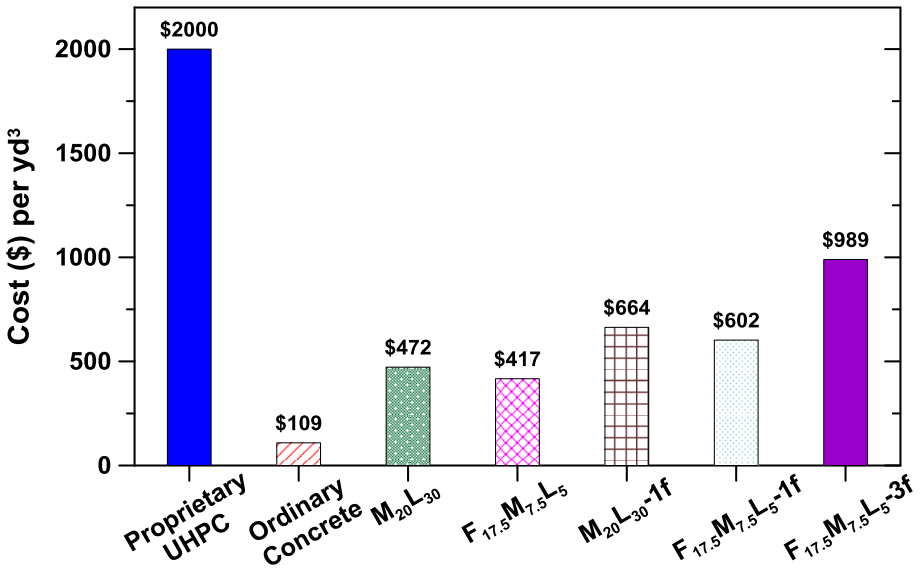

Figure 177. Comparison of raw material cost ($) per cubic yard of UHPCs designed in this study versus proprietary UHPC and ordinary concrete

Figure 178 shows that proprietary UHPC mixtures cost nearly 20 times as much (by volume) as ordinary concrete. While non-proprietary UHPC will cost several times more than ordinary concrete, their cost is only about one-fourth to one-half that of the proprietary product shown here. Compared to proprietary UHPC mixtures that are reported to cost between $2000 and $3500 per yd^3, the UHPC mixtures designed by the authors are a more economical alternative, making it a viable alternative for transportation and infrastructural agencies interested in high-strength and high-performance mixtures. From a compressive strength-normalized cost perspective, the fiber-reinforced mixtures appear less attractive, but realistically, they should be compared based on ductility or post-cracking, tensile-strength-normalized cost to ensure fair comparisons. Consideration of all known costs, not just those of construction or raw materials, can help ADOT make the best decision for each project.

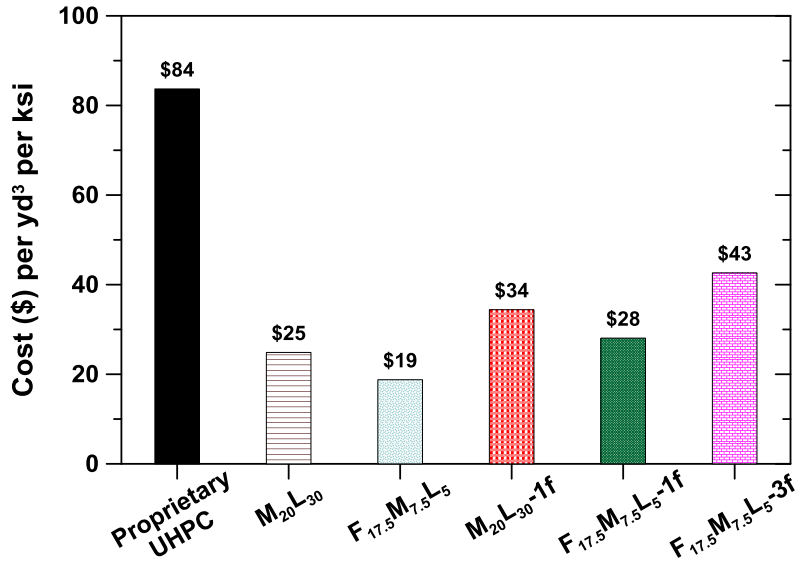

Figure 178. Comparison of volumetric cost ($) per ksi of compressive strength

Chapter 11 SUMMARY OF FINDINGS

This study provides state transportation agencies an opportunity to capitalize on the benefits of UHPC as a unique material capable of providing enhanced load carrying capacity, ductility, and extremely high durability to state infrastructures. The work focused on developing ultra high–performance (UHPC) mix designs for use in bridge element connections, but the findings may be applicable for other elements in transportation infrastructure. A systematic and structured approach based on fundamentals of materials science, mechanics of materials, structural analysis of nonlinear materials, and structural design based on load and resistance factor design (LRFD) approach was used. This study focused on the development of design equations when the tensile cracking in the material is suppressed and controlled so that the residual tensile strength of the fiber reinforced high-performance system can be accounted for in the design.

One of the key objectives of the study was to develop non-proprietary UHPC mix designs that incorporate materials that are commercially available in Arizona. Several such mix designs were developed and tested during the study. The mix designs exhibited characteristics that exceeded acceptable performance, and analysis shows these designs to be at a lower cost than UHPC incorporating proprietary materials. The information below includes many of the material requirements, performance results, and mixing needs. Note that the UHPC mixtures in this study can be proportioned at less than half of the cost of commercially available UHPC. (See Chapter 10 for more detail on Cost Analysis.)

Materials and Mix Design

- Ternary mixtures containing a combination of cement, pozzolans like fly ash or blast furnace slag, and highly reactive materials like metakaolin or silica fume perform better in terms of strength development. To make the ternary mixtures economical, a fraction of such higher-cost items as silica fume or metakaolin may be substituted by fine limestone to form quaternary UHPC mixtures.

- The ternary and quaternary mixtures can have cement substitution levels ranging from 20% to 50%. Cement is the primary material in terms of mass in these mixture compositions. Pozzolans like fly ash or blast furnace slag are the secondary materials, followed by silica fume and metakaolin as the tertiary materials, and lastly followed by limestone.

- The effective water to binder ratio for UHPC mixtures between 0.18 to 0.24 is suggested with a superplasticizer content ranging between 2% to 5% by weight of the binder. The higher the water to binder ratio, the less is the amount of superplasticizer required to maintain workability.

- The selection of paste to aggregate ratio is a critical component in the design of UHPC mixtures. The paste to aggregate ratio suggested in this study is 65:35 by volume.

- The type and size distribution of aggregates is a key factor in determining the packing density of UHPC and ultimately the mechanical properties. Aggregate sizes smaller than ¼" were used in this study and are recommended for future use.

- Determination of the appropriate amount of coarse aggregate sizes was explained using a compressible packing model. The aggregate compositions obtained using the model have nearly 20% higher packing densities as compared to standard aggregate stockpiles that are commercially available and used.

- The lower water to binder ratio in UHPC mixtures leads to complication in mixing the components. Commonly available drum mixers and planetary mixers were found to be unsuitable for preparing UHPC. Results of a mixer evaluation study showed that beams mixed with a high-shear mixer have a residual strength 12% greater than that of beams made using a hand-drill. This can be attributed to a more uniform fiber distribution during the mixing procedure. A shear mixer with a high RPM is part of capital equipment required for making UHPC mixtures. A medium size high shear mixer with a capacity of 10 cubic feet and RPM rate of 74 RPM was found to be suitable for producing small UHPC batches in this study. (See Chapter 6 for more detail)

- A steel fiber content of 1% to 3% is the appropriate fiber content based on ductility requirements for a UHPC application. A high fiber content leads to a higher ductility.

Performance and Cost

- The appropriate selection of water to binder ratio and superplasticizer directly influences the mechanical and durability properties of UHPC. A higher water to binder content would lower the mechanical strength as well as the durability, while a lower water to binder ratio will have opposite effects, however, one would reach a point of diminishing returns when there is not sufficient water for hydration of the cement and self-desiccation would affect the mechanical strength and durability.

- A lower water to binder ratio would also result in a higher material cost to manufacture UHPC.

- The ideal UHPC binder formulation was selected from several blends using a stepwise algorithm that considered the effects of microstructural packing and rheological properties of the binder. The proposed methodology allows the user to select mixtures based on acceptable ranges of microstructural packing and workability demanded by the application. The selected binder formulations were evaluated and 28-day compressive strengths close to 15 ksi were obtained for all binders. (See Chapter 5 for more details)

- Compressive strengths after 28 days were higher than 22 ksi for all the UHPC mixtures and flexural strengths exceeded 1500 psi. The UHPC samples with straight steel fibers demonstrated

high ductility under both compression and flexure loading. The addition of 1% steel fibers increased the toughness by over 40 times when compared to the mixtures with no fibers.

- The increase in fiber content from 1% to 3% leads increases flexural strength from 1500 psi to 3000 psi, increase in the elastic modulus by 20% and increase load carrying capacity by nearly 70 percent. Beams with higher fiber content show reduced crack opening, multiple cracking, and higher residual strengths in the post-peak region.
- UHPC beams containing 3% fibers can maintain 40% of its initial stiffness even after numerous cycles of loading and unloading.
- Durability testing using chloride transport tests show that UHPC mixtures designed in this study are nearly 10 times more resistant to chloride ion ingress and are more durable and reduce steel corrosion.
-

REFERENCES

Aaleti, Sriram, and Sri Sritharan. 2014. “Design of Ultrahigh-Performance Concrete Waffle Deck for Accelerated Bridge Construction.” *Transportation Research Record: Journal of the Transportation Research Board* 2406 (July): 12–22. https://doi.org/10.3141/2406-02.

Abbas, S., M. L. Nehdi, and M. A. Saleem. 2016a. “Ultra-High Performance Concrete: Mechanical Performance, Durability, Sustainability and Implementation Challenges.” *International Journal of Concrete Structures and Materials* 10 (3): 271–295.

———. 2016b. “Ultra-High Performance Concrete: Mechanical Performance, Durability, Sustainability and Implementation Challenges.” *International Journal of Concrete Structures and Materials*, June, 1–25. https://doi.org/10.1007/s40069-016-0157-4.

Abbas, Safeer, Ahmed M. Soliman, and Moncef L. Nehdi. 2015. “Exploring Mechanical and Durability Properties of Ultra-High Performance Concrete Incorporating Various Steel Fiber Lengths and Dosages.” *Construction and Building Materials* 75 (January): 429–41. https://doi.org/10.1016/j.conbuildmat.2014.11.017.

ACI 544. 2016. “544.7R-16 Report on Design and Construction of Fiber-Reinforced Precast Concrete Tunnel Segments.” ACI Committee 544.

ACI Committee 239. n.d. “ACI Committee 239, ‘Committee in Ultra-High Performance Concrete,.’”

ACI Committee 318, and American Concrete Institute. 2014. *Building Code Requirements for Structural Concrete (ACI 318-14): An ACI Standard : Commentary on Building Code Requirements for Structural Concrete (ACI 318R-14), an ACI Report*.

Ahlborn, Theresa, Devin Harris, Donald Misson, and Erron Peuse. 2011. “Characterization of Strength and Durability of Ultra-High-Performance Concrete Under Variable Curing Conditions.” *Transportation Research Record: Journal of the Transportation Research Board* 2251 (December): 68–75. https://doi.org/10.3141/2251-07.

Ahlborn, Theresa M., Donald Li Misson, Erron J. Peuse, and Christopher G. Gilbertson. 2008. “Durability and Strength Characterization of Ultra-High Performance Concrete under Variable Curing Regimes.” In *Proc. 2nd Int. Symp. on Ultra High Performance Concrete, Fehling, E., Schmidt, M., & Stürwald, S.(Eds.) Kassel, Germany*, 197–204.

Aim, R. Ben, and P. Le Goff. 1969. “Porosité Des Mélanges Binaires de Sphères et d’objets à Symétrie Cylindrique.” *Powder Technology* 2 (3): 169–74. https://doi.org/10.1016/0032-5910(69)80006-9.

Alkaysi, Mo, Sherif El-Tawil, Zhichao Liu, and Will Hansen. 2016. “Effects of Silica Powder and Cement Type on Durability of Ultra High Performance Concrete (UHPC).” *Cement and Concrete Composites* 66 (February): 47–56. https://doi.org/10.1016/j.cemconcomp.2015.11.005.

Almansour, H., and Z. Lounis. 2010. “Innovative Design Approach of Precast–Prestressed Girder Bridges Using Ultra High Performance Concrete.” *Canadian Journal of Civil Engineering* 37 (4): 511–521.

Antoni, M., J. Rossen, F. Martirena, and K. Scrivener. 2012. “Cement Substitution by a Combination of Metakaolin and Limestone.” *Cement and Concrete Research* 42 (12): 1579–89. https://doi.org/10.1016/j.cemconres.2012.09.006.

Ariño, Antonio M., and Barzin Mobasher. 1999. “Effect of Ground Copper Slag on Strength and Toughness of Cementitious Mixes.” *ACI Materials Journal* 96 (1). https://asu.pure.elsevier.com/en/publications/effect-of-ground-copper-slag-on-strength-and-toughness-of-cementi.

Arora, Aashay. 2018. “Evaluation of the Performance of Multi-Component Cementitious Composites: Multi-Scale Experimental Characterization and Numerical Simulation.” Ph.D., United States -- Arizona: Arizona State University.

https://search.proquest.com/pqdtglobal/docview/2154864839/abstract/9B029C95683F4B09PQ/1.
Arora, Aashay, Matthew Aguayo, Hannah Hansen, Cesar Castro, Erin Federspiel, Barzin Mobasher, and Narayanan Neithalath. 2018. "Microstructural Packing- and Rheology-Based Binder Selection and Characterization for Ultra-High Performance Concrete (UHPC)." *Cement and Concrete Research* 103 (January): 179–90. https://doi.org/10.1016/j.cemconres.2017.10.013.
Arora, Aashay, Gaurav Sant, and Narayanan Neithalath. 2016. "Ternary Blends Containing Slag and Interground/Blended Limestone: Hydration, Strength, and Pore Structure." *Construction and Building Materials* 102, Part 1 (January): 113–24. https://doi.org/10.1016/j.conbuildmat.2015.10.179.
Arora, Aashay, Kirk Vance, Gaurav Sant, and Narayanan Neithalath. 2016. "A Methodology to Extract the Component Size Distributions in Interground Composite (Limestone) Cements." *Construction and Building Materials* 121 (September): 328–37. https://doi.org/10.1016/j.conbuildmat.2016.06.006.
ASTM C 1202, Standard. 2017. "Standard Test Method for Electrical Indication of Concrete's Ability to Resist Chloride Ion Penetration." *West Conshohocken, PA: ASTM International*.
ASTM C 1585, C. 2013. "1585-04. Standard Test Method for Measurement of Rate of Absorption of Water by Hydraulic-Cement Concretes." *ASTM International*.
ASTM, C29. 1997. "Test Method for Bulk Density ('Unit Weight') and Voids in Aggregate." *Philadelphia, PA: American Society for Testing and Materials*.
ASTM C944. 2012. "ASTM C944 / C944M - 12. Standard Test Method for Abrasion Resistance of Concrete or Mortar Surfaces by the Rotating Cutter Method." *ASTM International, West Conshohocken, PA (2012)*.
"ASTM C1202 - 12. Standard Test Method for Electrical Indication of Concrete's Ability to Resist Chloride Ion Penetration." 2012. *ASTM International, West Conshohocken, PA (2012)*.
ASTM C1260. 2014. "ASTM C1260 - 14. Standard Test Method for Potential Alkali Reactivity of Aggregates (Mortar-Bar Method)." *ASTM International, West Conshohocken, PA (2014)*.
ASTM C1585. 2013. "ASTM C1585 - 13. Standard Test Method for Measurement of Rate of Water by Hydraulic-Cement Concretes." *ASTM International, West Conshohocken, PA (2013)*.
Attar, A., A. Bendada, R. Connolly, Y. Denomme, E. Dallaire, and P. C. Aitcin. 2000. "Novel Ultra-High Performance Concrete as Mold Material for the Blow Molding Process." *Sampe Journal* 36 (3): 45–49.
Bakhshi, Mehdi, Christopher Barsby, and Barzin Mobasher. 2014. "Comparative Evaluation of Early Age Toughness Parameters in Fiber Reinforced Concrete." *Materials and Structures* 47 (5): 853–72. https://doi.org/10.1617/s11527-013-0098-1.
Bakhshi, Mehdi, Busaba Laungrungrong, Aboozar Bonakdar, and Barzin Mobasher. 2013. "Economical Concrete Mix Design Utilizing Blended Cements, Performance-Based Specifications, and Pay Factors." ADOT AZ633. Arizona Department of Transportation. https://www.azdot.gov/planning/research-center/research/research-reports.
Bakhshi, Mehdi, Busaba Laungrungrong, Aboozar Bonakdar, Barzin Mobasher, Connie M. Borror, and Douglas C. Montgomery. 2013. "Economical Concrete Mix Design Utilizing Blended Cements, Performance-Based Specifications, and Pay Factors," May. https://trid.trb.org/view.aspx?id=1252518.
Balaguru, P., Ramesh Narahari, and Mehendra Patel. 1992. "Flexural Toughness of Steel Fiber Reinforced Concrete." *Materials Journal* 89 (6): 541–546.
Banthia, Nandakumar, and N. Nandakumar. 2003. "Crack Growth Resistance of Hybrid Fiber Reinforced Cement Composites." *Cement and Concrete Composites* 25 (1): 3–9.

Barros, Joaquim A. O., V. M. C. F. Cunha, A. F. Ribeiro, and J. a. B. Antunes. 2005. "Post-Cracking Behaviour of Steel Fibre Reinforced Concrete." *Materials and Structures* 38 (1): 47–56. https://doi.org/10.1007/BF02480574.

Batson, Gordon. 1976. "Steel Fiber Reinforced Concrete." *Materials Science and Engineering* 25: 53–58.

Bayasi, Ziad, and Jing Zhou. 1993. "Properties of Silica Fume Concrete and Mortar." *Materials Journal* 90 (4): 349–56.

Behloul, M., G. Bernier, and M. Cheyrezy. 1996. "Tensile Behavior of Reactive Powder Concrete (RPC)." In *Proceedings of the 4th International Symposium on Utilization of HSC/HPC, BHP*, 96:1375–1381.

Behloul, M., G. Chanvillard, P. Pimienta, A. Pineaud, and P. Rivillon. 2005. "Fatigue Flexural Behavior of Pre-Cracked Specimens of Special UHPFRC." *Special Publication* 228: 1253–1268.

Bencardino, Francesco, Lidia Rizzuti, Giuseppe Spadea, and Ramnath N. Swamy. 2008. "Stress-Strain Behavior of Steel Fiber-Reinforced Concrete in Compression." *Journal of Materials in Civil Engineering* 20 (3): 255–63. https://doi.org/10.1061/(ASCE)0899-1561(2008)20:3(255).

Benson, S. D. P., and B. L. Karihaloo. 2005. "CARDIFRC®-Development and Mechanical Properties. Part III: Uniaxial Tensile Response and Other Mechanical Properties." *Magazine of Concrete Research* 57 (8): 433–443.

Bentur, A., and S. Mindess. 1990. *Fiber Reinforced Cementitious Composites, London and New York*. Elsevier Applied Science.

Bernard, E. S. 2004. "Durability of Cracked Fibre Reinforced Shotcrete." *Shotcrete: More Engineering Developments, Taylor and Francis, London, ES Bernard (Ed)*, 59–66.

Bierwagen, D., B. Moore, and V. Perry. 2006. "Revolutionary Concrete Solutions." *Construction Specifier*.

Birchall, J. D., K. I. Majid, B. W. Staynes, A. A. Rahman, N. J. Dave, H. F. W. Taylor, F. Tamas, et al. 1983. "Cement in the Context of New Materials for an Energy-Expensive Future [and Discussion]." *Philosophical Transactions of the Royal Society of London A: Mathematical, Physical and Engineering Sciences* 310 (1511): 31–42. https://doi.org/10.1098/rsta.1983.0063.

Boddy, A. M, R. D Hooton, and M. D. A Thomas. 2000. "The Effect of Product Form of Silica Fume on Its Ability to Control Alkali–Silica Reaction." *Cement and Concrete Research* 30 (7): 1139–50. https://doi.org/10.1016/S0008-8846(00)00297-0.

Bonen, David, and Sidney Diamond. 1992. "Occurrence of Large Silica Fume-Derived Paticles in Hydrated Cement Paste." *Cement and Concrete Research* 22 (6): 1059–66. https://doi.org/10.1016/0008-8846(92)90036-U.

Cam, Hieu T., and Narayanan Neithalath. 2010. "Moisture and Ionic Transport in Concretes Containing Coarse Limestone Powder." *Cement and Concrete Composites* 32 (7): 486–96. https://doi.org/10.1016/j.cemconcomp.2010.04.002.

Camiletti, J., A. M. Soliman, and M. L. Nehdi. 2012. "Effects of Nano- and Micro-Limestone Addition on Early-Age Properties of Ultra-High-Performance Concrete." *Materials and Structures* 46 (6): 881–98. https://doi.org/10.1617/s11527-012-9940-0.

Cheng-yi, Huang, and R. F. Feldman. 1985. "Hydration Reactions in Portland Cement-Silica Fume Blends." *Cement and Concrete Research* 15 (4): 585–92. https://doi.org/10.1016/0008-8846(85)90056-0.

Cheyrezy, M., V. Maret, and L. Frouin. 1995. "Microstructural Analysis of Rpc (Reactive Powder Concrete)." *Cement and Concrete Research* 25 (7): 1491–1500. https://doi.org/10.1016/0008-8846(95)00143-Z.

Choi, Myoung Sung, Jung Soo Lee, Keum Seong Ryu, Kyung-Taek Koh, and Seung Hee Kwon. 2016. "Estimation of Rheological Properties of UHPC Using Mini Slump Test." *Construction and Building Materials* 106 (March): 632–39. https://doi.org/10.1016/j.conbuildmat.2015.12.106.

Committee 544, A. C. I. 2016. *ACI 544. 8R-16 Report on Indirect Method to Obtain Stress-Strain Response of Fiber-Reinforced Concrete (FRC)*. American Concrete Institute.

"Correlated Solutions – VIC-2D™." n.d. Accessed December 19, 2017. http://correlatedsolutions.com/vic-2d/.

D. P. Bentz. 2005. "CEMHYD3D: A Three-Dimensional Cement Hydration and Microstructure Development Modeling Package. Version 3.0. NISTIR 7232." *US Department of Commerce*.

Das, Sumanta, Matthew Aguayo, Vikram Dey, Robert Kachala, Barzin Mobasher, Gaurav Sant, and Narayanan Neithalath. 2014. "The Fracture Response of Blended Formulations Containing Limestone Powder: Evaluations Using Two-Parameter Fracture Model and Digital Image Correlation." *Cement and Concrete Composites* 53: 316–326.

Das, Sumanta, Matthew Aguayo, Gaurav Sant, Barzin Mobasher, and Narayanan Neithalath. 2015a. "Fracture Process Zone and Tensile Behavior of Blended Binders Containing Limestone Powder." *Cement and Concrete Research* 73: 51–62.

———. 2015b. "Fracture Process Zone and Tensile Behavior of Blended Binders Containing Limestone Powder." *Cement and Concrete Research* 73 (July): 51–62. https://doi.org/10.1016/j.cemconres.2015.03.002.

Daschbach, J. M., and Henry Apgar. 1988. "Design Analysis through Techniques of Parametric Cost Estimation." *Engineering Costs and Production Economics* 14 (2): 87–93. https://doi.org/10.1016/0167-188X(90)90111-T.

De Larrard, Francois. 1999. *Concrete Mixture Proportioning: A Scientific Approach*. CRC Press.

Destrée, Xavier, Yiming Yao, and Barzin Mobasher. 2015. "Sequential Cracking and Their Openings in Steel-Fiber-Reinforced Joint-Free Concrete Slabs." *Journal of Materials in Civil Engineering* 28 (4). https://doi.org/10.1061/(ASCE)MT.1943-5533.0001377.

Dewar, Joe. 2002. *Computer Modelling of Concrete Mixtures*. CRC Press.

Dils, J., V. Boel, and G. De Schutter. 2013. "Influence of Cement Type and Mixing Pressure on Air Content, Rheology and Mechanical Properties of UHPC." *Construction and Building Materials* 41 (April): 455–63. https://doi.org/10.1016/j.conbuildmat.2012.12.050.

Dinh, Hai H., Gustavo J. Parra-Montesinos, and James K. Wight. 2010. "Shear Strength Model for Steel Fiber Reinforced Concrete Beams without Stirrup Reinforcement." *Journal of Structural Engineering* 137 (10): 1039–1051.

Dugat, J., N. Roux, and G. Bernier. 1996. "Mechanical Properties of Reactive Powder Concretes." *Materials and Structures* 29 (188): 233–40. https://doi.org/10.1007/BF02485945.

Elrahman, Mohamed Abd, and Bernd Hillemeier. 2014. "Combined Effect of Fine Fly Ash and Packing Density on the Properties of High Performance Concrete: An Experimental Approach." *Construction and Building Materials* 58: 225–233.

Feylessoufi, A., F. Villieras, L. J. Michot, P. DeDonato, J. M. Cases, and P. Richard. 1996. "Water Environment and Nanostructural Network in a Reactive Powder Concrete." *Cement & Concrete Composites* 18 (1): 23–29. https://doi.org/10.1016/0958-9465(95)00036-4.

FHWA. 2011. "Ultra-High Performance Concrete, FHWA-HRT-11-038." March 2011. https://www.fhwa.dot.gov/publications/research/infrastructure/structures/11038/.

———. 2013. "Ultra-High Performance Concrete: A State-Of-The-Art Report for The Bridge Community , FHWA-HRT-13-060." June 2013. https://www.fhwa.dot.gov/publications/research/infrastructure/structures/hpc/13060/.

———. 2014. "Design and Construction of Field-Cast UHPC Connections , October 2014 - FHWA-HRT-14-084." 2014. https://www.fhwa.dot.gov/publications/research/infrastructure/structures/14084/index.cfm.

———. 2016. “ABC - Accelerated - Technologies and Innovations - Construction - Federal Highway Administration.” 2016. https://www.fhwa.dot.gov/bridge/abc/.
“Fillers in Action: How to Achieve High Particle Loadings.” 2015. *Polymer Innovation Blog* (blog). December 7, 2015. http://polymerinnovationblog.com/fillers-action-achieve-high-particle-loadings/.
Freytag, Bernhard, Michael Reichel, Lutz Sparowitz, Gerhard Santner, and Guenter Heinzle. 2009. “Full-Scale Experiment Bridge WILD - Design of an UHPC Arch Bridge based on Experiments.” *Beton- Und Stahlbetonbau* 104 (3): 134–44. https://doi.org/10.1002/best.200900663.
Fu, G., and W. Dekelbab. 2003. “3-D Random Packing of Polydisperse Particles and Concrete Aggregate Grading.” *Powder Technology* 133 (1): 147–55. https://doi.org/10.1016/S0032-5910(03)00082-2.
Gao, G., S. Huang, K. Xia, and Z. Li. 2015. “Application of Digital Image Correlation (DIC) in Dynamic Notched Semi-Circular Bend (NSCB) Tests.” *Experimental Mechanics* 55 (1): 95–104. https://doi.org/10.1007/s11340-014-9863-5.
Garcia-Lodeiro, I., A. Palomo, A. Fernández-Jiménez, and D. E. Macphee. 2011. “Compatibility Studies between N-A-S-H and C-A-S-H Gels. Study in the Ternary Diagram Na2O–CaO–Al2O3–SiO2–H2O.” *Cement and Concrete Research* 41 (9): 923–31. https://doi.org/10.1016/j.cemconres.2011.05.006.
Ghafari, Ehsan, Hugo Costa, Eduardo Júlio, António Portugal, and Luisa Durães. 2012. “Optimization of UHPC by Adding Nanomaterials.” In *Proceedings of 3rd International Symposium on Ultra-High-Performance Concrete and Nanotechnology for High Performance Construction Materials Kassel (Germany)*, 71–8. https://books.google.com/books?hl=en&lr=&id=LufCDwJ-sacC&oi=fnd&pg=PA71&dq=optimization+of+UHPC+by+adding+nanomaterials&ots=b3vHtOtO4s&sig=ukL-ei9dcXN5s36Sl4JpzeEk17Y.
———. 2014. “The Effect of Nanosilica Addition on Flowability, Strength and Transport Properties of Ultra High Performance Concrete.” *Materials & Design* 59 (July): 1–9. https://doi.org/10.1016/j.matdes.2014.02.051.
Ghasemi, Sahar, Pedram Zohrevand, Amir Mirmiran, Yulin Xiao, and Kevin Mackie. 2016. “A Super Lightweight UHPC-HSS Deck Panel for Movable Bridges.” *Engineering Structures* 113 (April): 186–93. https://doi.org/10.1016/j.engstruct.2016.01.046.
Goltermann, Per, Vagn Johansen, and Lars Palbøl. 1997. “Packing of Aggregates: An Alternative Tool to Determine the Optimal Aggregate Mix.” *Materials Journal* 94 (5): 435–43. https://doi.org/10.14359/328.
Gowripalan, N., and R. I. Gilbert. 2000. “Design Guidelines for RPC Prestressed Concrete Beams.” *Sydney, Australia: School of Civil and Environmental Engineering, University of New South Wales*.
Graybeal, B. 2011. “FHWA TECHNOTE: Ultra High Performance Concrete.” *FHWA Publication No: FHWA-HRT-11-038: Federal Highway Administration*.
Graybeal, B. A. 2004. “Fabrication of an Optimized UHPC Bridge.” In *PCI National Bridge Conference, Atlanta, GA, USA*.
Graybeal, Ben. 2010a. “Field-Cast UHPC Connections for Modular Bridge Deck Elements.” FHWA-HRT-11-022. Federal Highway Administration.
———. 2010b. “Finite Element Analysis of UHPC: Structural Performance of an AASHTO Type II Gurder and a 2nd Generation Pi-Girder.” FHWA-HRT-10-079. Federal Highway Administration.
———. 2011. “Ultra-High Performance Concrete.” *Technote*, March. https://trid.trb.org/view.aspx?id=1104239.
———. 2014a. “Design and Construction of Field-Cast UHPC Connections.”
———. 2014b. “Design and Construction of Field-Cast UHPC Connections.” FHWA-HRT-14-084. Federal Highway Administration.

Graybeal, Benjamin A. 2006. “Material Property Characterization of Ultra-High Performance Concrete,” August. https://trid.trb.org/view.aspx?id=798080.

———. 2011. “Fatigue Response in Bridge Deck Connection Composed of Field-Cast Ultra-High-Performance Concrete.” *Transportation Research Record*, no. 2251: 93–100. https://doi.org/10.3141/2251-10.

———. 2016. “UHPC Connections for Accelerated Bridge Construction.” *Accelerated Bridge Construction* (blog). 2016. https://abc-utc.fiu.edu/mc-events/uhpc-connections-for-accelerated-bridge-construction/.

Graybeal, Benjamin A., and Joseph L. Hartmann. 2003. “Strength and Durability of Ultra-High Performance Concrete.” In *Concrete Bridge Conference, Portland Cement Association*.

Graybeal, Benjamin, and Marshall Davis. 2008. “Cylinder or Cube: Strength Testing of 80 to 200 MPa (11.6 to 29 Ksi) Ultra-High-Performance Fiber-Reinforced Concrete.” *ACI Materials Journal* 105 (6): 603–609.

Graybeal, Benjamin, and Jussara Tanesi. 2007. “Durability of an Ultrahigh-Performance Concrete.” *Journal of Materials in Civil Engineering* 19 (10): 848–54. https://doi.org/10.1061/(ASCE)0899-1561(2007)19:10(848).

Gruber, K. A, Terry Ramlochan, Andrea Boddy, R. D Hooton, and M. D. A Thomas. 2001. “Increasing Concrete Durability with High-Reactivity Metakaolin.” *Cement and Concrete Composites* 23 (6): 479–84. https://doi.org/10.1016/S0958-9465(00)00097-4.

Grünewald, Steffen. 2004. *Performance-Based Design of Self-Compacting Fibre Reinforced Concrete*. TU Delft, Delft University of Technology. http://repository.tudelft.nl/view/ir/uuid:07a817aa-cba1-4c93-bbed-40a5645cf0f1/.

Gunes, Oguz, Seda Yesilmen, Burcu Gunes, and Franz-Joseph Ulm. 2012. “Use of UHPC in Bridge Structures: Material Modeling and Design.” *Advances in Materials Science and Engineering*, 319285. https://doi.org/10.1155/2012/319285.

Habel, Katrin, Marco Viviani, Emmanuel Denarié, and Eugen Brühwiler. 2006. “Development of the Mechanical Properties of an Ultra-High Performance Fiber Reinforced Concrete (UHPFRC).” *Cement and Concrete Research* 36 (7): 1362–70. https://doi.org/10.1016/j.cemconres.2006.03.009.

Haber, Zachary, and Benjamin A. Graybeal. n.d. “Performance of Multiple UHPC-Class Materials in Prefabricated Bridge Deck Connections.”

Hadl, Philipp, Regina della Pietra, Kim Huy Hoang, Erwin Pilch, and Nguyen Viet Tue. 2015. “Application of UHPC as road bridge topping within the adaptation of an existing conventional bridge to an integral abutment bridge in Austria.” *Beton- Und Stahlbetonbau* 110 (2): 162–70. https://doi.org/10.1002/best.201400091.

Hansen, Torben C., and Henrik Narud. 1983. “Strength of Recycled Concrete Made from Crushed Concrete Coarse Aggregate.” *Concrete International* 5 (01): 79–83.

Honarvar, Ebadollah, Sri Sritharan, Jon Matthews Rouse, and Sriram Aaleti. 2016. “Bridge Decks with Precast UHPC Waffle Panels: A Field Evaluation and Design Optimization.” *Journal of Bridge Engineering* 21 (1): 04015030. https://doi.org/10.1061/(ASCE)BE.1943-5592.0000775.

Igarashi, Shin-ichi, Akio Watanabe, and Mitsunori Kawamura. 2005. “Evaluation of Capillary Pore Size Characteristics in High-Strength Concrete at Early Ages.” *Cement and Concrete Research* 35 (3): 513–19. https://doi.org/10.1016/j.cemconres.2004.06.036.

Iyengar, KT Sundara Raja, S. Raviraj, and T. N. Jayaram. 2002. “Analysis of Crack Propagation in Strain-Softening Beams.” *Engineering Fracture Mechanics* 69 (6): 761–778.

Kadri, El-Hadj, Said Kenai, Karim Ezziane, Rafat Siddique, and Geert De Schutter. 2011. “Influence of Metakaolin and Silica Fume on the Heat of Hydration and Compressive Strength Development of Mortar.” *Applied Clay Science* 53 (4): 704–8. https://doi.org/10.1016/j.clay.2011.06.008.

Kamal, M. M., M. A. Safan, Z. A. Etman, and R. A. Salama. 2014. “Behavior and Strength of Beams Cast with Ultra High Strength Concrete Containing Different Types of Fibers.” *HBRC Journal* 10 (1): 55–63.

Kosmatka, Steven H., Beatrix Kerkhoff, and William C. Panarese. 2002. *Design and Control of Concrete Mixtures*. 14th edition. Skokie, Ill.: Portland Cement Association.

Kumar, Aditya, Tandre Oey, Seohyun Kim, Davis Thomas, Sondos Badran, Jialin Li, Fabio Fernandes, Narayanan Neithalath, and Gaurav Sant. 2013. “Simple Methods to Estimate the Influence of Limestone Fillers on Reaction and Property Evolution in Cementitious Materials.” *Cement and Concrete Composites* 42 (September): 20–29. https://doi.org/10.1016/j.cemconcomp.2013.05.002.

Lange, F., H. Mörtel, and V. Rudert. 1997. “Dense Packing of Cement Pastes and Resulting Consequences on Mortar Properties.” *Cement and Concrete Research*, Materials Research Society Symposium on Structure-Property Relationships in Hardened Cement Paste and Composites, 27 (10): 1481–88. https://doi.org/10.1016/S0008-8846(97)00189-0.

Larrard, F. de, and T. Sedran. 1994. “Optimization of Ultra-High-Performance Concrete by the Use of a Packing Model.” *Cement and Concrete Research* 24 (6): 997–1009. https://doi.org/10.1016/0008-8846(94)90022-1.

Laungrungrong, Busaba, Barzin Mobasher, and Douglas C. Montgomery. 2008. *Development of Rational Pay Factors Based on Concrete Compressive Strength Data*. Vol. 608. Arizona Department of Transportation. https://apps.azdot.gov/ADOTLibrary/publications/project_reports/PDF/AZ608.pdf.

Le, Ha Thanh, Matthias Müller, Karsten Siewert, and Horst-Michael Ludwig. 2015. “The Mix Design for Self-Compacting High Performance Concrete Containing Various Mineral Admixtures.” *Materials & Design* 72 (May): 51–62. https://doi.org/10.1016/j.matdes.2015.01.006.

Le, Ha Thanh, Sang Thanh Nguyen, and Horst-Michael Ludwig. 2014. “A Study on High Performance Fine-Grained Concrete Containing Rice Husk Ash.” *International Journal of Concrete Structures and Materials* 8 (4): 301–7. https://doi.org/10.1007/s40069-014-0078-z.

Lecomte, André. 2006. “The Measurement of Real and Virtual Packing Density of Soft Grains.” *Materials and Structures* 39 (1): 63–80.

Lee, Seong-Cheol, Jae-Yeol Cho, and Frank J. Vecchio. 2011. “Diverse Embedment Model for Steel Fiber-Reinforced Concrete in Tension: Model Development.” *Materials Journal* 108 (5): 516–525.

Li, Lungui, Zhongguo Ma, Mary E. Griffey, and Ralph G. Oesterle. 2009. “Improved Longitudinal Joint Details in Decked Bulb Tees for Accelerated Bridge Construction: Concept Development.” *Journal of Bridge Engineering* 15 (3): 327–336.

Li, Wengui, Zhengyu Huang, Fangliang Cao, Zhihui Sun, and Surendra P. Shah. 2015. “Effects of Nano-Silica and Nano-Limestone on Flowability and Mechanical Properties of Ultra-High-Performance Concrete Matrix.” *Construction and Building Materials* 95 (October): 366–74. https://doi.org/10.1016/j.conbuildmat.2015.05.137.

Lim, T. Y., P. Paramisivam, and S. L. Lee. 1987. “Bending Behavior of Steel-Fiber Concrete Beams.” *Structural Journal* 84 (6): 524–536.

Lim, Teck-Yong, P. Paramasivam, and Seng-Lip Lee. 1987. “Behavior of Reinforced Steel-Fiber-Concrete Beams in Flexure.” *Journal of Structural Engineering* 113 (12): 2439–2458.

Lok, Tat-Seng, and Jin-Song Pei. 1998. “Flexural Behavior of Steel Fiber Reinforced Concrete.” *Journal of Materials in Civil Engineering* 10 (2): 86–97.

Ma, Jianxin, Frank Dehn, Gert Koenig, Ying-shu Yuan, Surendra P. Shah, and Heng-lin Lü. 2003. "Autogenous Shrinkage of Self-Compacting Ultra-High Performance Concrete (UHPC)." In *Proceedings of the International Conference ICACS, Xuzhou, China*, 255–262. https://books.google.com/books?hl=en&lr=&id=RQR9Rpr1LW8C&oi=fnd&pg=PA255&dq=Ma+J,+Dehn+F,+Koenig+G+(2003)+Autogenous+shrinkage+of+self-compacting+ultra-high+performance+concrete+(UHPC).&ots=BeXJCMwmnH&sig=u4au7eWoUtQeNfzM70E66g1LeoQ.

Macedo, Vanessa Cruz, André Luis Faria e Silva, and Luis Roberto Marcondes Martins. 2010. "Effect of Cement Type, Relining Procedure, and Length of Cementation on Pull-out Bond Strength of Fiber Posts." *Journal of Endodontics* 36 (9): 1543–1546.

Maeder, Urs, Isabelle Lallemant-Gamboa, Joel Chaignon, and Jean-Pierre Lombard. 2004. "Ceracem, a New High Performance Concrete: Characterisations and Applications." In *First International Symposium on Ultra High Performance Concrete, Kassel*, 59–68. https://www.researchgate.net/profile/Lesday_Martinez/publication/271196269_Lime-pozzolan_binder_as_a_very_fine_mineral_admixture_in_concrete/links/54bffe160cf28a6324a03408.pdf#page=75.

Magureanu, Cornelia, Ioan Sosa, Camelia Negrutiu, and Bogdan Heghes. 2012. "Mechanical Properties and Durability of Ultra-High-Performance Concrete." *Materials Journal* 109 (2): 177–84.

Malhotra, V. M., V. S. Ramachandra, R. F. Feldman, and P. C. Aitcin. 1987. "CONDENSED SILICA FUME IN CONCRETE." https://trid.trb.org/view.aspx?id=286228.

Markovic, Ivan. 2006. "High-Performance Hybrid-Fibre Concrete: Development and Utilisation." TU Delft, Delft University of Technology. http://repository.tudelft.nl/view/ir/uuid:44ed51cd-fc27-4353-ab81-cf8348f52443/.

Matsubara, N., T. Ohno, G. Sakai, Y. Watanabe, S. Ishii, and M. Ashida. 2008. "Application of a New Type of Ultra High Strength Fiber Reinforced Concrete to a Prestressed Concrete Bridge." In *Second International Symposium on Ultra High Performance Concrete, Kassel*, 787–794.

Mazloom, M., A. A. Ramezanianpour, and J. J. Brooks. 2004. "Effect of Silica Fume on Mechanical Properties of High-Strength Concrete." *Cement and Concrete Composites* 26 (4): 347–57. https://doi.org/10.1016/S0958-9465(03)00017-9.

Means, R. S. 2012. "RSMeans Construction Cost Data." *Kingston, MA: RS Means Company*.

Meda, A., G. A. Plizzari, and P. Riva. 2004. "Fracture Behavior of SFRC Slabs on Grade." *Materials and Structures* 37 (6): 405–11. https://doi.org/10.1007/BF02479637.

Meda, Alberto, Fausto Minelli, and Giovanni A. Plizzari. 2012. "Flexural Behaviour of RC Beams in Fibre Reinforced Concrete." *Composites Part B: Engineering* 43 (8): 2930–2937.

Meng, Weina, Yiming Yao, Barzin Mobasher, and H. Kamal Khayat. 2017. "Effects of Loading Rate and Notch-to-Depth Ratio of Notched Beams on Flexural Performance of Ultra-High-Performance Concrete (Under Review)." *Cement and Concrete Composites*.

Minelli, F., G. A. Plizzari, and F. J. Vecchio. 2007. "Influence of Steel Fibers on Full-Scale RC Beams under Shear Loading." In *High Performance Concrete, Brick-Masonry and Environmental Aspects. Sixth International Conference of Fracture Mechanics of Concrete and Concrete Structures FRAMCOS6. Taylor & Francis Group (UK), London/Catania*, 3:1523–1531.

Mitchell, D. R. G., I. Hinczak, and R. A. Day. 1998. "Interaction of Silica Fume with Calcium Hydroxide Solutions and Hydrated Cement Pastes." *Cement and Concrete Research* 28 (11): 1571–84. https://doi.org/10.1016/S0008-8846(98)00133-1.

Mobasher, B., and Cheng Yu Li. 1995. "Modeling of Stiffness Degradation of the Interfacial Zone during Fiber Debonding." *Composites Engineering* 5 (10–11): 1349–1365.

Mobasher, Barzin. 2011. *Mechanics of Fiber and Textile Reinforced Cement Composites*. CRC press.

Mobasher, Barzin, and Kamil Kaloush. 2004. “Laboratory Evaluation of ADOT’s Ultra-Thin Whitetopping PCC Test Sections – Cottonwood.” Arizona Department of Transportation.
Mobasher, Barzin, and Cheng Yu Li. 1996. “Mechanical Properties of Hybrid Cement-Based Composites.” *ACI Materials Journal* 93: 284–92.
Mobasher, Barzin, Yiming Yao, and Chote Soranakom. 2015. “Analytical Solutions for Flexural Design of Hybrid Steel Fiber Reinforced Concrete Beams.” *Engineering Structures* 100: 164–77.
Mooney, M. 1951. “The Viscosity of a Concentrated Suspension of Spherical Particles.” *Journal of Colloid Science* 6 (2): 162–70. https://doi.org/10.1016/0095-8522(51)90036-0.
Moser, B, C Pfeifer, and J Stark. 2009. “Durability and Microstructural Development during Hydration in Ultra-High Performance Concrete.” *London, UK: Taylor and Francis Group*, 87–88.
Naaman, A. E., and H. W. Reinhardt. 2006. “Proposed Classification of HPFRC Composites Based on Their Tensile Response.” *Materials and Structures* 39 (5): 547–55. https://doi.org/10.1617/s11527-006-9103-2.
Naaman, Antoine E., George G. Namur, Jamil M. Alwan, and Husam S. Najm. 1991. “Fiber Pullout and Bond Slip. I: Analytical Study.” *Journal of Structural Engineering* 117 (9): 2769–2790.
Nagataki, S., N. Otsuki, and M. Hisoda. 1994. “Effects of Physical and Chemical Treatments of Silica Fume on the Strength and Microstructures of Mortar.” *Special Publication* 149 (October): 21–36.
Nehdi, M., and M. -A. Rahman. 2004. “Estimating Rheological Properties of Cement Pastes Using Various Rheological Models for Different Test Geometry, Gap and Surface Friction.” *Cement and Concrete Research* 34 (11): 1993–2007. https://doi.org/10.1016/j.cemconres.2004.02.020.
Neithalath, Narayanan, and Jitendra Jain. 2010. “Relating Rapid Chloride Transport Parameters of Concretes to Microstructural Features Extracted from Electrical Impedance.” *Cement and Concrete Research* 40 (7): 1041–51. https://doi.org/10.1016/j.cemconres.2010.02.016.
Neithalath, Narayanan, Jarrod Persun, and Akhter Hossain. 2009. “Hydration in High-Performance Cementitious Systems Containing Vitreous Calcium Aluminosilicate or Silica Fume.” *Cement and Concrete Research* 39 (6): 473–81. https://doi.org/10.1016/j.cemconres.2009.03.006.
Nochaiya, Thanongsak, Watcharapong Wongkeo, and Arnon Chaipanich. 2010. “Utilization of Fly Ash with Silica Fume and Properties of Portland Cement–Fly Ash–Silica Fume Concrete.” *Fuel* 89 (3): 768–774.
NT Build 492, NordTest. 1999. “Concrete, Mortar and Cement-Based Repair Materials: Chloride Migration Coefficient from Non-Steady-State Migration Experiments.” *Nordtest Method* 492.
Ouyang, C., A. Pacios, and S. P. Shah. 1994. “Pullout of Inclined Fibers from Cementitious Matrix.” *Journal of Engineering Mechanics* 120 (12): 2641–2659.
Paiva, H., A. Velosa, P. Cachim, and V. M. Ferreira. 2012. “Effect of Metakaolin Dispersion on the Fresh and Hardened State Properties of Concrete.” *Cement and Concrete Research* 42 (4): 607–12. https://doi.org/10.1016/j.cemconres.2012.01.005.
Park, Seung Hun, Dong Joo Kim, Gum Sung Ryu, and Kyung Taek Koh. 2012. “Tensile Behavior of Ultra High Performance Hybrid Fiber Reinforced Concrete.” *Cement and Concrete Composites* 34 (2): 172–84. https://doi.org/10.1016/j.cemconcomp.2011.09.009.
Perry, Vic, Raymond Krisciunas, and Bob Stofko. 2014. “Mackenzie River Twin Bridges North America’s Largest Field-Cast Ultra-High-Performance Concrete Connections Project.” *Pci Journal*, 40–48.
Peyvandi, Amirpasha, Libya Ahmed Sbia, Parviz Soroushian, and Konstantin Sobolev. 2013. “Effect of the Cementitious Paste Density on the Performance Efficiency of Carbon Nanofiber in Concrete Nanocomposite.” *Construction and Building Materials* 48 (November): 265–69. https://doi.org/10.1016/j.conbuildmat.2013.06.094.
Phaobunjong, Kan. 2002. “Parametric Cost Estimating Model for Conceptual Cost Estimating of Building Construction Projects.” PhD Thesis.

Philippot, S., S. Masse, H. Zanni, P. Nieto, V. Maret, and M. Cheyrezy. 1996. “Si-29 NMR Study of Hydration and Pozzolanic Reactions in Reactive Powder Concrete (RPC).” *Magnetic Resonance Imaging* 14 (7–8): 891–93. https://doi.org/10.1016/S0730-725X(96)00174-9.

Poon, C. S., S. C. Kou, and L. Lam. 2006a. “Compressive Strength, Chloride Diffusivity and Pore Structure of High Performance Metakaolin and Silica Fume Concrete.” *Construction and Building Materials* 20 (10): 858–65. https://doi.org/10.1016/j.conbuildmat.2005.07.001.

———. 2006b. “Compressive Strength, Chloride Diffusivity and Pore Structure of High Performance Metakaolin and Silica Fume Concrete.” *Construction and Building Materials* 20 (10): 858–65. https://doi.org/10.1016/j.conbuildmat.2005.07.001.

Poon, C. -S, L Lam, S. C Kou, Y. -L Wong, and Ron Wong. 2001. “Rate of Pozzolanic Reaction of Metakaolin in High-Performance Cement Pastes.” *Cement and Concrete Research* 31 (9): 1301–6. https://doi.org/10.1016/S0008-8846(01)00581-6.

Porteneuve, C., H. N. Zanni, C. Vernet, K. O. Kjellsen, J. P. Korb, and D. Petit. 2001. “Nuclear Magnetic Resonance Characterization of High- and Ultrahigh-Performance Concrete - Application to the Study of Water Leaching.” *Cement and Concrete Research* 31 (12): 1887–93. https://doi.org/10.1016/S0008-8846(01)00648-2.

Prem, Prabhat Ranjan, Avadhanam Ramachandra Murthy, and Bhajantri H. Bharatkumar. 2015. “Influence of Curing Regime and Steel Fibres on the Mechanical Properties of UHPC.” *Magazine of Concrete Research* 67 (18): 1400333. https://doi.org/10.1680/macr.14.00333.

Prisco, Marco di, Giovanni Plizzari, and Lucie Vandewalle. 2009. “Fibre Reinforced Concrete: New Design Perspectives.” *Materials and Structures* 42 (9): 1261–81. https://doi.org/10.1617/s11527-009-9529-4.

Puerta-Falla, Guillermo, Magdalena Balonis, Gwenn Le Saout, Aditya Kumar, Melanie Rivera, Gabriel Falzone, Narayanan Neithalath, and Gaurav Sant. 2016. “The Influence of Slightly and Highly Soluble Carbonate Salts on Phase Relations in Hydrated Calcium Aluminate Cements.” *Journal of Materials Science* 51 (12): 6062–74. https://doi.org/10.1007/s10853-016-9912-9.

Pyo, Sukhoon, Kay Wille, Sherif El-Tawil, and Antoine E. Naaman. 2015. “Strain Rate Dependent Properties of Ultra High Performance Fiber Reinforced Concrete (UHP-FRC) under Tension.” *Cement and Concrete Composites* 56 (February): 15–24. https://doi.org/10.1016/j.cemconcomp.2014.10.002.

Rajan, S. D., B. Mobasher, S. Sankaran, D. Naik, and Z. Stahlecker. 2010. “Explicit Finite Element Modeling of Multilayer Composite Fabric for Gas Turbine Engine Containment Systems, Phase III, Part 1: Arizona State University Material Model and Numerical Simulations.” *FAA Rep. DOT/FAA/AR-10/24, Federal Aviation Administration (FAA), Washington, DC*.

Rallabhandhi, Saipavan. 2016. *Evaluation of Ultra High Performance Concrete in Joints of Bridge Girders*. Missouri University of Science and Technology.

Rao, Akash, Kumar N. Jha, and Sudhir Misra. 2007. “Use of Aggregates from Recycled Construction and Demolition Waste in Concrete.” *Resources, Conservation and Recycling* 50 (1): 71–81.

Rao, G. Appa. 2003. “Investigations on the Performance of Silica Fume-Incorporated Cement Pastes and Mortars.” *Cement and Concrete Research* 33 (11): 1765–70. https://doi.org/10.1016/S0008-8846(03)00171-6.

Reda, M. M, N. G Shrive, and J. E Gillott. 1999. “Microstructural Investigation of Innovative UHPC.” *Cement and Concrete Research* 29 (3): 323–29. https://doi.org/10.1016/S0008-8846(98)00225-7.

Reichel, Michael. 2009. “Special Features of Material and Structure in the Application of UHPC for Bridge Construction exemplified by three Pilot Projects.” *Beton- Und Stahlbetonbau* 104 (9): 589–98. https://doi.org/10.1002/best.200900023.

Reichel, Michael, Lutz Sparowitz, and Bernhard Freytag. 2011. “Bridge WILD Volkermarkt - Prestressed Arched Structure Made of Precast UHPC-Segments. Part 2-Erection, Accompanying Research, Quality Control.” *Beton- Und Stahlbetonbau* 106 (12): 827–35. https://doi.org/10.1002/best.201110054.

Richard, Pierre, and Marcel Cheyrezy. 1995. “Composition of Reactive Powder Concretes.” *Cement and Concrete Research* 25 (7): 1501–11. https://doi.org/10.1016/0008-8846(95)00144-2.

Richardson, I. G. 1999. “The Nature of CSH in Hardened Cements.” *Cement and Concrete Research* 29 (8): 1131–1147.

Ríos, José D., Héctor Cifuentes, Rena C. Yu, and Gonzalo Ruiz. 2017. “Probabilistic Flexural Fatigue in Plain and Fiber-Reinforced Concrete.” *Materials* 10 (7): 767.

Royce, Mathew. 2014. “Implementing Ultra-High-Performance Concrete for Accelerated Bridge Construction in New York.” *Pci Journal*, 38–47.

Russell, Henry G., and Benjamin A. Graybeal. 2013. “Ultra-High Performance Concrete: A State-of-the-Art Report for the Bridge Community.”

Sagoe-Crentsil, Kwesi K., Trevor Brown, and Alan Harry Taylor. 2001. “Performance of Concrete Made with Commercially Produced Coarse Recycled Concrete Aggregate.” *Cement and Concrete Research* 31 (5): 707–712.

Schiessl, P., K. Beckhaus, I. Schachinger, and P. Rucker. 2004. “New Results on Early-Age Cracking Risk of Special Concrete.” *Cement Concrete and Aggregates* 26 (2): 139–47.

Schrefler, Bernhard A., Gabriel A. Khoury, Dariusz Gawin, and Carmelo E. Majorana. 2002. “Thermo-Hydro-Mechanical Modelling of High Performance Concrete at High Temperatures.” *Engineering Computations* 19 (7/8): 787–819.

Schröfl, Ch., M. Gruber, and J. Plank. 2012. “Preferential Adsorption of Polycarboxylate Superplasticizers on Cement and Silica Fume in Ultra-High Performance Concrete (UHPC).” *Cement and Concrete Research* 42 (11): 1401–8. https://doi.org/10.1016/j.cemconres.2012.08.013.

Schwartzentruber, L. D’Aloia, R. Le Roy, and J. Cordin. 2006. “Rheological Behaviour of Fresh Cement Pastes Formulated from a Self Compacting Concrete (SCC).” *Cement and Concrete Research* 36 (7): 1203–13. https://doi.org/10.1016/j.cemconres.2004.10.036.

Shekarchi, M., A. Bonakdar, M. Bakhshi, A. Mirdamadi, and B. Mobasher. 2010. “Transport Properties in Metakaolin Blended Concrete.” *Construction and Building Materials* 24 (11): 2217–23. https://doi.org/10.1016/j.conbuildmat.2010.04.035.

Simon, A., Z. Hajar, D. Lecointre, and J. Petitjean. 2002. “Realization of Two Road Bridges with Ultra-High-Performance Fibre-Reinforced Concrete.” In *Proceedings of the 6th International Symposium on Utilisation of High Strength/High Performance Concrete, Leipzig*.

Singh, Bhupinder, and Kranti Jain. 2014. “Appraisal of Steel Fibers as Minimum Shear Reinforcement in Concrete Beams.” *ACI Structural Journal* 111 (5): 1191.

Skazlić, Marijan, Marijana Serdar, and Dubravka Bjegović. 2008. “Influence of Test Specimen Geometry on Compressive Strength of Ultra High Performance Concrete.” In . http://bib.irb.hr/prikazi-rad?rad=326094.

Soranakom, C., and B. Mobasher. 2007. “Closed-Form Solutions for Flexural Response of Fiber-Reinforced Concrete Beams.” *Journal of Engineering Mechanics* 133 (8): 933–41. https://doi.org/10.1061/(ASCE)0733-9399(2007)133:8(933).

Soranakom, Chote, and Barzin Mobasher. 2007. “Closed-Form Solutions for Flexural Response of Fiber-Reinforced Concrete Beams.” *Journal of Engineering Mechanics* 133: 933–41.

———. 2008. “Correlation of Tensile and Flexural Responses of Strain Softening and Strain Hardening Cement Composites.” *Cement and Concrete Composites* 30: 465–77.

———. 2009. “Flexural Design of Fiber-Reinforced Concrete.” *Materials Journal* 106 (5): 461–69. https://doi.org/10.14359/51663147.

Sorelli, L. G., P. Fanning, and F. Toutlemonde. 2006. “INNOVATIVE BRIDGE SYSTEM OF ULTRA HIGH PERFORMANCE FIBRE REINFORCED CONCRETE: EXPERIMENTS, MODELING AND DESIGN.” In *7th International Conference on Short and Medium Span Bridges*, 23–25. https://www.gci.ulaval.ca/fileadmin/gci/documents/10.pdf.

Standard, J. C. I. 2003. “Method of Test for Fracture Energy of Concrete by Use of Notched Beam.” JCI-S-001-2003. Japan Concrete Institute (JCI).

Stovall, T., F. de Larrard, and M. Buil. 1986. “Linear Packing Density Model of Grain Mixtures.” *Powder Technology* 48 (1): 1–12. https://doi.org/10.1016/0032-5910(86)80058-4.

Stroeven, Piet, and Martijn Stroeven. 1999a. “Assessment of Packing Characteristics by Computer Simulation.” *Cement and Concrete Research* 29 (8): 1201–6. https://doi.org/10.1016/S0008-8846(99)00020-4.

———. 1999b. “Assessment of Packing Characteristics by Computer Simulation.” *Cement and Concrete Research* 29 (8): 1201–6. https://doi.org/10.1016/S0008-8846(99)00020-4.

Suleiman, Muhannad T., Thomas Vande Voort, and Sri Sritharan. 2010. “Behavior of Driven Ultrahigh-Performance Concrete H-Piles Subjected to Vertical and Lateral Loadings.” *Journal of Geotechnical and Geoenvironmental Engineering* 136 (10): 1403–13. https://doi.org/10.1061/(ASCE)GT.1943-5606.0000350.

Suraneni, Prannoy, Vahid Jafari Azad, Burkan O. Isgor, and William Jason Weiss. 2016. “Calcium Oxychloride Formation in Pastes Containing Supplementary Cementitious Materials: Thoughts on the Role of Cement and Supplementary Cementitious Materials Reactivity.” *RILEM Technical Letters* 1: 24–30.

Tabsh, Sami W., and Akmal S. Abdelfatah. 2009. “Influence of Recycled Concrete Aggregates on Strength Properties of Concrete.” *Construction and Building Materials* 23 (2): 1163–1167.

Tafraoui, Ahmed, Gilles Escadeillas, Soltane Lebaili, and Thierry Vidal. 2009. “Metakaolin in the Formulation of UHPC.” *Construction and Building Materials* 23 (2): 669–74. https://doi.org/10.1016/j.conbuildmat.2008.02.018.

Tafraoui, Ahmed, Gilles Escadeillas, and Thierry Vidal. 2016. “Durability of the Ultra High Performances Concrete Containing Metakaolin.” *Construction and Building Materials* 112 (June): 980–87. https://doi.org/10.1016/j.conbuildmat.2016.02.169.

Taheri, Mahsa, Joaquim A. O. Barros, and Hamidreza Salehian. 2011. “A Design Model for Strain-Softening and Strain-Hardening Fiber Reinforced Elements Reinforced Longitudinally with Steel and FRP Bars.” *Composites Part B: Engineering* 42 (6): 1630–40. https://doi.org/10.1016/j.compositesb.2011.04.009.

Tennis, P., M.D.A. Thomas, and W.J. Weiss. 2011. *State-of-the-Art Report on Use of Limestone in Cements at Levels of up to 15%, SN3148*. Skokie, Illinois, USA: Portland Cement Association.

Tjiptobroto, Prijatmadi, and Will Hansen. 1993. “Tensile Strain Hardening and Multiple Cracking in High-Performance Cement-Based Composites Containing Discontinuous Fibers.” *Materials Journal* 90 (1): 16–25.

Toufar, W., M. Born, and E. Klose. 1976. “Contribution of Optimisation of Components of Different Density in Polydispersed Particles Systems.” *Freiberger Booklet A* 558: 29–44.

Van Mier, Jan GM. 2017. *Fracture Processes of Concrete*. CRC press.

Vance, Kirk, Matthew Aguayo, Tandre Oey, Gaurav Sant, and Narayanan Neithalath. 2013a. “Hydration and Strength Development in Ternary Portland Cement Blends Containing Limestone and Fly Ash or Metakaolin.” *Cement and Concrete Composites* 39 (May): 93–103. https://doi.org/10.1016/j.cemconcomp.2013.03.028.

———. 2013b. “Hydration and Strength Development in Ternary Portland Cement Blends Containing Limestone and Fly Ash or Metakaolin.” *Cement and Concrete Composites* 39 (May): 93–103. https://doi.org/10.1016/j.cemconcomp.2013.03.028.

Vance, Kirk, Aashay Arora, Gaurav Sant, and Narayanan Neithalath. 2015. “Rheological Evaluations of Interground and Blended Cement–Limestone Suspensions.” *Construction and Building Materials* 79 (March): 65–72. https://doi.org/10.1016/j.conbuildmat.2014.12.054.

Vance, Kirk, Aditya Kumar, Gaurav Sant, and Narayanan Neithalath. 2013. “The Rheological Properties of Ternary Binders Containing Portland Cement, Limestone, and Metakaolin or Fly Ash.” *Cement and Concrete Research* 52 (October): 196–207. https://doi.org/10.1016/j.cemconres.2013.07.007.

Vance, Kirk, Gaurav Sant, and Narayanan Neithalath. 2015. “The Rheology of Cementitious Suspensions: A Closer Look at Experimental Parameters and Property Determination Using Common Rheological Models.” *Cement and Concrete Composites* 59 (May): 38–48. https://doi.org/10.1016/j.cemconcomp.2015.03.001.

Vandewalle, Lucie. 1999. “Influence of Tensile Strength of Steel Fibre on the Toughness of High Strength Concrete.” In *Third International Workshop" High Performance Fiber Reinforced Cement Composites"*, 331–340.

———. 2002. “RILEM TC162-TDF : Test and Design Methods for Steel Fibre Reinforced Concrete : Bending Test (Final Recommendation).” *Materials and Structures* 35 (November): 579–82.

Vic Perry, FCSCE, P. Eng, Dick Dykstra, Philip Murray, M. Eng, Biljana Rajlic, and Nova Scota Halifax. 2010. “Innovative Field Cast UHPC Joints for Precast Bridge Systems–3-Span Live Load Continuous.”

Vikan, Hedda, and Harald Justnes. 2007. “Rheology of Cementitious Paste with Silica Fume or Limestone.” *Cement and Concrete Research* 37 (11): 1512–17. https://doi.org/10.1016/j.cemconres.2007.08.012.

Voo, Yen Lei, Stephen J. Foster, and Chen Cheong Voo. 2015. “Ultrahigh-Performance Concrete Segmental Bridge Technology: Toward Sustainable Bridge Construction.” *Journal of Bridge Engineering* 20 (8): B5014001. https://doi.org/10.1061/(ASCE)BE.1943-5592.0000704.

Wang, Chong, Changhui Yang, Fang Liu, Chaojun Wan, and Xincheng Pu. 2012. “Preparation of Ultra-High Performance Concrete with Common Technology and Materials.” *Cement and Concrete Composites* 34 (4): 538–44. https://doi.org/10.1016/j.cemconcomp.2011.11.005.

Wang, Xian, Xuejin Liu, Haibin Zhu, and Shaopeng Ma. 2017. “Spatial-Temporal Subset Based Digital Image Correlation Considering the Temporal Continuity of Deformation.” *Optics and Lasers in Engineering* 90 (March): 247–53. https://doi.org/10.1016/j.optlaseng.2016.10.021.

Wille, K., and C. Boisvert-Cotulio. 2013. “Development of Non-Proprietary Ultra-High Performance Concrete for Use in the Highway Bridge Sector.” *Report No. PB2013-110587, National Technical Information Service, Springfield, VA*.

Wille, Kay, and Christopher Boisvert-Cotulio. 2015. “Material Efficiency in the Design of Ultra-High Performance Concrete.” *Construction and Building Materials* 86 (July): 33–43. https://doi.org/10.1016/j.conbuildmat.2015.03.087.

Wille, Kay, Dong Joo Kim, and Antoine E. Naaman. 2011. “Strain-Hardening UHP-FRC with Low Fiber Contents.” *Materials and Structures* 44 (3): 583–98. https://doi.org/10.1617/s11527-010-9650-4.

Xing, H. Z., Q. B. Zhang, C. H. Braithwaite, B. Pan, and J. Zhao. 2017. “High-Speed Photography and Digital Optical Measurement Techniques for Geomaterials: Fundamentals and Applications.” *Rock Mechanics and Rock Engineering* 50 (6): 1611–59. https://doi.org/10.1007/s00603-016-1164-0.

Yajun, Ji, and Jong Herman Cahyadi. 2003. “Effects of Densified Silica Fume on Microstructure and Compressive Strength of Blended Cement Pastes.” *Cement and Concrete Research* 33 (10): 1543–48. https://doi.org/10.1016/S0008-8846(03)00100-5.

Yang, In Hwan, Changbin Joh, and Byung-Suk Kim. 2010. “Structural Behavior of Ultra High Performance Concrete Beams Subjected to Bending.” *Engineering Structures* 32 (11): 3478–87. https://doi.org/10.1016/j.engstruct.2010.07.017.

Yang, Jian, and Jianqiao Ye. 2002. “Interfacial Stresses in Plated Beams with Cracks.” *Composite Structures* 57: 125–34.

Yao, Yiming, Mehdi Bakhshi, Verya Nasri, and Barzin Mobasher. 2018. “Interaction Diagrams for Design of Hybrid Fiber-Reinforced Tunnel Segments.” *Materials and Structures* 51 (1): 35.

Yao, Yiming, Xinmeng Wang, Karan Aswani, and Barzin Mobasher. 2017. “Analytical Procedures for Design of Strain Softening and Hardening Cement Composites.” *International Journal of Advances in Engineering Sciences and Applied Mathematics* 9 (3): 181–194.

Yazıcı, Halit, Hüseyin Yiğiter, Anıl Ş Karabulut, and Bülent Baradan. 2008. “Utilization of Fly Ash and Ground Granulated Blast Furnace Slag as an Alternative Silica Source in Reactive Powder Concrete.” *Fuel* 87 (12): 2401–2407.

Yoo, Doo-Yeol, and Young-Soo Yoon. 2015. “Structural Performance of Ultra-High-Performance Concrete Beams with Different Steel Fibers.” *Engineering Structures* 102 (November): 409–23. https://doi.org/10.1016/j.engstruct.2015.08.029.

Young, Wade F., and Jasan Boparai. 2013. “Whiteman Creek Bridge: A Synthesis of Accelerated Bridge Construction, Ultra-High-Performance Concrete, and Fiber-Reinforced Polymer.” *Pci Journal*, 37–47.

Yu, R., P. Spiesz, and H. J. H. Brouwers. 2014. “Mix Design and Properties Assessment of Ultra-High Performance Fibre Reinforced Concrete (UHPFRC).” *Cement and Concrete Research* 56 (February): 29–39. https://doi.org/10.1016/j.cemconres.2013.11.002.

———. 2015. “Development of Ultra-High Performance Fibre Reinforced Concrete (UHPFRC): Towards an Efficient Utilization of Binders and Fibres.” *Construction and Building Materials* 79 (March): 273–82. https://doi.org/10.1016/j.conbuildmat.2015.01.050.

Zachary B. Haber, Igor De la Varga, Benjamin A. Graybeal, Brian Nakashoji, and Rafic El-Helou. 2018. “Properties and Behavior of UHPC-Class Materials.” FHWA-HRT-18-036.

Zanni, H., M. Cheyrezy, V. Maret, S. Philippot, and P. Nieto. 1996. “Investigation of Hydration and Pozzolanic Reaction in Reactive Powder Concrete (RPC) Using Si-29 NMR.” *Cement and Concrete Research* 26 (1): 93–100. https://doi.org/10.1016/0008-8846(95)00197-2.

Zhang, X. X., A. M. Abd Elazim, G. Ruiz, and R. C. Yu. 2014. “Fracture Behaviour of Steel Fibre-Reinforced Concrete at a Wide Range of Loading Rates.” *International Journal of Impact Engineering* 71 (September): 89–96. https://doi.org/10.1016/j.ijimpeng.2014.04.009.

Zhu, Deju, Barzin Mobasher, and Subramaniam D. Rajan. 2010. “Dynamic Tensile Testing of Kevlar 49 Fabrics.” *Journal of Materials in Civil Engineering* 23 (3): 230–239.

Zohrevand, Pedram, and Amir Mirmiran. 2013. “Seismic Response of Ultra-High Performance Concrete-Filled FRP Tube Columns.” *Journal of Earthquake Engineering* 17 (1): 155–70. https://doi.org/10.1080/13632469.2012.713560.

APPENDIX A – PACKING FRACTION CALCULATION

Question – Three aggregate sizes 1/4", #4 and #8 are combined in weight fractions of 45%, 30% and 25% respectively. The specific gravity of the three aggregates is known to be 2.4, 2.5 and 2.7 respectively. Calculate the packing fraction of this mixture of aggregates using the compressible packing model

Solution –

Step 1 – Calculate the volume fractions of the aggregates from the weight fractions and density values (using Equation 6.12). These values correspond to the y_i values in Equation 6.11.

Table A.1 – Aggregate fractions for given aggregate mixture

	1/4"	**#4**	**#8**
Aggregate Weight Fractions	0.45	0.30	0.25
Specific Gravity (g/cc)	2.40	2.50	2.70
Average Diameter (in.)	0.31"	0.22"	0.14"
Aggregate Volume Fractions (calculated), y_i values in Equation 6.11.	0.47	0.30	0.23

Procedure

Equation 6.12 is used here to determine the aggregate volume fraction from the aggregate weight fractions given in the problem. Equation 6.12 is shown below

$$V_i = \frac{W_i/\rho_i}{\sum_{j=1}^{n} W_j/\rho_j} \qquad (6.12)$$

Here,

V_i is the absolute volume fraction of aggregate size "i" (Note: Since this is absolute volume fraction of aggregates, the volume of voids in the bulk aggregate stockpile is not considered here),

W_i , Wj are the weight fractions of aggregate sizes "i" and "j" and

ρ_i and ρ_j are the specific gravity values corresponding to aggregate sizes "i" and "j".

$$V_1 = \frac{W_1/\rho_1}{\sum_{j=1}^{3} W_1/\rho_1} \Rightarrow V_1 = \frac{0.45/2.40}{0.45/2.40 + 0.30/2.50 + 0.25/2.70} = 0.47$$

Similarly, values for V_2 and V_3 can be calculated as 0.30 and 0.23.

It should be noted that the sum of is V_1 ,V_2 and V_3 is 1.0 sine these are absolute volume fractions, i.e. no voids in the bulk aggregate stockpile are considered in this calculations.

Step 2 – Determine the packing density values for each aggregate size experimentally using DRUW test. These values correspond to the β_i values in Equation 6.11.

Table A.2 – Packing density values obtained from experiment

	1/4"	**#4**	**#8**
DRUW	0.586	0.562	0.542

Procedure

The dry rodded unit weight test was conducted on each of the aggregate sizes separately. For the ¼" aggregate size, the weight of aggregate that filled up the entire container was determined to be 21.95 lbs. Therefore,

$M_{aggregate}$ = 21.95 lbs

$V_{container}$ = 0.25 ft^3 (standard volume for a DRUW test container)

Using equation 6.9, we have:

$$\rho_{bulk} = M_{aggregate}/V_{container} \tag{6.9}$$

$$\Rightarrow \rho_{bulk} = \frac{21.95}{0.25} = 87.8\ lb/ft^3$$

Now, using equation 6.10, we have:

$$\phi_{aggregate} = \rho_{bulk}/\rho_{aggregate} \tag{6.10}$$

Here, aggregate specific gravity is given in the problem as 2.4, therefore in lb/ft3, the aggregate density can be calculated as:

$$\rho_{aggregate} = 2.4 * 62.429 = 149.83\ lb/ft^3$$

Therefore, we can determine the packing density of aggregate as:

$$\Rightarrow \phi_{aggregate} = \frac{87.8}{149.83} = 0.586$$

Step 3 – Calculate the wall effect and loosening coefficients (using Equations 6.6 and 6.7).

Procedure

Equations 6.6 and 6.7 are shown below:

$$a_{ij} = \sqrt{1 - \left(1 - d_j/d_i\right)^{1.02}}; d_j > d_i \quad (6.6)$$

$$b_{ij} = 1 - \left(1 - d_i/d_j\right)^{1.50};\ d_i > d_j \quad (6.7)$$

Since we have three different aggregate sizes, the size of the matrices containing the loosening and wall effect coefficients is 3 x 3. Note that both coefficient matrices have zeroes in one half of the matrix. This is because the calculation of the loosening coefficient (a_{ij}) is only valid when $d_i < d_j$ and the calculation of wall coefficient is only valid when $d_i > d_j$.

We can write the calculations for loosening coefficient as:

$$a_{11} = \sqrt{1 - (1 - d_1/d_1)^{1.02}} = 1$$

Similarly,

$$a_{12} = \sqrt{1 - (1 - d_2/d_1)^{1.02}} = \sqrt{1 - (1 - 0.22/0.31)^{1.02}} = 0.84$$

And,

$$a_{23} = \sqrt{1 - (1 - d_3/d_2)^{1.02}} = \sqrt{1 - (1 - 0.14/0.22)^{1.02}} = 0.81$$

Also, a_{21}=0, a_{31}=0 and a_{32}=0, since the equation for loosening coefficient is not valid when $d_i > d_j$

We can write the calculations for wall effect coefficient as:

$$b_{11} = 1 - (1 - d_1/d_1)^{1.50} = 1$$

Similarly,

$$b_{21} = 1 - (1 - d_2/d_1)^{1.50} = 1 - (1 - 0.22/0.31)^{1.50} = 0.84$$

And,

$$b_{32} = 1 - (1 - d_3/d_2)^{1.50} = 1 - (1 - 0.14/0.22)^{1.50} = 0.79$$

Also, b_{12}=0, b_{13}=0 and b_{23}=0, since the equation for wall effect coefficient is not valid when $d_i < d_j$

Table A.3 and A.4 show the calculated coefficients in a matrix format.

Table A.3 – Loosening effect coefficients (a_{ij})

	1/4"	#4	#8
1/4"	1	0.84	0.68
#4	0	1	0.81
#8	0	0	1

Table A.4 – Wall Effect Coefficients (b_{ij})

	1/4"	#4	#8
1/4"	1	0	0
#4	0.84	1	0
#8	0.59	0.79	1

Step 4 – The values for β_i, y_i and the wall and loosening effect coefficients are used to evaluate γ_i values using equation 6.8.

Procedure

Equation 6.8 is shown below.

$$\gamma_i = \frac{\beta_i}{1 - \sum_{j=1}^{i-1}\left[1 - \beta_i + b_{ij}\beta_i\left(1 - 1/\beta_j\right)\right]y_j - \sum_{j=i+1}^{n}\left[1 - a_{ij}\,\beta_i/\beta_j\right]y_j}$$

For the calculation of γ_1, all te other required values have been determined in the previous steps. So we can express γ_2 as:

$$\gamma_2 = \frac{\beta_2}{1 - \sum_{j=1}^{1}\left[1 - \beta_2 + b_{1j}\beta_2\left(1 - 1/\beta_j\right)\right]y_j - \sum_{j=3}^{3}\left[1 - a_{1j}\,\beta_2/\beta_j\right]y_j}$$

$$\Rightarrow \gamma_2 = \frac{0.562}{1 - \left(1 - 0.562 + 1 * 0.562 * \left(1 - \frac{1}{0.586}\right)\right) * 0.47 - \left(1 - 1 * \frac{0.562}{0.542}\right) * 0.23} = 0.617$$

Similarly, the values for γ_1 and γ_3 can be determined. The calculated values for γ_1, γ_2 and γ_3 are shown in Table A.5.

Table A.5 – Virtual packing density values calculated for every aggregate size

	1/4"	**#4**	**#8**
Virtual Packing Density (γ)	0.654	0.617	0.631

Step 5 – Solve for Packing Density ϕ

Procedure

Select a value of compaction index "K" (value of 9 is selected here assuming compaction using vibration and compression). Finally, the values of "K", γ_i, β_i and y_i are used in equation 6.11 to solve for the packing density ϕ. Equation 6.11 is shown below:

$$K = \sum_{i=1}^{n} \frac{y_i/\beta_i}{1/\Phi - 1/\gamma_i} \qquad (6.11)$$

All of the calculated values are substituted here to get:

$$9 = \sum_{i=1}^{3} \frac{y_i/\beta_i}{1/\Phi - 1/\gamma_i}$$

$$\Rightarrow 9 = \frac{y_1/\beta_1}{1/\Phi - 1/\gamma_1} + \frac{y_2/\beta_2}{1/\Phi - 1/\gamma_2} + \frac{y_3/\beta_3}{1/\Phi - 1/\gamma_3}$$

$$\Rightarrow 9 = \frac{0.47/0.586}{1/\Phi - 1/0.654} + \frac{0.30/0.562}{1/\Phi - 1/0.617} + \frac{0.23/0.542}{1/\Phi - 1/0.631}$$

This equation needs to be solved for the unknown packing density ϕ using Newton's iteration method, which can be done using any numerical software package such as Excel or MATLAB.

Result – The packing density ϕ is found to be 0.563.

APPENDIX B - SOLVED EXAMPLE PROBLEMS FOR – PARAMETRIC BASED DESIGN FOR UHPC

The sample problem can be constructed in three different cases:

Case A - The sizes of the beam and the residual strength of the material are known; the maximum allowable load is required for a given geometry.

Case B - Size of the beam and the loading condition (moment demand) are known; the level of residual strength is required.

Case C - The residual strength of the material and the loading condition (moment demand) are known; the size of the section is required.

Case A- Calculation of the moment capacity of a given section

The aim of this section is to use the simplified ultimate strength approach and compare the parametric design of FRC with the solutions obtained from ACI 544.8R-16, in order to illustrate the process of obtaining moment capacity for a section and compute the allowable service load.

Problem Statement- Compute the maximum allowable load on a simply supported beam with a span of $L = 10\,\text{ft}\ (3.04\,\text{m})$ and a rectangular section 6 in × 12 in (152 mm × 305 mm). UHPC concrete has a compressive strength, f_c', of 22 ksi (151.6 MPa). Design for a material with $f^D_{150} = 580\,\text{psi}\ (4\,\text{MPa})$. Assume a concrete density as $\rho_c = 150\,\text{lb/ft}^3$ $(2402.7\,\text{kg/m}^3)$ and compute unfactored moment by assuming $\phi = 1$ (ϕ is strength reduction factor, which is less than one in accordance with ACI 318-14 Section 10.5.1(ACI Committee 318 and American Concrete Institute 2014).

For an illustration of the calculation and comparison, Case A is addressed in this example. Figure B-1 shows a schematic side view of the simply supported beam under a center loading.

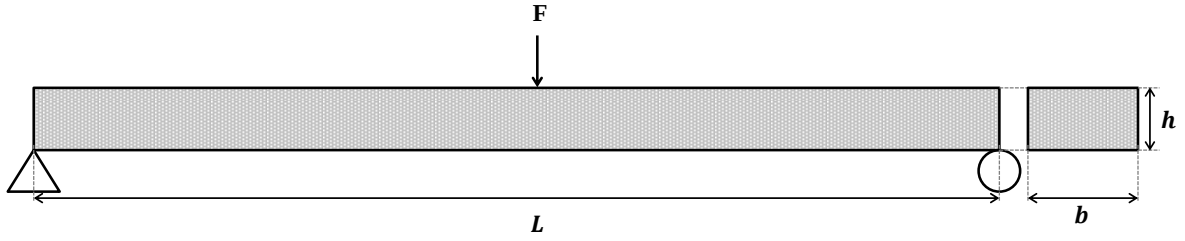

Figure B - 1. Sample problem, simply supported beam with center point loading.

- **Step 1: Define geometric and material parameters**

$L = 10$ ft (3.3 m), $b = 12$" (0.3 m), $h = 6$" (0.15 m), $\phi = 1$, $f_c' = 22$ ksi (151.6 MPa)

Assume $\gamma = 1$, thus: $E_c = E$; also $\sigma_{cr} = 0.04 f_c'$

$$E = 49000\sqrt{f_c'} = 7.27 \times 10^6 \text{ psi } (50 \text{ GPa})$$

$$\sigma_{cr} = 0.04 f'_c = 0.04 \times 22000 = 880 \text{ psi } (6.07 \text{ MPa})$$

$$\varepsilon_{cr} = \frac{\sigma_{cr}}{E} = \frac{880 \text{ psi}}{7270000 \text{ psi}} = 1.21 \times 10^{-4}$$

$$\varepsilon_{cy} = \beta_2 \times \frac{f_c'}{E} = 0.85 \times \frac{22000 \text{ psi}}{7270000 \text{ psi}} = 0.85 \times 0.003 = 2.57 \times 10^{-3}$$

β_{tu} is the normalized ultimate tensile strain in the section, since it is assumed that the section will maintain its residual tensile strength. This value is expected to be imposed as a large number. In this example, it is considered to be equal to 50, i.e., $\beta_{tu} = \varepsilon_{tu} / \varepsilon_{cr} = 50$. Therefore, maximum tensile strain allowed is $\varepsilon_{tu} = 0.0055$ or 0.55%.

- **Step 2: Calculate demand moment**

$$M_u = M_{DL} + M_F$$

Where M_{DL} is moment due to dead weight and M_F is the moment due to point load.

$$\text{w} = \frac{72 \text{ in}^2}{144} \times 150 \text{ lb/ft}^3 = 75 \text{ lb/ft} = 6.25 \text{ lb/in} (1.09 \text{ kN/m})$$

$$M_{DL} = \frac{wL^2}{8} = \frac{75 \text{ lb/ft} \times 10^2 \text{ ft}^2}{8} = 937.5 \text{ lb-ft} = 11250 \text{ lb-in} (1.27 \text{ kN-m})$$

For a simply supported beam the maximum moment is at the center of the beam:

$$\phi \text{M}_\text{n} = M_u = 937.5 + \frac{F \times 10}{4} \text{ lb-ft} = 11250 + 30F \text{ lb-in}$$

- **Step 3: Calculate the cracking moment**

The cracking moment is given by:

$$M_{cr} = \frac{1}{6}\sigma_{cr} bh^2 = \frac{1}{6}(880 \text{ psi}) \times 12" \times (6")^2 = 63360 \text{ lb-in} = 5.28 \text{ kips-ft } (7.16 \text{ kN-m})$$

- **Step 4: Determine post-crack tensile strength (ACI 544.8R-16)**

Use the formula for plain FRC (according to $M_n = \frac{3f^D_{150}}{2.42\sigma_{cr}} M_{cr} = \frac{31f^D_{150}}{f_c'} M_{cr}$ Equation **65**)

$$M_n = \frac{31f^D_{150}}{f_c'} M_{cr}$$

$$= \left[\frac{31\times 580}{22000}\right] \times 5.28 = 4314 \text{ lb-ft (5.84 kN-m)}$$

$$\phi M_u = M_n \Rightarrow \left(937.5 + \frac{F\times 10}{4}\right) = 4314 \text{ lb-ft}$$

$$F = 1350.6 \text{ lb (6.0 kN)}$$

Simplified Approach:

Here the results of the previous method are compared with the results from the simplified approach.

From $M_n = \frac{\omega\mu(3\omega + 8\mu)}{(\omega + 2\mu)^2} \times M_{cr}$ Equation 32, we have

$$M_n = \frac{\omega\mu(3\omega + 8\mu)}{(\omega + 2\mu)^2} \times M_{cr}$$

Where

$$\omega = \frac{\varepsilon_{cr}}{\varepsilon_{cr}} = \frac{2.57\times 10^{-3}}{1.21\times 10^{-4}} = 21.25 \text{ and } \mu = \frac{f^D_{150}}{2.42\sigma_{cr}} = \frac{580}{2.42\times 880} = 0.27$$

Thus

$$M_n = 50895 \text{lb-in} = 4241 \text{lb-ft} \ (5.75 \text{ kN-m})$$

Moment capacity obtained from the simplified method is 11 percent higher than the value obtained from the ULS method. The simulated moment-curvature diagram for this example is shown in Figure B-2. Both ULS and the simplified approach give an acceptable result. However, before reaching the ultimate state, the section is able to carry higher bending moments than the ultimate moment capacity.

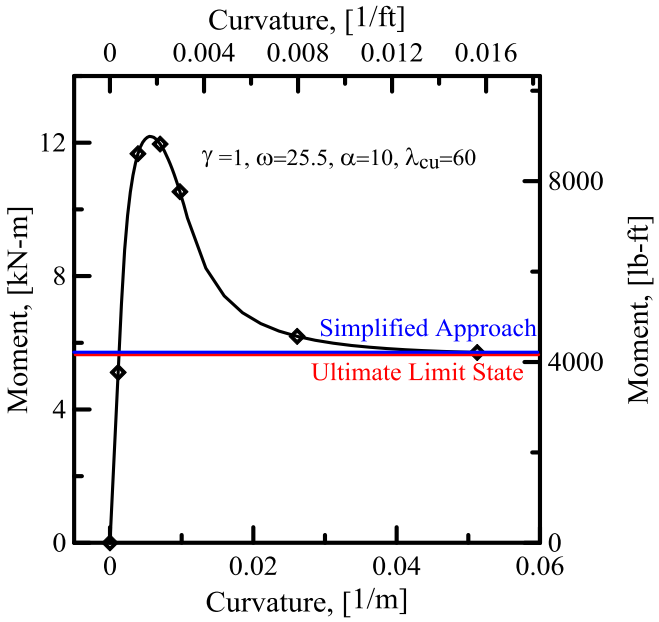

Figure B - 2. Comparison between different analytical models.

Case B- Calculation of the moment capacity of a given reinforced joint

This part presents a design example for the reinforced section with a joint at the middle section of the beam. The design procedure will be calculated using the solutions obtained from ACI 544.8R-16, to illustrate the process of obtaining moment capacity for a UHPC joint under specific loading conditions and compute the allowable service load. All of the dimensions are similar to the previous example; only the parameters for the reinforcement and the UHPC joint are extra parameters in this example.

Problem Statement- Compute the maximum bending capacity of the UHPC joint as a function of allowable load, F, on a simply supported single reinforced beam with a span of $L = 10\,\text{ft}\ (3.04\,\text{m})$ and a rectangular section 6in × 12in (152 × 305 millimeters). The reinforcement consisted of 3 Grade 60 #4 rebars, $E_s = 30\times10^6$ psi $(210\,\text{GPa})$ (see Figure A.1.b), with a yield strength σ_{sy} (or f_y) of 74 ksi (510 MPa), yield strain ε_{sy} of 0.24 percent, and the reinforcement depth is $d = 5\text{in}$. Two loads with a loading gage of L/3 are applied on top of the beam and the joint length, $L_j = 6\text{in}\ (152\ \text{mm})$.

Normal concrete has $f_{c1}^{'} = 6$ ksi (41.4 MPa) and $\sigma_{cr1} = 0.3$ ksi (2 MPa); UHPC concrete has $f_{c2}^{'} = 22$ ksi (151.6 MPa) and $\sigma_{cr2} = 1.2$ ksi (8.27 MPa). Design for a UHPC material with $f^{D}_{150} = 580$ psi $(4\,\text{MPa})$. Assume a concrete density as $\rho_c = 150\,\text{lb/ft}^3$ $(2402.7\,\text{kg/m}^3)$ for both normal concrete and UHPC.

To illustrate the calculation, Figure B-3 shows a schematic side view of the simply supported beam under two equal loadings.

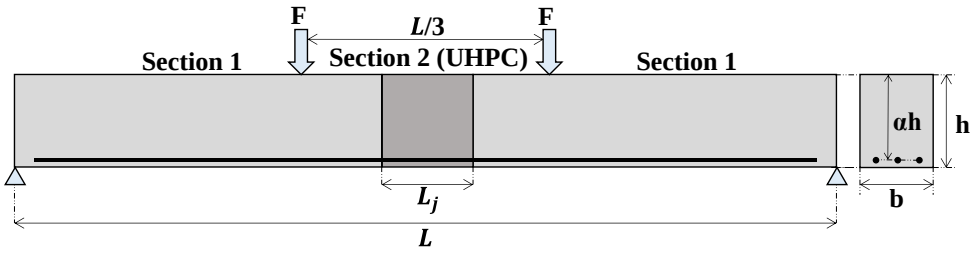

Figure B - 3. Sample problem, simply supported beam with center point loading.

- **Step 1: Define geometric and material parameters**

$L = 10$ ft (3.3 m), $b = 12$" (0.305 m), $h = 6$" (0.152 m), $\phi = 1$

Also,, $\sigma_{cr2} = 0.04 f_{c2}$' and $E_{c2} = 49000\sqrt{f_{c2}'}$, thus:

$$E_{c1} = 57000\sqrt{f_{c1}'} = 4.4\times10^{6} \text{ psi } (30 \text{ GPa})$$

$\sigma_{cr1} = 6.7\sqrt{f_{c1}'} = 519$ psi (3.6 MPa)

$E_{c2} = 49000\sqrt{f_{c2}'} = 7.27\times10^{6}$ psi (50 GPa)

$$\sigma_{cr2} = 0.04 f'_c = 0.04\times22000 = 880 \text{ psi } (6.07 \text{ MPa})$$

$$\varepsilon_{cr1} = \frac{\sigma_{cr1}}{E_{c1}} = \frac{519 \text{ psi}}{4400000 \text{ psi}} = 1.18\times10^{-4}$$

$$\varepsilon_{cr2} = \frac{\sigma_{cr2}}{E_{c2}} = \frac{880 \text{ psi}}{7270000 \text{ psi}} = 1.21\times10^{-4}$$

β_{tu} is the normalized ultimate tensile strain in the section. Since it is assumed that the section will maintain its residual tensile strength, this value is expected to be imposed as a large number. In this example, it is considered to be equal to 50, i.e. $\beta_{tu} = \varepsilon_{tu} / \varepsilon_{cr} = 50$. Therefore, maximum tensile strain allowed is $\varepsilon_{tu} = 0.0055$ or 0.55% .

ω is the ratio of compressive strength to tensile strength and obtained as

$$\omega = \beta_2 \times \frac{f_c^{'}}{\sigma_{cr}} = 0.85 \times \frac{22000 \text{ psi}}{880 \text{ psi}} = 21.25$$

- **Step 2: Calculate the demand moment**

$$M_u = M_{DL} + M_F$$

Where M_{DL} is the moment due to dead weight and M_F is the moment due to point load.

$$\text{w} = \frac{72 \text{ in}^2}{144} \times 150 \text{ lb/ft}^3 = 75 \text{ lb/ft} = 6.25 \text{ lb/in} (1.09 \text{ kN/m})$$

$$M_{DL} = \frac{wL^2}{8} = \frac{75 \text{ lb/ft} \times 10^2 \text{ ft}^2}{8} = 937.5 \text{ lb-ft} = 11250 \text{ lb-in} (1.27 \text{ kN-m})$$

For a simply supported beam the maximum moment is at the center of the beam:

$$\phi \text{M}_\text{n} = M_u = 937.5 \text{ ft} + \frac{F \times 10}{3} \text{ lb-ft}$$

- **Step 3: Calculate the cracking moment**

Is this problem there are two different sections. The RC section is likely to fail before UHPC joint failure, so the design should be based on the properties of the beam section (section 1). However, the purpose of this example is to introduce the design process of the UHPC joint section and its bending capacity. Therefore, the calculations for the RC section are not represented here and only the comparative results are demonstrated in Figure B - 4.

Cracking moment of the joint is given by:

$$M_{cr} = \frac{1}{6} \sigma_{cr} bh^2 = \frac{1}{6} (880 \text{ psi}) \times 12'' \times (6'')^2 = 63360 \text{ lb-in} = 5.28 \text{ kips-ft (7.16 kN-m)}$$

- **Step 4: Minimum and balanced reinforcement**

Minimum reinforcement is given by (ACI Committee 318, 2014)

$$\rho_{\text{min}} = \text{Max}[\frac{200}{f_y}, \frac{3\sqrt{f_c^{'}}}{f_y}] = \text{Max}[\frac{200}{74000}, \frac{3\sqrt{22000}}{74000}] = \text{Max}[0.0027, 0.006] = 0.006$$

For this example we have

$$\rho_g = \frac{3 \times 0.2 \text{ in}^2}{12 \times 5 \text{ in}^2} = 0.01 \geq \rho_{\text{min}} \text{ , Passed}$$

To calculate the balanced reinforcement ρ_{bal} from $\rho_b = \frac{\beta_1\beta_2\varepsilon_{cy}f_c' - \varepsilon_{sy}\mu\sigma_{cr}}{(\varepsilon_{sy}+\varepsilon_{cy})f_y} = \frac{\beta_1\omega^2 - \kappa\mu}{(\kappa+\omega)n\kappa}$

Equation 48, we have

$$\rho_b = \frac{\beta_1\omega^2 - \kappa\mu}{(\kappa+\omega)n\kappa}$$

From $\kappa = \frac{\varepsilon_{sy}}{\varepsilon_{cr}}$ Equation 35, Equation 36 and Equation 64

$$\kappa = \frac{\varepsilon_{sy}}{\varepsilon_{cr}} = \frac{2.4\times10^{-3}}{1.21\times10^{-4}} = 20$$

$$n = \frac{E_s}{E_c} = \frac{30\times10^6 \text{ psi}}{7.27\times10^6 \text{ psi}} = 4.1$$

$$\mu = \frac{f^D_{150}}{2.42\sigma_{cr}} = \frac{580 \text{ psi}}{2.42\times880 \text{ psi}} = 0.27$$

Thus,

$$\rho_b = \frac{0.65\times0.85\times21.25^2 - 0.27\times20}{(20+0.27)\times4.1\times20} = 0.082 >> \rho_g \text{, Passed}$$

The current reinforcement is much lower than the balanced reinforcement (i.e., $\rho_g << \rho_b$ = 8%).

- **Step 5: Determine post-crack tensile strength (ACI 544.8R-16)**

Use the formula for the single reinforced section, according to Equation 67.

$$M_n \approx m_\infty M_{cr} = \frac{6\rho_g n\kappa\left(\mu\alpha - \mu + \alpha\omega\right) + 3\omega\mu - 3\left(\rho_g n\kappa\right)^2}{\omega + \mu} M_{cr}$$

Where

$$\alpha = \frac{d}{h} = \frac{5 \text{ in}}{6 \text{ in}} = 0.83$$

Thus

$$M_n = 4.74\times M_{cr} = 4.87\times63360 = 307 \text{ kip-in} = 25600 \text{ lb-ft (34.7 kN-m)}$$

$$\phi M_u = M_n \Rightarrow \left(937.5 + \frac{F \times 10}{3}\right) = 25600 \text{ lb-ft}$$

$$F = 7.4 \text{ kip } (32.9 \text{kN})$$

Simplified approach:

Here the results of the ULS method is compared with the results from the simplified approach. From Equation 45, we have

$$M_n = 3\left[\mu(1-A)\left(1+A(1-\beta_1)\right) + 2\rho\kappa n\left(\alpha - \frac{A\beta_1}{2}\right)\right] \times M_{cr}$$

Where

$$A = \frac{\mu + \rho\kappa n}{\beta_1 \omega + \mu}$$

Thus

$$M_n = 307.2 \text{ kip-in} = 25.6 \text{ kip-ft } (34.71 \text{ kN-m})$$

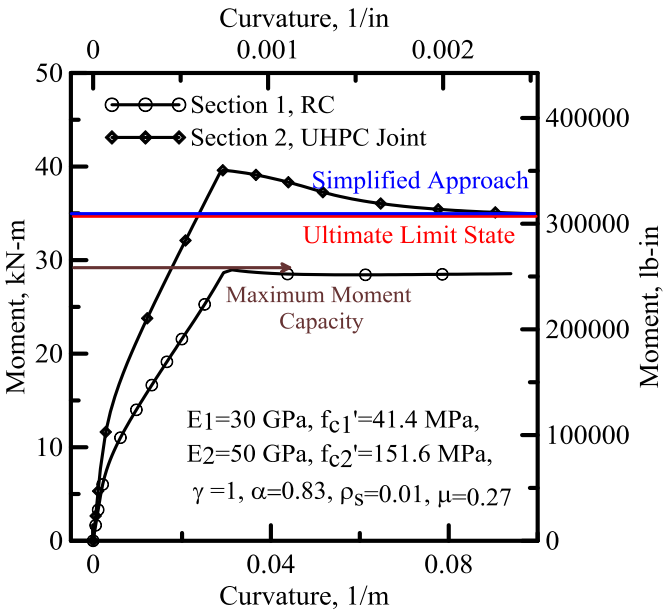

Figure B - 4. Comparative results for different design approaches (1 MPa = 145 psi).

This figure shows a comparison between different design methods for the UHPC joint (section 2). As can be observed from the figure, there is a very good agreement between different approaches at ULS. However, the RC section (section 1) has a lower bending strength (about 20 percent) and will dominate the failure of the element, regardless of the UHPC joint's strength. Therefore, the proper design approach is to first design the RC beam and then control the joint.

APPENDIX C - TOOLS FOR DESIGNING UHPC MIXTURES

APM – Aggregate Packing Model - A Software Package to Calculate the Packing Fraction of Poly Disperse Aggregate Mixtures

Developed By – Aashay Arora

Doctoral Student,

School of Sustainable Engineering and the Built Environment,

Arizona State University, Tempe, AZ, USA

INFORMATION - This software is provided as a tool for the proportioning of the aggregate blends and in fulfilment of the ADOT sponsored project SPR-745 conducted at Arizona State University. This software is intended to be used by an experienced user. Please refer to the documentation provided with the program to become familiar with its capabilities.

Overview

APM version 1.0 is a software package designed to calculate the packing fraction of aggregates in an aggregate mixture containing aggregates of two or more sizes. Packing fraction of an aggregate mixture is defined as the volume fraction occupied by aggregates in a unit volume. The remainder of this quantity is the porosity of the mixture (Porosity = 1 – Packing Fraction). The packing fraction of an aggregate mixture depends on several factors such as the gradation of aggregate sizes, the shape and size of aggregates and the degree of packing. A well graded aggregate distribution will have aggregates from large to small sizes in such a way so that they interlock well and result in a compact distribution with a very low porosity. On the other hand, a poorly graded distribution will result in a very low packing fraction and consequently high porosity because the smaller aggregates are not able to fill in the voids created by the larger aggregates. Similarly, rounded aggregates may not pack as efficiently as angular aggregates. The current model considers all of these factors and calculates the packing fraction.

The model accepts as inputs the sizes of aggregates in the aggregate mixture and the packing fractions of each aggregate size derived using DRUW method (ASTM 1997). The output of the model is a text file containing combinations of aggregates (volume fractions) and the packing fraction of the corresponding aggregate mixture.

Model Description

APM version 1.0 utilizes an analytical approach to determine the packing fraction of an aggregate mixture (Arora 2018). The model is based on the compressible packing model by De Larrard (De Larrard 1999). The packing fraction of a poly-disperse aggregate mixture can be expressed as a function of the individual packing fractions of each aggregate size present in the mixture. The software uses a scalar

index “K”, also known as the compaction index, which depends on the physical effort involved in packing these particles in the mixture. A higher compaction index implies fewer voids and a higher packing density of aggregates. For instance, a “K” value of 9 is used when a combination of vibration and compression is used to pack the particles and a “K” value of 4.75 is used when only vibration is used. The packing fraction is evaluated as the solution to Equation C - 1.

$$K = \sum_{i=1}^{n} \frac{y_i/\beta_i}{1/\Phi - 1/\gamma_i}$$ **Equation C - 1**

Here,

K is the compaction index; K = 9 is used when aggregates are vibrated and compacted,

“n” is the number of different aggregate sizes in the aggregate mixture,

β_i is the residual packing density of aggregate size “i,” determined using DRUW testing,

y_i is the individual volume fraction of the aggregate size “i” in the mixture,

ϕ is the packing density of the aggregate mixture, and

γ_i is the packing density of the aggregate mixture considering aggregate size “i” as the dominant aggregate size.

Here K, n and β_i are inputs to the program, γ_i is calculated internally in the software for different values of y_i. A detailed description to calculate γ_i is given in Chapter 6. Equation C - 1 is numerically solved in the software for different volume fractions of aggregates ranging from 0 to 1, and ϕ values are determined for each aggregate mixture. Finally, calculated values of packing fraction are tabulated in a text file.

Inputs Required

Prior to running this software to calculate the packing density of aggregate mixtures, the user of the software should know the following:

- Aggregate sizes to be used (eg. ¼”, #4, #8, #10). The program accepts aggregate sizes in inches. The conversion for a few standard ASTM sizes in inches is given in Table C- 1.

Table C- 1. Conversion of ASTM sizes to inches

ASTM Sizes	Size (in inches)
No.4	0.187in
No.6	0.132in
No.8	0.093in
No.10	0.079in
No.16	0.046in
No.20	0.033in

No.30	0.024in

- DRUW for each aggregate size – The output from the DRUW test is used as an input for the program. The user must perform the DRUW test on every aggregate size that they wish to use in the aggregate gradation.
- BSG (bulk specific gravity) – The program measures the optimized aggregate proportions in terms of volume fractions. User must know the bulk density of the aggregate as measured by ASTM C127 and 128 to convert the volume fractions into equivalent mass fractions.
- K (compression index) - a dimensionless number between 0 to 10 representing the compaction ratio. i.e. a compression index of 1 represents loose aggregate and 9 represents a fully compacted, rodded, and vibrated blend of aggregates.

Software Documentation

The software is distributed as an .exe file and runs on any Windows operating system. The opening screen contains details of the model name, version, last compiled date and developer's credentials. Figure C- 1 shows the opening screen of the software.

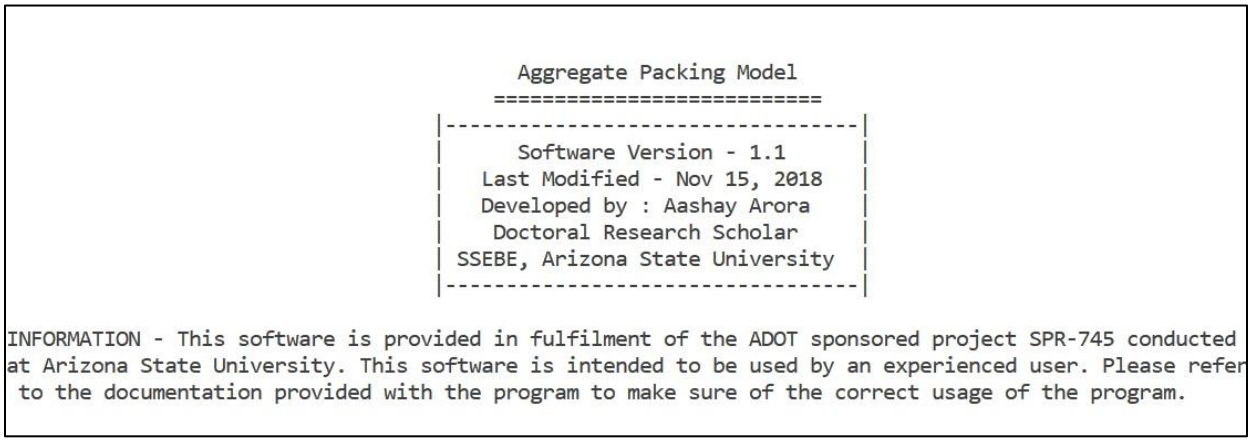

Figure C- 1. Opening screen of APM

The opening screen is followed by step 1, where the user is asked to enter the number of aggregate classes. The term "aggregate class" refers to the number of aggregate sizes to be used in the design of UHPC. The minimum number of aggregate sizes to be entered is 2 and the maximum number of aggregate sizes that can be entered is 10. Standard aggregate stockpiles contain aggregates of five to six different sizes, so having 10 aggregate sizes is more than enough to determine an optimized gradation which can be implemented in field. Figure C- 2 shows step 1.

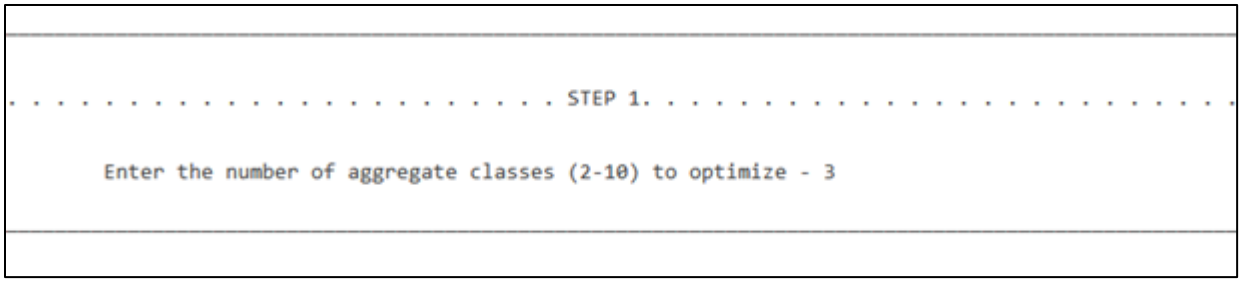

Figure C- 2. Step 1: Enter the number of aggregate classes

Step 2 takes user input for aggregate sizes and their corresponding packing fractions. User must enter aggregates for the number of aggregate sizes as entered in Step 1. User must be extremely careful here to enter the sizes of aggregates in decreasing order (that is, largest size first), else the program will return an error code when it runs. The aggregate size must be specified in inches. The step also asks the user to enter the packing fraction of the aggregate. The value of packing fraction for the particular aggregate class/size is the volume fraction occupied by that aggregate class/size in a unit volume and is experimentally determined using the DRUW method. Since this is a fraction, its value lies between 0 and 1. Figure C- 3 shows step 2.

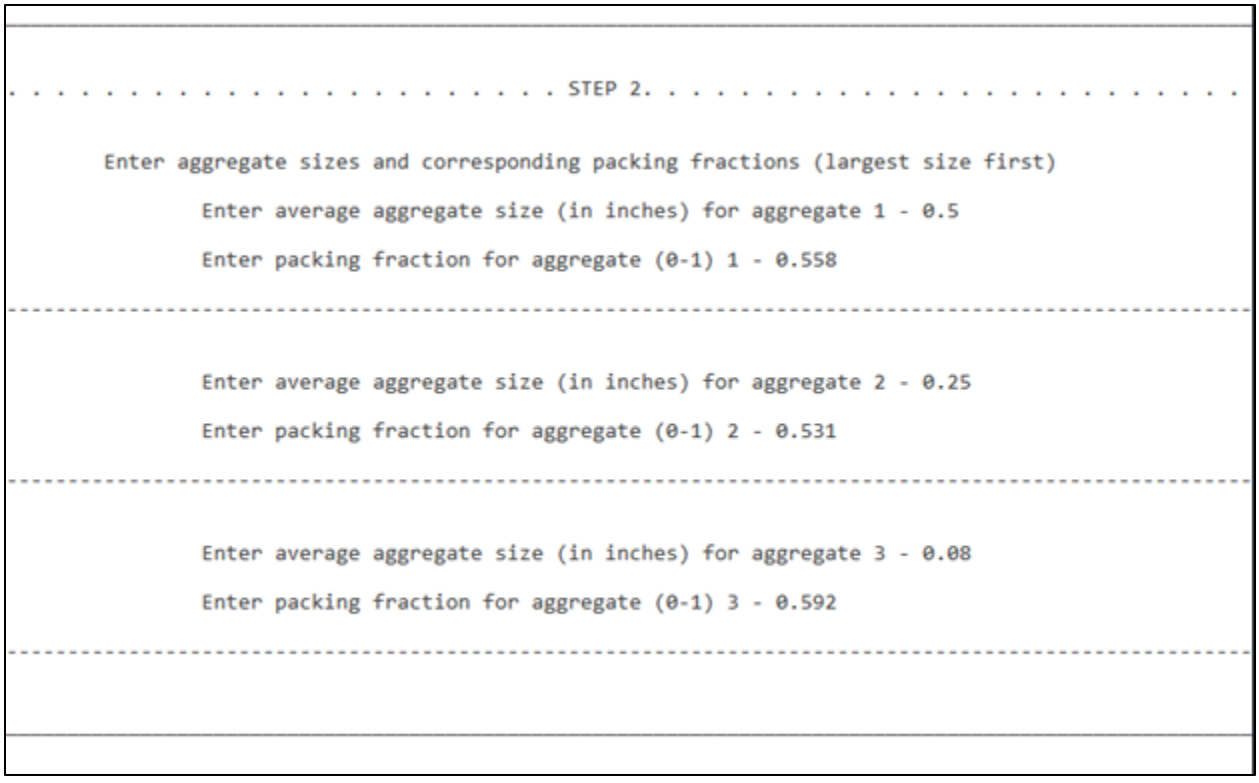

Figure C- 3. Step 2: Enter aggregate sizes and packing fractions

Step 3 takes the user input for compression index (K) and test precision. As a guideline, a "K" value of 9 is used when a combination of vibration and compression is used to pack the aggregates and a "K" value of 4.75 is used when only vibration is used. The test precision is for the software to recognize the number of levels of individual volume fractions (y_i) of aggregates to check for an optimized aggregate gradation. The y_i values are selected by the software between 0 and 1 based on the test precision specified by the user. Test precision has ten levels ranging from one to ten. The precision levels are given in Table C- 2.

Table C- 2. Test precision levels

Test Precision Level	Individual Volume Fraction Interval
1	0.25
2	0.20
3	0.15
4	0.12
5	0.10
6	0.08
7	0.05
8	0.04
9	0.02
10	0.01

For instance, if test precision level is selected as 0.2, the software will run the packing simulation for the individual volume fractions of the aggregates at an interval of 0.2, that is 0, 0.2, 0.4, 0.6, 0.8 and 1.0. Similarly, if the test precision level of 10 is selected, the software will run the packing simulation for the individual volume fractions of the aggregates at an interval of 0.01, that is 0, 0.01, 0.02, 0.03 … 0.97, 0.98, 0.99, 1.00.

It is sufficient to say that the greater the test precision, the more accurate the results will be; however, it will affect the time it takes to run the program. For instance, if there are three aggregate classes, then the number of times the program will run the packing simulation at a precision level one is 15, whereas, for three aggregate classes at a precision level 10, the number of packing simulations required is 5050. These numbers will be even higher if the number of aggregate classes is more than three. Therefore, users are advised to select the test precision level carefully. A default test precision level between 5 to 7 is suggested for number of aggregate classes greater than five. For aggregate classes less than or equal to five, the user may go to a test precision of 10. Figure C- 4 shows step 3.

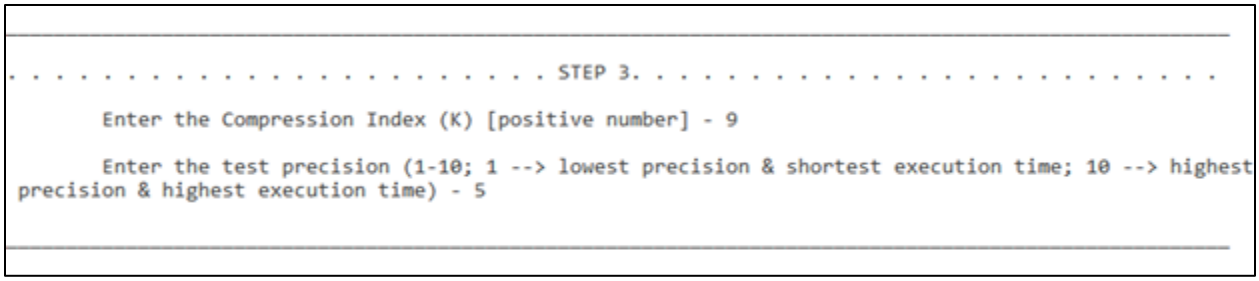

Figure C- 4. Step 3: Enter compression index (K) and test precision

Step 4 requires the user to enter the name of the file under which to save the report. The report is written in a tab delimited format in a text file. The file extension (*.dat) is automatically applied to the filename. Figure C- 5 shows step 4.

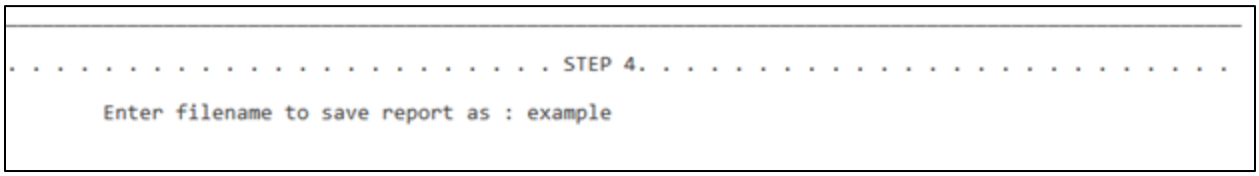

Figure C- 5. Step 4: Enter filename

Based on all the above information, the software runs the packing simulations and generates a report using the name recorded in Step 4. If all inputs are correct, the software displays the statement "Success. Run Completed." Figure C- 6 shows step 5.

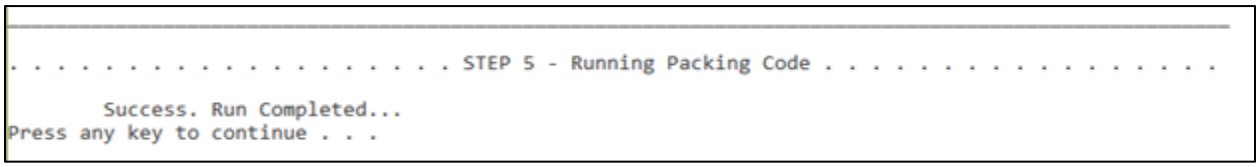

Figure C- 6. Step 5: Run completed

Post Processing of Results

The report generated by the software is saved in the folder where the .exe file is located. A .dat file is generated which may be opened in any text editor such as Notepad. The first few rows of the output file show the software name, last compiled and developer information. The next few lines show the input given by user. The following lines show a tabulated result of aggregate combinations and corresponding packing fraction obtained. Figure C- 7 shows a snapshot of the text file generated.

```
          Aggregate Packing Model
          ========================
         |----------------------------------|
         |      Software Version - 1.0      |
         |   Last Modified - June 4, 2018   |
         |   Developed by : Aashay Arora    |
         |    Doctoral Research Scholar     |
         | SSEBE, Arizona State University  |
         |----------------------------------|

Aggregate#  Size (mm)   Packing Fraction
1   12.7    0.558
2   6.35    0.531
3   2.032   0.592
Compression Index (K)   9
Test Precision  0.1
Size = 12.7 Size = 6.35 Size = 2.032    Packing Fraction
0   0   1   0.532459
0   0.1 0.9 0.545227
0   0.2 0.8 0.558607
0   0.3 0.7 0.571588
0   0.4 0.6 0.583378
0   0.5 0.5 0.590823
0   0.6 0.4 0.583336
0   0.7 0.3 0.559723
0   0.8 0.2 0.531029
0   0.9 0.1 0.503109
0   1   1.11022e-016    0.477588
0.1 0   0.9 0.551947
0.1 0.1 0.8 0.565483
0.1 0.2 0.7 0.579645
0.1 0.3 0.6 0.592444
0.1 0.4 0.5 0.602143
0.1 0.5 0.4 0.599124
0.1 0.6 0.3 0.575944
```

Figure C- 7. Report generated in text format

The report generated is a tab delimited text file and can be imported in Microsoft Excel to view the results. A snapshot of the imported file is shown in Figure C- 8.

	A	B	C	D
1	Column1	Column2	Column3	Column4
2				Aggregate Packing Model
3				==========
4			|----------|	
5			| Software Version - 1.0 |	
6			| Last Modified - June 4, 2018 |	
7			| Developed by : Aashay Arora |	
8			| Doctoral Research Scholar |	
9			| SSEBE, Arizona State University |	
10			|----------|	
11				
12	Aggregate#	Size (mm)	Packing Fraction	
13	1	12.7	0.558	
14	2	6.35	0.531	
15	3	2.032	0.592	
16	Compression Index (K)	9		
17	Size = 12.7	Size = 6.35	Size = 2.032	Packing Fraction
18	0	0	1	0.532459
19	0	0.1	0.9	0.545227
20	0	0.2	0.8	0.558607
21	0	0.3	0.7	0.571588
22	0	0.4	0.6	0.583378
23	0	0.5	0.5	0.590823
24	0	0.6	0.4	0.583336
25	0	0.7	0.3	0.559723
26	0	0.8	0.2	0.531029
27	0	0.9	0.1	0.503109

Figure C- 8. Report exported to Microsoft Excel

The aggregate combination with the maximum packing fraction can be determined by sorting the excel file by the packing fraction column. Figure C- 9 shows the sorted data organized in descending order of packing fraction.

A	B	C	D
Size = 12.7	Size = 6.35	Size = 2.032	Packing Fraction
0.5	0.1	0.4	0.643536
0.6	0	0.4	0.64146
0.4	0.2	0.4	0.637982
0.5	0	0.5	0.636767
0.5	0.2	0.3	0.631877
0.4	0.1	0.5	0.630817
0.3	0.3	0.4	0.62733
0.6	0.1	0.3	0.627224
0.4	0.3	0.3	0.624042
0.3	0.2	0.5	0.622381
0.4	0	0.6	0.616677
0.2	0.4	0.4	0.613828
0.7	0	0.3	0.612818
0.2	0.3	0.5	0.612734
0.3	0.4	0.3	0.609857
0.3	0.1	0.6	0.609497
0.5	0.3	0.2	0.602781
0.1	0.4	0.5	0.602143
0.6	0.2	0.2	0.601972
0.2	0.2	0.6	0.601209
0.1	0.5	0.4	0.599124
0.3	0	0.7	0.594292
0.2	0.5	0.3	0.592895
0.4	0.4	0.2	0.592481
0.1	0.3	0.6	0.592444

Figure C- 9. Results sorted by packing fraction

The aggregate combination with the maximum packing fraction is selected as the optimized gradation for the given set of aggregates.

Example Simulation

Suppose we have a sample #57 aggregate gradation (Table C- 3) and the objective is to determine the maximum packing density that can be achieved using all aggregate sizes present in this gradation.

Table C- 3. Aggregate Gradation for ASTM #57

ASTM Sizes	Size (in)	%	%
1.5	1.5	100	0
1	1	95	5
3/8	0.38	42.5	52.5
#4	0.187	10	32.5
#8	0.093	5	5
#10	0.079	0	5

Step A – In this case, the first step is to sieve the aggregate into individual aggregate stockpiles corresponding to 1 inch, 3/8 inch, #4, #8 and #10 sizes.

Step B – The next step is to determine the DRUW values for each of these aggregate sizes. The DRUW values obtained are then converted into packing density values ($\phi_{aggregate}$) using Equation C - 2 and Equation C - 3.

$$\rho_{bulk} = M_{aggregate} / V_{container}$$ **Equation C - 2**

$$\phi_{aggregate} = \rho_{bulk} / \rho_{aggregate}$$ **Equation C - 3**

Here,

ρ_{bulk} is the bulk density of aggregate,

$M_{aggregate}$ is the measured DRUW of aggregate,

$V_{container}$ is the volume of the cylindrical measure, and

$\phi_{aggregate}$ is the packing density of the aggregate.

The calculated packing density values are shown in Table C- 4.

Table C- 4. Packing Density values obtained from DRUW Test

Aggregate Size (ASTM)	1”	3/8”	#4	#8	#10
Aggregate Size (inch)	1	0.38	0.187	0.093	0.079
Packing Density	0.562	0.558	0.593	0.529	0.565

Step C – At this stage, the user has obtained all necessary values required for APM and is ready to run the software. The user can follow Steps 1-5 listed above to run the software and obtain the packing results. Figure C- 10 and Figure C- 11 show the user inputs in the program. Note here that the inputs for Step 3 (Compression Index and Precision) depend on the user’s preferences.

```
. . . . . STEP 1. . . . . .
       Enter the number of aggregate classes (2-10) to optimize - 5

. . . . . STEP 2. . . . . .
       Enter aggregate sizes and corresponding packing fractions (largest size first)
              Enter average aggregate size (in inches) for aggregate 1 - 1
              Enter packing fraction for aggregate (0-1) 1 - 0.562
-------------------------------------------------------------------------------------------------------------
              Enter average aggregate size (in inches) for aggregate 2 - 0.38
              Enter packing fraction for aggregate (0-1) 2 - 0.558
-------------------------------------------------------------------------------------------------------------
              Enter average aggregate size (in inches) for aggregate 3 - 0.187
              Enter packing fraction for aggregate (0-1) 3 - 0.593
-------------------------------------------------------------------------------------------------------------
              Enter average aggregate size (in inches) for aggregate 4 - 0.093
              Enter packing fraction for aggregate (0-1) 4 - 0.529
-------------------------------------------------------------------------------------------------------------
              Enter average aggregate size (in inches) for aggregate 5 - 0.079
              Enter packing fraction for aggregate (0-1) 5 - 0.565
-------------------------------------------------------------------------------------------------------------
```

Figure C- 10. User input in steps 1 and 2 for example simulation

```
. . . . . STEP 3. . . . . .
       Enter the Compression Index (K) [positive number] - 9
       Enter the test precision (1-10; 1 --> lowest precision & shortest execution time; 10 --> highest preci
sion & highest execution time) - 5

. . . . . STEP 4. . . . . .
       Enter filename to save report as : example_run

. . . . . STEP 5 - Running Packing Code . . . . . .
       Success. Run Completed...
Press any key to continue . . .
```

Figure C- 11. User inputs in steps 3-5 in example simulation

The results obtained are imported in Microsoft Excel and sorted to get the maximum packing density. In this case, the maximum value of packing density obtained is 0.6774 for an aggregate combination corresponding to (1 in. – 50%; 3/8 in. – 10%, #4 – 10%, #8 – 0%, #10 – 30%).

Depending on these results obtained, the user may wish to apply certain constraints on the volume fraction of aggregates that need to be present in the optimized aggregate mixture. The available aggregate stockpile has about 50% by volume of 3/8 in. aggregate and 30% by volume of #4 aggregate size. So, it is highly likely that the user may want to have at least 40% of 3/8 in. aggregate and at least 30% of #4 aggregate size in the final gradation. In that case, user can filter the values obtained using this criterion. Table C- 5 shows the filtered results. Note here that the maximum packing fraction for such a criterion is 0.627 which is much lower than the maximum packing fraction of 0.6774 which is possible to be obtained.

Table C- 5. Packing fraction results filtered by criteria (at least 40% of 3/8 in. aggregate and at least 30% of #4 aggregate)

Size = 1 in.	Size = 0.38 in.	Size = 0.187 in.	Size = 0.093 in.	Size = 0.079 in.	Packing Fraction
0.1	0.4	0.3	0	0.2	0.627
0.2	0.4	0.3	0	0.1	0.622
0	0.4	0.3	0	0.3	0.622
0.1	0.4	0.3	0.1	0.1	0.620
0	0.4	0.3	0.1	0.2	0.616
0	0.5	0.3	0	0.2	0.611
0	0.4	0.4	0	0.2	0.609
0	0.4	0.3	0.2	0.1	0.608
0.1	0.4	0.4	0	0.1	0.607
0	0.5	0.3	0.1	0.1	0.605
0.1	0.5	0.3	0	0.1	0.604
0	0.4	0.4	0.1	0.1	0.602
0.2	0.4	0.4	0	0	0.601
0	0.5	0.4	0	0.1	0.592
0.2	0.5	0.3	0	0	0.591
0	0.4	0.5	0	0.1	0.588
0	0.6	0.3	0	0.1	0.587
0.1	0.4	0.5	0	0	0.585
0.1	0.5	0.4	0	0	0.585
0.1	0.6	0.3	0	0	0.574
0	0.5	0.5	0	0	0.572
0	0.6	0.4	0	0	0.569
0	0.4	0.6	0	0	0.567
0	0.7	0.3	0	0	0.557

APPENDIX D - OPTICAL MICROGRAPHS OF CRACK PATTERNS IN FAILED SAMPLES

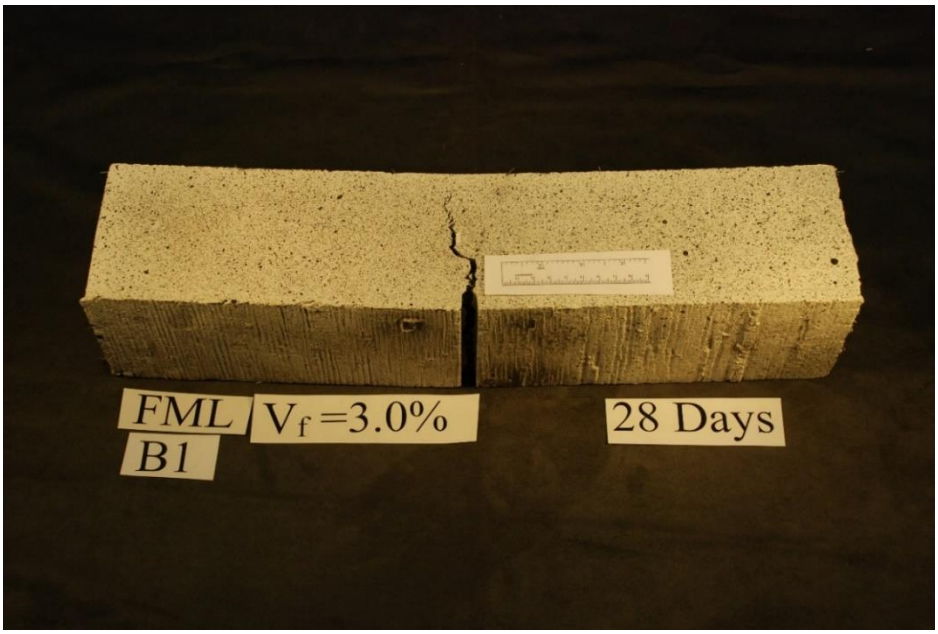

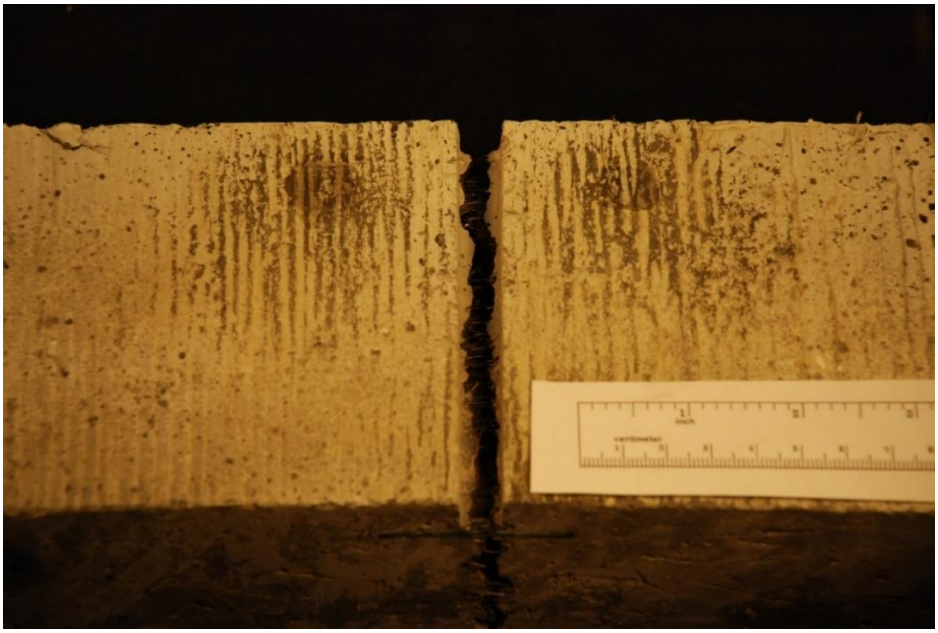

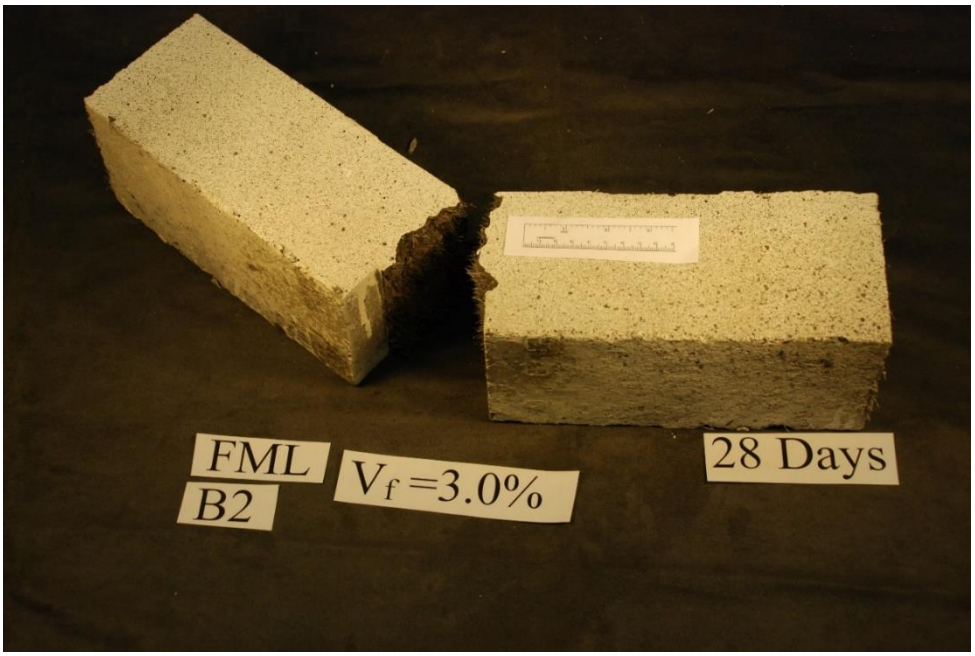
FML
B2
V_f =3.0%
28 Days

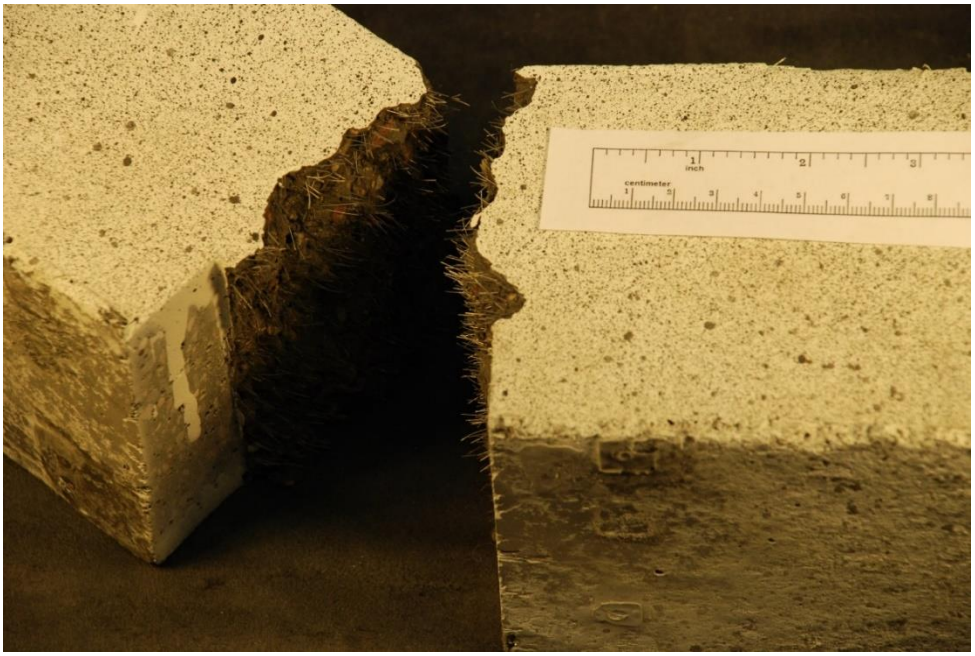

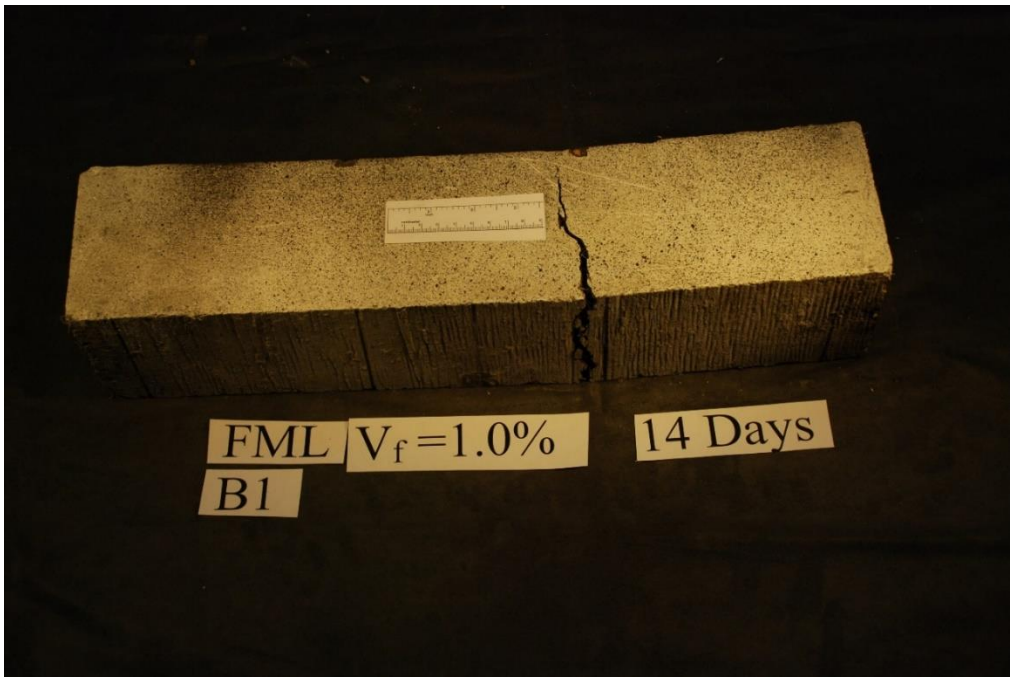
FML
V_f =1.0%
14 Days
B1

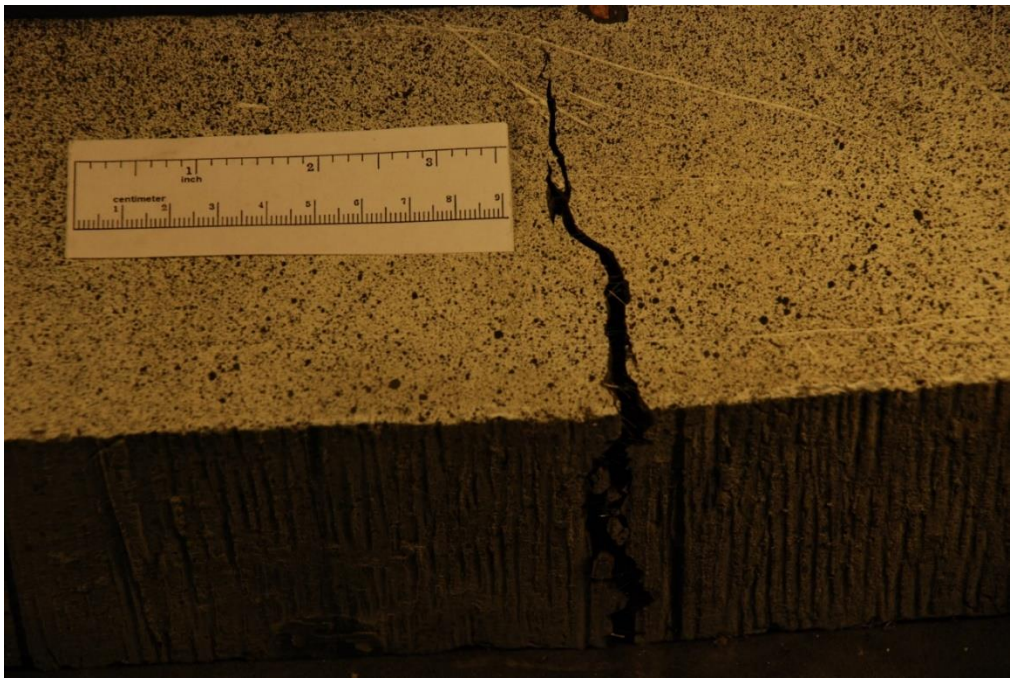
inch
centimeter

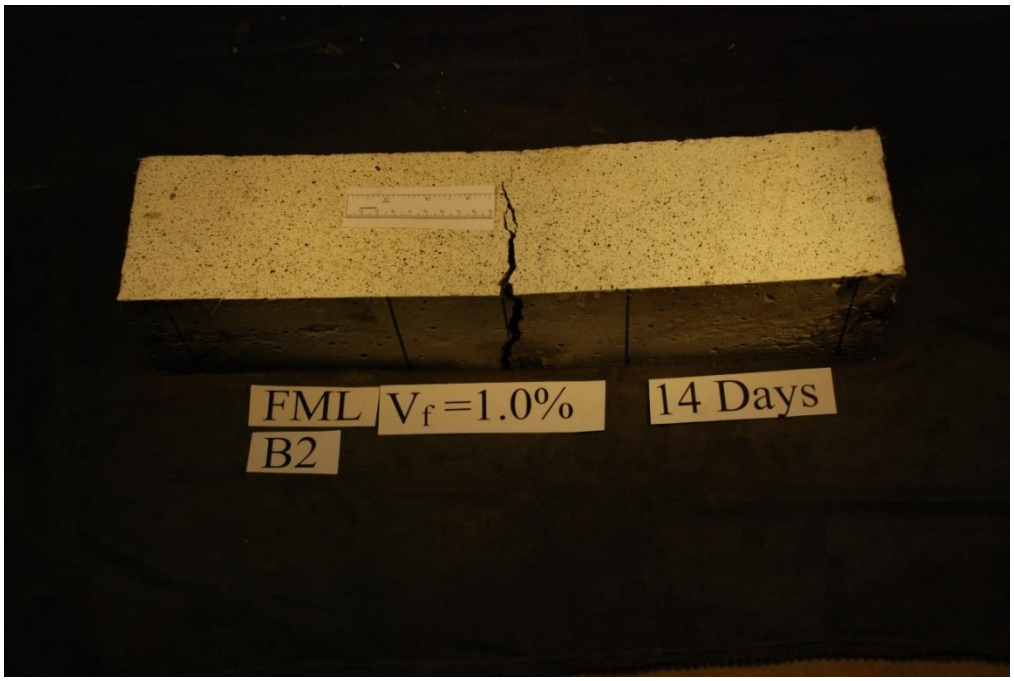
FML
V_f =1.0%
14 Days
B2

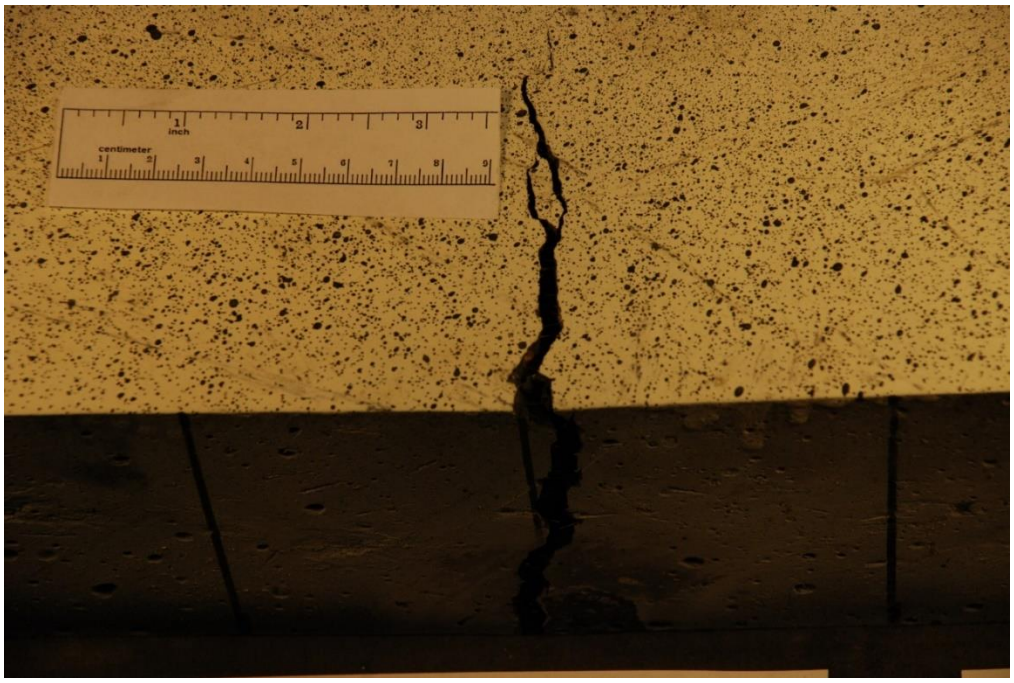
1
inch
2
3
centimeter
1
2
3
4
5
6
7
8
9

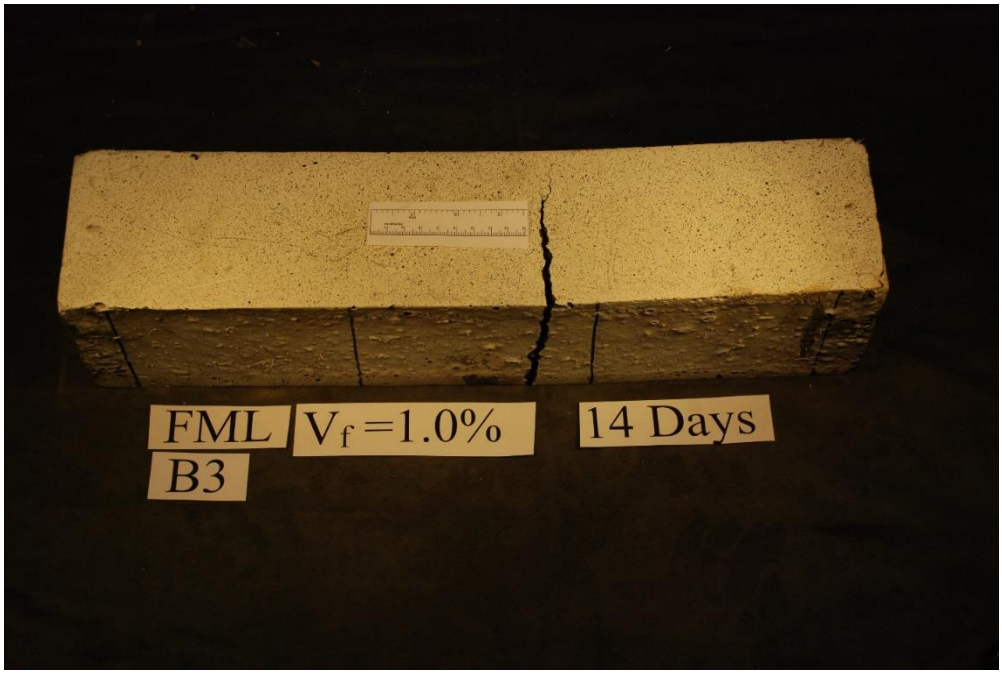
FML
V_f =1.0%
14 Days
B3

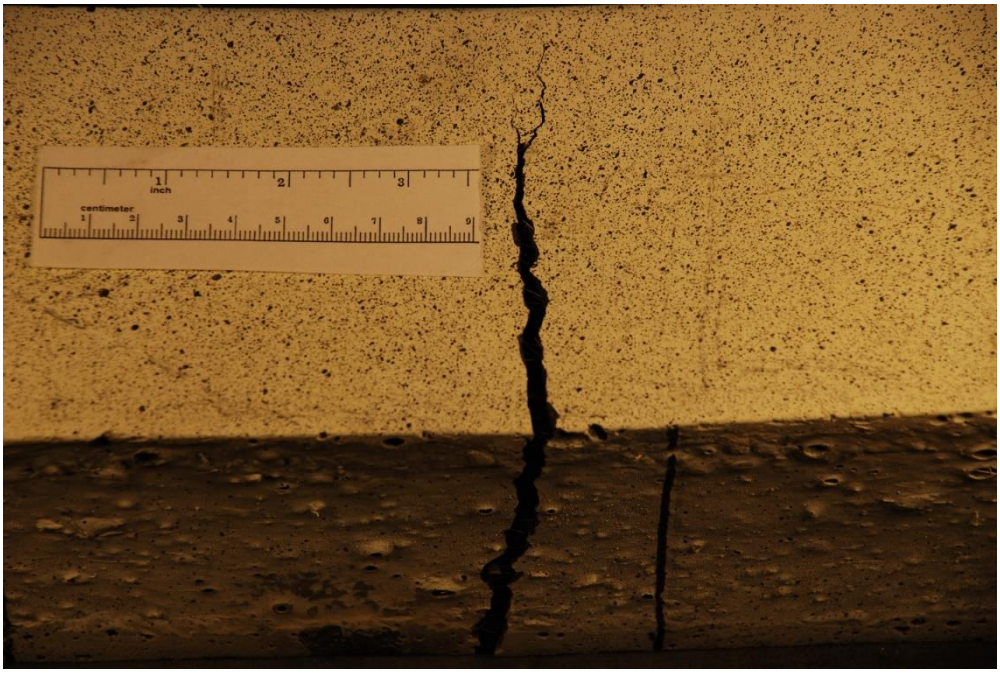
inch
centimeter

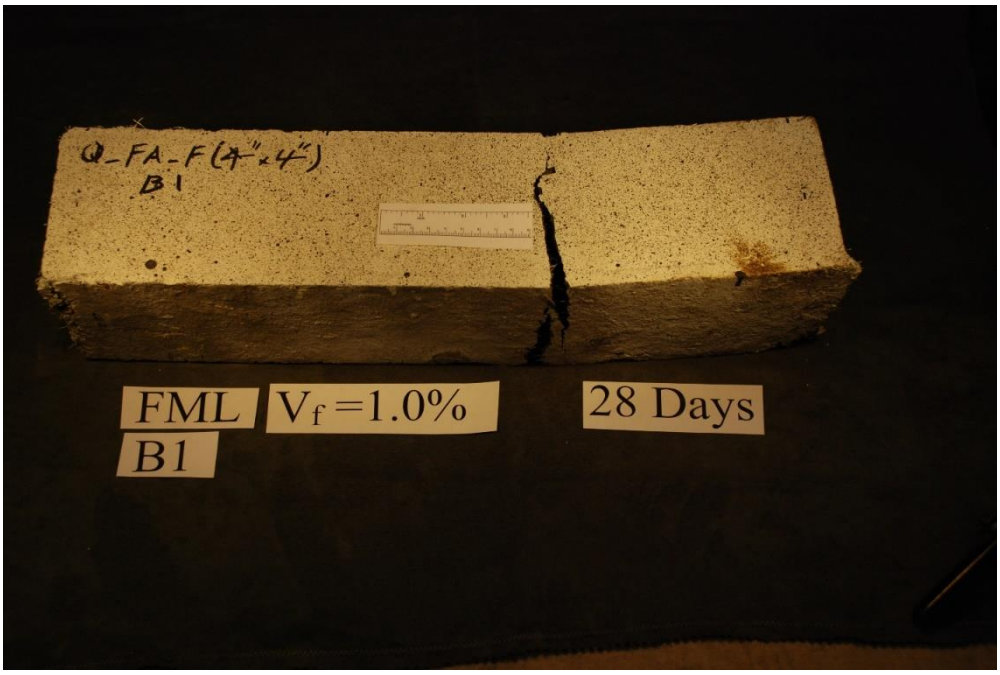
Q_FA_F(4"x4")
B1
FML
B1
V_f =1.0%
28 Days

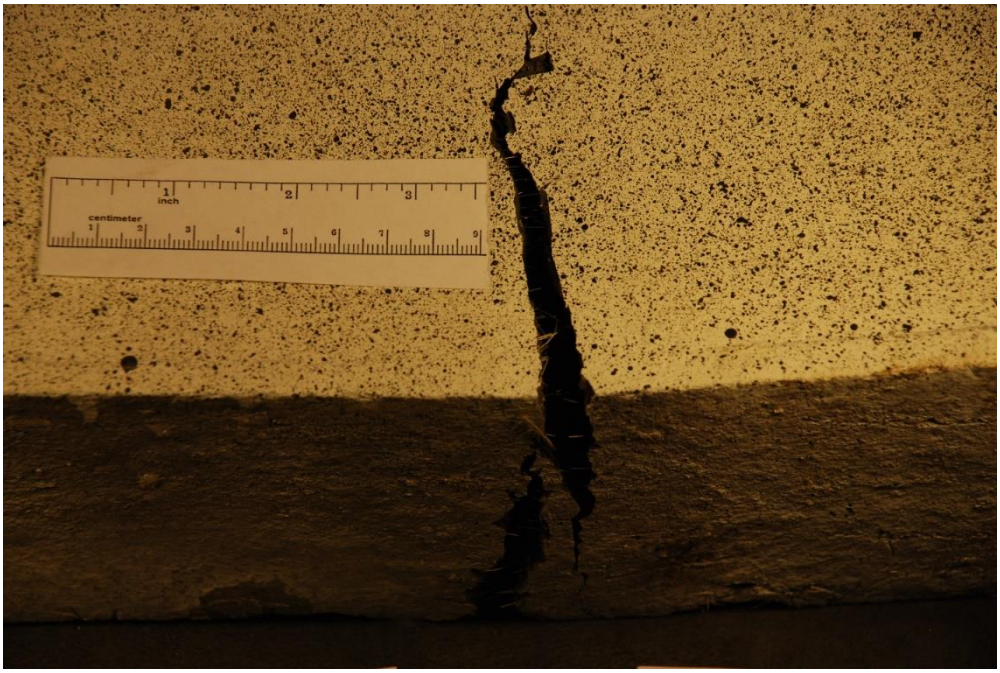
1
inch
2
3
centimeter
1
2
3
4
5
6
7
8
9

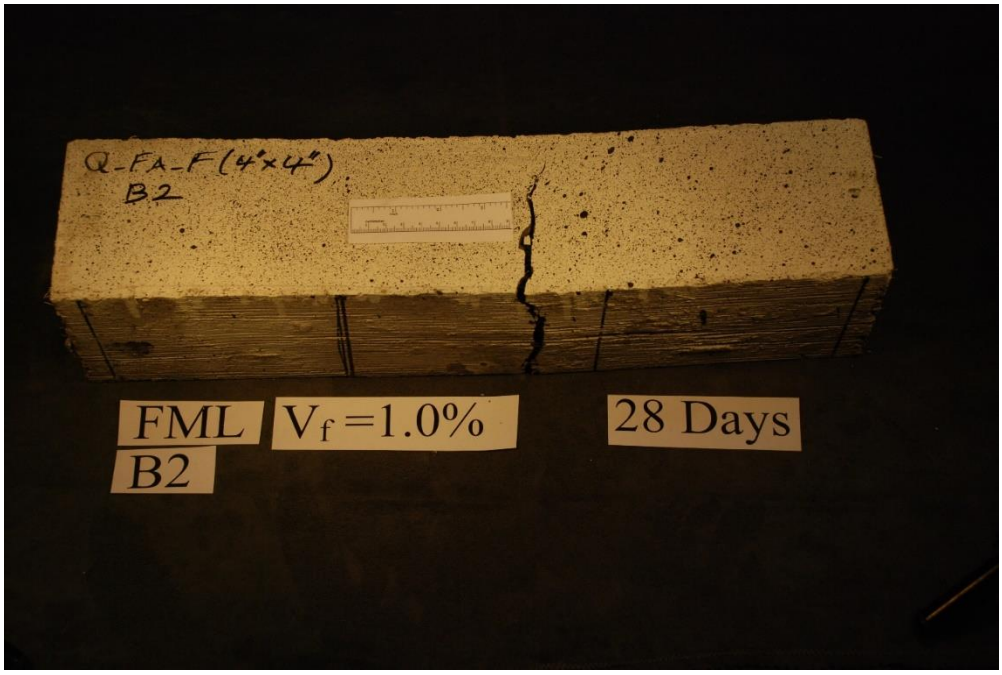
Q-FA-F(4"x4")
B2
FML
B2
V_f =1.0%
28 Days

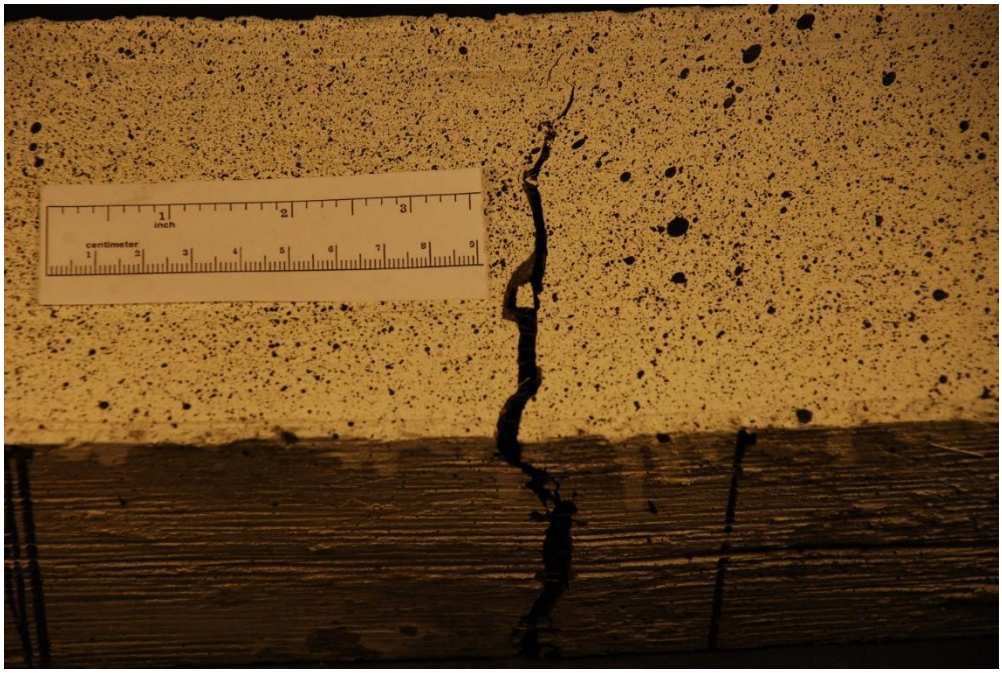
inch
centimeter

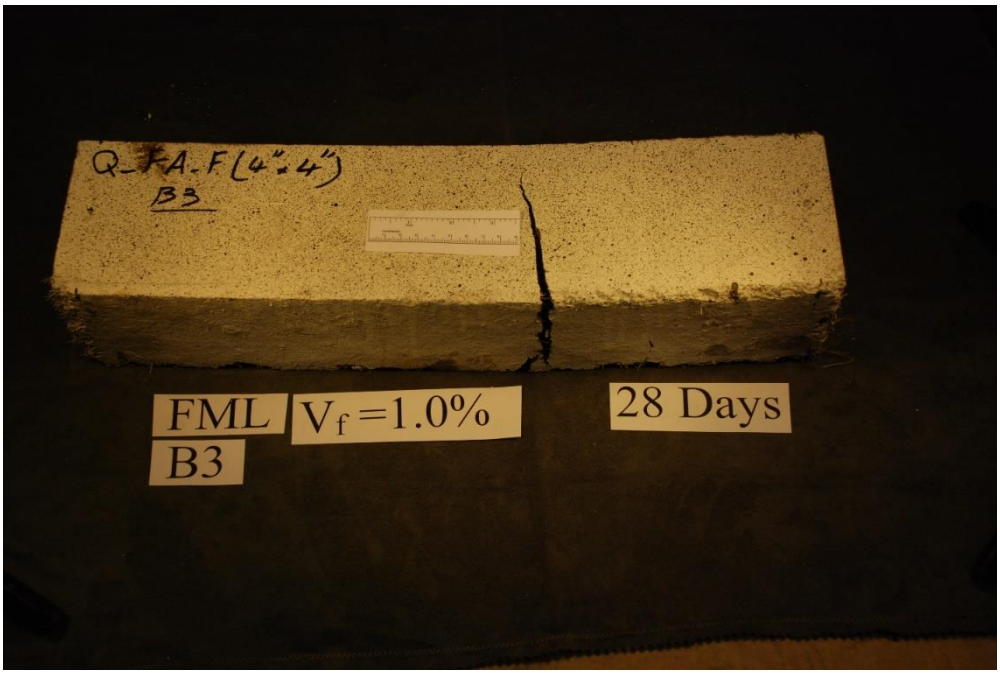
Q_FA_F(4"x4")
B3
FML
B3
V_f =1.0%
28 Days

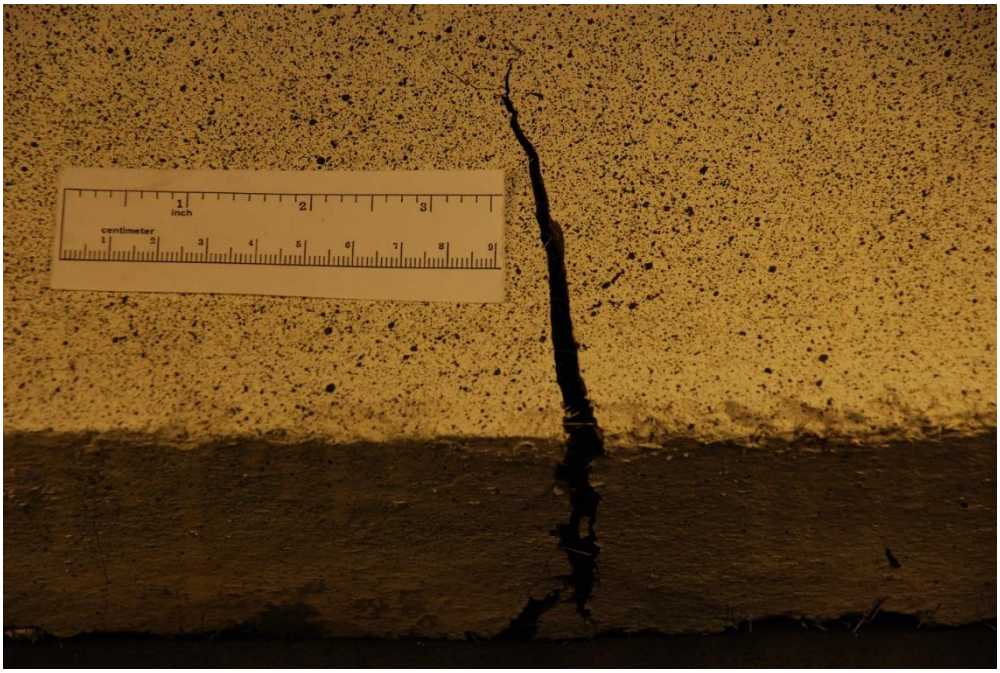
1
inch
2
3
centimeter
1
2
3
4
5
6
7
8
9


inch
centimeter


centimeter
inch

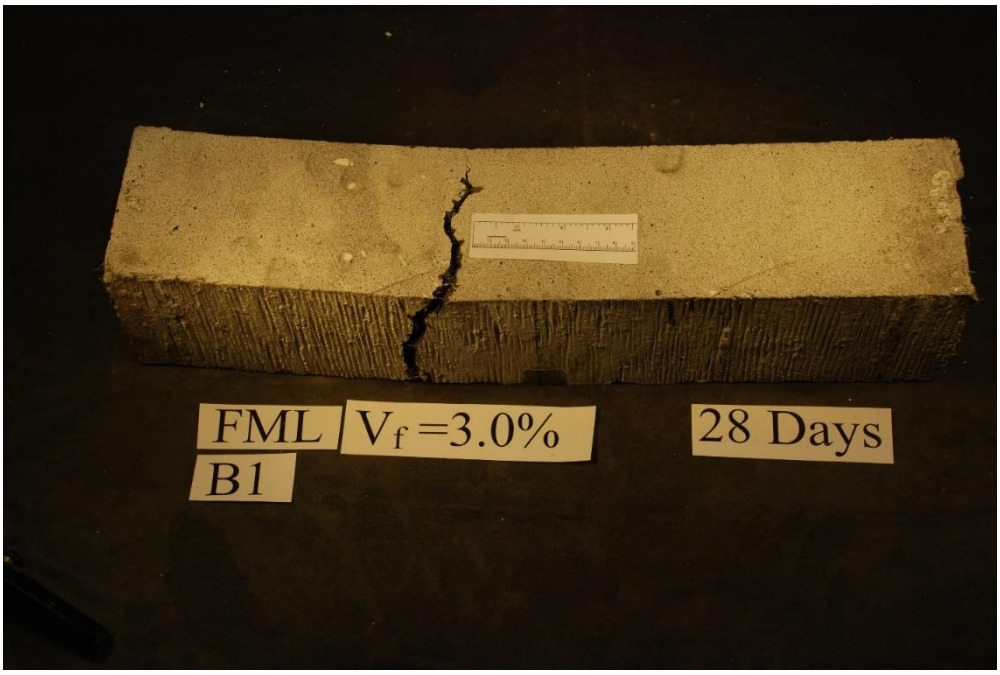
FML
B1
V_f =3.0%
28 Days


inch
centimeter

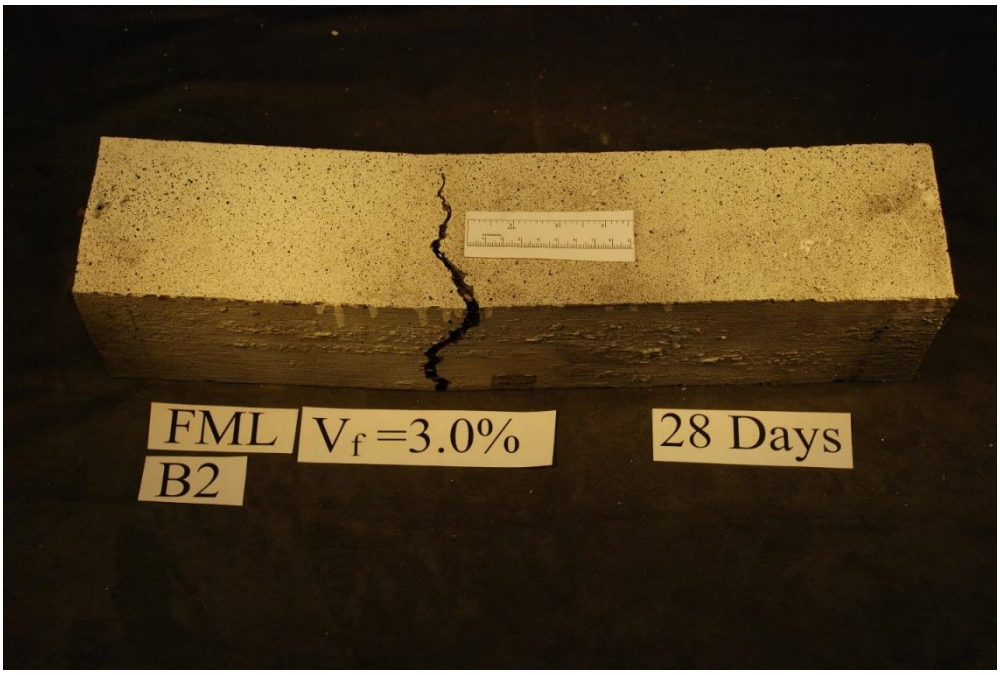
FML
B2
V_f =3.0%
28 Days

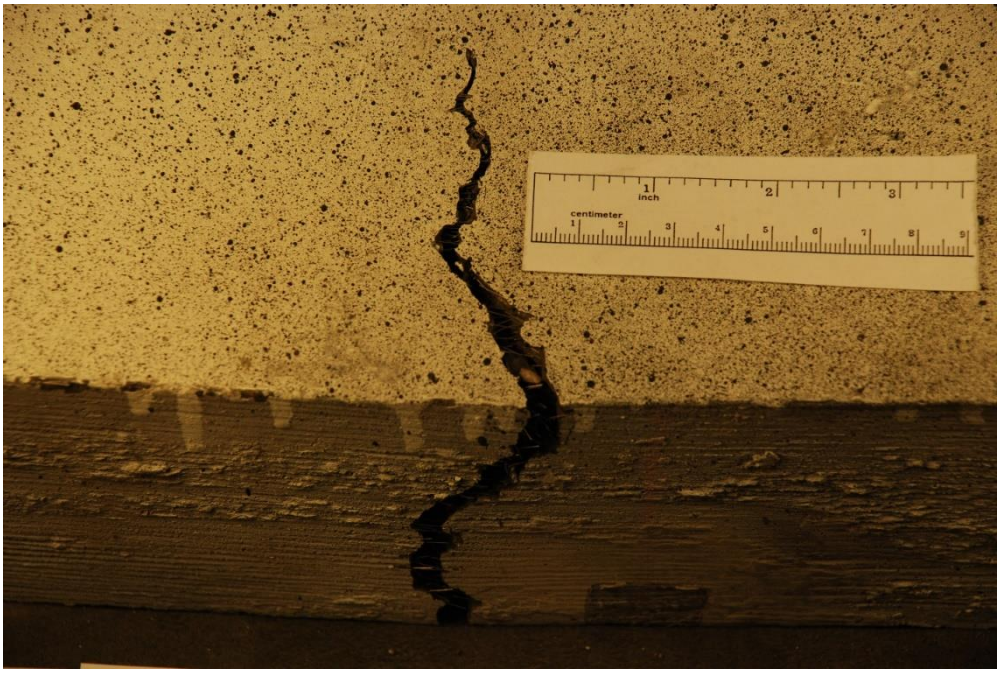
inch
centimeter

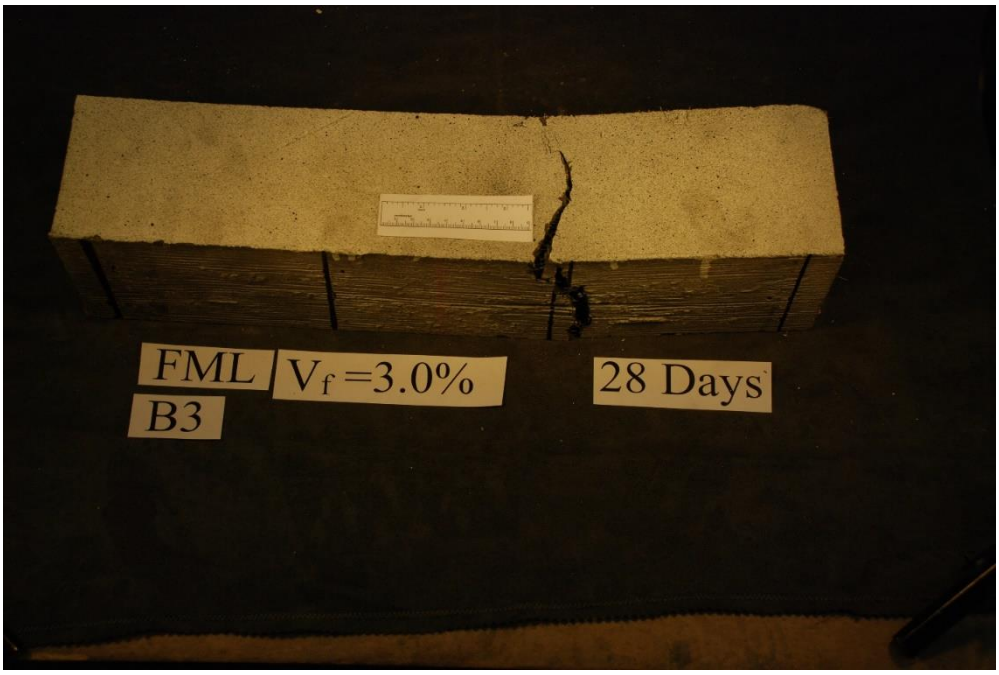
FML
V_f =3.0%
28 Days
B3

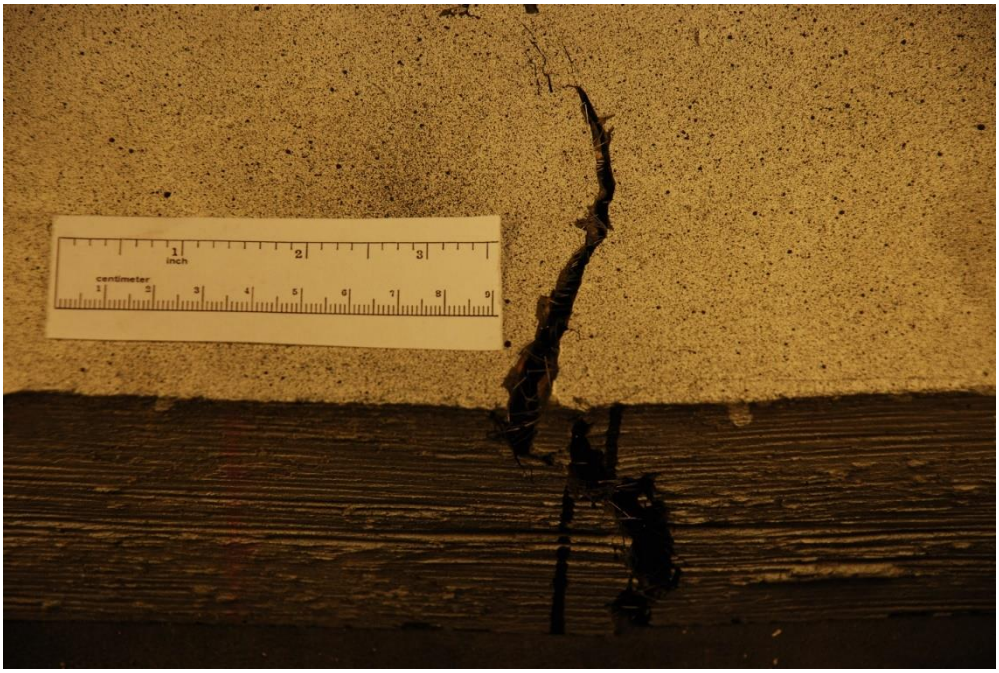
inch
centimeter

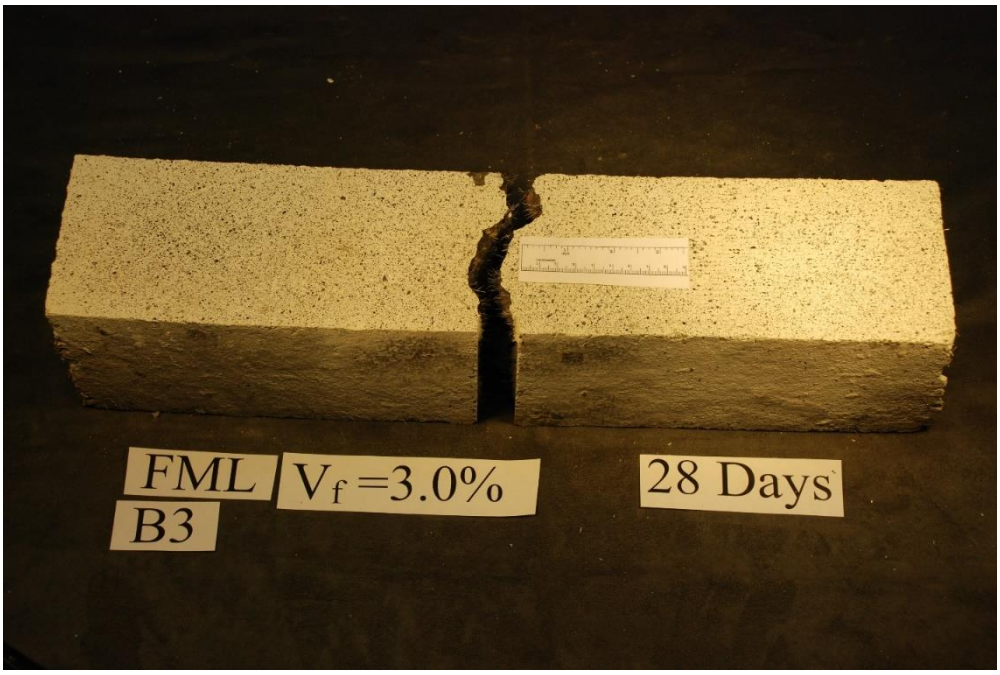
FML
B3
V_f =3.0%
28 Days

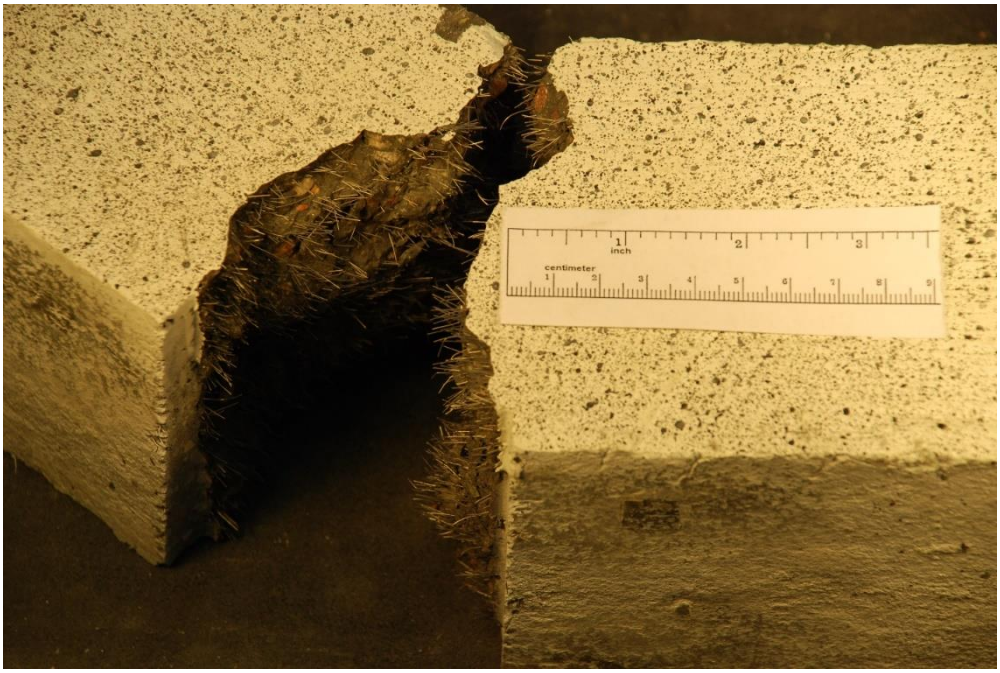
centimeter
inch

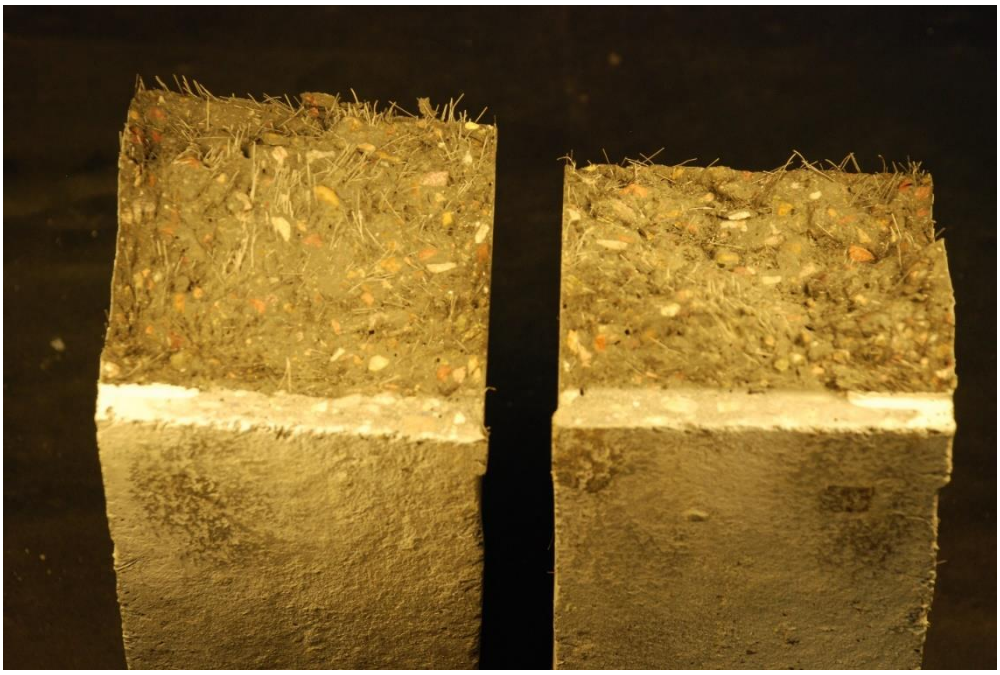

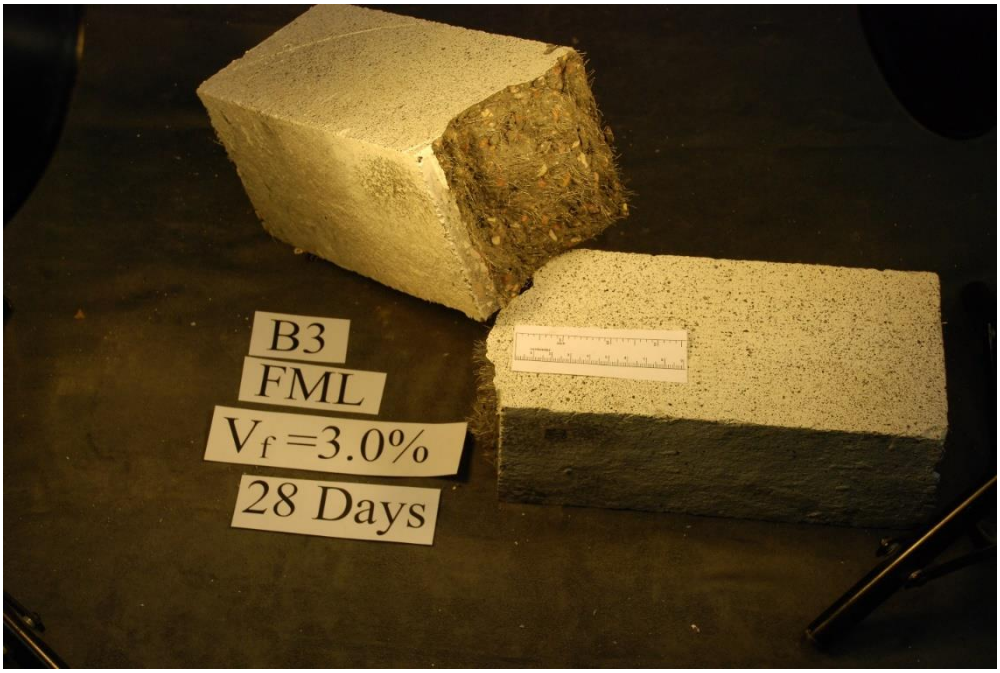
B3
FML
V_f =3.0%
28 Days

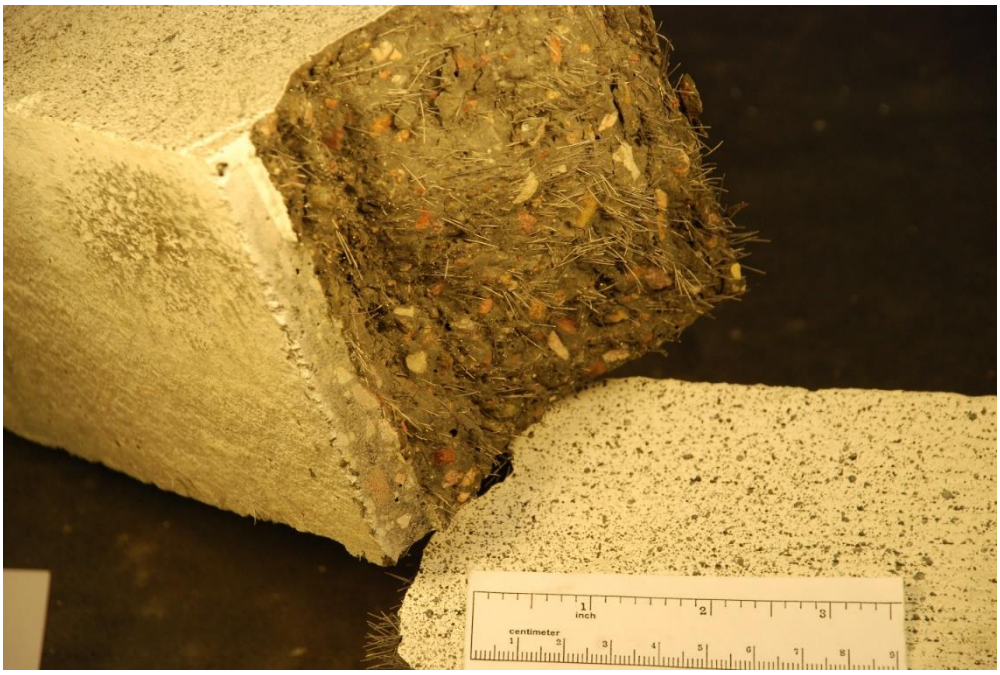
inch
centimeter

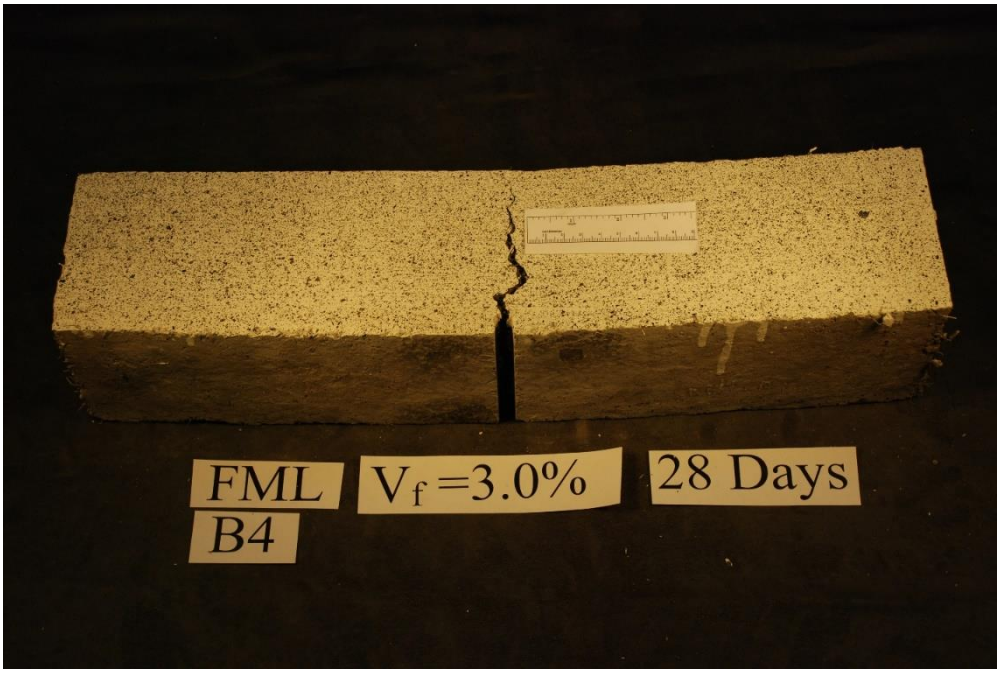
FML
B4
V_f =3.0%
28 Days

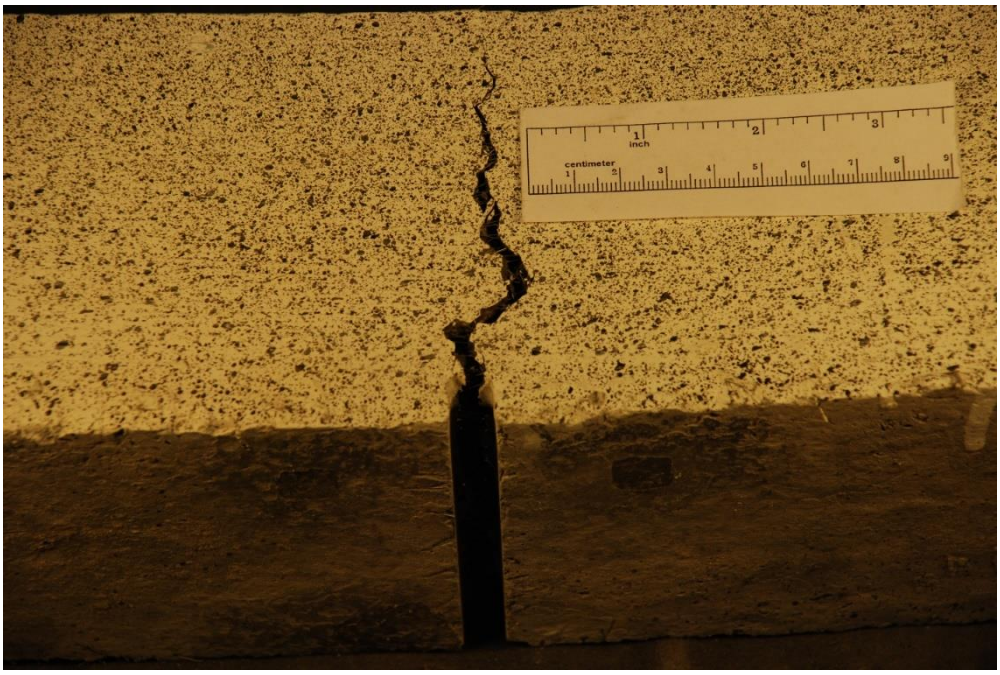
inch
centimeter


inch
centimeter

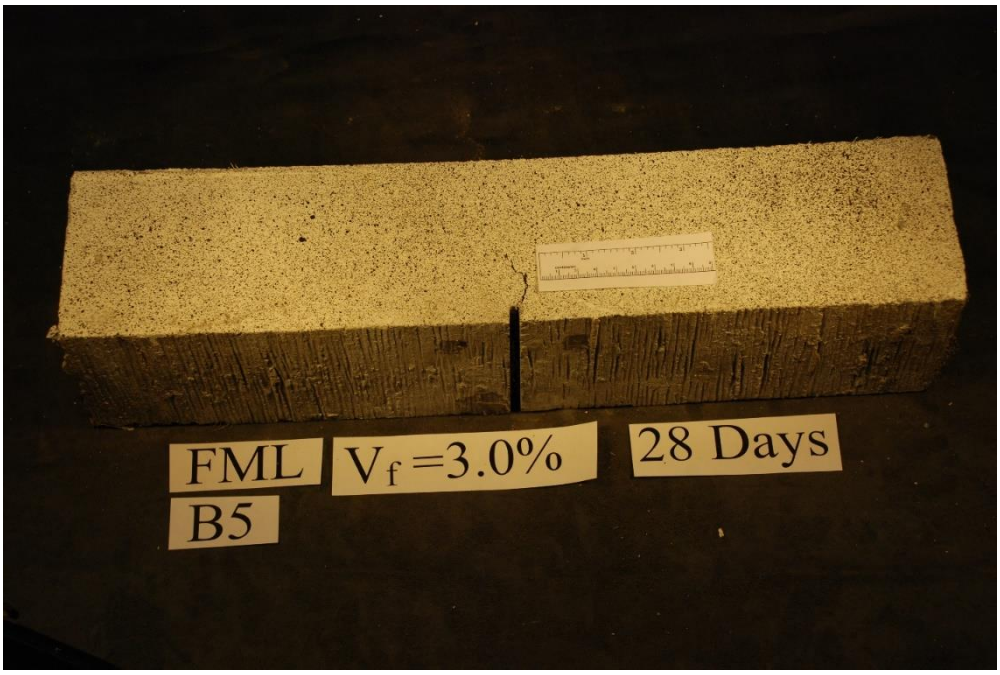
FML
V_f =3.0%
28 Days
B5

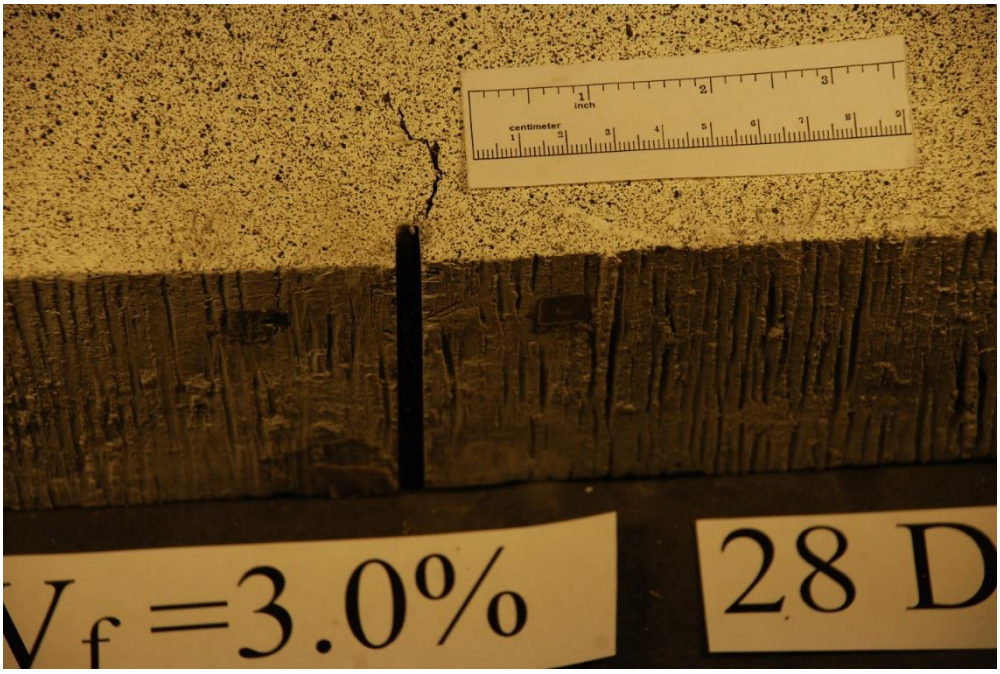
V_f =3.0%
28 D

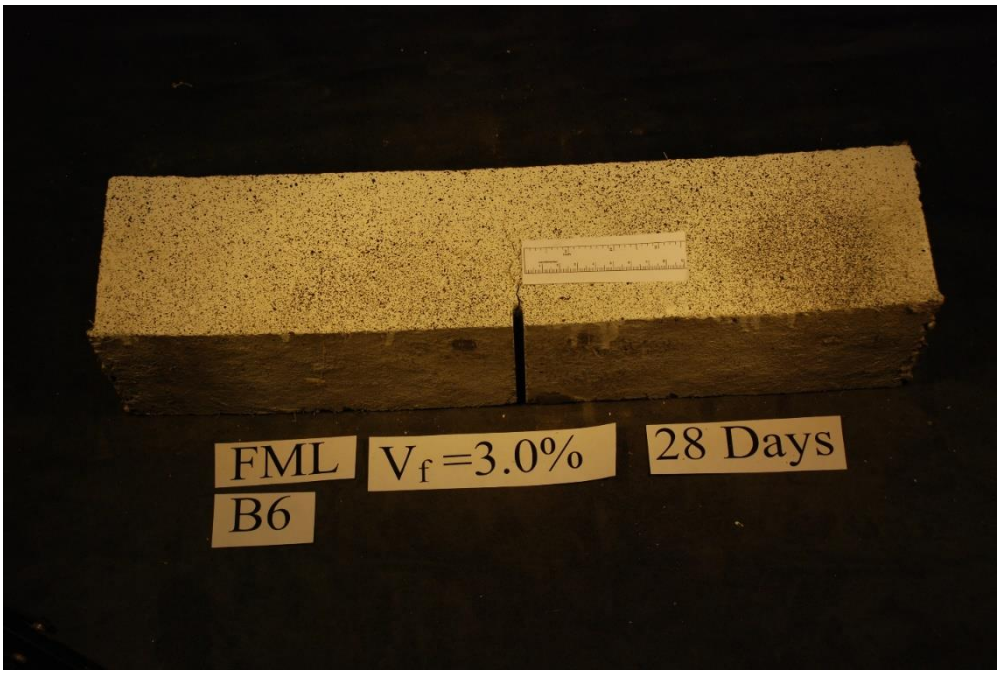
FML
B6
V_f =3.0%
28 Days

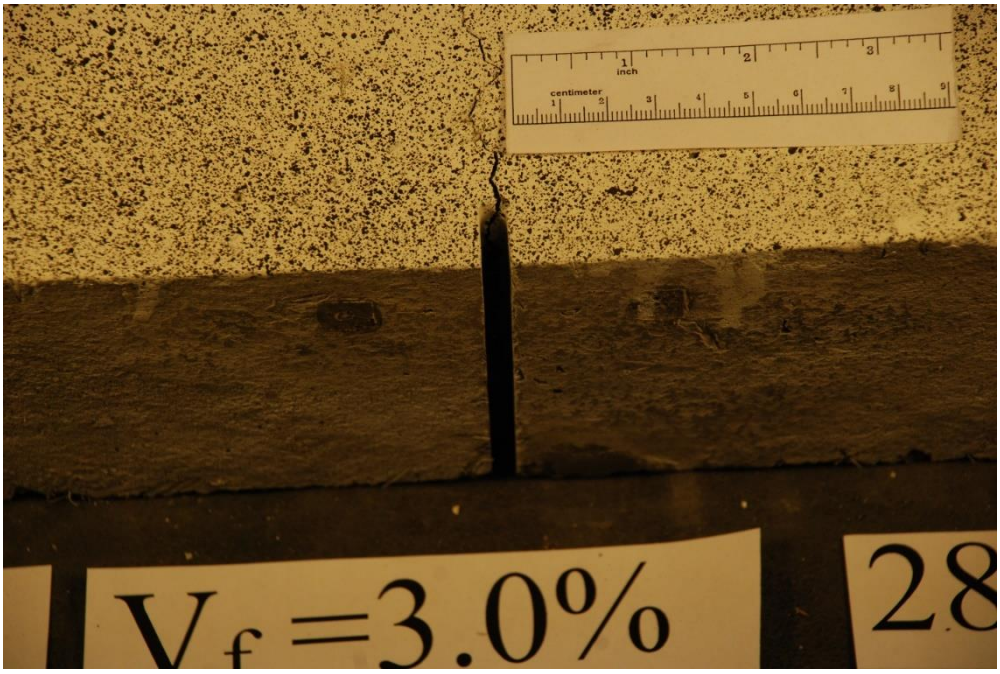
V_f =3.0%
28

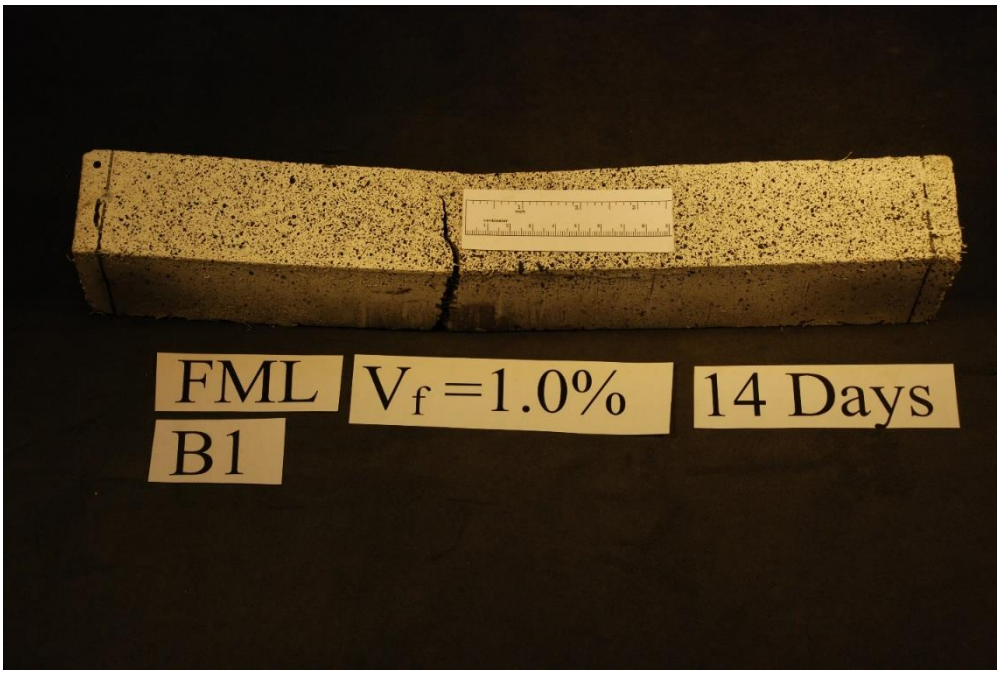
FML
V_f =1.0%
14 Days
B1

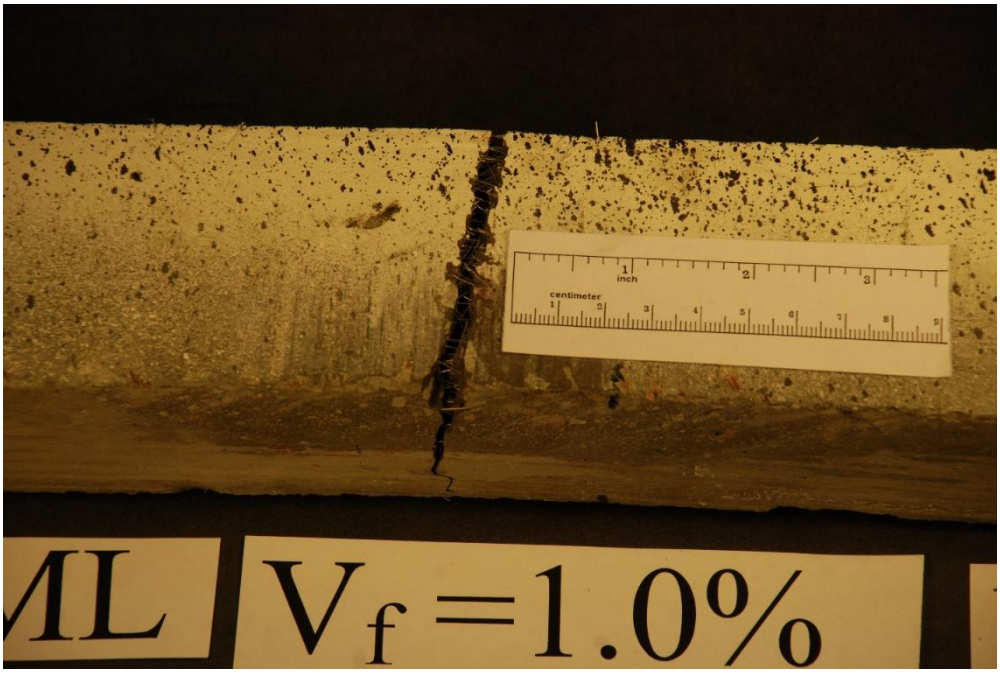
centimeter
inch
ML
V_f =1.0%

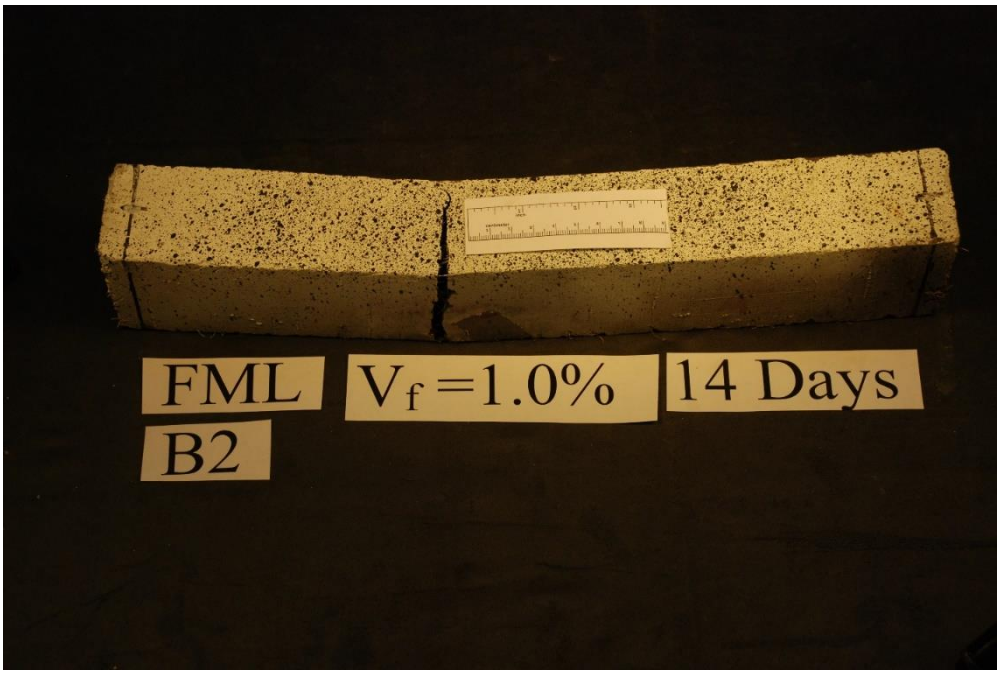
FML
V_f =1.0%
14 Days
B2

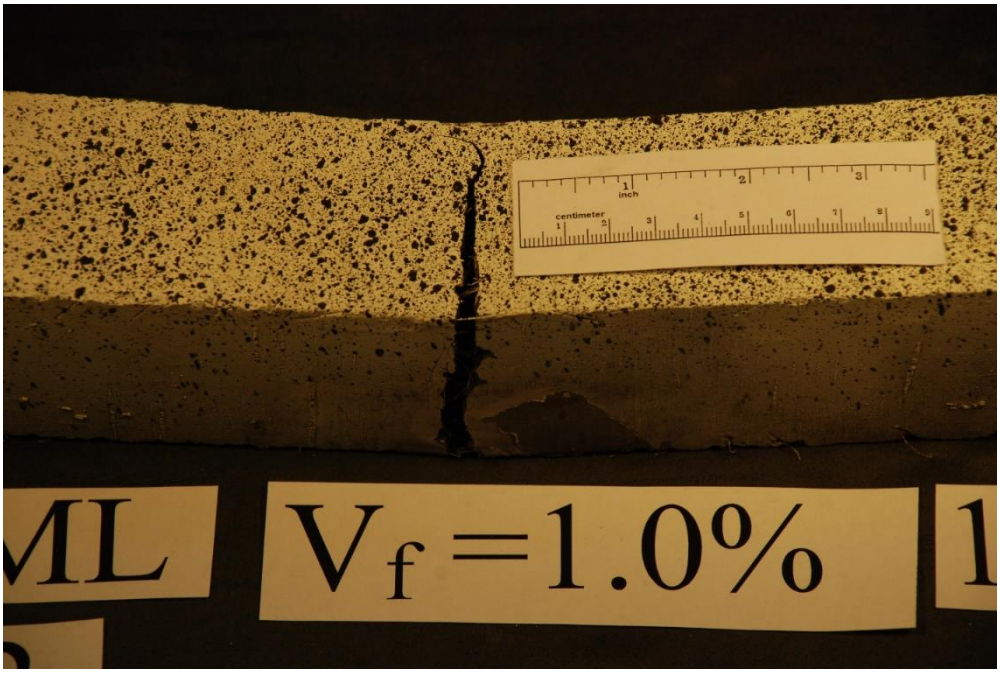
ML
V_f =1.0%
1

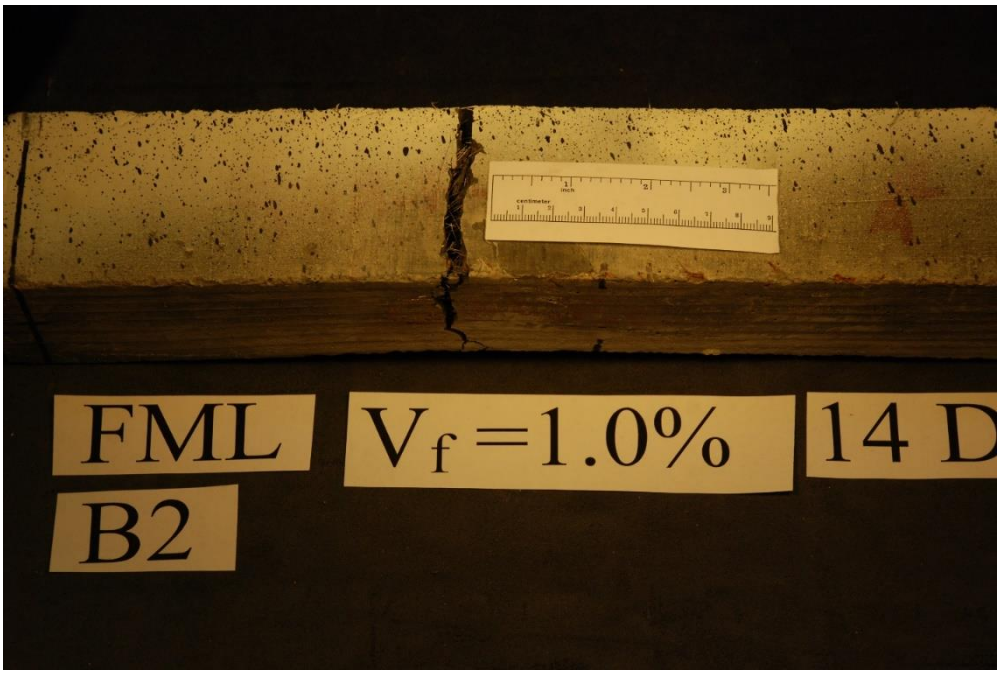
FML
V_f =1.0%
14 D
B2

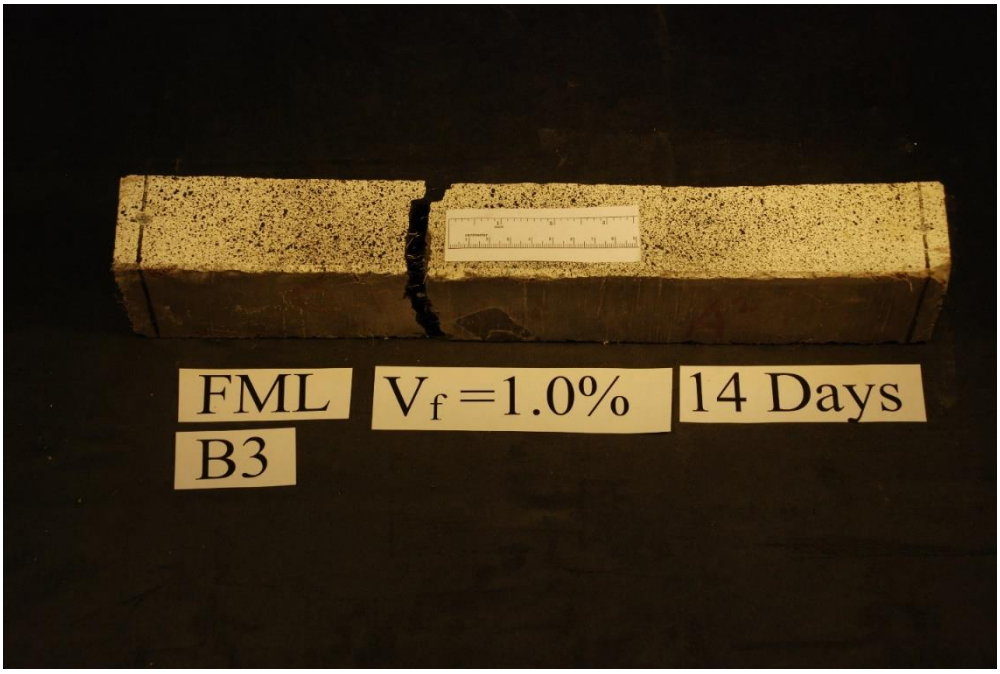
FML
V_f =1.0%
14 Days
B3

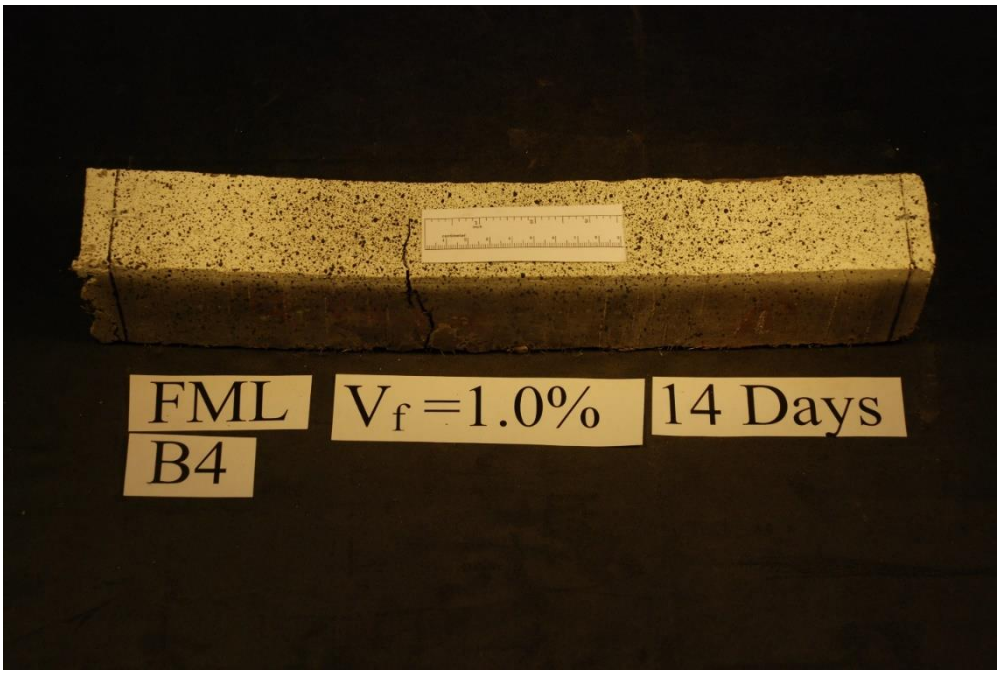
FML
B4
V_f =1.0%
14 Days

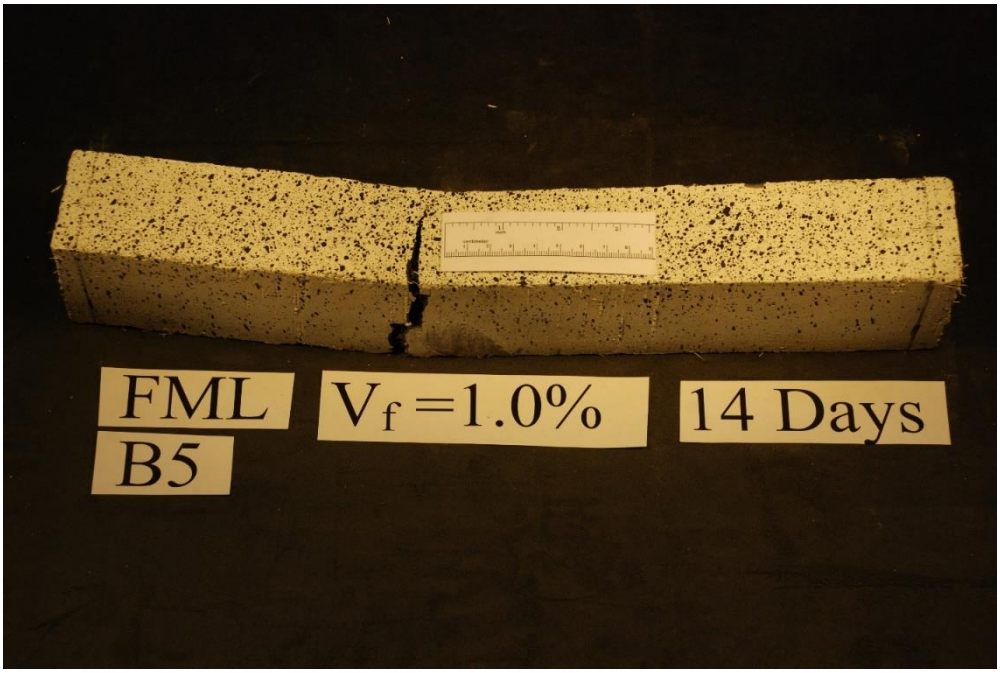
FML
B5
V_f =1.0%
14 Days

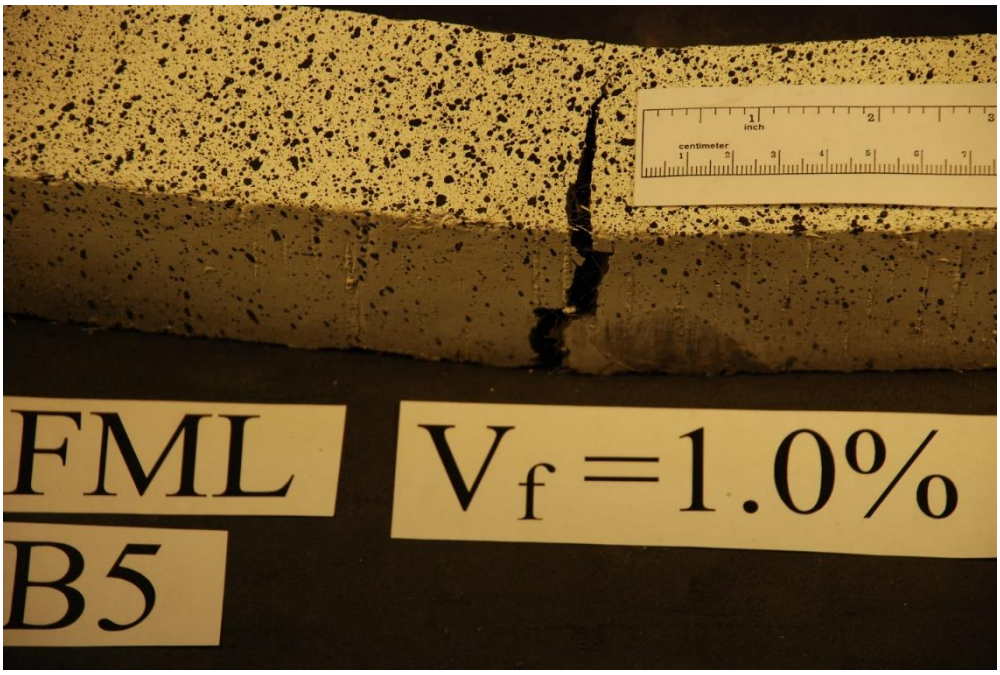
FML
B5
V_f =1.0%

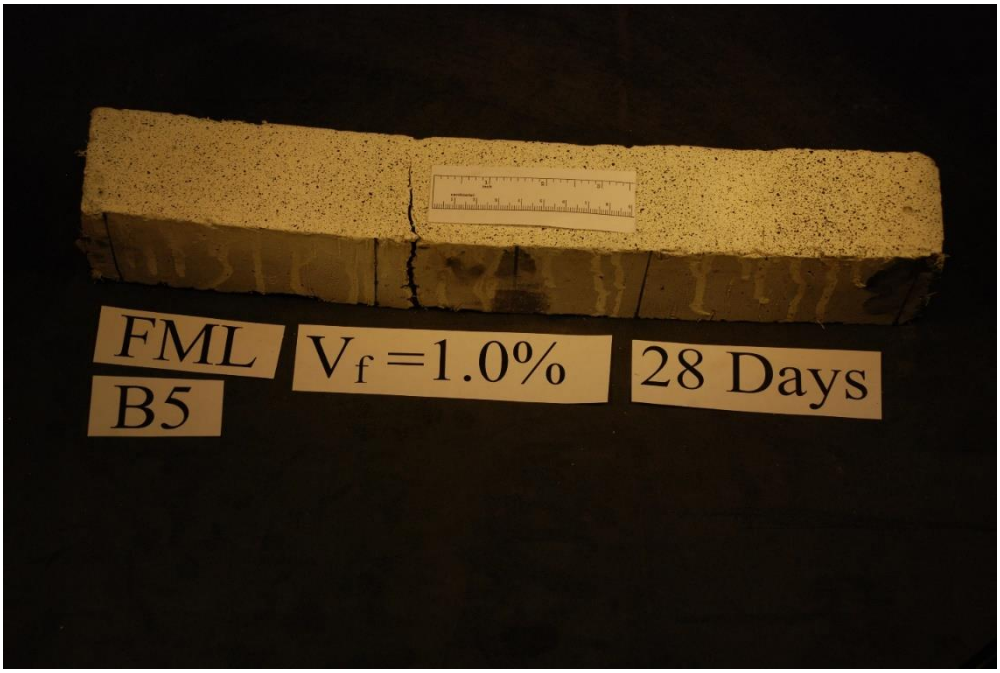
FML
B5
V_f =1.0%
28 Days

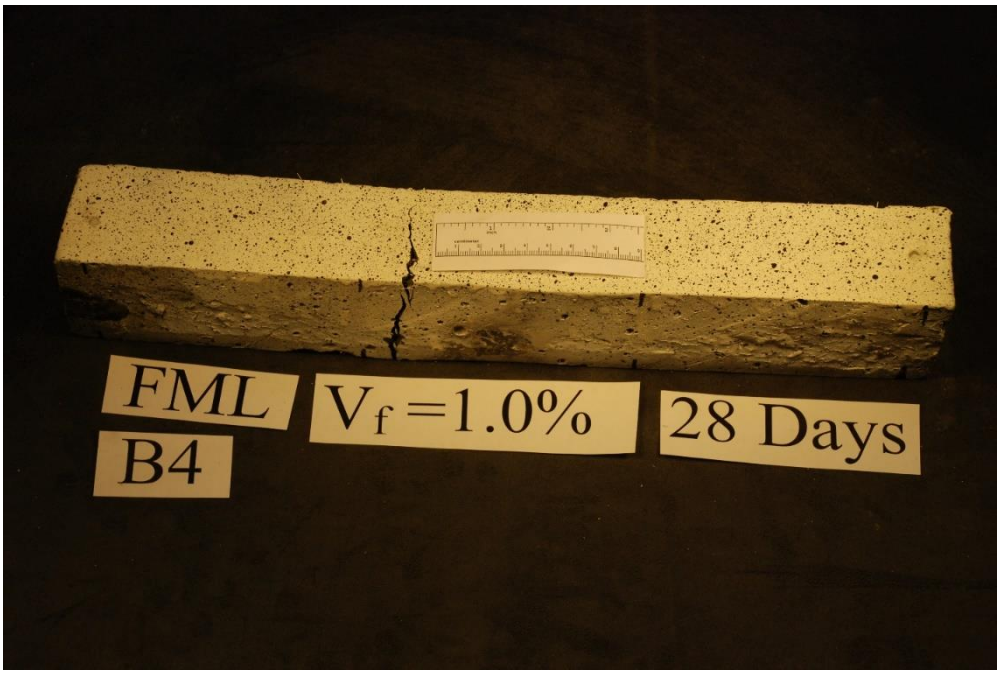
FML
B4
V_f =1.0%
28 Days

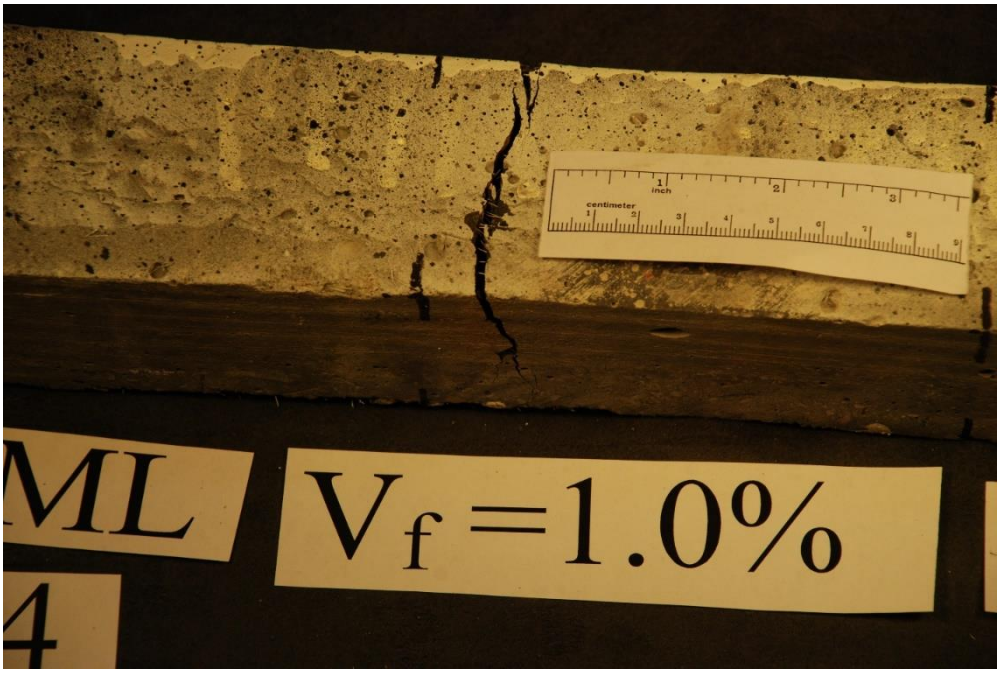
ML
4
V_f =1.0%

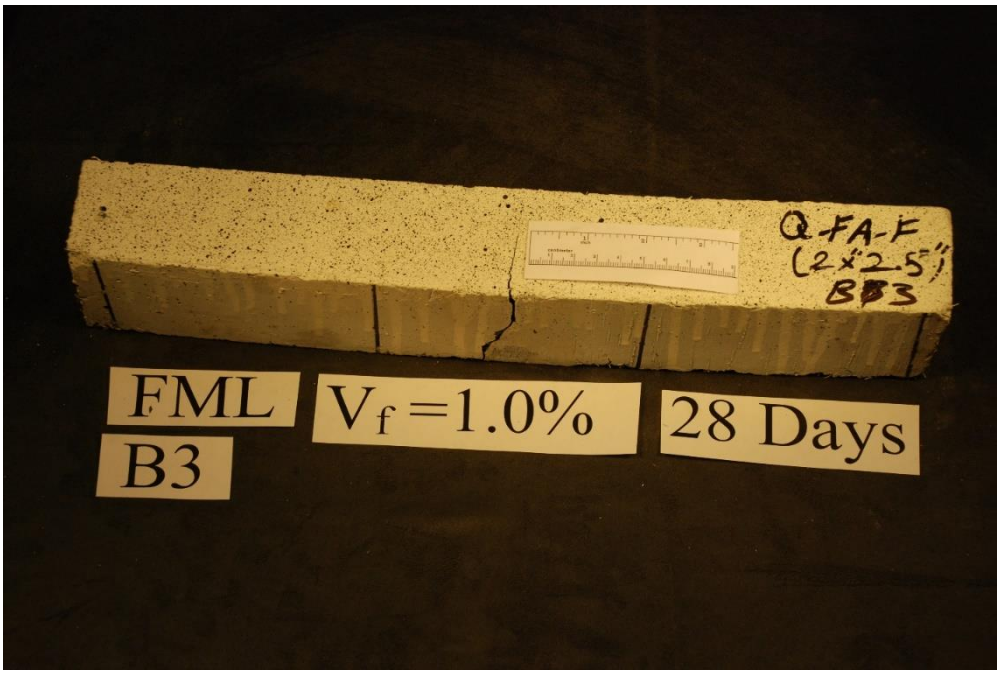
Q-FA-F
(2×2.5")
BB3
FML
B3
V_f =1.0%
28 Days

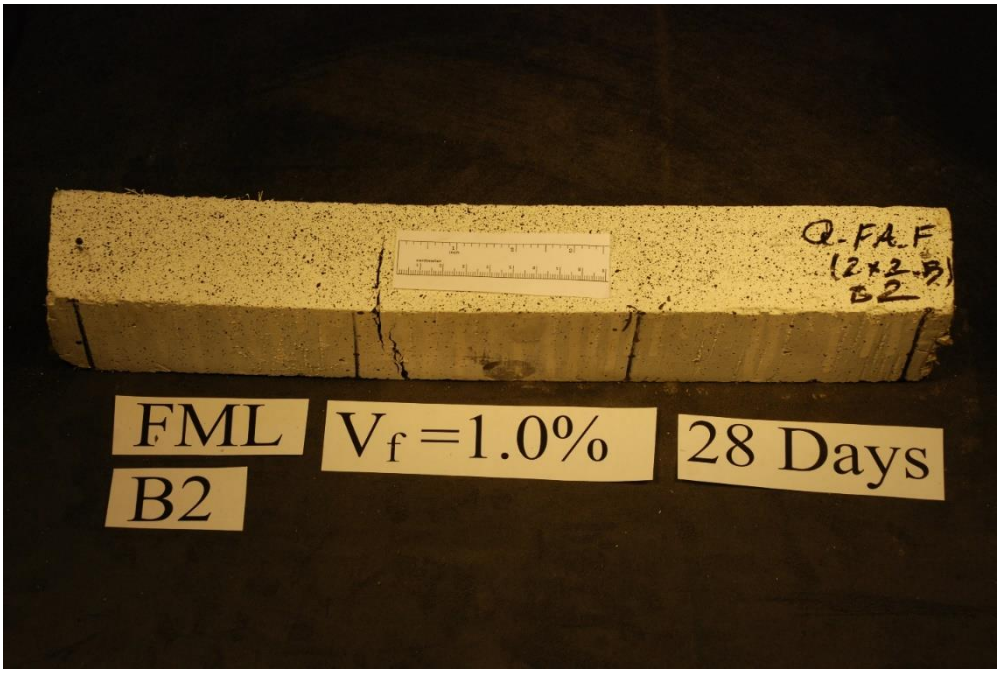
Q-FA-F
(2×2-B)
B2
FML
B2
V_f =1.0%
28 Days

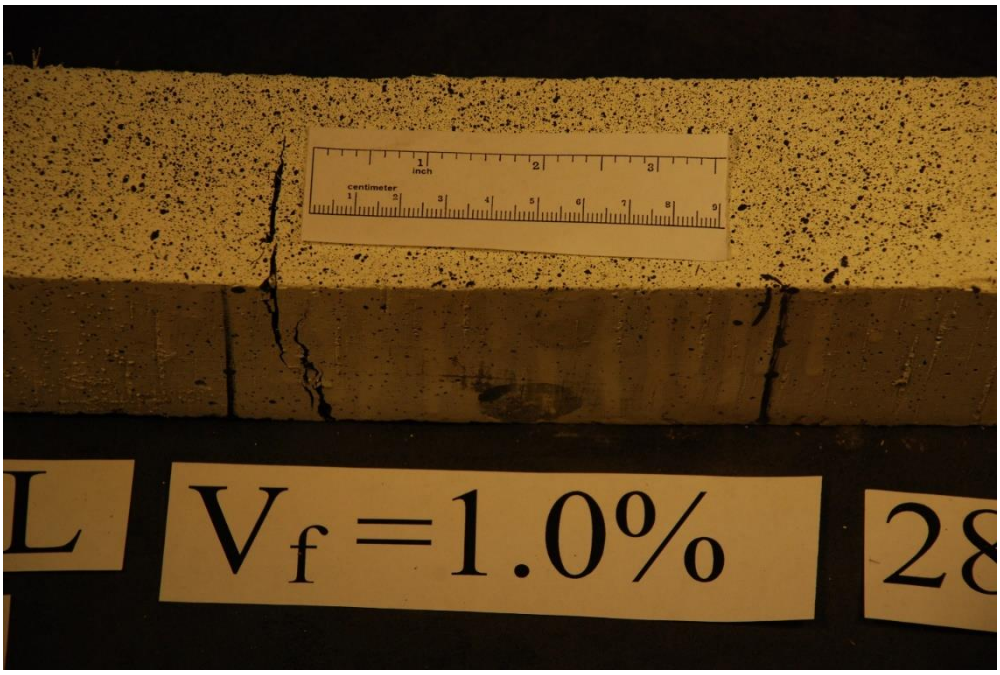
L
V_f =1.0%
28

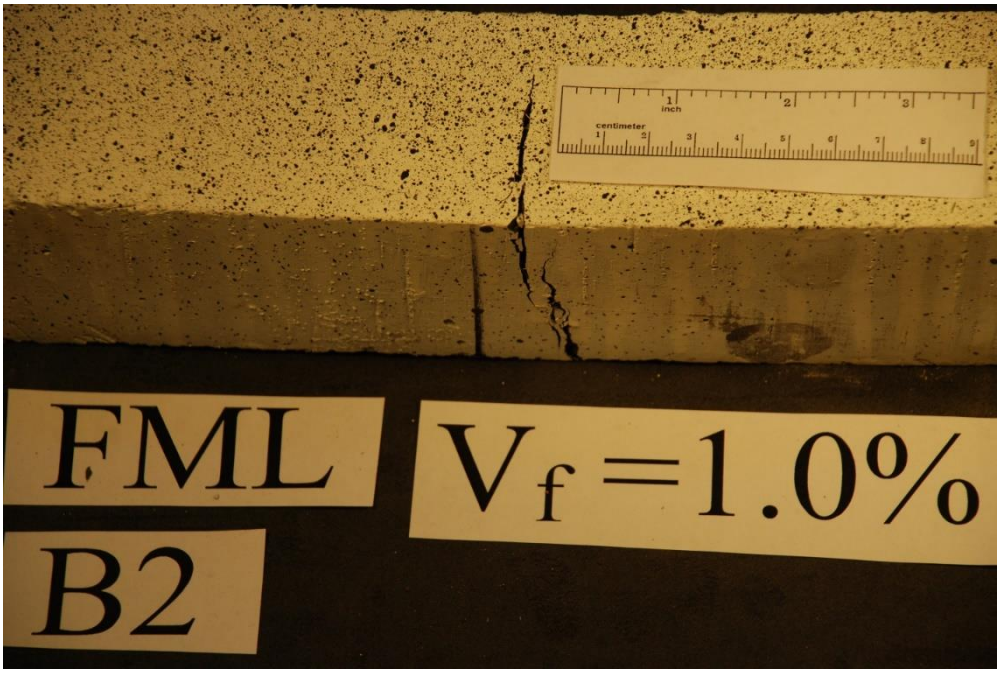
FML
B2
V_f =1.0%

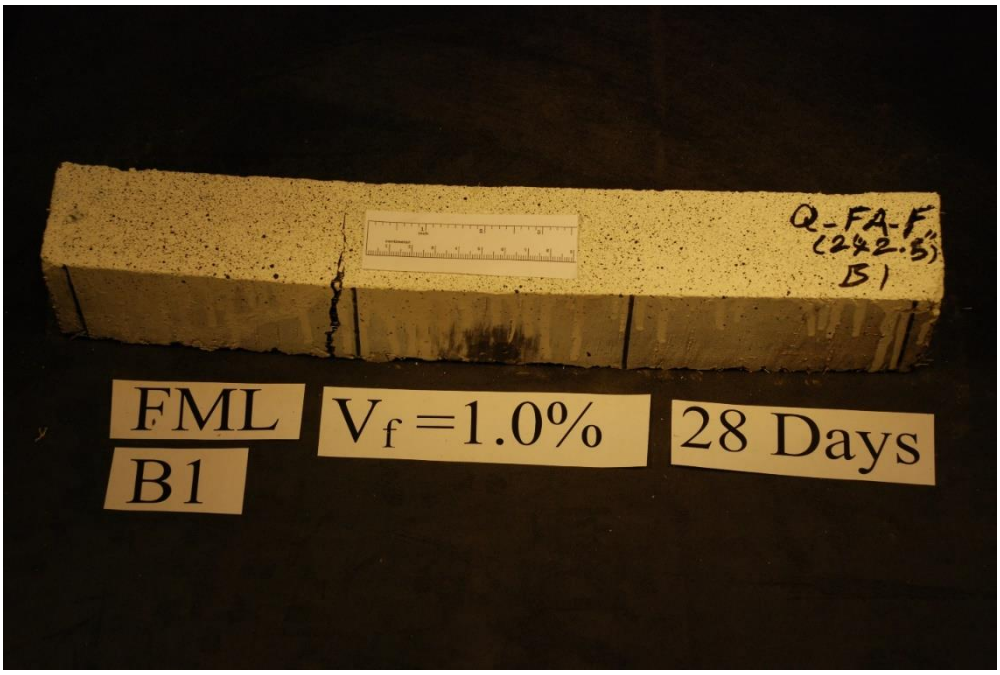
Q-FA-F
(2&2.5)
B1
FML
B1
V_f =1.0%
28 Days

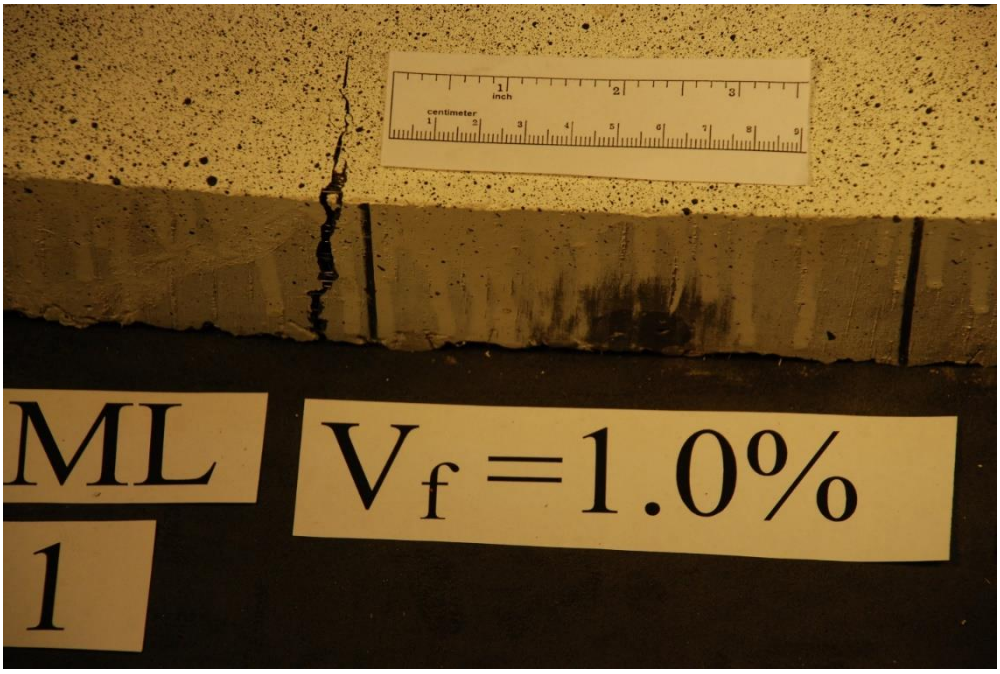
ML
1
V_f =1.0%

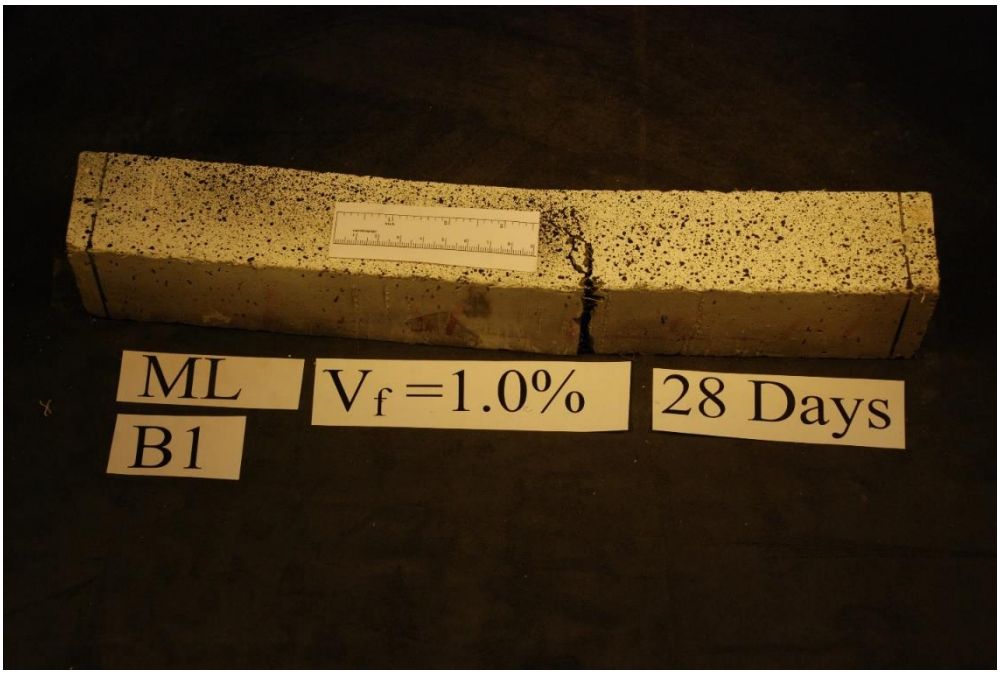
ML
B1
V_f =1.0%
28 Days

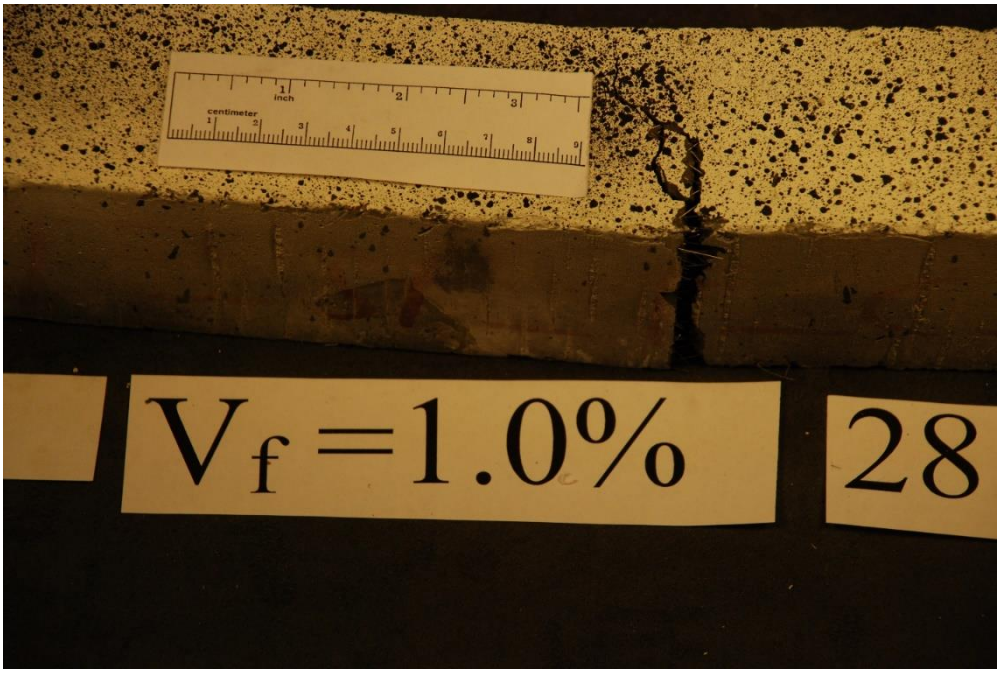
V_f =1.0%
28

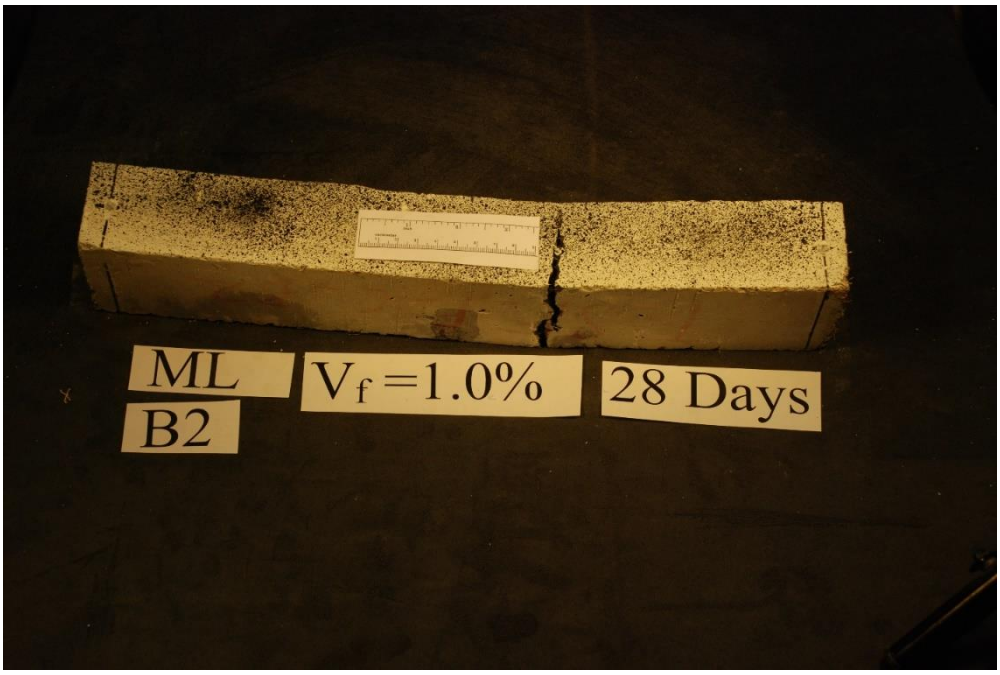
ML
B2
V_f =1.0%
28 Days

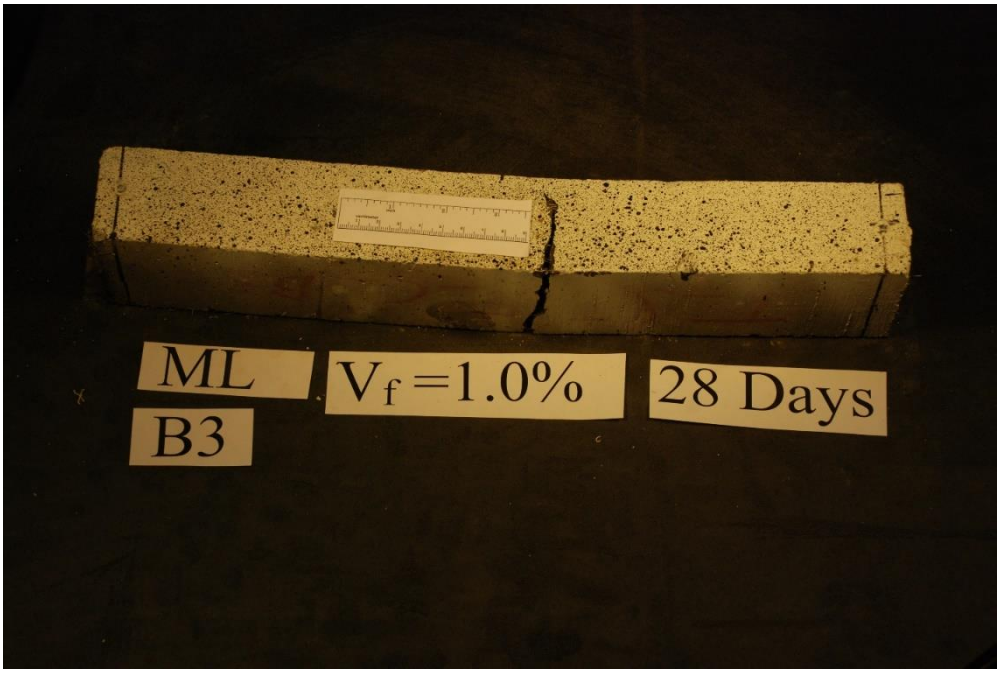
ML
B3
V_f =1.0%
28 Days

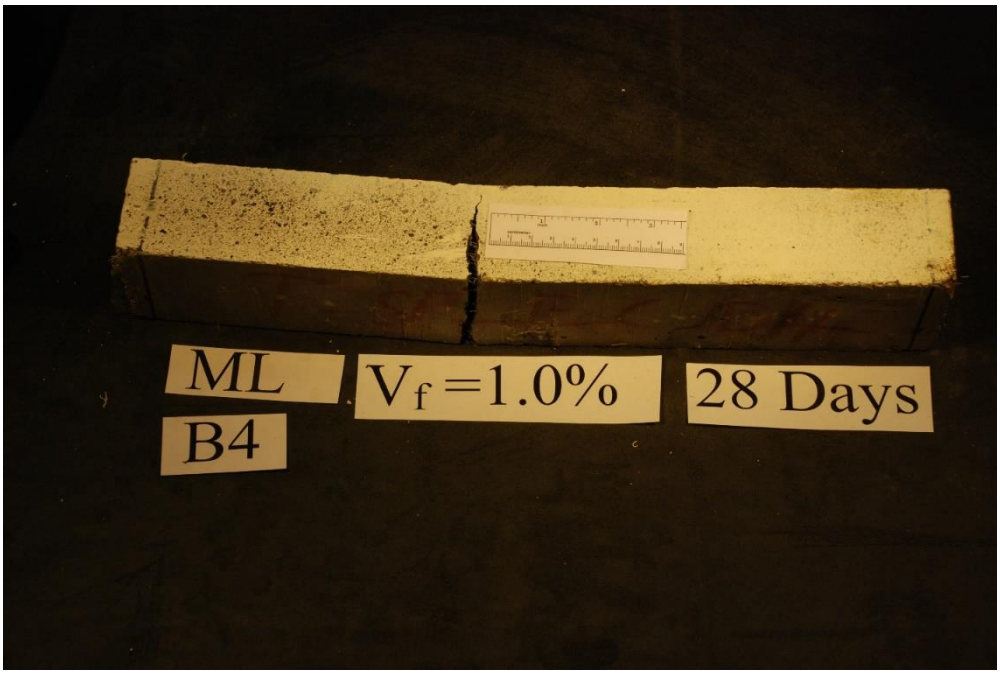
ML
B4
V_f =1.0%
28 Days

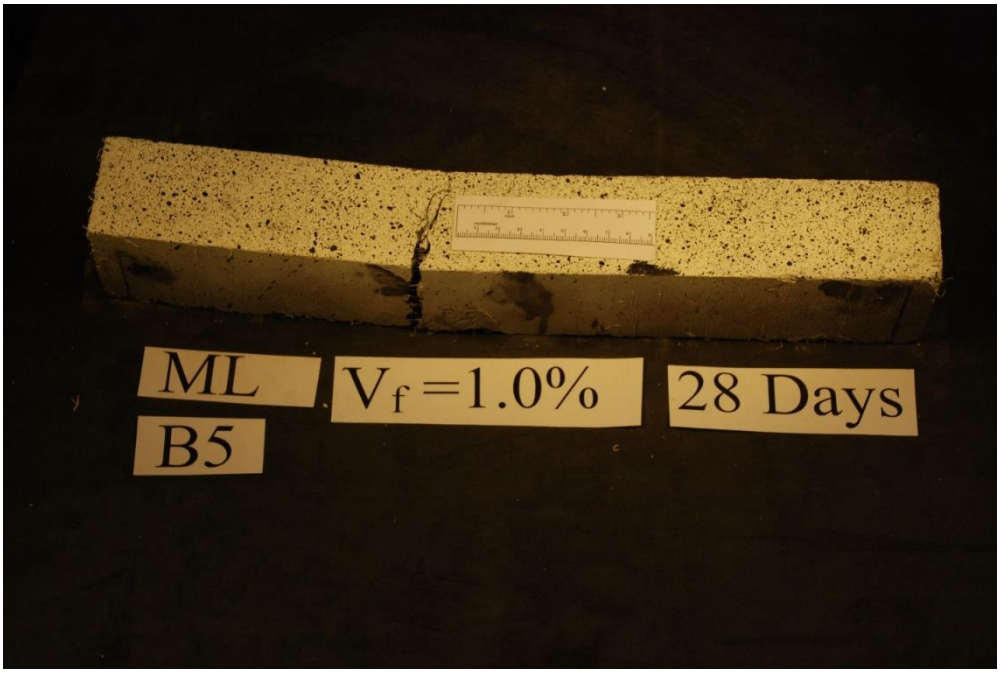
ML
B5
V_f =1.0%
28 Days

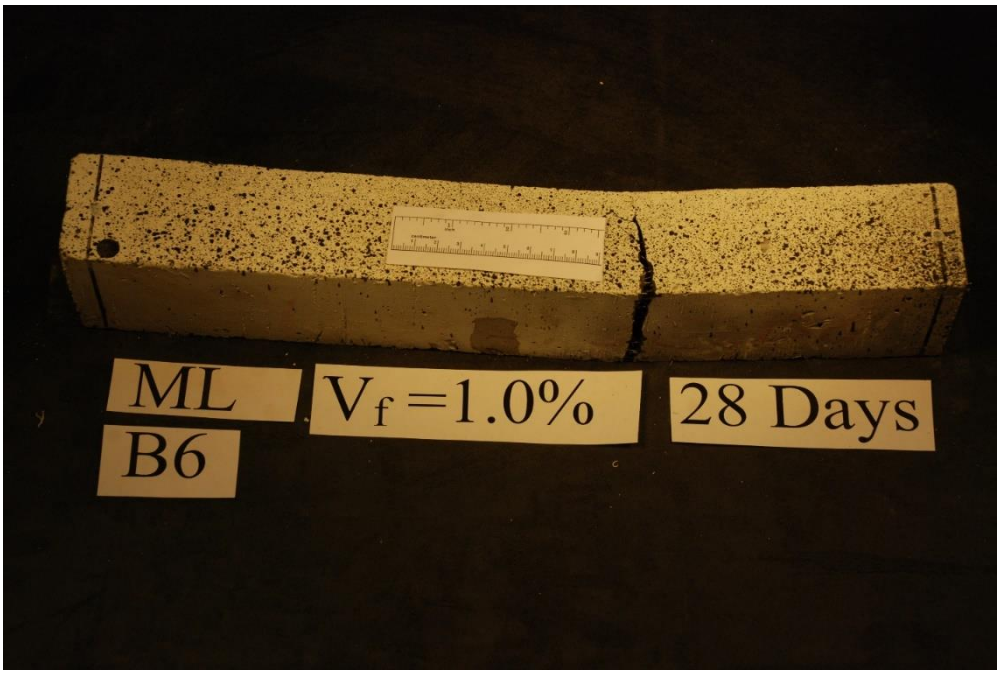
ML
B6
V_f =1.0%
28 Days

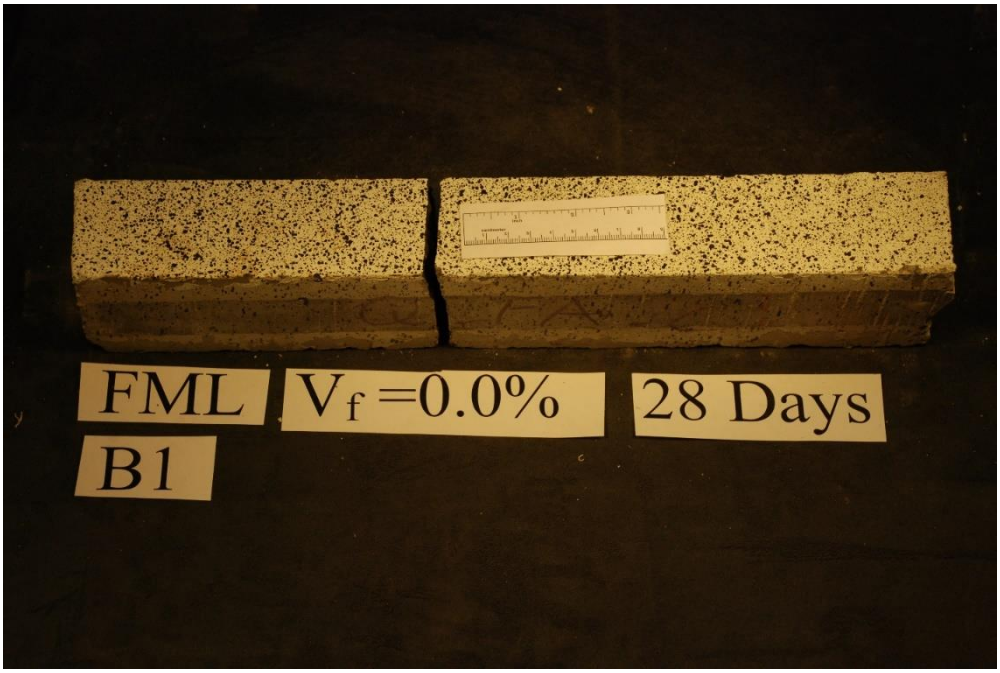
FML
B1
V_f =0.0%
28 Days

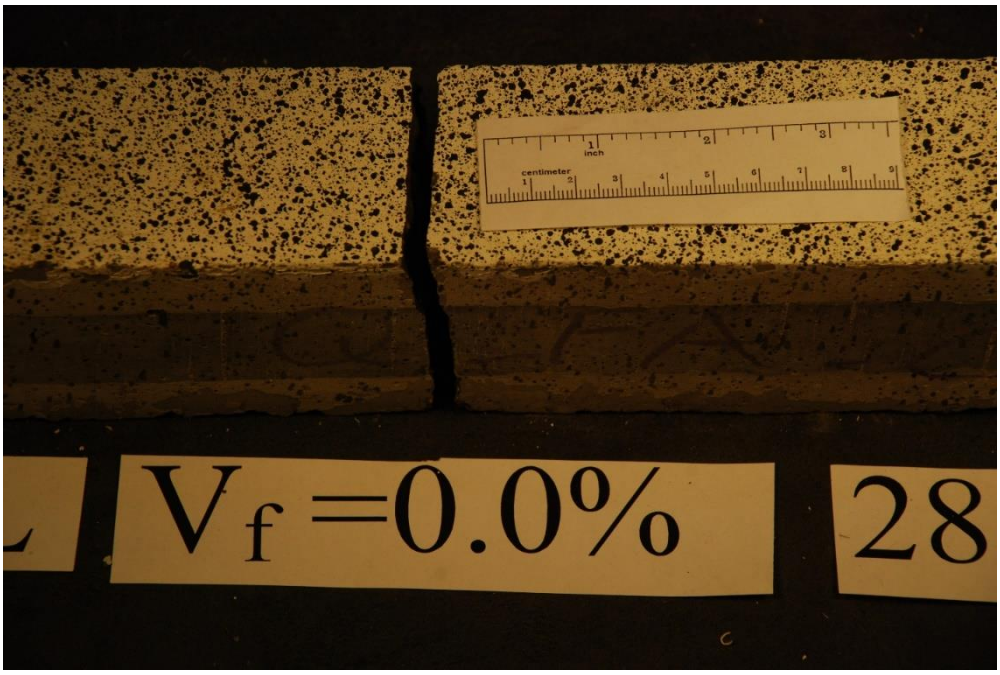
V_f =0.0%
28

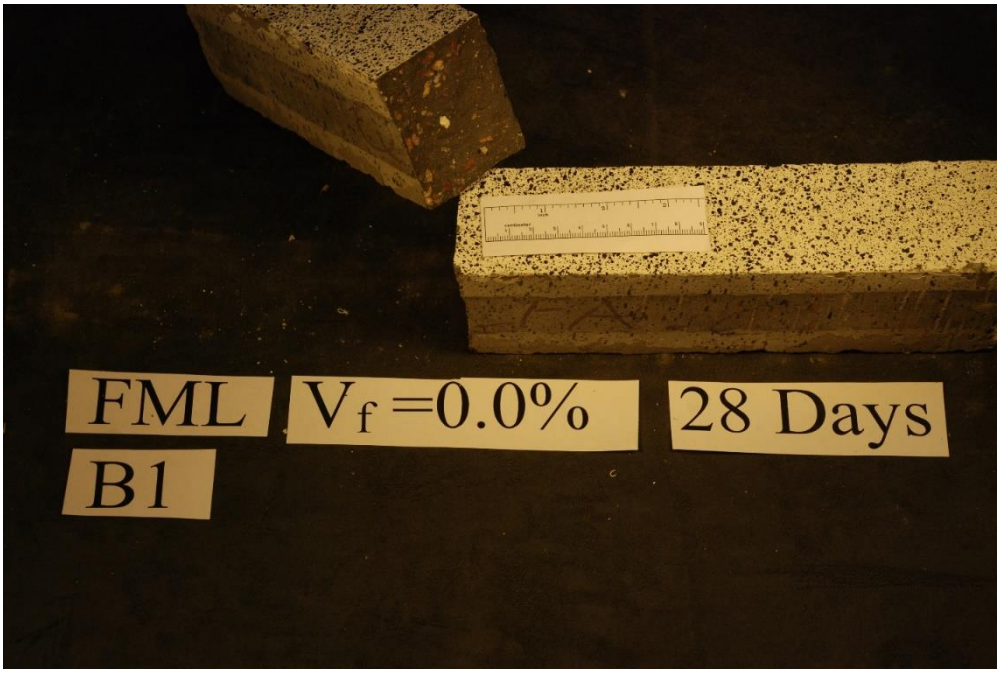
FML
V_f =0.0%
28 Days
B1

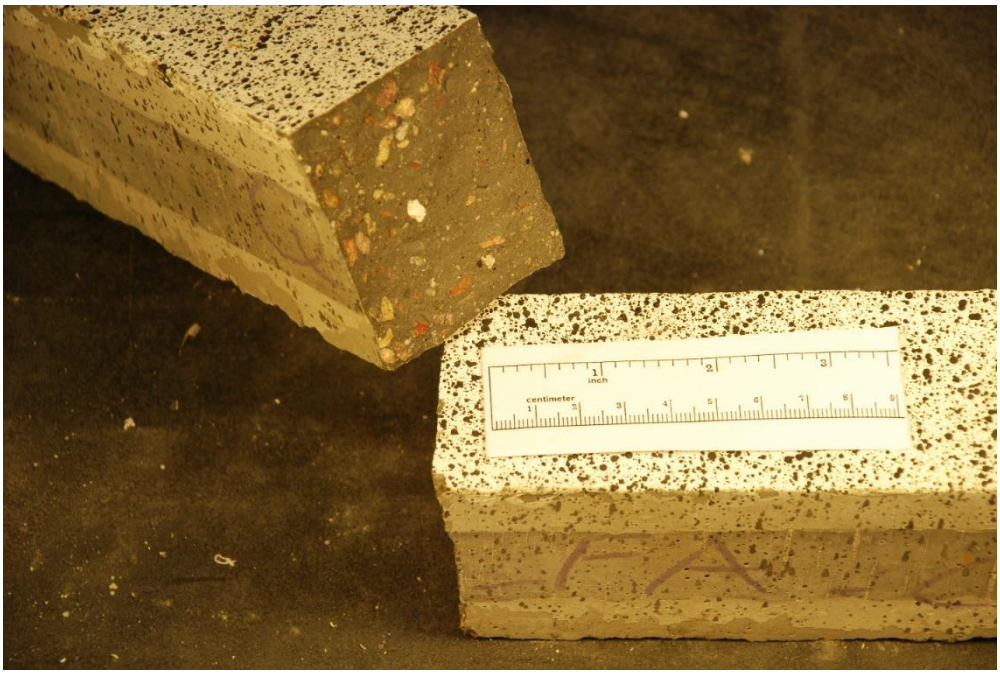
centimeter
inch

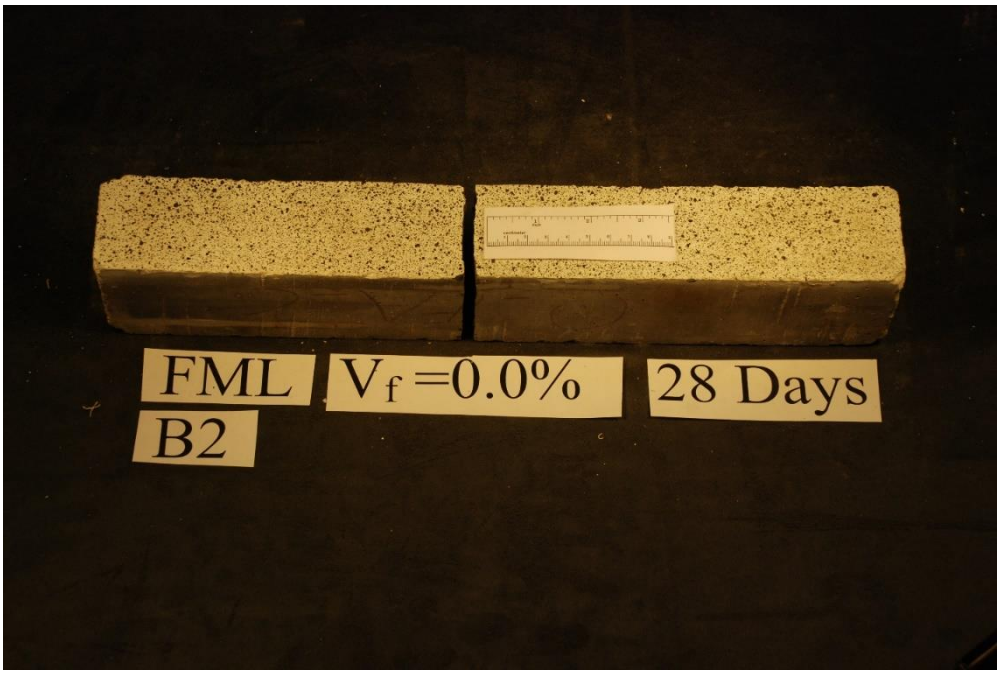
FML
V_f =0.0%
28 Days
B2

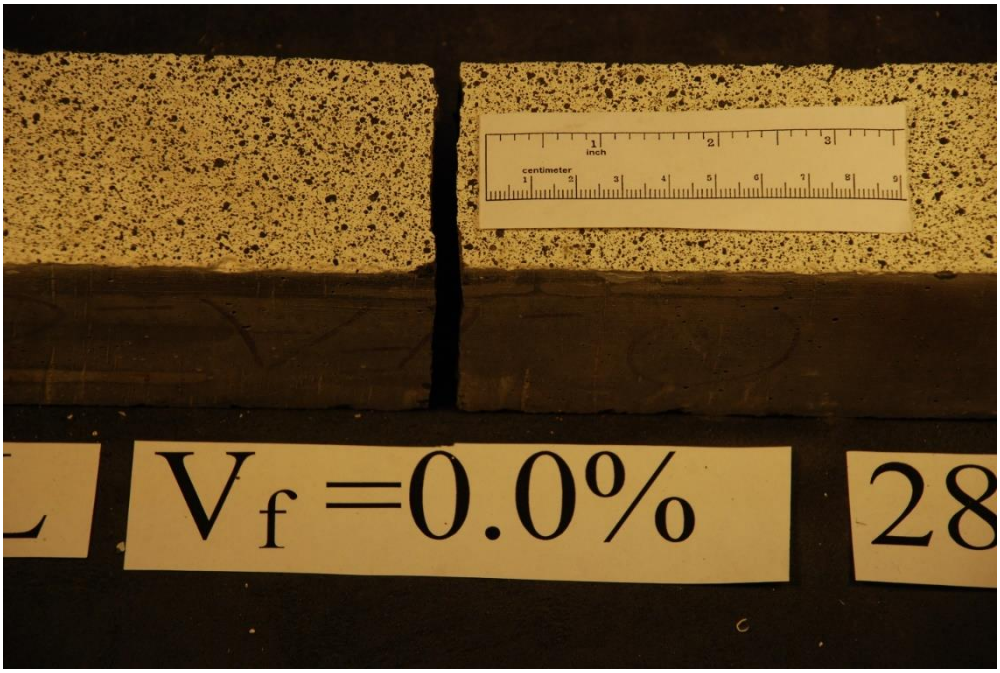
V_f =0.0%
28

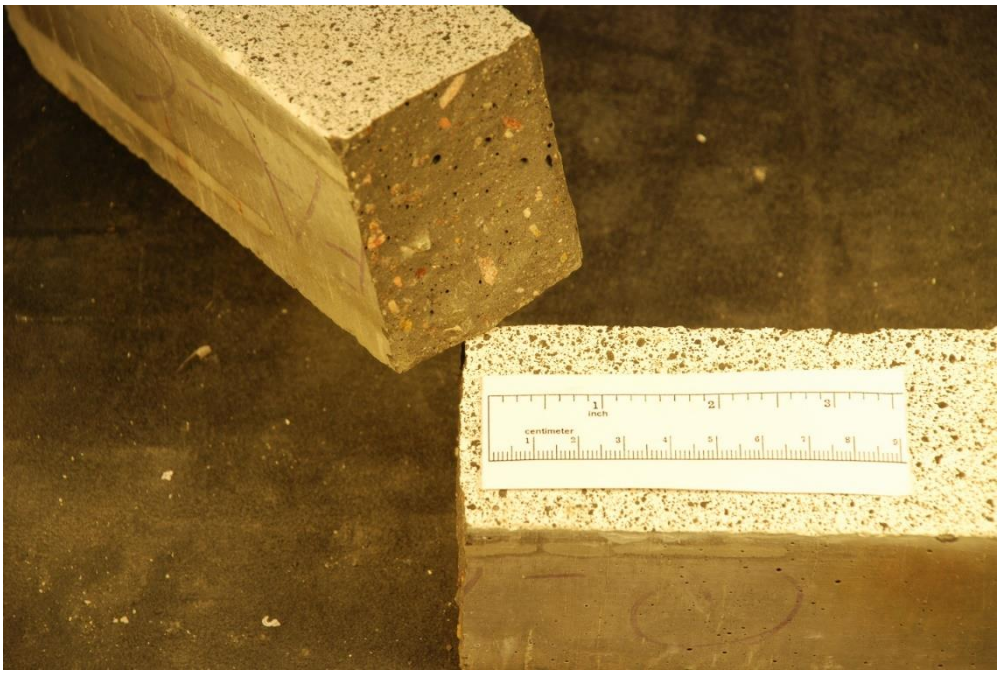

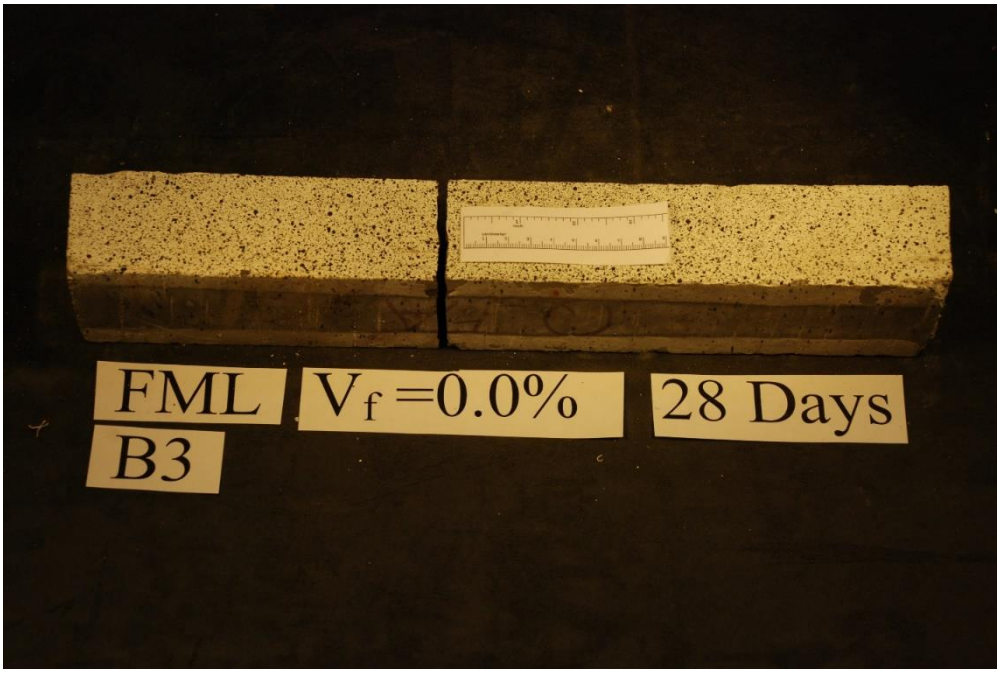
FML
V_f =0.0%
28 Days
B3

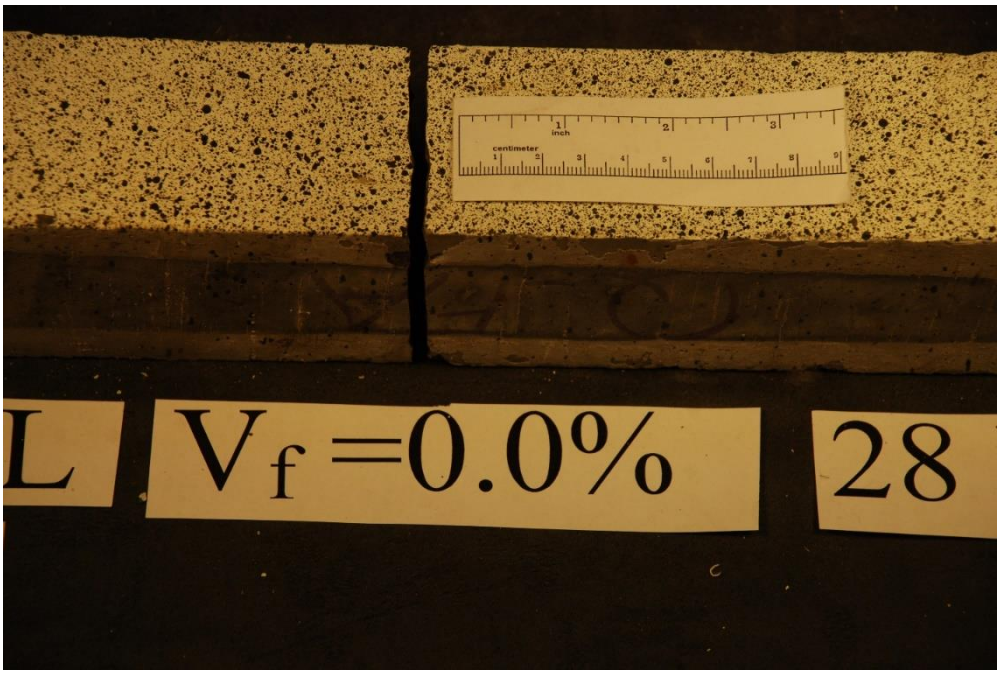
L
V_f =0.0%
28

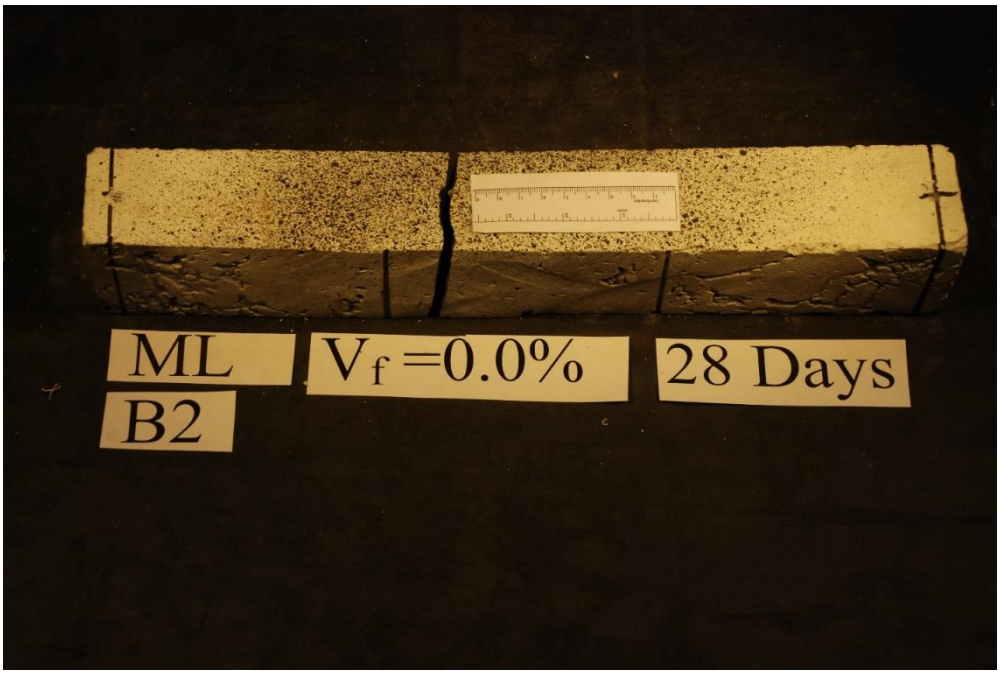
ML
B2
Vf =0.0%
28 Days

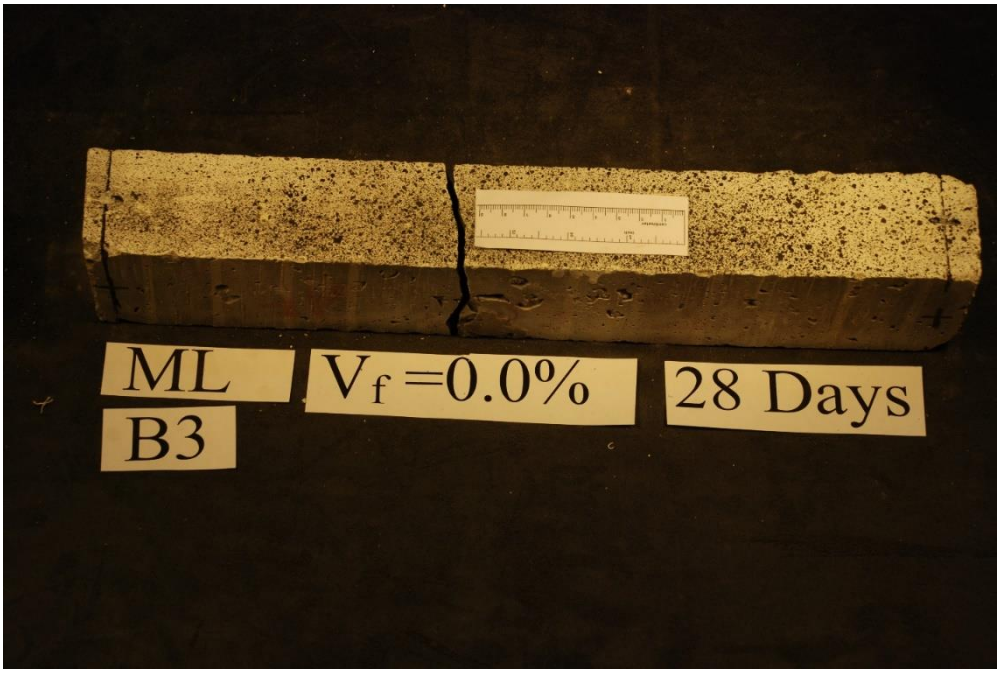
ML
B3
Vf =0.0%
28 Days